TESIS DE LA UNIVERSIDAD DE ZARAGOZA

2018

58

Alberto Concellón Allueva

Advanced functional materials based on liquid crystal dendrimers: novel dendritic architectures for applications in material science and biomedicine

Departamento

Química Orgánica

Director/es

MARCOS MARTÍNEZ, MERCEDES

ROMERO SORIA, PILAR

ISSN 2254-7606

Prensas de la Universidad Universidad Zaragoza

ISSN 2254-7606

Universidad Zaragoza
1542

Tesis Doctoral

ADVANCED FUNCTIONAL MATERIALS BASED ON LIQUID CRYSTAL DENDRIMERS: NOVEL DENDRITIC ARCHITECTURES FOR APPLICATIONS IN MATERIAL

Autor

Alberto Concellón Allueva

Director/es

MARCOS MARTÍNEZ, MERCEDES
ROMERO SORIA, PILAR

UNIVERSIDAD DE ZARAGOZA

Química Orgánica

2018

ADVANCED FUNCTIONAL MATERIALS BASED ON LIQUID CRYSTAL DENDRIMERS: NOVEL DENDRITIC ARCHITECTURES FOR APPLICATIONS IN MATERIAL SCIENCE AND BIOMEDICINE

Alberto Concellón Allueva

Memoria presentada en la Universidad de Zaragoza para optar al Grado de Doctor

Dpto. Química Orgánica
Facultad de Ciencias – ICMA
Universidad de Zaragoza – CSIC

Zaragoza, Abril 2018

This work was supported by the MINECO-FEDER funds (Projects CTQ2012-35692 and CTQ2015-70174; PhD Fellowship BES-2013-064705), and Gobierno de Aragón-FSE (Research Group E04). The use of the SAI (Universidad de Zaragoza) and CEQMA (Universidad de Zaragoza-CSIC) Services is also acknowledged.

La Dra. MERCEDES MARCOS MARTÍNEZ, Investigadora Científica del Consejo Superior de Investigaciones Científicas, y la Dra. PILAR ROMERO SORIA, Científica Titular del Consejo Superior de Investigaciones Científicas, pertenecientes al Instituto de Ciencia de Materiales de Aragón y al Departamento de Química Orgánica de la Universidad de Zaragoza

HACEN CONSTAR

Que el trabajo original titulado "ADVANCED FUNCTIONAL MATERIALS BASED ON LIQUID CRYSTAL DENDRIMERS: NOVEL DENDRITIC ARCHITECTURES FOR APPLICATIONS IN MATERIAL SCIENCE AND BIOMEDICINE", ha sido realizado por D. ALBERTO CONCELLÓN ALLUEVA bajo nuestra supervisión en el Departamento de Química Orgánica de la Universidad de Zaragoza y reúne las condiciones para su presentación como tesis doctoral.

En Zaragoza, a 9 de Abril de 2018

Fdo.: Mercedes Marcos Martínez Fdo.: Pilar Romero Soria

Acronyms List

1D	One-Dimensional
2D	Two-Dimensional
3D	Three-Dimensional
a	Lattice Parameter of a Columnar Mesophase
AFM	Atomic Force Microscopy
BH	Bulk Heterojunction
BisMPA	2,2-Bis(hydroxymethyl)propionic acid
CAC	Critical Aggregation Concentration
Col_h	Hexagonal Columnar Mesophase
Col_r	Rectangular Columnar Mesophase
c	Stacking Distance of a Columnar Mesophase
CPMAS	Cross-Polarization Magic-Angle Spinning
Cr	Crystal
CuAAC	Copper-Catalyzed Azide-Alkyne Cycloaddition
CV	Cyclic Voltammetry
d	Layer Spacing of a Smectic Mesophase
DCC	*N,N*-Dicyclohexylcarbodiimide
DCM	Dichloromethane
DCTB	*trans*-2-[3-(4-*tert*-Butylphenyl)-2-methyl-2-propenylidene]malononitrile
D_h	Hydrodynamic Diameter
DIAD	Diisopropyl azodicarboxylate
DCM	Dichloromethane
DLC	Discotic Liquid Crystal
DLS	Dynamic Light Scattering
DMAP	4-(Dimethylamino)pyridine
DMF	*N,N*-Dimethylformamide

DMSO	Dimethylsulfoxide
DPTS	4-(Dimethylamino)pyridinium *p*-toluenesulfonate
DSC	Differential Scanning Calorimetry
FRET	Fluorescence Resonance Energy Transfer
FTIR	Fourier Transform Infrarred Spectroscopy
g	Glass
h_d	Disk Thickness
h l k	Miller Indices
HOMO	Highest Occupied Molecular Orbital
I	Isotropic Liquid
ITO	Indium Tin Oxide
LC	Liquid Crystal
LUMO	Lowest Unoccupied Molecular Orbital
MS	Mass Spectroscopy
MALDI	Matrix-Assisted Laser Desorption/Ionization
N	Nematic Mesophase
N_{Col}	Nematic Columnar Mesophase
N_D	Nematic Discotic Mesophase
N_L	Lateral Nematic Mesophase
NMR	Nuclear Magnetic Resonance
OFET	Organic Field-Effect Transistor
OLED	Organic Light-Emitting Diode
OPV	Organic Photovoltaic Device
PAMAM	Poly(amidoamine)
POM	Polarized Optical Microscopy
PPI	Poly(propylene imine)
RT	Room Temperature
SCLC	Space Charge-Limited Current
SEC	Size Exclusion Chromatography

SmA	Smectic A Mesophase
TBAB	Tetrabutylammonium Bromide
TBAF	Tetrabutylammonium Fluoride
TCE	1,1,2,2-Tetrachloroethane
TEM	Transmission Electron Microscopy
TGA	Thermogravimetric Analysis
THF	Tetrahydrofuran
TsCl	4-Toluenesulfonyl Chloride
TOF	Time-of-Flight
UV	Ultraviolet
Vis	Visible
XPS	X-Ray Photoelectron Spectroscopy
XRD	X-Ray Diffraction
λ	Wavelength
μ_{hole}	Hole Mobility
ϕ_{ET}	Energy Transfer Efficiency
ϕ_{F}	Fluorescence Quantum Yield
Ø	Diameter

Contents

Preface

Thesis Outline

Abstract. *The Preface introduces the scientific research questions addressed in this thesis and provides an overview of the principles that can be used for the construction of smart materials based on liquid crystalline dendrimers. The final section of the Preface covers the objectives of this research and the structure of the thesis.*

"We must not forget that when radium was discovered no one knew that it would prove useful in hospitals. The work was one of pure science. And this is a proof that scientific work must not be considered from the point of view of the direct usefulness of it. It must be done for itself, for the beauty of science, and then there is always the chance that a scientific discovery may become like the radium a benefit for humanity."

Marie Curie

The term *dendrimer* is derived from the Greek words *dendron* and *meros*, meaning *tree* and *part*, respectively. These molecules were first called *cascade molecules* by Vögtle,[1] and later *arborols* by Newkome.[2] However, the term dendrimer is commonly used and accepted and it has displaced the original one.

Dendritic polymers are highly branched polymers that exhibit very different properties compared with their linear analogues.[3-5] Depending on the control over the branching units there are five main subgroups in dendritic polymers: dendrimers, dendrons, hyperbranched polymers, dendronized polymers and dendrigraft polymers (**Figure 1**).

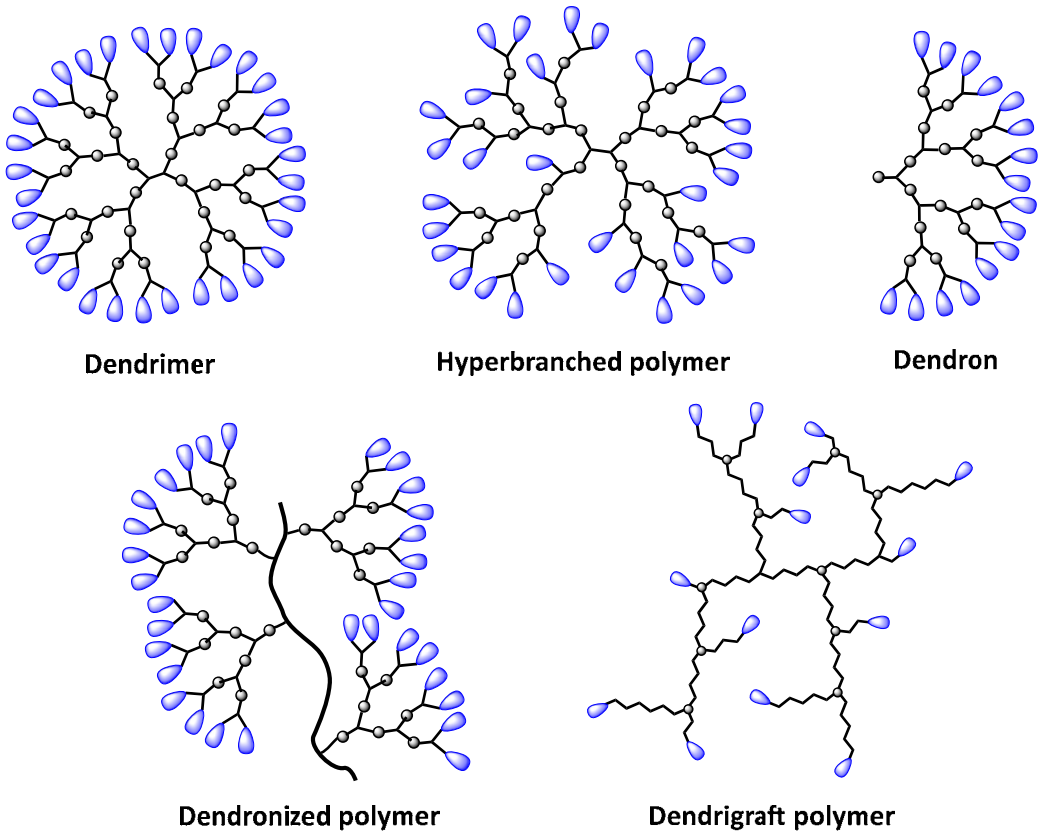

Figure 1. Schematic representation of the subclasses of dendritic polymers.

Dendrimers are monodisperse and perfectly branched molecular architectures (**Figure 2**). They consist of a central multifunctional core with layers of repeating units that are radially branched. Each layer is called a generation and the branched structures linked to the central core are termed dendrons. A large number of end-groups are present at the periphery of the dendrimer. The dendrimer periphery is probably the most interesting aspect because it is accessible for further functionalization and permits modification of dendrimer properties. In addition,

the number of functional end-groups increases with each generation, leading to an amplification effect called the dendritic effect.[6]

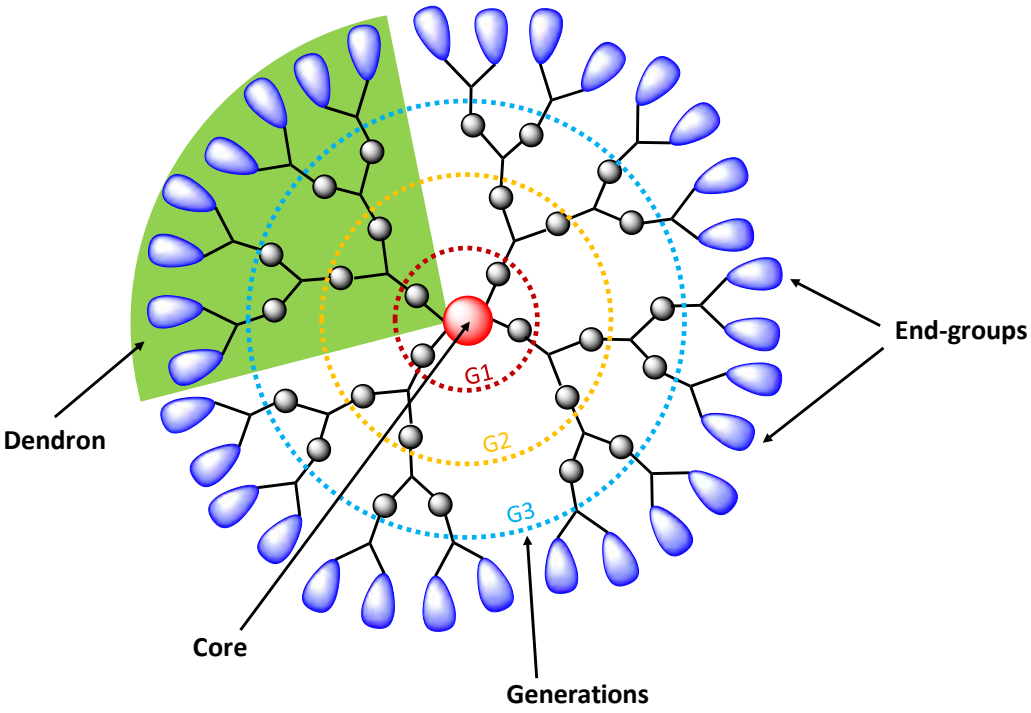

Figure 2. Schematic representation of a dendrimer.

Such highly branched architecture gives dendrimers unique properties that have been exploited in the design of functional materials with applications in target drug delivery, optoelectronics, light-harvesting, sensors, among others.[7-9]

Likewise, liquid crystals (LCs) represent a fascinating state of matter which combines order and mobility from molecular to macroscopic level. In such state of matter, molecules possess orientational and various degrees of translational/positional molecular orderings like in crystalline solids and also share the mechanical properties of liquids (**Figure 3**). There are several ways of classifying LCs, however, the most widely utilized classification is the distinction between thermotropic and lyotropic LCs. Thermotropic LCs form mesophases within a certain temperature range, while the formation of lyotropic mesophases is solvent and concentration dependent.

LCs are the advanced materials found in low-power-consuming flat-panel displays (liquid crystal displays, LCD) which have drastically revolutionized daily life and constitute a $100 billion market, globally. Nevertheless, the “beyond display” applications are also important and numerous.[10]

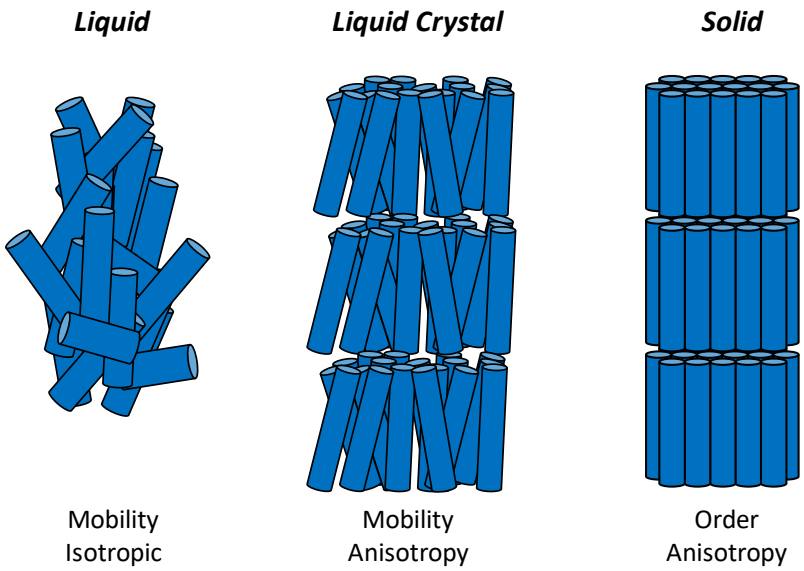

Figure 3. Schematic representation of the supramolecular organization in the states of matter.

LCs are now playing a very important role in nanoscience and nanotechnology.[11] For instance, they can potentially be used as new functional materials for electron, ion, and molecular transporting, as well as for sensory, catalytic, optical and bioactive materials.[12, 13] Due to their dynamic nature, LCs are able to respond to different external stimuli such as temperature, magnetic field, electric field, light, mechanical stress, among others. Thus, they can be used for the preparation of stimuli-responsive multifunctional materials.[14] Moreover, the biomedical applications of LCs have been demonstrated recently.[15, 16]

Molecular engineering of LCs is an important method to control the self-organizing process of single moieties into periodically nanostructured mesophases.[17] Additionally, ordered supramolecular assemblies can enhance the functions of single molecules. Therefore, dendrimers are attractive candidates as novel scaffolds for the preparation of new LC materials.[18-20] In these materials, the mesogenic units are arranged in a highly congested environment which leads to the formation of singular supramolecular organizations that are not achievable with conventional LCs.[21]

LC dendrimers are usually prepared by the introduction of mesogenic units within a dendritic structure (**Figure 4**). The most commonly used approach are the so-called side-chain LC dendrimers. It consists of the attachment of mesogenic units to the periferial end-groups of a conventional dendrimer. Main-chain LC

dendrimers are a less employed method that involves the introduction of mesogenic groups as repeating units within the central dendritic structure.

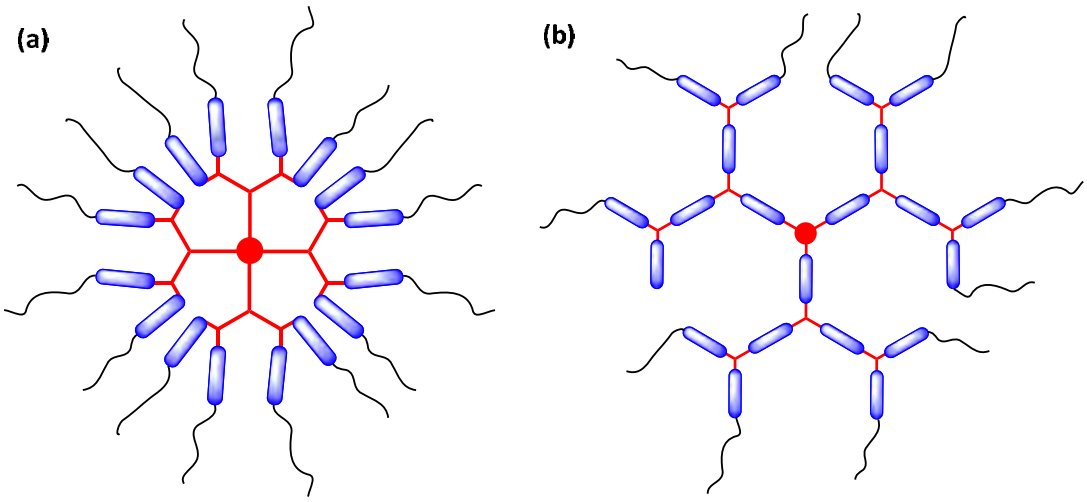

Figure 4. Schematic representation of **(a)** side-chain and **(b)** main-chain LC dendrimers.

Nowadays, obtaining LC behavior in dendrimers is not the main aim, it is the way to enhance other interesting functionalities. Thus, current research in LC dendrimers is focused on the search of applications in these materials.[22] LC dendrimers represent an attractive tool for the preparation of functional materials as they combine the inherent properties of the dendritic scaffold with the anisotropic properties provided by the LC state.

The main objective of this doctoral thesis was the development of organic materials based on LC dendrimers with applications both in materials science and biomedicine.

CHAPTER 1 describes the preparation of LC dendrimers and their use as potential efficient **organic semiconductors**. In the field of organic electronics, the structural versatility of dendrimers is really interesting because it allows the introduction of different functional units (donor-acceptor systems) in the dendritic structure. These functionalities self-assemble into a LC arrangement with a supramolecular order that facilitates charge transport.

CHAPTER 2 describes a versatile method to obtain **ion transporting materials** by using an easy and quantitative method of synthesis. Ionic LC dendrimers are used for the preparation of 1D and 2D proton conductive materials. The formation of ionic nanosegregated areas (formed by ionic salts) generates the continuous

pathways necessary for proton conduction to occur. These ionic pathways are not disrupted after photocrosslinking, thus nanostructured, thermally and mechanically stable membrane materials with permanent pathways for proton transport are obtained. The proton conduction in these ionic LC dendrimers may open a new path in the search for electrolyte materials for the preparation of electrochemical devices.

The research described in **CHAPTER 3** focuses on the development of organic **nanoporous materials** from hydrogen-bonded columnar LC dendrimers. The obtained nanoporous materials show remarkable size selectivity in adsorption experiments because our strategy allows us to control the size of the pores and, consequently, the adsorption selectivity of the obtained polymers. Moreover, the obtained nanoporous polymers are highly versatile because their adsorption selectivity can be tuned on demand by *in situ* chemical treatment of the polymer films. Such results can potentially be used to control the size and the chemical nature of the pores and the group of molecules and ions that can be separated by these nanoporous polymers.

In **CHAPTER 4**, luminescent LC dendrimers were employed for the preparation of different nanostructures such as micelles, vesicles or nanospheres. These nanostructures are used as nanocarriers, being of interest for **drug delivery**.

References

(1) E. Buhleier, W. Wehner & F. Vögtle. "Cascade"- and "Nonskid-Chain-like" Syntheses of Molecular Cavity Topologies. *Synthesis* **1978**, 155-158.

(2) G. R. Newkome, Z. Yao, G. R. Baker & V. K. Gupta. Micelles. Part 1. Cascade molecules: a new approach to micelles. A [27]-arborol. *J. Org. Chem.* **1985,** *50*, 2003-2004.

(3) D. A. Tomalia & J. M. J. Fréchet, In *Dendrimers and Other Dendritic Polymers*, John Wiley & Sons, Ltd: **2002**.

(4) A. M. Caminade, D. Yan & D. K. Smith. Dendrimers and hyperbranched polymers. *Chem. Soc. Rev.* **2015,** *44*, 3870-3873.

(5) D. Yan, C. Gao & H. Frey, *Hyperbranched polymers: synthesis, properties, and applications*. Wiley: Hoboken, N.J., **2011**.

(6) A. M. Caminade, A. Ouali, R. Laurent, C. O. Turrin & J. P. Majoral. The dendritic effect illustrated with phosphorus dendrimers. *Chem. Soc. Rev.* **2015,** *44*, 3890-3899.

(7) G. R. Newkome, C. N. Moorefield & F. Vögtle, In *Dendrimers and Dendrons*, Wiley-VCH Verlag GmbH & Co. KGaA: **2004**.

(8) F. Vögtle, G. Richardt & N. Werner, In *Dendrimer Chemistry*, Wiley-VCH Verlag GmbH & Co. KGaA: **2009**.

(9) D. Astruc, E. Boisselier & C. Ornelas. Dendrimers Designed for Functions: From Physical, Photophysical, and Supramolecular Properties to Applications in Sensing, Catalysis, Molecular Electronics, Photonics, and Nanomedicine. *Chem. Rev.* **2010,** *110*, 1857-1959.

(10) J. W. Goodby, P. J. Collings, T. Kato, C. Tschierske, H. Gleeson & P. Raynes, In *Handbook of Liquid Crystals, Second ed., Volume 8: Applications of Liquid Crystals.*, Wiley-VCH Verlag GmbH & Co. KGaA: **2014**.

(11) Q. Li, *Nanoscience with liquid crystals: from self-organized nanostructures to applications*. Springer: Cham, Heidelberg, **2014**.

(12) H. K. Bisoyi & S. Kumar. Liquid-crystal nanoscience: an emerging avenue of soft self-assembly. *Chem. Soc. Rev.* **2011,** *40*, 306-319.

(13) T. Kato, N. Mizoshita & K. Kishimoto. Functional liquid-crystalline assemblies: Self-organized soft materials. *Angew. Chem. Int. Ed.* **2006,** *45*, 38-68.

(14) D. J. Broer, C. M. W. Bastiaansen, M. G. Debije & A. P. H. J. Schenning. Functional Organic Materials Based on Polymerized Liquid-Crystal Monomers: Supramolecular Hydrogen-Bonded Systems. *Angew. Chem. Int. Ed.* **2012,** *51*, 7102-7109.

(15) J. P. F. Lagerwall & G. Scalia. A new era for liquid crystal research: Applications of liquid crystals in soft matter nano-, bio- and microtechnology. *Curr. Appl. Phys.* **2012,** *12*, 1387-1412.

(16) S. J. Woltman, G. D. Jay & G. P. Crawford. Liquid-crystal materials find a new order in biomedical applications. *Nature Mater.* **2007,** *6*, 929.

(17) B. M. Rosen, C. J. Wilson, D. A. Wilson, M. Peterca, M. R. Imam & V. Percec. Dendron-Mediated Self-Assembly, Disassembly, and Self-Organization of Complex Systems. *Chem. Rev.* **2009,** *109*, 6275-6540.

(18) J. Barberá, B. Donnio, L. Gehringer, D. Guillon, M. Marcos, A. Omenat & J. L. Serrano. Self-organization of nanostructured functional dendrimers. *J. Mater. Chem.* **2005,** *15*, 4093-4105.

(19) I. M. Sáez & J. W. Goodby. Supermolecular liquid crystals. *J. Mater. Chem.* **2005,** *15*, 26-40.

(20) B. Donnio, S. Buathong, I. Bury & D. Guillon. Liquid crystalline dendrimers. *Chem. Soc. Rev.* **2007,** *36*, 1495-1513.

(21) M. Marcos, R. Martín-Rapún, A. Omenat & J. L. Serrano. Highly congested liquid crystal structures: dendrimers, dendrons, dendronized and hyperbranched polymers. *Chem. Soc. Rev.* **2007,** *36*, 1889-1901.

(22) S. Hernández-Ainsa, M. Marcos & J. L. Serrano, Dendrimeric and Hyperbranched Liquid Crystal Structures. In *Handbook of Liquid Crystals*, Second ed.; J. W. Goodby, P. J. Collings, T. Kato, C. Tschierske, H. Gleeson & P. Raynes, Eds. Wiley-VCH Verlag GmbH & Co. KGaA: **2014**; Vol. 7, pp 259-300.

Chapter 1

Organic Semiconductors Based on Liquid Crystalline Porphyrin-Core Dendrimers

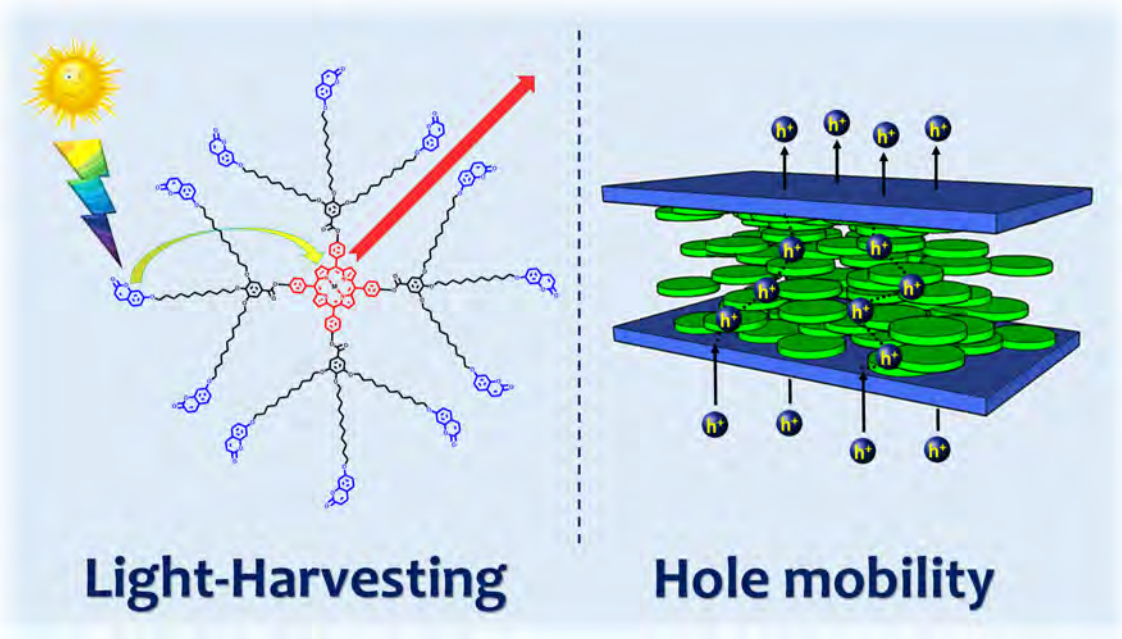

Abstract. *We report a new class of nematic discotic porphyrin-core dendrimers that have coumarin or carbazole functional units around the porphyrin core. Such dendrimers exhibit nematic discotic mesophases. Their high tendency for homeotropic alignment makes these LC dendrimers excellent candidates for device applications, due to their easy processability, spontaneous alignment between electrodes, and self-healing of defects, because of their dynamic nature. The charge mobility values of these materials are the highest ever reported for nematic discotic mesophases. Moreover, these values are similar to the highest values reported for ordered columnar mesophases, and this shows that a supramolecular organization in columns is not necessary to achieve high charge mobility.*

“Those who can imagine anything, can create the impossible”

Alan Turing

1. INTRODUCTION

1.1 Liquid Crystals as Organic Semiconductors

Organic electronic devices such as organic light-emitting diodes (OLEDs), organic field-effect transistors (OFETs) and organic photovoltaic devices (OPVs) are based on the transport of electrical charges between electrodes.[1-7] In these devices, the electronically active materials are organic semiconductors which consist of π-conjugated small molecules or polymers. The speed of the charge carriers through this active material is one of the main factors that governs the performance of organic semiconductors in devices.[8] The ideal organic semiconductor must have closely-packed molecules with few defects between molecules or domains because charge transport depends on molecular order.[9-11]

The highest charge carrier mobility in organic systems has been measured in single crystals of pentacene and rubrene (20 $cm^2 \cdot V^{-1} \cdot s^{-1}$).[12] However, the preparation of single-crystalline thin films is very tedious and not applicable industrially. To overcome this limitation, liquid crystals (LCs) offer an interesting approach as they bring order and dynamics.[13-15] They self-organize into nanostructured phases which provide similar properties to the organic single crystals, while the dynamics is vital for the processability and the self-healing of structural defects.[16]

Molecules with LC ordering, so-called mesogens, are typically composed of a rigid anisotropic core and flexible alkyl side chains. In the case of semiconducting materials, the core of the mesogen consists of a large π-conjugated system that allows charge carrier transport. The LC order is facilitated by strong π-π interations between the conjugated cores, whereas the disordered alkyl chains prevent a “true long-range order” by filling space and favoring molecular mobility.

Depending on the shape of the mesogenic units, LCs can be mainly classified into calamitic (rod-like), discotic (disk-like), and bent-core (banana-shaped) LCs (**Figure 1.1**).

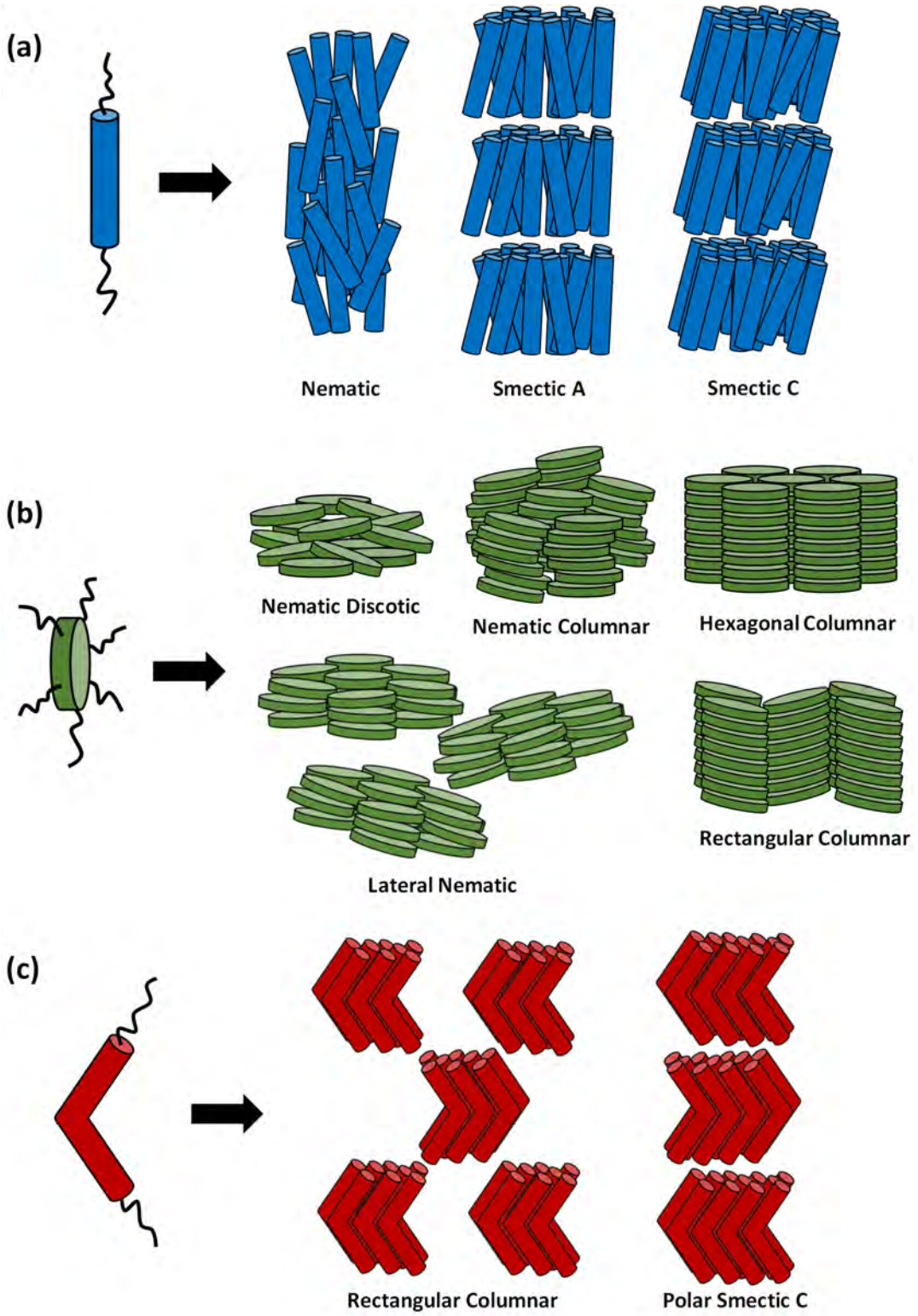

Figure 1.1 Different types of mesogens and the most common **(a)** calamitic, **(b)** discotic and **(c)** bent-core mesophases.

Calamitic LCs tend to form nematic or smectic mesophases. Smectic phases, in which molecules are arranged in layers, demonstrate two-dimensional charge transport with charge carrier mobilities up to 10^{-1} $cm^2 \cdot V^{-1} \cdot s^{-1}$.[17-19] Such mobility is

anisotropic with the highest values in the directions within the layer plane, because the smectic phase favors π-π intermolecular interactions within the plane.

Discotic LCs (DLCs) arrange into nematic or columnar phases.[20-23] In the nematic discotic (N_D) phase, the disk-shaped molecules stay more or less parallel having orientational order but no long-range positional order. The lateral nematic phase (N_L) is built of aggregates formed by multiple discotic mesogens. These supramolecular aggregates then organize into a nematic phase. In columnar phases, the disks stack on top of each other and arrange primarily in columns. In addition, the columns pack in various lattices, including hexagonal (Col_h) or rectangular (Col_r) unit cells. The nematic columnar (N_{Col}) phase is characterized by a columnar stacking of the molecules. However, these columns do not form two-dimensional lattice structures.

Conduction in columnar LCs is highly anisotropic as charges move preferentially along the conducting aromatic cores of the columns.[24, 25] Flexible alkyl chains linked to the π-conjugated core act as an insulating hydrocarbon matrix and decrease the probability of intercolumnar tunneling of the charge carriers. Therefore, columnar LCs represent one-dimensional conducting molecular wires. Depending on the π-conjugated core and the degree of order in the columnar stacking, charge carrier mobilities of 10^{-3}–1 $cm^2 \cdot V^{-1} \cdot s^{-1}$ along the direction of the columns have been reported.[26-29] Depending on the ionization potential (HOMO) or electron affinity (LUMO), these discotic molecules are able to transport either positive holes or negative electrons and accordingly, the materials can be classified as *p*-type or *n*-type semiconductors.

These structural and electronic properties of columnar LCs enable their application as an alternative to conventional inorganic semiconductors. Currently, there are many companies that are focused on the fabrication of flexible OFETs displays based on organic semiconducting materials.[30] Moreover, OLEDs and organic solar cells devices are commonly found commercialy.[31]

1.2 Charge Transport in Discotic Liquid Crystals

The charge transport mechanism in LC semiconductors seems to be an incoherent hopping process.[32, 33] The disk-like molecules self-assemble into columns with a significant intermolecular overlap of the delocalized π-electrons, providing quasi-one-dimensional channels for charge transport.[34] There are several techniques to determine the charge carrier mobility such as pulsed radiolysis time-resolved microwave conductivity (PR-TRMC), time of flight (TOF), space charge-limited current (SCLC), and field-effect transistor (FET) techniques.[35] In recent years, charge carrier mobility measurements in many DLC mesophases have been reported. The charge carrier mobility in organic semiconducting materials is one of the crucial parameters as it determines the performance of the material in electronic and optoelectronic devices. Mobility is related with the switching speed of OFETs, the intensity of light in OLEDs, and the separation of charges in OPVs.

To achieve high charge carrier mobility, it is important to have a high degree of molecular order within the columnar phase. This implies that the columns must be appropriately aligned in the direction that charge carriers are likely to flow. DLCs can align either perpendicular to the substrate surface (homeotropic alignment) or parallel to the substrate surface (planar alignment) (**Figure 1.2**). A planar alignment is required for OFETs, whereas a homeotropic alignment is preferred for OPV and OLED applications.[25] However, columnar mesophases still suffer from the disadvantage that orientationally uniform domains that are large enough to be used in most devices are often hard to obtain, even with the help of long thermal annealing, surface treatments or complex processing techniques.[36-41]

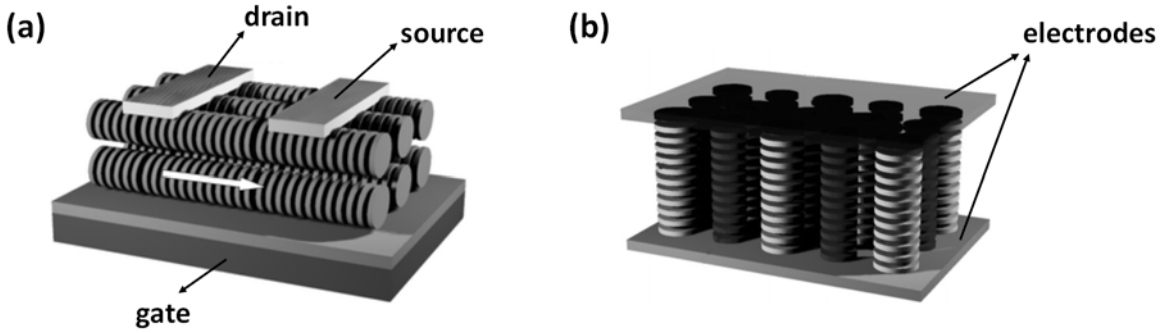

Figure 1.2 Schematic representation of **(a)** a planar orientation of the molecules desired in OFETs and **(b)** homeotropic alignment, which is considered to favor the performance of OPVs and OLEDs. (Adapted from reference 26)

Charge carrier mobility does not depend just on the degree of order, but also on the π-π stacking distance between the molecules within the columnar organization. Therefore, to achieve high charge carrier mobility, several chemical modifications have been introduced in semiconducting DLCs to increase the order along the column by decreasing the π-π stacking distance.

Most of the DLCs described today are derived from electron-rich aromatic cores and are known to be hole transporting materials. Representative examples include derivatives of triphenylene, hexa-peri-benzocoronenes, porphyrins or pthalocyanines, among others (**Figure 1.3**). Several charge mobility studies with triphenylene-based DLCs have been carried out.[42-45] Short-side alkyl chains derivatives allow better interactions of the cores resulting in higher mobilities in comparison to long-side chain analogs (**Figure 1.3a**). Additionally, the substitution of the lateral ether bonds by thioether resulted in a hexagonal columnar helical mesophase with considerably higher charge mobility values. The higher order in the columnar helical mesophase increases the hole mobility up to 10^{-1} $cm^2 \cdot V^{-1} \cdot s^{-1}$ in comparison to only 10^{-3} $cm^2 \cdot V^{-1} \cdot s^{-1}$ in the hexagonal columnar phase.[46]

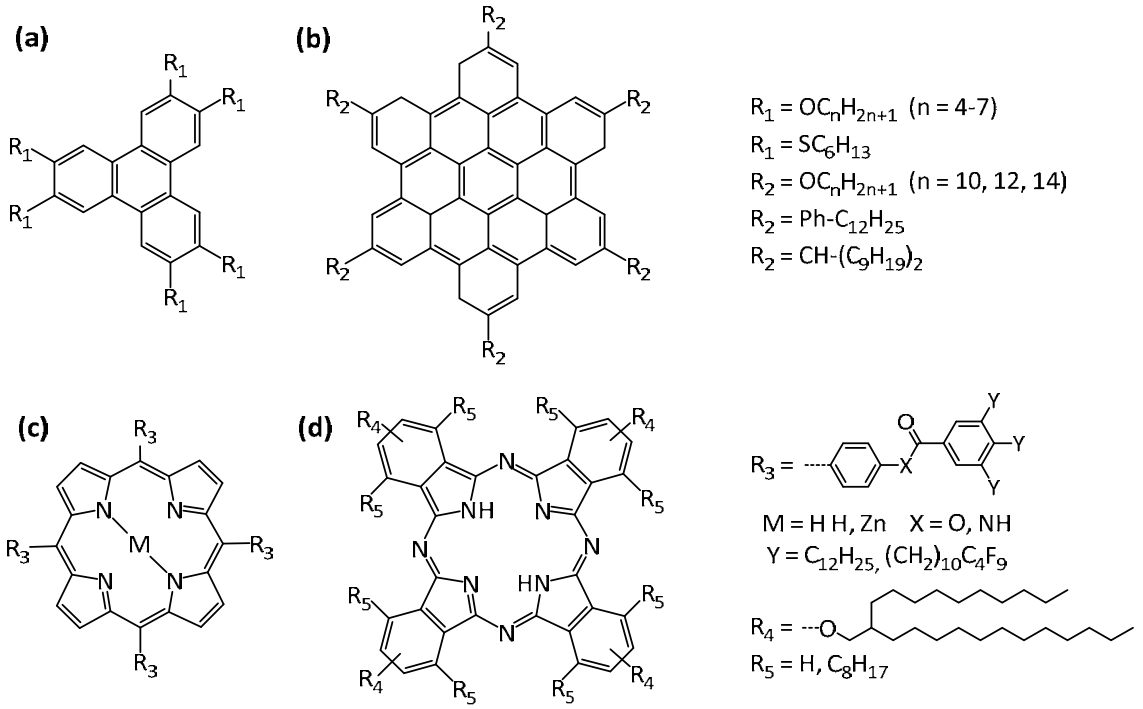

Figure 1.3 Chemical structures of **(a)** triphenylene, **(b)** hexa-peri-benzocoronene, **(c)** porphyrin and **(d)** pthalocyanine discotics studied for charge carrier mobility.

Müllen and coworkers developed a new family of DLCs based on hexa-peri-benzocoronenes with charge carrier mobilities in the range of 10^{-1}–1 $cm^2 \cdot V^{-1} \cdot s^{-1}$

(**Figure 1.3b**).[47, 48] These high charge carrier mobilities were attributed to highly ordered columnar phases that resulted in a large intermolecular π-orbital overlap between aromatic cores.[49, 50] Thus, hexa-peri-benzocoronenes derivatives have been extensively used as active conducting layers in molecular devices.[51] Aida and coworkers also reported a series of hexa-peri-benzocoronenes with two hydrophobic dodecyl chains and two hydrophilic triethylene glycol chains (**Figure 1.4**).[52] The mixture of both derivatives self-assembled in a coaxial nanotube structure with an intratubular hole mobility of 2 $cm^2 \cdot V^{-1} \cdot s^{-1}$.

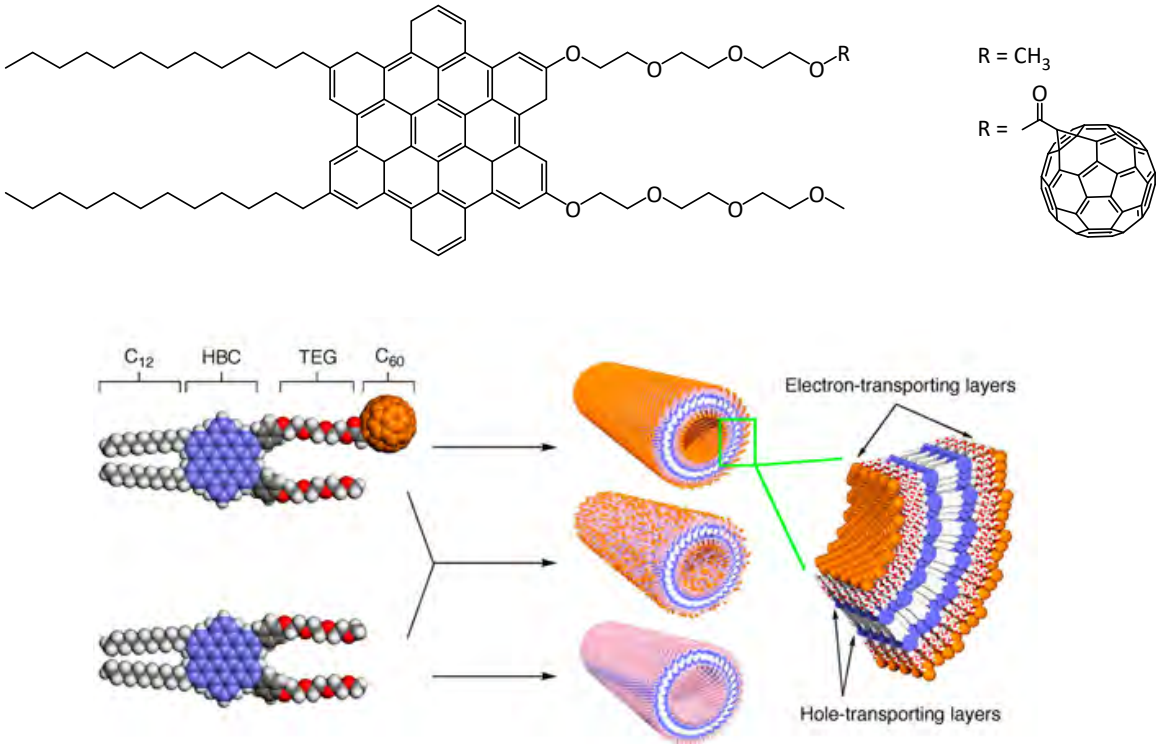

Figure 1.4 Schematic representation of the hexa-peri-benzocoronene derivatives and their nanotubes. (Adapted from reference 52)

Porphyrin and phthalocyanines macrocycles have also been used as electron-rich systems which may display columnar LC behavior. Charge carrier mobility studies were carried out on these systems obtaining mobilities in the 10^{-3}–10^{-1} $cm^2 \cdot V^{-1} \cdot s^{-1}$ range.[53-57] Li and coworkers reported some porphyrin-based DLCs that formed spontaneously defect-free large-area monodomain films with homeotropic alignment.[58, 59] With these materials they prepared bilayer- and bulk-heterojunction solar cells, obtaining the highest power conversions efficiencies of any reported solar cells using columnar LCs.[60]

Gómez-Lor and coworkers reported columnar LCs based on triindole with different linking groups between the core and the side chains (**Figure 1.5**). In these systems, the mobility values increased from 6×10^{-4} to 2.8 $cm^2 \cdot V^{-1} \cdot s^{-1}$ by improving the intramolecular order, reducing the stacking distance from 4.4 to 3.3 Å, respectively.[61-64]

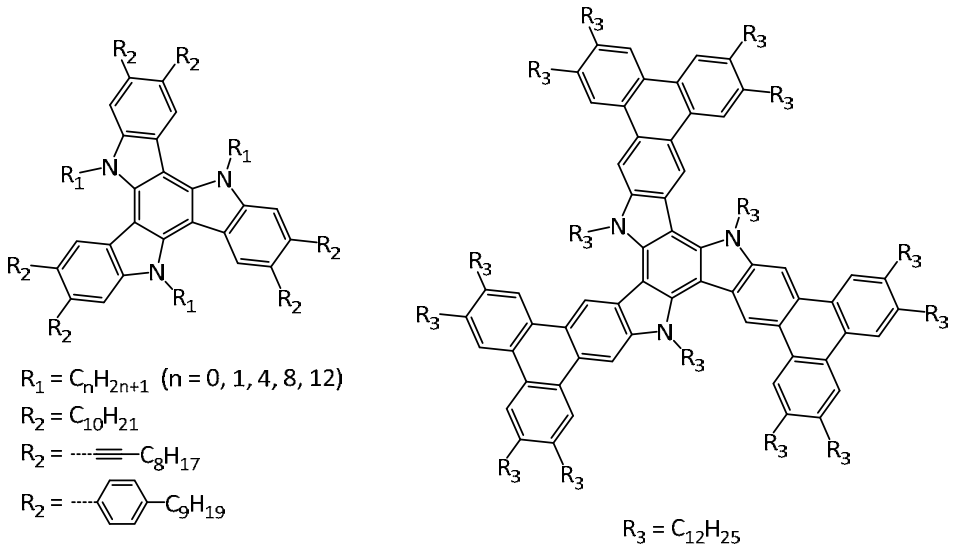

Figure 1.5 Chemical structures of triindol derivatives reported by Gómez-Lor and coworkers for charge carrier mobility.

While *p*-type discotics are abundant and well-studied for charge transport properties, *n*-type discotics are rare and there are only few reports on their charge transport behavior. They can be obtained either by substitution of electron-withdrawing peripheral groups onto a *p*-type discotic core or by designing new electron-deficient aromatic cores. Perylene derivatives are probably the most studied *n*-type semiconducting materials and they have been widely used as active layers in prototype devices such as organic solar cells, OFETs and OLEDs (**Figure 1.6a**). Charge mobilities in perylene derivatives was found to lie within the range of 10^{-2}–10^{-1} $cm^2 \cdot V^{-1} \cdot s^{-1}$.[65-68]

In recent years, other π-conjugated systems have been identified as promising DLCs cores for electron transport. For instance, hexaazatriphenylene is an electron-deficient aromatic heterocyclic core that exhibited a columnar mesophase with mobilities up to 2×10^{-2} $cm^2 \cdot V^{-1} \cdot s^{-1}$ (**Figure 1.6b**).[69, 70] Lehmann *et al.* reported DLCs based on an electron-deficient hexaazatrinaphthylene core with charge carrier mobilities of 9×10^{-1} and 3×10^{-1} $cm^2 \cdot V^{-1} \cdot s^{-1}$ for crystalline and columnar LC phases, respectively (**Figure 1.6c**).[71] Demenev *et al.* reported electron mobilities of

2×10^{-3} $cm^2 \cdot V^{-1} \cdot s^{-1}$ in benzotristhiophene derivatives with hexagonal columnar LC phases (**Figure 1.6d**).[72] In our research group, Beltrán *et al.* synthesized hexagonal columnar LCs based on a tris(triazolyl)triazine aromatic core (**Figure 1.6e**). The electrochemical studies confirmed the electron deficient nature of this core and its potential for electron transport.[73, 74] So far, electron mobilities in the 10^{-2}–10^{-1} $cm^2 \cdot V^{-1} \cdot s^{-1}$ range were found for these tris(triazolyl)triazine-based columnar LCs.[75]

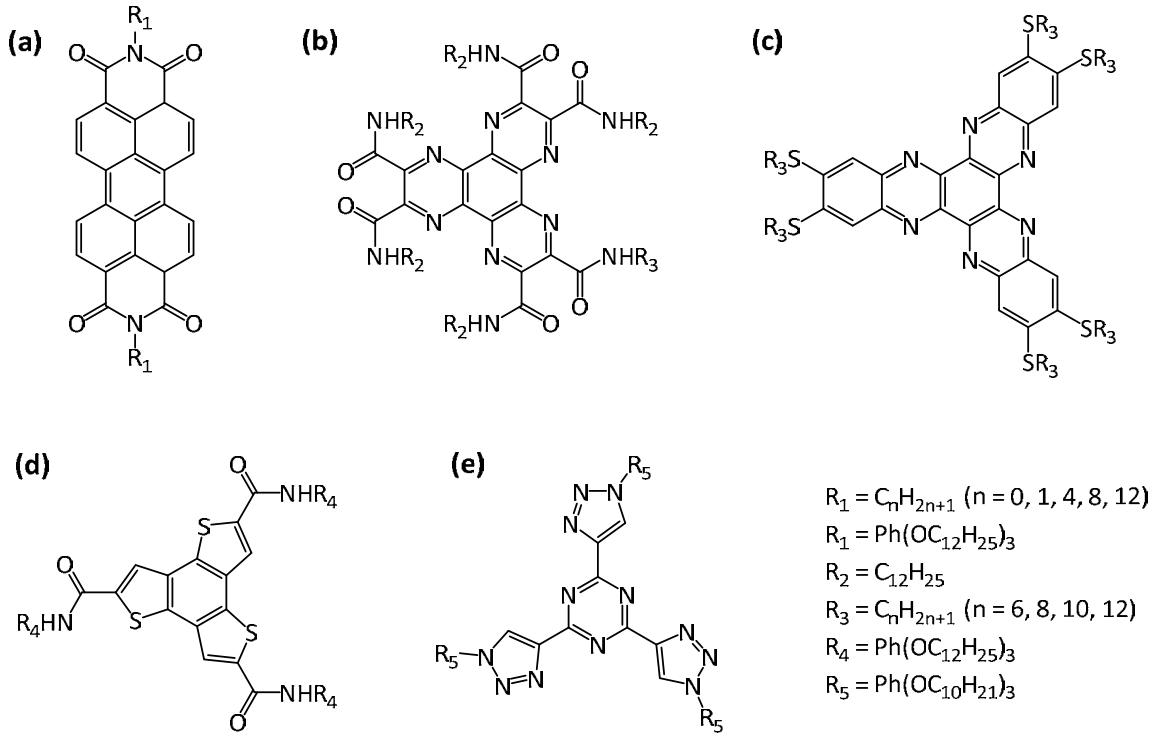

Figure 1.6 Chemical structures of **(a)** perylene, **(b)** hexaazatriphenylene, **(c)** hexaazatrinaphthylene **(d)** benzotristhiophene and **(e)** tris(triazolyl)triazine DLCs studied for charge carrier mobility.

Aida's research group synthesized a fused metalloporphyrin dimer that formed a LC mesophase with a π-stacked columnar structure at room temperature. High charge carrier mobilities of 2.7×10^{-1} $cm^2 \cdot V^{-1} \cdot s^{-1}$ were found for these derivatives.[76, 77] In another interesting approach, Percec and coworkers reported hole and electron mobilities (ranged from 10^{-4} to 7×10^{-3} $cm^2 \cdot V^{-1} \cdot s^{-1}$) in columnar LC dendrons with the donor/acceptor groups filling the central space of the columns.[78, 79]

1.3 Porphyrin

Porphyrins are natural products that are important in biological systems. Natural porphyrin derivatives, including hemes, chlorophylls, and bacteriochlorophylls, are integrated into proteins scaffolds and are essential for their biological activities.[80] Porphyrin and their metal complexes are also relevant in material science due to their photo-stability, photo-absorption over a broad range of wavelengths, interesting photophysical properties, and convenient chemical synthesis. These attractive properties make them suitable for many organic electronic applications.[81-86]

The porphyrin macrocycle consists of four pyrrole rings joined by four interpyrrolic methine bridges to give a highly conjugated macrocycle. Porphyrins can be prepared by several methods such as the tetramerization of monopyrroles, the dimerization of dipyrromethanes and from open chain pyrrolic derivatives.[87-89] Nevertheless, all methods give only moderate yields and the purification of the product is generally tedious.

1.3.1 Porphyrin-Based Liquid Crystals

Porphyrin derivatives have been extensively incorporated into self-organizing supramolecular LC systems due to their attractive properties. The first porphyrin-based LC was reported by Goodby and coworkers and it was prepared from commercially available uroporphyrin I dihydrochloride.[90] Since them several works have described the incorporation of porphyrins and their metal complexes into self-organizing LC systems. Although there are some examples of porphyrin derivatives displaying calamitic mesophases, the porphyrin core has been frequently used as central platform to obtain DLC materials. LC porphyrin derivatives can be divided into two broad categories depending on the location of the substitution in the macrocyclic ring (**Figure 1.7**): porphyrins octa-substituted at the β-positions of the pyrrole rings, and porphyrins di- and tetra-substituted at the *meso*-positions.

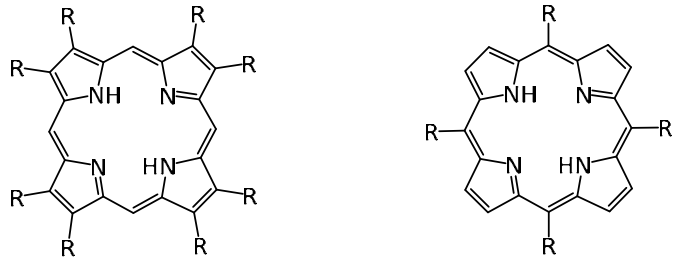

Figure 1.7 Structures of β-substituted (left) and *meso*-substituted (right) porphyrins.

1.3.1.1 β-*Substituted Porphyrin Derivatives*

Gregg *et al.* reported a series of *n*-alkyl octaesters and octaethers of β-substituted porphyrins and their metal complexes (**Figure 1.8a**).[91, 92] In general, the compounds showed columnar LC behavior and the incorporation of metal ions into the porphyrin core enhanced the thermal stability of the mesophases. The central metal ion increased the strength of the π-π interactions between neighboring porphyrins because metalation increases both the rigidity of the porphyrin rings and their electrostatic attraction. In a similar way, more recently Shearman *et al.* prepared a series of octaalkyl β-substituted porphyrins with LC behavior. The metal-free derivatives were not mesomorphic whereas their Zn^{2+} complexes displayed rectangular columnar phases.[93]

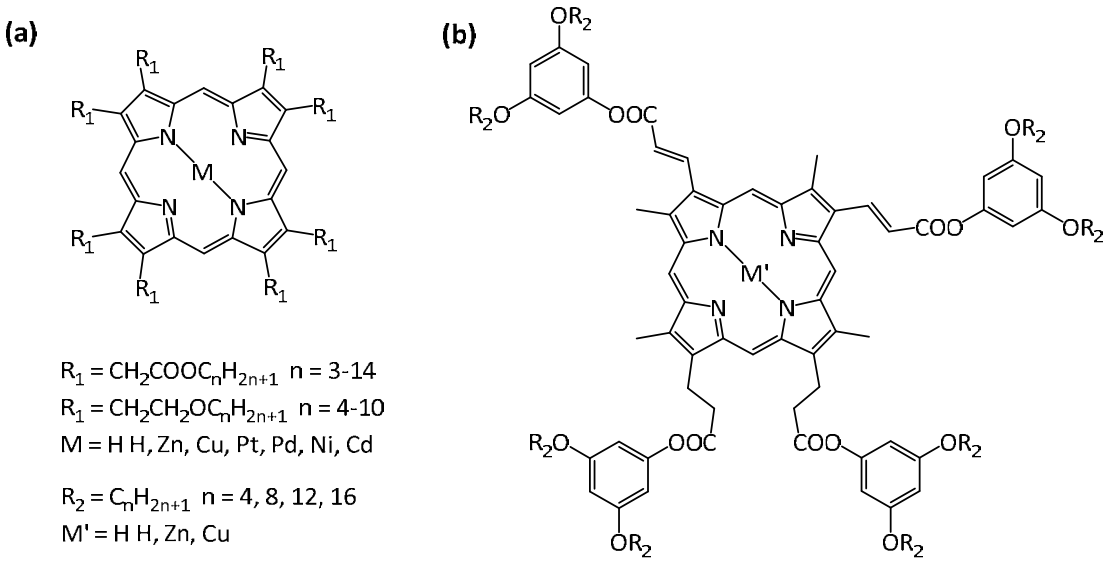

Figure 1.8 Chemical structures of **(a)** octaesters and octaethers and **(b)** hemin-based β-substituted porphyrins and their metal complexes.

Velasco and coworkers reported a family of asymmetrical β-substituted porphyrins prepared from hemin (ferriprotoporphyrin IX chloride), a naturally occurring iron-containing asymmetrically substituted porphyrin (**Figure 1.8b**).[94-96] These hemin-

derived discotics exhibited columnar LC properties from room temperature with a wide mesophase range. As expected, the alkyl chain lengths affected the melting and the clearing points and metalation enhanced the thermal stability of the mesophases due to the enhancement of the interactions between the porphyrin cores.

Würthner and coworkers prepared a hexagonal columnar LC by the attachment of a second-generation dendritic unit onto a commercially available chlorophyll derivative (**Figure 1.9**).[97] The Percec-type dendron governed the self-assembly into cyclic structures composed of 5–6 slices that led to columnar mesophases. Hole mobilities of around 10^{-2} $cm^2 \cdot V^{-1} \cdot s^{-1}$ were obtained, revealing that these organized columnar superstructures hold promise for optoelectronic and photovoltaic applications.

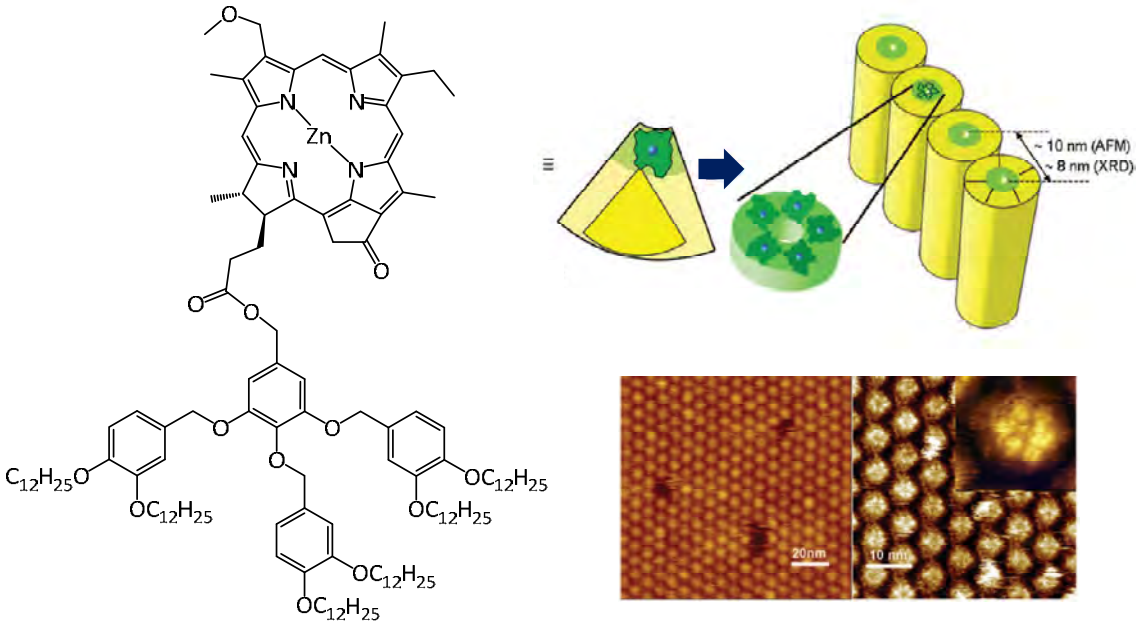

Figure 1.9 Chemical structure, proposed arrangement within the column stratum and AFM (left) and STM (right) images of the LC arrangement. (Adapted from reference 97)

1.3.1.2 *meso-Substituted Porphyrin Derivatives*

Meso-substituted porphyrins, though not naturally occurring, are widely preferred candidates in various fields due to their much simpler synthesis compared to β-substituted porphyrins. A large number of *meso*-tetra-substituted porphyrins which displayed columnar LC behavior have been prepared.[98] While simple tetraalkyl-substituted porphyrins are generally non-mesomorphic, many tetra-(4-

alkylphenyl), tetra-(4-alkoxyphenyl), tetra-(3,4-dialkylphenyl), tetra-(3,4-dialkoxyphenyl), etc. displayed LC behavior.[99]

Li and coworkers reported a family of tetrakis-(3,4,5-trialkoxybenzoate)phenyl porphyrins that exhibited hexagonal columnar mesophases (**Figure 1.10**).[59] The flat porphyrin core promoted the formation of homeotropic aligned mesophases making these products excellent candidates for device applications.[60] These porphyrin derivatives were also blended with fullerene C_{60} obtaining a LC arrangement in which C_{60} was sandwiched between two porphyrin cores due to π-π interactions.[100] The supramolecular adduct retained the homeotropic aligned LC nanostructure providing efficient paths for electrons and holes along the columnar axis. In addition, introducing fluorine into the alkyl chains provided a structural change that enhanced the tendency towards defect-free homeotropic alignment of interest for high performance electronic applications.[58]

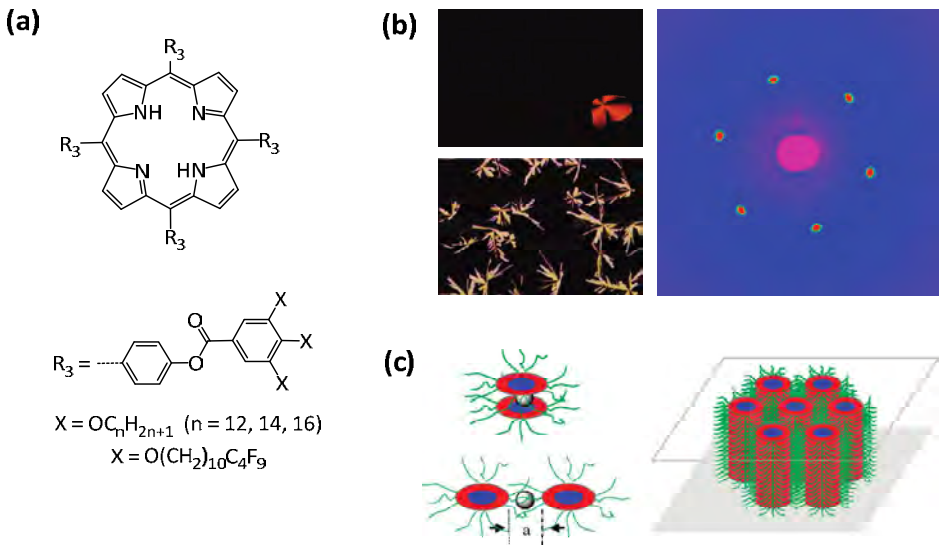

Figure 1.10 (a) Chemical structure of porphyrin derivatives reported by Li and coworkers, **(b)** POM textures and XRD patterns of the homeotropic monodomain, **(c)** schematic representations of the possible arrangements with C_{60}. (Adapted from reference 100)

Wu *et al.* reported fatty acid meta-octaesters of tetraphenylporphyrins.[101] Temperature ranges of the hexagonal columnar mesophase were considerably increased by complexation with several metal ions (Zn^{2+}, Cu^{2+}, Ni^{2+} and Mg^{2+}). Interestingly, the corresponding Cu^{2+} complexes displayed no fluorescence emission due to the paramagnetism of this metal ion.

The introduction of additional functional units around the porphyrin core was a strategy employed by Kimura *et al*. They reported the preparation of a perylene-based dendritic porphyrin derivatives with columnar mesomorphism.[102] The inclusion of C_{60} in the dendritic structure modified the LC arrangement resulting in the quenching of the fluorescence properties. In addition, DLCs based on a porphyrin core surrounded by triphenylene functional units were reported by Miao *et al.*[103] These compounds presented a microphase separation between the porphyrin and the triphenylene columns that may be useful for organic photovoltaic and photochemical applications.

Aida and coworkers reported the preparation of LC materials based on fused metalloporphyrin dimers that formed LC mesophases with a π-stacked columnar structure (**Figure 1.11**).[76, 77] These materials behaved as charge-transporting semiconductors with mobilities in the 10^{-3}–10^{-1} cm^2 V^{-1} s^{-1} range.

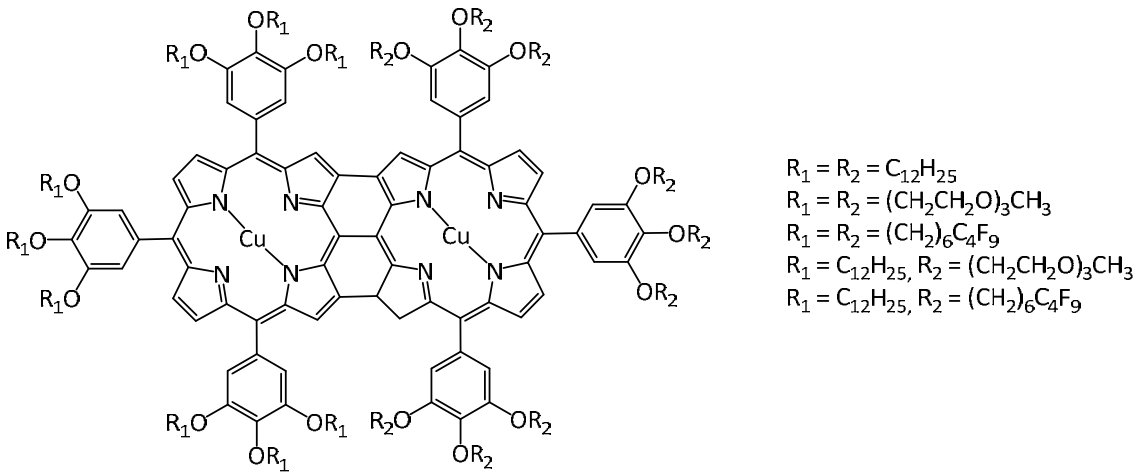

Figure 1.11 Molecular structures of fused metalloporphyrin dimers.

Bruce and coworkers demonstrated that extending the porphyrin macrocycle in one direction transformed the discotic porphyrins into rod-like molecules that showed calamitic nematic and smectic phases at elevated temperatures (**Figure 1.12**).[104-106] More recently, Mehl *et al.* also synthesized rod-like porphyrin-based materials but in this case the lamellar mesomorphism was achieved at room temperature.[107]

X = H, $R_1 = R_2 = OC_nH_{2n+1}$ n = 8, 10, 12, 14, 16

X = H, R_1 = OH, R_2 = 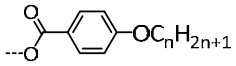 n = 7, 8, 14

X = OC_8H_{17}, R_1 = OH, R_2 = 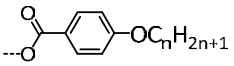 n = 7, 8, 14

Figure 1.12 Chemical structure of calamitic porphyrin derivatives reported by Bruce and coworkers.

Supramolecular interactions were also employed to functionalize porphyrin macrocycles. The first example was described by Camerel *et al.* who reported an easy way to produce porphyrin-based LC materials by ionic self-assembly.[108] Ionic complexes were prepared by mixing tetrakis(4-sulfonatophenyl)porphyrin and ammonium functionalized amido derivatives of 3,4,5-trialkyloxybenzoic acid (**Figure 1.13**). In all cases, hexagonal columnar phases were obtained.

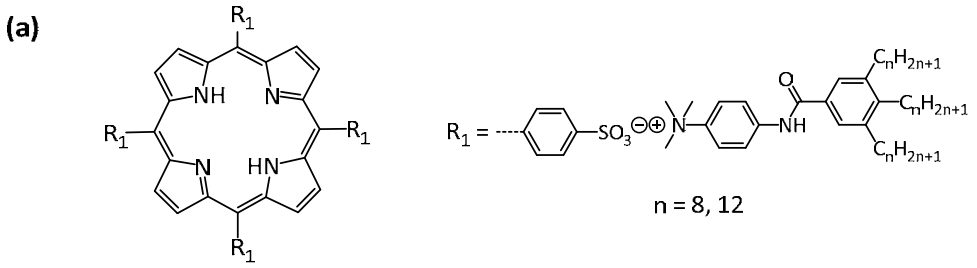

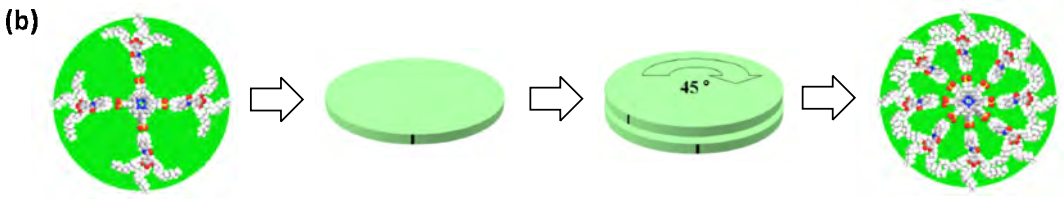

Figure 1.13 (a) Chemical structure of the ionic porphyrin derivatives reported by Camerel *et al.* and **(b)** their organization along the column in the hexagonal columnar mesophase. (Adapted from reference 108)

Very recently, our research group reported the preparation of hydrogen-bonded LC dendrimers formed between 5,10,15,20-tetra(4-pyridyl)porphyrin and its zinc metalated derivative and four peripheral bifunctionalized dendrons derived from bisMPA with coumarin and pyrene moieties as functional groups (**Figure 1.14**).[109]

The supramolecular dendrimers showed LC behavior. However, it is noteworthy that *a priori* the molecular structure seemed to induce a discotic arrangement, although the flexibility of the bisMPA dendrons resulted in the formation of calamitic superstructures and smectic mesophases were observed.

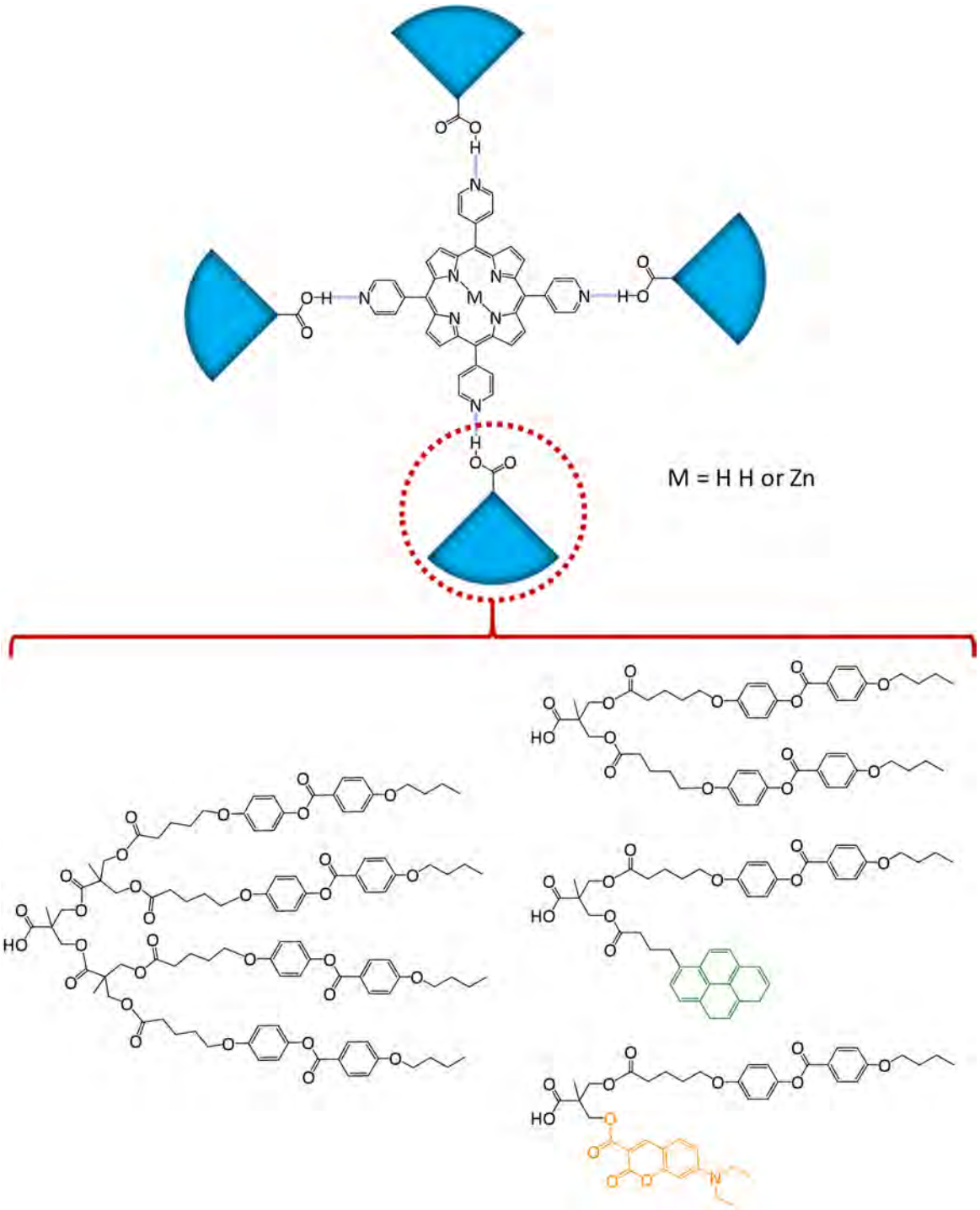

Figure 1.14 Schematic representation of the supramolecular porphyrin-core dendrimers prepared by hydrogen bonding.

1.3.2 Porphyrin-Core Dendrimers for Light-Harvesting

Sunlight is the most abundant renewable energy available to our planet, and thus, nature has developed several complex photosynthetic processes to convert solar radiation into a useful source of fuel. The photosynthesis starts with the collection of light energy and energy transfer to the photosynthetic reaction center. The light-harvesting complexes play a vital role in absorbing photons in the visible region and funneling the acquired energy to the reaction center with an efficiency of 100%.[110-112] Artificial light-harvesting antenna systems are a fascinating challenge for chemists because they may offer potential technological advantages with a variety of applications in molecular electronics and molecular optics.[113]

In the design of artificial light-harvesting systems, a great number of chromophores must be incorporated to acquire a large absorption cross-section.[114-117] In addition, these chromophores have to be spatially organized in order to facilitate directional energy transfer in a cooperative way. The use of synthetic dendritic building blocks permits the introduction of a large number of chromophoric pigments at the periphery of the dendrimer. In fact, several multichromophoric dendrimers have been reported for carrying out the so-called “antenna effect”.[118-120] Dendritic light-harvesting antennas for the collection of photons have attracted attention not only from a fundamental point of view but also for their potential applications in optoelectronics, bioimaging or photodynamic therapy.[113, 121]

Among these light-harvesting systems, dendrimers built from a porphyrin core with different branching functional units have been studied as synthetic analogous of biological systems closely imitating the function of the natural photosynthetic machinery. One of the first examples was reported by Aida and coworkers (**Figure 1.15a**).[122] They found highly efficient energy transfer from poly(benzyl ether) dendrons to the free-base porphyrin core (ϕ_{ET}= 80.3%). The energy transfer efficiency depended on the morphology and the generation number of the dendritic units. The dendritic architecture provided a densely packed configuration which allowed an efficient energy-migration from one benzyl ether unit to the next one (through-space Förster mechanism). Similarly, Kimura *et al.* prepared polyphenylene-based rigid dendritic porphyrins with efficient energy transfer (ϕ_{ET}= 42–98%) from the polyphenylene dendritic side groups to the focal porphyrin unit (**Figure 1.15b**).[123]

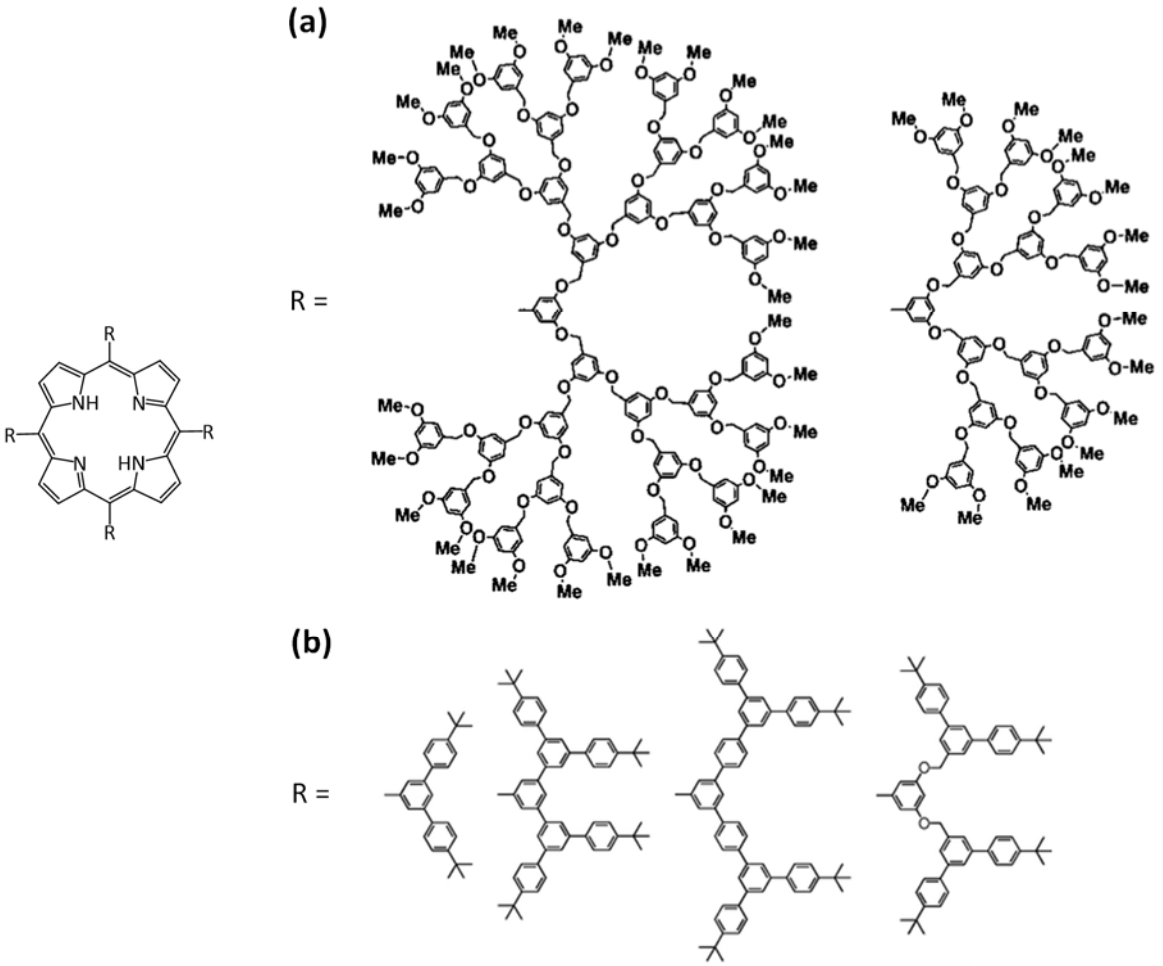

Figure 1.15 Dendritic porphyrin derivatives described by **(a)** Aida and coworkers and **(b)** Kimura *et al.* (Adapted from reference 122 and 123)

Fréchet and coworkers compared the intramolecular energy transfer of three different macromolecular architectures: a four-generation dendrimer and its eight- and four-arm star-shaped isomers (**Figure 1.16**).[124] They found that the dendrimer exhibited a much higher efficiency (ϕ_{ET}= 83.9%) than the eight- (ϕ_{ET}= 57.0%) and four-arm (ϕ_{ET}= 34.2%) star-shaped isomers. These results demonstrated the great advantage of using dendritic scaffolds for energy transfer from the periphery to the core.

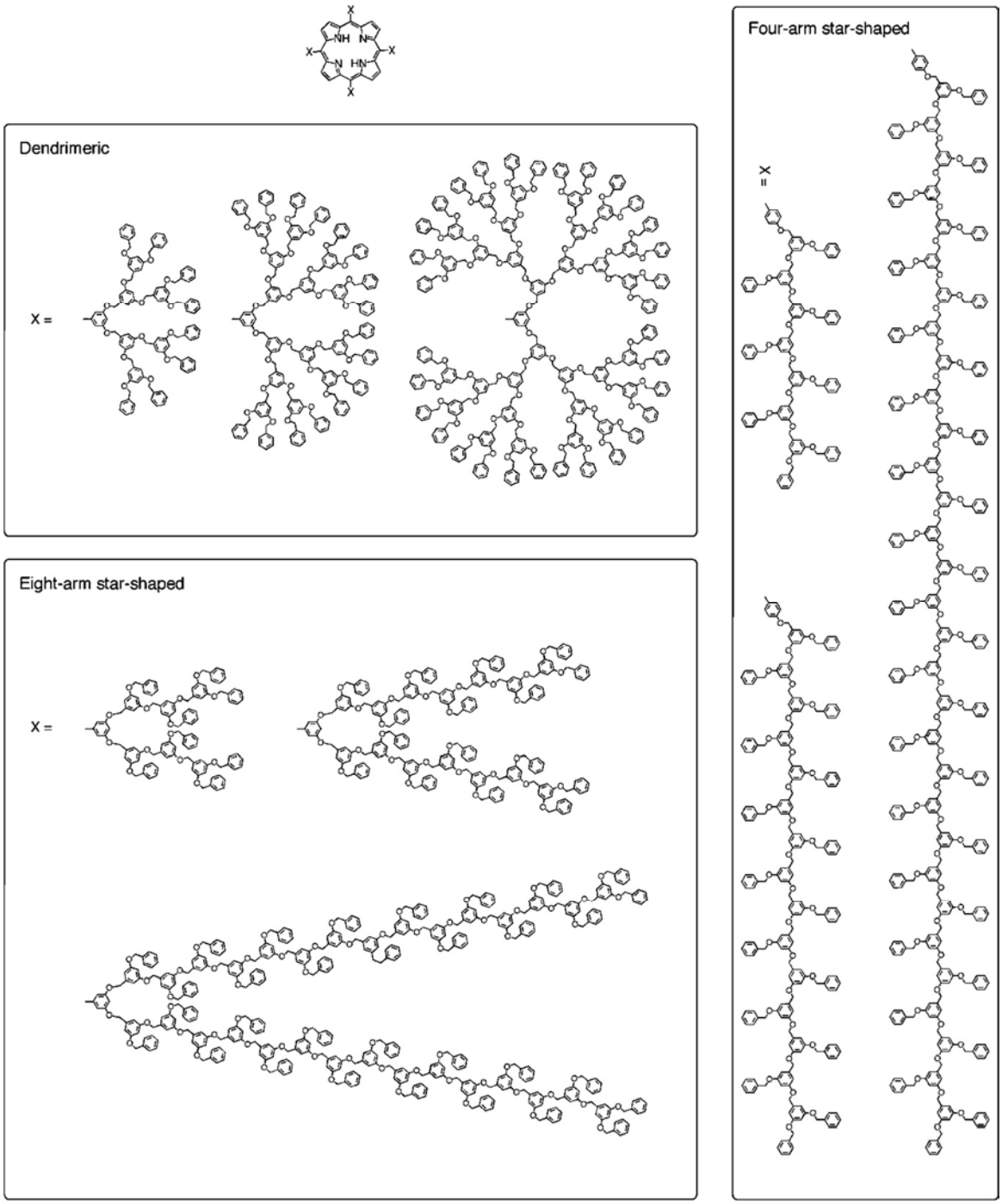

Figure 1.16 Chemical structures of a four-generation dendrimer and its eight- and four-arm star-shaped isomers described by Fréchet and coworkers (Adapted from reference 124)

Fréchet's research group also obtained efficient energy transfer (ϕ_{ET}= 65–98%) by using polycaprolactone branches functionalized with coumarin moieties (**Figure 1.17a**).[125, 126] In addition, they prepared dendrimers that consisted of a porphyrin core with both coumarin and naphthopyranone functional units (**Figure 1.17b**).[127] Excitation of the outer coumarin units gave an energy transfer cascade from the outer layer, where the coumarins are located, to the inner layer containing the

naphthopyranones, and then to the focal porphyrin unit (ϕ_{ET}= 97%). Therefore, the system absorbs light over a wide spectral range and transferred to the porphyrin acceptor where the light is emitted at a single wavelength.

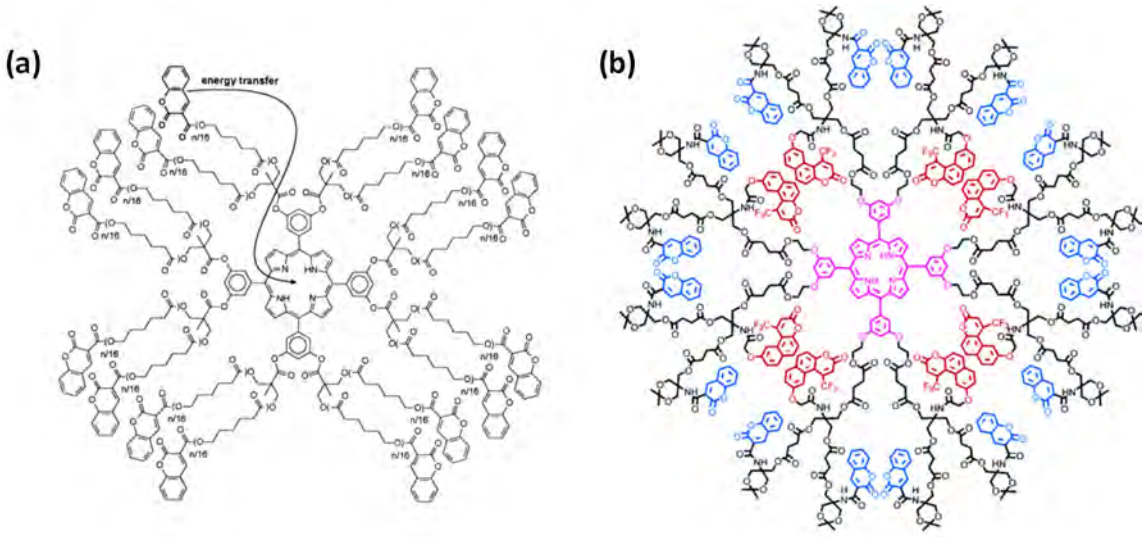

Figure 1.17 Porphyrin-core dendrimers containing **(a)** polycaprolactone branches functionalized with coumarin donor moieties, and **(b)** naphtopyranone and coumarin donor chromophores. (Adapted from references 125 and 127)

Due to its special electronic and optical properties, carbazole is also a promising building block for the construction of light-harvesting dendritic porphyrins. Loiseau *et al.* reported the first example of porphryrin-core dendrimers with carbazole-based branching subunits.[128] In these dendrimers, light was absorbed by the peripheral carbazole chromophores and efficiently transferred to the porphyrin core. The efficiency of energy transfer decreased with the generation (ϕ_{ET}= 40–69%).[129] Similarly, Yamamoto and coworkers reported several carbazole-phenylazomethine dendrimers with a porphyrin core.[130] Such molecular architectures were also able to complex metal ions or fullerene derivatives at the imine sites.[131, 132]

Beside of this, intramolecular energy transfer in other porphyrin-core dendrimers was investigated using platinum-acetylide,[133] truxene,[134] or triphenylamine[135-137] derivatives around the porphyrin macrocycle.

1.4 Coumarin

Coumarins are an important class of heterocyclic compounds which are used in biology, medicine and material science.[138] Coumarin derivatives have found optical applications such as OLEDs, optical sensors, laser dyes, light-harvesting materials, fluorescent probes in biology and medicine, among others.[139-142] They are also present in perfumes and cosmetics, cigarettes, alcoholic beverages, and drugs.

Upon UV irradiation, coumarins undergo [2+2] cycloadditions to yield cyclobutane dimers (**Figure 1.18**). The photodimerization reaction has been studied both in solution and in the solid state and it can be reversed *via* UV irradiation at a shorter wavelength.

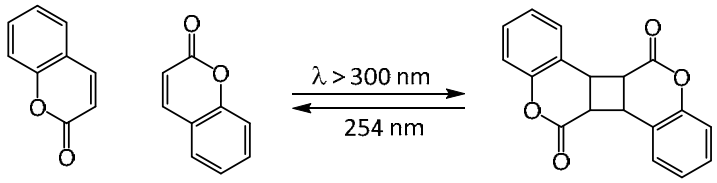

Figure 1.18 Coumarin photodimerization reaction

1.4.1 Liquid Crystalline Coumarins

Due to their exceptional optical properties, several mesogenic coumarin derivatives have been reported.[143-149] LC coumarins possess wide range of potential applications from display devices to biological systems.[138]

On the other hand, LC polymers bearing coumarin moieties as side-chains have been reported as a new kind of photoalignment layer for LCs in which the photodimerization of the coumarin units occurs by exposure to UV light.[150-154] The direction of the orientation of the LCs could be tailored by the polarization direction of the irradiated light. Photoalignment is a noncontact method employed to avoid the problems that originate with mechanical rubbing. The uniaxial orientation of LCs is the basis of some electronic devices.[155]

Our research group has described several LC dendrimers that incorporate coumarin fluorescent units in order to study their photoconductivity. The dendrimers were prepared by hydrogen bonding between a melamine central core

and coumarin-containg bifunctional dendrons based on bisMPA (**Figure 1.19**). It was concluded that this type of dendritic system may be useful in the preparation of polymeric materials with potential applications in organic electronic devices.[156] So far, we essayed a similar approach using a porphyrin central core (**Figure 1.14**).[109] Beside of this, more recently we reported the preparation of new PPI dendrimers bearing coumarin units that displayed LC behavior.[157]

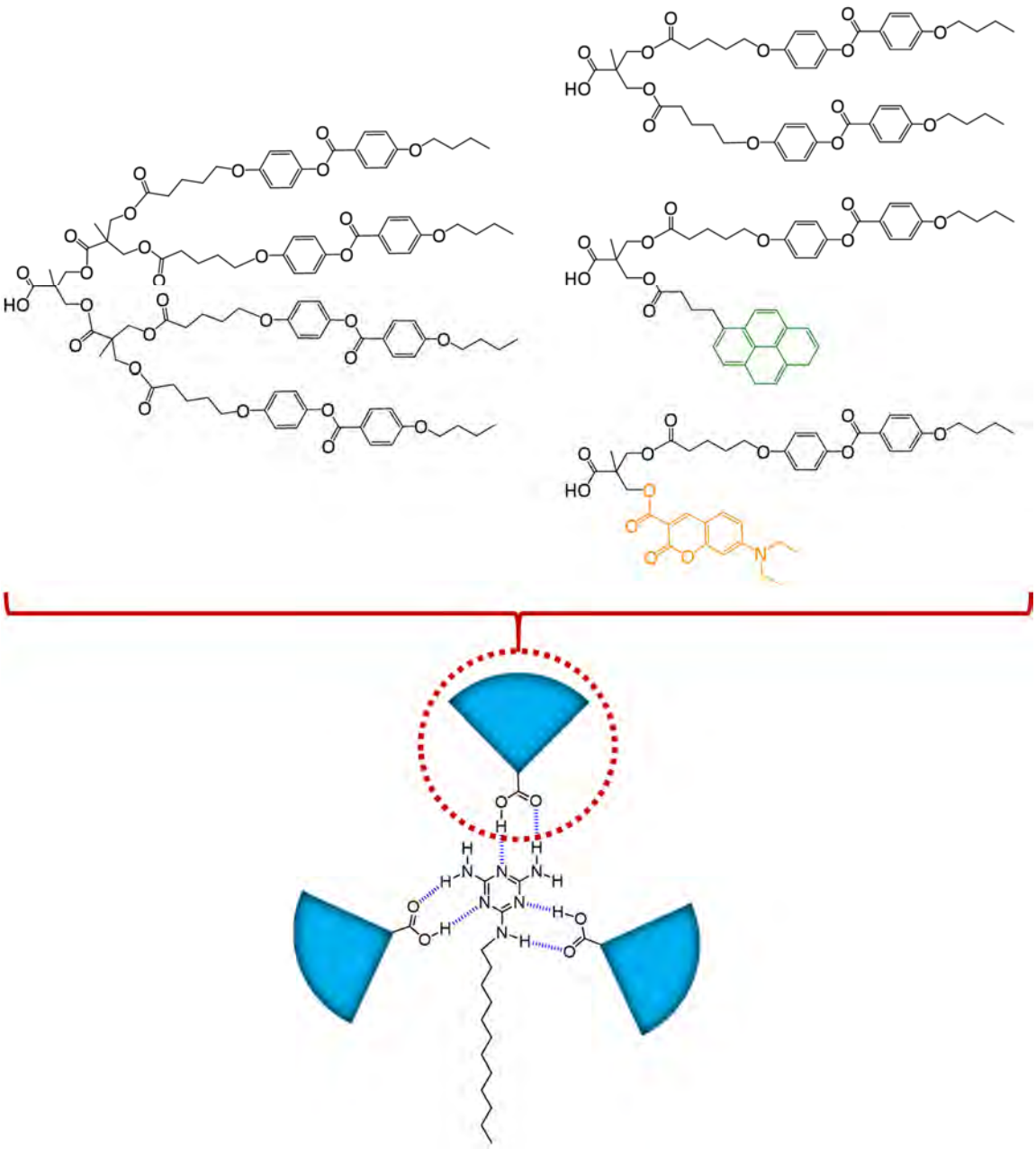

Figure 1.19 Schematic representation of hydrogen-bonded dendrimers containing pyrene or coumarin luminescent units.

1.4.2 Coumarin-Based Light-Harvesting Systems

As mentioned in *Section 1.3.2 (Porphyrin-Core Dendrimers for Light-Harvesting),* the design of artificial systems for harvesting solar energy has been a topic of interest due to their potential optoelectronic and biomedical applications.[113, 121] The first works incorporated coumarins into polymers in an attempt to harvest and transfer the solar radiation energy. For instance, Palmans *et al.* prepared a poly(*p*-phenylene ethylene) derivative with coumarin units attached to the polymer backbone (**Figure 1.20**).[158] Energy transfer was evidenced by the absence of the emission of the coumarin groups (donor) and the presence of the emission of the polymer backbone when coumarins were excited (ϕ_{ET}= 80%).

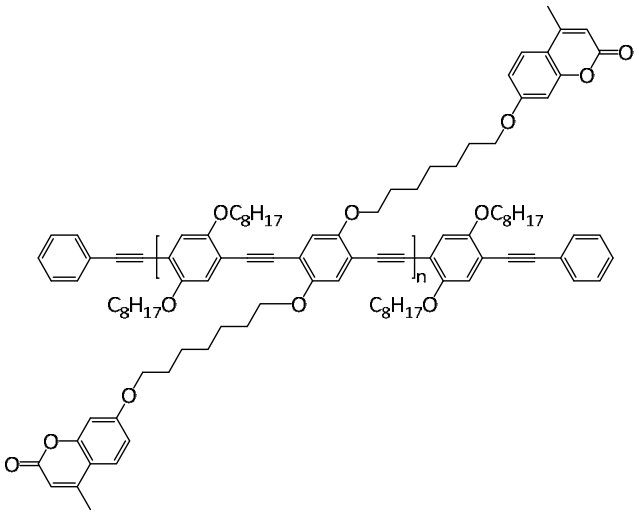

Figure 1.20 Coumarin-containing poly(*p*-phenylene ethylene) derivative.

Fréchet and coworkers also studied energy transfer in coumarin-containing polymers and dendrimers. The dendrimers were synthesized using two different coumarin units (**Figure 1.21a**). The coumarin located at the focal point (acceptor) absorbed the emission from the coumarin units at the periphery of the dendrimer (donors). As the dendrimer increased in generation, the number of donor coumarins increased, thus the dendrimer was able to absorb more light resulting in a more efficient antenna effect (ϕ_{ET}= 86–97%).[159-161] Due to the difficult synthetic methods for Fréchet's harvesting dendrimers, linear polymers with chemical compositions mimicking such dendrimers were synthesized (**Figure 1.21b**).[162] The linear polymers had comparable energy transfer efficiencies to dendrimers. However, the polymers also had some undesirable properties not present in the dendrimers such as low fluorencence quantum yields and low solubility.

In addition to this, coumarin units have also been incorporated into porphyrin derivatives with the aim of taking advantage from the efficient energy transfer between coumarin and porphyrins for light harvesting applications.[163] However, these coumarin-porphyrin systems have already been reviewed in *Section 1.3.2 (Porphyrin-Core Dendrimers for Light-Harvesting)*.

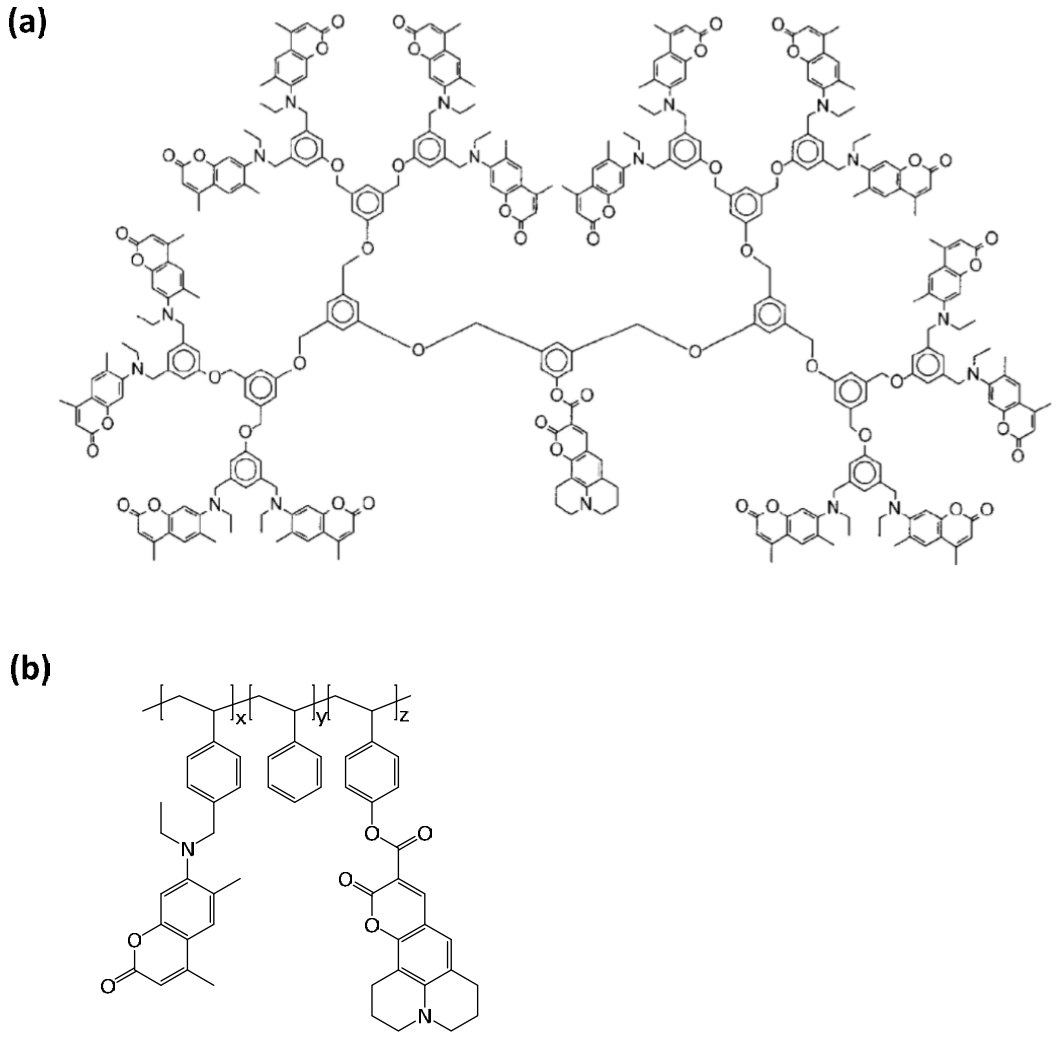

Figure 1.21 Chemical structure of coumarin-containing **(a)** G4 poly(arylether) dendrimer, and **(b)** linear polymers.

1.4.3 Coumarin Photodimerization as a Crosslinking Reaction

Very recently, Barner-Kowollik and coworkers reviewed the formation of precision polymeric networks using advanced photoinduced ligation techniques including coumarin photodimerization as a promising alternative to (meth)acrylate or epoxy materials.[164] One of the appealing properties of this strategy is its reversibility. This

approach allows both the light-triggered formation and cleavage (reverse reaction of photodimerization) of covalent networks. Coumarin photodimerization is particularly attractive as it does not require an initiator or catalyst and side reactions may be avoided.

Chujo *et al.* reported for first time the preparation of a polyoxazoline-based hydrogel by coumarin photodimerization.[165] The photoclevage of the gel was carried out by 253 nm irradiation and was almost quantitative. The reversible photocrosslinking and photoclevage behavior was investigated by Zhang and coworkers using a hyperbranched polymer functionalized with 4-methylcoumarin units.[166]

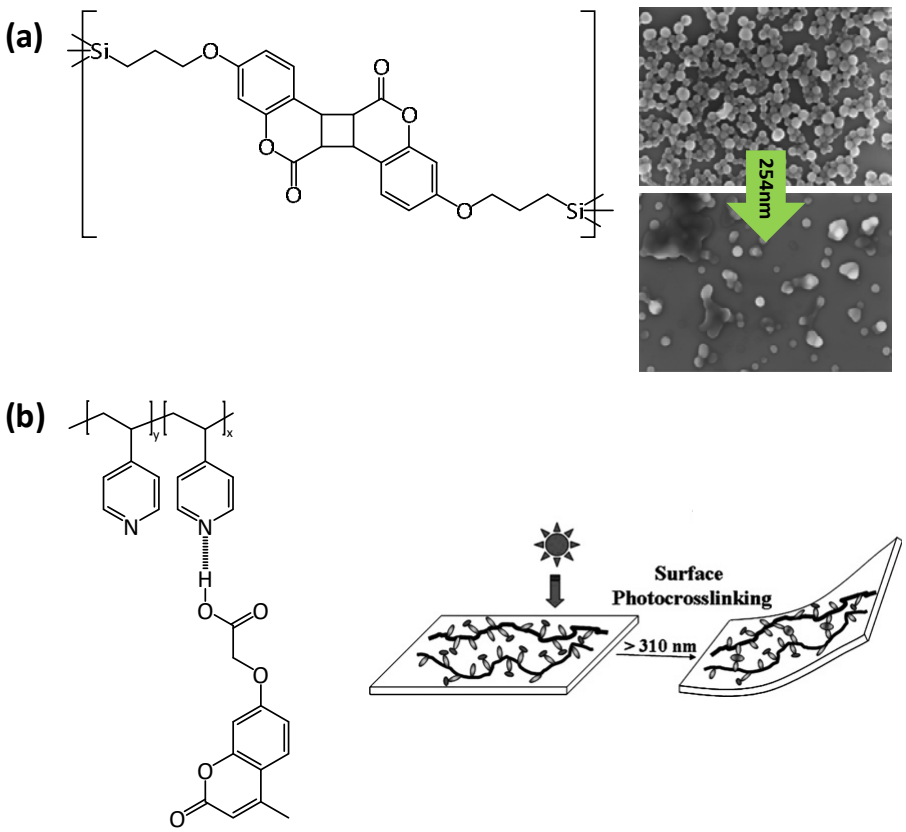

Figure 1.22 (a) Chemical structure of polysilesquioxane polymer and its nanoparticles (before and after irradiation). **(b)** Chemical structure of the coumarin-containing actuator and schematic illustration of the mechanism of the photoinduced film bending. (Adapted from reference 167 and 168)

Shea and coworkers reported the synthesis of photoresponsive spherical nanoparticles. The polysilesquioxane-based nanoparticles incorporated a coumarin dimer as light-responsive moiety (**Figure 1.22a**). Photoclevage of coumarin dimers resulted in deformation of the nanoparticles by 254 nm

irradiation.[167] Zhao *et al.* found that coumarin photodimerization could be employed for the preparation of photodeformable polymers networks (**Figure 1.22b**).[168] The plausible mechanism was based on the photodimerization of coumarin pendant groups occurring on one side of the film which created imbalanced surface stresses leading to the bending.

Zhao *et al*. also employed coumarin photodimerization for the preparation of well-defined single chain nanoparticles. They employed these nanoparticles as nanoreactors for the synthesis of Au nanoparticles.[169] So far, the same authors reported the preparation of photorresponsive LC single-chain nanoparticles that underwent photoinduced deformation upon exposure to linearly polarized light (**Figure 1.23**). These nanoparticles were deformed from an initially spherical form to a stretched shape.[170]

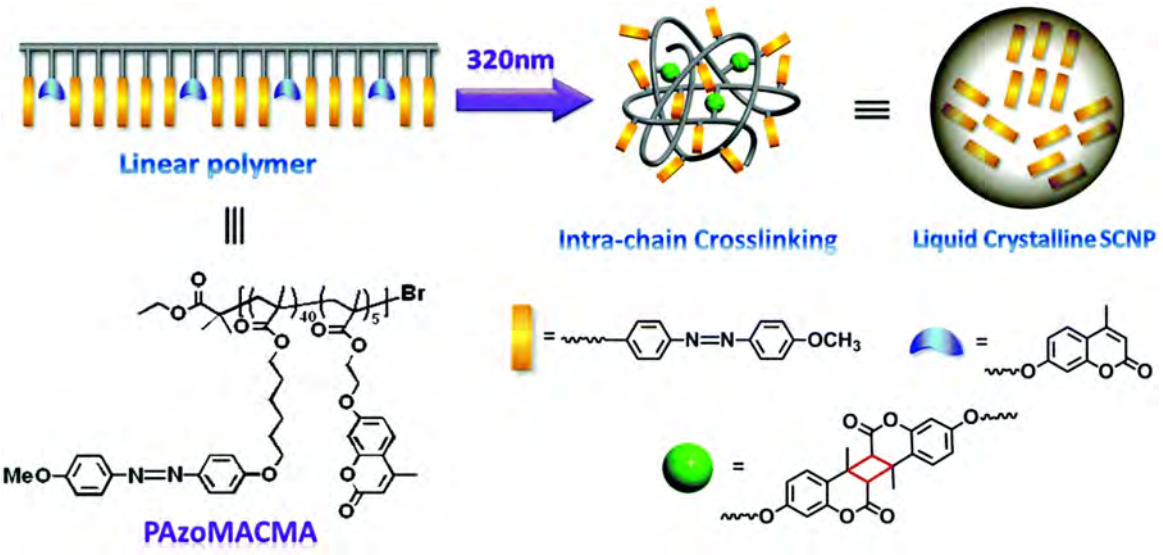

Figure 1.23 Schematic illustration for the preparation of photorresponsive LC single-chain nanoparticles based on the intra-chain photodimerization of coumarin moieties. (Adapted from reference 170)

Joy and coworkers synthesized two novel polyesters in which coumarin units were incorporated into the polymer chain.[171, 172] The coumarin-based polyesters exhibited dual photoresponsive properties: crosslinking upon 350 nm irradiation and polymer chain scission and uncrosslinking at 254 nm irradiation. In addition, micropatterned surfaces were created by irradiation at 350 or 254 nm. The prepared materials were mechanically robust and stable in the absence of light and preliminary studies with cells showed their biocompatibility.

1.5 Carbazole

Carbazole is an aromatic heterocyclic compound which consists of two benzene rings fused on a pyrrole ring. The chemistry of carbazole has been studied for many years due to their extensive biological activity.[173] However, in recent years carbazole-based materials have attracted considerable attention for optoelectronic applications.[174, 175]

Carbazole derivatives have been recognized for their good charge transport properties. They undergo reversible oxidation processes and they are able to transport positive charges (holes) *via* the radical cation species (**Figure 1.24**).[176] In addition, carbazole derivatives generally exhibit high thermal and photochemical stability. The photoconductivity and hole-transport properties of carbazole units have been extensively exploited in several fields such as xerography, light-emitting diodes or photorefractive materials.

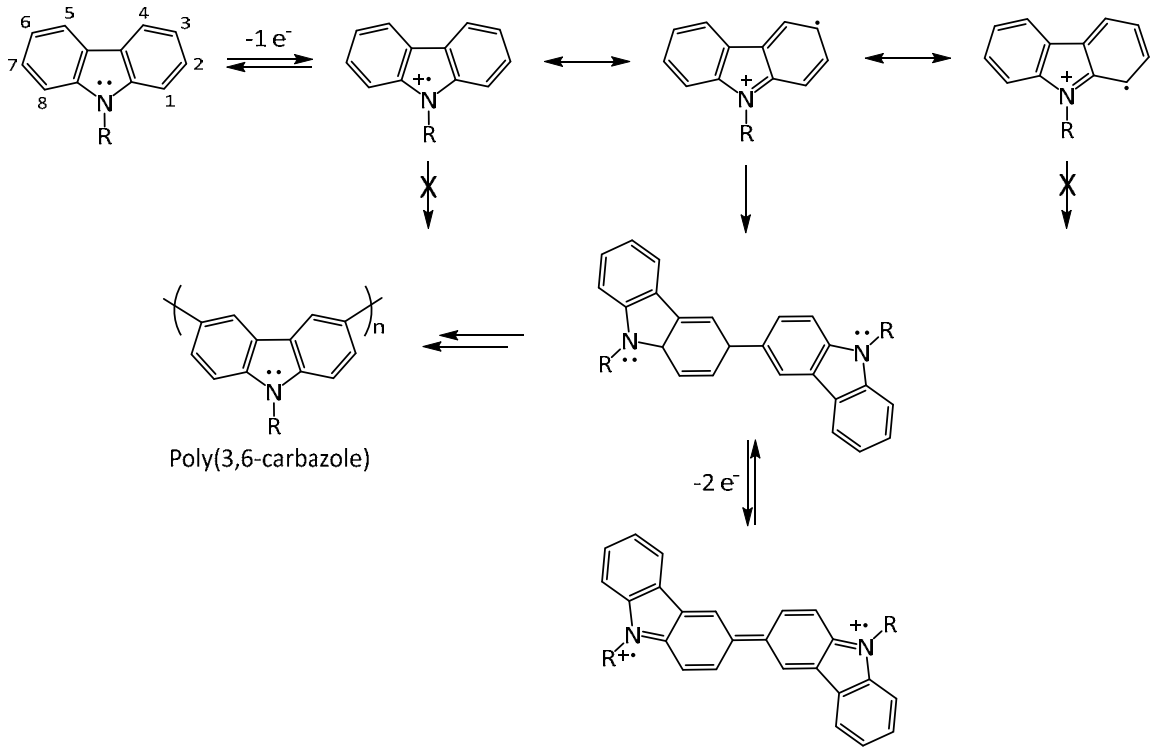

Figure 1.24 Mechanism of the electrochemical oxidation of carbazole.

1.5.1 Carbazole-Based Liquid Crystals

Carbazole-based LCs are attractive for the preparation of photorefractive materials as they combine the self-organization into LC phases with the photoconductivity and charge transport properties in the same molecule.[177] Thus, there are several works in which carbazole moiety has been incorporated into low-molecular weight and polymeric LC materials. These include both calamitic and discotic mesogens.

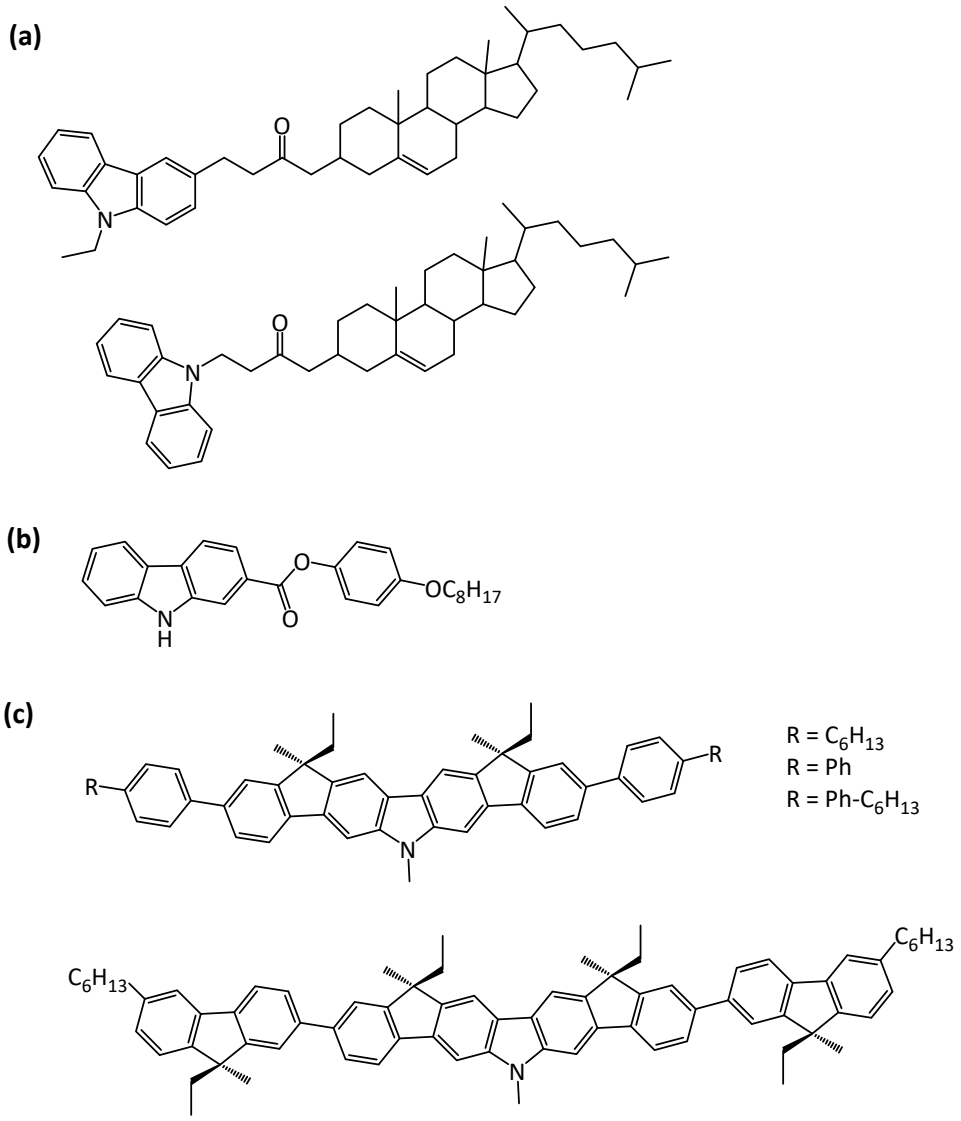

Figure 1.25 Chemical structure of carbazole-based low molecular weight mesogenic derivatives.

The first example was reported by Kawaguchi *et al.* and it consisted of cholesteryl-carbazole LC derivatives (**Figure 1.25a**).[178] Photochemical studies on these molecules were carried out, obtaining low photocurrent values. Since then, several examples of carbazole-based LCs were synthesized with the aim of studying the relationship between the mesomorphic properties and the photoconductive

behavior.[179, 180] Iric *et al.* reported the synthesis of a smectic A LC which contained a carbazole chromophore (**Figure 1.25b**).[181] Low fluorescence quantum yields were obtained due to the formation of intermolecular hydrogen bonds. Moreover, a large number of bisindenocarbazoles derivatives that exhibit LC phases have been reported (**Figure 1.25c**).[182-185] These compounds showed blue photoluminescence with high fluorescence efficiencies and good stability to oxidation.

Regarding DLCs containing carbazole, Manickam *et al.* reported a series of triphenylene derivatives with carbazole units linked to the periphery (**Figure 1.26a**).[186, 187] None of the materials displayed LC behavior. However, a hexagonal columnar phase was observed upon doping some of the triphenylene-carbazole derivatives with 2,4,7-trinitrofluorenone. Perea *et al.* reported hexagonal columnar mesophases with a 9-phenylcarbazole derivative as the central core (**Figure 1.26b**).[188, 189]

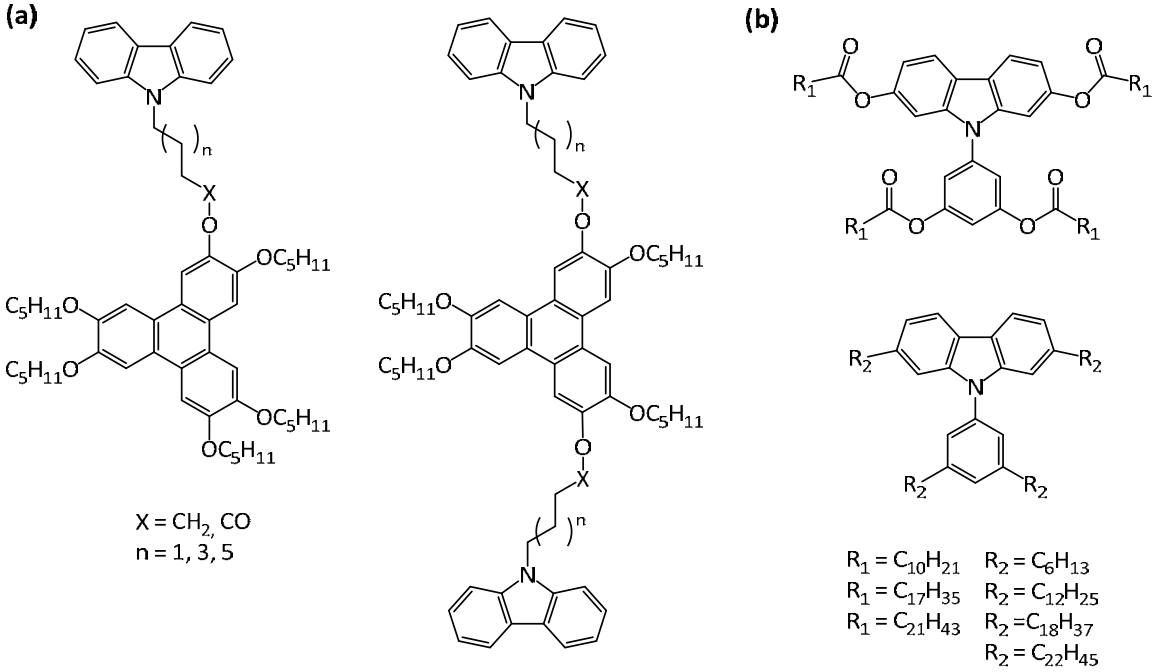

Figure 1.26 Chemical structure of: **(a)** mono- and bi-carbazole-triphenylene derivatives, and **(b)** polysubstituted N-arylcarbazole derivatives.

Gómez-Lor's research group reported the synthesis of several triindole compounds (tricarbazole core) (**Figure 1.5**).[61-64] Highly ordered hexagonal columnar phases with high charge mobility values were obtained by extending the conjugation in these systems. Camerel *et al.* grafted trialkoxybenxamide residues to carbazole- and naphthalene-based core (**Figure 1.27**).[190] The amide groups played a crucial

role in the stabilization of the hexagonal columnar mesophases by hydrogen bonding. In addition, spectroscopic measurements showed that these compounds were luminescent in solution and in the solid state.

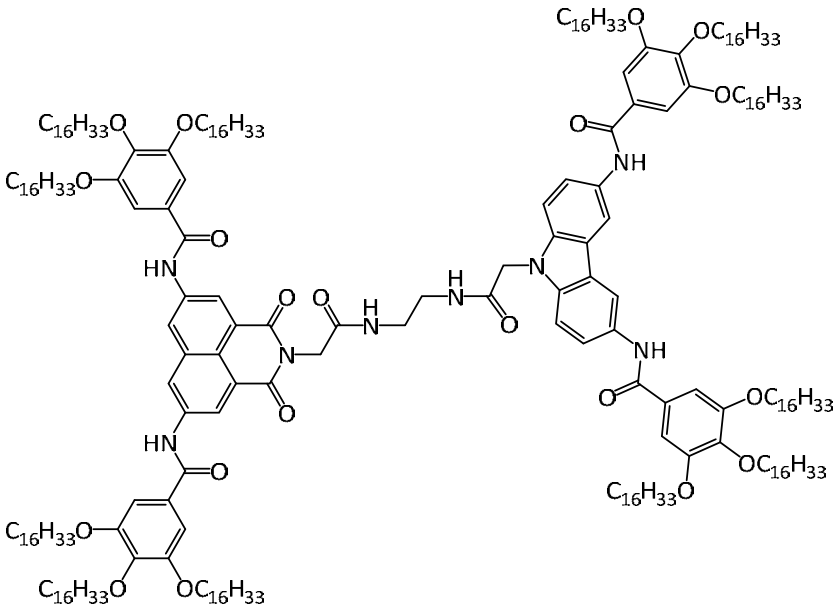

Figure 1.27 Chemical structure of carbazole-based derivative reported by Camerel *et al.*

Percec and coworkers demonstrated that the attachment of carbazole moieties to dendrons mediated the self-assembly of these functional units in a π-stack located in the center of the columns (**Figure 1.28**).[191, 192] The supramolecular columns self-organized into various columnar LC phases that enhanced the charge carrier mobility of the carbazole molecules.[78, 79]

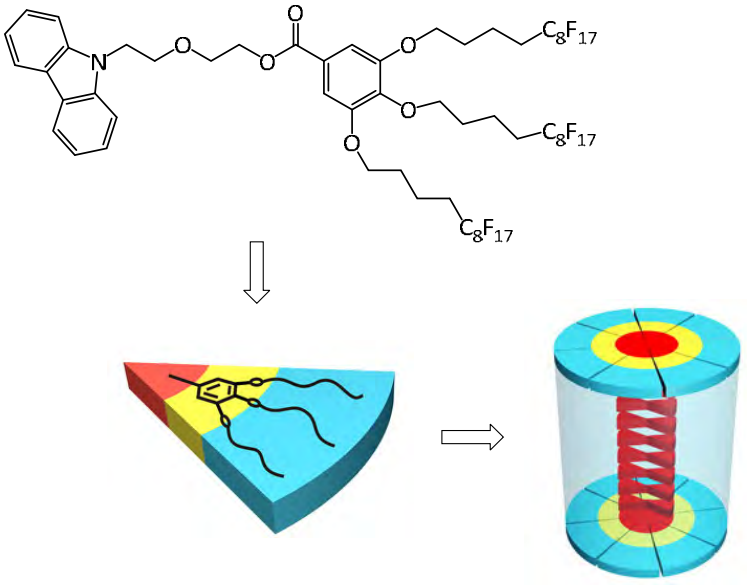

Figure 1.28 Chemical structure and proposed arrangement within the column stratum. (Adapted from reference 192)

Carbazole moieties were also incorporated into macrocycles to obtained materials for non-linear optics.[193, 194] So far, Müllen and coworkers described the charge transport properties of carbazole macrocycles with a hexagonal columnar mesophase.[195, 196] These systems allowed charge transport in three dimensions due to inward-facing side chains. Following this synthetic approach, Kawano *et al.* described hexagonal columnar metallomacrocycle with carbazole units (**Figure 1.29**).[197] The inner cavity was able to interact with various metal ion guest molecules.

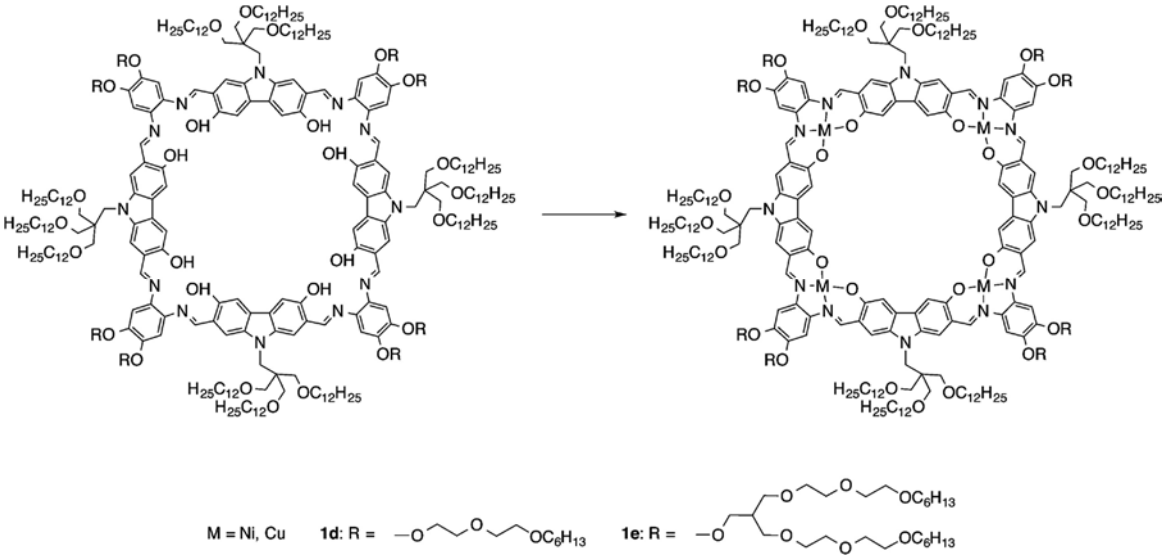

Figure 1.29 Chemical structure of carbazole-based macrocycles reported by Kawano *et al.* (Adapted from reference 197)

Our research group has done pioneering research on LC dendrimers containing carbazole units with potential optoelectronic applications. For instance, Castelar *et al.* described two families of supramolecular dendrimers based on ionic or hydrogen bonding self-assembly between carbazole-containing dendrons and poly(propylene imine) (PPI)[198] or melamine[199] cores. The carbazole functional groups provided luminescent and photoconductive properties to these dendrimers. In another interesting approach, Gracia *et al.* developed functional carbazole block codendrimers with hexagonal columnar LC behavior (**Figure 1.30**).[200] Due to the presence of carbazole units, hole mobilities of 10^{-8} cm^2 V^{-1} s^{-1} were obtained. In addition, these block codendrimers were able to form organogels with a pronounced photoluminescence.[201]

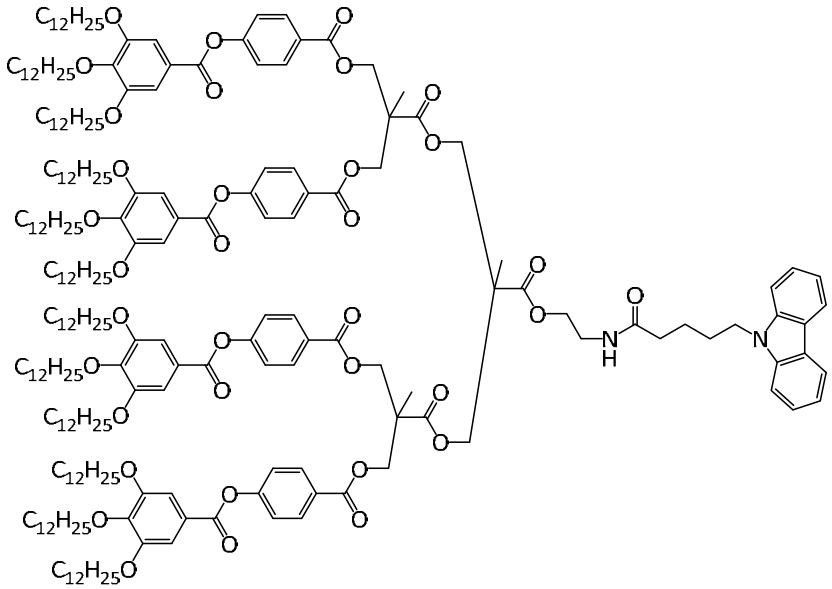

Figure 1.30 Chemical structure of carbazole-containing block codendrimer with hexagonal columnar mesomorphism.

1.5.2 Dendrimers with Carbazole Units

Although the physical properties of carbazole containing polymers have been extensively studied in the development of organic optoelectronic devices, the three-dimentional architecture of dendrimers allows additional control over the intermolecular interactions of the photoactive moieties leading to an interesting improvement of their physical properties. Carbazole-containing dendrimers have been widely used for the preparation of OLEDs due to their light emission and charge transporting properties.[202] Li *et al.* reported a new carbazole-based hyperbranched polymer with promising hole-transporting properties for applications in organic electronics.[203] The OFET devices prepared with the carbazole-based hyperbranched polymer exhibited remarkably enhanced efficiency compared to the linear polymer.

In the development of highly efficient materials for OLED devices, it is desirable to use dendrimers with more than one functional unit. Therefore, carbazole-based dendrons were attached to conjugated cores such as triazine,[204] pyrene,[205] ethynylbenzene,[206, 207] biphenyl,[208] perylene bisimide,[209] oligothiophene,[210] triphenylamine,[211, 212] or porphyrin derivatives.[128-132, 213, 214]

Furthermore, due to their high luminescence quantum yields carbazole-based dendrons were also introduced into transition-metal-based complexes such as iridium, gold or europium (**Figure 1.31**).[215-219] The presence of a heavy-metal center enhanced the performance of OLED devices.

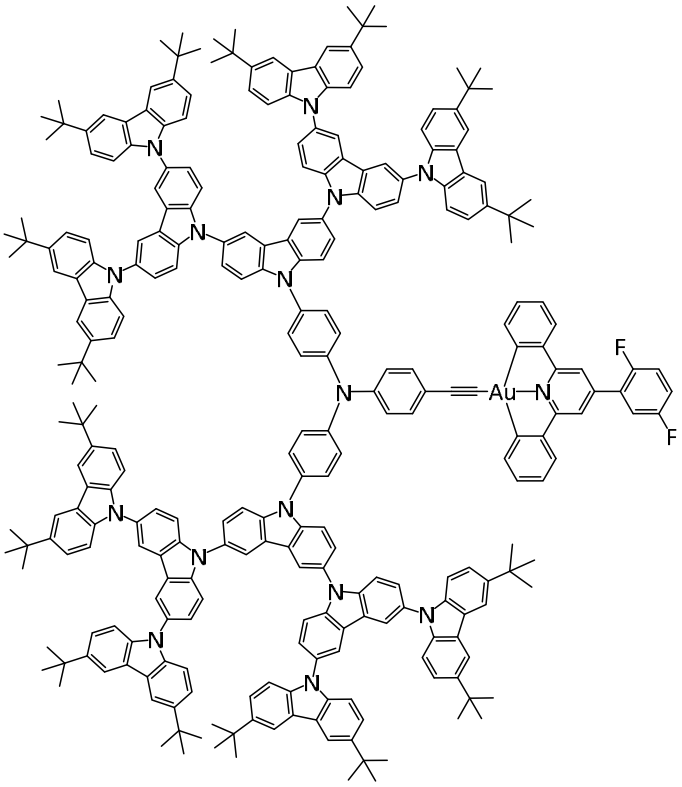

Figure 1.31 Chemical structure of a gold (III) carbazole-based dendrimer.

Advincula's research group investigated several carbazol-terminated dendrimers for their interest in the development of optoelectronic devices and other photonic applications (**Figure 1.32**).[220-223] They reported the preparation of carbazole-terminated Fréchet-type poly(benzyl ether) dendrimers. The electrochemical crosslinking of the peripheral carbazole units at 3,6-positions led to the formation of polycarbazole units. The electroactive carbazole side groups facilitated electrodeposition forming oligocarbazole polymer nanoparticles on the surface of the electrode. They found that the electro-optical properties and electrodeposition of these dendrimers and dendrons were generation dependent.

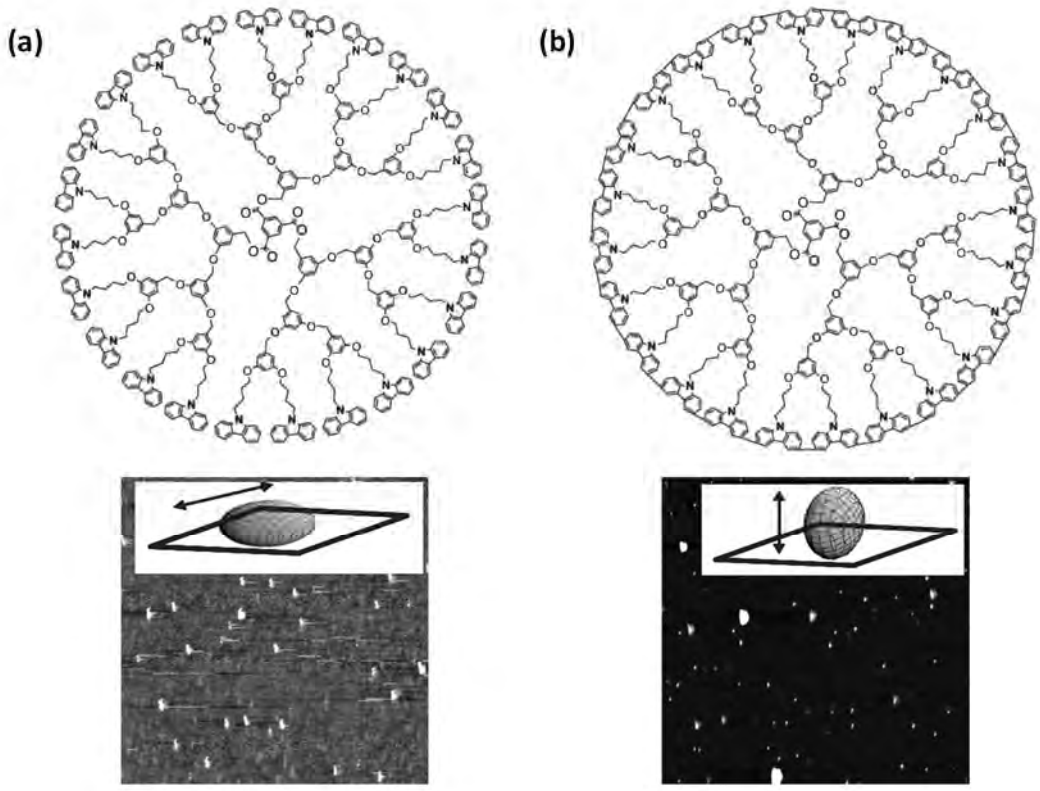

Figure 1.32 Chemical structure of carbazole-terminated dendrimers (top) and AFM pictures (bottom): **(a)** before and **(b)** after electrochemical crosslinking. (Adapted from reference 223)

The same research group employed carbazole electrodeposition for the preparation of oligo(ethylene glycol)-functionalized biocompatible surfaces for protein adsorption resistance (**Figure 1.33**).[224, 225]

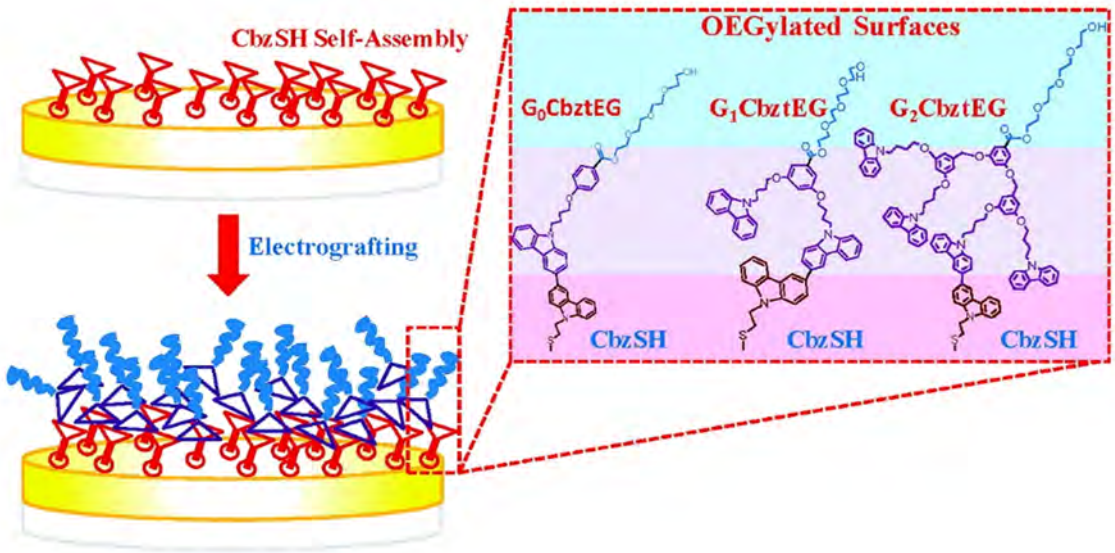

Figure 1.33 Surface modification by electrodeposition of oligo(ethylene glycol)-functionalized linear carbazole dendrons. (Adapted from reference 227)

Advincula and coworkers also reported the complexation between carboxylic acid-terminated carbazole-containing dendrons and amine groups of poly(amidoamine) (PAMAM) dendrimer and hyperbranched polyethylenimine (PEI) (**Figure 1.34**). The electrochemical oxidation of ionic dendrimers showed the formation of nano-ring structures composed of the PAMAM core and a carbazole dendron shell.[226] Additionally, these compounds were utilized for the encapsulation of anionic guests and for the *in situ* formation of gold and silver nanoparticles without any reducing agent.[227]

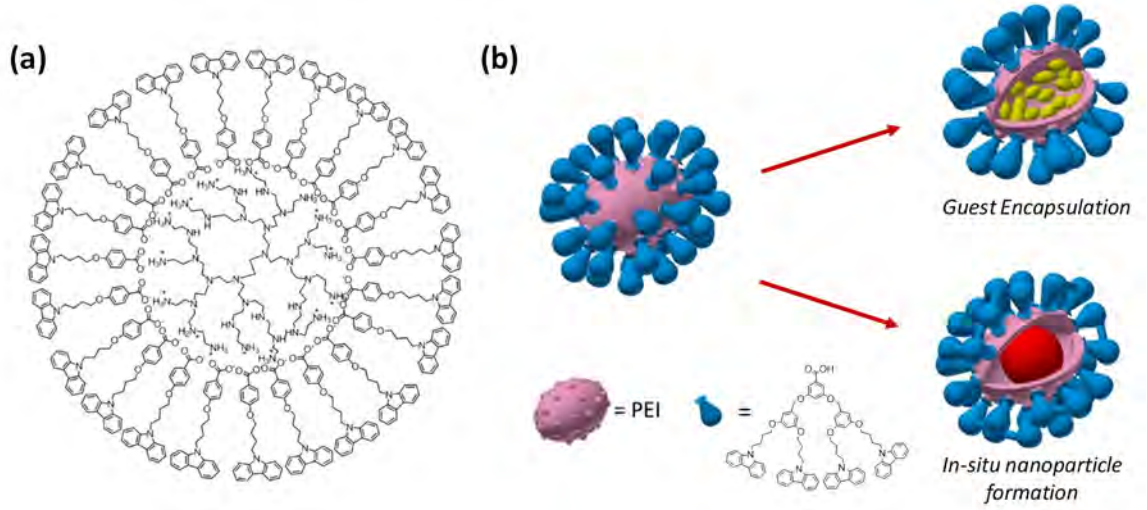

Figure 1.34 (a) Chemical structure of carbazole-containing ionic dendrimer, and **(b)** schematic representation of the encapsulation of anionic guests and the *in situ* formation of gold and silver nanoparticles. (Adapted from reference 230)

2. HIGH CHARGE MOBILITY IN A NEMATIC DISCOTIC MESOPHASE FORMED BY PORPHYRIN-CORE DENDRIMERS WITH COUMARIN MOIETIES*

2.1 Objectives

The structural and synthetic versatility of LC dendrimers has been exploited in the design of functional materials. The topology of these molecules bearing several external reactive groups allows the introduction of different active moieties that modify their physical properties. LC dendrimers combine in the same molecule the dendritic structure with the self-organization into LC phases. Therefore, they have been recognized as an attractive tool for the preparation of polymeric materials for optoelectronic applications.

In this context, our research group has studied new families of supramolecular LC dendrimers prepared by hydrogen bonding between a porphyrin central core and bifunctional dendrons, based on bisMPA structure, containing a carboxyl group at their focal point (**Figure 1.14**).[109] The dendrons were functionalized with a promesogenic unit and coumarin or pyrene moieties. The aim of this work was to obtain materials with potential applications in organic electronics by exploiting the LC properties as a tool to organize these functional dendrimers. However, their performance was limited due to the dynamic nature of hydrogen bonding which broke down as temperature increased. Moreover, the flexible external bisMPA-based dendrons avoided obtaining columnar organizations and only lamellar phases were observed.

To overcome all these limitations, we planned the synthesis of a new family of multifunctional discotic dendrimeric LCs that consist of a porphyrin central core covalently linked to four dendritic structures, derived from 3,4,5-trialkoxicarboxylic acid, bearing coumarin moieties (**Figure 2.1**). Porphyrin metalation has a marked effect on the photophysical properties and therefore the Cu^{2+} and Zn^{2+} derivatives were also prepared. In addition, coumarin functional units were chosen to

* Published in: A. Concellón, M. Marcos, P. Romero, J. L. Serrano, R. Termine & A. Golemme. Not Only Columns: High Hole Mobility in a Discotic Nematic Mesophase Formed by Metal-Containing Porphyrin-Core Dendrimers. *Angew. Chem. Int. Ed.* **2017,** *56*, 1259-1263.
This work was carried out in collaboration with Prof. Attilio Golemme (University of Calabria, Italy) during a 3 months stay financed by MINECO (EEBB-I-15-09927).

introduce luminescent and hole transporting properties. In this section, we report the synthesis, chemical and physical characterization of these systems with the aim of assessing their possible use in the preparation of organic electronic devices.

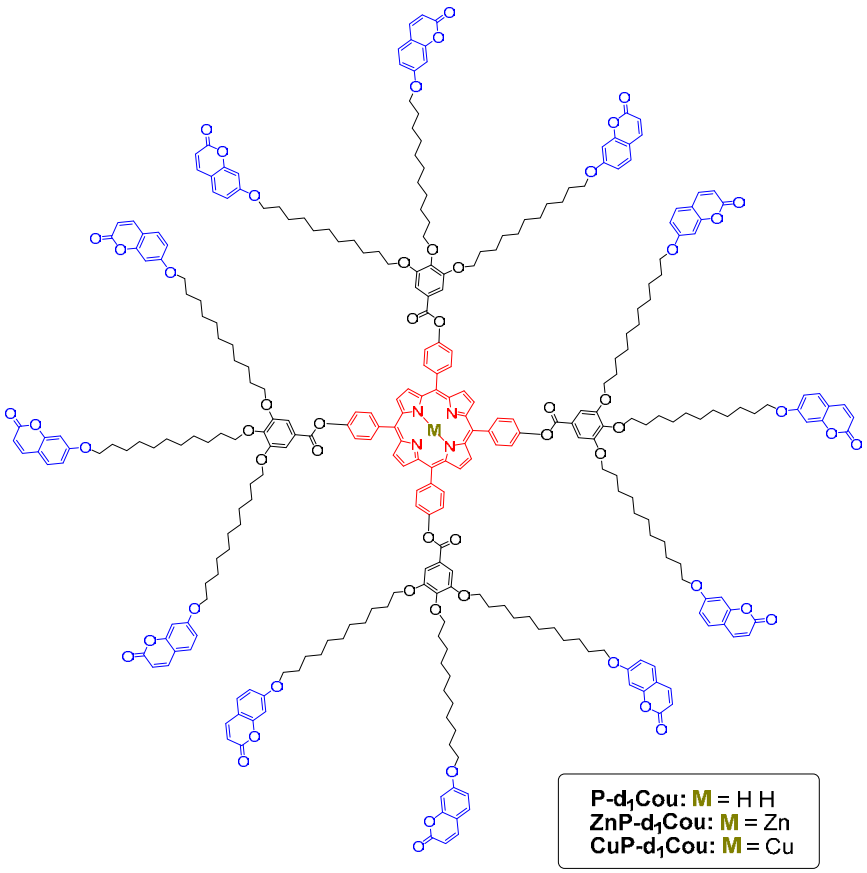

Figure 2.1 Chemical structure of the porphyrin-core dendrimers.

2.2 Results and Discussion

2.2.1 Synthesis and Structural Characterization

The dendron containing coumarin units (**d_1Cou**) was obtained following the synthetic methodology given in **Scheme 2.1**. In the first step umbelliferone was alkylated with 11-bromo-1-undecanol under standard Mitsunobu etherifications conditions to yield **1**. Subsequent etherification with methyl gallate under Williamson conditions yielded **2**. **d_1Cou** was obtained by alkaline hydrolysis of the methyl ester group of **2**.

The porphyrin-core dendrimer **P-d_1Cou** was synthesized by Steglich esterification using *meso*-tetra(*p*-hydroxyphenyl)porphine (**P-OH**) and dendron **d_1Cou** (3 equiv. per phenol group) (**Scheme 2.1**). Thin layer chromatography was not sufficient for monitoring the progress of the reaction because some of the partially functionalized cores exhibit an *Rf* value similar to that of the fully functionalized product. Therefore, MALDI-TOF mass spectroscopy was used to monitore the reaction. The free-base porphyrin-core dendrimer **P-d_1Cou** was quantitatively metalated by dissolving the macromolecule and the corresponding salt in methanol-chloroform (1:1) and heating at reflux overnight. Confirmation of the metalation was provided by NMR and MALDI-TOF mass spectroscopy. The MALDI-TOF mass spectra showed the expected peak and no other signals corresponding to dendrimers with a partial metalation were detected. The ^{1}H NMR spectrum of the product containing Zn^{2+} (**ZnP-d_1Cou**) no longer exhibited the characteristic signal at around δ= -3 ppm of the two protons located inside the porphyrin ring of the free-base starting material (**Figure 2.2**). The NMR spectrum of the dendrimer containing Cu^{2+} (**CuP-d_1Cou**) was not measured because of the paramagnetism of this metal ion.

The chemical structures of all the compounds were confirmed by IR spectroscopy, one-dimensional ^{1}H and ^{13}C NMR spectroscopy (**Figure 2.2**, and **Figures 6.1-6.4**) and two-dimensional ^{1}H-^{1}H COSY, DOSY, ^{1}H-^{13}C HSQC and ^{1}H-^{13}C HMBC experiments, MALDI-TOF mass spectroscopy (**Figure 6.25**) and elemental analysis.

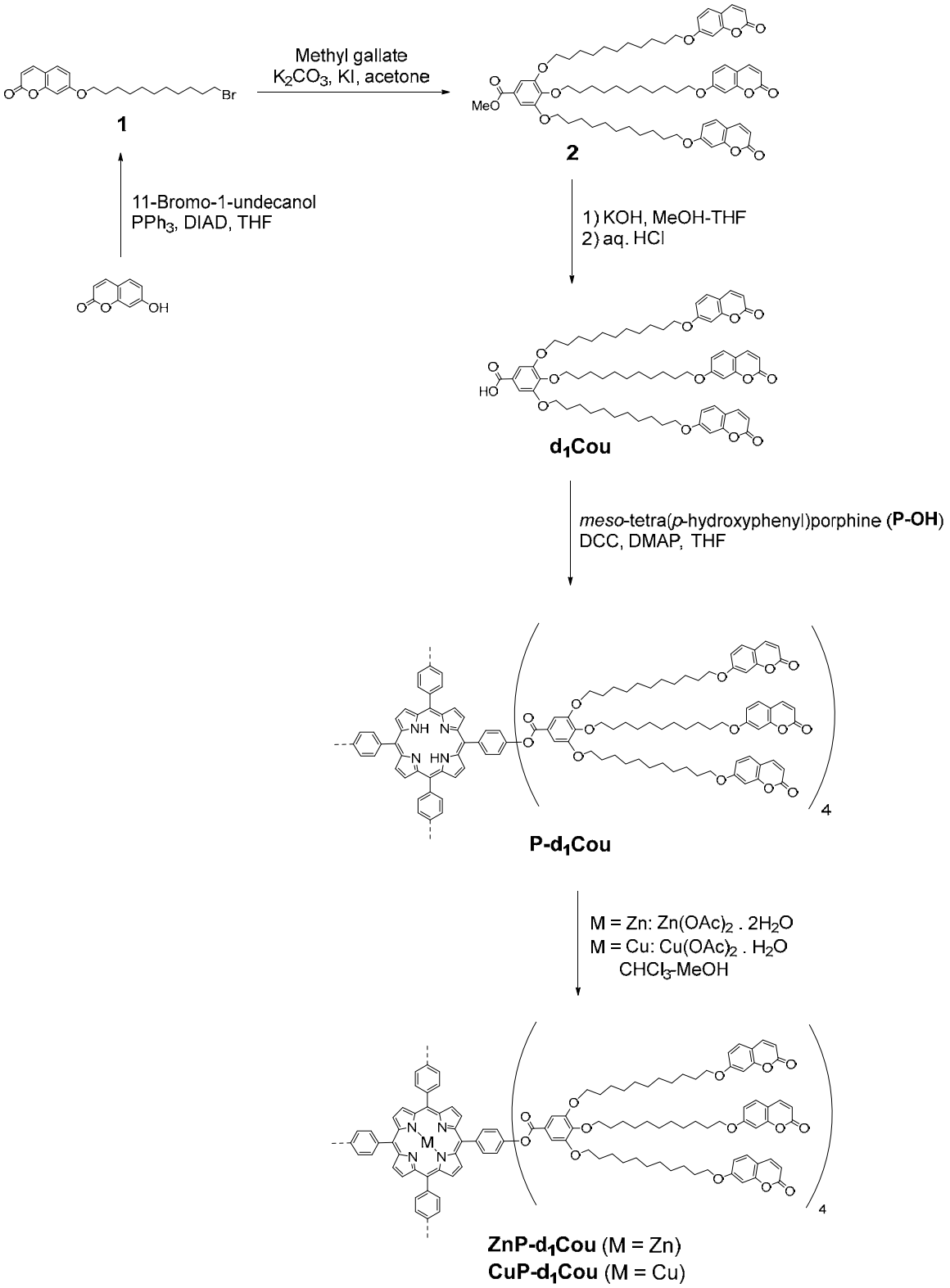

Scheme 2.1 Synthetic route of the porphyrin-core dendrimer with coumarin units and their metal complexes.

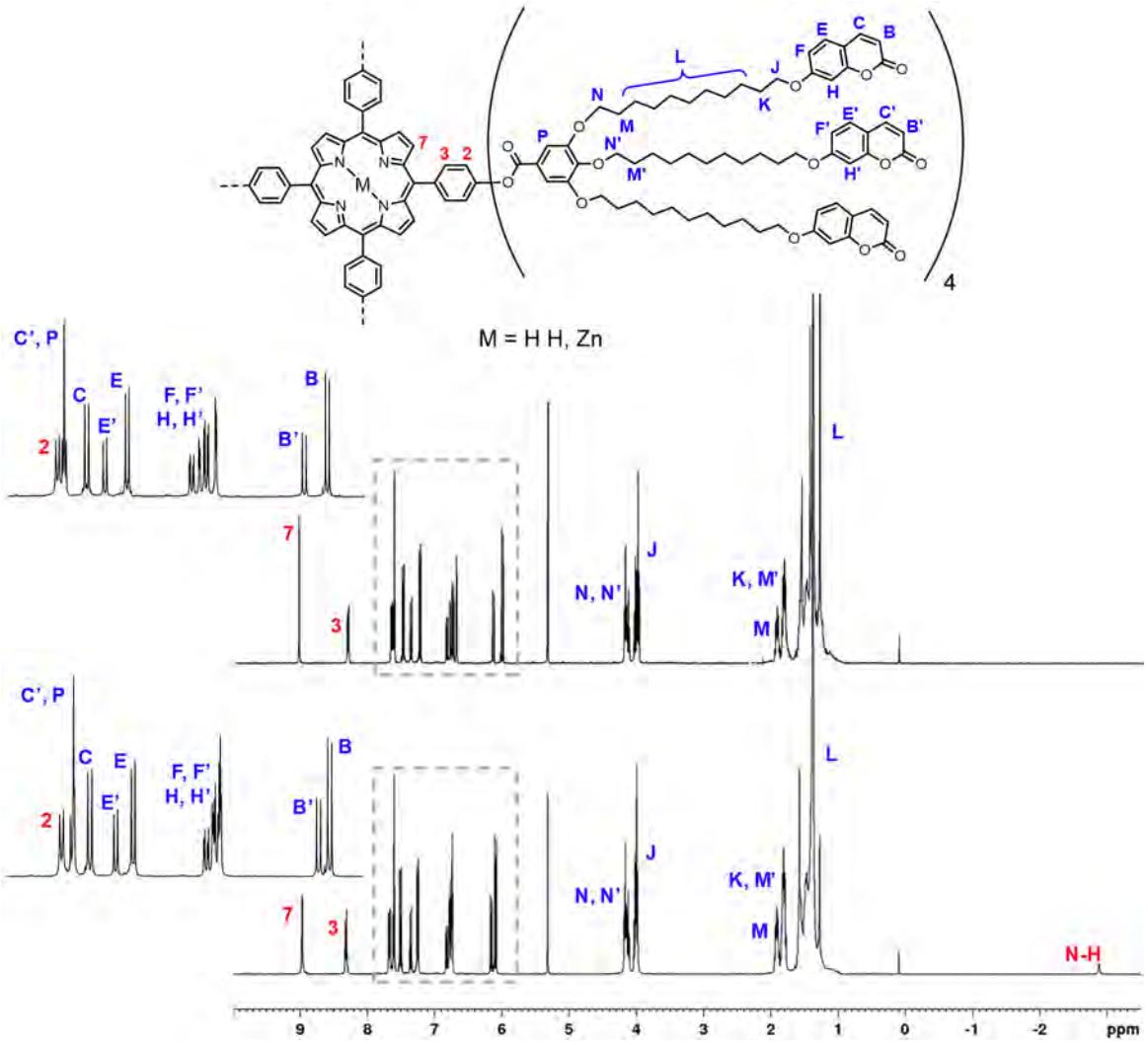

Figure 2.2 ^{1}H NMR spectra (400 MHz, CD_2Cl_2) of **P-d$_1$Cou** (bottom) and **ZnP-d$_1$Cou** (top).

2.2.2 Thermal Stability and Liquid Crystalline Properties

The thermal stability was studied by thermogravimetric analysis (TGA). All the samples showed good thermal stability and in all cases the 2% weight loss temperature ($T_{2\%}$) was detected more than 100 °C above the clearing point (**Table 2.1**). Thermal transitions and mesomorphic properties were studied by polarized optical microscopy (POM) and differential scanning calorimetry (DSC) and the results are listed in **Table 2.1**.

Table 2.1 Thermal properties.

	$T_{2\%}$ (°C)[a]	Phase transitions[b]
d_1Cou	242	g 28 (-32.4) Cr 89 (71.5) I
P-d_1Cou	232	g 16 N_D 61[c] I
ZnP-d_1Cou	271	g 11 N_D 74[c] I
CuP-d_1Cou	215	g 17 N_D 73[c] I

[a] Temperature at which 2% mass lost is detected in the thermogravimetric curve.

[b] DSC data of the second heating process at a rate of 10 °C/min. Temperatures are read at the maximum of the corresponding peak, and enthalpies (kJ/mol) are in brackets. g: glass, Cr: crystal, N_D: nematic discotic mesophase, I: isotropic liquid.

[c] POM data.

The DSC curves of free-base and metal porphyrin-core dendrimers showed only a glass transition (**Figure 2.3a**). All the compounds displayed enantiotropic liquid crystalline mesophases from room temperature. The clearing temperatures were established from POM observations because transition peaks were not detected in DSC curves. Due to their tendency to homeotropic alignment, the mesophase was observed by POM on applying mechanical stress to the samples (**Figure 2.3b**).

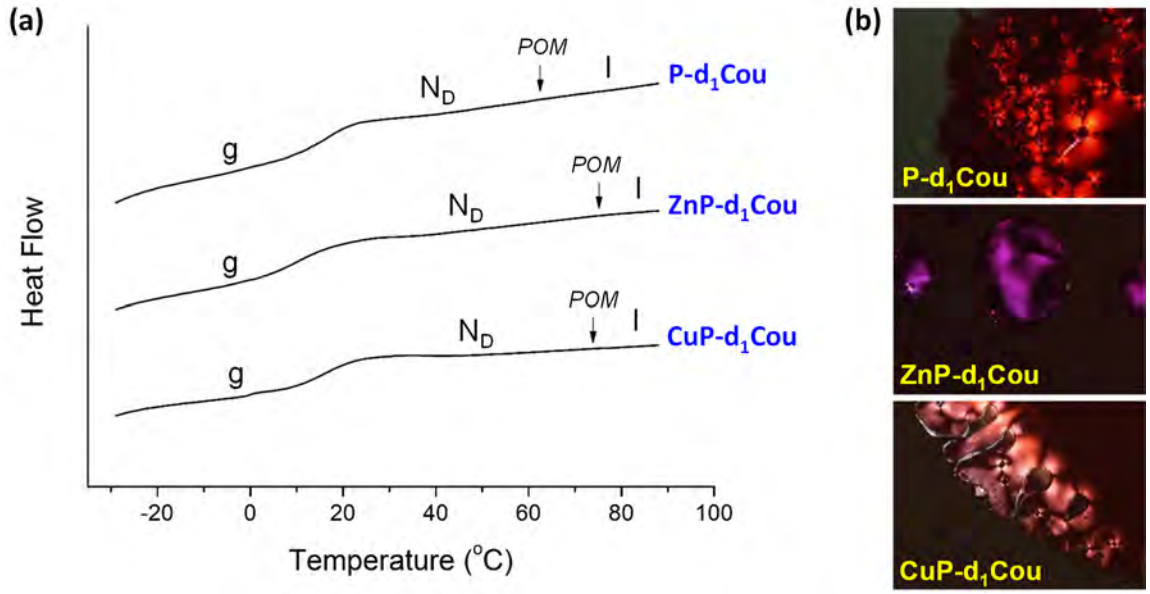

Figure 2.3 (a) DSC traces corresponding to the second heating scan for the porphyrin-core dendrimers (10 °C/min, Exo down). **(b)** POM microphotographs observed in the cooling process at room temperature after applying mechanical stress.

The incorporation of Zn^{2+} and Cu^{2+} into the porphyrins enhanced the thermal stability of mesophases, raising their clearing temperatures by 10–15°C. The enhanced interactions between neighboring porphyrins is believed to be responsible for this improvement, as metalation has been shown to increase both the rigidity of the porphyrin rings and their electrostatic attraction.[96, 101]

The nature of the mesophase was identified by XRD. The diffractograms recorded for all porphyrin-core dendrimers showed only diffuse scattering in the low-angle region owing to the lateral disk-disk distance (**Figure 2.4**). In the high-angle region a broad diffuse halo was observed and this is related to the conformational disorder of the liquid-like hydrocarbon chains. These patterns, along with the POM textures shown in **Figure 2.3b**, are consistent with a nematic discotic (N_D) mesophase, which has only orientational order.[228, 229] Indeed, the absence of Bragg reflections and the presence of only diffuse reflections indicate that there is no periodical order and thus the presence of columnar structures can be ruled out.

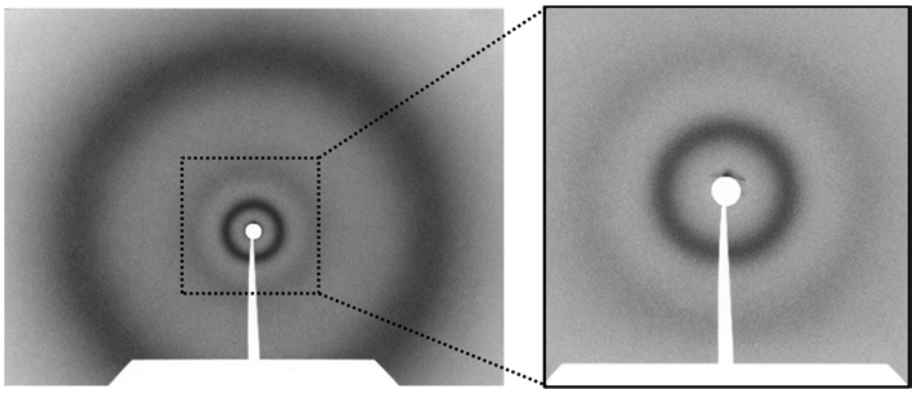

Figure 2.4 Room temperature XRD patterns of **CuP-d$_1$Cou** in the N_D mesophase: complete (left) and low-angle region (right).

2.2.3 Absorption and Emission Properties

The UV-Vis absorption and fluorescence spectra of porphyrin-core dendrimers were collected on dilute solutions (10^{-5} to 10^{-7} M) in dichloromethane (DCM) and in thin films. Relevant data are presented in **Table 2.2**.

Table 2.2 Photophysical data in DCM solutions and in thin film.

		λ_{abs} (nm) *Coumarin*	λ_{abs} (nm) *Soret band*	λ_{abs} (nm) *Q-bands*	λ_{em} (nm) *Coumarin*	λ_{em} (nm) *Q (0–1)*	λ_{em} (nm) *Q (0–2)*	ϕ_F[a]	ϕ_{ET}
P-d$_1$Cou	*DCM*	320	420	516, 551, 591, 646	384	650	713	0.07	15%
	film	319	427	520, 556, 594, 651	–[b]	656	722	–	–
ZnP-d$_1$Cou	*DCM*	320	423	550, 592	383	600	642	0.12	17%
	film	320	434	562, 603	–[b]	605	649	–	–
CuP-d$_1$Cou	*DCM*	320	417	540	382	–[b]	–[b]	0.00	20%
	film	317	424	544	–[b]	–[b]	–[b]	–	–

[a] The ϕ_F values were calculated from DCM solutions with tetraphenylporphyrin (0.11 in benzene) as a standard, excitation at 420 nm.

[b] Not detectable.

The UV-Vis absorption spectra of the free-base porphyrin-core dendrimer (**P-d$_1$Cou**) in DCM included four Q-bands in the region of 500–700 nm, the Soret band at 420 nm, and the peripheral coumarin units at 320 nm (**Figure 2.5a**). In general terms, the absorption of **P-d$_1$Cou** in solution was, within experimental error, a combination of the spectra of the corresponding building blocks, and this implies no conjugation effect between the two chromophores (**Figure 2.5a**). After complexation with metal ions, the number of Q-bands was modified and the absorption frequencies were red-shifted due to the increased molecular symmetry of metal complexes (**Figure 2.5b**). Thin solid films of these compounds were prepared by casting DCM solutions onto quartz substrates. The absorption bands for the porphyrin-core dendrimers in solid films exhibited a bathochromic shift of about 7–13 nm in relation to those in solution, due to the aggregation effect.

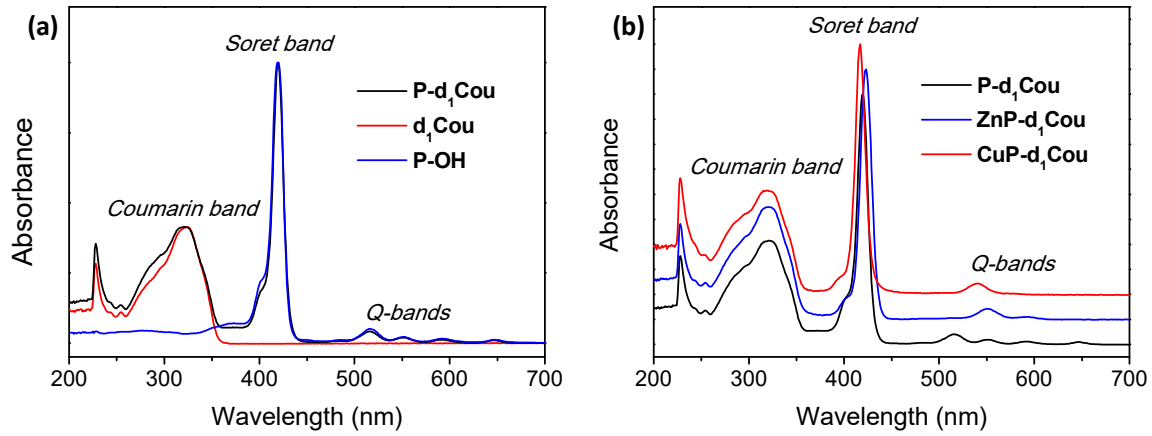

Figure 2.5 UV-Vis absorption spectra in DCM solution

The fluorescence emission spectra of the free-base porphyrin-core dendrimer

(**P-d$_1$Cou**) in DCM, obtained at an excitation wavelength (λ_{exc}) of 420nm, consisted of two bands at 650 nm (Q(0–1)) and at 712 nm (Q(0–2)) (**Figure 2.6a**). After complexation with Zn^{2+}, the emission spectrum exhibited hypsochromic shifts of about 50 nm. In contrast, the copper porphyrin displayed no fluorescence emission, as expected, considering the paramagnetism of the Cu^{2+} ion.[101] The fluorescence quantum yields (ϕ_F) of the porphyrin-core dendrimers were also measured with tetraphenylporphyrin (ϕ_F= 0.11 in benzene) as a standard, obtaining low quantum yield values. Moreover, the fluorescence spectra were recorded in thin film. Compared to the data from DCM solutions, the emission Q(0–1) and Q(0–2) peaks are red-shifted ca. 5–10 nm (**Figure 2.6a**).

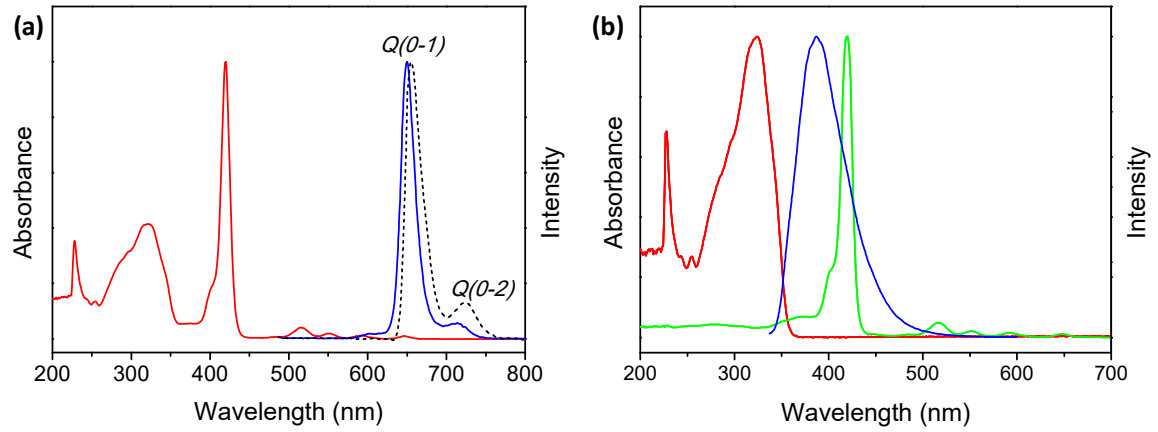

Figure 2.6 (a) UV-Vis absorption spectra in DCM solution (red line) and emission spectra (λ_{exc} = 420 nm) in DCM solution (blue line) and in thin film (dashed line) of **P-d$_1$Cou**. **(b)** UV-Vis absorption spectra of **d$_1$Cou** (red line), UV-Vis absorption spectra of **P-OH** (green line) and emission spectra of **d$_1$Cou** (blue line).

The absorption and fluorescence spectra for **d$_1$Cou** and **P-OH** are shown in **Figure 2.6b**. There is a partial overlap of the **P-OH** absorption spectrum (λ_{abs}= 420 nm) and **d$_1$Cou** emission spectrum (λ_{em}= 388 nm). In the present porphyrin-core dendrimers, the porphyrin unit serves as an acceptor whereas multiple coumarin donors are present in the dendrimer periphery. When coumarin donors were excited selectively (λ_{exc}= 320 nm), emission from both the coumarin units and the porphyrin acceptor was observed, thus demonstrating that fluorescence resonance energy-transfer (FRET) was facile but not quantitative in these systems (**Figure 2.7**). Intramolecular energy transfer occurs from coumarin moieties to the porphyrin core (antenna effect), despite the low degree of overlap between the emission spectrum of the donor and the absorption spectrum of the acceptor (**Figure 2.6b**). FRET efficiencies (ϕ_{ET}) were calculated by comparing the donor emission in the presence of the acceptor relative to that in the absence of the acceptor, and moderate ϕ_{ET} values were obtained.

The fluorescence spectra at an excitation wavelength of 320 nm were also recorded in thin film and compared to the data from DCM solutions; almost no residual emission of the coumarin moieties was observed (**Figure 2.7**). This finding demonstrates that FRET from coumarin units to the porphyrin core is more efficient in thin film than in DCM solution. This behavior probably reflects the fact that in the solid state the porphyrin-core dendrimers are in the N_D mesophase and this forces the porphyrin ring to be within the same plane as the coumarin units, leading to enhanced electronic communication with this arrangement.[230]

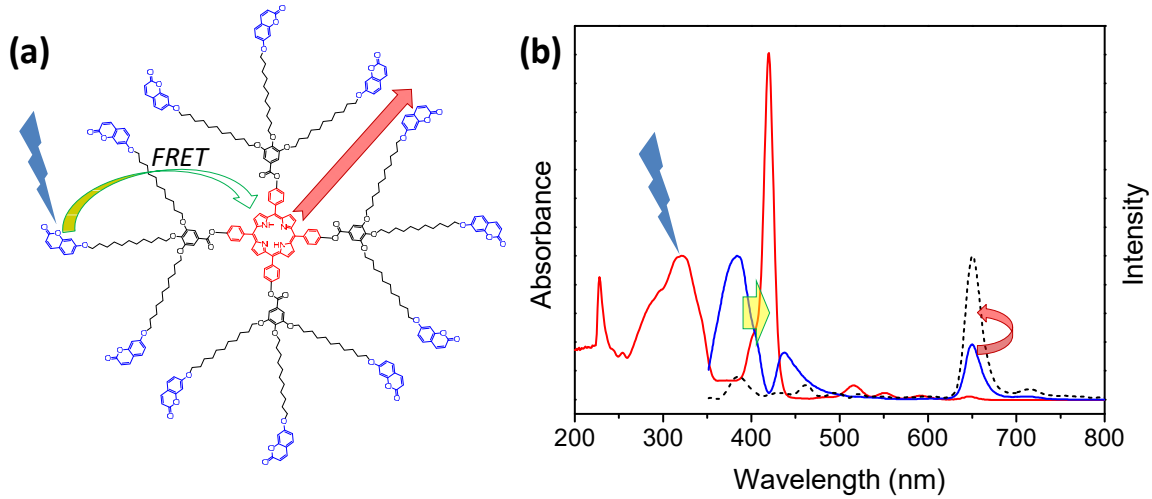

Figure 2.7 (a) Schematic representation of intramolecular energy transfer in the porphyrin-core dendrimers, **(b)** UV-Vis absorption spectra in DCM solution (red line) and emission spectra (λ_{exc} = 320 nm) in DCM solution (blue line) and in thin film (dashed line) of **P-d$_1$Cou**.

2.2.4 Electrochemical and Charge Transport Properties

To investigate the feasibility of electron- and hole-injection processes in these new porphyrin-core dendrimers, cyclic voltammetry (CV) measurements were carried out. All the porphyrin-core dendrimers exhibited similar cyclic voltammograms that show that these compounds can be easily oxidized. However, meaningful reduction processes were not detected. The HOMO and LUMO energy levels referred to the vacuum level were estimated by combining electrochemical and optical data. The values are summarized in **Table 2.3**

The charge carrier mobilities of the porphyrin-core dendrimers were measured by using the space charge-limited current (SCLC) technique. In such measurements, substances are sandwiched between two electrodes, with one of them injecting charges of a given sign (ohmic contact) while the other one should be non-injecting for charges of the opposite sign.[35] Considering the HOMO energy values of the materials (see **Table 2.3**), gold electrodes were used as positive electrodes because its work function (W_{Au}≈ -5.1 eV) matches the HOMO values and thus ensures the formation of an ohmic contact. As a counter-electrode, indium tin oxide (ITO) was used because its work function (W_{ITO}≈ -4.6 eV) is significantly lower than the estimated LUMO energy values (see **Table 2.3**) and because being transparent allows to check the macroscopic orientation by POM. All the cells were filled by capillarity by heating the material above the isotropic liquid transition. After sample filling, the cells were cooled down to room temperature.

Table 2.3 Electrochemical parameters and hole mobilities at room temperature.

	E_{ox} (V)[a]	E_{HOMO} (eV)[b]	λ_{edge} (nm)[c]	ΔE_g (eV)[d]	E_{LUMO} (eV)[e]	$\mu_{0,hole}$ ($cm^2V^{-1}s^{-1}$)	$\beta/10^{-2}$ ($cm^{0.5}V^{-0.5}$)	$\mu_{hole(at\ E=5\ V/\mu m)}$ ($cm^2V^{-1}s^{-1}$)
P-d$_1$Cou	0.94	-5.26	592.0	2.09	-3.17	5×10^{-10}	2.5	1.2×10^{-7}
ZnP-d$_1$Cou	0.61	-4.93	554.5	2.24	-2.69	0.12	1.0	1.10
CuP-d$_1$Cou	0.88	-5.20	545.7	2.27	-2.93	0.03	1.1	0.34

[a] Onset potential for the first oxidation process.

[b] $E_{HOMO} = -(E_{ox} - E_{1/2,\ FOC} + 4.8)\ eV$.

[c] Intersection of the normalized UV-Vis absorption spectrum and the fluorescence spectrum.

[d] Optical band gap, calculated by $\Delta E_g = hc/\lambda_{edge}$.

[e] $E_{LUMO} = E_{HOMO} + \Delta E_g$

A typical double logarithmic plot of the current density (*J*) versus applied voltage (*V*) is shown in **Figure 2.8a**. All materials showed ohmic behavior at low voltages with a typical linear relationship. At higher voltages, for which the current becomes space-charge-limited, a quadratic relationship was observed. In the SCLC region the mobility could be calculated from the modified Mott-Gurney equation:[231]

$$J = \frac{9}{8}\varepsilon_0\varepsilon_r\mu_0 \exp\left(\beta\sqrt{\frac{V}{d}}\right)\frac{V^2}{d^3}$$

in which *J* is the measured current density, μ_0 is the zero-field charge mobility, ε_0 is the free-space permittivity, ε_r is the relative dielectric constant of the material, *V* is the applied voltage, *d* is the thickness of the device and β is a constant describing the field dependence of the mobility. Within this model, the mobility is expressed as:[232]

$$\mu = \mu_0 \exp\left(\beta\sqrt{\frac{V}{d}}\right)$$

and the two parameters μ_0 and β can be extracted from fits of the SCLC sections of the experimental data. The resulting hole mobility values are summarized in **Table 2.3**. The effect of the presence of the metal on charge mobility is dramatic and can be seen by comparing the mobilities of the compounds at an applied field *E*= 5 $V\cdot\mu m^{-1}$, within the range of the SCLC sections of the experimental *J*-*V* curves. In fact, the metal-porphyrin derivatives exhibit a hole mobility 6–7 orders of magnitude higher than the metal-free porphyrin, which shows a very low μ_{hole} value (1.2×10^{-7} $cm^2\cdot V^{-1}\cdot s^{-1}$). Regardless of the presence of the metal, these porphyrin-core dendrimers showed a strong tendency to orient with their short molecular axes perpendicular to the substrate. That is, without any surface treatment the alignment of the director was perfectly homeotropic for all compounds (with the director perpendicular to the plane of the substrates; dark view observed by POM between crossed polarizers). This situation rules out the possibility that the large difference in mobility associated with metalation is due to a difference in macroscopic orientational order. The hole mobility of **CuP-d$_1$Cou** in the N_D mesophase was also measured at different temperatures, while an SCLC regime was not observed when experiments were performed in the isotropic phase. The mobility was constant within experimental error up to 25–30 ºC below the N_D–I

transition and then it gradually decreased with increasing temperature as the isotropic transition was approached (**Figure 2.8b**). Such gradual decrease is probably associated with the very weakly first order nature of the N_D–I transition.

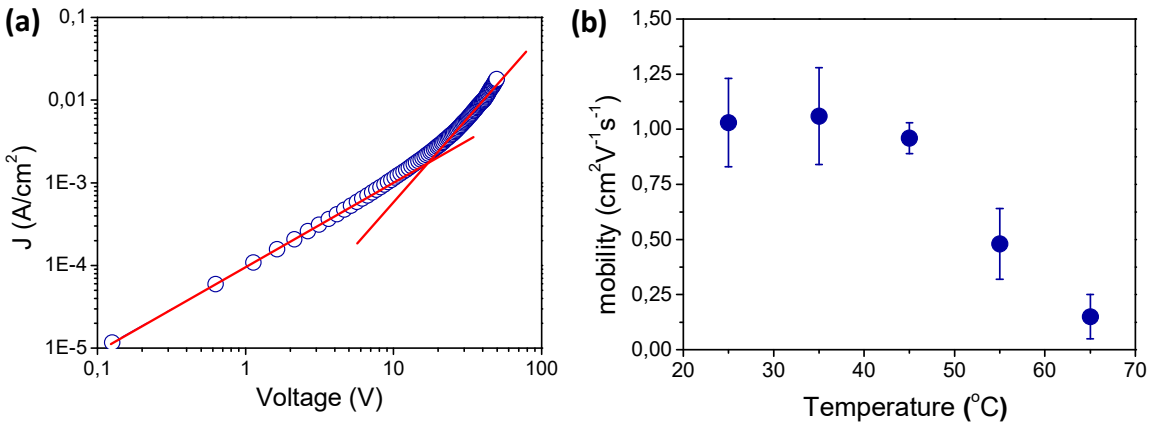

Figure 2.8 (a) Typical *J-V* curve for a 8.8 µm thick **CuP-d$_1$Cou** (circles represent experimental data and the two continuous lines represent the ideal linear and quadratic dependence of *J* on *V*). **(b)** Temperature dependence of mobility for a 9.3 µm thick sample of **CuP-d$_1$Cou** (these data are taken over the best performing area of the sample).

In order to check the injecting performance of the gold electrodes and to exclude ionic contributions to the measured currents, cells with one gold electrode and one aluminum electrode were prepared. In these cells, the measured mobilities were within the range observed in samples with gold/ITO electrodes when the positive voltage was applied on the gold side. However, in measurements with the positive voltage on the aluminum side, currents were 6-7 orders of magnitude lower and an SCLC regime was not observed. Therefore, ionic currents are negligible and their effect can be excluded.

To our knowledge, the hole mobility values measured for these metal porphyrin-core dendrimers are the highest ever reported for nematic discotic phases.[233] In fact, the charge carrier mobility values obtained for **ZnP-d$_1$Cou** and **CuP-d$_1$Cou** are comparable to the highest values described to date in the more ordered hexagonal columnar mesophases.[63, 64] In columnar phases, the high mobility values are commonly rationalized in terms of the high charge transfer rates allowed within the stack by the π-π intermolecular interactions between the cores of neighboring molecules. However, the phase structure of the N_D phase does not exhibit any long-range columnar order, and this leaves an open question as to why such a high mobility is observed in the N_D phases formed by **ZnP-d$_1$Cou** and **CuP-d$_1$Cou** that,

given the data illustrated above, must be connected with metalation. A certain degree of short-range columnar order cannot be excluded but, given the lack of influence of metalation on the XRD patterns, a direct influence of metalation on the orientational properties can be excluded. It seems instead more reasonable to invoke either or both 1) a direct involvement of the metal in the charge transfer through metal-metal or metal-nitrogen intermolecular interactions and 2) an increase in the transfer integral owing to the metal-induced variation of the ring shape, leading to stronger intermolecular interactions, as also suggested by the increase in the clearing temperature with metalation. The decisive influence that metalation has on the physical properties of some LC derivatives has been reported in previous works, although in many cases it is not possible to propose a plausible explanation for the experimental results.[98, 234-236] The data presented in this work do not allow further conclusions to be drawn regarding this important issue, and more experimental and theoretical investigations are required.

2.3 Conclusions

In conclusion, we have prepared a new family of disk-like liquid crystalline dendrimers with a porphyrin core and luminescent coumarin units at the periphery. All of the porphyrin-core dendrimers display a nematic discotic mesophase and are stable up to 200 ºC. It has also been demonstrated that excitation of coumarin moieties leads to energy transfer to the luminescent porphyrin core. Despite the fact that the compounds exhibit a nematic discotic phase, the charge mobility values measured in the metal-porphyrin derivatives are among the highest reported for discotic mesogens to this date, including the values observed in the much more ordered columnar phases. In their nematic discotic phases, the studied compounds show a high tendency to form large homogeneously oriented domains, with very low density of defects and scattering losses, as observed by POM. In addition, the compounds have a high viscosity and a good processability and, in this respect, they are quite similarly to thermoplastic polymers. For the reasons outline above, the results described in this work could open a new way to the design of organic materials for optoelectronic applications.

3. LIQUID CRYSTALLINE DENDRITIC METALLOPORPHYRINS *VIA* CLICK CHEMISTRY: LIGHT-HARVESTING AND HOLE-TRANSPORTING SYSTEMS[†]

3.1 Objectives

Although the preparation of dendrimers has been improved over the past decades, their synthesis requires extremely efficient reactions. 'Click' chemistry, introduced into the field of materials chemistry by Sharpless, provides efficient routes for the synthesis of dendrimers.[237-239] Among the wide variety of 'click' reactions described to date, the copper-catalyzed azide-alkyne "click" cycloaddition (CuAAC) has been widely used for the synthesis of several dendrimeric architectures as it requires mild reaction conditions and simple work-up procedure, tolerates a wide range of functional groups, and leads to high yields.[240-243]

In Section 2 we have described a new family of LC dendrimers which consist of a porphyrin core and luminescent coumarin units at the periphery. In spite of exhibiting good charge transport properties, the synthetic methodology followed for their preparation gave only low yields and their purification was very tedious. Therefore, the aim of the work reported in this section was to exploit 'click' chemistry as an effective and elegant approach for the preparation of LC dendrimers with potential applications in organic optoelectronic devices.

Herein, we have described a new approach which allows us to connect four azido functionalized dendrons with an alkyne functionalized porphyrin core. This strategy gives high yields and resulted in products that can be easily purified by non-chromatographic procedures. What's more, the new triazole groups introduce an additional electronic density which may increase the conductive properties.[73]

Following this synthetic approach, four porphyrin-core dendrimers have been synthetized and their chemical structure are shown in **Figure 3.1**. Two of them are

[†] Published in: A. Concellón, M. Marcos, P. Romero, J. L. Serrano, R. Termine & A. Golemme. Light-harvesting and hole-transporting systems based on liquid crystalline dendritic metalloporphyrins formed via 'click' chemistry. *In preparation* **2018**; A. Concellón, M. Marcos, P. Romero, J. L. Serrano, R. Termine & A. Golemme. High efficient artificial light-harvesting antenna with a porphyrin-core dendrimer with fluorinated coumarins as peripheral units. *In preparation* **2018**.
This work was carried out in collaboration with Prof. Attilio Golemme (University of Calabria, Italy) during a 3 months stay financed by MINECO (EEBB-I-15-09927).

the first- and second-generation dendrimers bearing coumarin moieties (**ZnP-*t*-d$_1$Cou** and **ZnP-*t*-d$_2$Cou**). The third porphyrin-core dendrimer is synthesized in an attempt to enhance the antenna effect efficiency, thus we introduce a chemical modification in the peripheral coumarin units (**ZnP-*t*-d$_1$Cou-CF$_3$**). The fourth porphyrin-core dendrimer is prepared to evaluate the role of coumarin peripheral units in these supermolecular systems. It is formed by a first-generation dendron cointaining dodecyloxy alkyl chains without coumarin moieties (**ZnP-*t*-d$_1$C12**).

In this section, we report the synthesis, characterization and mesomorphic properties of these porphyrin-core dendrimers. In addition, their physical properties were studied by absorption and emission spectroscopy, cyclic voltammetry and charge transport experiments.

Nomenclature: the porphyrin core dendrimers are denoted as **ZnP-*t*-d$_n$X** where:

- **n** indicates the generation of the dendron (n =1: first generation dendron, n = 2: second generation dendron).
- **X** represents the functional dendron (X = Cou: dendron containing coumarin units, X = Cou-CF$_3$: dendron containing fluorinated-coumarin units, and X = C12: dendron cointaining dodecyloxy alkyl chains).
- ***t*** refers to the triazole moiety which links the dendron and the porphyrin core.

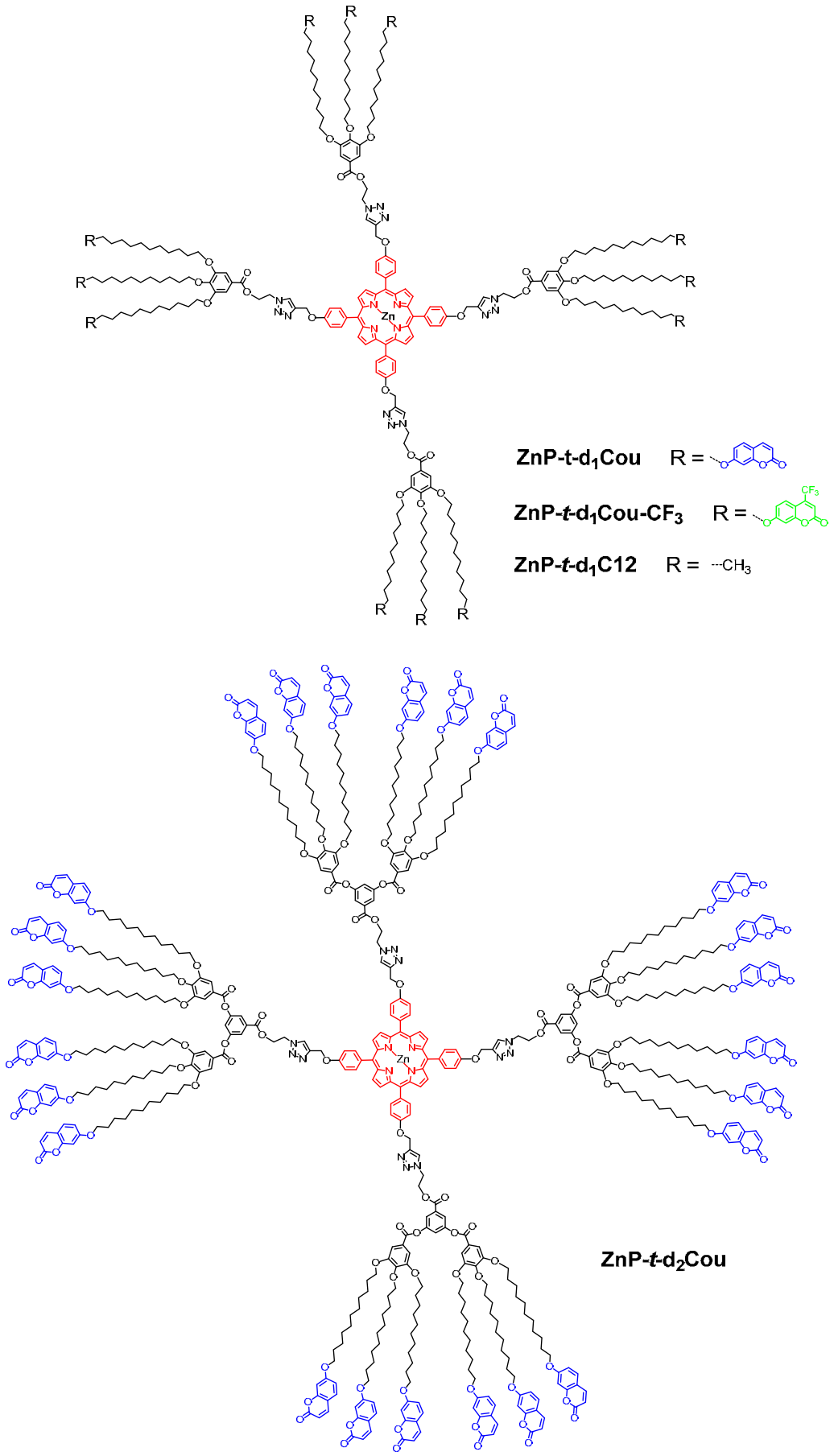

Figure 3.1 Chemical structure of the porphyrin-core dendrimers prepared by 'click' chemistry.

3.2 Results and discussion

3.2.1 Synthesis and Structural Characterization

The synthesis of the alkyne functionalized porphyrin core (**ZnP-YNE**) was carried out following a previously reported procedure.[244] The azido functionalized dendrons (**N_3-d_1Cou**, **N_3-d_2Cou**, **N_3-d_1Cou-CF_3** and **N_3-d_1C12**) were obtained following the synthetic methodology given in **Scheme 3.1**.

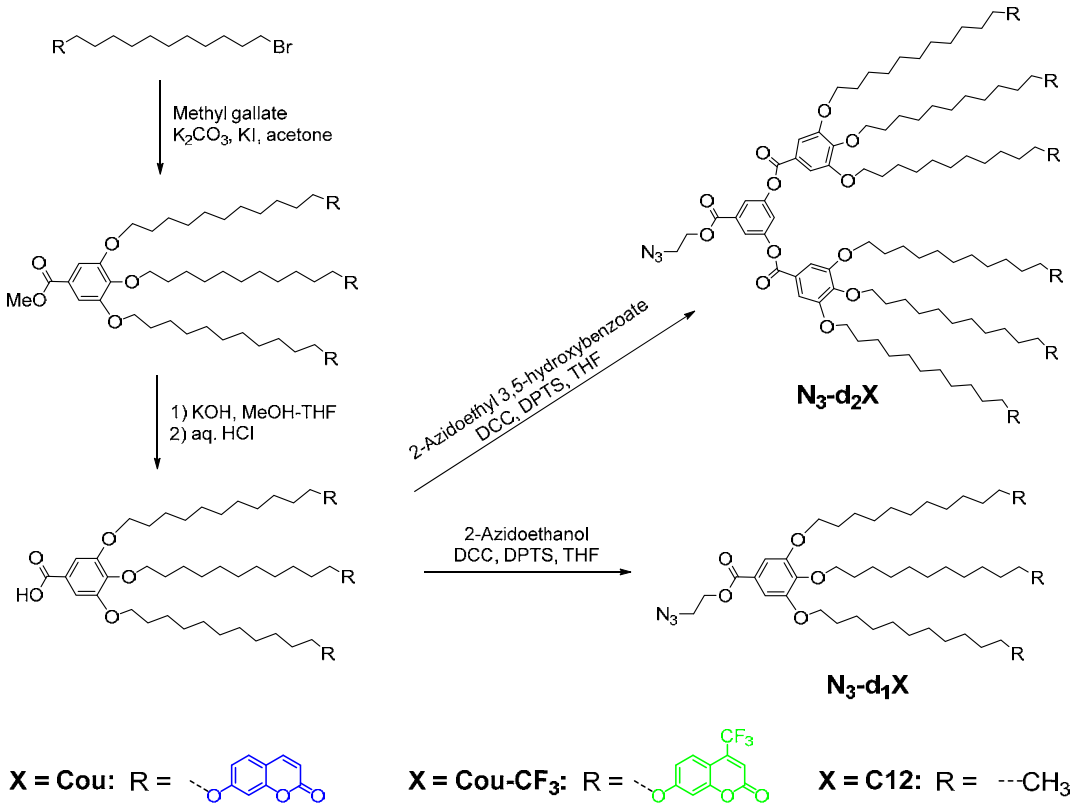

Scheme 3.1 General synthetic approach used for the preparation of the azido functionalized dendrons.

In the final synthetic step, the azido functionalized dendrons and the alkyne functionalized porphyrin were coupled by CuAAC using THF/water as solvent and $CuSO_4 \cdot 5H_2O$/sodium ascorbate as the catalytic system (**Scheme 3.2**). An excess of the azide dendron (1.5 equivalents per alkyne group) was employed to ensure the completeness of the reaction and was removed using a previously synthesized alkyne-functionalized Wang resin. The efficiency of the CuAAC coupling was determined by FTIR, NMR spectroscopy (**Figures 6.5-6.18**), MALDI-TOF MS (**Figures 6.26-6.29**), and size exclusion chromatography (SEC).

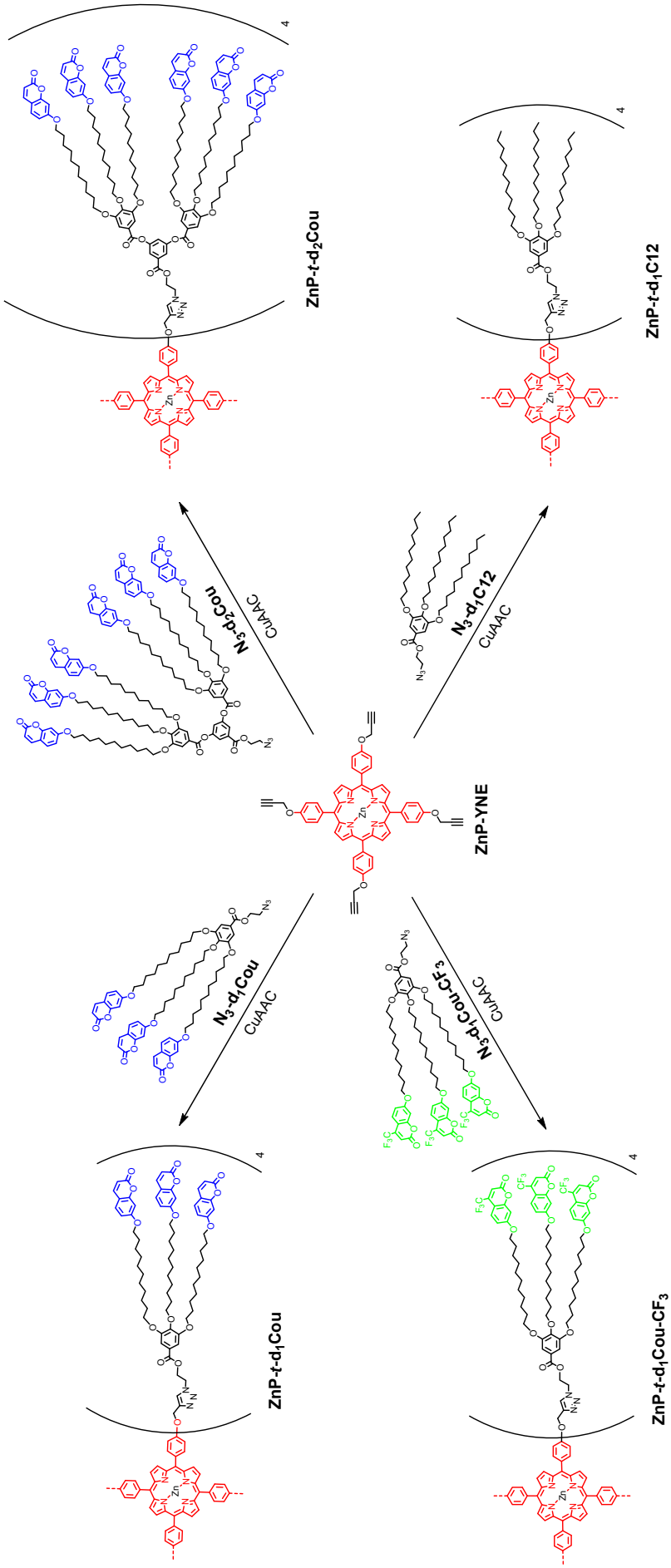

Scheme 3.2 Convergent synthetic approach used for the preparation of the porphyrin-core dendrimers (CuAAC: $CuSO_4{\cdot}H_2O$, sodium ascorbate, THF/H_2O)

FTIR spectra confirmed the coupling, the bands at around 3280 (≡C-H), 2120 (C≡C) and 2110 (N_3) disappeared after the CuAAC reaction (**Figure 3.2a**). Further confirmation of the coupling was provided by SEC analysis and MALDI-TOF mass spectroscopy. The MALDI-TOF mass spectra showed the expected peak and no other signals corresponding to dendrimers with a partial functionalization were detected (**Figure 3.2b**). The SEC curves showed monomodal molar mass distributions and residual precursors were not detected (**Figure 3.2c**). As can be observed, CuAAC coupling of the precursor blocks gave rise to a shift of the molar mass distribution towards lower retention times that indicates the porphyrin-core dendrimer's formation.

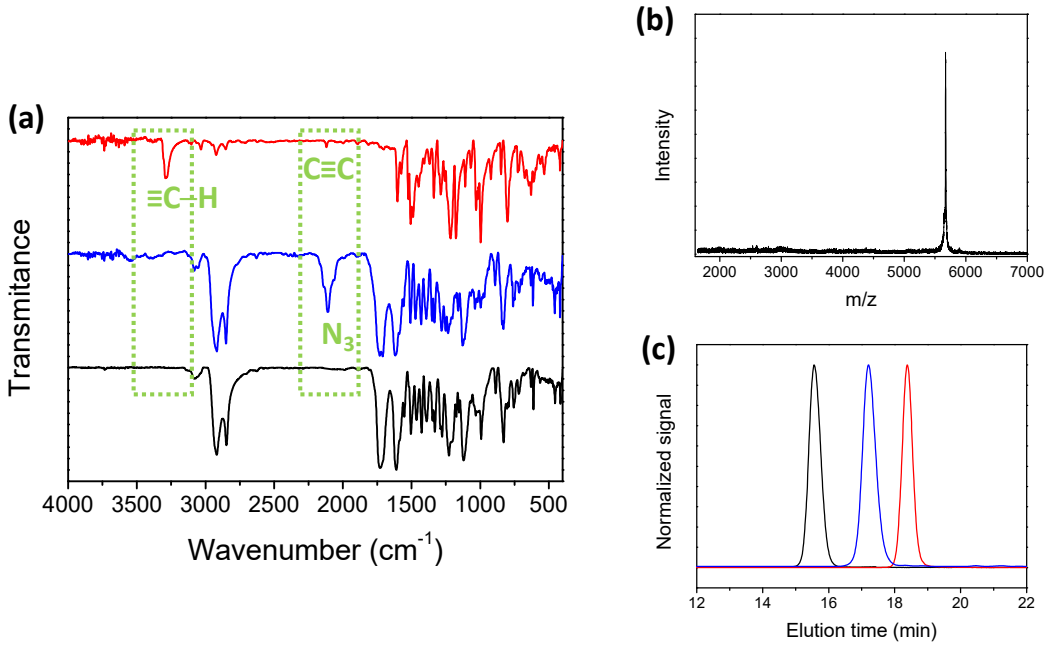

Figure 3.2 (a) FTIR spectra of **ZnP-YNE** (red), **ZnP-*t*-d$_1$Cou** (black) and **N$_3$-d$_1$Cou** (blue). **(b)** MALDI mass spectrum of **ZnP-*t*-d$_1$Cou**. **(c)** SEC traces of: **ZnP-YNE** (red), **ZnP-*t*-d$_1$Cou** (black) and **N$_3$-d$_1$Cou** (blue).

Further evidence for the formation of the dendrimers was collected from ^{1}H NMR spectra (**Figure 3.3**), where new peaks corresponding to the newly formed triazol ring appeared at around 7.95 ppm (H_V) and the ethynyl proton signal of the alkyne functionalized porphyrin core disappeared upon CuAAC coupling. Furthermore, there were changes in the shift of the methylenic protons linked to the newly formed triazol (H_U and H_T).

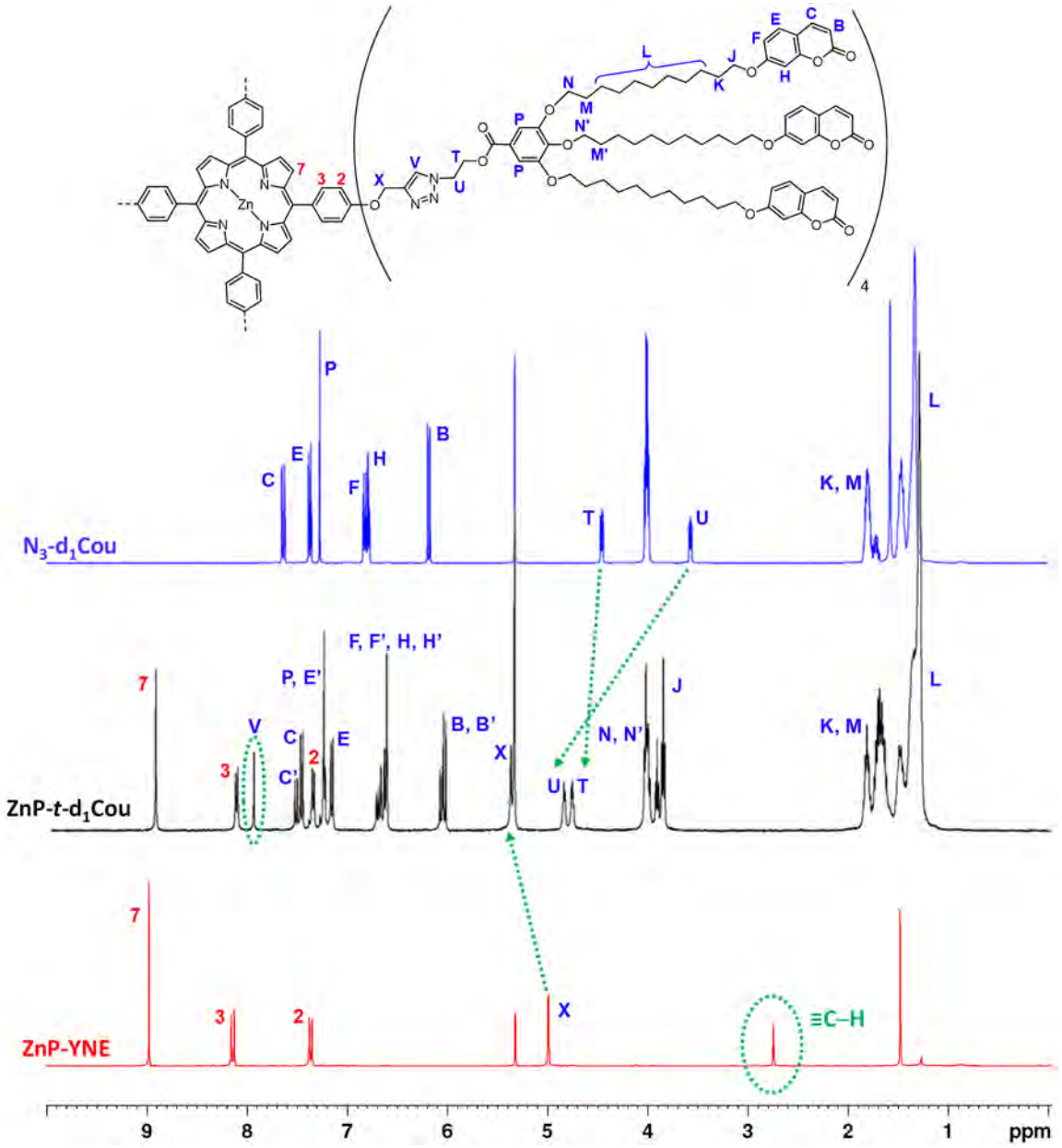

Figure 3.3 ^{1}H NMR spectra (400 MHz, CD_2Cl_2, 298K) of: **ZnP-YNE** (red), **ZnP-*t*-d$_1$Cou** (black) and **N$_3$-d$_1$Cou** (blue).

3.2.2 Thermal Stability and Liquid Crystalline Properties

The thermal stability of all the compounds were studied by TGA. All of the samples showed good thermal stability with the 2% weight loss temperature more than 150 °C above the clearing point (**Table 3.1**). Thermal transitions and mesomorphic properties were studied by POM, DSC and XRD, and the results are listed in **Table 3.1**. Three cycles were carried out in DSC experiments and data were taken from

the second cycle. In some cases, temperatures were taken from POM observations because transition peaks were not detected in DSC curves.

Table 3.1 Thermal properties.

	$T_{2\%}$ (°C)[a]	Phase transitions[b]
N_3-d_1Cou	213	g 20 (-14.9) Cr (63.9) 61 I
N_3-d_2Cou	230	g 11 N 73[c] I
N_3-d_1Cou-CF_3	190	g -16 SmA 59[c] I
N_3-d_1C12	241	Cr 30 (19.8) I
ZnP-*t*-d_1Cou	344	g 24 N_D 112[c] I
ZnP-*t*-d_2Cou	309	g 21 N_D 98[c] I
ZnP-*t*-d_1Cou-CF_3	305	g 9 N_D 69[c] I
ZnP-*t*-d_1C12	335	g 122 (-15.55) Cr 151[c] M 155[c] I

[a] Temperature at which 2% mass lost is detected in the thermogravimetric curve.
[b] DSC data of the second heating process at a rate of 10 °C/min. Temperatures are read at the maximum of the peak, and enthalpies (kJ/mol) are in brackets. g: glass, Cr: crystal, N: nematic mesophase, N_D: nematic discotic mesophase, M: unidentified mesophase, I: isotropic liquid.
[c] POM data.

Only two azido functionalized dendrons, **N_3-d_2Cou** and **N_3-d_1Cou-CF_3**, exhibited LC behavior. The other azido functionalized dendrons (**N_3-d_1Cou** and **N_3-d_1C12**) were not mesomorphic. **N_3-d_2Cou** showed a birefringent texture by POM at room temperature on applying mechanical stress (**Figure 3.4a**). The XRD pattern showed only diffuse scattering, suggesting the absence of long-range positional order in the LC phase (**Figure 3.4b**). This kind of pattern corresponds to a nematic mesophase.

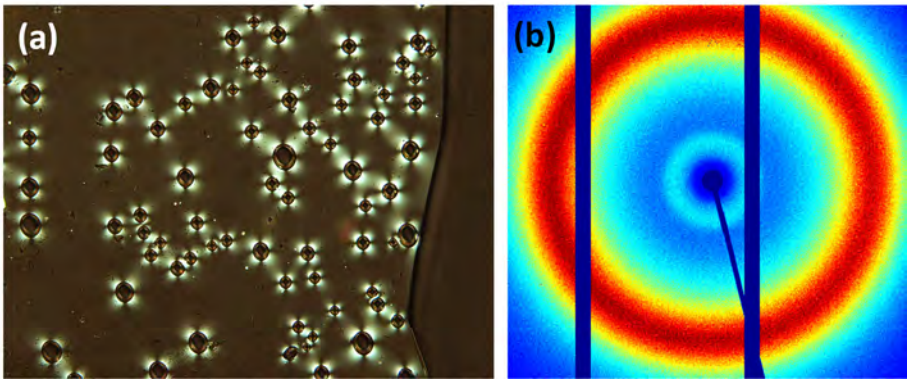

Figure 3.4 (a) POM microphotograph of **N_3-d_2Cou** taken at room temperature in the second cooling process. **(b)** XRD pattern of **N_3-d_2Cou.**

In the case of **N_3-d_1Cou-CF_3**, it showed a enantiotropic smectic A mesophase (**Figure 3.5a**). The XRD pattern consisted of a diffuse halo in the high-angle region and one sharp strong maxima in the small-angle region (**Figure 3.5b**). This maximum is assigned to the first order reflection of the smectic layers and it was used to deduce the layer spacing by applying Bragg's law. The diffuse halo is related to the conformational disorder of the liquid-like chains. This kind of pattern corresponds to a smectic A organization, given the orthogonal character of the mesophase deduced from the presence of homeotropic domains in the textures observed by POM (**Figure 3.5a**). The experimentally measured layer thickness (40.8 Å) was significantly larger than the molecule length in its most extended conformation (28.6 Å). This suggests that the mesophase adopts a bilayer structure.

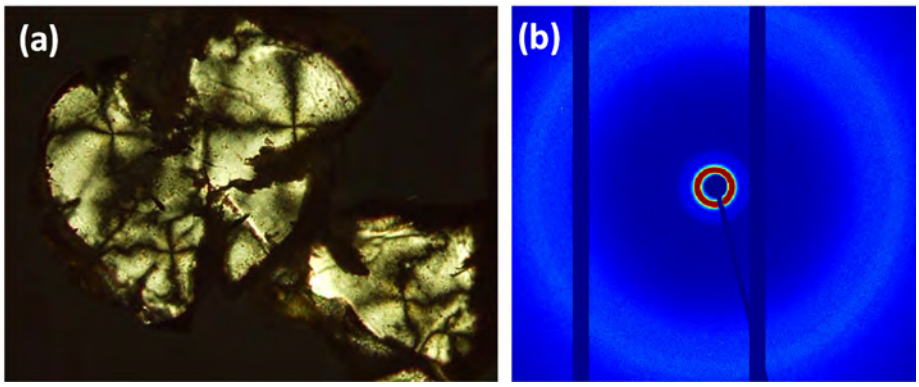

Figure 3.5 (a) POM microphotograph of **N_3-d_1Cou-CF_3** taken at room temperature in the second cooling process. **(b)** XRD pattern of **N_3-d_1Cou-CF_3**.

All the porphyrin-core dendrimers exhibited mesogenic properties and the thermal behavior was different depending on the compound. In the case of the porphyrin-core dendrimers with coumarin functional units around the porphyrin core (**ZnP-*t*-d_1Cou**, **ZnP-*t*-d_2Cou** and **ZnP-*t*-d_1Cou-CF_3**), they displayed enantiotropic LC mesophases. The DSC curves showed only a glass transition freezing the mesomorphic order at room temperature, while clearing temperatures were established from POM observations. All the compounds had a high tendency to homeotropic alignment and the mesophase was observed by POM on applying mechanical stress to the samples showing birefringent textures (**Figure 3.6**).

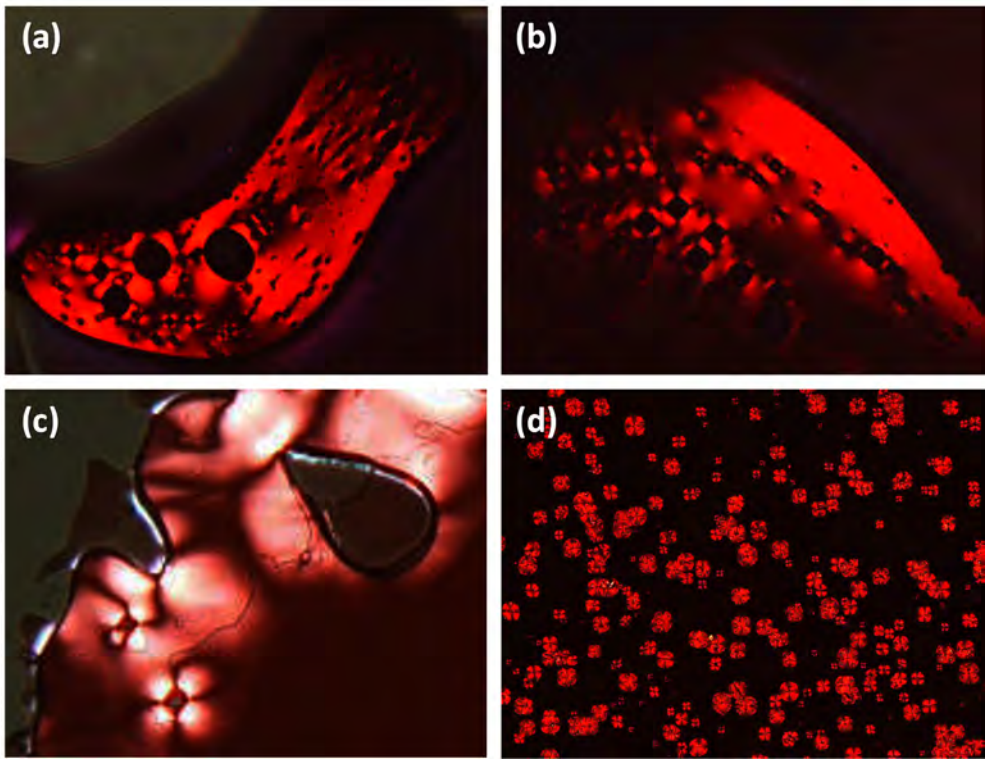

Figure 3.6 POM microphotographs of: **(a) ZnP-t-d_1Cou** taken at room temperature in the second cooling process, **(b) ZnP-t-d_2Cou** taken at room temperature in the second cooling process, **(c) ZnP-t-d_1Cou-CF_3** taken at room temperature in the second cooling process, and **(d) ZnP-t-d_1C12** at 152 °C in the second heating process.

Assignment of mesophase type was carried out by XRD (**Figure 3.7**). The XRD pattern recorded for **ZnP-*t*-d_1Cou** showed one diffuse reflection in the low-angle region. It corresponds to intra and intermolecular interactions between porphyrin units and approximates the diameter of the porphyrin core (26 Å). In the high-angle region a broad diffuse halo was detected at 4.5 Å which corresponds to short-range correlations between the conformationally disordered alkyl chains. On the other hand, the XRD pattern of **ZnP-*t*-d_2Cou** and **ZnP-*t*-d_1Cou-CF_3** only showed diffuse scattering in the low-angle region and in the high-angle region a broad diffuse halo was detected, corresponding to a mean distance of about 4.5 Å. All the obtained XRD patterns were consistent with N_D mesophases.[228, 229]

With **ZnP-*t*-d_1C12**, the DSC curve showed an exothermic peak at 122 °C (cold crystallization) and an endothermic peak corresponding both to the crystal-to-mesophase transition and the transition from mesophase to isotropic liquid. These two transitions were observed by POM and detected as only one endothermic peak in the DSC which corresponds to the sum of the two transition peaks, so the nature of the mesophase could not be identified by XRD.

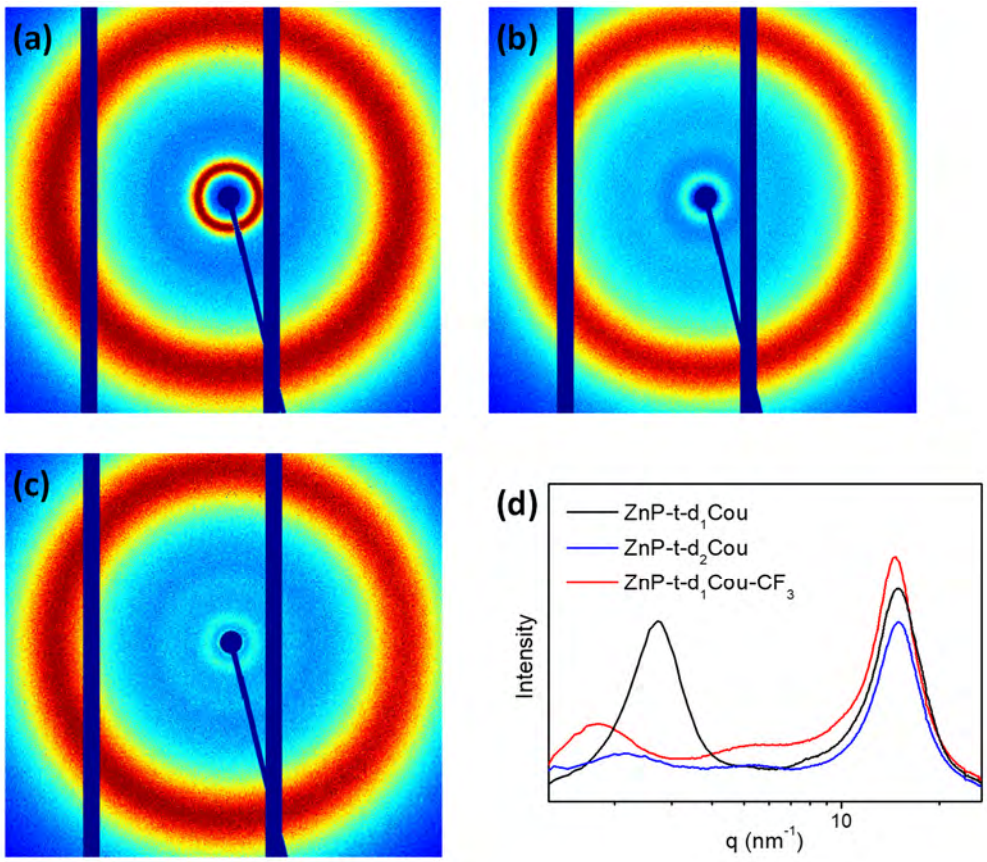

Figure 3.7 (a) XRD pattern of **ZnP-*t*-d$_1$Cou**, **(b)** XRD pattern of **ZnP-*t*-d$_2$Cou**, **(c)** XRD pattern of **ZnP-*t*-d$_1$Cou-CF$_3$**, and **(d)** 1D XRD profiles.

3.2.3 Absorption and Emission Properties

The UV-Vis absorption and fluorescence spectra of porphyrin-core dendrimers were collected on dilute solutions (10^{-5} to 10^{-7} M) in DCM and in thin film. Relevant data are presented in **Table 3.2**. The UV-Vis absorption spectra of the four porphyrin-core dendrimers in DCM are, within experimental error, a combination of the spectra of the corresponding azido functionalized dendron and the alkyne functionalized porphyrin. Thin solid films of these compounds were prepared by casting DCM solutions onto quartz substrates. The absorption bands for the porphyrin-core dendrimers in thin films exhibited a bathochromic shift of about 10 nm in relation to those in solution, due to the aggregation effect.

Table 3.2 Photophysical data in DCM solutions and in thin film.

		λ_{abs} (nm) *Coumarin*	λ_{abs} (nm) *Soret band*	λ_{abs} (nm) *Q-bands*	λ_{em} (nm) *Coumarin*	λ_{em} (nm) *Q (0–1)*	λ_{em} (nm) *Q (0–2)*	ϕ_F[a]	ϕ_{ET}
ZnP-*t*-d$_1$Cou	*DCM*	322	426	552, 595	383	603	643	0.12	16%
	film	322	434	562, 603	–[b]	605	649	–	–
ZnP-*t*-d$_2$Cou	*DCM*	321	427	552, 594	383	601	642	0.11	23%
	film	322	436	563, 604	–[b]	605	648	–	–
ZnP-*t*-d$_1$Cou-CF$_3$	*DCM*	336	424	552, 593	–[b]	600	645	0.09	92%
	film	334	438	566, 608	–[b]	610	648	–	–
ZnP-*t*-d$_1$C12	*DCM*	–	417	540	–	600	644	0.14	–
	film	–	424	544	–	611	650	–	–

[a] The ϕ_F values were calculated from DCM solutions with tetraphenylporphyrin (0.11 in benzene) as a standard, excitation at 420 nm.

[b] Not detectable.

The fluorescence emission spectra of the four porphyrin-core dendrimers (λ_{exc}= 425 nm) consisted of two bands with a Q(0–1)-band at around 600 nm and a Q(0–2)-band at around 645 nm. The fluorescence quantum yields of the porphyrin-core dendrimers were also measured with tetraphenylporphyrin (ϕ_F= 0.11 in benzene) as a standard, which led to low quantum yield values. The fluorescence spectra were also recorded in thin films. Compared to the data from DCM solutions, the emission Q(0–1) and Q(0–2) peaks are red-shifted ca. 5–10 nm.

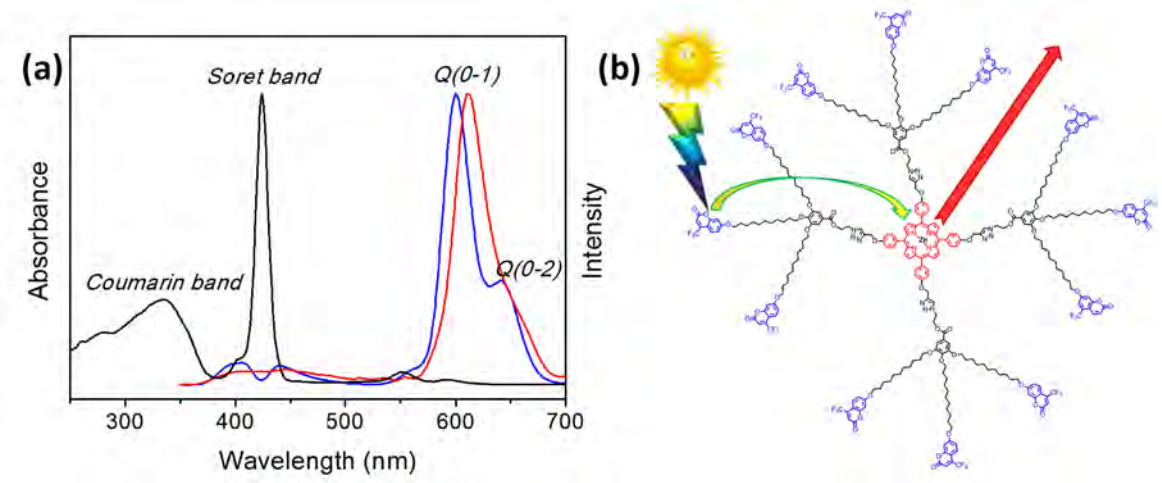

Figure 3.8 (a) UV-Vis absorption spectra in DCM solution (black line) and emission spectra (λ_{exc}= 340 nm) in DCM solution (blue line) and in thin film (red line) of **ZnP-*t*-d$_1$Cou-CF$_3$**. **(b)** Schematic representation of **ZnP-*t*-d$_1$Cou-CF$_3$** intramolecular energy transfer.

When coumarin units were excited at 320 nm for **ZnP-*t*-d$_1$Cou** and **ZnP-*t*-d$_2$Cou** and 335 nm for **ZnP-*t*-d$_1$Cou-CF$_3$**, significant fluorescence emission is observed with the porphyrin, while the fluorescence of the coumarins was suppressed (**Figure 3.8a**). This indicates that energy transfer from coumarins donors to the porphyrin acceptor occurs efficiently. The ϕ_{ET} values were calculated by comparing the donor emission in the presence of the acceptor relative to that in the absence of the acceptor and are summarized in **Table 3.2**. These results indicate that light energy collected by peripheral coumarin chromophores is transfered to the porphyrin core (**Figure 3.8b**). Therefore, **ZnP-*t*-d$_1$Cou-CF$_3$** is an efficient light-harvesting antenna (ϕ_{ET}= 92%), with the porphyrin acting as the energy trap. By contrast, in the fluorescence spectra of **ZnP-*t*-d$_1$Cou** and **ZnP-*t*-d$_2$Cou** obtained by exciting at 320 nm, emission from both the coumarin units and the porphyrin was observed, demonstrating that energy transfer from the coumarin moiety to the porphyrin core is less efficient than that of **ZnP-*t*-d$_1$Cou-CF$_3$**. This result is in agreement with one of the principles of resonance energy transfer: ϕ_{ET} increases with increasing

spectral overlap between the absorption spectrum of the acceptor and the emission spectrum of the donor (**Figure 3.9**).

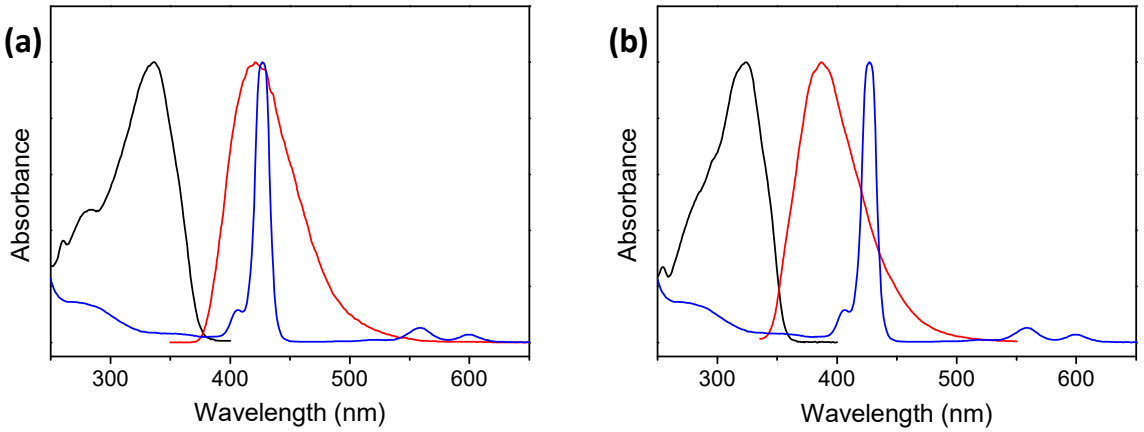

Figure 3.9 (a) UV-Vis absorption spectra of **N_3-d_1Cou-CF_3** (black line), UV-Vis absorption spectra of **ZnP-YNE** (blue line), and emission spectra of **N_3-d_1Cou-CF_3** (red line). **(b)** UV-Vis absorption spectra of **N_3-d_1Cou** (black line), UV-Vis absorption spectra of **ZnP-YNE** (blue line), and emission spectra of **N_3-d_1Cou** (red line).

The fluorescence spectra at excitation wavelength of 320 or 335 were also recorded in thin film and compared to the data from DCM solutions; almost no residual emission of the coumarin moieties was observed (**Figure 3.8a**). Energy transfer from coumarin units to the porphyrin core is more efficient in thin film than in solution.[230]

3.2.4 Electrochemical and Charge Transport Properties

Cyclic voltammetry experiments (CV) were performed to study the electrochemical properties of the porphyrin-core dendrimers. **ZnP-*t*-d_1Cou**, **ZnP-*t*-d_2Cou**, **ZnP-*t*-d_1Cou-CF_3** and **ZnP-*t*-d_1C12** exhibit similar cyclic voltammograms with reduction and oxidation processes. These results are consistent with the electron and acceptor character of the porphyrin core. The HOMO and LUMO energy levels, referred to the vacuum level have been estimated from the oxidation and reduction waves. The values are summarized in **Table 3.3**.

Table 3.3 Electrochemical parameters and hole mobilities.

	E_{ox} (V)[a]	E_{HOMO} (eV)[b]	E_{red} (V)[a]	E_{LUMO} (eV)[c]	μ_{hole} ($cm^2V^{-1}s^{-1}$)
ZnP-*t*-d$_1$Cou	0.60	-4.92	-1.33	-2.99	0.15
ZnP-*t*-d$_2$Cou	0.62	-4.94	-1.35	-2.97	0.90[d]
ZnP-*t*-d$_1$Cou-CF$_3$	0.58	-4.90	-1.31	-3.01	4.40[d]
ZnP-*t*-d$_1$C12	0.60	-4.92	-1.56	-2.76	2.0×10^{-9}

[a] Onset potential for the first oxidation/reduction process.

[b] $E_{HOMO} = -(E_{ox} - E_{1/2,\,FOC} + 4.8)$ eV.

[c] $E_{LUMO} = -(E_{red} - E_{1/2,\,FOC} + 4.8)$ eV.

[d] Lower estimation of the charge carrier mobility (measured in areas with the lowest currents).

The charge carrier mobility measurements were performed by using the space charge-limited current (SCLC) technique.[35] As explained in *Section 2.2.4*, the SCLC method was chosen by considering the HOMO energy value of the materials, which matches the work function of gold (W_{Au}≈ -5.1 eV) and thus ensures the formation of an ohmic contact. As a counter-electrode, indium tin oxide (ITO) was used because its work function (W_{ITO}≈ -4.6 eV) is significantly lower than the LUMO energy values and because being transparent allows to check the macroscopic orientation by POM. All the cells were filled by capillarity by heating the material above the isotropic liquid transition temperature. After sample filling, the cells were cooled down to room temperature. **ZnP-*t*-d$_1$Cou**, **ZnP-*t*-d$_2$Cou** and **ZnP-*t*-d$_1$Cou-CF$_3$** showed a strong tendency for homeotropic alignment. That is, without any surface treatment, the samples were perfectly oriented with their short molecular axes perpendicular to the substrate. However, cells filled with compound **ZnP-*t*-d$_1$C12**, which did not display liquid crystal properties, showed non-homeotropic alignment with large domains of various orientations.

The current-voltage curves typically exhibit a linear region at low applied voltages, where the behavior is ohmic. However, at higher voltages, where the current becomes space-charge-limited, a quadratic dependence can be observed. In this regime the current depends only on the charge carrier mobility and it is calculated from Mott-Gurney equation:[245]

$$J = \frac{9}{8}\varepsilon_0\varepsilon_r\mu\frac{V^2}{d^3}$$

where *J* is the measured current density, μ is the charge mobility, ε_0 is the free-space permittivity, ε_r is the dielectric constant of the material, *V* is the applied voltage, and *d* is the thickness of the device. From this equation, since the relative dielectric constant and the sample thickness can be easily measured, charge mobilities can be easily obtained from *J*–*V* curves. The hole mobilities values (μ_{hole}) obtained by the SCLC technique are summarized in **Table 3.3**.

Typical *J*–*V* curves were obtained for **ZnP-*t*-d$_1$Cou** and **ZnP-*t*-d$_1$C12** (**Figure 3.10**), and the resulting mobilities were 0.15 and 2.0×10^{-9} $cm^2 \cdot V^{-1} \cdot s^{-1}$, respectively. The low mobility value of **ZnP-*t*-d$_1$C12** can be explained by taking into account that this compound did not display liquid crystal properties and thus all the measurements were carried out in macroscopically disordered crystalline phases. In the case of **ZnP-*t*-d$_1$Cou**, the introduction of coumarin units around the porphyrin core contributes to the appearance of the N_D mesophase, leading to a remarkable increase of μ_{hole} by 8 orders of magnitude. However, the measured hole mobility values for **ZnP-*t*-d$_1$Cou** were of the same order of magnitude as the values measured for **ZnP-d$_1$Cou** (described in *Section 2*) which has a similar chemical structure and mesomorphic behavior.

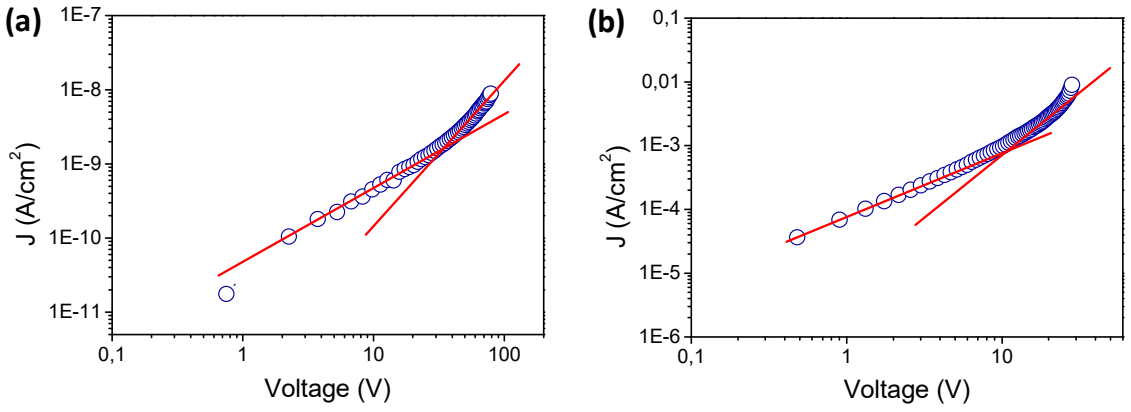

Figure 3.10 Typical *J*–*V* curves for: **(a) ZnP-*t*-d$_1$C12** and **(b) ZnP-*t*-d$_1$Cou** (circles represent experimental data and the two continuous lines represent the ideal linear and quadratic dependence of *J* on *V*).

On the other hand, very high currents were measured for **ZnP-*t*-d$_2$Cou** and **ZnP-*t*-d$_1$Cou-CF$_3$** and the mobility values reported in **Table 3.3** were obtained in areas with the lowest currents. This can be explained by taking into account that only in these areas the injected charges reach a local density high enough to enter the space-charge regime. In areas with higher mobility (higher currents), the

density of the injected charges never reaches a level high enough to obtain the space-charge regime. This means that the measured mobilities are a lower estimation of the mobility of these materials and thus the real μ_{hole} is probably one of the highest values ever reported for a non-crystalline organic material. Therefore, additional measurements are being collected with an alternative method (Hall Effect technique) in order to confirm these high charge carrier mobility values.

Although differences are not dramatic among the three liquid crystalline porphyrin-core dendrimers, **ZnP-*t*-d$_1$Cou-CF$_3$** gave the highest mobility. The difference, which is especially relevant when comparing with **ZnP-*t*-d$_1$Cou**, could be attributed to the trifluoromethyl-substitution of the peripheral coumarin units, leading to an efficient energy transfer (ϕ_{ET}= 92%, see *Section 3.2.3*) and inducing an enhanced electronic communication between the porphyrin ring and the coumarin units, with a consequent increase in charge mobility. In a similar way, a comparison between the mobilities of **ZnP-*t*-d$_2$Cou** and **ZnP-*t*-d$_1$Cou** indicates that increasing generation of the dendrimer, which results in a more efficient energy transfer due to the higher number of coumarin units around the porphyrin core, also increases the mobility.

3.3 Conclusions

We have developed a convenient and highly versatile route involving 'click' chemistry to prepare novel LC dendrimers based on a porphyrin core and different coumarin units at the periphery of the dendrimer. As we proved in analogous materials described in *Section 2*, we have found that combining a metalloporphyrin core with coumarin moieties in the same scaffold is a good strategy for the preparation of polymeric materials for optoelectronic applications.

On one hand, it has been demonstrated that excitation of coumarin donors results in energy transfer to the porphyrin central core. The efficiency of this antenna effect strongly depends on the degree of overlap between the absorption spectrum of the acceptor and the emission spectrum of the donor.

On the other hand, the supramolecular organization in nematic discotic mesophases gives high charge mobility values (of the order of 1 $cm^2 \cdot V^{-1} \cdot s^{-1}$) which show the importance of tuning the optical and electronic properties of these new LC dendrimers upon dendrimer periphery modification. In particular, determining which compound is characterized by the highest mobility can be extremely useful for understanding the relationship between charge transport properties and molecular structure, with the final goal of tuning the functional performance of the materials in organic electronic devices.

4. LIQUID CRYSTALLINE CARBAZOLE-CONTAINING PORPHYRIN-CORE DENDRIMERS WITH OPTICAL AND ELECTRONIC PROPERTIES‡

4.1 Objectives

Due to their photorefractive properties, carbazole derivatives have been used in plastic electronics since the early 2000s. The ongoing peak of interest in carbazole-containing polymers is connected mostly with their ability as efficient light-emitting diodes, charge transport and photorefractive properties.[174, 175] Furthermore, carbazole-based dendrimers have shown similar properties to polymers. However, the three-dimensional architecture of dendrimers allows additional control over the intermolecular interactions of the photoactive moieties. In this context, our research group has explored different approaches for the preparation of carbazole-containing LC dendrimers with optoelectronic applications.[198-200]

As a continuation of our research programme in this area, and taking into account the new approach for the synthesis of porphyrin-core dendrimers which has been described in Section 3, we decided the introduction of carbazole moieties around a porphyrin core. Herein, we describe the synthesis of two carbazole-containing LC porphyrin-core dendrimers that were denoted as **ZnP-*t*-d$_n$X** (**Figure 4.1**). The subscript **n** indicates the generation of the dendron (n=1: first generation dendron). The letter **X** represents the functional dendron (X = Cz: dendron containing carbazol units, X = PhCz: dendron containing phenylcarbazole units). The letter ***t*** refers to the triazole moiety which links the dendron and the porphyrin core.

The aim of the work described here was to exploit the capability of these porphyrin-core dendrimers to self-assemble into LC organizations, and the study of their electronic properties by absorption and emission spectroscopy, cyclic voltammetry and charge transport experiments.

‡ *This work was carried out in collaboration with Prof. Attilio Golemme (University of Calabria, Italy).*

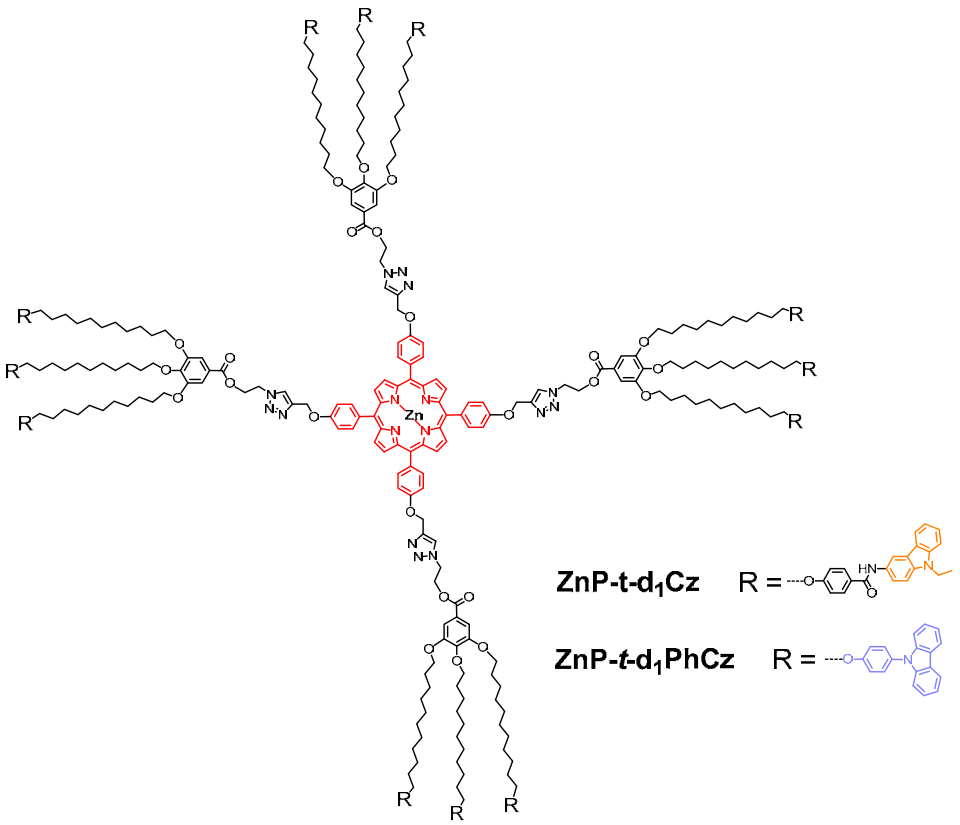

Figure 4.1 Chemical structure of the carbazole-containing porphyrin-core dendrimers.

4.2 Results and Discussion

4.2.1 Synthesis and Structural Characterization

The azido functionalized dendrons bearing carbazole units (**N_3-d_1Cz** and **N_3-d_1PhCz**) were obtained following the synthetic methodology described in Section 3 (**Scheme 3.1**). The synthesis of the porphyrin-core dendrimers with carbazole units at the periphery (**ZnP-*t*-d_1Cz** and **ZnP-*t*-d_1PhCz**) was carried out by using the same coupling strategy presented in Section 3 where first generation dendrons with an azido group at the focal point (**N_3-d_1Cz** and **N_3-d_1PhCz**) were 'click' coupled to an alkyne functionalized porphyrin (**ZnP-YNE**) by CuAAC (**Scheme 4.1**).

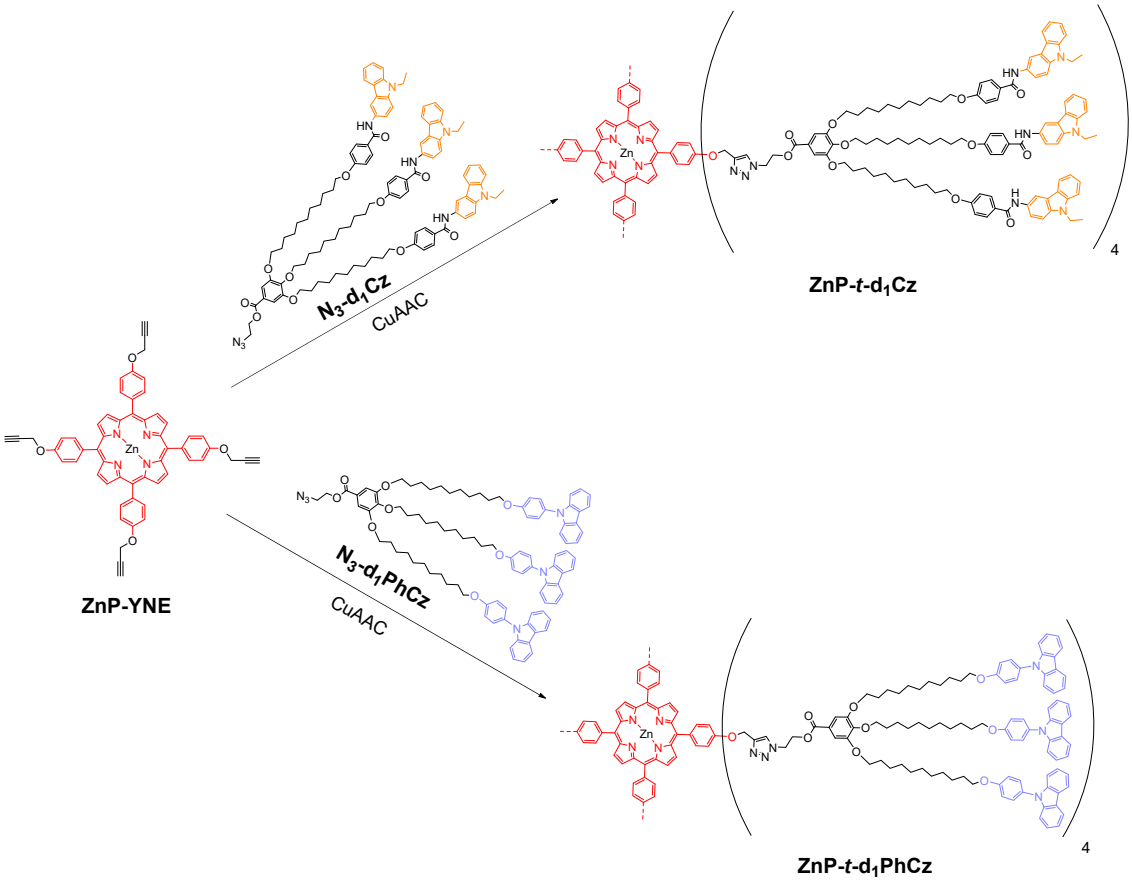

Scheme 4.1 Convergent synthetic approach used for the preparation of the porphyrin-core dendrimers (CuAAC: $CuSO_4 \cdot H_2O$, sodium ascorbate, THF/H_2O)

The chemical structures of all the compounds were confirmed by FTIR spectroscopy, one-dimensional ^1H and ^{13}C NMR spectroscopy (**Figure 4.2** and **Figures 6.19-6.24**) and two-dimensional ^1H-^1H COSY, DOSY, ^1H-^{13}C HSQC and ^1H-^{13}C HMBC experiments, MALDI-TOF mass spectroscopy (**Figures 6.30-6.31**) and

elemental analysis. For instance, **Figure 4.2** depicts the ^{1}H NMR spectra of **ZnP-*t*-d$_1$Cz** and **ZnP-*t*-d$_1$PhCz,** where new peaks corresponding to the formed triazol ring appeared at 7.5–8.5 ppm (H_M in **Figure 4.2**), and at 4.5–5.0 ppm corresponding to the methylenic protons linked to it (H_K and H_L in **Figure 4.2**).

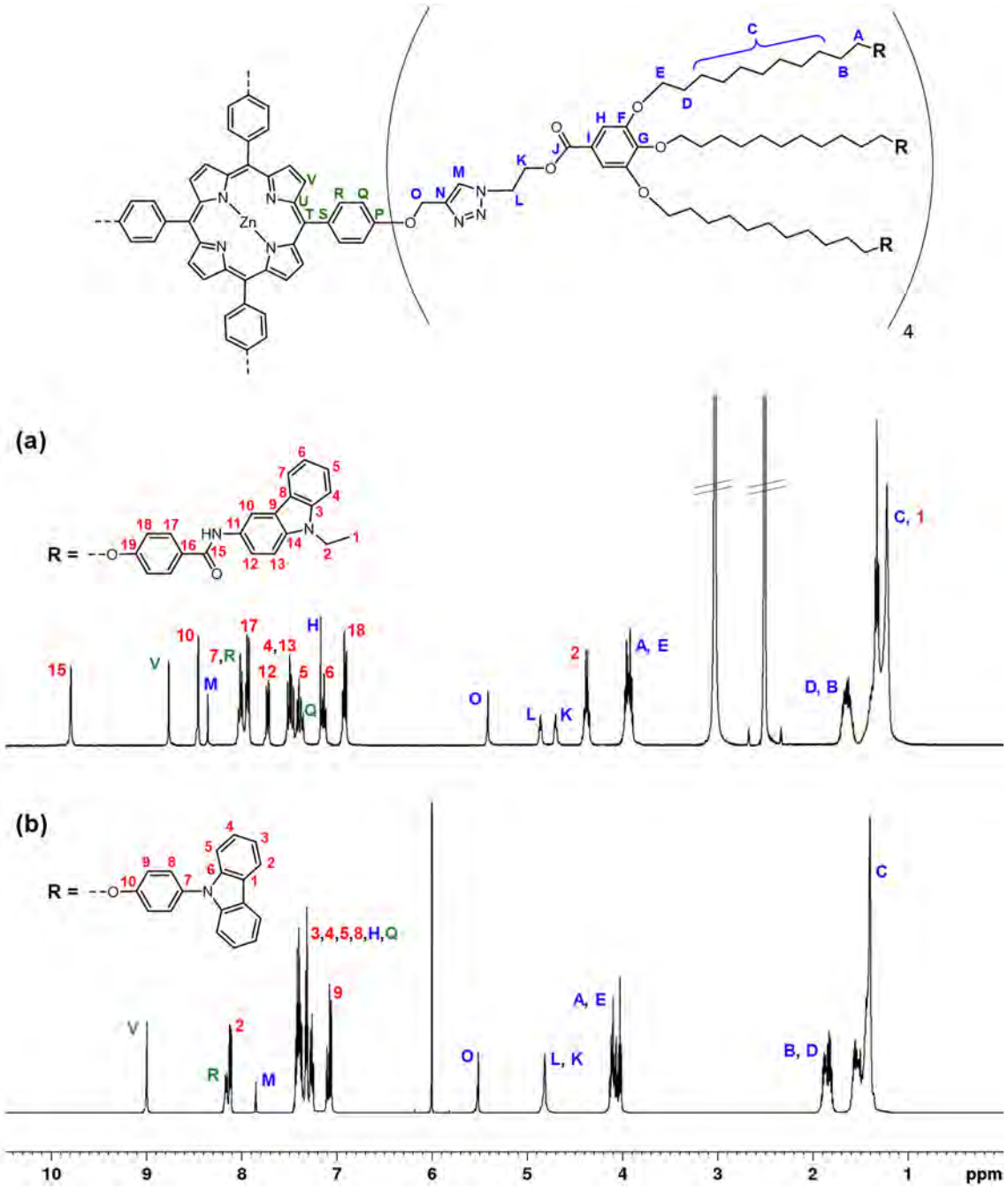

Figure 4.2 (a) ^{1}H NMR spectrum (500 MHz, DMSO-d$_6$, 353K) of **ZnP-*t*-d$_1$Cz**, and **(b)** ^{1}H NMR spectrum (500 MHz, TCE-d$_2$, 373K) of **ZnP-*t*-d$_1$PhCz**.

4.2.2 Thermal Stability and Liquid Crystalline Properties

The thermal stability of all the compounds were studied by TGA. All of the samples showed good thermal stability with 2% weight loss temperature more than 150 °C above the clearing point (**Table 4.1**). Thermal transitions and mesomorphic properties were studied by POM, DSC and XRD, and the results are listed in **Table 4.1**.

Table 4.1 Thermal properties.

	$T_{2\%}$ (°C)[a]	Phase transitions[b]
N_3-d_1Cz	255	g 61 N 107[c] I
N_3-d_1PhCz	190	g -4 I
ZnP-*t*-d_1Cz	320	g 82 N_D 155[c] I
ZnP-*t*-d_1PhCz	315	g 50 N_D 89[c] I

[a] Temperature at which 2% mass lost is detected in the thermogravimetric curve.
[b] DSC data of the second heating process at a rate of 10 °C/min. g: glass, N: nematic mesophase, N_D: nematic discotic mesophase, I: isotropic liquid.
[c] POM data.

Only **N_3-d_1Cz** exhibited LC behavior, showing a birefringent texture by POM at room temperature on applying mechanical stress (**Figure 4.3a**). The XRD pattern showed diffuse scattering in the low-angle region, suggesting the absence of long-range positional order in the LC phase (**Figure 4.3b**). This kind of XRD pattern is consistent with a nematic mesophase. The other azido functionalized dendron, **N_3-d_1PhCz**, did not show LC behavior.

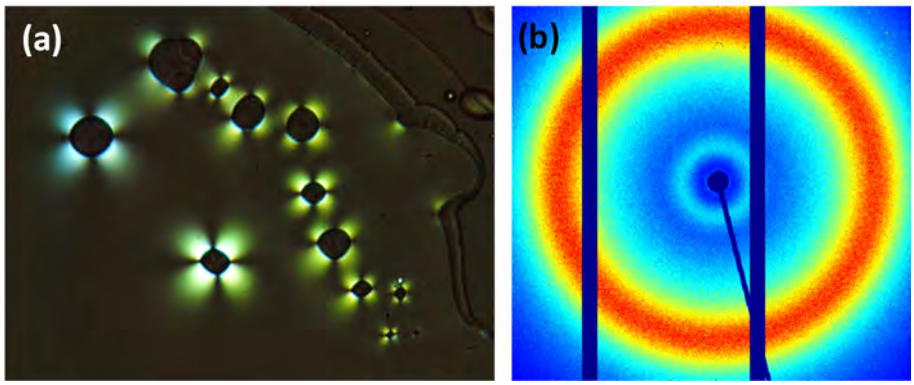

Figure 4.3 (a) POM microphotograph of **N_3-d_1Cz** taken at room temperature in the second cooling process. **(b)** XRD pattern of **N_3-d_1Cz.**

Both porphyrin-core dendrimers (**ZnP-*t*-d$_1$Cz** and **ZnP-*t*-d$_1$PhCz**) exhibited enantiotropic LC mesophases. The DSC traces showed only a glass transition freezing the mesomorphic order at room temperature. The clearing temperatures were taken from POM observations because transition peaks were not detected in DSC curves. Both compounds had a high tendency to homeotropic alignment, thus the mesophase was observed by POM on applying mechanical stress to the samples which showed birefringent textures (**Figure 4.4**).

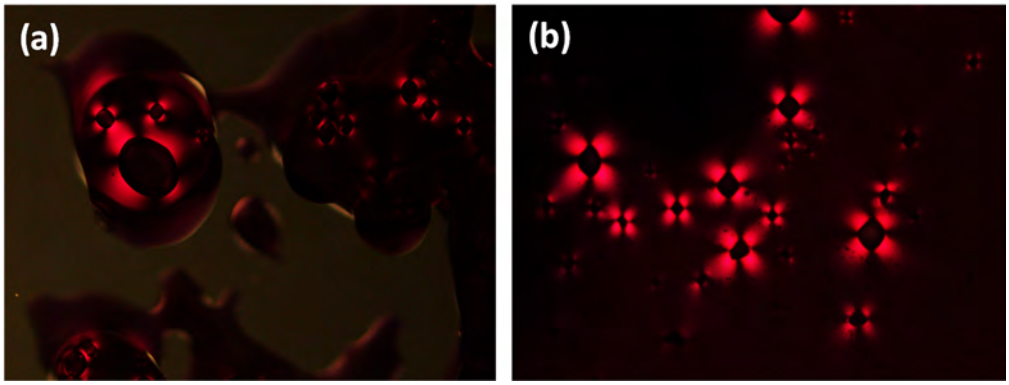

Figure 4.4 POM microphotographs for: **(a) ZnP-t-d$_1$Cz** taken at room temperature in the second cooling process, and **(b) ZnP-t-d$_1$PhCz** taken at room temperature in the second cooling process.

The nature of the mesophase was identified by XRD (**Figure 4.5**). The XRD patterns recorded for **ZnP-*t*-d$_1$Cz** and **ZnP-*t*-d$_1$PhCz** showed diffuse scattering in the low-angle region. In the high-angle region, a broad diffuse halo was detected due to the conformational disorder of the liquid-like hydrocarbon chains. These patterns, along with the POM textures (*vide supra*) are consistent with nematic discotic mesophases (N_D).

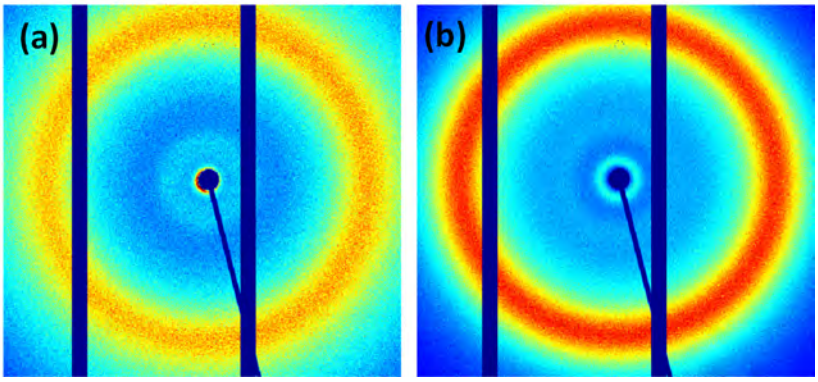

Figure 4.5 XRD pattern of: **(a) ZnP-*t*-d$_1$Cz**, **(b) ZnP-*t*-d$_1$PhCz**.

4.2.3 Absorption and Emission Properties

The UV-Vis absorption and fluorescence spectra of porphyrin-core dendrimers were collected on dilute solutions (10^{-5} to 10^{-7} M) and in thin films at room temperature. Relevant data are shown in **Table 4.2**.

The UV-Vis absorption spectra of **ZnP-*t*-d$_1$Cou** and **ZnP-*t*-d$_1$Cou** in solution consisted of porphyrin Soret (425 nm) and Q (500–700 nm) bands, and the characteristic carbazole π-π* (295–305 nm) and n-π* (340–370 nm) bands (**Figure 4.6**). These absorption spectra are a combination of the spectra of the corresponding building blocks and the presence of new bands was not observed. This result implies no conjugation effect between the two chromophores as the porphyrin core and the dendritic structure itself do not interfere with the absorption properties of the carbazole. The absorption bands for the porphyrin-core dendrimers in thin film exhibited a bathochromic shift of about 5–10 nm in relation to those in solution, due to the aggregation effect.

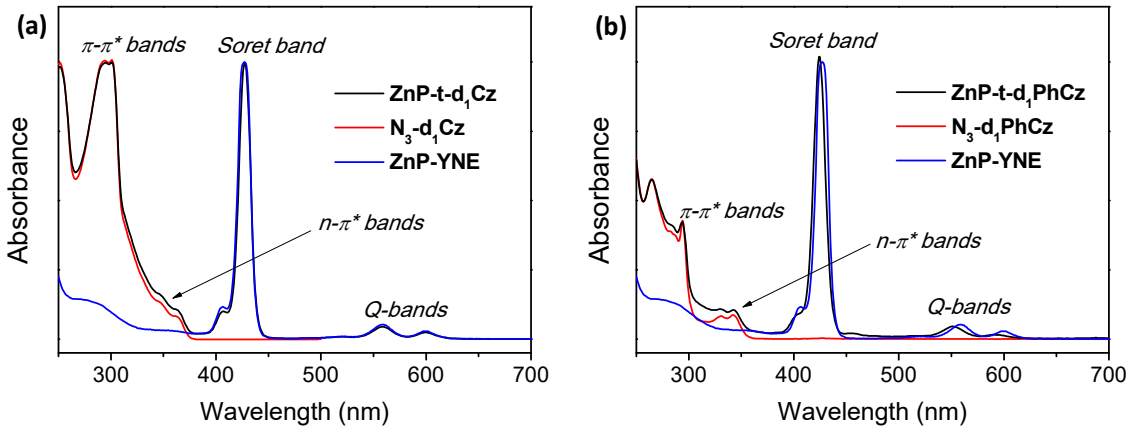

Figure 4.6 UV-Vis absorption spectra in: **(a)** THF and **(b)** DCM solution.

The fluorescence emission spectra of the porphyrin-core dendrimers (λ_{exc}= 425 nm) consisted of two bands with a Q(0–1)-band at around 600 nm and a Q(0–2)-band at around 650 nm. The fluorescence quantum yields were also measured with tetraphenylporphyrin (Φ_F= 0.11 in benzene) as a standard, resulting in low quantum yield values. Fluorescence spectra were also collected in thin films. Compared to the data from solution, the emission Q(0–1) and Q(0–2) peaks are red-shifted ca. 5–10 nm.

Table 4.2 Photophysical data in THF or DCM solutions and in thin film.

		λ_{abs} (nm) *Carbazole*	λ_{abs} (nm) *Soret band*	λ_{abs} (nm) *Q-bands*	λ_{em} (nm) *Carbazole*	λ_{em} (nm) *Q (0–1)*	λ_{em} (nm) *Q (0–2)*	Φ_F[a]	ϕ_{ET}
ZnP-*t*-d$_1$Cz	*THF*	301	427	559, 600	389	609	650	0.10	16%
	film	306	436	562, 603	–[b]	610	654	–	–
ZnP-*t*-d$_1$PhCz	*DCM*	294	424	551, 592	385	601	643	0.12	23%
	film	297	437	564, 606	–[b]	614	651	–	–

[a] The Φ_F values were calculated from THF or DCM solutions with tetraphenylporphyrin (0.11 in benzene) as a standard, excitation at 420 nm.

[b] Not detectable.

Similarly to the compounds described in Section 3, in **ZnP-*t*-d$_1$Cz** and **ZnP-*t*-d$_1$PhCz**, the porphyrin unit serves as an acceptor whereas multiple carbazole donors are present in the dendrimer periphery. When carbazole donors were excited selectively in their π-π* band (λ_{exc}= 295 nm), emissions from both the carbazole units and the porphyrin acceptor were observed (**Figure 4.7**). This result indicates that light energy collected by peripheral carbazole chromophores transfers to the porphyrin core (antenna effect). The ϕ_{ET} values are summarized in **Table 4.2** and were calculated by comparing the donor emission in the presence of the acceptor relative to that in the absence of the acceptor. Low ϕ_{ET} efficiencies were obtained because of the low degree of overlap between the emission spectrum of the carbazole and the absorption spectrum of the porphyrin. Fluorescence spectra at an excitation wavelength of 295 nm were also collected from the thin films and compared to the data from solution, almost no residual emission of the carbazole moieties was observed (**Figure 4.7**). Energy transfer from carbazole units to the porphyrin core is more efficient in the thin film than in solution.

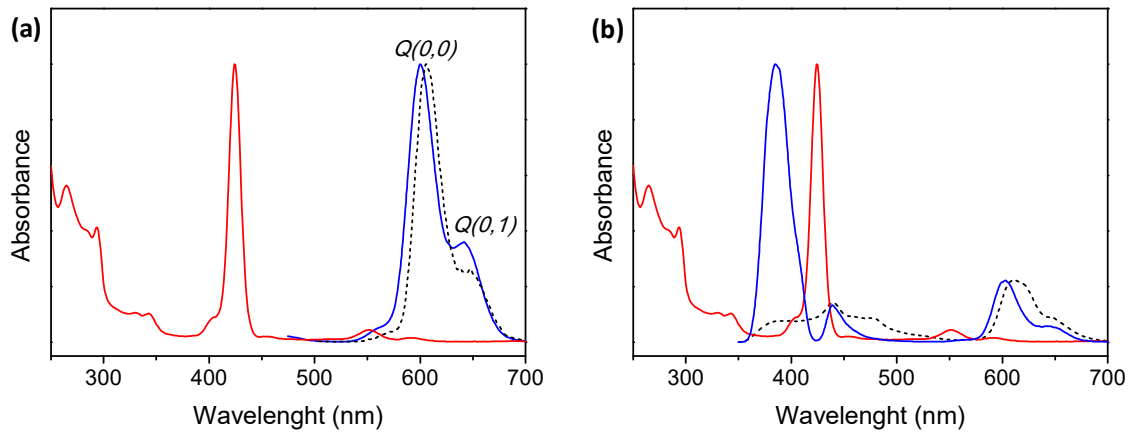

Figure 4.7 UV-Vis absorption spectra in DCM solution (red line) and emission spectra in DCM solution (blue line) and in thin film (dashed line) of **ZnP-t-d$_1$PhCz**: **(a)** λ_{exc} = 425 nm, and **(b)** λ_{exc} = 295 nm.

4.2.4 Electrochemical Crosslinking of Carbazole Units

Advincula's research group has studied for some time the electrochemical crosslinking of carbazole-containing dendrimers at the 3,6-positions to form poly(3,6-carbazole) derivatives.[220-227] The mechanism has been shown in **Figure 1.24**. Therefore, carbazole has potential for producing new electro-optical

materials because it is not only polymerizable, but also potentially electrically conductive when polymerized.[174]

The precursor azido-functionalized dendrons (**N_3-d_1Cz** and **N_3-d_1PhCz**) and the porphyrin-core dendrimers (**ZnP-*t*-d_1Cz** and **ZnP-*t*-d_1PhCz**) were electropolymerized and deposited on ITO substrates. In all cases, 10 cyclic voltammetry cycles were applied by scanning the electrodes from -0.2 to 1.2 V. Cyclic voltammetry (CV) results are shown in **Figure 4.8**, with the arrows pointing from the 1st to the 10th cycle.

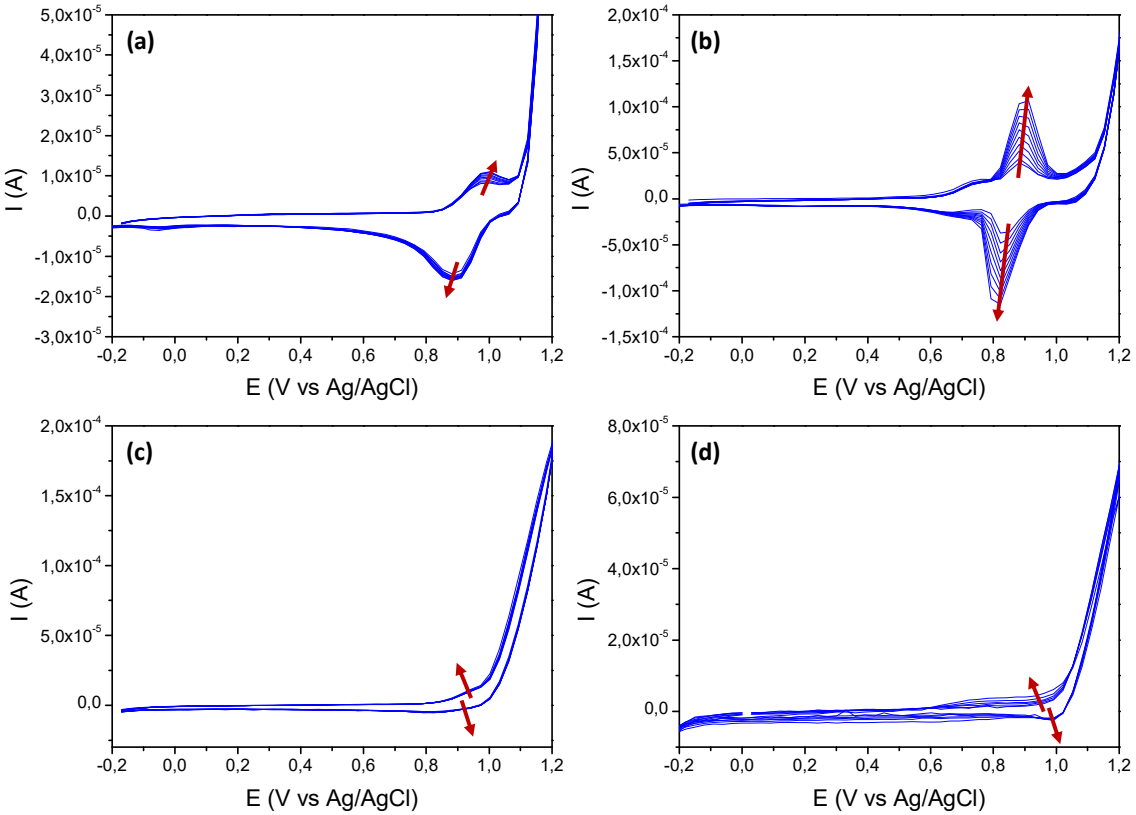

Figure 4.8 Cyclic voltammograms of the electrochemical polymerization (100 mV/s, 10 cycles) of: **(a) N_3-d_1Cz**, **(b) ZnP-*t*-d_1Cz**, **(c) N_3-d_1PhCz**, and **(d) ZnP-*t*-d_1PhCz**. Arrows indicate from 1st to 10th cycle.

In the first cycle of **ZnP-*t*-d_1PhCz**, the onset of porphyrin and carbazol oxidation was found at around 0.63 and 0.79 V, respectively. **N_3-d_1PhCz** exhibited one oxidation peak at 0.85 V corresponding to carbazole units. Starting from the second CV cycle, the oxidation waves ranged from 0.8 to 1.0 V corresponded to the doping process of the polymerized carbazoles and formation of polaronic and bipolaronic species. The reduction peaks from 1.0 to 0.7 V corresponded to the dedoping process, in which the polarons and bipolarons gained electrons to give the neutral

coupled carbazole species. Upon further cycling, the oxidation and reduction currents increased progressively, indicating a continous mass deposition of **N_3-d_1PhCz** and **ZnP-*t*-d_1PhCz** with more charges built up in the electropolymerized films. The anodic and cathodic currents of **N_3-d_1PhCz** were significally lower than those of **ZnP-*t*-d_1PhCz** due to the lower number of active species (carbazole) per molecule. Nevertheless, in **ZnP-*t*-d_1PhCz**, which has a higher number of carbazole moieties per molecule, the anodic and cathodic peaks moved further apart with increasing CV cycles. This suggests that more **ZnP-*t*-d_1PhCz** was electrochemically deposited onto the electrodes.

On the other hand, **N_3-d_1Cz** and **ZnP-*t*-d_1Cz** were not electrochemically deposited onto ITO electrodes, as deduced from the CV voltammograms. These compounds have 3-substituted carbazole units and consequently, the coupling of carbazoles at 3,6-position and subsequent polymerization is not expected.

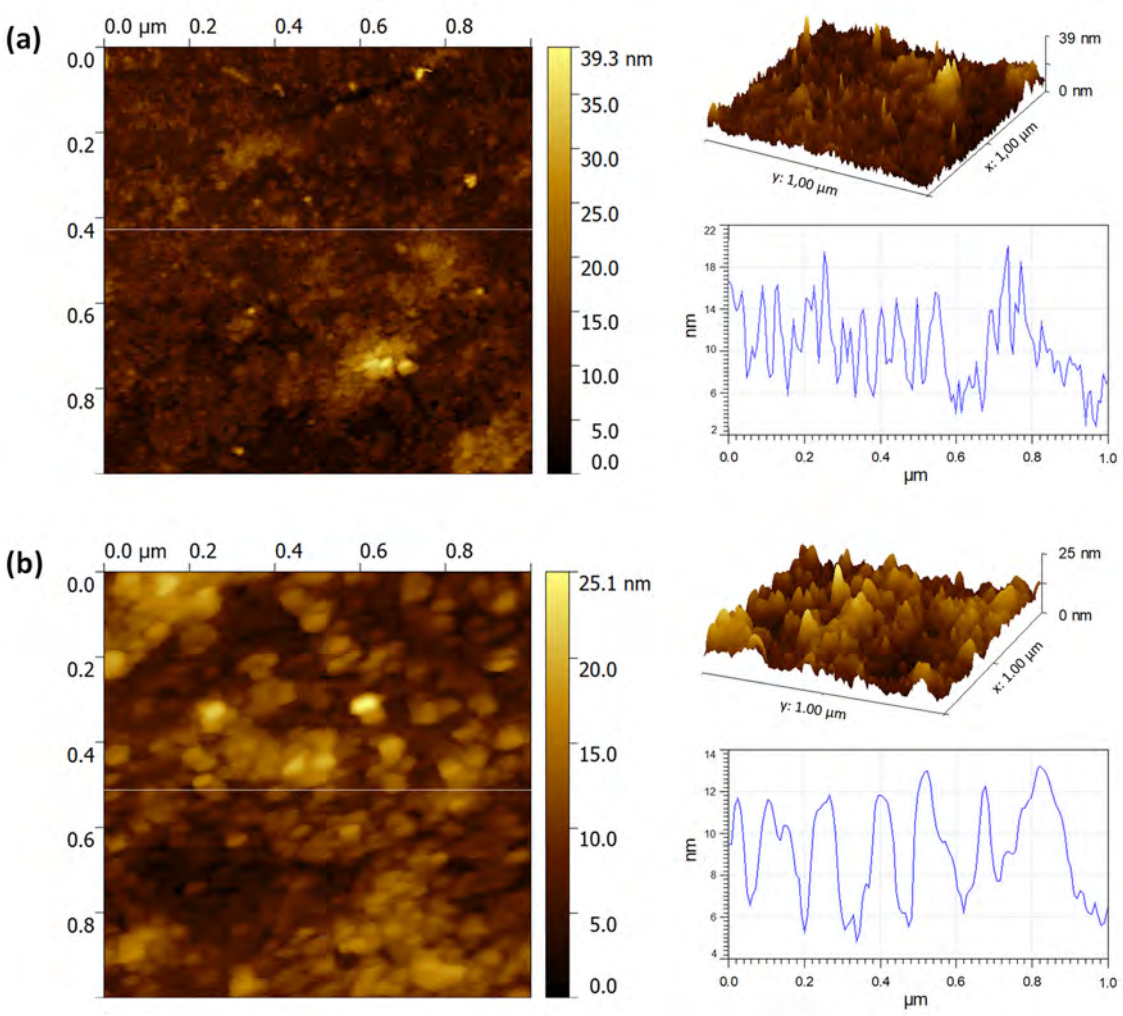

Figure 4.9 Tapping-mode AFM topography images of the electropolymerized films from: **(a) N_3-d_1Cz**, and **(b) ZnP-*t*-d_1Cz**.

The crosslinking of the peripheral carbazoles at the 3,6-position leads to the formation of electrodeposited films onto ITO electrodes. The morphology of these electrodeposited films was studied using AFM measurements (**Figure 4.9**). In the case of **N_3-d_1PhCz**, small globular particles (<40 nm) were formed, while for the porphyrin-core dendrimer (**ZnP-*t*-d_1PhCz**), the size increased up to 150 nm. The increasing number of electropolymerizable units has a decisive influence on the final size of the particles. An increase of the number of cycles (up to 20) does not modify the size of the particles, which suggests that the equilibrium is readily achieved.

The morphology of **N_3-d_1PhCz** and **ZnP-*t*-d_1PhCz** after electrochemical deposition onto ITO electrodes was also studied by SEM to confirm agreement with the AFM measurements. As shown in **Figure 4.10**, the size of the globular particules was found to be around 50 nm (for **N_3-d_1PhCz**) and 170 nm (for **ZnP-*t*-d_1PhCz**).

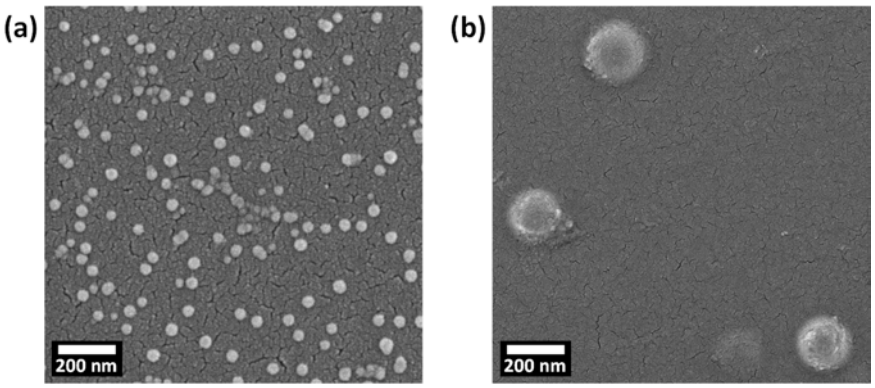

Figure 4.10 SEM images of the electropolymerized films from: **(a) N_3-d_1Cz**, and **(b) ZnP-*t*-d_1Cz**.

4.2.5 Electrochemical and Charge Transport Properties

To study the possible use of these porphyrin-core dendrimers (**ZnP-*t*-d_1Cz** and **ZnP-*t*-d_1PhCz**) in optoelectronics, it is important to investigate the feasibility of electron- and hole-injection processes in these materials which can be deduced from CV experiments. **ZnP-*t*-d_1Cz** and **ZnP-*t*-d_1PhCz** exhibit similar cyclic voltammograms with one reduction wave, corresponding to the porphyrin core, which is consistent with the electron acceptor character of this unit. Moreover, several oxidation processes were observed and they corresponded to the porphyrin and carbazol electron donating moieties. The HOMO and LUMO energy

values, calculated from the oxidation and reduction waves, are summarized in **Table 4.3**.

Table 4.3 Electrochemical parameters and hole mobilities.

	E_{ox} (V)[a]	E_{HOMO} (eV)[b]	E_{red} (V)[a]	E_{LUMO} (eV)[b]	μ_{hole} ($cm^2V^{-1}s^{-1}$)
ZnP-*t*-d$_1$Cz	0.82	-5.14	-1.36	-2.96	0.54
ZnP-*t*-d$_1$PhCz	0.59	-4.91	-1.38	-2.94	1.30[d]

[a] Onset potential for the first oxidation/reduction process.

[b] $E_{HOMO} = -(E_{ox} - E_{1/2,\,FOC} + 4.8)$ eV.

[c] $E_{LUMO} = -(E_{red} - E_{1/2,\,FOC} + 4.8)$ eV.

[d] Lower estimation of the charge carrier mobility (measured in areas with the lowest currents).

As explained in *Section 2.2.4*, the charge carrier mobility measurements were performed using the space charge-limited current (SCLC) technique.[35] SCLC was chosen by considering the HOMO energy values (see **Table 4.3**) which matches the work function of gold (W_{Au}≈ -5.1 eV) which ensures the formation of an ohmic contact in samples consisting of films placed between gold- and ITO-coated glass electrodes. All the cells were filled by capillarity by heating the material above the isotropic liquid transition. After sample filling, the cells were cooled down to room temperature. In current-voltage measurements, at low fields the observed current is ohmic and has a linear relationship with the field, while at higher fields the current becomes space-charge limited following the Mott-Gurney equation:[245]

$$J = \frac{9}{8}\varepsilon_0\varepsilon_r\mu\frac{V^2}{d^3}$$

where *J* is the measured current density, μ is the charge mobility, ε_0 is the free-space permittivity, ε_r is the dielectric constant of the material, *V* is the applied voltage, and *d* is the thickness of the device. As all the other parameters in the equation are measurable, charge mobilities can be easily obtained from *J*–*V* curves. The resulting charge mobilities are quite high, and the values are summarized in **Table 4.3**. Moreover, very high currents were measured for **ZnP-*t*-d$_1$PhCz** and thus μ_{hole} was obtained in areas with the lowest currents. As explained in *Section 3.2.4*, in this sense, the measured mobility values can be considered lower limits (to confirm them, additional measurements are in progress with an alternative technique).

4.2.6 Preparation of Organic Photovoltaic Devices

Given its high charge mobility, **ZnP-*t*-d$_1$Cz** is suitable for application in organic electronic devices. In particular, the value of its frontier orbital energy is appropriate for a use as donor in bulk heterojunction (BH) solar cells. In these devices, a blend of two bicontinuous phases is present as the active medium. The acceptor-rich phase is often based on soluble fullerene derivatives, while the donor phase can be polymeric or low molecular weight compounds. Polymeric phases are better suited to form pinhole-free films deposited by spin-coating. This is another reason to use **ZnP-*t*-d$_1$Cz**, whose high molecular weight is reflected in a polymer-like behavior in terms of viscosity, glass-phase forming properties, and is readily made into films. **PC$_{70}$BM** (see chemical structure in **Figure 4.11a**) was the molecule of choice as an acceptor. It has been widely used in BH solar cells for its good electron transport properties and its solubility in common organic solvents.

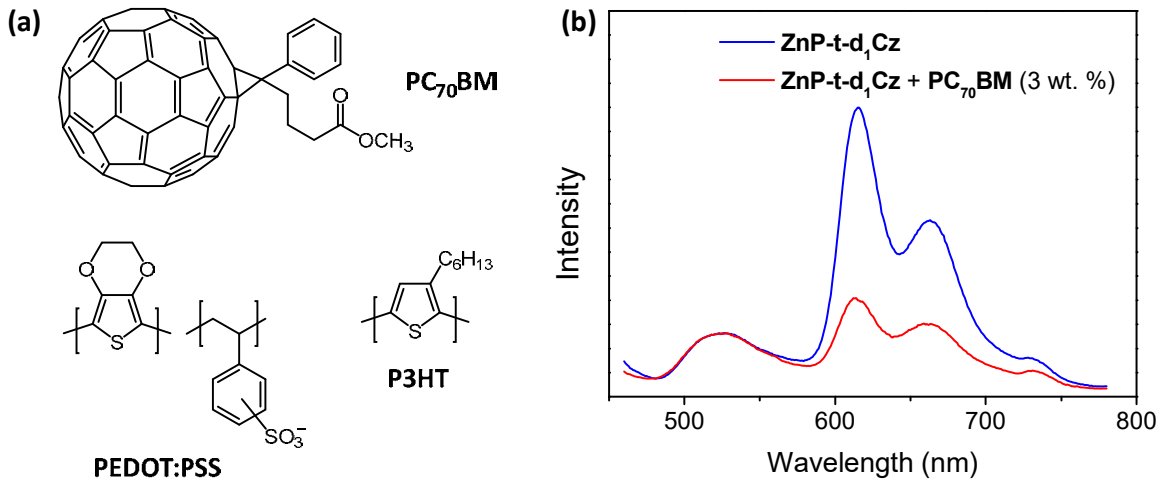

Figure 4.11 (a) Chemical structures of **PC$_{70}$BM**, **PEDOT:PSS** and **P3HT**. **(b)** Emission spectra in thin film deposited by spin-coating (λ_{exc} = 420 nm).

In fact, the spin-coating film deposition method requires both the acceptor and the donor to be soluble in a common solvent. This was the first problem to solve because **PC$_{70}$BM** is soluble in non-polar solvents (toluene and dichlorobenzene are the most often used) while **ZnP-*t*-d$_1$Cz** is soluble in more polar solvents. After several trials, the only common solvent found was 1,1,2,2-tetrachloroethane (TCE).

The first characterization was the evaluation of the fluorescence quenching of **ZnP-*t*-d$_1$Cz** in presence of **PC$_{70}$BM**. As illustrated in **Figure 4.11b**, films of **ZnP-*t*-d$_1$Cz** containing 3% of **PC$_{70}$BM** showed a reduced emission, an observation that can be

interpreted as an electron transfer from **ZnP-*t*-d$_1$Cz** to **PC$_{70}$BM**. This electron transfer is one of the necessary steps for the operation of the solar cell.

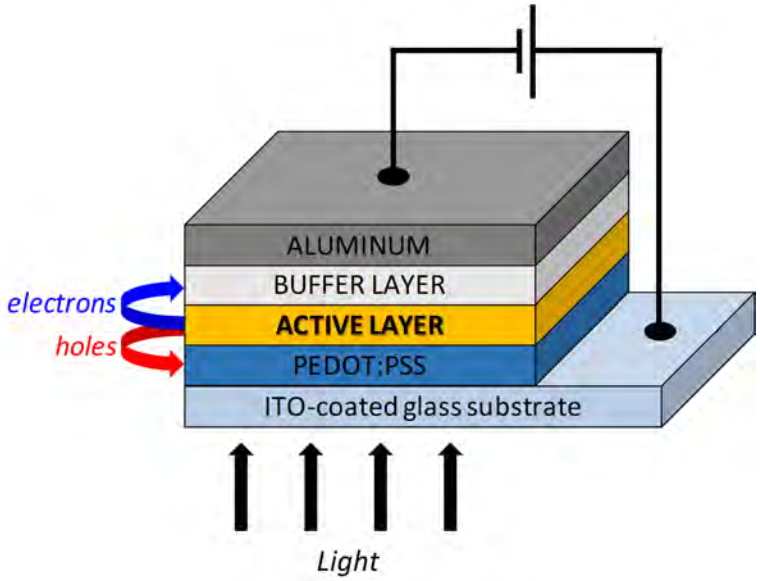

Figure 4.12 Schematic representation of a standard BH solar cell.

The next step consisted of the construction of the BH device (**Figure 4.12**). The solar cell support consisted of a rigid glass substrate, covered with a thin layer of semiconducting ITO. Then, a 40–50 nm thick layer of **PEDOT:PSS** was spin-coated from an aqueous solution onto the ITO. **PEDOT:PSS** is a thiophene-based hole-conducting polymer (see chemical structure in **Figure 4.11a**), used to improve the hole injection processes into the ITO and to block electrons from being injected. On top of the **PEDOT:PSS** layer, the active layer was deposited by spin-coating from a solution containing the donor and the acceptor. Finally, the top electrode, which consisted of aluminum, was deposited by high vacuum thermal evaporation. It is also quite common to introduce an electron transport layer (called the buffer layer) between the active layer and the top electrode. Lithium fluoride and calcium are the most common substances used for this purpose.

The performance of BH devices depends on several factors. Some of them are directly tied to the properties of the substances used, such as light absorption and emission, energy transfer behavior in both phases, donor/acceptor electron transfer properties, and charge mobilities for both electrons and holes. However, there are other parameters that control the performance of BH devices based on the morphology of the BH, which are the size and connectivity of the domains of the two interpenetrating phases. In most cases, highly interconnected domains of

around 10–20 nm give the best results. This morphology mainly depends on the kinetics of the phase separation process that occurs during and after the end of spin-coating.

In order to control the phase separation kinetics, several processing parameters can be varied. The main one is choice of solvent, but in this case it could not be changed because TCE was the only common solvent available for **ZnP-*t*-d$_1$Cz** and **PC$_{70}$BM**. Thus, we proceeded to change the **ZnP-*t*-d$_1$Cz**:**PC$_{70}$BM** weight ratio, the temperature during spin-coating, and tried adding small amounts of a co-solvent or a commonly used nucleation agent. Unfortunately, variations in morphology were unsatisfactory and the overall performance of the solar cells did not improve (**Figure 4.13**).

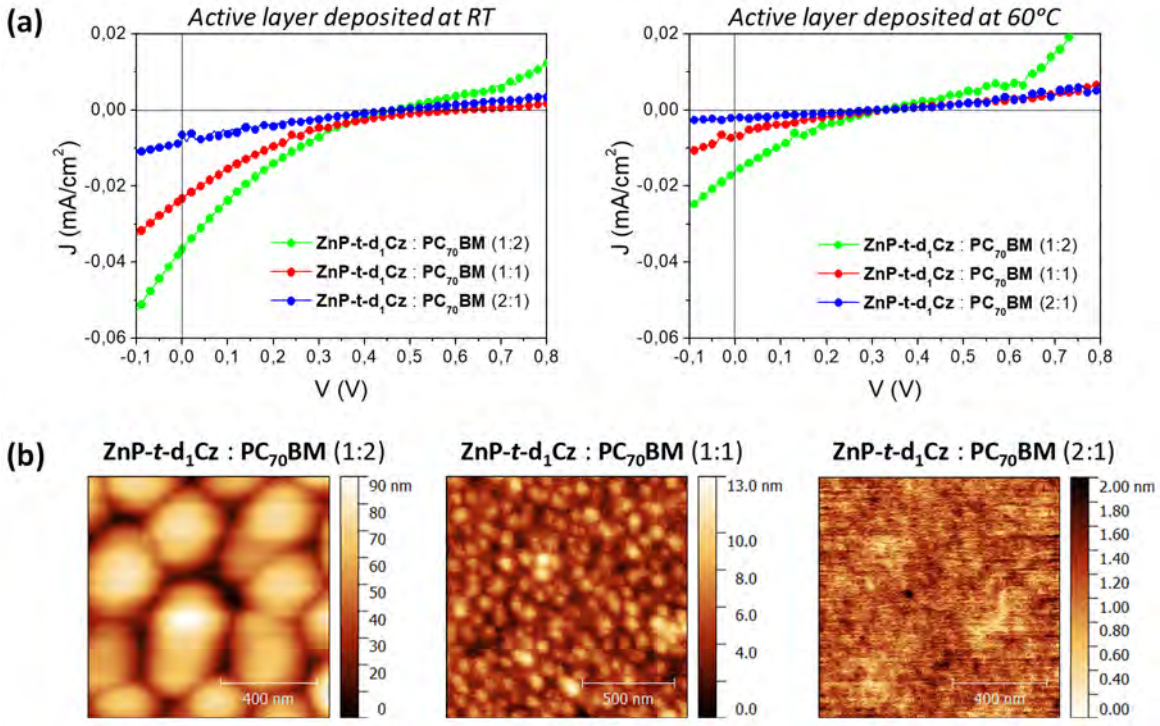

Figure 4.13 (a) Representative *J*-*V* curves of the BH cells (active layers deposited at different temperatures). **(b)** AFM images (tapping-mode topography) showed a growth of globular structures on the surface of the films upon increasing the content of **PC$_{70}$BM**.

From the shape of the *J*–*V* curves, it was hypothesized that either an incorrect formation of the BH morphology occurred or an interfacial problem existed with the aluminum counter electrode which caused poor electron collection. Thus, we tried to introduce a buffer layer of lithium fluoride between the active layer and the aluminum electrode in order to improve the electron extraction at the counter

electrode. Additionally, we carried out a post-deposition treatment to selectively remove **ZnP-*t*-d$_1$Cz** from the active layer. After several trials, the post-deposition treatment consisted of spin-coating with a mixture of isopropyl alcohol:chlorobenzene (3:1) or a **PC$_{70}$BM** solution in that mixture. In both cases, we observed a slight improvement of the solar cells performance, confirming that the morphology in the bulk of the active layer (and not just at the surface) is at the origin of this problem (**Figure 4.14**).

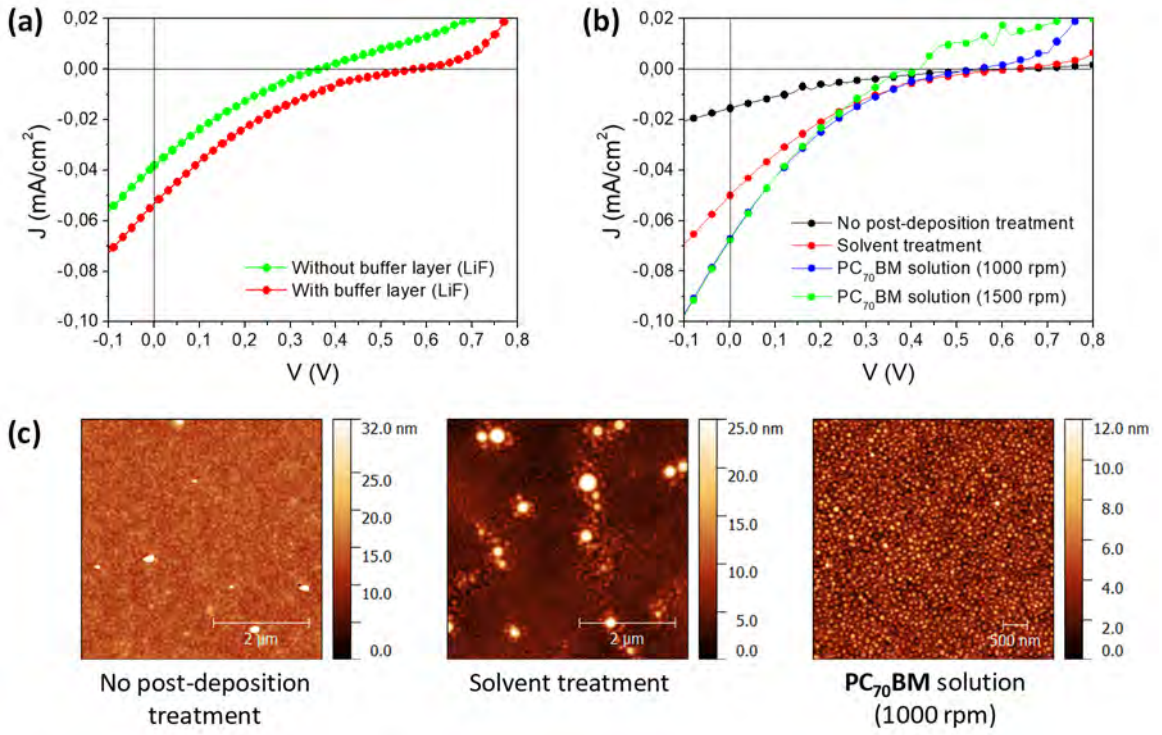

Figure 4.14 (a) Representative *J-V* curves of BH cells with active layer of **ZnP-*t*-d$_1$Cz**:**PC$_{70}$BM** (1:2) deposited at RT. **(b)** Representative *J-V* curves of BH cells with active layer of **ZnP-*t*-d$_1$Cz**:**PC$_{70}$BM** (1:1) deposited at RT. **(c)** AFM images (tapping-mode topography) showed the effect of the post-deposition treatments.

Finally, we tried using **ZnP-*t*-d$_1$Cz** to substitute **PEDOT:PSS** as a hole transporting layer. To accomplish this, the BH solar cell support consisted of a ITO-covered glass substrate. Then, a 25–70 nm thick layer of **ZnP-*t*-d$_1$Cz** was spin-coated from a TCE solution onto the ITO. On top of this hole transporting layer, the active layer which consisted of a 1:1 mixture of **PC$_{70}$BM** and **P3HT** (see chemical structure in **Figure 4.11a**) was deposited by spin-coating from a chlorobencene solution. Finally, the top electrode consisted of aluminium which was deposited by high vacuum thermal evaporation. In general, the results were very poor (**Figure 4.15**), which

was likely a result of low charge carrier density, despite the high mobility of **ZnP-*t*-d$_1$Cz**, or possibly because of its lack of electron blocking properties.

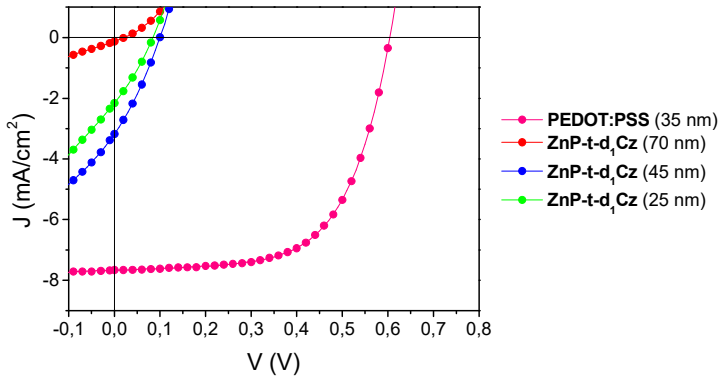

Figure 4.15 Representative *J-V* curves of BH cells with different hole transporting layers.

4.3 Conclusions

We have synthesized new liquid crystalline carbazole-containing porphyrin-core dendrimers which displayed a nematic discotic mesophase. In this LC arrangement, the compounds can be easily processed due to their high tendency to form large oriented homeotropic domains. Moreover, all the compounds displayed electrochemical properties with a high HOMO energy level (of around -5.0 eV) that make these products suitable for applications where charge injection from an electrode is required. Notably, we have carried out experimental investigations of spherical nanoparticle deposition on ITO by electrochemical crosslinking of carbazole units.

The charge mobility studies revealed that the nematic discotic mesophase displays semiconductor properties with hole mobility values of around 1 $cm^2 \cdot V^{-1} \cdot s^{-1}$ and accordingly these porphyrin-core dendrimers have great potential as semiconducting soft materials with high charge mobility.

5. EXPERIMENTAL PART

5.1 Characterization techniques

5.1.1 Materials

Meso-tetra(*p*-hydroxyphenyl)porphine (**P-OH**) was purchased from Frontier Scientific. Pyrrole was dried over CaH_2 and vacuum-distilled before use. All other commercially reagents were purchased from Sigma-Aldrich and used as received. Anhydrous THF and DCM were purchased from Scharlab and dried using a solvent purification system.

5.1.2 Structural Characterization

Infrared spectroscopy spectra were obtained on a Bruker Vertex 70 FT-IR spectrophotometer using KBr pellets.

Solution **nuclear magnetic resonance** experiments were carried out on Bruker Avance spectrometers operating at 500/400 MHz for ^{1}H and 125/100 for ^{13}C, using standard pulse sequences. Chemical shifts are given in ppm relative to TMS and the residual solvent peak was used as internal reference.

Elemental analysis was performed using a Perkin-Elmer 2400 microanalyzer.

MALDI-TOF mass spectrometry was performed on an Autoflex mass spectrometer (Bruker Daltonics) using dithranol or DCTB as matrix.

5.1.3 Liquid Crystal Characterization

Mesogenic behavior was investigated by **polarized-light optical microscopy** using an Olympus BH-2 polarizing microscope fitted with a Linkam THMS600 hot stage.

Thermogravimetric analysis was performed using a Q5000IR from TA Instruments at heating rate of 10 °C/min under nitrogen atmosphere.

Thermal transitions were determined by **differential scanning calorimetry** using a DSC Q20 and Q2000 from TA Instruments at a scan rate of 10 °C/min with powdered samples (2–5 mg) sealed in aluminum pans under nitrogen atmosphere. Glass transition temperatures (T_g) were determined at the half-height of the baseline jump, and first-order transition temperatures were read at the maximum of the corresponding peak.

X-ray diffraction was performed with an evacuated Pinhole camera (Anton-Paar) operating a point-focused Ni-filtered Cu-K_α beam. The patterns were collected on flat photographic films perpendicular to the X-ray beam. Powdered samples were placed in Lindemann glass capillaries (0.9 mm diameter).

X-ray diffraction was also performed with a Ganesha Lab Instrument equipped with a GeniX-Cu ultralow divergence source producing X-ray photons with a wavelength of 1.54 Å and a flux of 1×10^8 ph·s^{-1}. Scattering patterns were collected using a Pilatus 300 K silicon pixel detector. The beam center and the *q* range were calibrated using the diffraction peaks of silver behenate. Powdered samples were placed in Lindemann glass capillaries (1 mm diameter).

5.1.4 Optical Properties

Ultraviolet-visible spectra were recorded on an ATI-Unicam UV4-200 spectrophotometer.

Fluorescence measurements were recorded on a Perkin-Elmer LS 50B fluorescence spectrophotometer.

All the measurements were performed in dilute DCM or THF solutions (10^{-5} to 10^{-7} M) using quartz cuvettes. Thin films for UV-vis absorption experiments were prepared by casting from DCM or THF solutions (1 mg/mL) onto quartz substrates. Films for fluorescence measurements were prepared between two quartz plates by heating the compounds above their isotropization temperature and cooling down to RT.

5.1.5 Electrochemical Properties

Cyclic voltammetry was carried out using a μ-Autolab ECO-Chemie potentiostat over a scanning range from -2.0 to 2.0 V (*vs* Ag/AgCl) and at a scan rate of 100 mV/s. A three-electrode system (a glassy carbon working electrode, Pt counter electrode, and Ag/AgCl reference electrode) was used in all cases. The experiments were carried out under argon in DCM with tetrabutylammonium hexafluorophosphate ($TBAPF_6$) as supporting electrolyte (0.1 M). A ferrocene solution (0.1 M in DCM) was tested by the same procedure to obtain the half-wave potential ($E_{1/2,\,FOC}$) in order to correlate all measurements. The energy of the HOMO level was calculated by the empirical relationship: $E_{HOMO} = -(E_{ox} - E_{1/2,\,FOC} + 4.8)$ eV, where E_{ox} is the onset potential for the oxidation wave. The energy of the LUMO level was calculated by the empirical relationship: $E_{LUMO} = -(E_{red} - E_{1/2,\,FOC} + 4.8)$ eV, where E_{red} is the onset potential for the reduction wave. When no reduction processes were detected, the energy of the LUMO level was deduced from the optical band gap (ΔE_g). ΔE_g was calculated upon the intersection of the normalized UV-Vis absorption spectrum and the fluorescence spectra. The energy of the LUMO was determined according to the expression: $E_{LUMO} = E_{HOMO} - \Delta E_g$.

The electrochemical measurements for electropolymerization were carried out using a μ-Autolab ECO-Chemie potentiostat. **Cyclic volammetry** was performed over a scanning range from -0.2 to 1.2 V (*vs* Ag/AgCl) and at a scan rate of 100 mV/s. A three-electrode system (ITO supported on glass working electrode, Pt counter electrode, and Ag/AgCl reference electrode) was used in all cases. The experiments were carried out under argon with tetrabutylammonium hexafluorophosphate ($TBAPF_6$) as supporting electrolyte (0.1 M).

Atomic force microscopy (AFM) imaging was examined in ambient conditions with a Multimode 8 from Veeco-Bruker in the tapping mode.

Field emission scanning electron microscopy (FESEM) measurements were performed using a Carl Zeiss MERLIN™ microscope. Samples for FESEM measurements were coated with platinum.

5.1.6 Charge Transport Properties

Glass substrates with five 0.6 mm wide Indium Tin Oxide (ITO) electrodes were prepared by photolithography, starting from commercial glasses entirely covered by ITO (VisionTek, 120 nm ITO thickness, 12 Ω/sq resistivity). Thermal evaporation of gold or aluminum on glass substrates covered by a mask was used to prepare substrates with three 1.2 mm wide metal electrodes.

The cells for SCLC measurements were assembled by superimposing one substrate with gold electrodes and one with ITO electrodes, controlling the thickness within the 7–12 µm range by using glass spacers and thus obtaining 15 independent overlapping areas per sample. The cells were then placed on a hot plate with some of the active material on one open side and heated up to a few degrees above the melting point of the liquid crystal. Due to the high viscosity of the materials, the filling of the cells by capillarity usually lasted 10–12 h. Once the space between the two substrates was completely filled with the material, the hot plate was turned off and the samples reached room temperature in about one hour.

Either a Keithley 6517A or a Keithley 2636B electrometer were used to acquire voltage/current characteristic curves, while the dielectric constant was obtained by capacity measurements performed by using a HP 4284A Precision LCR Meter.

Given the extremely uniform macroscopic orientation of the director, the values of the mobility measured in different areas of each sample and in different samples showed very little variation, with a difference between the highest and the lowest values of less than one order of magnitude but with most measurements much closer to the average. This is in marked contrast to the behavior usually observed for columnar phases, where a uniform macroscopic orientational order is much harder to achieve.

5.2 Synthetic Procedures

5.2.1 Porphyrin-Core Dendrimers Prepared by Steglich Esterification

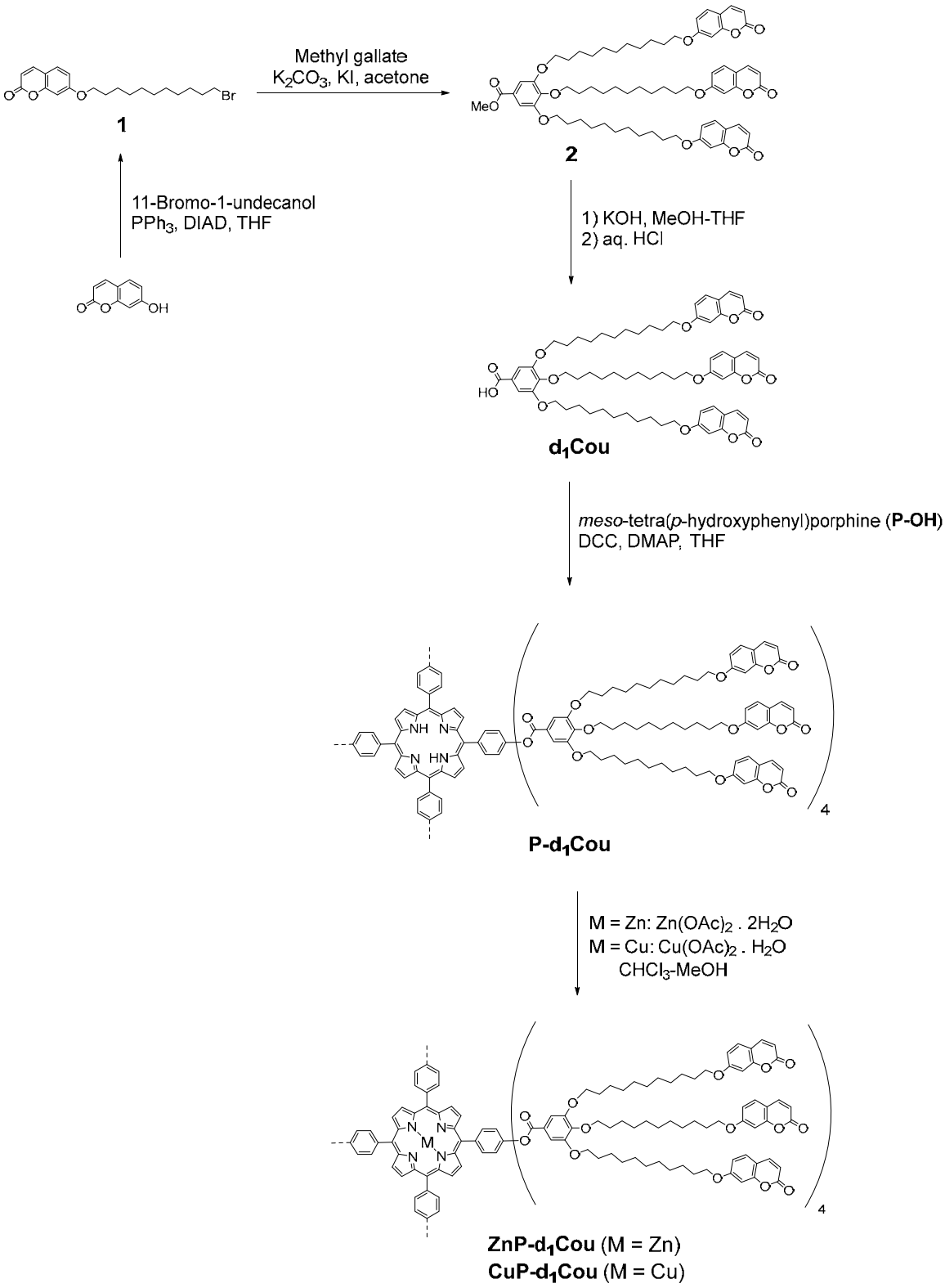

Scheme 5.1 Synthetic route of the porphyrin-core dendrimer with coumarin units and their metal complexes.

7-((11-bromoundecyl)oxy)-2*H*-chromen-2-one (1). Umbelliferone (8.00 g, 49.34 mmol), 11-bromo-1-undecanol (12.39 g, 49.34 mmol) and triphenylphosphine (12.94 g, 49.34 mmol) were dissolved in anhydrous THF (450 mL). The reaction flask was cooled in an ice bath and flushed with argon, then diisopropyl azodicarboxylate (9.98 g, 49.34 mmol) was added dropwise. The mixture was stirred at RT for 12 h under an argon atmosphere. The white precipitate was filtered off. The solvent was evaporated and the crude product was recrystallized in ethanol. Yield: 91%. IR (KBr, ν, cm^{-1}): 3076 (=C-H), 2917 (C-H), 1722 (C=O), 1620, 1471 (Ar), 1236, 1132 (C-O). ^{1}H NMR (CD_2Cl_2, 298K, 400 MHz, δ, ppm): 7.65 (d, *J*= 9.4 Hz, 1H), 7.43-7.35 (m, 1H), 6.87-6.78 (m, 2H), 6.18 (d, *J*= 9.4 Hz, 1H), 4.02 (t, *J*= 6.6 Hz, 2H), 3.42 (t, *J*= 6.6 Hz, 2H), 1.90-1.74 (m, 4H), 1.52-1.21 (m, 14H). ^{13}C NMR (CD_2Cl_2, 298K, 100 MHz, δ, ppm): 162.99, 161.43, 156.53, 143.94, 129.33, 113.37, 113.28, 112.95, 101.74, 69.29, 34.82, 33.44, 30.03, 29.99, 29.95, 29.85, 29.53, 29.29, 28.70, 26.45. MS (MALDI$^+$, dithranol, m/z): calcd. for $C_{20}H_{27}BrO_3$, 394.1; found, 417.0 $[M + Na]^+$. Anal. calcd. for $C_{20}H_{27}BrO_3$: C, 60.76%; H, 6.88%. Found: C, 61.02%; H, 7.13%.

Methyl 3,4,5-tris((11-((2-oxo-2*H*-chromen-7-yl)oxy)undecyl)oxy)benzoate (2). A mixture of compound **1** (5 g, 12.71 mmol), methyl gallate (0.71 g, 3.85 mmol), potassium carbonate (5.32 g, 38.52 mmol), a teaspoon of potassium iodide and acetone (125 mL) was stirred and heated under reflux for 24 h. The reaction mixture was allowed to cool down to RT and the solids were filtered off and washed with acetone. The solvent was evaporated and the crude product was purified by flash column chromatography on silica gel using DCM as eluent and gradually changing the composition of the eluent to DCM/ethyl acetate (9:1). Yield: 75%. IR (KBr, ν, cm^{-1}): 3080 (=C-H), 2916 (C-H), 1739 (C=O), 1616, 1507, 1471 (Ar), 1230, 1122 (C-O). ^{1}H NMR (CD_2Cl_2, 298K, 400 MHz, δ, ppm): 7.69-7.60 (m, 3H), 7.42-7.33 (m, 3H), 7.23 (s, 2H), 6.88-6.73 (m, 6H), 6.22-6.13 (m, 3H), 4.07-3.95 (m, 12H), 3.85 (s, 3H), 1.88-1.65 (m, 12H), 1.56-1.20 (m, 42H). ^{13}C NMR (CD_2Cl_2, 298K, 100 MHz, δ, ppm): 167.22, 162.99, 161.44, 156.33, 153.41, 143.94, 142.67, 129.33, 125.36, 113.37, 133.27, 112.96, 108.17, 101.73, 73.94, 69.65, 69.30, 52.49, 30.89, 30.25, 30.17, 30.15, 30.12, 30.10, 29.96, 29.94, 29.92, 29.89, 29.58, 29.58, 29.56, 26.64, 26.52, 26.49. MS (MALDI$^+$, dithranol, m/z): calcd. for $C_{68}H_{86}O_{14}$, 1126.6; found, 1149.5 $[M + Na]^+$. Anal. calcd. for $C_{68}H_{86}O_{14}$: C, 72.44%; H, 7.69%. Found: C, 72.05%; H, 7.94%.

3,4,5-Tris((11-((2-oxo-2*H*-chromen-7-yl)oxy)undecyl)oxy)benzoic acid (d_1Cou). An aqueous solution of potassium hydroxide (1.00 g, 10 mL) was added to a solution of compound **2** (2.00 g, 1.77 mmol) in THF-methanol 1:1 (50 mL). The mixture was stirred and heated under reflux and the evolution of the reaction was followed by thin layer chromatography. When all of the starting material had been consumed, the reaction mixture was neutralized with concentrated hydrochloric acid until pH 2. The organic solvents were evaporated under reduced pressure and the resulting aqueous phase was extracted with DCM. The combined organic phases were washed with brine and dried over anhydrous magnesium sulfate. The solution was filtered and the solvent was removed under reduced pressure. The product was purified by flash chromatography on silica gel using DCM as eluent and gradually changing the composition of the eluent to DCM/ethyl acetate (7:3). Yield: 78%. IR (KBr, ν, cm^{-1}): 3240 (O-H), 3080 (=C-H), 2921 (C-H), 1740 (C=O ester), 1680 (C=O acid), 1617, 1511, 1468 (Ar), 1233, 1128 (C-O). ^{1}H NMR (CD_2Cl_2, 298K, 400 MHz, δ, ppm): 7.69-7.59 (m, 3H), 7.41-7.34 (m, 3H), 7.32 (s, 2H), 6.87-6.74 (m, 6H), 6.21-6.15 (m, 3H), 4.12-3.91 (m, 12H), 1.90-1.66 (m, 12H), 1.57-1.20 (m, 42H). ^{13}C NMR (CD_2Cl_2, 298K, 100 MHz, δ, ppm): 170.74, 162.45, 160.94, 160.91, 155.95, 152.91, 143.39, 142.99, 128.76, 123.68, 112.78, 112.72, 112.39, 108.30, 101.20, 73.44, 69.17, 68.75, 30.33, 29.67, 29.60, 29.56, 29.52, 29.38, 29.35, 29.32, 29.02, 28.99, 26.06, 26.04, 25.95, 25.92. MS (MALDI$^+$, dithranol, m/z): calcd. for $C_{67}H_{84}O_{14}$, 1112.6; found, 1135.5 $[M + Na]^+$, 1157.5 $[M – H + 2Na]^+$. Anal. calcd. for $C_{67}H_{84}O_{14}$: C, 72.28%; H, 7.60%. Found: C, 71.95%; H, 7.49%.

P-d_1Cou. *Meso*-tetra(*p*-hydroxyphenyl)porphine (**P-OH**) (25 mg, 0.04 mmol), compound **d_1Cou** (0.50 g, 0.45 mmol), and 4-(dimethylamino)pyridine (0.17 g, 1.35 mmol) were dissolved in anhydrous THF (10 mL). The reaction flask was cooled in an ice bath and flushed with argon and *N*,*N*′-dicyclohexylcarbodiimide (1.08 g, 5.23 mmol) was added dropwise. The mixture was stirred at 60 °C for 48 h under an argon atmosphere. The organic solvent was evaporated under reduced pressure, the resulting product was dissolved in DCM and washed with water, sodium hydroxide 5% (aq.) and brine. The solution was dried over anhydrous magnesium sulfate and filtered. The product was purified by flash chromatography on silica gel using DCM as eluent and gradually changing the composition of the eluent to DCM/ethyl acetate (7:3). Yield: 55%. IR (KBr, ν, cm^{-1}): 3335 (N-H), 2925 (C-H), 1734 (C=O), 1613, 1508, 1469 (Ar), 1192, 1122 (C-O). ^{1}H NMR (CD_2Cl_2, 298K, 400 MHz, δ,

ppm): 9.01-8.89 (m, 8H). 8.39-8.25 (m, 8H), 7.72-7.57 (m, 20H), 7.56-7.46 (m, 8H), 7.43-7.32 (m, 4H), 7.32-7.21 (m, 8H), 6.88-6.71 (m, 24H), 6.21-6.14 (m, 4H), 6.12-6.06 (m, 8H), 4.20-4.08 (m, 24H), 4.05-3.94 (m, 24H), 1.99-1.74 (m, 48H), 1.63-1.18 (m, 168H), -2.88 (s, 2H). ^{13}C NMR (CD_2Cl_2, 298K, 100 MHz, δ, ppm): 165.61, 162.99, 162.93, 161.42, 161.35, 156.53, 156.44, 153.70, 151.79, 143.92, 143.82, 143.62, 140.09, 136.01, 129.33, 129.23, 128.34 (detected by ^{1}H-^{13}C HSQC, H7-C7), 124.63, 120.78, 119.94, 113.37, 113.28, 113.19, 112.95, 112.85, 109.06, 101.73, 101.67, 74.13, 69.90, 69.32, 69.29, 30.98, 30.31, 30.20, 30.16, 30.00, 29.96, 29.61, 29.58, 26.71, 26.68, 26.56, 26.53. MS (MALDI$^+$, dithranol, m/z): calcd. for $C_{312}H_{358}N_4O_{56}$, 5056.5; found, 5079.6 $[M + Na]^+$. Anal. calcd. for $C_{312}H_{358}N_4O_5$: C, 74.06%; H, 7.13%; N, 1.11%. Found: C, 73.95%; H, 7.19%; N, 1.43%.

ZnP-d$_1$Cou. The free-base porphyrin-core dendrimer (**P-d$_1$Cou**) (75 mg, 0.015 mmol) and zinc acetate dihydrate (32 mg, 0.15 mmol) were dissolved in chloroform-methanol 1:1 (10 mL). The solution was stirred and heated under reflux for 12 h under an argon atmosphere. Then, the solution was diluted with chloroform and washed with water and brine. The solvent was evaporated under reduced pressure, and the residual solid was purified by flash chromatography on silica gel using DCM as eluent and gradually changing the composition of the eluent to DCM/ethyl acetate (7:3). Yield: 59%. IR (KBr, ν, cm^{-1}): 2924 (C-H), 1733 (C=O), 1614, 1508, 1468 (Ar), 1190, 1121 (C-O). ^{1}H NMR (CD_2Cl_2, 298K, 400 MHz, δ, ppm): 9.08-8.86 (m, 8H). 8.35-8.24 (m, 8H), 7.71-7.56 (m, 20H), 7.51-7.42 (m, 8H), 7.39-7.31 (m, 4H), 7.27-7.15 (m, 8H), 6.88-6.62 (m, 24H), 6.19-6.09 (m, 4H), 6.03-5.93 (m, 8H), 4.21-4.08 (m, 24H), 4.05-3.93 (m, 24H), 1.97-1.72 (m, 48H), 1.64-1.19 (m, 168H). ^{13}C NMR (CD_2Cl_2, 298K, 100 MHz, δ, ppm): 165.65, 163.00, 162.91, 161.42, 161.32, 156.51, 156.33, 153.69, 151.54, 150.77, 143.93, 143.78, 143.61, 141.04, 135.93, 132.53, 129.33, 129.17, 124.69, 120.65, 120.50, 113.34, 113.29, 113.23, 113.15, 112.94, 112.77, 109.09, 101.73, 101.60, 74.11, 69.90, 69.31, 30.95, 30.23, 30.15, 29.97, 29.59, 26.67, 26.54. MS (MALDI$^+$, dithranol, m/z): calcd. for $C_{312}H_{356}N_4O_{56}Zn$, 5118.5; found, 5141.4 $[M+Na]^+$. Anal. calcd. for $C_{312}H_{356}N_4O_{56}Zn$: C, 73.14%; H, 7.00%; N, 1.09%. Found: C, 73.35%; H, 6.89%; N, 1.23%.

CuP-d$_1$Cou. The free-base porphyrin-core dendrimer (**P-d$_1$Cou**) (100 mg, 0.02 mmol) and copper (II) acetate monohydrate (24 mg, 0.2 mmol) were dissolved in chloroform-methanol 1:1 (10 mL). The solution was stirred and heated under reflux for 12 h under an argon atmosphere. Then, the solution was diluted with

chloroform and washed with water and brine. The solvent was evaporated under reduced pressure, and the residual solid was purified by flash chromatography on silica gel using DCM as eluent and gradually changing the composition of the eluent to DCM/ethyl acetate (7:3). Yield: 65%. IR (KBr, ν, cm^{-1}): 2924 (C-H), 1734 (C=O), 1614, 1505, 1467 (Ar), 1192, 1121 (C-O). MS (MALDI$^+$, dithranol, m/z): calcd. for $C_{312}H_{356}N_4O_{56}Cu$, 5117.4; found, 5140.5 $[M + Na]^+$. Anal. calcd. for $C_{312}H_{356}N_4O_{56}Cu$: C, 73.17%; H, 7.01%; N, 1.09%. Found: C, 73.15%; H, 7.33%; N, 0.93%.

5.2.2 Porphyrin-Core Dendrimers Prepared by 'Click' Chemistry

5.2.2.1 *Synthesis of the Alkyne-Functionalized Porphyrin Core*

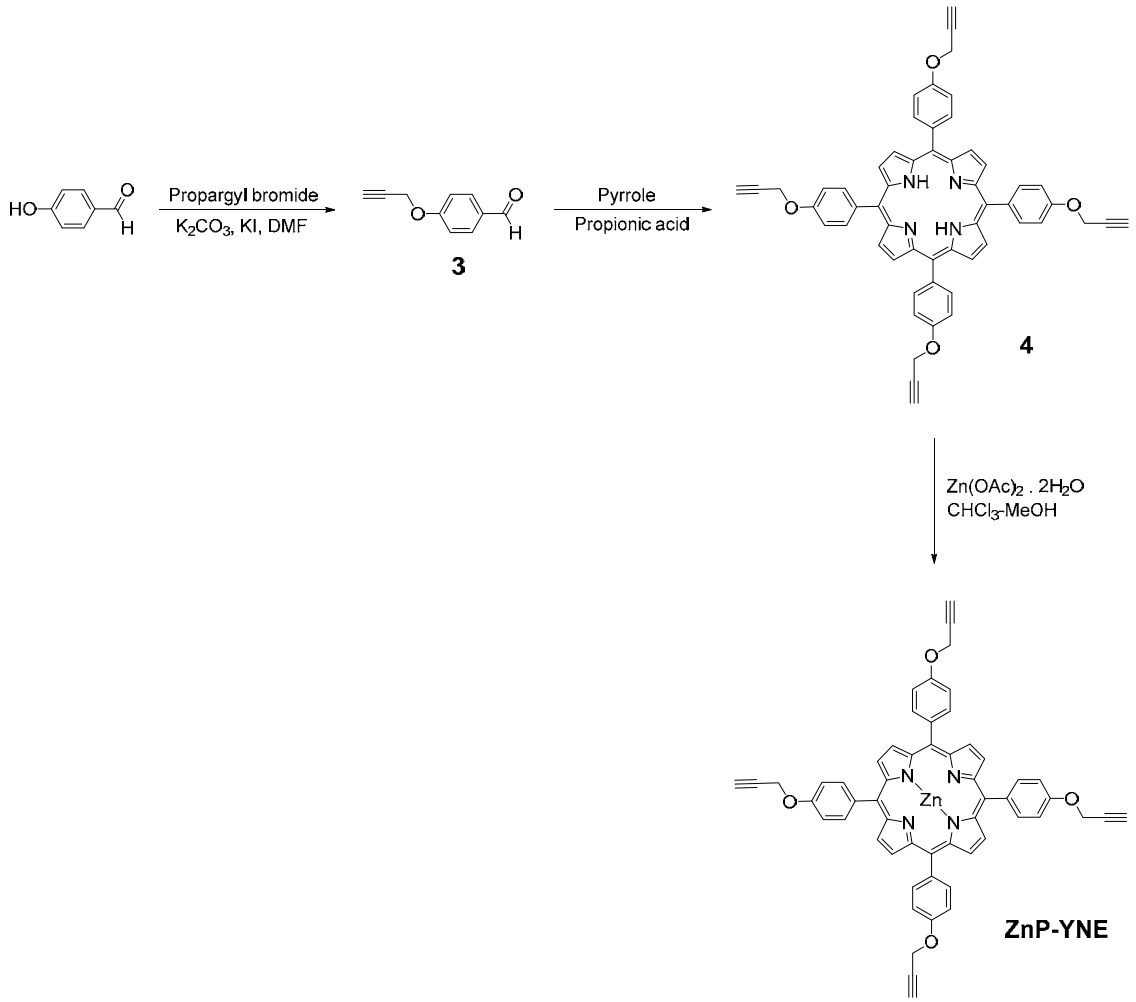

Scheme 5.2 Synthetic route of the alkyne-functionalized porphyrin core.

4-(Propargyloxy)benzaldehyde (3). 4-Hydroxybenzaldehyde (10 g, 81.9 mmol), potassium carbonate (22.6 g, 163.8 mmol) and a teaspoon of potassium iodide were stirred in DMF (150 mL). The mixture was heated to 110 °C and then propargyl bromide (8.8 mL, 98.3 mmol) was slowly added. The reaction was stirred at 110 °C for 8 h. The mixture was allowed to cool down to RT and poured into water and extracted with hexane/ethyl acetate (1:1). The combined organic phases were washed with brine and dried over anhydrous magnesium sulfate. The solution was filtered and the solvent was removed under reduced pressure. The crude product was recrystallized in ethanol. Yield: 93%. IR (KBr, ν, cm^{-1}):, 3277 (≡C-H), 2144 (C≡C), 1701 (C=O), 1600, 1507, 1475 (Ar). ^{1}H NMR ($CDCl_3$, 298K, 400 MHz, δ, ppm): 9.90 (s, 1H), 7.93-7.80 (m, 2H), 7.15-7.04 (m, 2H), 5.77 (d, *J*= 2.4 Hz, 2H), 2.57 (t, *J*= 2.4

Hz, 1H). ^{13}C NMR ($CDCl_3$, 298K, 100 MHz, δ, ppm): 190.91, 162.51, 132.03, 130.75, 115.32, 77.68, 76.50, 56.09.

5,10,15,20-Tetrakis(4-propargyloxyphenyl)-2*H*-porphyrin (4). A solution of 4-(propargyloxy)benzaldehyde (**3**) (3.60 g, 22.5 mmol) and pyrrole (1.60 mL, 22.5 mmol) in propionic acid (100 mL) was flushed with argon and stirred 1 h at 120 °C. Then the propionic acid solvent was evaporated under reduced pressure. The crude residue was precipitated into cold methanol twice. Yield: 23%. IR (KBr, ν, cm^{-1}): 3326 (N-H), 3280 (≡C-H), 2150 (C≡C), 1604, 1501, 1471 (Ar). ^{1}H NMR (CD_2Cl_2, 298K, 400 MHz, δ, ppm): 8.87 (s, 8H), 8.20-8.10 (m, 8H), 7.39-7.29 (m, 8H), 4.99 (d, *J*= 2.4 Hz, 8H), 2.70 (t, *J*= 2.4 Hz, 4H), -2.76 (s, 2H). ^{13}C NMR (CD_2Cl_2, 298K, 100 MHz, δ, ppm): 158.14, 136.14, 135.92, 131.81, 120.23, 113.73, 79.31, 76.13, 56.76. MS (MALDI$^+$, dithranol, m/z): calcd. for $C_{56}H_{38}N_4O_4$, 830.3; found, 830.2 $[M]^+$, 853.2 $[M+Na]^+$ Anal. calcd. for $C_{56}H_{38}N_4O_4Zn$: C, 80.95%; H, 4.61%; N, 6.74%. Found: C, 81.13%; H, 4.65%; N, 3.02%.

5,10,15,20-tetrakis(4-propargyloxyphenyl)-Zn-porphyrin (ZnP-YNE). The free-base porphyrin (**4**) (0.20 g, 0.24 mmol) and zinc acetate dihydrate (0.53 g, 2.41 mmol) were dissolved in chloroform-methanol 1:1 (5 mL). The reaction mixture was stirred and heated under reflux for 12 h under an argon atmosphere. The solution was diluted with chloroform and washed with water and brine. The solvent was evaporated under reduced pressure to give pure **ZnP-YNE**. Yield: 91%. IR (KBr, ν, cm^{-1}): 3283 (≡C-H), 2120 (C≡C), 1601, 1487 (Ar). ^{1}H NMR (CD_2Cl_2, 298K, 400 MHz, δ, ppm): 8.95 (s, 8H), 8.19-8.10 (m, 8H), 7.41-7.30 (m, 8H), 4.98 (d, *J*= 2.4 Hz, 8H), 2.74 (t, *J*= 2.4 Hz, 4H). ^{13}C NMR (CD_2Cl_2, 298K, 100 MHz, δ, ppm): 157.98, 151.04, 136.65, 135.99, 132.43, 121.15, 113.58, 79.38, 76.09, 56.78. MS (MALDI$^+$, dithranol, m/z): calcd. for $C_{56}H_{36}N_4O_4Zn$, 892.2; found, 892.2 $[M]^+$, 915.2 $[M+Na]^+$. Anal. calcd. for $C_{56}H_{36}N_4O_4Zn$: C, 75.21%; H, 4.06%; N, 6.26%. Found: C, 75.03%; H, 4.19%; N, 6.01%.

5.2.2.2 *Synthesis of the Alkyne-Functionalized Wang Resin*

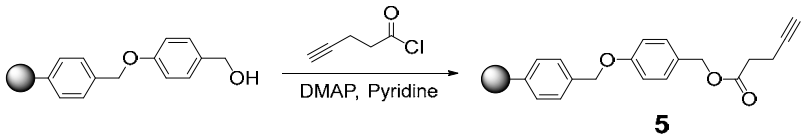

5

Scheme 5.3 Synthetic route of the alkyne-functionalized Wang resin.

Wang resin (2.0 g, 2.0 mmol) and a teaspoon of 4-(dimethylamino)pyridine were stirred in anhydrous pyridine (20 mL) for 1 h. Then 4-pentynoyl chloride (0.70 g, 6.0 mmol) was added and the reaction mixture was stirred at 60 °C for 24 h. The resin was filtered and washed with acetone-water (1:1), water, acetone and DCM. Yield: 98%. IR (KBr, ν, cm^{-1}): 3295 (≡C-H), 3023 (=C-H), 2120 (C≡C), 1731 (C=O), 1605, 1511, 1492 (Ar), 1137 (C-O).

5.2.2.3 *Synthesis of the Azide Precursors*

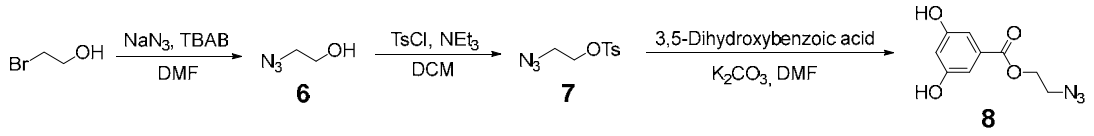

Scheme 5.4 Synthetic route of the azide precursor.

2-Azidoethanol (6). A mixture of 2-bromoethanol (1 mL, 14.11 mmol), sodium azide (1.83 g, 28.22 mmol) and tetrabutylammonium bromide (0.23 g, 0.71 mmol) in DMF (5 mL) was stirred overnight at 100 °C. Then the reaction mixture was poured into water and extracted with diethyl ether. The combined organic phases were washed with brine and dried over anhydrous magnesium sulfate. The solution was filtered and the solvent was removed under reduced pressure. Yield: 83%. IR (KBr, ν, cm^{-1}): 3368 (O-H), 2922 (C-H), 2105 (N_3). ^{1}H NMR ($CDCl_3$, 298K, 400 MHz, δ, ppm): 3.75 (t, *J*= 5.0 Hz, 2H), 3.42 (t, *J*= 5.0 Hz, 2H). ^{13}C NMR ($CDCl_3$, 298K, 100 MHz, δ, ppm): 58.42, 49.32.

2-Azidoethyl 4-metylbenzenesulfonate (7). 2-Azidoethanol (**6**) (0.50 g, 5.74 mmol) and triethylamine (1.60 mL, 11.48 mmol) were dissolved in anhydrous DCM (10 mL) and cooled in an ice bath. 4-Toluenesulfonyl chloride (1.64 g, 8.61 mmol) was added dropwise and the reaction mixture was stirred 2 h. After 2 h, the reaction mixture was poured into water and extracted with diethyl ether. The combined organic phases were washed with hydrochloric acid 2M (aq.), sodium bicarbonate 5% (aq.), brine and dried over anhydrous magnesium sulfate. The solution was filtered and the solvent was removed under reduced pressure. The residue was purified by flash column chromatography using DCM as eluent. Yield: 87%. IR (KBr, ν, cm^{-1}): 2111 (N_3), 2920 (C-H), 1142 (S=O). ^{1}H NMR (CD_2Cl_2, 298K, 400 MHz, δ, ppm): 7.82-7.77 (m, 2H), 7.42-7.37 (m, 2H), 4.17-4.09 (m, 2H), 3.52-3.43 (m, 2H), 2.46 (s, 3H). ^{13}C NMR (CD_2Cl_2, 298K, 100 MHz, δ, ppm): 145.91, 141.87, 130.41, 128.28, 68.75, 50.07, 21.81.

2-Azidoethyl 3,5-hydroxybenzoate (8). 2-Azidoethyl 4-metylbenzenesulfonate (**7**) (0.5 g, 2.07 mmol) was added dropwise to a solution of 3,5-dihydroxybenzoic acid (0.29 g, 1.88 mmol) and potassium carbonate (0.39 g, 2.82 mmol) in DMF (10 mL). The mixture was stirred overnight at room temperature. Then the reaction mixture was poured into water and extracted with diethyl ether. The combined organic phases were washed with brine and dried over anhydrous magnesium sulfate. The

solution was filtered and the solvent was removed under reduced pressure. The crude product was purified by flash column chromatography using DCM as eluent and gradually changing the composition of the eluent to DCM/ethyl acetate (8:2). Yield: 74%. IR (KBr, ν, cm^{-1}): 3400 (O-H), 2922 (C-H), 2100 (N_3), 1701 (C=O), 1610, 1502, 1447 (Ar), 1230, 1011 (C-O). ^{1}H NMR (CD_2Cl_2, 298K, 400 MHz, δ, ppm): 8.26 (s_{broad}, 2H), 7.27 (t, *J*= 2.3 Hz, 1H), 7.00 (d, *J*= 2.3 Hz, 2H), 4.46-4.35 (m, 2H), 3.63-3.50 (m, 2H). ^{13}C NMR (CD_2Cl_2, 298K, 100 MHz, δ, ppm): 166.67, 158.60, 131.83, 108.78, 108.66, 63.80, 50.42.

5.2.2.4 *Synthesis of Porphyrin-Core Dendrimers with Coumarin Units*

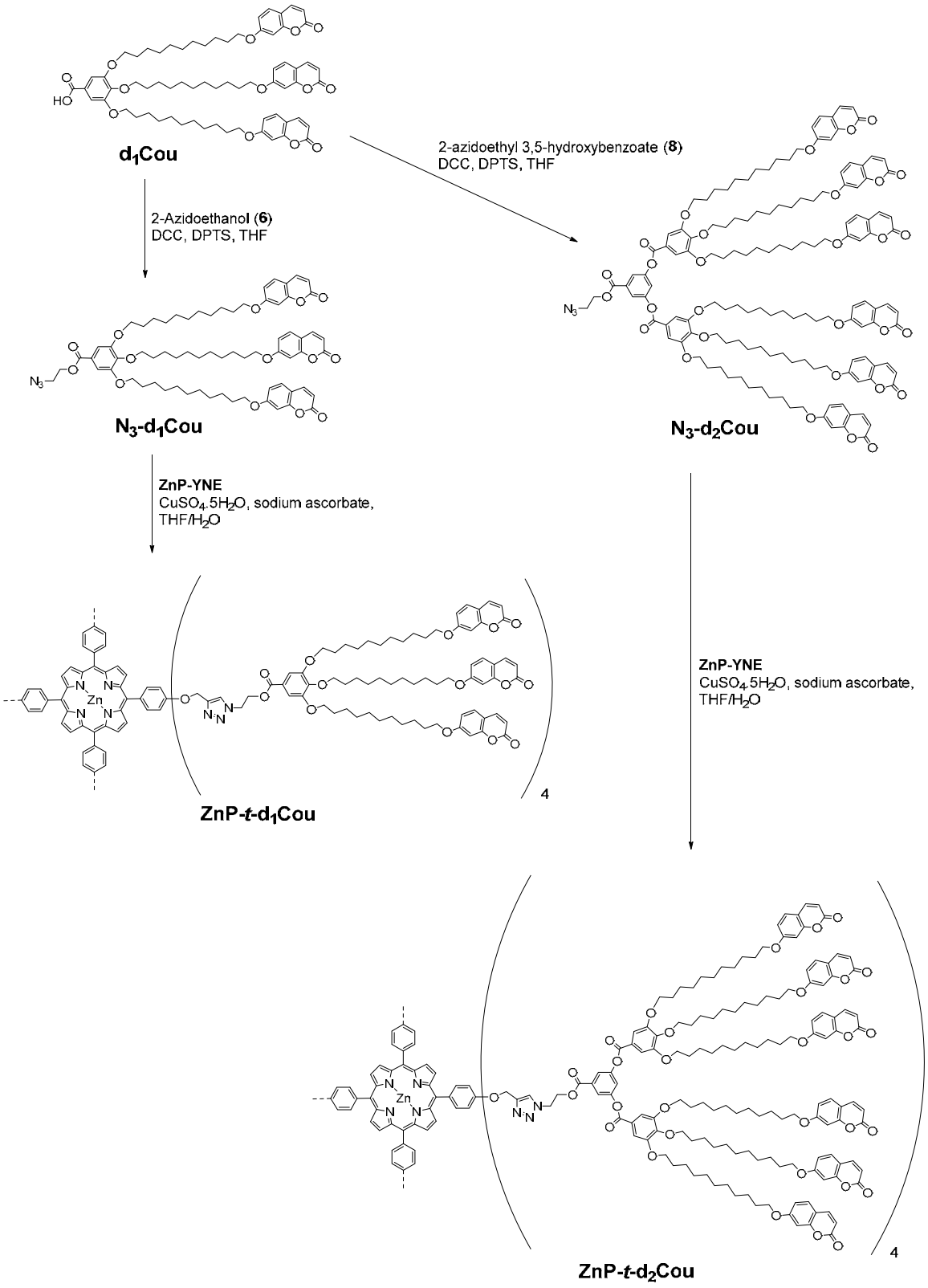

Scheme 5.5 Synthetic route of the porphyrin-core dendrimers with coumarin units.

2-Azidoethyl 3,4,5-tris((11-((2-oxo-2*H*-chromen-7-yl)oxy)undecyl)oxy)benzoate (N_3-d_1Cou). Compound **d_1Cou** (0.75 g, 0.67 mmol), 2-azidoethanol (**6**) (88 mg, 1.01 mmol) and 4-(dimethylamino)pyridinium *p*-toluenesulfonate (0.11 g, 0.34 mmol) were dissolved in anhydrous DCM (12 mL). The reaction flask was cooled in an ice bath and flushed with argon, then *N,N'*-dicyclohexylcarbodiimide (0.21 g, 1.01 mmol) was added dropwise. The mixture was stirred at RT for 24 h under argon atmosphere. The white precipitate was filtered off and washed with DCM. The solvent was evaporated and the crude product was purified by flash column chromatography on silica gel using DCM as eluent and gradually changing the composition of the eluent to DCM/ethyl acetate (9:1). Yield: 68%. IR (KBr, ν, cm^{-1}): 3070 (=C-H), 2921 (C-H), 2106 (N_3), 1737 (C=O), 1613, 1471 (Ar), 1231, 1127 (C-O). ^{1}H NMR (CD_2Cl_2, 298K, 400 MHz, δ, ppm): 7.67-7.58 (m, 3H), 7.42-7.33 (m, 3H), 7.27 (s, 2H), 6.86-6.76 (m, 6H), 6.21-6.15 (m, 3H), 4.49-4.41 (m, 2H), 4.08-3.92 (m, 12H), 3.60-3.53 (m, 2H), 1.89-1.64 (m, 12H), 1.53-1.23 (m, 42H). ^{13}C NMR (CD_2Cl_2, 298K, 100 MHz, δ, ppm): 166.43, 163.02, 161.46, 156.54, 153.49, 143.96, 142.97, 129.34, 124.72, 113.38, 113.29, 112.96, 108.36, 101.75, 73.98, 69.69, 69.32, 64.52, 50.67, 30.89, 30.26, 30.18, 30.16, 30.11, 29.97, 29.94, 29.92, 29.89, 29.57, 26.64, 26.53, 26.50. MS (MALDI$^+$, dithranol, m/z): calcd. for $C_{69}H_{87}N_3O_{14}$, 1181.6; found, 1182.1 $[M]^+$, 1205.1 $[M+Na]^+$. Anal. calcd. for $C_{69}H_{87}N_3O_{14}$: C, 70.09%; H, 7.42%; N, 3.55%. Found: C, 70.30%; H, 7.81%; N, 3.16.

2-Azidoethyl 3,5-bis(3,4,5-Tris((11-((2-oxo-2*H*-chromen-7-yl)oxy)undecyl)oxy) benzoyloxy)benzoate (N_3-d_2Cou). Compound **d_1Cou** (0.50 g, 0.45 mmol), 2-azidoethyl 3,5-hydroxybenzoate (**8**) (50 mg, 0.22 mmol) and 4-(dimethylamino) pyridinium *p*-toluenesulfonate (70 mg, 0.22 mmol) were dissolved in anhydrous DCM (10 mL). The reaction flask was cooled in an ice bath and flushed with argon, then *N,N'*-dicyclohexylcarbodiimide (0.10 g, 0.49 mmol) was added dropwise. The mixture was stirred at RT for 24 h under argon atmosphere. The white precipitate was filtered off and washed with THF. The solvent was evaporated and the crude product was purified by flash column chromatography on silica gel using DCM as eluent and gradually changing the composition of the eluent to DCM/ethyl acetate (8:2). Yield: 65%. IR (KBr, ν, cm^{-1}): 3075 (=C-H), 2922 (C-H), 2112 (N_3), 1731 (C=O), 1613, 1508 (Ar), 1190, 1122 (C-O). ^{1}H NMR (CD_2Cl_2, 298K, 400 MHz, δ, ppm): 7.85-7.79 (m, 2H), 7.67-7.59 (m, 6H), 7.45-7.31 (m, 11H), 6.86-6.73 (m, 12H), 6.23-6.13 (m, 6H), 4.56-4.44 (m, 2H), 4.13-3.91 (m, 24H), 3.68-3.55 (m, 2H), 1.92-1.64 (m,

24H), 1.61-1.18 (m, 84H). ^{13}C NMR (CD_2Cl_2, 298K, 100 MHz, δ, ppm): 165.14, 165.04, 163.01, 161.44, 156.54, 153.64, 152.17, 143.94, 143.76, 132.46, 129.34, 123.78, 121.54, 121.10, 113.38, 113.28, 112.97, 108.96, 101.76, 74.10, 69.84, 69.32, 64.63, 50.48, 30.93, 30.27, 30.19, 30.16, 30.12, 29.96, 29.92, 29.60, 29.57, 26.66, 26.63, 26.54, 26.51. MS (MALDI$^+$, dithranol, m/z): calcd. for $C_{143}H_{173}N_3O_{30}$, 2412.2; found, 2412.1 $[M]^+$, 2435.1 $[M+Na]^+$. Anal. calcd. for $C_{143}H_{173}N_3O_{30}$: C, 71.15%; H, 7.22%; N, 1.74%. Found: C, 71.03%; H, 6.99%; N, 2.02%.

ZnP-*t*-d$_1$Cou. A Schlenk flask was charged with **ZnP-YNE** (25.2 mg, 0.028 mmol), **N$_3$-d$_1$Cou** (200 mg, 0.17 mmol), sodium ascorbate (5.6 mg, 0.028 mmol) and THF (4 mL). Copper (II) sulfate pentahydrate (3.5 mg, 0.014 mmol) was dissolved in water (1 mL) and was added to the reaction. The reaction flask was degassed by three freeze-pump-thaw cycles and flushed with argon. The reaction mixture was stirred at 40 °C for 48 h. Then, the alkyne-functionalized resin (**5**) was added under argon flow to remove azide excess and the reaction mixture was stirred for further 24 h. The resin was filtered off, the mixture was diluted with THF and then passed through a short column of aluminum oxide, using THF as eluent, to remove copper salts. The resulting product was carefully precipitated into cold acetone. Yield: 91%. IR (KBr, ν, cm^{-1}): 2923 (C-H), 1730 (C=O), 1612, 1507 (Ar), 1230, 1123 (C-O). ^{1}H NMR (CD_2Cl_2, 298K, 400 MHz, δ, ppm): 8.92 (s, 8H), 8.15-8.05 (m, 8H), 7.93 (s, 4H), 7.56-7.42 (m, 12H), 7.40-7.31 (m, 8H), 7.31-7.11 (m, 20H), 6.75-6.55 (m, 24H), 6.12-5.96 (m, 12H), 5.36 (s, 8H), 4.87-4.79 (m, 8H), 4.79-4.69 (m, 8H), 4.09-3.78 (m, 48H), 1.86-1.56 (m, 48H), 1.52-1.17 (m, 168H). ^{13}C NMR (CD_2Cl_2, 298K, 100 MHz, δ, ppm): 166.23, 162.80, 161.38, 158.61, 156.27, 153.52, 150.85, 144.74, 143.81, 143.17, 136.57, 136.17, 132.28, 129.13, 124.47, 124.17, 120.91, 113.37, 113.14, 112.75, 108.37, 101.56, 74.00, 69.72, 69.18, 63.42, 62.76, 49.96, 30.87, 30.14, 30.07, 29.90, 29.51, 29.45, 26.67, 26.41. MS (MALDI$^+$, DCTB, m/z): calcd. for $C_{334}H_{390}N_{16}O_{60}Zn$, 5648.7; found, 5648.7 $[M]^+$. Anal. calcd. for $C_{334}H_{390}N_{16}O_{60}Zn$: C, 70.95%; H, 6.95%; N, 3.96%. Found: C, 71.20%; H, 6.95%; N, 4.02%.

ZnP-*t*-d$_2$Cou. A Schlenk flask was charged with **ZnP-YNE** (15.4 mg, 0.017 mmol), **N$_3$-d$_2$Cou** (250 mg, 0.104 mmol), sodium ascorbate (3.4 mg, 0.017 mmol) and THF (5 mL). Copper (II) sulfate pentahydrate (2.2 mg, 0.009 mmol) was dissolved in water (1 mL) and was added to the reaction. The reaction flask was degassed by three freeze-pump-thaw cycles and flushed with argon. The reaction mixture was stirred at 40 °C for 48 h. Then, the alkyne-functionalized resin (**5**) was added under

argon flow to remove azide excess and the reaction mixture was stirred for further 24 h. The resin was filtered off, the mixture was diluted with THF and then passed through a short column of aluminum oxide, using THF as eluent, to remove copper salts. The resulting product was carefully precipitated into cold acetone. Yield: 71%. IR (KBr, ν, cm^{-1}): 2917 (C-H), 1732 (C=O), 1610, 1511 (Ar), 1230, 1125 (C-O). ^{1}H NMR (CD_2Cl_2, 298K, 500 MHz, δ, ppm): 9.00-8.77 (m, 8H), 8.22-7.89 (m, 12H), 7.88-7.72 (m, 8H), 7.71-7.05 (m, 76H), 6.92-6.55 (m, 48H), 6.28-5.95 (m, 24H), 5.48-5.36 (m, 8H), 4.98-4.42 (m, 16H), 4.15-3.73 (m, 96H), 1.98-0.95 (m, 432H). ^{13}C NMR (CD_2Cl_2, 298K, 125 MHz, δ, ppm): 165.02, 162.92, 161.45, 156.39, 153.57, 152.20, 150.83, 143.93, 143.73, 136.52, 136.16, 132.12, 129.24, 123.69, 121.70, 121.10, 120.81, 113.38, 113.22, 108.95, 101.64, 74.02, 69.79, 69.24, 63.64, 62.39 (detected by ^{1}H-^{13}C HSQC, H5-C5), 49.51 (detected by ^{1}H-^{13}C HSQC, H2-C2), 30.87, 30.12, 30.06, 29.92, 29.87, 29.55, 29.50, 26.61, 26.50, 26.44. MS (MALDI^{+}, DCTB, m/z): calcd. for $C_{630}H_{734}N_{16}O_{124}Zn$, 10571.1; found, 10571.2 $[M]^{+}$, 10594.3 $[M+Na]^{+}$. Anal. calcd. for $C_{630}H_{734}N_{16}O_{124}Zn$: C, 71.52%; H, 6.99%; N, 2.12%. Found: C, 71.13%; H, 6.75%; N, 2.05%.

5.2.2.5 *Synthesis of Porphyrin-Core Dendrimers with 4-(Trifluoromethyl) Coumarin Units*

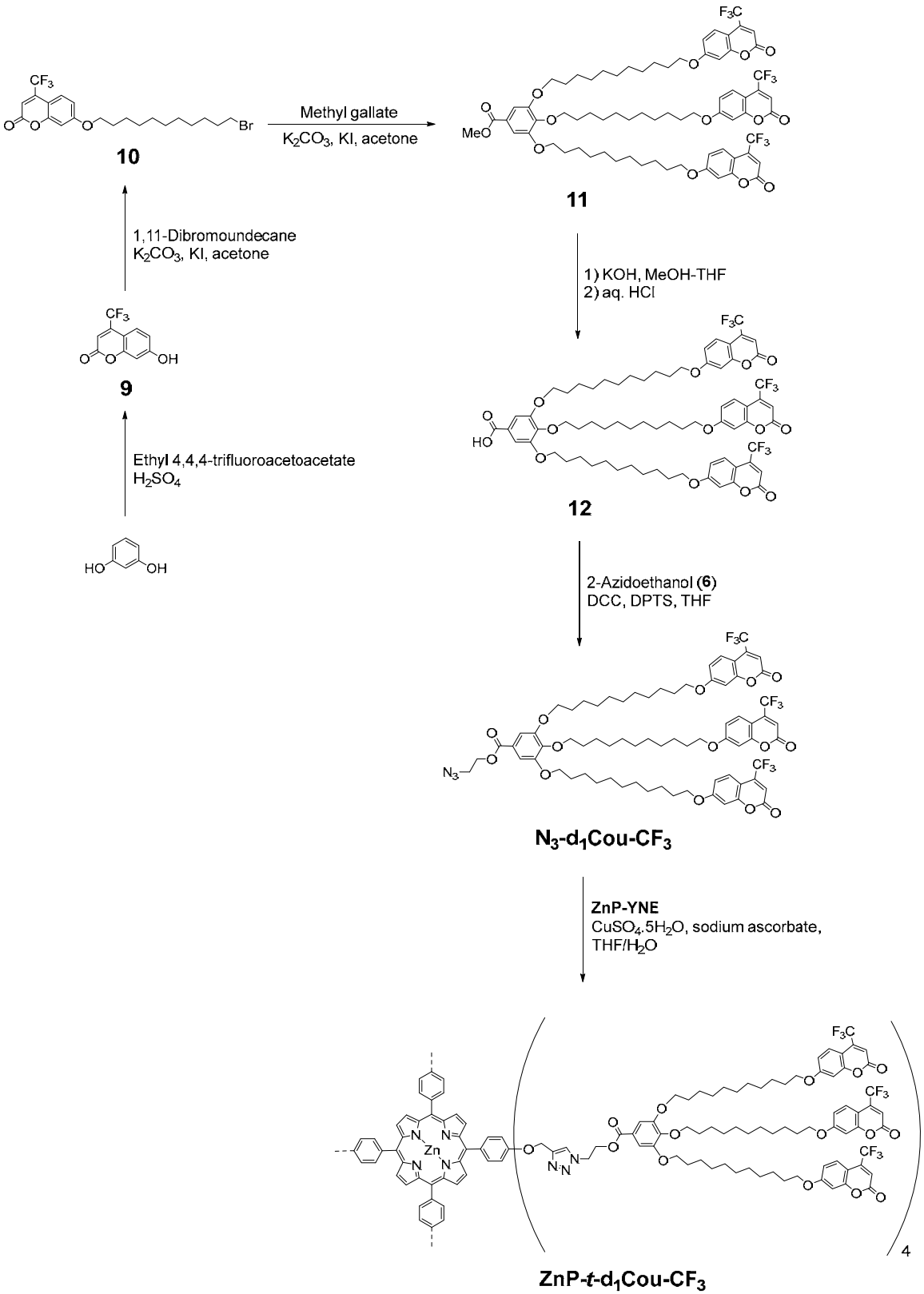

Scheme 5.6 Synthetic route of the porphyrin-core dendrimer with 4-(trifluoromethyl)coumarin units.

7-Hydroxy-4-(trifluoromethyl)-2*H*-chromen-2-one (9). Resorcinol (2.00 g, 18.2 mmol) was dissolved in concentrated sulfuric acid (7 mL) and cooled to 0 °C with stirring. After 30 min, a solution of ethyl 4,4,4-trifluoroacetoacetate (4 mL, 27.4 mmol) in concentrated sulfuric acid (10 mL) was added dropwise. The reaction mixture was allowed to warm up to RT and stirred overnight. After that, the reaction mixture was poured into ice water and the precipitate was filtered and washed with water. Yield: 79%. IR (KBr, ν, cm^{-1}): 3398 (O-H), 3106 (=C-H), 1713 (C=O), 1611, 1518, 1442 (Ar), 1194, 1130 (C-O). ^{1}H NMR (DMSO-d_6, 298K, 400 MHz, δ, ppm): 10.98 (s_{broad}, 1H), 7.58-7.49 (m, 1H), 6.89 (dd, *J*= 8.9, 2.4 Hz, 1H), 6.81 (d, *J*= 2.4 Hz, 1H), 6.70 (s, 1H). ^{13}C{^{1}H} NMR (DMSO-d_6, 298K, 100 MHz, δ, ppm): 162.26, 158.90, 155.97, 139.93 (q, $^{2}J_{C-F}$= 32.1 Hz), 126.15, 121.78 (q, $^{1}J_{C-F}$= 275.6 Hz), 114.12, 111.84 (q, $^{3}J_{C-F}$= 5.9 Hz), 105.26, 103.18. ^{19}F{^{1}H} NMR (DMSO-d_6, 298K, 282 MHz, δ, ppm): -63.57.

7-((11-bromoundecyl)oxy)-4-(trifluoromethyl)-2*H*-chromen-2-one (10). A solution of 7-hydroxy-4-(trifluoromethyl)-2*H*-chromen-2-one (**9**) (5.00 g, 21.73 mmol) in acetone (100 mL) was added dropwise over more than 1 h to a mixture of 1,11-dibromoundecane (13.65 g, 43.45 mmol), potassium carbonate (6.00 g, 43.45 mmol) a teaspoon of 18-crown-6 in acetone (50 mL) at reflux. The reaction was allowed to cool down to RT and the solids filtered off and washed with acetone. The solvent was evaporated under reduced pressure and the residue was purified by flash column chromatography using hexane/DCM (1:1) as eluent. Yield: 48%. IR (KBr, ν, cm^{-1}): 3087 (=C-H), 2921 (C-H), 1735 (C=O), 1615, 1556 (Ar), 1207, 1133 (C-O). ^{1}H NMR (CD_2Cl_2, 298K, 500 MHz, δ, ppm): 7.67-7.59 (m, 1H), 6.94 (dd, *J*= 9.0, 2.5 Hz, 1H), 6.90 (d, *J*= 2.5 Hz, 1H), 6.61 (s, 1H), 4.07 (t, *J*= 6.6 Hz, 2H), 3.44 (t, *J*= 6.6 Hz, 2H), 1.93-1.77 (m, 4H), 1.57-1.24 (m, 14H).^{13}C{^{1}H} NMR (CD_2Cl_2, 298K, 125 MHz, δ, ppm): 163.80, 159.82, 157.01, 141.84 (q, $^{2}J_{C-F}$= 32.6 Hz), 126.74, 122.36 (q, $^{1}J_{C-F}$= 275.5 Hz), 114.15, 112.79 (q, $^{3}J_{C-F}$= 5.7 Hz), 107.34, 102.41, 69.56, 34.81, 33.47, 30.04, 30.01, 29.97, 29.85, 29.46, 29.31, 28.72, 26.43. ^{19}F{^{1}H} NMR (CD_2Cl_2, 298K, 282 MHz, δ, ppm): -65.05.

Methyl 3,4,5-tris((11-((2-oxo-4-(trifluoromethyl)-2H-chromen-7-yl)oxy)undecyl) oxy)benzoate (11). A mixture of compound **10** (2.5 g, 5.42 mmol), methyl gallate (0.30 g, 1.64 mmol), potassium carbonate (2.27 g, 16.42 mmol), a teaspoon of potassium iodide and acetone (75 mL) was stirred and heated under reflux for 24 h. The reaction mixture was allowed to cool down to RT and the solids were filtered

off and washed with acetone. The solvent was evaporated and the crude product was purified by flash column chromatography on silica gel using DCM as eluent and gradually changing the composition of the eluent to DCM/ethyl acetate (19:1). Yield: 70%. IR (KBr, ν, cm^{-1}): 3085 (=C-H), 2923 (C-H), 1731 (C=O), 1615, 1557, 1430 (Ar), 1281, 1134 (C-O). ^{1}H NMR (CD_2Cl_2, 298K, 400 MHz, δ, ppm): 7.66-7.55 (m, 3H), 7.24 (s, 2H), 6.95-6.83 (m, 6H), 6.60-6.55 (m, 3H), 4.08-3.96 (m, 12H), 3.85 (s, 3H), 1.88-1.67 (m, 12H), 1.53-1.25 (m, 42H). $^{13}C\{^{1}H\}$ NMR (CD_2Cl_2, 298K, 100 MHz, δ, ppm): δ 167.22, 163.77, 159.80, 156.99, 153.42, 142.69, 141.82 (q, $^{2}J_{C-F}$= 33.4 Hz), 126.72, 125.38, 122.34 (q, $^{1}J_{C-F}$= 275.3 Hz), 114.13, 112.79 (q, $^{3}J_{C-F}$= 5.9 Hz), 108.20, 107.33, 102.38, 73.95, 69.67, 69.56, 52.50, 30.90, 30.26, 30.17, 30.12, 29.95, 29.91, 29.49, 26.65, 26.47. $^{19}F\{^{1}H\}$ NMR (CD_2Cl_2, 282 MHz, δ, ppm): -65.05.

3,4,5-Tris((11-((2-oxo-4-(trifluoromethyl)-2*H*-chromen-7-yl)oxy)undecyl)oxy) benzoic acid (12). An aqueous solution of potassium hydroxide (0.32 g, 2 mL) was added to a solution of compound **11** (0.75 g, 0.56 mmol) in THF-methanol 1:1 (20 mL). The mixture was stirred and heated under reflux and the evolution of the reaction was followed by thin layer chromatography. When all of the starting material had been consumed, the reaction mixture was neutralized with concentrated hydrochloric acid until pH 2. The organic solvents were evaporated under reduced pressure and the resulting aqueous phase was extracted with DCM. The combined organic phases were washed with brine and dried over anhydrous magnesium sulfate. The solution was filtered and the solvent was removed under reduced pressure. The product was purified by flash chromatography on silica gel using DCM as eluent and gradually changing the composition of the eluent to ethyl acetate. Yield: 70%. IR (KBr, ν, cm^{-1}): 3240 (O-H), 3084 (=C-H), 2922 (C-H), 1735, 1680 (C=O), 1617, 1541, 1468 (Ar), 1235, 1129 (C-O). ^{1}H NMR (CD_2Cl_2, 298K, 400 MHz, δ, ppm): 7.65-7.53 (m, 3H), 7.30 (s, 2H), 6.96-6.83 (m, 6H), 6.60-6.55 (m, 3H), 4.12-3.93 (m, 12H), 1.90-1.66 (m, 12H), 1.57-1.21 (m, 42H). $^{13}C\{^{1}H\}$ NMR (CD_2Cl_2, 298K, 100 MHz, δ, ppm): 170.72, 163.79, 159.85, 156.99, 153.50, 143.55, 141.84 (q, $^{2}J_{C-F}$= 31.8 Hz), 126.73, 124.11, 122.35 (q, $^{1}J_{C-F}$= 275.7 Hz), 114.14, 112.79 (q, $^{3}J_{C-F}$= 5.8 Hz), 108.86, 107.34, 102.41, 74.03, 69.75, 69.57, 30.91, 30.25, 30.15, 30.11, 29.94, 29.90, 29.48, 26.64, 26.47. $^{19}F\{^{1}H\}$ NMR (CD_2Cl_2, 298K, 282 MHz, δ, ppm): -65.05.

2-Azidoethyl 3,4,5-Tris((11-((2-oxo-4-(trifluoromethyl)-2H-chromen-7-yl)oxy) undecyl)oxy)benzoate (N_3-d_1Cou-CF_3). Compound **12** (0.3 g, 0.23 mmol),

2-azidoethanol (**6**) (29.7 mg, 0.34 mmol) and 4-(dimethylamino)pyridinium *p*-toluenesulfonate (36 mg, 0.12 mmol) were dissolved in anhydrous DCM (10 mL). The reaction flask was cooled in an ice bath and flushed with argon, then *N,N'*-dicyclohexylcarbodiimide (70.5 mg, 0.34 mmol) was added dropwise. The mixture was stirred at RT for 24 h under argon atmosphere. The white precipitate was filtered off and washed with DCM. The solvent was evaporated and the crude product was purified by flash column chromatography on silica gel using DCM as eluent and gradually changing the composition of the eluent to DCM/ethyl acetate (9:1). Yield: 72%. IR (KBr, ν, cm^{-1}): 3080 (=C-H), 2918 (C-H), 2111 (N_3), 1733 (C=O), 1609, 1537, 1422 (Ar), 1291, 1135 (C-O). ^{1}H NMR (CD_2Cl_2, 298K, 400 MHz, δ, ppm): 7.65-7.56 (m, 3H), 7.27 (s, 2H), 6.96-6.84 (m, 6H), 6.61-6.55 (m, 3H), 4.52-4.36 (m, 2H), 4.15-3.91 (m, 12H), 3.61-3.41 (m, 2H), 1.86-1.62 (m, 12H), 1.54-1.06 (m, 42H). ^{13}C{^{1}H} NMR (CD_2Cl_2, 298K, 100 MHz, δ, ppm): 166.43, 163.78, 159.81, 156.98, 153.49, 142.97, 141.83 (q, $^2J_{C\text{-}F}$= 32.8 Hz), 126.73, 124.74, 122.34 (q, $^1J_{C\text{-}F}$= 275.2 Hz), 114.13, 112.79 (q, $^3J_{C\text{-}F}$= 5.8 Hz), 108.36, 107.33, 102.39, 73.98, 69.69, 69.56, 64.53, 50.67, 30.90, 30.26, 30.16, 30.11, 29.94, 29.90, 29.49, 26.64, 26.47. ^{19}F{^{1}H} NMR (CD_2Cl_2, 298K, 282 MHz, δ, ppm): -65.05. MS (MALDI$^+$, dithranol, m/z): calcd. for $C_{72}H_{84}F_9N_3O_{14}$, 1385.6; found, 1385.7 $[M]^+$, 1408.7 $[M+Na]^+$. Anal. calcd. for $C_{72}H_{84}F_9N_3O_{14}$: C, 62.37%; H, 6.11%; N, 3.03%. Found: C, 62.18%; H, 6.37%; N, 3.16.

ZnP-*t*-d$_1$Cou-CF$_3$. A Schlenk flask was charged with the **ZnP-YNE** (15.5 mg, 0.017 mmol), compound **N$_3$-d$_1$Cou-CF$_3$** (150 mg, 0.104 mmol), sodium ascorbate (3.4 mg, 0.017 mmol) and THF (3 mL). Copper (II) sulfate pentahydrate (2.2 mg, 0.009 mmol) was dissolved in water (1 mL) and was added to the reaction. The reaction flask was degassed by three freeze-pump-thaw cycles and flused with argon. The reaction mixture was stirred at 40 °C for 48 h. Then, the alkyne-functionalized resin (**5**) was added under argon flow to remove azide excess and the reaction mixture was stirred for further 24 h. The resin was filtered off, the mixture was diluted with THF and then passed through a short column of aluminum oxide, using THF as eluent, to remove copper salts. The resulting product was carefully precipitated into cold methanol. Yield: 82%. IR (KBr, ν, cm^{-1}): 2924 (C-H), 1731 (C=O), 1605, 1507, 1471 (Ar), 1234, 1118 (C-O). ^{1}H NMR ($C_2D_2Cl_4$, 373K, 500 MHz, δ, ppm): 9.07-8.94 (m, 8H), 8.25-8.14 (m, 8H), 7.97-7.89 (m, 4H), 7.69-7.54 (m, 12H), 7.50-7.38 (m, 8H), 7.35-7.25 (m, 8H), 7.00-6.80 (m, 24H), 6.66-6.49 (m, 12H), 5.63-5.46 (m, 8H), 4.96-4.78 (m, 16H), 4.17-3.94 (m, 48H), 1.92-1.72 (m, 48H), 1.62-1.28 (m,

168H). ^{13}C {^{1}H} NMR ($C_2D_2Cl_4$, 373K, 500 MHz, δ, ppm): 165.62, 163.08, 158.80, 158.13, 156.26, 152.93, 150.35, 144.52, 143.83, 141.28 (q, $^{2}J_{C-F}$= 32.5 Hz), 135.93, 135.35, 131.66, 125.98, 123.62, 122.94, 122.69 (q, $^{1}J_{C-F}$= 312.9 Hz), 120.45, 113.45, 113.18, 111.99 (q, $^{3}J_{C-F}$= 5.3 Hz), 109.18, 106.76, 102.16, 69.65, 68.95, 62.70, 62.44, 49.17, 30.16, 29.28, 29.21, 29.12, 28.99, 28.70, 25.90, 25.83, 25.65. ^{19}F{^{1}H} NMR ($C_2D_2Cl_4$, 298K, 282 MHz, δ, ppm): -65.05. MS (MALDI^{+}, DCTB, m/z): calcd. for $C_{346}H_{378}F_{36}N_{16}O_{60}Zn$, 6464.6; found, 6464.5 $[M]^{+}$, 6487.5 $[M+Na]^{+}$. Anal. calcd. for $C_{346}H_{378}F_{36}N_{16}O_{60}Zn$: C, 64.23%; H, 5.89%; N, 3.46%. Found: C, 64.20%; H, 5.99%; N, 3.09%.

5.2.2.6 *Synthesis of Porphyrin-Core Dendrimers with Dodecyl Alkyl Chains*

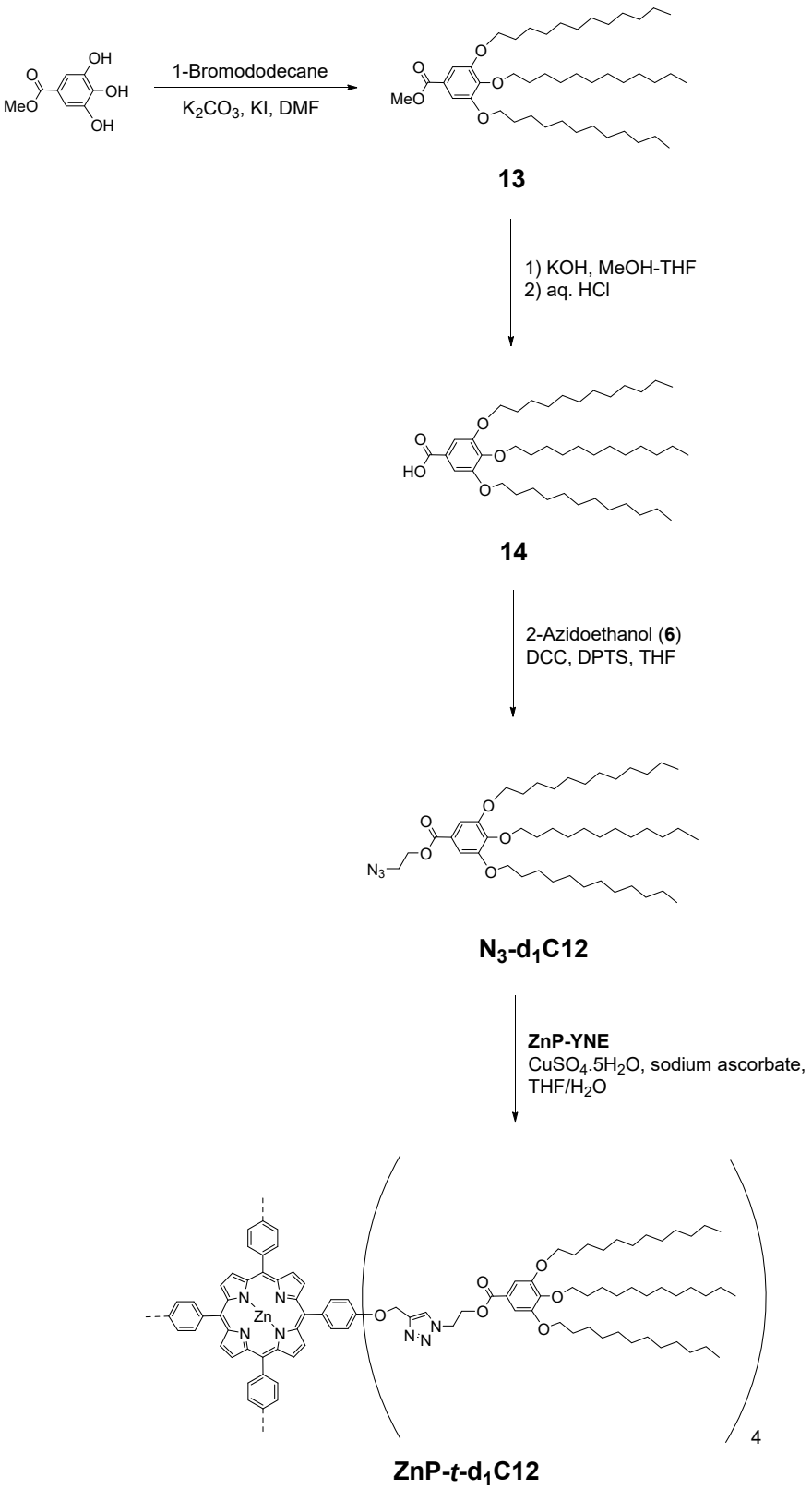

Scheme 5.7 Synthetic route of the porphyrin-core dendrimer with dodecyl alkyl chains.

Methyl 3,4,5-tris(dodecyloxy)benzoate (13). Methyl gallate (1.5 g, 8.15 mmol), potassium carbonate (6.1 g, 43.6 mmol) and a teaspoon of potassium iodide were stirred in DMF (75 mL). The mixture was heated to 110 ºC and then 1-bromododecane (6.0 mL, 25.0 mmol) was slowly added. The reaction was stirred at 110 ºC for 12 h. The mixture was allowed to cool down to RT and poured into water and extracted with hexane/ethyl acetate (1:1). The combined organic phases were washed with sodium hydroxide 10% (aq.), brine and dried over anhydrous magnesium sulfate. The solution was filtered and the solvent was removed under reduced pressure. The crude product was recrystallized in ethanol. Yield: 88%. IR (KBr, ν, cm^{-1}): 2933 (C-H), 1717 (C=O), 1589, 1504 (Ar), 1234, 1132 (C-O). ^{1}H NMR (CD_2Cl_2, 298K, 400 MHz, δ, ppm): 7.24 (s, 2H), 4.09-3.92 (m, 6H), 3.85 (s, 3H), 1.89-1.65 (m, 6H), 1.55-1.18 (m, 54H), 0.88 (t, *J*= 6.8 Hz, 9H). ^{13}C NMR (CD_2Cl_2, 298K, 100 MHz, δ, ppm): 167.10, 153.30, 142.63, 125.22, 108.11, 73.83, 69.56, 32.36, 30.76, 30.13, 30.06, 29.83, 29.79, 26.52, 23.12, 14.29.

3,4,5-Tri(dodecyloxy)benzoic acid (14). An aqueous solution of potassium hydroxide (0.81. g, 2 mL) was added to a solution of compound **13** (2.00 g, 2.90 mmol) in ethanol (10 mL). The mixture was stirred and heated under reflux and the evolution of the reaction was followed by thin layer chromatography. When all of the starting material had been consumed, the crude product was precipitated by addition of concentrated hydrochloric acid until pH 2 and it was filtered. The product was purified by recrystallization in ethanol. Yield: 96%. IR (KBr, ν, cm^{-1}): 3240 (O-H), 2923 (C-H), 1736, 1685 (C=O), 1617, 1508, 1472 (Ar), 1234, 1128 (C-O). ^{1}H NMR (CD_2Cl_2, 298K, 400 MHz, δ, ppm): 7.22 (s, 2H), 4.04-3.84 (m, 6H), 1.87-1.63 (m, 6H), 1.54-1.16 (m, 54H), 0.88 (t, *J*= 6.8 Hz, 9H). ^{13}C NMR (CD_2Cl_2, 298K, 100 MHz, δ, ppm): 172.80, 153.30, 143.79, 124.29, 108.11, 73.83, 69.56, 32.38, 30.76, 30.19, 30.13, 29.83, 29.78, 26.52, 23.12, 14.29.

2-Azidoethyl 3,4,5-tris(dodecyloxy)benzoate (N_3-d_1C12). Compound **14** (0.75 g, 1.11 mmol), 2-azidoethanol (**6**) (0.15 g, 1.67 mmol) and 4-(dimethylamino) pyridinium *p*-toluenesulfonate (0.17 g, 0.55 mmol) were dissolved in anhydrous DCM (10 mL). The reaction flask was cooled in an ice bath and flushed with argon, then *N,N'*-dicyclohexylcarbodiimide (0.34 g, 1.67 mmol) was added dropwise. The mixture was stirred at RT for 24 h under argon atmosphere. The white precipitate was filtered off and washed with DCM. The solvent was evaporated and the crude product was purified by flash column chromatography on silica gel using

hexane/ethyl acetate (9:1). Yield: 83%. IR (KBr, ν, cm^{-1}): 2921 (C-H), 2115 (N_3), 1735 (C=O), 1608, 1512, 1469 (Ar), 1228, 1126 (C-O). ^{1}H NMR (CD_2Cl_2, 298K, 500 MHz, δ, ppm): 7.27 (s, 2H), 4.49-4.42 (m, 2H), 4.06-3.95 (m, 6H), 3.63-3.53 (m, 2H), 1.85-1.68 (m, 6H), 1.51-1.20 (m, 54H), 0.88 (t, *J*= 7.0 Hz, 9H). ^{13}C NMR (CD_2Cl_2, 298K, 125 MHz, δ, ppm): 166.30, 153.37, 142.93, 124.57, 108.28, 73.87, 69.59, 64.33, 50.54, 32.37, 30.76, 30.15, 30.13, 30.09, 30.07, 29.99, 29.82, 29.80, 29.77, 26.52, 26.49, 23.12, 14.29. MS (MALDI$^+$, dithranol, m/z): calcd. for $C_{45}H_{81}N_3O_5$, 743.6; found, 743.7 $[M]^+$, 766.7 $[M+Na]^+$. Anal. calcd. for $C_{45}H_{81}N_3O_5$: C, 72.63%; H, 10.97%; N, 5.65%. Found: C, 72.33%; H, 10.83%; N, 5.72.

ZnP-*t*-d_1C12. A Schlenk flask was charged with **ZnP-YNE** (70.7 mg, 0.079 mmol), **N_3-d_1C12** (0.25 g, 0.336 mmol), sodium ascorbate (15.7 mg, 0.079 mmol) and THF (3 mL). Copper (II) sulfate pentahydrate (9.9 mg, 0.040 mmol) was dissolved in water (1 mL) and was added to the reaction. The reaction flask was degassed by three freeze-pump-thaw cycles and flushed with argon. The reaction mixture was stirred at 40 °C for 48 h. Then, the alkyne-functionalized resin (**5**) was added under argon flow to remove azide excess and the reaction mixture was stirred for further 24 h. The resin was filtered off, the mixture was diluted with THF and then passed through a short column of aluminum oxide, using THF as eluent, to remove copper salts. The resulting product was carefully precipitated into cold methanol. Yield: 82%. IR (KBr, ν, cm^{-1}): 2924 (C-H), 1732 (C=O), 1610, 1509, 1470 (Ar), 1232, 1125 (C-O). ^{1}H NMR (CD_2Cl_2, 298K, 500 MHz, δ, ppm): 8.97-8.91 (m, 8H), 8.12-8.06 (m, 8H), 7.76-7.68 (m, 4H), 7.29-7.21 (m, 8H), 7.20 (s, 2H), 5.02-4.85 (m, 8H), 4.72-4.56 (m, 16H), 4.09-3.88 (m, 24H), 1.86-1.62 (m, 24H), 1.50-1.10 (m, 216H), 0.89-0.73 (m, 54H). ^{13}C NMR (CD_2Cl_2, 298K, 125 MHz, δ, ppm): 166.03, 158.34, 153.40, 150.86, 144.42, 143.18, 136.59, 136.05, 132.14, 124.25, 123.58, 120.83, 113.21, 108.30, 100.45, 73.88, 69.62, 63.11, 62.32, 49.70, 32.31, 30.75, 30.11, 30.06, 29.96, 29.84, 29.78, 26.55, 26.47, 23.07, 14.27. MS (MALDI$^+$, DCTB, m/z): calcd. for $C_{238}H_{366}N_{16}O_{24}Zn$, 3896.7; found, 3896.9 $[M]^+$. Anal. calcd. for $C_{238}H_{366}N_{16}O_{24}Zn$: C, 73.28%; H, 9.46%; N, 5.74%. Found: C, 73.00%; H, 9.49%; N, 6.02%.

5.2.2.7 *Synthesis of Porphyrin-Core Dendrimers with Carbazole Units*

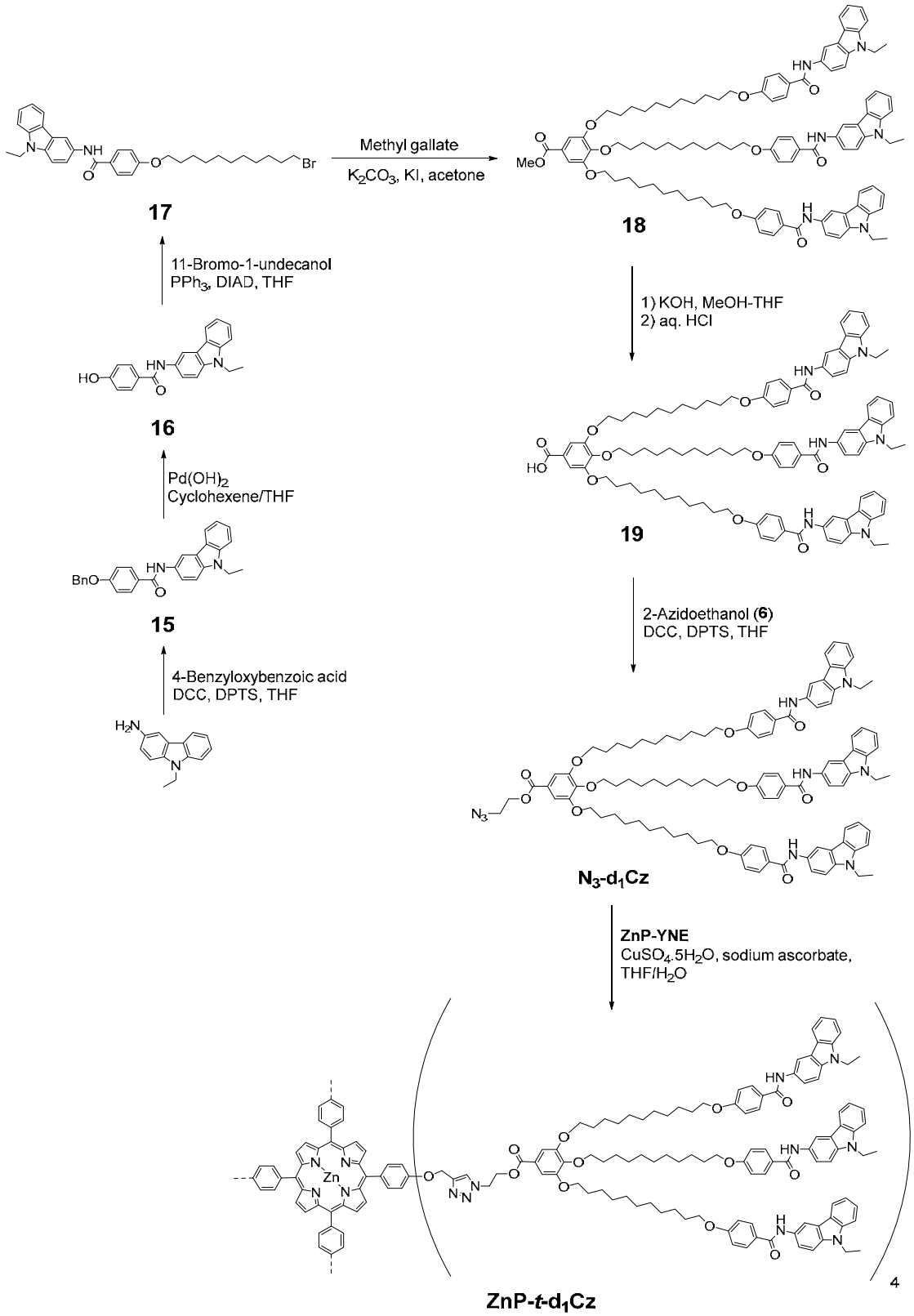

Scheme 5.8 Synthetic route of the porphyrin-core dendrimer with carbazole units.

4-Benzyloxy-*N*-(9-ethyl-9*H*-carbazol-3-yl)benzamide (15). 4-Benzyloxybenzoic acid (10 g, 43.81 mmol), 9-ethyl-9*H*-carbazol-3-amine (9.21 g, 43.81 mmol) and 4-(dimethylamino)pyridinium *p*-toluenesulfonate (3.42 g, 10.95 mmol) were dissolved in anhydrous THF (250 mL). The reaction flask was cooled in an ice bath and flushed with argon, then *N,N'*-dicyclohexylcarbodiimide (9.94 g, 48.19 mmol) was added dropwise. The mixture was stirred at RT for 24 h under argon atmosphere. The precipitate was filtered off and the solvent was evaporated. The crude product was recrystallized in ethanol. Yield: 78%. IR (KBr, ν, cm^{-1}): 3327 (N-H), 2922 (C-H), 1638 (C=O), 1607, 1509, 1472 (Ar). ^{1}H NMR (DMSO-d_6, 298K, 400 MHz, δ, ppm): 10.14 (s, 1H), 8.59-8.48 (m, 1H), 8.12-8.05 (m, 1H), 8.05-7.98 (m, 2H), 7.80-7.71 (m, 1H), 7.64-7.54 (m, 2H), 7.53-7.31 (m, 6H), 7.23-7.11 (m, 3H), 5.22 (s, 2H), 4.44 (q, *J*= 7.1 Hz, 2H), 1.32 (t, *J*= 7.1 Hz, 3H). ^{13}C NMR (DMSO-d_6, 298K, 100 MHz, δ, ppm): 164.57, 160.78, 139.98, 136.72, 136.40, 131.12, 129.44, 128.50, 127.97, 127.80, 127.44, 125.73, 122.13, 121.80, 120.34, 120.17, 118.58, 114.44, 112.75, 109.17, 108.82, 69.40, 36.99, 13.72.

***N*-(9-ethyl-9*H*-carbazol-3-yl)-4-hydroxybenzamide (16).** Compound **15** (3.5 g, 8.32 mmol) and $Pd(OH)_2$/C (20% wt.) (0.75 g) were dissolved in a mixture of THF (75 mL) and cyclohexene (150 mL) under reflux. After 12 h, the catalyst was filtered off using Celite® and carefully washed with DCM. The solvent was evaporated to give pure compound **16**. Yield: 98%. IR (KBr, ν, cm^{-1}): 3325 (N-H), 2925 (C-H), 1640 (C=O), 1607, 1506, 1471 (Ar). ^{1}H NMR (DMSO-d_6, 298K, 400 MHz, δ, ppm): 10.06 (s, 1H), 10.04 (s, 1H), 8.54-8.49 (m, 1H), 8.11-8.03 (m, 1H), 7.95-7.88 (m, 2H), 7.77-7.69 (m, 1H), 7.62-7.52 (m, 2H), 7.48-7.41 (m, 1H), 7.24-7.14 (m, 1H), 6.95-6.83 (m, 2H), 4.43 (q, *J* = 7.1 Hz, 2H), 1.31 (t, *J* = 7.1 Hz, 3H). ^{13}C NMR (DMSO-d_6, 298K, 100 MHz, δ, ppm): 164.82, 160.34, 139.98, 136.34, 131.25, 129.56, 125.68, 122.15, 121.80, 120.37, 120.16, 118.56, 114.89, 112.73, 109.16, 108.79, 36.99, 13.72.

4-((11-bromoundecyl)oxy]-*N*-(9-ethyl-9*H*-carbazol-3-yl)benzamide (17). Compound **16** (2.75 g, 8.32 mmol), 11-bromo-1-undecanol (2.30 g, 9.16 mmol) and triphenylphosphine (2.40 g, 9.16 mmol) were dissolved in anhydrous THF (120 mL). The reaction flask was cooled in an ice bath and flushed with argon, then diisopropylazadicarboxylate (1.85 g, 9.16 mmol) was added dropwise. The mixture was stirred at RT for 12 h under argon atmosphere. The white precipitate was filtered off. The solvent was evaporated and the crude product was recrystallized in ethanol. Yield: 88%. IR (KBr, ν, cm^{-1}): 3296 (N-H), 2931 (C-H), 1634 (C=O), 1609,

1509, 1468 (Ar), 1258, 1238 (C-O). ^{1}H NMR (CD_2Cl_2, 298K, 400 MHz, δ, ppm): 8.44-8.37 (m, 1H), 8.11-8.02 (m, 2H), 7.94-7.84 (m, 2H), 7.68-7.59 (m, 1H), 7.53-7.35 (m, 2H), 7.24-7.16 (m, 1H), 7.01-6.92 (m, 2H), 4.36 (q, *J*= 7.2 Hz, 2H), 4.01 (t, *J*= 6.6 Hz, 2H), 3.43 (t, *J*= 6.6 Hz, 2H), 1.92-1.74 (m, 4H), 1.56-1.21 (m, 17H). ^{13}C NMR (CD_2Cl_2, 298K, 400 MHz, δ, ppm): 165.50, 162.08, 140.61, 137.45, 130.05, 128.98, 127.29, 125.99, 123.25, 122.96, 120.84, 119.94, 118.89, 114.56, 113.30, 108.67, 68.37, 37.76, 34.20, 32.97, 29.64, 29.59, 29.55, 29.49, 29.29, 28.90, 28.31, 26.14, 13.96.

Methyl 3,4,5-tris((11-(4-((9-ethyl-9*H*-carbazol-3-yl)carbamoyl)phenoxy)undecyl) oxy)benzoate (18). A mixture of compound **17** (2.5 g, 4.44 mmol), methyl gallate (0.25 g, 1.34 mmol), potassium carbonate (1.86 g, 13.44 mmol), a teaspoon of potassium iodide and acetone (125 mL) was stirred at reflux temperature for 24 h. Then, the reaction was allowed to cool down to RT and the solids were filtered off and washed with acetone. The solvent was evaporated and the crude product was purified by flash column chromatography on silica gel using DCM as eluent and gradually changing the composition of the eluent to DCM/ethyl acetate (19:1). Yield: 73%. IR (KBr, ν, cm^{-1}): 3294 (N-H), 2920 (C-H), 1717, 1639 (C=O), 1608, 1509, 1472 (Ar), 1252, 1011 (C-O). ^{1}H NMR (DMSO-d_6, 298K, 400 MHz, δ, ppm): 10.15-10.04 (m, 3H), 8.54-8.50 (m, 3H), 8.11-7.94 (m, 9H), 7.78-7.68 (m, 3H), 7.62-7.51 (m, 6H), 7.46-7.39 (m, 3H), 7.22-7.11 (m, 5H), 7.06-6.96 (m, 6H), 4.47-4.36 (m, 6H), 4.09-3.88 (m, 12H), 3.81 (s, 3H), 1.79-1.56 (m, 12H), 1.50-1.17 (m, 51H). ^{13}C NMR (DMSO-d_6, 298K, 100 MHz, δ, ppm): 165.89, 164.55, 161.16, 152.40, 141.44, 139.97, 136.37, 131.14, 129.42, 127.01, 125.69, 124.40, 122.14, 121.80, 120.34, 120.14, 118.55, 113.93, 112.73, 109.15, 108.76, 107.25, 72.52, 68.44, 67.68, 52.13, 36.97, 29.03, 28.92, 28.81, 28.75, 28.63, 25.55, 13.70.

3,4,5-Tris((11-(4-((9-ethyl-9*H*-carbazol-3-yl)carbamoyl)phenoxy)undecyl)oxy) benzoic acid (19). An aqueous solution of potassium hydroxide (0.34 g, 10 mL) was added to a solution of compound **18** (1.00 g, 0.61 mmol) in dioxane (50 mL). The mixture was stirred and heated under reflux and the evolution of the reaction was followed by thin layer chromatography. When all the starting material had been consumed, the reaction mixture was neutralized with concentrated hydrochloric acid until pH 2. The organic solvents were evaporated under reduced pressure and the resulting aqueous phase was extracted with DCM. The combined organic phases were washed with brine and dried over anhydrous magnesium sulfate. The solution was filtered and the solvent was removed under reduced pressure. The

product was purified by flash chromatography on silica gel using DCM as eluent and gradually changing the composition of the eluent to DCM/ethyl acetate (9:1). Yield: 79%. IR (KBr, ν, cm^{-1}): 3291 (N-H), 2922 (C-H), 1702, 1639 (C=O), 1607, 1509, 1472 (Ar), 1252, 1122 (C-O). ^{1}H NMR (DMSO-d_6, 298K, 500 MHz, δ, ppm): 12.76 (s_{broad}, 1H), 10.14-10.05 (m, 3H), 8.58-8.48 (m, 3H), 8.10-7.95 (m, 9H), 7.78-7.71 (m, 3H), 7.61-7.50 (m, 6H), 7.46-7.40 (m, 3H), 7.22-7.13 (m, 5H), 7.05-6.97 (m, 6H), 4.48-4.36 (m, 6H), 4.08-3.86 (m, 12H), 1.79-1.56 (m, 12H), 1.50-1.15 (m, 51H). ^{13}C NMR (DMSO-d_6, 298K, 125 MHz, δ, ppm): 166.97, 164.52, 161.13, 152.24, 141.12, 139.95, 136.35, 131.13, 129.37, 127.00, 125.64, 122.12, 121.78, 120.31, 120.08, 118.50, 113.90, 112.69, 109.09, 108.70, 107.45, 72.45, 68.37, 67.66, 36.94, 29.76, 29.10, 29.05, 28.99, 28.88, 28.81, 28.77, 28.71, 28.59, 25.52, 25.46, 13.63.

2-Azidoethyl 3,4,5-tris((11-(4-((9-ethyl-9*H*-carbazol-3-yl)carbamoyl)phenoxy) undecyl)oxy)benzoate (N_3-d_1Cz). Compund **19** (0.75 g, 0.46 mmol), 2-azidoethanol (61 mg, 0.70 mmol) and 4-(dimethylamino)pyridinium *p*-toluenesulfonate (72 mg, 0.23 mmol) were dissolved in anhydrous THF (10 mL). The reaction flask was cooled in an ice bath and flushed with argon, then *N,N'*-dicyclohexylcarbodiimide (0.14 g, 0.70 mmol) was added dropwise. The mixture was stirred at RT for 24 h under argon atmosphere. The white precipitate was filtered off and washed with THF. The crude product was recrystallized in acetone. Yield: 74%. IR (KBr, ν, cm^{-1}): 3294 (N-H), 2922 (C-H), 2104 (N_3), 1715, 1640 (C=O), 1607, 1534, 1471 (Ar), 1251, 1111 (C-O). ^{1}H NMR (DMSO-d_6, 298K, 500 MHz, δ, ppm): 10.16-10.04 (m, 3H), 8.59-8.47 (m, 3H), 8.12-7.94 (m, 9H), 7.82-7.68 (m, 3H), 7.64-7.50 (m, 6H), 7.49-7.39 (m, 3H), 7.22 (s, 2H), 7.21-7.12 (m, 3H), 7.08-6.93 (m, 6H), 4.51-4.32 (m, 8H), 4.08-3.86 (m, 12H), 3.66-3.59 (m, 2H), 1.80-1.55 (m, 12H), 1.52-1.14 (m, 51H). ^{13}C NMR (DMSO-d_6, 298K, 125 MHz, δ, ppm): 165.09, 164.54, 161.15, 152.41, 141.68, 139.96, 136.37, 131.14, 129.40, 127.01, 125.68, 124.00, 122.13, 121.79, 120.33, 120.12, 118.53, 113.92, 112.72, 109.13, 108.73, 107.45, 72.55, 68.45, 67.67, 64.18, 49.43, 36.96, 29.78, 29.12, 29.08, 29.00, 28.90, 28.84, 28.79, 28.71, 28.61, 25.52, 25.48, 13.67. MS (MALDI$^+$, dithranol, m/z): calcd. for $C_{105}H_{123}N_9O_{11}$, 1685.9; found, 1686.2 $[M]^+$, 1709.2 $[M+Na]^+$. Anal. calcd. for $C_{105}H_{123}N_9O_{11}$: C, 74.75%; H, 7.35%; N, 7.47%. Found: C, 74.75%; H, 7.00%; N, 7.65%.

ZnP-*t*-d_1Cz. A Schlenk flask was charged with **ZnP-YNE** (17.7 mg, 0.020 mmol), compound **N_3-d_1Cz** (200 mg, 0.12 mmol), sodium ascorbate (3.9 mg, 0.020 mmol) and THF (9 mL). Copper (II) sulfate pentahydrate (2.5 mg, 0.010 mmol) was

dissolved in water (1 mL) and was added to the reaction. The reaction flask was degassed by three freeze-pump-thaw cycles and flused with argon. The reaction mixture was stirred at 40 °C for 48 h. Then, the alkyne-functionalized resin (**5**) was added under argon flow to remove azide excess and the reaction mixture was stirred for further 24 h. The resin was filtered off, the mixture was diluted with THF and then passed through a short column of aluminum oxide, using THF as eluent, to remove copper salts. The solvent was partially evaporated, and the resulting polymer solution was carefully precipitated into cold acetone. Yield: 83%. IR (KBr, ν, cm^{-1}): 3299 (N-H), 2932 (C-H), 1718, 1641 (C=O), 1607, 1492 (Ar), 1250, 1174 (C-O). ^{1}H NMR (DMSO-d_6, 353K, 500 MHz, δ, ppm): 9.81 (s, 12H), 8.78 (s, 8H), 8.52-8.43 (m, 12H), 8.37 (s, 4H), 8.09-7.90 (m, 44H), 7.80-7.68 (m, 12H), 7.59-7.30 (m, 44H), 7.24-7.07 (m, 20H), 6.99-6.85 (m, 24H), 5.46-5.35 (m, 8H), 4.86 (t, *J*= 5.1 Hz, 8H), 4.70 (t, *J*= 5.1 Hz, 8H), 4.45-4.31 (m, 24H), 4.05-3.81 (m, 48H), 1.81-1.51 (m, 48H), 1.51-1.09 (m, 204H). ^{13}C NMR (DMSO-d_6, 353K, 125 MHz, δ, ppm): 164.57, 164.26, 160.81, 152.07, 149.27, 142.80, 142.12, 139.78, 136.20, 134.67, 134.10, 133.85, 130.89, 128.90, 126.95, 125.19, 124.36, 123.67, 121.96, 121.63, 120.02, 119.59, 118.09, 113.63, 112.56, 112.40, 108.63, 108.19, 107.92, 72.28, 68.56, 67.44, 62.57, 61.61, 48.36, 36.65, 29.33, 28.44, 28.27, 28.17, 25.09, 24.97, 13.08. MS (MALDI$^+$, DCTB, m/z): calcd. for $C_{478}H_{534}N_{40}O_{48}Zn$, 7666.0; found, 7666.0 $[M]^+$. Anal. calcd. for $C_{478}H_{534}N_{40}O_{48}Zn$: C, 74.82%; H, 7.02%; N, 7.30%. Found: C, 74.62%; H, 6.99%; N, 7.02%.

5.2.2.8 *Synthesis of Porphyrin-Core Dendrimers with N-Phenylcarbazole Units*

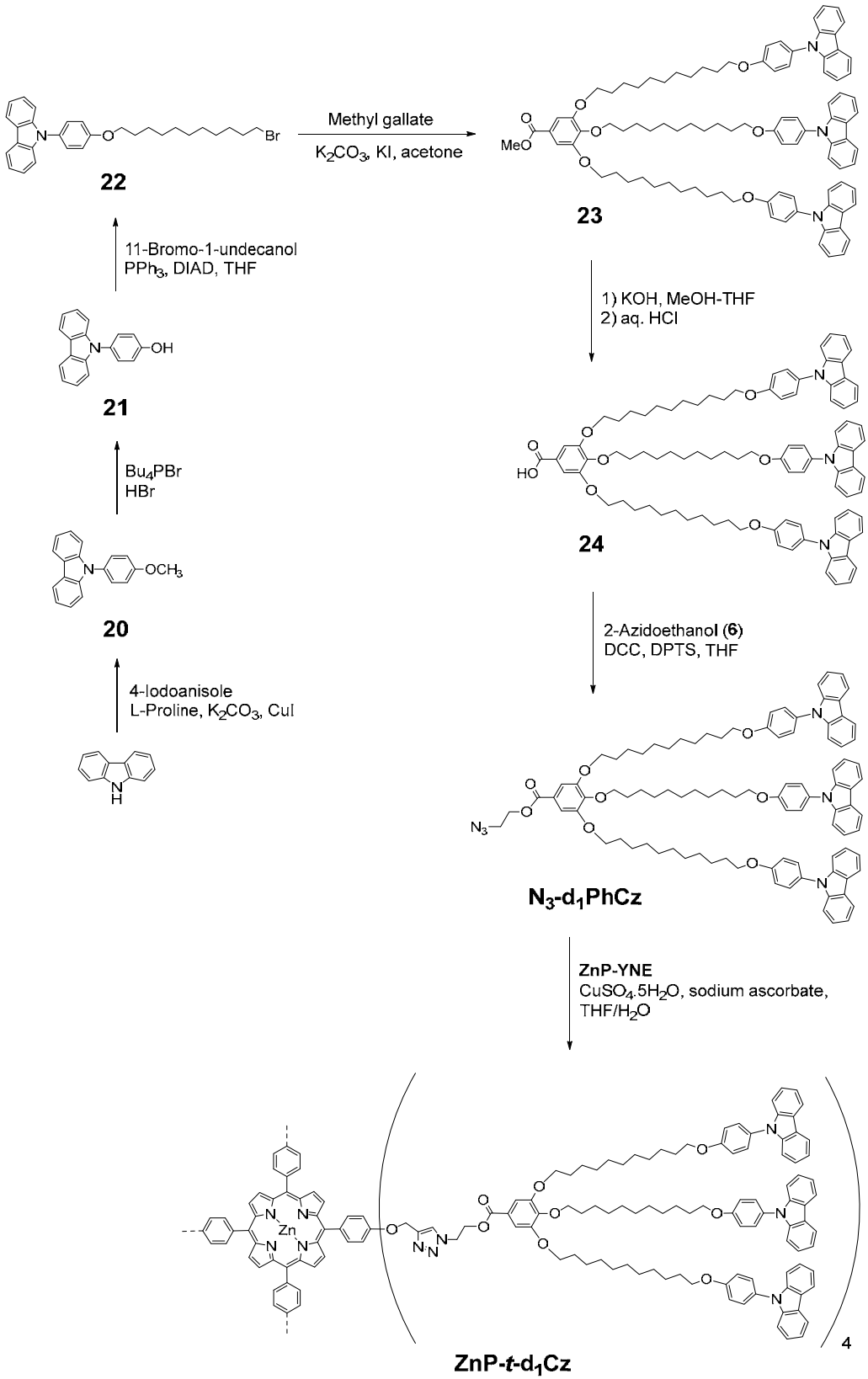

Scheme 5.9 Synthetic route of the porphyrin-core dendrimer with 9-phenyl-carbazole.

9-(4-Methoxyphenyl)-9*H*-carbazole (20). A Schlenk flask was charged with carbazole (6.50 g, 38.84 mmol), 4-iodoanisole (10.00 g, 42.72 mmol), *L*-proline (1.23 g, 10.68 mmol), copper (I) iodide (0.74 g, 3.88 mmol), potassium carbonate (10.74 g, 77.68 mmol) and DMSO (30 mL). The reaction flask was degassed by three freeze-pump-thaw cycles and flushed with argon. The reaction mixture was stirred at 90 °C for 48 h. The reaction crude was poured into water and extracted with DCM. The combined organic phases were washed with brine and dried over anhydrous magnesium sulfate. The solution was filtered and the solvent was removed under reduced pressure. The product was purified by recrystallization in acetonitrile. Yield: 77%. IR (KBr, ν, cm^{-1}): 3015 (=C-H), 1513, 1451 (Ar), 1248, 1181 (C-O).^{1}H NMR ($CDCl_3$, 298K, 400 MHz, δ, ppm): 8.19-8.11 (m, 2H), 7.50-7.37 (m, 4H), 7.37-7.30 (m, 2H), 7.30-7.24 (m, 2H), 7.17-7.09 (m, 2H), 3.91 (s, 3H). ^{13}C NMR ($CDCl_3$, 298K, 100 MHz, δ, ppm): 158.98, 141.50, 130.42, 128.69, 125.97, 123.23, 120.37, 119.76, 115.18, 109.82, 55.71.

4-(9*H*-Carbazol-9-yl)phenol (21). A mixture of compound **20** (6.00 g, 21.96 mmol), tetrabutylphosphonium bromide (7.52 g, 22.17 mmol) and hydrobromic acid (45 wt. % solution, 225 mL) was stirred at 100 °C for 48 h. The reaction mixture was extracted with DCM. The combined organic phases were washed with sodium bicarbonate solution, brine and dried over anhydrous magnesium sulfate. The solution was filtered and the solvent was removed under reduced pressure. The product was purified by flash chromatography on silica gel using hexane/DCM (1:1) as eluent and gradually changing the composition of the eluent to DCM. Yield: 91%. IR (KBr, ν, cm^{-1}): 3368 (O-H), 3015 (=C-H), 1515, 1452 (Ar). ^{1}H NMR ($CDCl_3$, 298K, 400 MHz, δ, ppm): 8.19-8.10 (m, 2H), 7.44-7.35 (m, 4H), 7.35-7.22 (m, 4H), 7.08-6.99 (m, 2H), 5.09 (s_{broad}, 1H). ^{13}C NMR ($CDCl_3$, 298K, 100 MHz, δ, ppm): 155.05, 141.48, 130.62, 128.96, 125.99, 123.24, 120.40, 119.80, 116.71, 109.81.

9-(4-((11-bromoundecyl)oxy)phenyl)-9H-carbazole (22). Compound **21** (5.00 g, 19.28 mmol), 11-bromo-1-undecanol (4.84 g, 19.28 mmol) and triphenylphosphine (4.29 g, 21.21 mmol) were dissolved in anhydrous DCM (125 mL). The reaction flask was cooled in an ice bath and flushed with argon, then diisopropylazadicarboxylate (5.56 g, 21.21 mmol) was added dropwise. The mixture was stirred at RT for 12 h under argon atmosphere. The white precipitate was filtered off. The solvent was evaporated and the crude product was purified by flash chromatography on silica gel using hexane/DCM (1:1) as eluent. Yield: 83%. IR (KBr, ν, cm^{-1}): 2922 (C-H), 1513,

1452 (Ar), 1230, 1179 (C-O). ^{1}H NMR (CD_2Cl_2, 298K, 500 MHz, δ, ppm): 8.17-8.12 (m, 2H), 7.47-7.37 (m, 4H), 7.35-7.31 (m, 2H), 7.30-7.24 (m, 2H), 7.14-7.09 (m, 2H), 4.07 (t, *J*= 6.9 Hz, 2H), 3.43 (t, *J*= 6.9 Hz, 2H), 1.92-1.80 (m, 4H), 1.59-1.25 (m, 14H). ^{13}C NMR (CD_2Cl_2, 298K, 125 MHz, δ, ppm): 159.15, 141.95, 130.48, 128.99, 126.39, 123.56, 120.68, 120.14, 116.11, 110.23, 69.02, 34.85, 33.48, 30.12, 30.06, 30.01, 29.96, 29.86, 29.34, 28.74, 26.62.

Methyl 3,4,5-tris((11-(4-(9H-carbazol-9-yl)phenoxy)undecyl)oxy)benzoate (23). Compound **22** (4.00 g, 8.12 mmol), methyl gallate (0.45 g, 2.46 mmol), potassium carbonate (3.40 g, 24.60 mmol), a teaspoon of potassium iodide and acetone (125 mL) was stirred at reflux temperature for 24 h. Then, the reaction was allowed to cool down to RT and the solids were filtered off and washed with acetone. The solvent was evaporated and the crude product was purified by flash column chromatography on silica gel using hexane/DCM (1:1) as eluent and gradually changing the composition of the eluent to DCM. Yield: 80%. IR (KBr, ν, cm^{-1}): 3047 (=C-H), 2924 (C-H), 1719 (C=O), 1596, 1513, 1453 (Ar), 1231 (C-O). ^{1}H NMR (CD_2Cl_2, 298K, 500 MHz, δ, ppm): 8.18-8.10 (m, 6H), 7.47-7.35 (m, 12H), 7.35-7.29 (m, 6H), 7.29-7.22 (m, 8H), 7.14-7.06 (m, 6H), 4.09-3.98 (m, 12H), 3.85 (s, 3H), 1.96-1.66 (m, 12H), 1.60-1.22 (m, 42H). ^{13}C NMR (CD_2Cl_2, 298K, 125 MHz, δ, ppm): 167.06, 159.13, 152.96, 142.53, 141.93, 130.48, 128.97, 126.39, 124.85, 123.55, 120.68, 120.14, 116.10, 110.22, 108.19, 74.05, 69.73, 69.01, 52.25, 30.94, 30.65, 30.26, 30.20, 30.02, 29.97, 29.90, 26.66.

3,4,5-Tris((11-(4-(9*H*-carbazol-9-yl)phenoxy)undecyl)oxy)benzoic acid (24). An aqueous solution of potassium hydroxide (0.40 g, 1 mL) was added to a solution of compound **23** (1.00 g, 0.72 mmol) in THF-methanol 1:1 (10 mL). The mixture was stirred and heated under reflux and the evolution of the reaction was followed by thin layer chromatography. When all of the starting material had been consumed, the reaction mixture was neutralized with concentrated hydrochloric acid until pH 2. The organic solvents were evaporated under reduced pressure and the resulting aqueous phase was extracted with DCM. The combined organic phases were washed with brine and dried over anhydrous magnesium sulfate. The solution was filtered and the solvent was removed under reduced pressure. The product was purified by flash chromatography on silica gel using DCM as eluent and gradually changing the composition of the eluent to DCM/ethyl acetate (9:1). Yield: 72%. IR (KBr, ν, cm^{-1}): 3243 (O-H), 3055 (=C-H), 2923 (C-H), 1682 (C=O), 1603, 1513, 1453

(Ar), 1235, 1129 (C-O). ^{1}H NMR (CD_2Cl_2, 298K, 500 MHz, δ, ppm): 8.17-8.10 (m, 6H), 7.47-7.34 (m, 12H), 7.34-7.29 (m, 8H), 7.29-7.22 (m, 6H), 7.13-7.05 (m, 6H), 4.13-3.96 (m, 12H), 1.91-1.68 (m, 12H), 1.59-1.21 (m, 42H). ^{13}C NMR (CD_2Cl_2, 298K, 125 MHz, δ, ppm): 170.76, 159.13, 153.51, 143.53, 141.93, 130.48, 128.97, 126.39, 124.12, 123.55, 120.68, 120.14, 116.10, 110.22, 108.83, 74.05, 69.73, 69.01, 30.94, 30.65, 30.26, 30.20, 30.02, 29.97, 29.90, 26.66.

2-Azidoethyl 3,4,5-tris((11-(4-(9*H*-carbazol-9-yl)phenoxy)undecyl)oxy)benzoate (N_3-d_1PhCz). Compound **24** (0.50 g, 0.36 mmol), 2-azidoethanol (47.6 mg, 0.55 mmol) and 4-(dimethylamino)pyridinium *p*-toluenesulfonate (57 mg, 0.18 mmol) were dissolved in anhydrous DCM (5 mL). The reaction flask was cooled in an ice bath and flushed with argon, then *N,N'*-dicyclohexylcarbodiimide (0.112 g, 0.55 mmol) was added dropwise. The mixture was stirred at RT for 24 h under argon atmosphere. The white precipitate was filtered off and washed with THF. The crude product was purified by flash column chromatography on silica gel using hexane/DCM (1:2) as eluent and gradually changing the composition of the eluent to DCM. Yield: 76%. IR (KBr, ν, cm^{-1}): 3042 (=C-H), 2921 (C-H), 2111 (N_3), 1735 (C=O), 1608, 1515, 1465 (Ar), 1228, 1129 (C-O). ^{1}H NMR (CD_2Cl_2, 298K, 500 MHz, δ, ppm): 8.17-8.11 (m, 6H), 7.48-7.35 (m, 12H), 7.35-7.22 (m, 14H), 7.13-7.07 (m, 6H), 4.47-4.42 (m, 2H), 4.10-3.97 (m, 12H), 3.61-3.48 (m, 2H), 1.90-1.71 (m, 12H), 1.58-1.29 (m, 42H). ^{13}C NMR (CD_2Cl_2, 298K, 125 MHz, δ, ppm): 166.44, 159.14, 153.52, 143.03, 141.94, 130.49, 128.98, 126.39, 124.74, 123.57, 74.02, 69.73, 69.02, 64.52, 50.68, 30.94, 30.26, 30.21, 30.17, 30.03, 29.98, 29.92, 26.67. MS (MALDI$^+$, dithranol, m/z): calcd. for $C_{96}H_{108}N_6O_8$, 1472.8; found, 1473.1 $[M]^+$, 1496.1 $[M+Na]^+$. Anal. calcd. for $C_{96}H_{108}N_6O_8$: C, 78.23%; H, 7.39%; N, 5.70%. Found: C, 78.48%; H, 7.21%; N, 6.00%.

ZnP-*t*-d_1PhCz. A Schlenk flask was charged with **ZnP-YNE** (15.5 mg, 0.017 mmol), compound **N_3-d_1PhCz** (150 mg, 0.104 mmol), sodium ascorbate (3.4 mg, 0.017 mmol) and THF (3 mL). Copper (II) sulfate pentahydrate (2.2 mg, 0.009 mmol) was dissolved in water (1 mL) and was added to the reaction. The reaction flask was degassed by three freeze-pump-thaw cycles and flused with argon. The reaction mixture was stirred at 40 °C for 48 h. Then, the alkyne-functionalized resin (**5**) was added under argon flow to remove azide excess and the reaction mixture was stirred for further 24 h. The resin was filtered off, the mixture was diluted with THF and then passed through a short column of aluminum oxide, using THF as eluent,

to remove copper salts. The solvent was partially evaporated, and the resulting polymer solution was carefully precipitated into cold methanol. Yield: 90%. IR (KBr, ν, cm^{-1}): 3048 (=C-H), 2932 (C-H), 1732 (C=O), 1610, 1509, 1469 (Ar), 1228, 1129 (C-O). ^{1}H NMR ($C_2D_2Cl_4$, 353K, 500 MHz, δ, ppm): 9.00 (s, 8H), 8.22-8.06 (m, 32H), 7.85 (s, 4H), 7.49-7.21 (m, 112H), 7.13-7.02 (m, 24H), 5.51 (s, 8H), 4.85-4.78 (m, 16H), 4.23-3.94 (m, 48H), 1.97-1.73 (m, 48H), 1.66-1.29 (m, 168H). ^{13}C NMR ($C_2D_2Cl_4$, 373K, 125 MHz, δ, ppm): 167.17, 159.98, 159.67, 154.51, 151.90, 146.07, 145.44, 142.99, 137.51, 136.90, 133.24, 131.73, 129.73, 127.23, 125.17, 124.59, 124.43, 121.97, 121.50, 121.08, 117.41, 114.73, 111.18, 110.77, 71.24, 70.15, 64.24, 63.96, 50.67, 31.75, 30.89, 30.85, 30.72, 27.49, 27.43. MS ($MALDI^+$, DCTB, m/z): calcd. for $C_{442}H_{474}N_{28}O_{36}Zn$, 6813.5; found, 6813.3 $[M]^+$. Anal. calcd. for $C_{442}H_{474}N_{28}O_{36}Zn$: C, 77.84%; H, 7.01%; N, 5.75%. Found: C, 78.11%; H, 7.15%; N, 5.64%.

6. APPENDIX

6.1 NMR Spectra

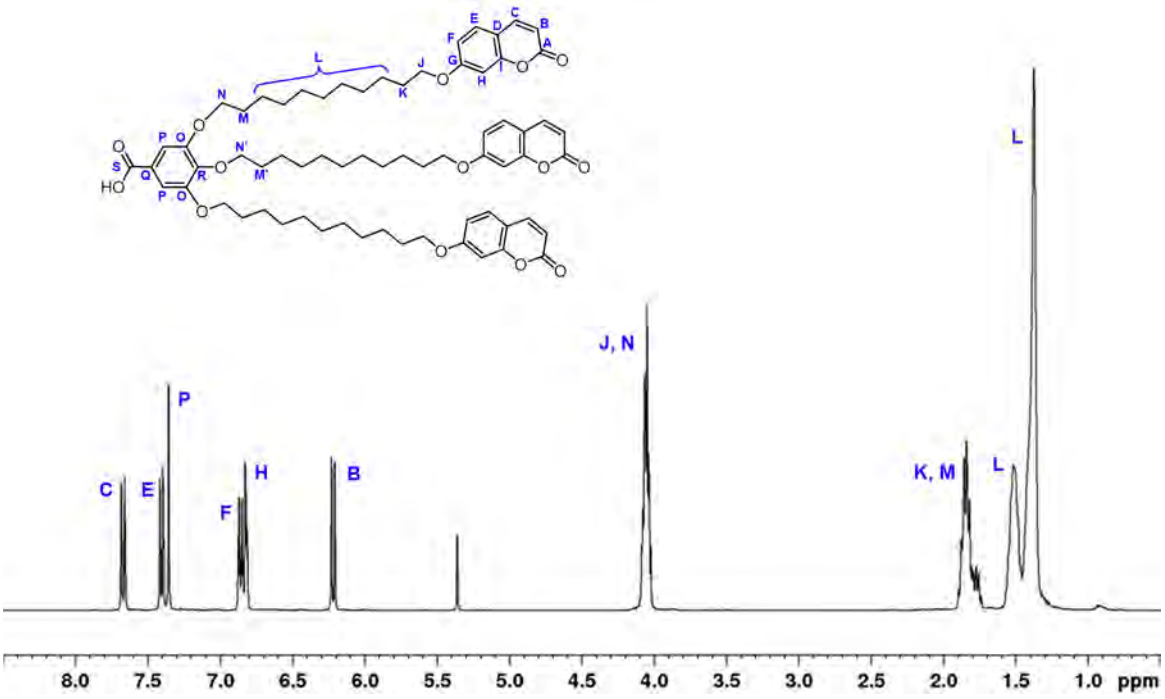

Figure 6.1 ^{1}H NMR spectrum (400 MHz, CD_2Cl_2) of **d_1Cou**

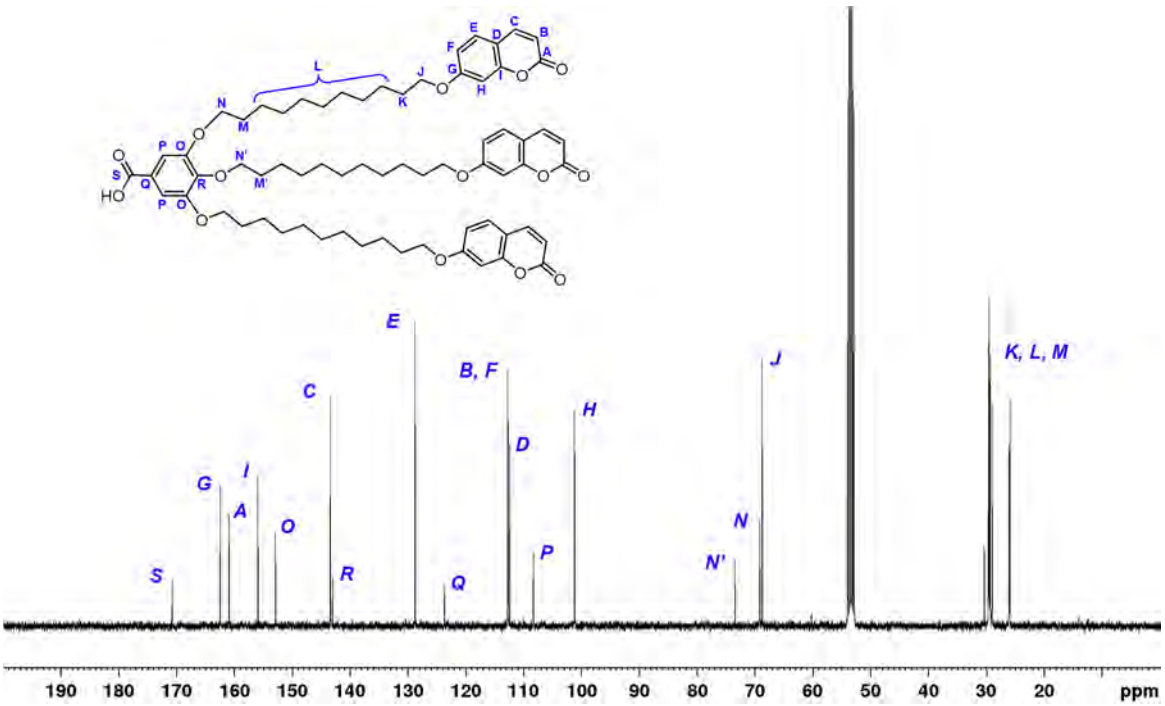

Figure 6.2 ^{13}C NMR spectrum (100 MHz, CD_2Cl_2) of **d_1Cou**

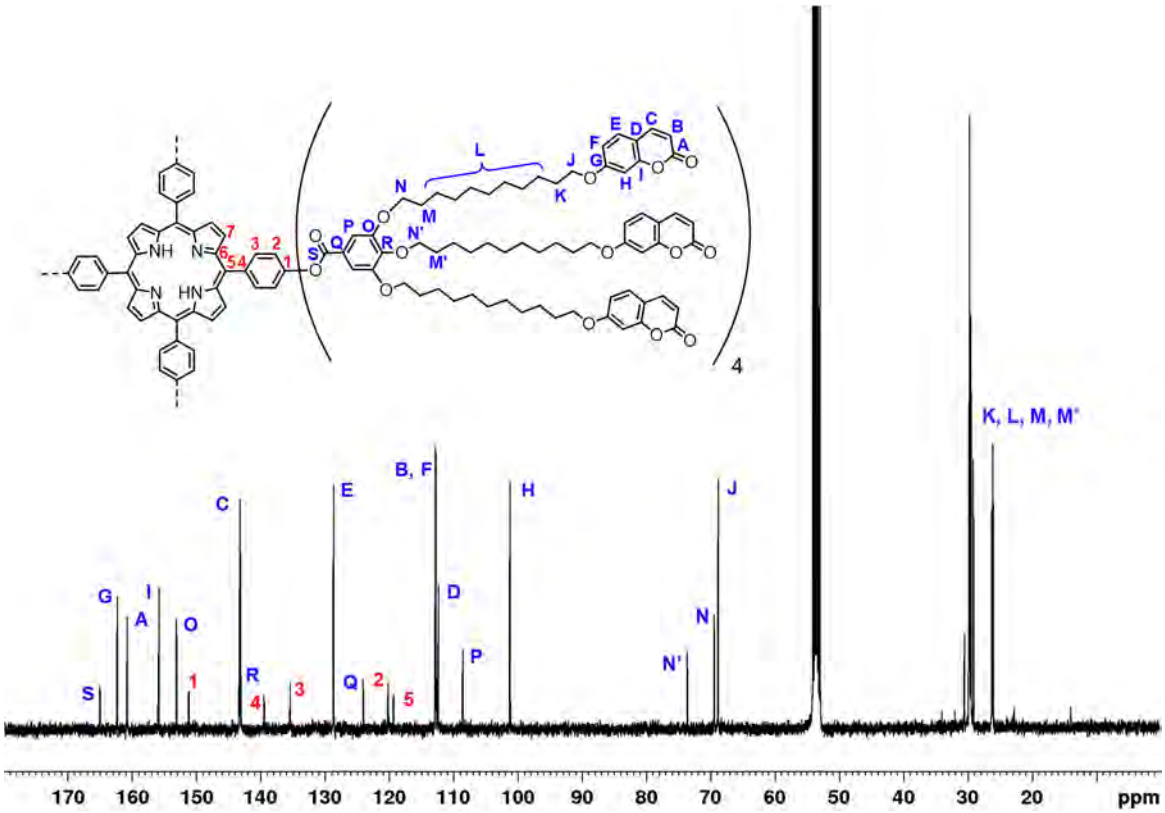

Figure 6.3 ^{13}C NMR spectrum (100 MHz, CD_2Cl_2) of **P-d$_1$Cou**

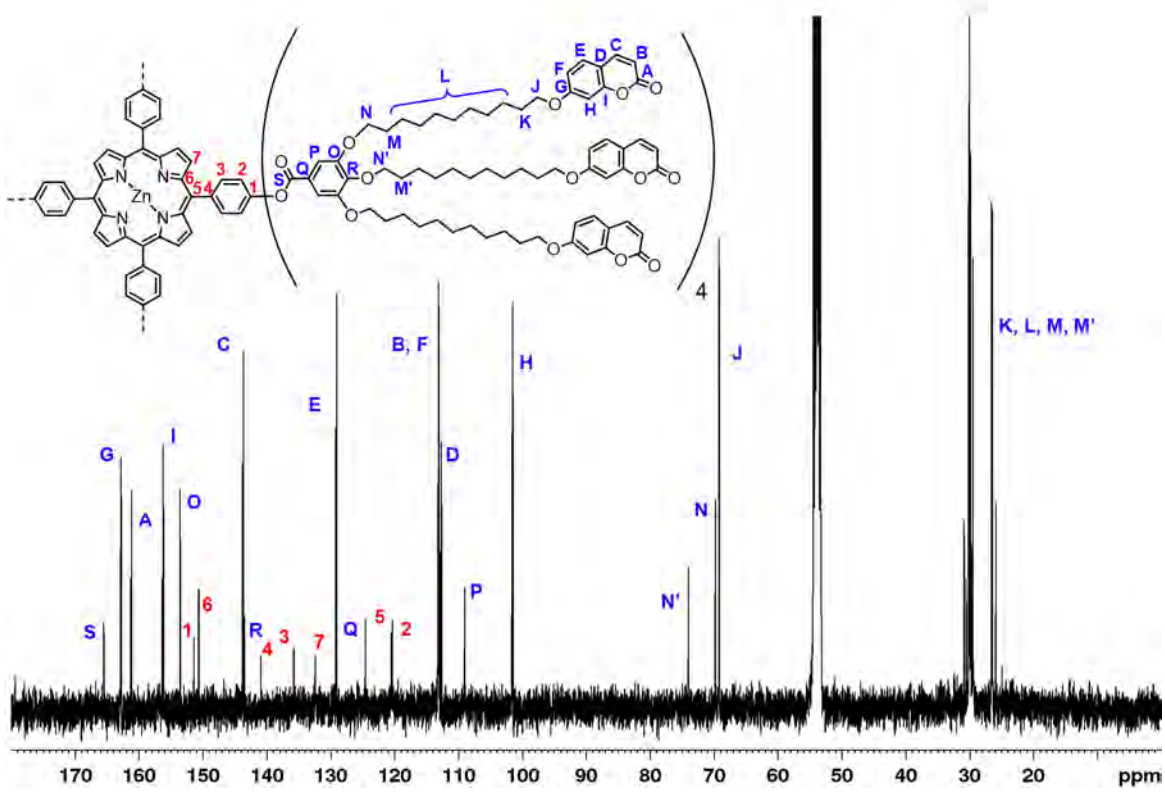

Figure 6.4 ^{13}C NMR spectrum (100 MHz, CD_2Cl_2) of **ZnP-d$_1$Cou**

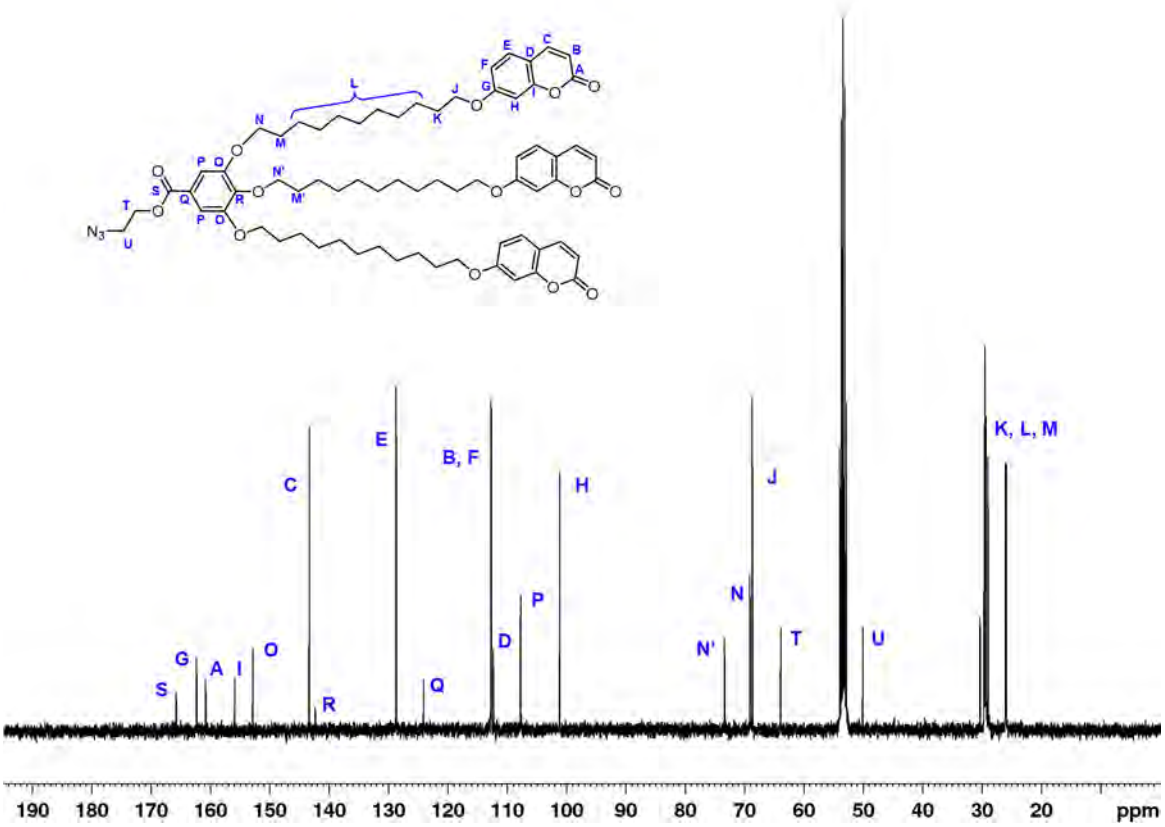

Figure 6.5 ^{13}C NMR spectrum (100 MHz, 298K, CD_2Cl_2) of **N_3-d_1Cou**

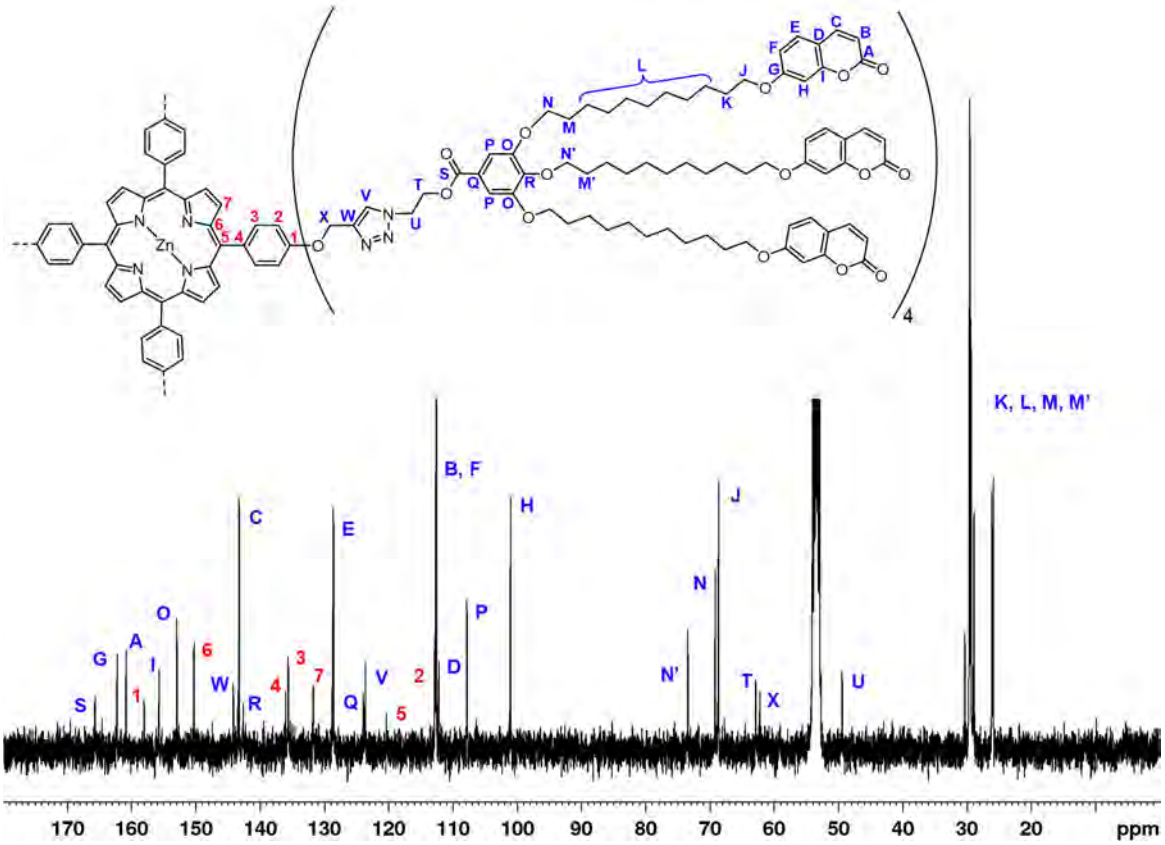

Figure 6.6 ^{13}C NMR spectrum (100 MHz, 298K, CD_2Cl_2) of **ZnP-*t*-d_1Cou**

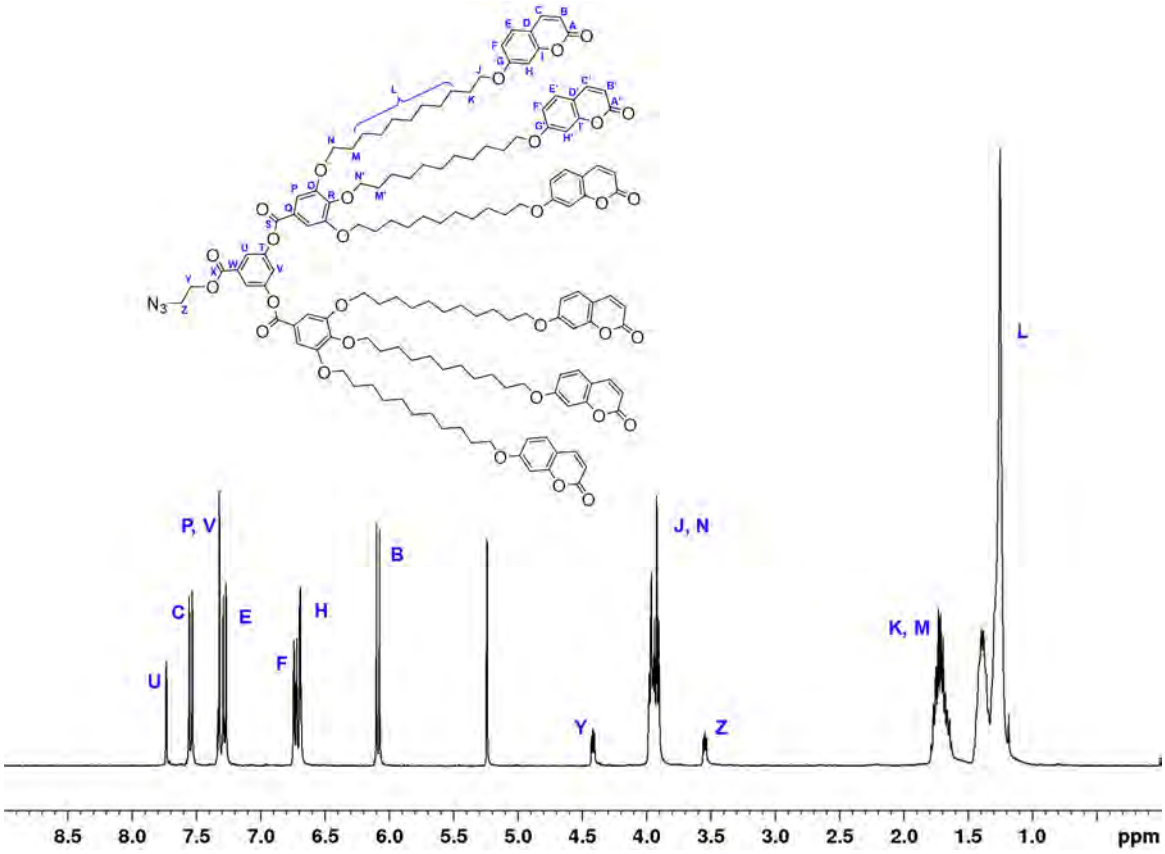

Figure 6.7 ^{1}H NMR spectrum (400 MHz, 298K, CD_2Cl_2) of **N_3-d_2Cou**

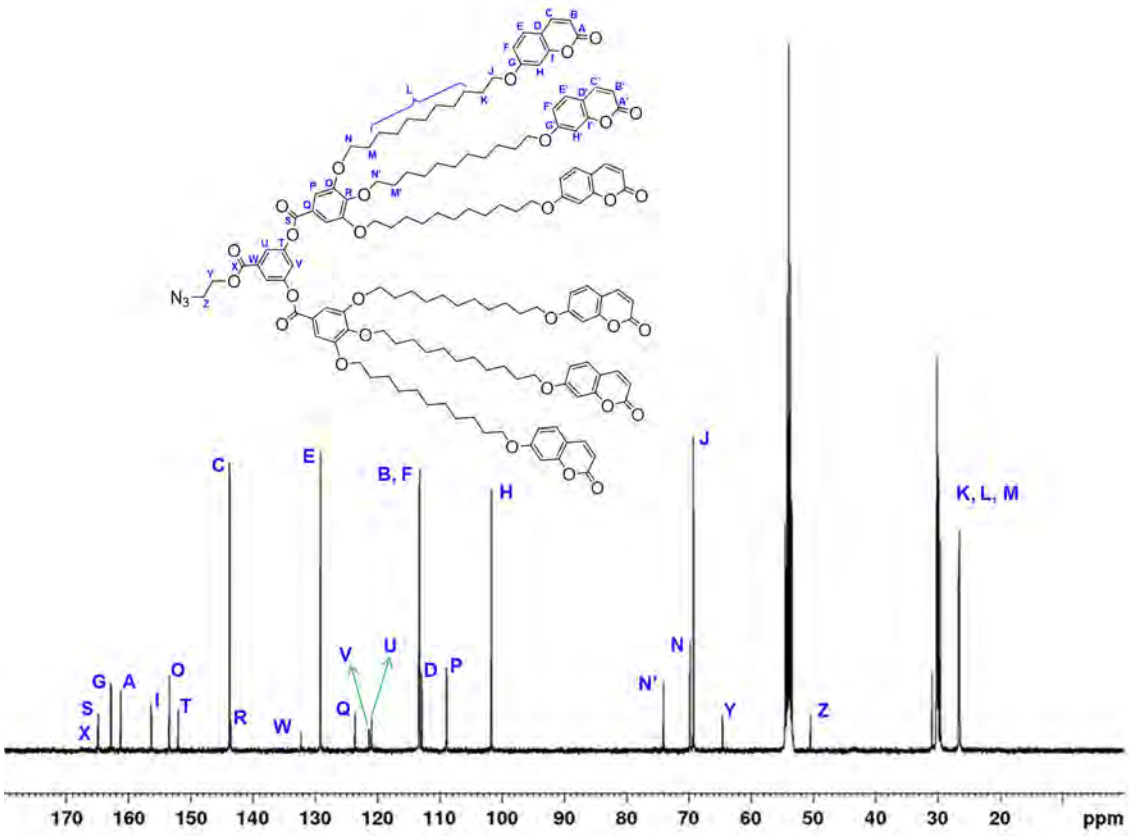

Figure 6.8 ^{13}C NMR spectrum (100 MHz, 298K, CD_2Cl_2) of **N_3-d_2Cou**

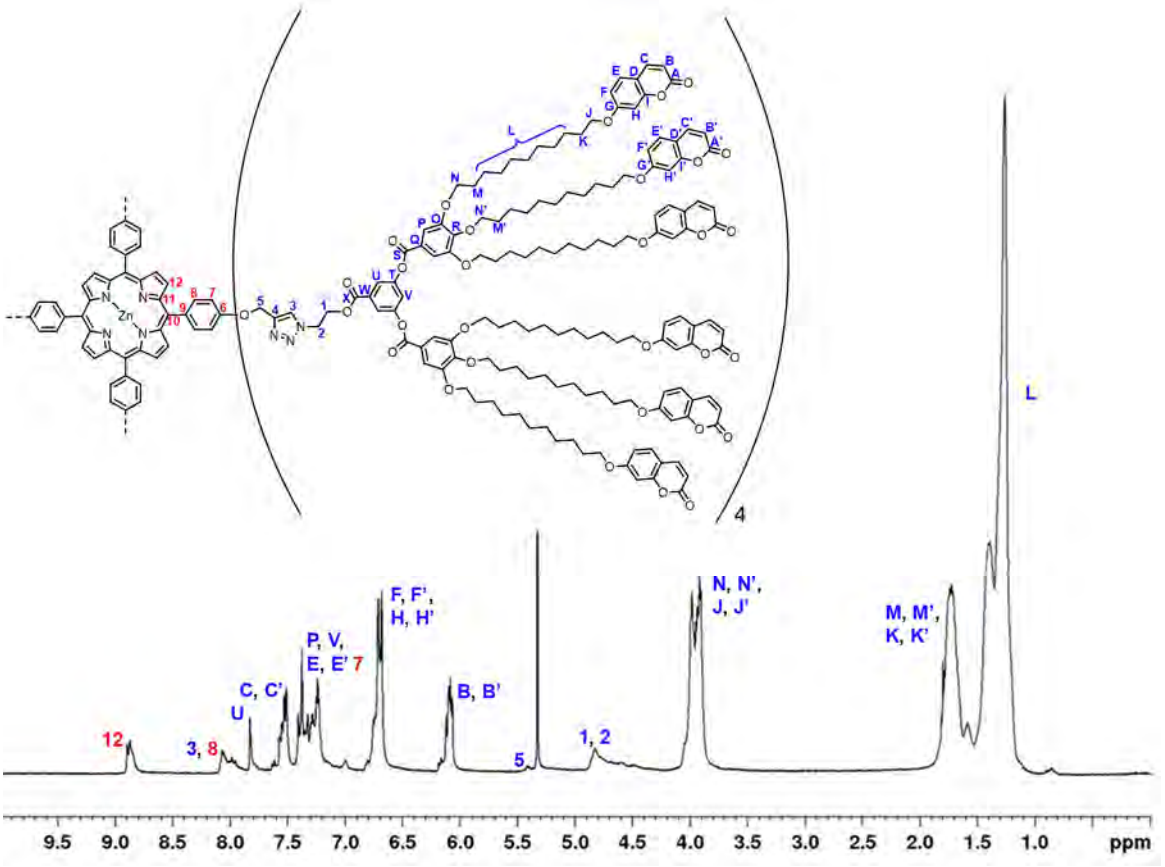

Figure 6.9 ^{1}H NMR spectrum (500 MHz, 298K, CD_2Cl_2) of **ZnP-*t*-d$_2$Cou**

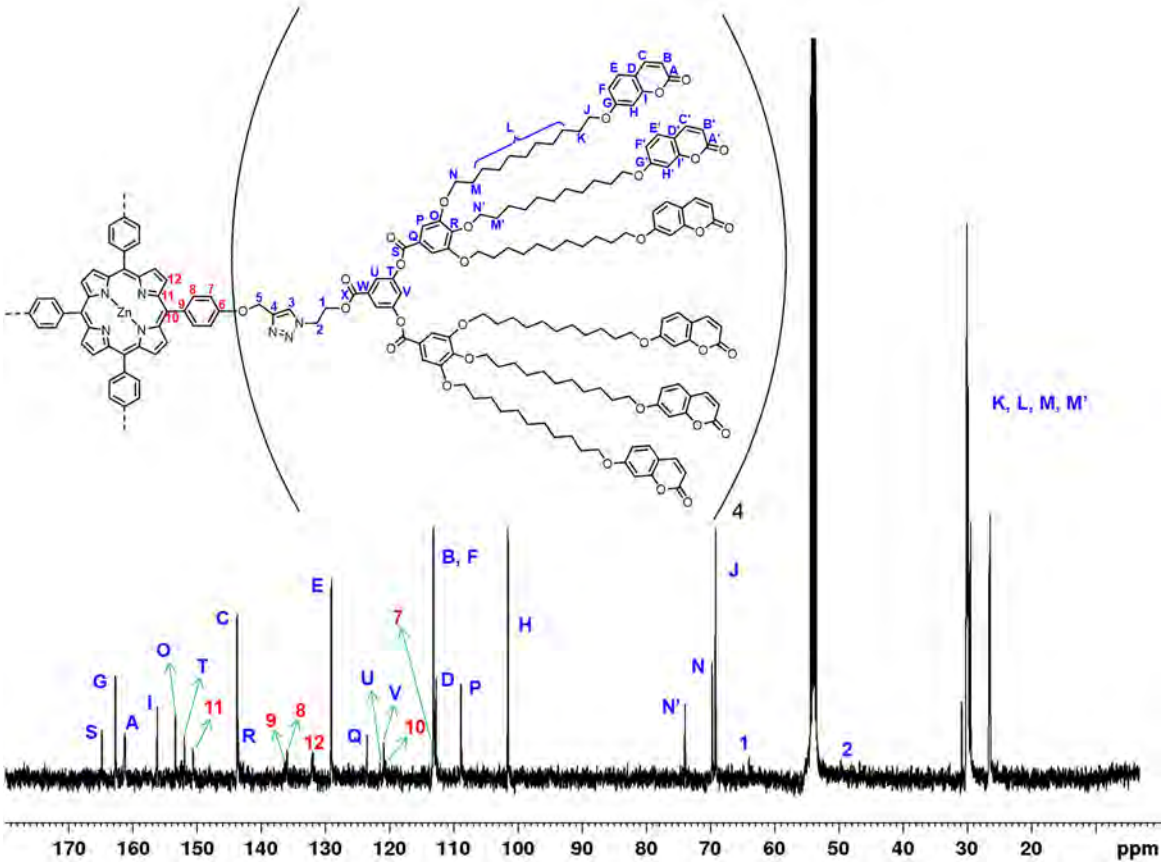

Figure 6.10 ^{13}C NMR spectrum (125 MHz, 298K, CD_2Cl_2) of **ZnP-*t*-d$_2$Cou**

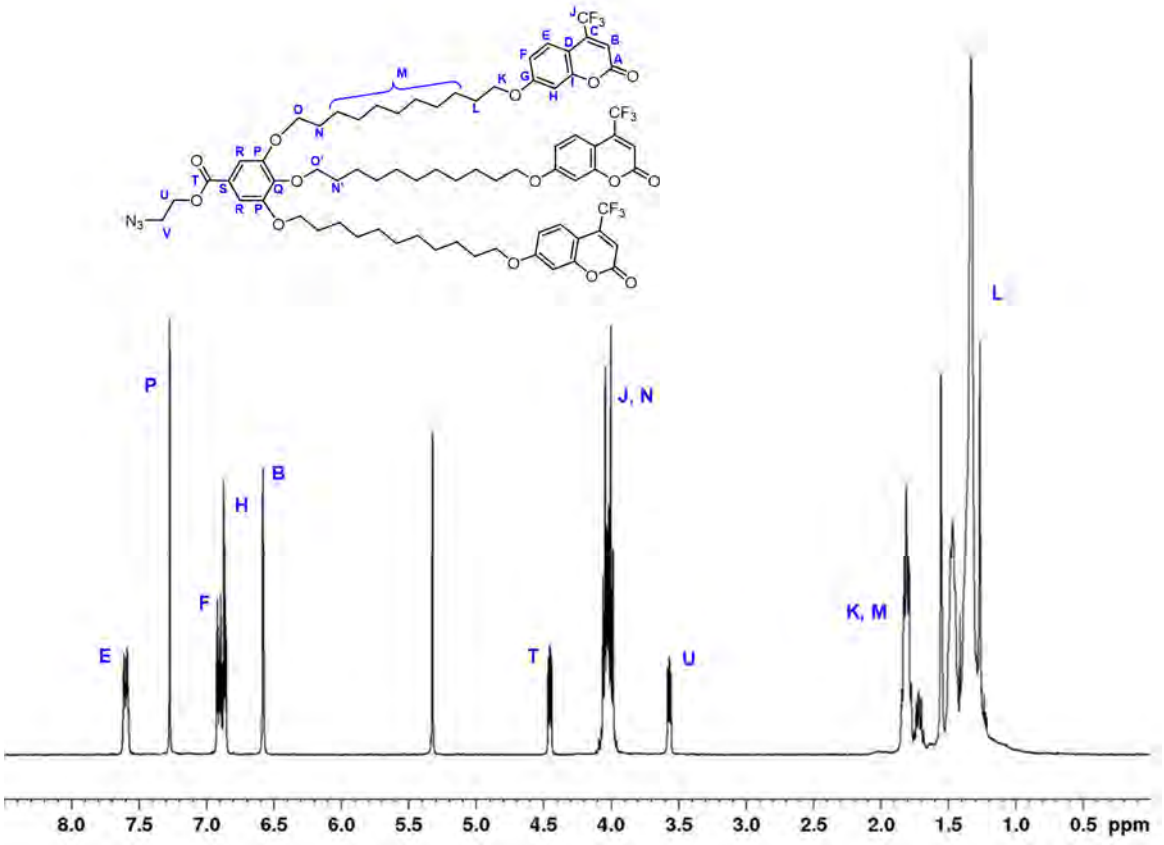

Figure 6.11 ^{1}H NMR spectrum (400 MHz, 298K, CD_2Cl_2) of **N_3-d_1Cou-CF_3**

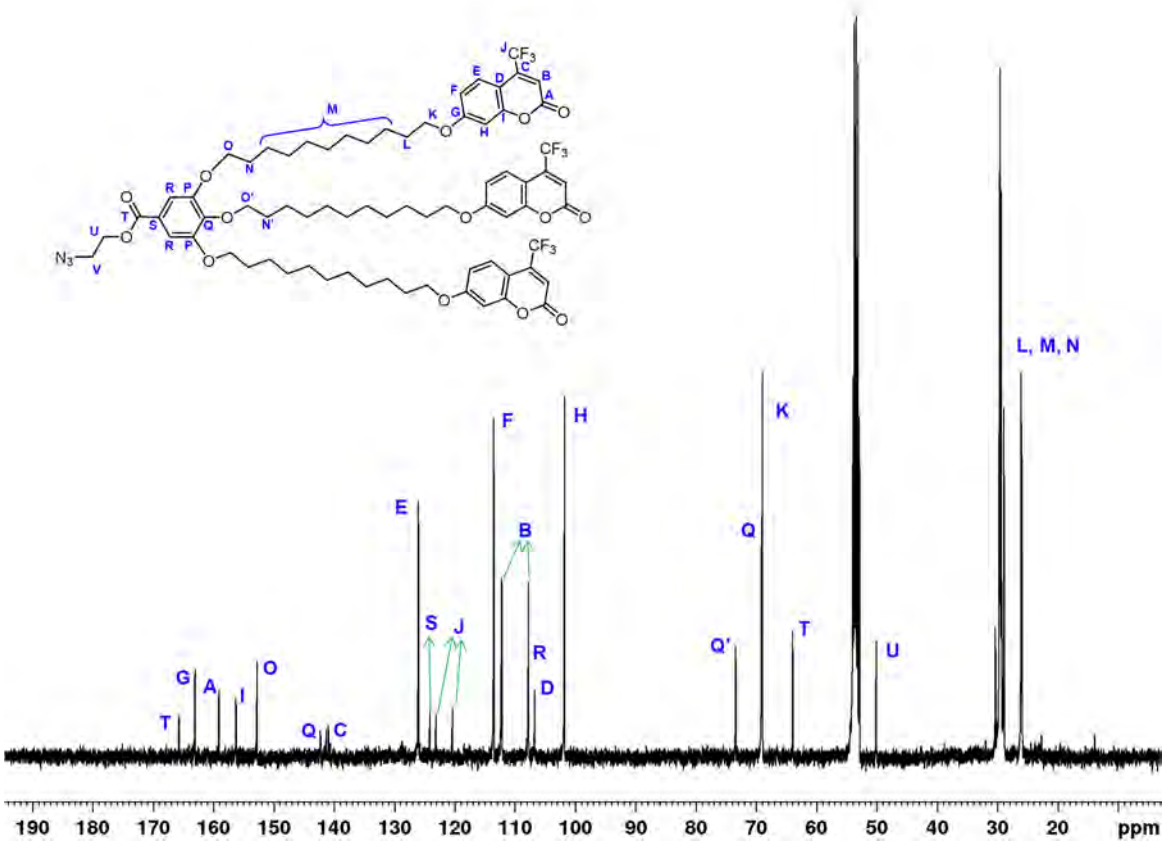

Figure 6.12 ^{13}C NMR spectrum (100 MHz, 298K, CD_2Cl_2) of **N_3-d_1Cou-CF_3**

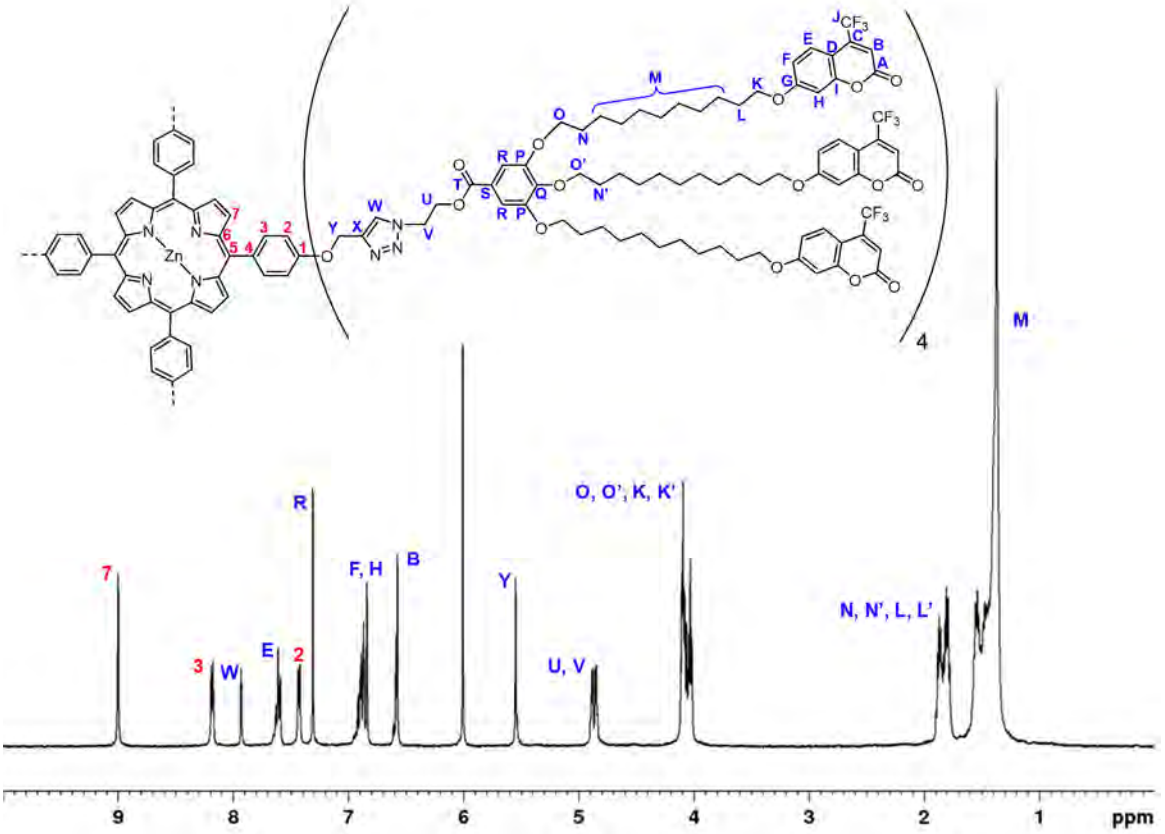

Figure 6.13 ^{1}H NMR spectrum (500 MHz, 373K, $C_2D_2Cl_4$) of **ZnP-*t*-d$_1$Cou-CF$_3$**

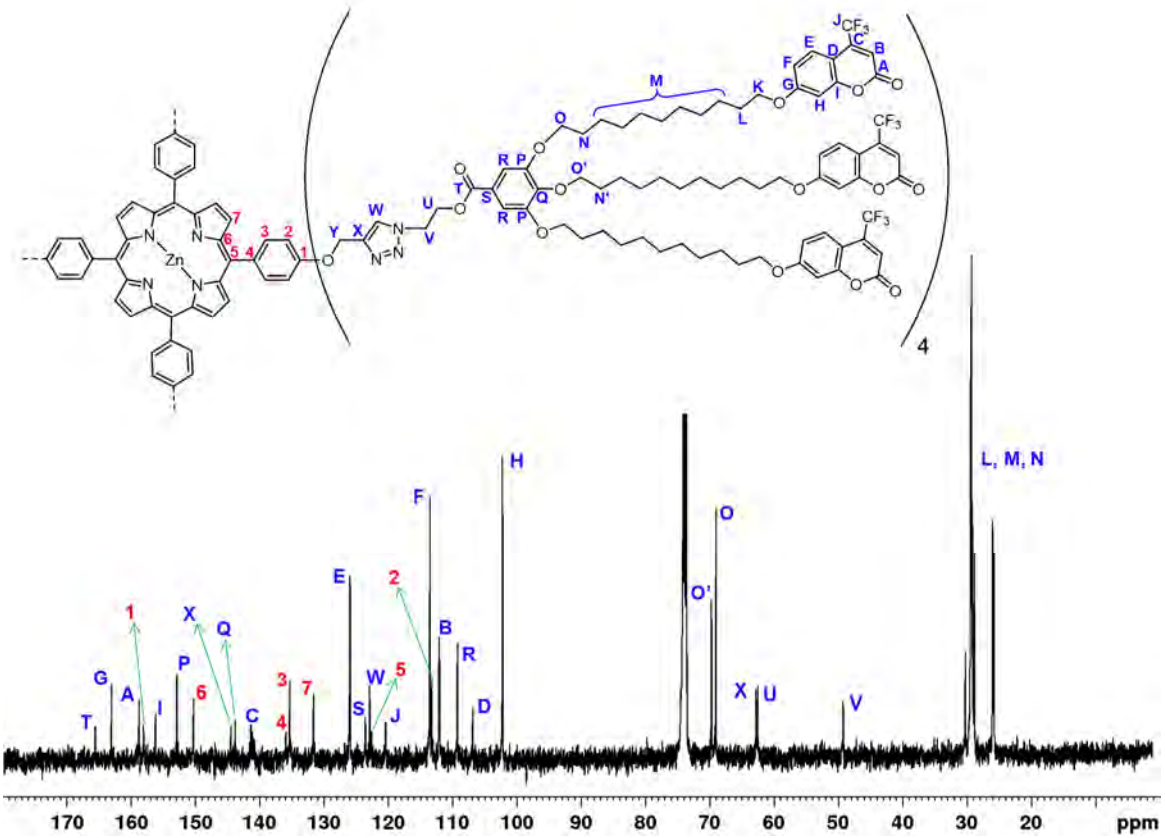

Figure 6.14 ^{13}C NMR spectrum (125 MHz, 373K, $C_2D_2Cl_4$) of **ZnP-*t*-d$_1$Cou-CF$_3$**

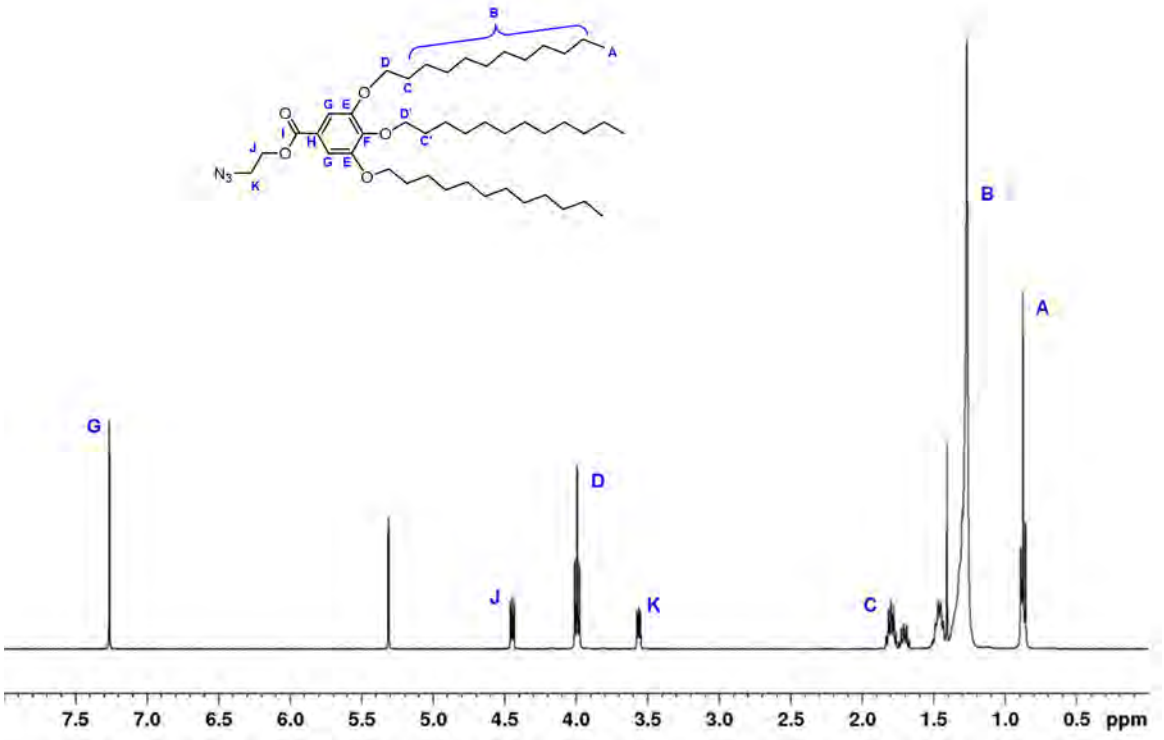

Figure 6.15 ^{1}H NMR spectrum (500 MHz, 298K, CD_2Cl_2) of **N_3-d_1C12**

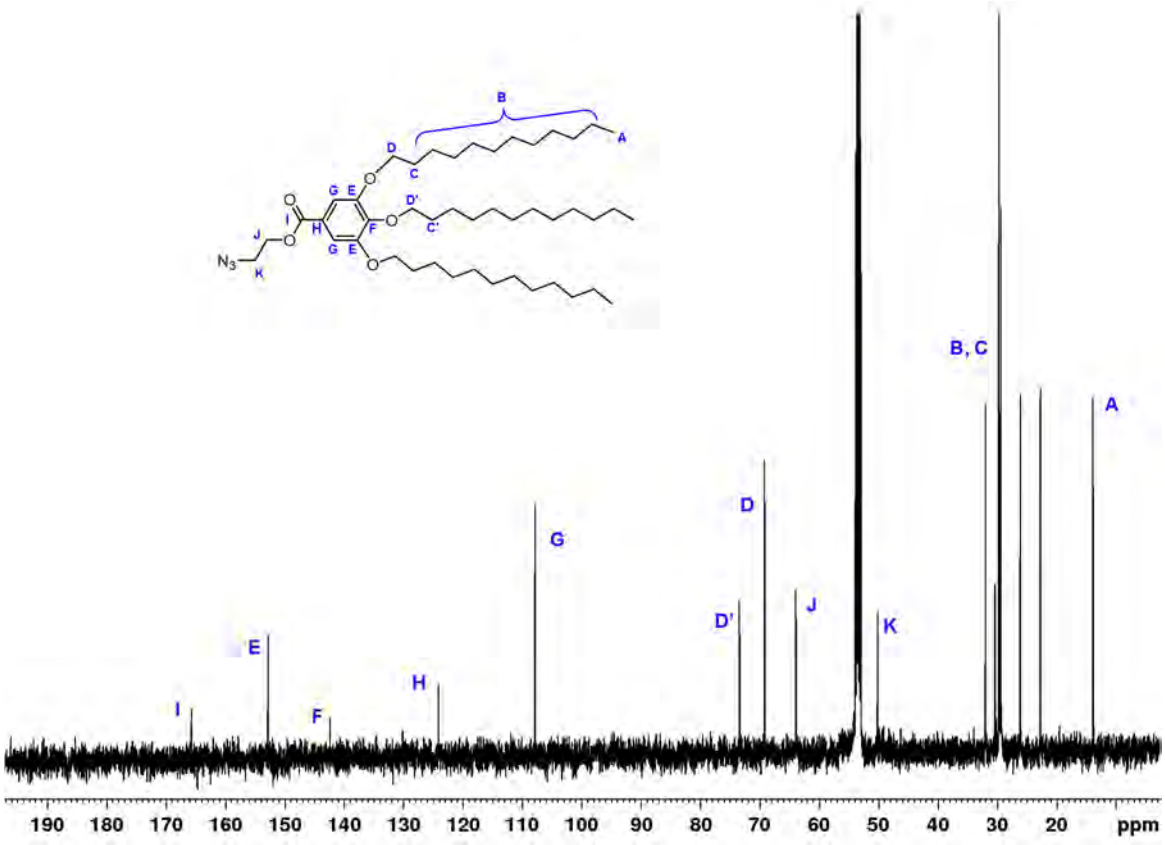

Figure 6.16 ^{13}C NMR spectrum (125 MHz, 298K, CD_2Cl_2) of **N_3-d_1C12**

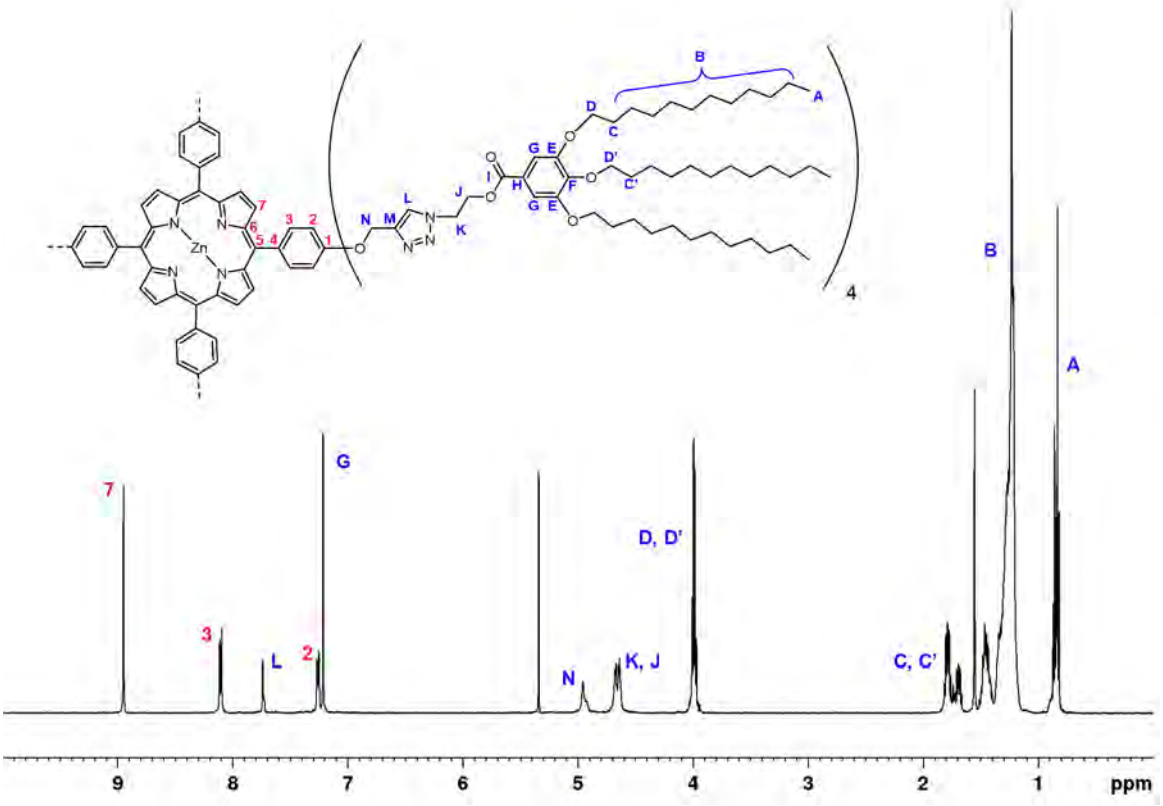

Figure 6.17 ^{1}H NMR spectrum (500 MHz, 298K, CD_2Cl_2) of **ZnP-*t*-d$_1$C12**

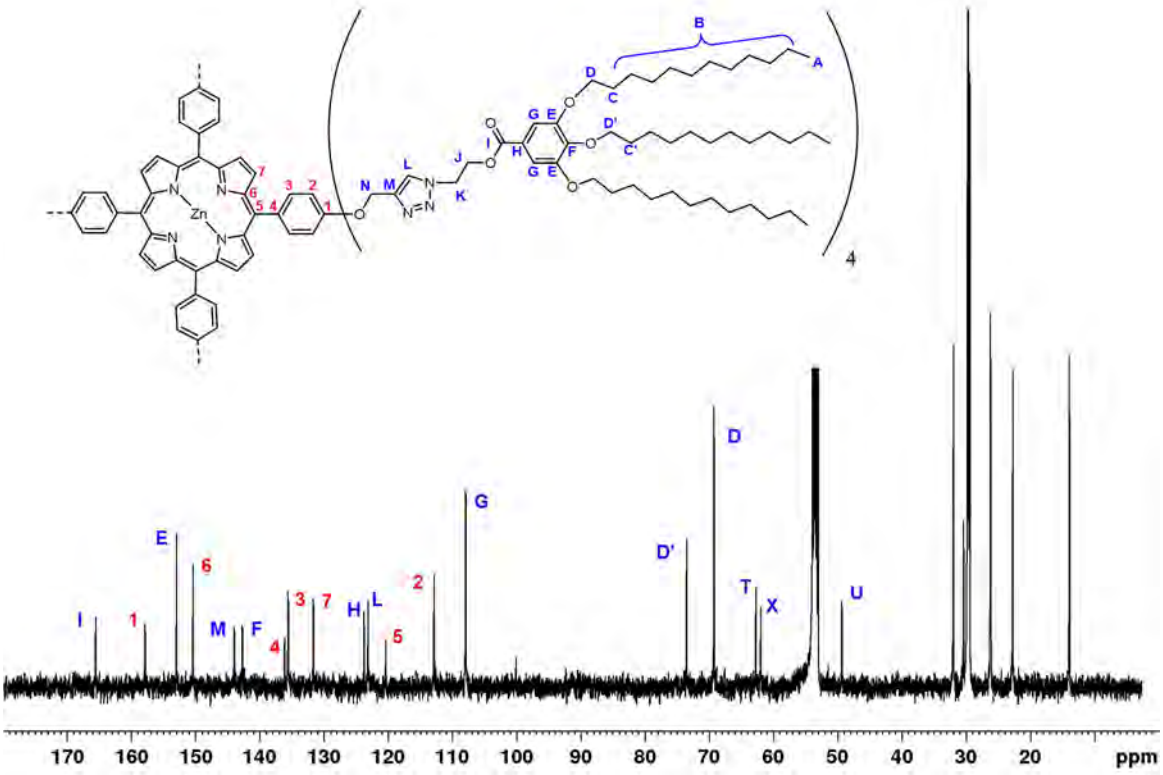

Figure 6.18 ^{13}C NMR spectrum (125 MHz, 298K, CD_2Cl_2) of **ZnP-*t*-d$_1$C12**

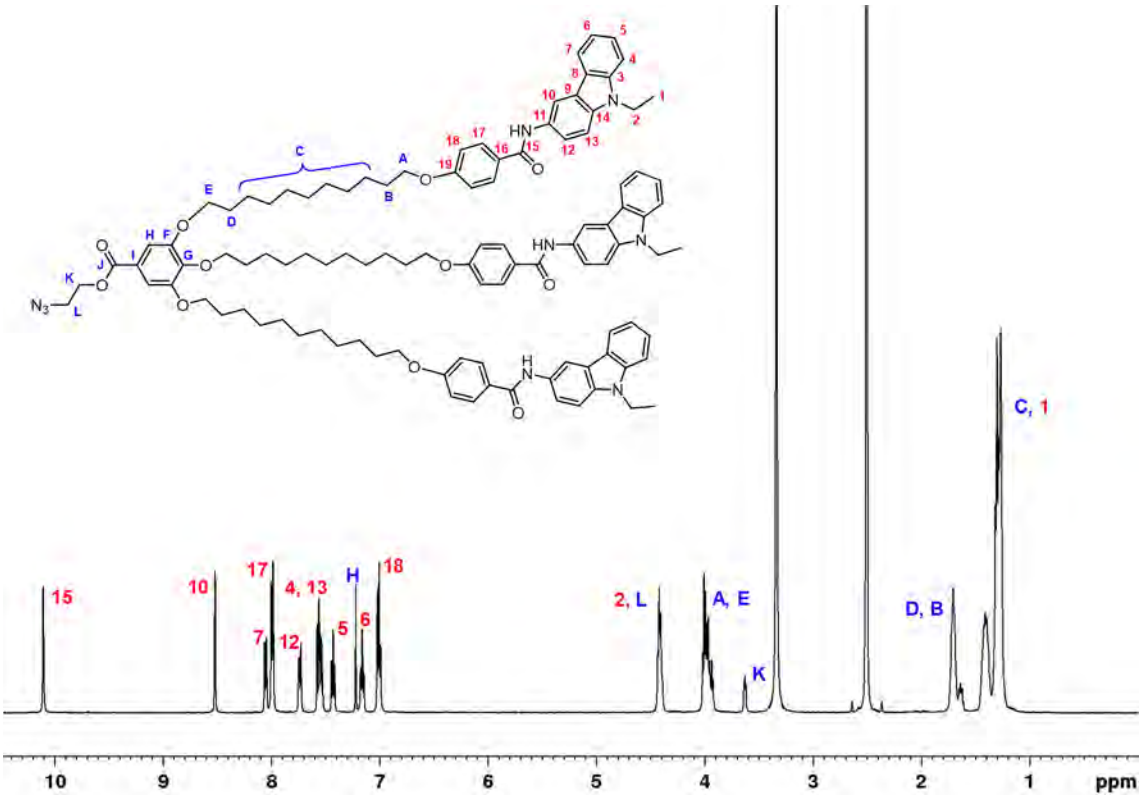

Figure 6.19 ^{1}H NMR spectrum (500 MHz, 353K, DMSO-d_6) of **N_3-d_1Cz**

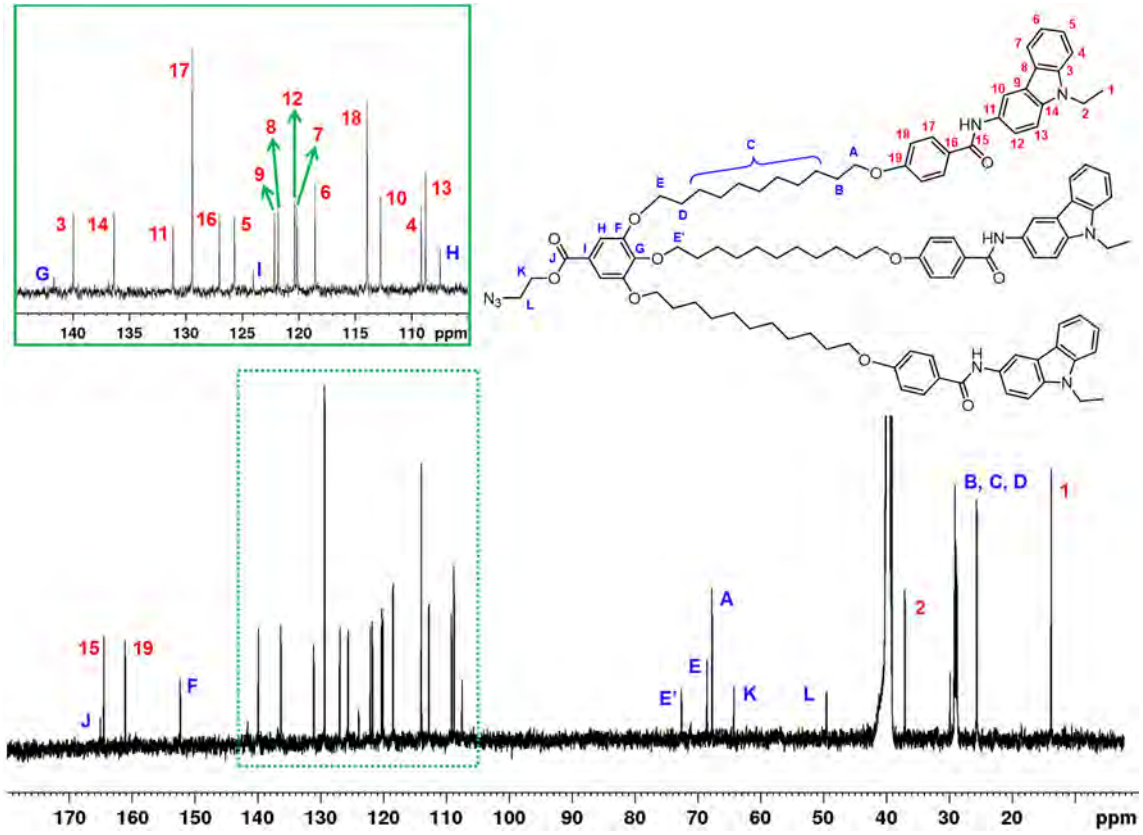

Figure 6.20 ^{13}C NMR spectrum (125 MHz, 353K, DMSO-d_6) of **N_3-d_1Cz**

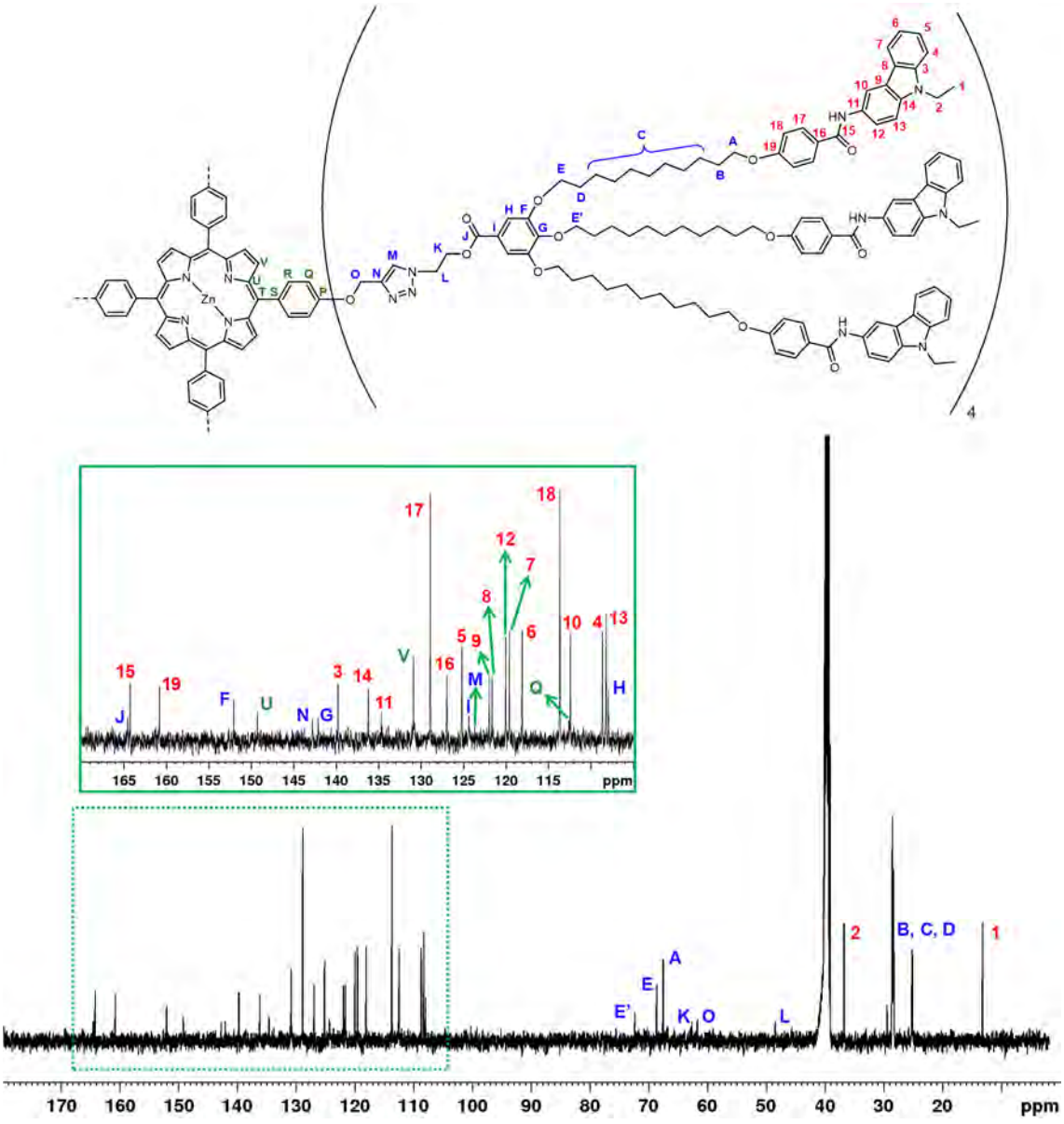

Figure 6.21 ^{13}C NMR spectrum (125 MHz, 353K, DMSO-d_6) of **ZnP-*t*-d_1Cz**

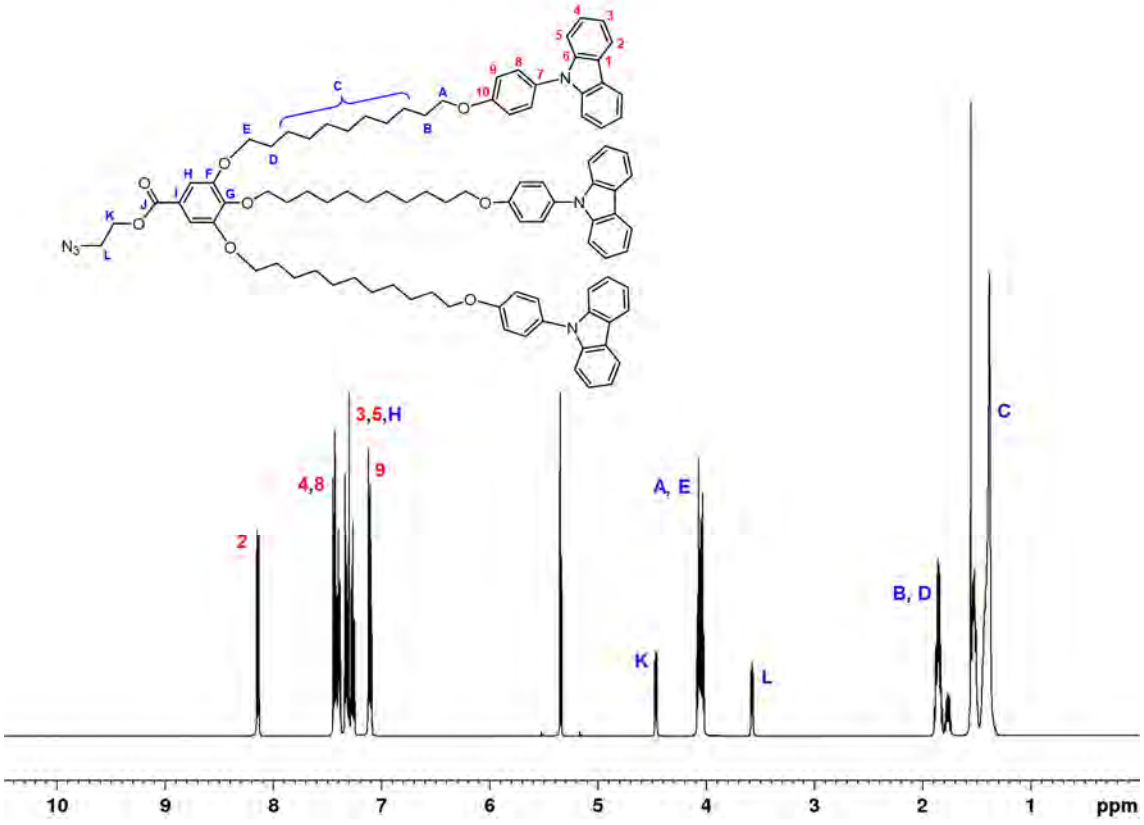

Figure 6.22 ^{1}H NMR spectrum (500 MHz, 298K, CD_2Cl_2) of **N_3-d_1PhCz**

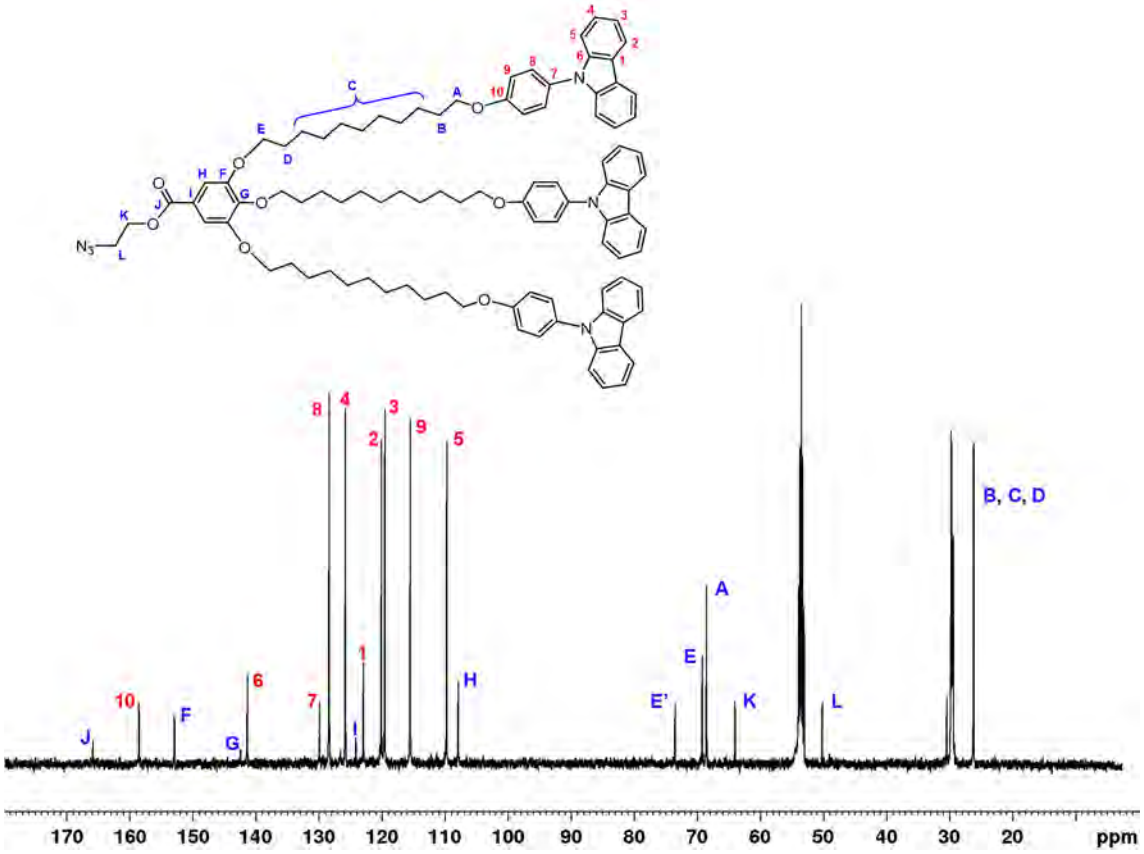

Figure 6.23 ^{13}C NMR spectrum (125 MHz, 298K, CD_2Cl_2) of **N_3-d_1PhCz**

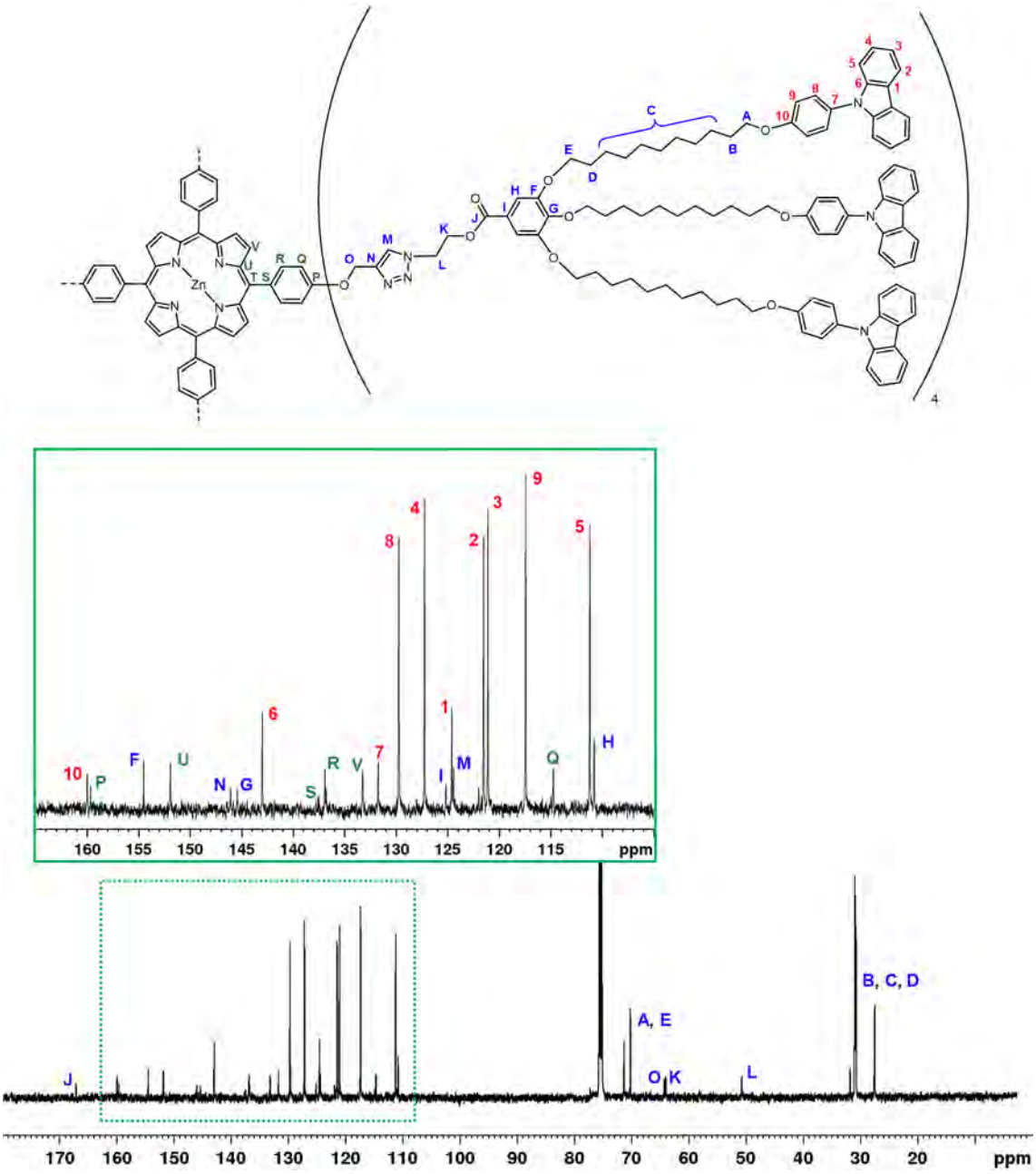

Figure 6.24 ^{13}C NMR spectrum (125 MHz, 353K, $C_2D_2Cl_4$) of **ZnP-*t*-d$_1$PhCz**

6.2 MALDI-TOF MS Spectra

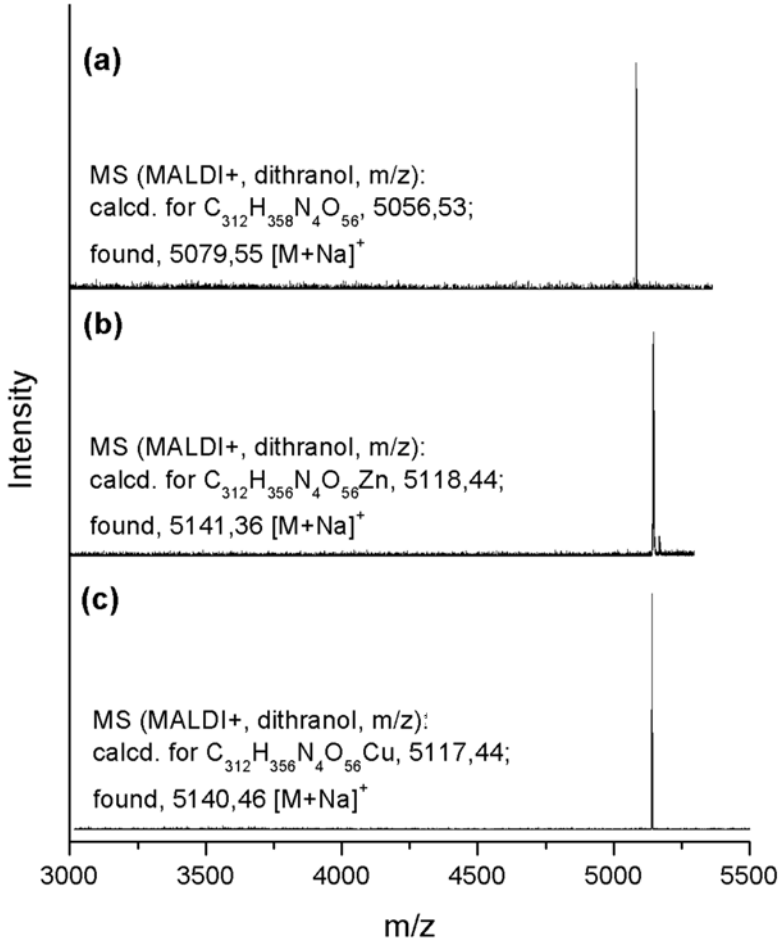

Figure 6.25 MALDI-TOF mass spectrum (MALDI$^+$, dithranol) of: **(a) P-d_1Cou, (b) ZnP-d_1Cou**, and **(c) CuP-d_1Cou**.

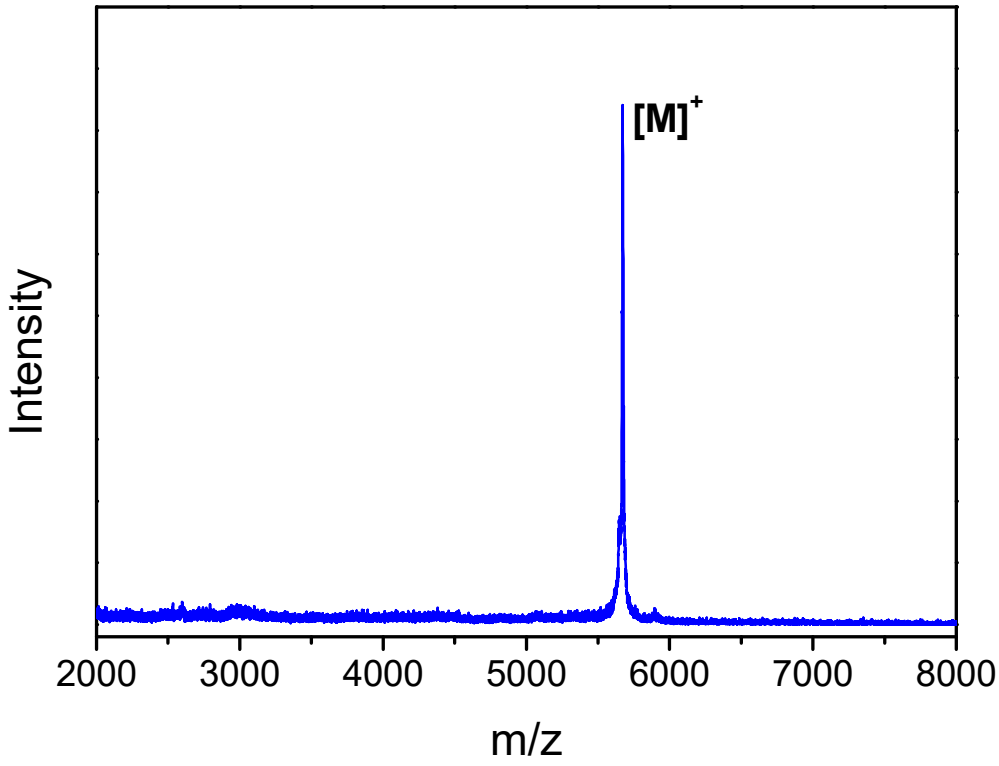

Figure 6.26 MALDI-TOF mass spectrum (MALDI$^+$, DCTB) of **ZnP-*t*-d$_1$Cou**.

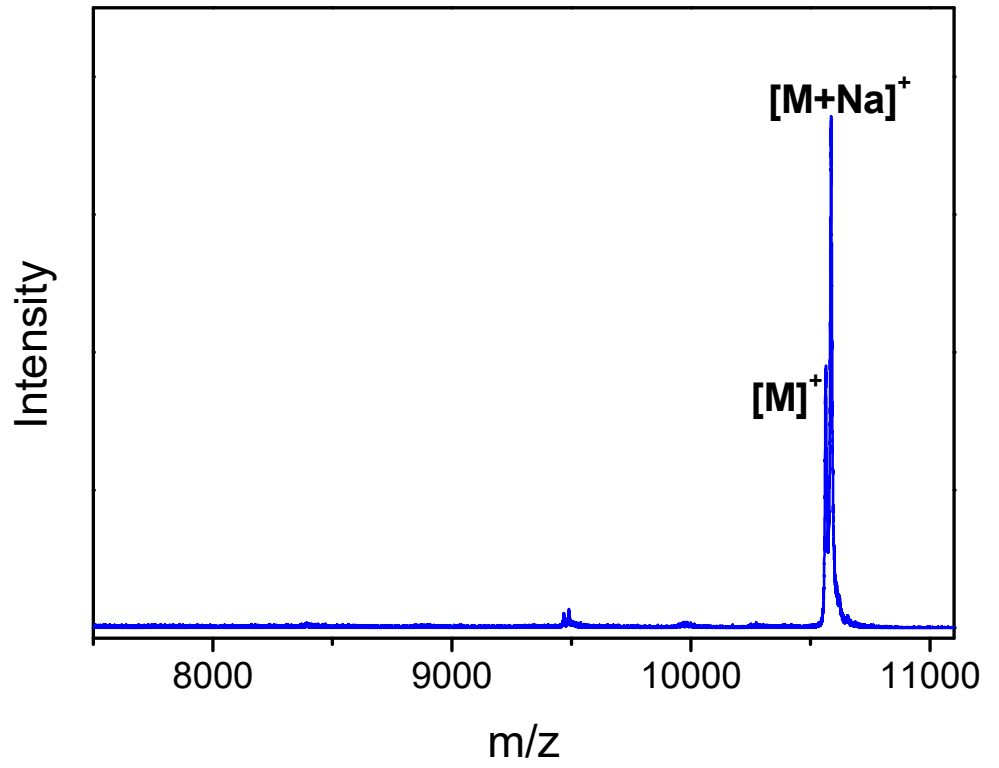

Figure 6.27 MALDI-TOF mass spectrum (MALDI$^+$, DCTB) of **ZnP-*t*-d$_2$Cou**.

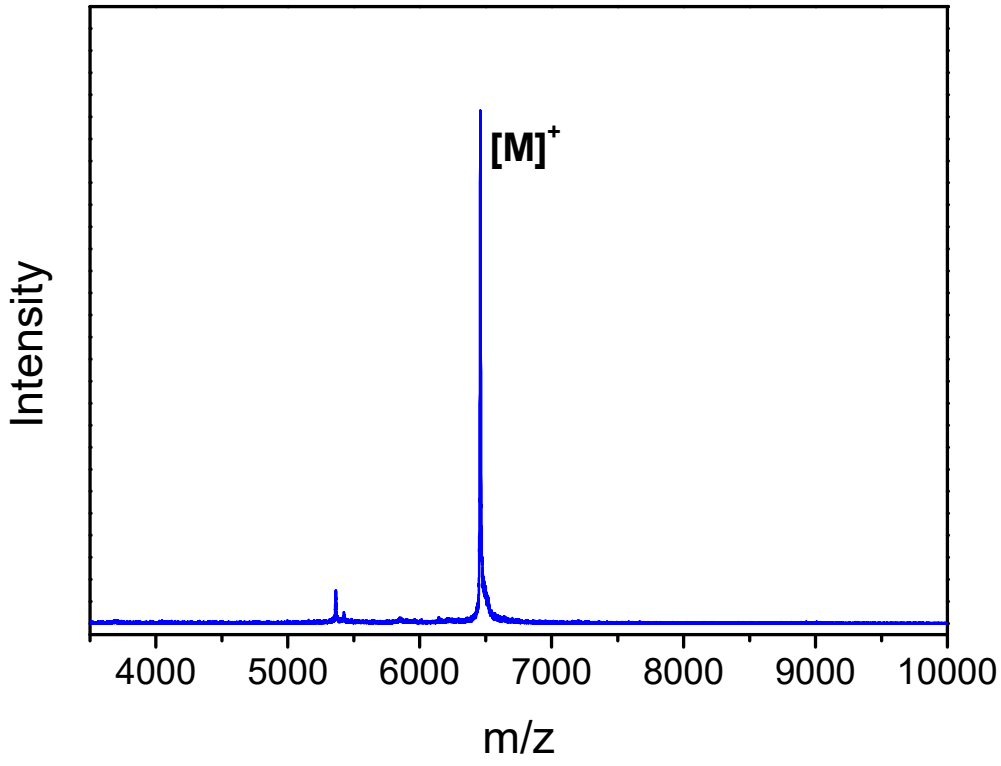

Figure 6.28 MALDI-TOF mass spectrum (MALDI$^+$, DCTB) of **ZnP-*t*-d$_1$Cou-CF$_3$**.

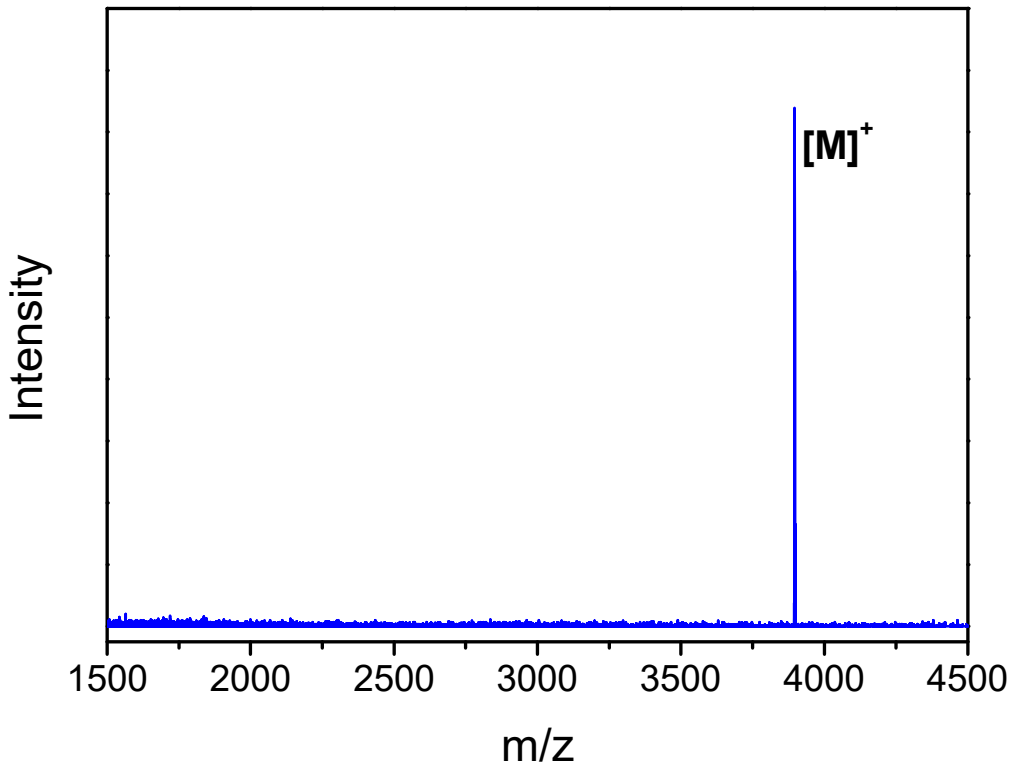

Figure 6.29 MALDI-TOF mass spectrum (MALDI$^+$, DCTB) of **ZnP-*t*-d$_1$C12**.

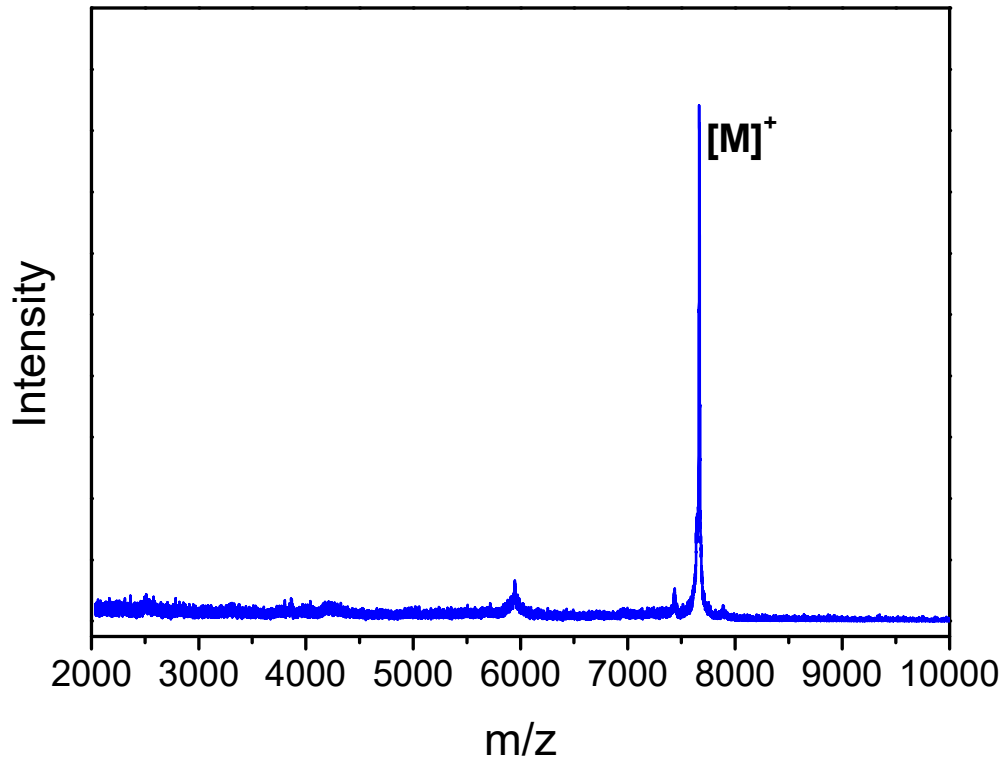

Figure 6.30 MALDI-TOF mass spectrum (MALDI$^+$, DCTB) of **ZnP-*t*-d$_1$Cz**.

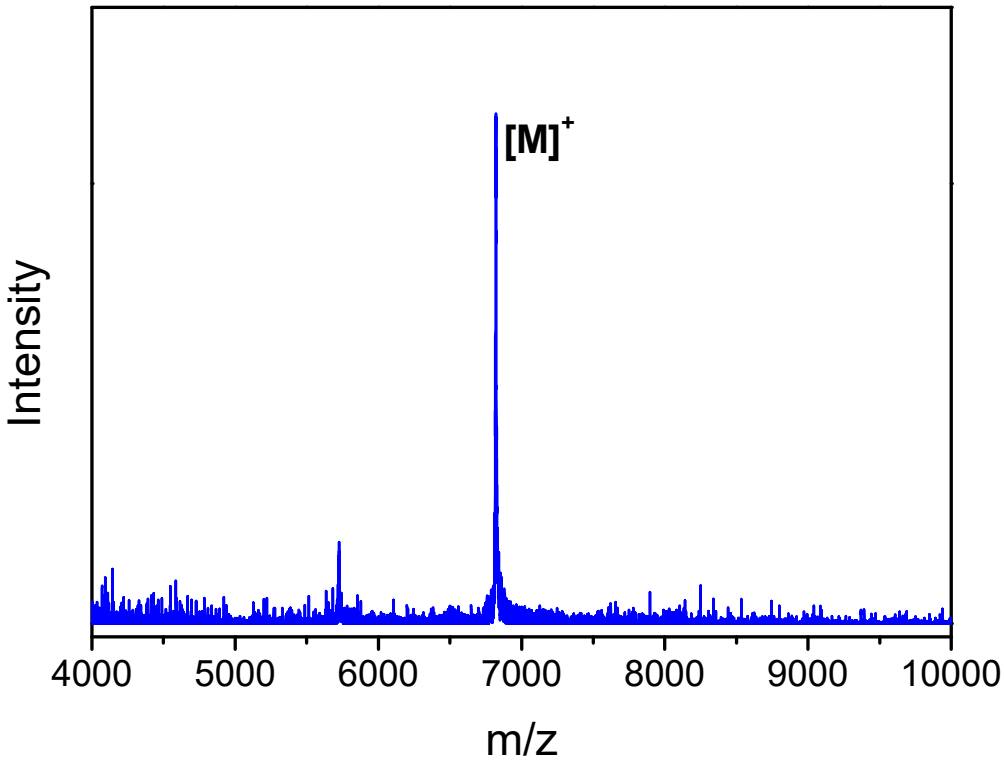

Figure 6.31 MALDI-TOF mass spectrum (MALDI$^+$, DCTB) of **ZnP-*t*-d$_1$PhCz**.

7. REFERENCES

(1) T. W. Kelley, P. F. Baude, C. Gerlach, D. E. Ender, D. Muyres, M. A. Haase, D. E. Vogel & S. D. Theiss. Recent Progress in Organic Electronics: Materials, Devices, and Processes. *Chem. Mater.* **2004,** *16*, 4413-4422.

(2) M. Gsänger, D. Bialas, L. Huang, M. Stolte & F. Würthner. Organic Semiconductors based on Dyes and Color Pigments. *Adv. Mater.* **2016,** *28*, 3615-3645.

(3) C. Wang, H. Dong, W. Hu, Y. Liu & D. Zhu. Semiconducting π-Conjugated Systems in Field-Effect Transistors: A Material Odyssey of Organic Electronics. *Chem. Rev.* **2012,** *112*, 2208-2267.

(4) A. Facchetti. Semiconductors for organic transistors. *Mater. Today* **2007,** *10*, 28-37.

(5) A. W. Hains, Z. Liang, M. A. Woodhouse & B. A. Gregg. Molecular Semiconductors in Organic Photovoltaic Cells. *Chem. Rev.* **2010,** *110*, 6689-6735.

(6) Y. J. Cheng, S. H. Yang & C. S. Hsu. Synthesis of Conjugated Polymers for Organic Solar Cell Applications. *Chem. Rev.* **2009,** *109*, 5868-5923.

(7) A. Hagfeldt, G. Boschloo, L. Sun, L. Kloo & H. Pettersson. Dye-Sensitized Solar Cells. *Chem. Rev.* **2010,** *110*, 6595-6663.

(8) V. Coropceanu, J. Cornil, D. A. da Silva Filho, Y. Olivier, R. Silbey & J. L. Brédas. Charge Transport in Organic Semiconductors. *Chem. Rev.* **2007,** *107*, 926-952.

(9) M. Mas-Torrent & C. Rovira. Role of Molecular Order and Solid-State Structure in Organic Field-Effect Transistors. *Chem. Rev.* **2011,** *111*, 4833-4856.

(10) O. Ostroverkhova. Organic Optoelectronic Materials: Mechanisms and Applications. *Chem. Rev.* **2016,** *116*, 13279-13412.

(11) L. Wang, G. Nan, X. Yang, Q. Peng, Q. Li & Z. Shuai. Computational methods for design of organic materials with high charge mobility. *Chem. Soc. Rev.* **2010,** *39*, 423-434.

(12) J. Takeya, M. Yamagishi, Y. Tominari, R. Hirahara, Y. Nakazawa, T. Nishikawa, T. Kawase, T. Shimoda & S. Ogawa. Very high-mobility organic single-crystal transistors with in-crystal conduction channels. *Appl. Phys. Lett.* **2007,** *90*, 102120.

(13) W. Pisula, M. Zorn, J. Y. Chang, K. Müllen & R. Zentel. Liquid Crystalline Ordering and Charge Transport in Semiconducting Materials. *Macromol. Rapid Commun.* **2009,** *30*, 1179-1202.

(14) M. O'Neill & S. M. Kelly. Ordered Materials for Organic Electronics and Photonics. *Adv. Mater.* **2011,** *23*, 566-584.

(15) E. K. Fleischmann & R. Zentel. Liquid-Crystalline Ordering as a Concept in Materials Science: From Semiconductors to Stimuli-Responsive Devices. *Angew. Chem. Int. Ed.* **2013,** *52*, 8810-8827.

(16) T. Kato, M. Yoshio, T. Ichikawa, B. Soberats, H. Ohno & M. Funahashi. Transport of ions and electrons in nanostructured liquid crystals. *Nat. Rev. Mater.* **2017,** *2*, 17001.

(17) J.-i. Hanna, A. Ohno & H. Iino. Charge carrier transport in liquid crystals. *Thin Solid Films* **2014,** *554*, 58-63.

(18) H. Iino, T. Usui & J.-i. Hanna. Liquid crystals for organic thin-film transistors. *Nat. Commun.* **2015,** *6*, 6828.

(19) J. Ma & Q. Li, Self-Organized Semiconducting Smectic Liquid Crystals. In *Self-Organized Organic Semiconductors*, John Wiley & Sons, Inc.: **2011**; pp 131-163.

(20) S. Kumar, *Chemistry of discotic liquid crystals: from monomers to polymers*. CRC Press: Boca Raton, **2011**.

(21) T. Wöhrle, I. Wurzbach, J. Kirres, A. Kostidou, N. Kapernaum, J. Litterscheidt, J. C. Haenle, P. Staffeld, A. Baro, F. Giesselmann & S. Laschat. Discotic Liquid Crystals. *Chem. Rev.* **2016,** *116*, 1139-1241.

(22) S. Kumar. Self-organization of disc-like molecules: chemical aspects. *Chem. Soc. Rev.* **2006,** *35*, 83-109.

(23) H. K. Bisoyi & S. Kumar. Discotic nematic liquid crystals: science and technology. *Chem. Soc. Rev.* **2010,** *39*, 264-285.

(24) M. Mathews & Q. Li, Self-Organized Discotic Liquid Crystals as Novel Organic Semiconductors. In *Self-Organized Organic Semiconductors*, John Wiley & Sons, Inc.: **2011**; pp 83-129.

(25) W. Pisula & K. Müllen, Discotic Liquid Crystals as Organic Semiconductors. In *Handbook of Liquid Crystals*, Second ed.; J. W. Goodby, P. J. Collings, T. Kato, C. Tschierske, H. Gleeson & P. Raynes, Eds. Wiley-VCH Verlag GmbH & Co. KGaA: **2014**; Vol. 8, pp 627-673.

(26) S. Sergeyev, W. Pisula & Y. H. Geerts. Discotic liquid crystals: a new generation of organic semiconductors. *Chem. Soc. Rev.* **2007,** *36*, 1902-1929.

(27) B. R. Kaafarani. Discotic Liquid Crystals for Opto-Electronic Applications. *Chem. Mater.* **2011,** *23*, 378-396.

(28) R. J. Bushby & K. Kawata. Liquid crystals that affected the world: discotic liquid crystals. *Liq. Cryst.* **2011,** *38*, 1415-1426.

(29) S. Laschat, A. Baro, N. Steinke, F. Giesselmann, C. Hägele, G. Scalia, R. Judele, E. Kapatsina, S. Sauer, A. Schreivogel & M. Tosoni. Discotic Liquid Crystals: From Tailor-Made Synthesis to Plastic Electronics. *Angew. Chem. Int. Ed.* **2007,** *46*, 4832-4887.

(30) http://www.emd-performance-materials.com/en/index.html

(31) http://www.heliatek.com/en/

(32) N. Boden, R. J. Bushby, J. Clements, B. Movaghar, K. J. Donovan & T. Kreouzis. Mechanism of charge transport in discotic liquid crystals. *Phys. Rev. B* **1995,** *52*, 13274-13280.

(33) K. Kohary, H. Cordes, S. D. Baranovskii, P. Thomas, S. Yamasaki, F. Hensel & J. H. Wendorff. One-dimensional hopping transport in disordered organic solids. II. Monte Carlo simulations. *Phys. Rev. B* **2001,** *63*, 094202.

(34) J. I. Hanna & A. Ohno, Charge-Carrier Transport and Its Modeling in Liquid Crystals. In *Self-Organized Organic Semiconductors*, John Wiley & Sons, Inc.: **2011**; pp 39-81.

(35) A. Kokil, K. Yang & J. Kumar. Techniques for characterization of charge carrier mobility in organic semiconductors. *J. Polym. Sci. Part B: Polym. Phys.* **2012,** *50*, 1130-1144.

(36) A. M. van de Craats, N. Stutzmann, O. Bunk, M. M. Nielsen, M. Watson, K. Müllen, H. D. Chanzy, H. Sirringhaus & R. H. Friend. Meso-Epitaxial Solution-Growth of Self-Organizing Discotic Liquid-Crystalline Semiconductors. *Adv. Mater.* **2003,** *15*, 495-499.

(37) W. Pisula, Ž. Tomović, M. Stepputat, U. Kolb, T. Pakula & K. Müllen. Uniaxial Alignment of Polycyclic Aromatic Hydrocarbons by Solution Processing. *Chem. Mater.* **2005,** *17*, 2641-2647.

(38) I. O. Shklyarevskiy, P. Jonkheijm, N. Stutzmann, D. Wasserberg, H. J. Wondergem, P. C. M. Christianen, A. P. H. J. Schenning, D. M. de Leeuw, Ž. Tomović, J. Wu, K. Müllen & J. C. Maan. High Anisotropy of the Field-Effect Transistor Mobility in Magnetically Aligned Discotic Liquid-Crystalline Semiconductors. *J. Am. Chem. Soc.* **2005,** *127*, 16233-16237.

(39) W. Pisula, X. Feng & K. Müllen. Charge-Carrier Transporting Graphene-Type Molecules. *Chem. Mater.* **2011,** *23*, 554-567.

(40) J. H. Lee, S. M. Choi, B. D. Pate, M. H. Chisholm & Y. S. Han. Magnetic uniaxial alignment of the columnar superstructure of discotic metallomesogens over the centimetre length scale. *J. Mater. Chem.* **2006,** *16*, 2785-2791.

(41) A. Tracz, J. K. Jeszka, M. D. Watson, W. Pisula, K. Müllen & T. Pakula. Uniaxial Alignment of the Columnar Super-Structure of a Hexa (Alkyl) Hexa-peri-hexabenzocoronene on Untreated Glass by Simple Solution Processing. *J. Am. Chem. Soc.* **2003,** *125*, 1682-1683.

(42) D. Adam, F. Closs, T. Frey, D. Funhoff, D. Haarer, P. Schuhmacher & K. Siemensmeyer. Transient photoconductivity in a discotic liquid crystal. *Phys. Rev. Lett.* **1993,** *70*, 457-460.

(43) J. Simmerer, B. Glüsen, W. Paulus, A. Kettner, P. Schuhmacher, D. Adam, K.-H. Etzbach, K. Siemensmeyer, J. H. Wendorff, H. Ringsdorf & D. Haarer. Transient photoconductivity in a discotic hexagonal plastic crystal. *Adv. Mater.* **1996,** *8*, 815-819.

(44) D. Adam, P. Schuhmacher, J. Simmerer, L. Haussling, K. Siemensmeyer, K. H. Etzbachi, H. Ringsdorf & D. Haarer. Fast photoconduction in the highly ordered columnar phase of a discotic liquid crystal. *Nature* **1994,** *371*, 141-143.

(45) H. Bengs, F. Closs, T. Frey, D. Funhoff, H. Ringsdorf & K. Siemensmeyer. Highly photoconductive discotic liquid crystals Structure–property relations in the homologous series of hexa-alkoxytriphenylenes. *Liq. Cryst.* **1993,** *15*, 565-574.

(46) A. M. van de Craats, J. M. Warman, M. P. de Haas, D. Adam, J. Simmerer, D. Haarer & P. Schuhmacher. The mobility of charge carriers in all four phases of the columnar discotic material hexakis(hexylthio)triphenylene: Combined TOF and PR-TRMC results. *Adv. Mater.* **1996,** *8*, 823-826.

(47) A. M. v. d. Craats, J. M. Warman, A. Fechtenkötter, J. D. Brand, M. A. Harbison & K. Müllen. Record Charge Carrier Mobility in a Room-Temperature Discotic Liquid-Crystalline Derivative of Hexabenzocoronene. *Adv. Mater.* **1999,** *11*, 1469-1472.

(48) M. Kastler, F. Laquai, K. Müllen & G. Wegner. Room-temperature nondispersive hole transport in a discotic liquid crystal. *Appl. Phys. Lett.* **2006,** *89*, 252103.

(49) J. Wu, W. Pisula & K. Müllen. Graphenes as Potential Material for Electronics. *Chem. Rev.* **2007,** *107*, 718-747.

(50) X. Feng, V. Marcon, W. Pisula, M. R. Hansen, J. Kirkpatrick, F. Grozema, D. Andrienko, K. Kremer & K. Mullen. Towards high charge-carrier mobilities by rational design of the shape and periphery of discotics. *Nat. Mater.* **2009,** *8*, 421-426.

(51) M. G. Debije, J. Piris, M. P. de Haas, J. M. Warman, Ž. Tomović, C. D. Simpson, M. D. Watson & K. Müllen. The Optical and Charge Transport Properties of Discotic Materials with Large Aromatic Hydrocarbon Cores. *J. Am. Chem. Soc.* **2004,** *126*, 4641-4645.

(52) Y. Yamamoto, G. Zhang, W. Jin, T. Fukushima, N. Ishii, A. Saeki, S. Seki, S. Tagawa, T. Minari, K. Tsukagoshi & T. Aida. Ambipolar-transporting coaxial nanotubes with a tailored molecular graphene–fullerene heterojunction. *PNAS* **2009,** *106*, 21051-21056.

(53) P. G. Schouten, J. M. Warman, M. P. de Haas, M. Anne Fox & H.-L. Pan. Charge migration in supramolecular stacks of peripherally substituted porphyrins. *Nature* **1991,** *353*, 736-737.

(54) P. G. Schouten, J. M. Warman, M. P. De Haas, J. F. Van der Pol & J. W. Zwikker. Radiation-induced conductivity in polymerized and nonpolymerized columnar aggregates of phthalocyanine. *J. Am. Chem. Soc.* **1992,** *114*, 9028-9034.

(55) H. Fujikake, T. Murashige, M. Sugibayashi & K. Ohta. Time-of-flight analysis of charge mobility in a Cu-phthalocyanine-based discotic liquid crystal semiconductor. *Appl. Phys. Lett.* **2004,** *85*, 3474-3476.

(56) H. Iino, J. i. Hanna, R. J. Bushby, B. Movaghar, B. J. Whitaker & M. J. Cook. Very high time-of-flight mobility in the columnar phases of a discotic liquid crystal. *Appl. Phys. Lett.* **2005,** *87*, 132102.

(57) K. Ban, K. Nishizawa, K. Ohta, A. M. van de Craats, J. M. Warman, I. Yamamoto & H. Shirai. Discotic liquid crystals of transition metal complexes 29: mesomorphism and charge transport properties of alkylthio-substituted phthalocyanine rare-earth metal sandwich complexes. *J. Mater. Chem.* **2001,** *11*, 321-331.

(58) L. Li, S. W. Kang, J. Harden, Q. Sun, X. Zhou, L. Dai, A. Jakli, S. Kumar & Q. Li. Nature-inspired light‐harvesting liquid crystalline porphyrins for organic photovoltaics. *Liq. Cryst.* **2008,** *35*, 233-239.

(59) S. W. Kang, Q. Li, B. D. Chapman, R. Pindak, J. O. Cross, L. Li, M. Nakata & S. Kumar. Microfocus X-ray Diffraction Study of the Columnar Phase of Porphyrin-Based Mesogens. *Chem. Mater.* **2007,** *19*, 5657-5663.

(60) Q. Sun, L. Dai, X. Zhou, L. Li & Q. Li. Bilayer- and bulk-heterojunction solar cells using liquid crystalline porphyrins as donors by solution processing. *Appl. Phys. Lett.* **2007,** *91*, 253505.

(61) M. Talarico, R. Termine, E. M. García-Frutos, A. Omenat, J. L. Serrano, B. Gómez-Lor & A. Golemme. New Electrode-Friendly Triindole Columnar phases with High Hole Mobility. *Chem. Mater.* **2008,** *20*, 6589-6591.

(62) E. M. Garcia-Frutos, A. Omenat, J. Barberá, J. L. Serrano & B. Gomez-Lor. Highly ordered [small pi]-extended discotic liquid-crystalline triindoles. *J. Mater. Chem.* **2011,** *21*, 6831-6836.

(63) E. M. García-Frutos, U. K. Pandey, R. Termine, A. Omenat, J. Barberá, J. L. Serrano, A. Golemme & B. Gómez-Lor. High Charge Mobility in Discotic Liquid-Crystalline Triindoles: Just a Core Business? *Angew. Chem. Int. Ed.* **2011,** *50*, 7399-7402.

(64) A. Benito-Hernández, U. K. Pandey, E. Cavero, R. Termine, E. M. García-Frutos, J. L. Serrano, A. Golemme & B. Gómez-Lor. High Hole Mobility in Triindole-Based Columnar phases: Removing the Bottleneck of Homogeneous Macroscopic Orientation. *Chem. Mater.* **2013,** *25*, 117-121.

(65) C. W. Struijk, A. B. Sieval, J. E. J. Dakhorst, M. van Dijk, P. Kimkes, R. B. M. Koehorst, H. Donker, T. J. Schaafsma, S. J. Picken, A. M. van de Craats, J. M. Warman, H. Zuilhof & E. J. R. Sudhölter. Liquid Crystalline Perylene Diimides: Architecture and Charge Carrier Mobilities. *J. Am. Chem. Soc.* **2000,** *122*, 11057-11066.

(66) Z. An, J. Yu, S. C. Jones, S. Barlow, S. Yoo, B. Domercq, P. Prins, L. D. A. Siebbeles, B. Kippelen & S. R. Marder. High Electron Mobility in Room-Temperature Discotic Liquid-Crystalline Perylene Diimides. *Adv. Mater.* **2005,** *17*, 2580-2583.

(67) P. R. L. Malenfant, C. D. Dimitrakopoulos, J. D. Gelorme, L. L. Kosbar, T. O. Graham, A. Curioni & W. Andreoni. N-type organic thin-film transistor with high field-effect

mobility based on a N,N'-dialkyl-3,4,9,10-perylene tetracarboxylic diimide derivative. *Appl. Phys. Lett.* **2002,** *80*, 2517-2519.

(68) J. Y. Kim, I. J. Chung, Y. C. Kim & J. W. Yu. Mobility of electrons and holes in a liquid crystalline perylene diimide thin film with time of flight technique. *Chem. Phys. Lett.* **2004,** *398*, 367-371.

(69) K. Pieterse, P. A. van Hal, R. Kleppinger, J. A. J. M. Vekemans, R. A. J. Janssen & E. W. Meijer. An Electron-Deficient Discotic Liquid-Crystalline Material. *Chem. Mater.* **2001,** *13*, 2675-2679.

(70) R. I. Gearba, M. Lehmann, J. Levin, D. A. Ivanov, M. H. J. Koch, J. Barberá, M. G. Debije, J. Piris & Y. H. Geerts. Tailoring Discotic Mesophases: Columnar Order Enforced with Hydrogen Bonds. *Adv. Mater.* **2003,** *15*, 1614-1618.

(71) M. Lehmann, G. Kestemont, R. Gómez Aspe, C. Buess-Herman, M. H. J. Koch, M. G. Debije, J. Piris, M. P. de Haas, J. M. Warman, M. D. Watson, V. Lemaur, J. Cornil, Y. H. Geerts, R. Gearba & D. A. Ivanov. High Charge-Carrier Mobility in π-Deficient Discotic Mesogens: Design and Structure–Property Relationship. *Chem. Eur. J.* **2005,** *11*, 3349-3362.

(72) A. Demenev, S. H. Eichhorn, T. Taerum, D. F. Perepichka, S. Patwardhan, F. C. Grozema, L. D. A. Siebbeles & R. Klenkler. Quasi Temperature Independent Electron Mobility in Hexagonal Columnar Mesophases of an H-Bonded Benzotristhiophene Derivative. *Chem. Mater.* **2010,** *22*, 1420-1428.

(73) E. Beltrán, J. L. Serrano, T. Sierra & R. Giménez. Tris(triazolyl)triazine via Click-Chemistry: A C3 Electron-Deficient Core with Liquid Crystalline and Luminescent Properties. *Org. Lett.* **2010,** *12*, 1404-1407.

(74) E. Beltran, J. L. Serrano, T. Sierra & R. Giménez. Functional star-shaped tris(triazolyl)triazines: columnar liquid crystal, fluorescent, solvatofluorochromic and electrochemical properties. *J. Mater. Chem.* **2012,** *22*, 7797-7805.

(75) B. Feringán, P. Romero, J. L. Serrano, C. L. Folcia, J. Etxebarria, J. Ortega, R. Termine, A. Golemme, R. Giménez & T. Sierra. H-Bonded Donor–Acceptor Units Segregated in Coaxial Columnar Assemblies: Toward High Mobility Ambipolar Organic Semiconductors. *J. Am. Chem. Soc.* **2016,** *138*, 12511-12518.

(76) T. Sakurai, K. Shi, H. Sato, K. Tashiro, A. Osuka, A. Saeki, S. Seki, S. Tagawa, S. Sasaki, H. Masunaga, K. Osaka, M. Takata & T. Aida. Prominent Electron Transport Property Observed for Triply Fused Metalloporphyrin Dimer: Directed Columnar Liquid Crystalline Assembly by Amphiphilic Molecular Design. *J. Am. Chem. Soc.* **2008,** *130*, 13812-13813.

(77) T. Sakurai, K. Tashiro, Y. Honsho, A. Saeki, S. Seki, A. Osuka, A. Muranaka, M. Uchiyama, J. Kim, S. Ha, K. Kato, M. Takata & T. Aida. Electron- or Hole-Transporting Nature Selected by Side-Chain-Directed π-Stacking Geometry: Liquid Crystalline Fused Metalloporphyrin Dimers. *J. Am. Chem. Soc.* **2011,** *133*, 6537-6540.

(78) V. Percec, M. Glodde, M. Peterca, A. Rapp, I. Schnell, H. W. Spiess, T. K. Bera, Y. Miura, V. S. K. Balagurusamy, E. Aqad & P. A. Heiney. Self-Assembly of Semifluorinated Dendrons Attached to Electron-Donor Groups Mediates Their π-Stacking via a Helical Pyramidal Column. *Chem. Eur. J.* **2006,** *12*, 6298-6314.

(79) V. Percec, M. Glodde, T. K. Bera, Y. Miura, I. Shiyanovskaya, K. D. Singer, V. S. K. Balagurusamy, P. A. Heiney, I. Schnell, A. Rapp, H. W. Spiess, S. D. Hudson & H. Duan. Self-organization of supramolecular helical dendrimers into complex electronic materials. *Nature* **2002,** *417*, 384-387.

(80) K. M. Kadish, K. M. Smith & R. Guilard, Cumulative Index to Volumes 1–34. In *Handbook of Porphyrin Science*, World Scientific Publishing Company: **2014**; pp 1-399.

(81) S. C. Zimmerman, M. S. Wendland, N. A. Rakow, I. Zharov & K. S. Suslick. Synthetic hosts by monomolecular imprinting inside dendrimers. *Nature* **2002,** *418*, 399-403.

(82) D. Wróbel & A. Dudkowiak. Porphyrins and Phthalocyanines-Functional Molecular Materials for Optoelectronics and Medicine. *Mol. Cryst. Liq. Cryst.* **2006,** *448*, 617-640.

(83) C. M. Drain, A. Varotto & I. Radivojevic. Self-Organized Porphyrinic Materials. *Chem. Rev.* **2009,** *109*, 1630-1658.

(84) I. Beletskaya, V. S. Tyurin, A. Y. Tsivadze, R. Guilard & C. Stern. Supramolecular Chemistry of Metalloporphyrins. *Chem. Rev.* **2009,** *109*, 1659-1713.

(85) M. G. Walter, A. B. Rudine & C. C. Wamser. Porphyrins and phthalocyanines in solar photovoltaic cells. *J. Porphyrins Phthalocyanines* **2010,** *14*, 759-792.

(86) M. Urbani, M. Grätzel, M. K. Nazeeruddin & T. Torres. Meso-Substituted Porphyrins for Dye-Sensitized Solar Cells. *Chem. Rev.* **2014,** *114*, 12330-12396.

(87) S. Hiroto, Y. Miyake & H. Shinokubo. Synthesis and Functionalization of Porphyrins through Organometallic Methodologies. *Chem. Rev.* **2017,** *117*, 2910-3043.

(88) M. Taniguchi & J. S. Lindsey. Synthetic Chlorins, Possible Surrogates for Chlorophylls, Prepared by Derivatization of Porphyrins. *Chem. Rev.* **2017,** *117*, 344-535.

(89) K. M. Smith. Development of porphyrin syntheses. *New. J. Chem.* **2016,** *40*, 5644-5649.

(90) J. W. Goodby, P. S. Robinson, B.-K. Teo & P. E. Cladi. The Discotic Phase of Uro-Porphyrin I Octa-N-Dodecyl Estei. *Mol. Cryst. Liq. Cryst.* **1980,** *56*, 303-309.

(91) B. A. Gregg, M. A. Fox & A. J. Bard. Porphyrin octaesters: new discotic liquid crystals. *J. Chem. Soc., Chem. Commun.* **1987**, 1134-1135.

(92) B. A. Gregg, M. A. Fox & A. J. Bard. 2,3,7,8,12,13,17,18-Octakis(β-hydroxyethyl)porphyrin (octaethanolporphyrin) and its liquid crystalline derivatives: synthesis and characterization. *J. Am. Chem. Soc.* **1989,** *111*, 3024-3029.

(93) G. C. Shearman, G. Yahioglu, J. Kirstein, L. R. Milgrom & J. M. Seddon. Synthesis and phase behaviour of β-octaalkyl porphyrins. *J. Mater. Chem.* **2009,** *19*, 598-604.

(94) M. Castella, F. López-Calahorra, D. Velasco & H. Finkelmann. First asymmetrically beta-tetrasubstituted porphyrin-based discotic lamellar liquid crystal. *Liq. Cryst.* **2002,** *29*, 559-565.

(95) M. Castella, F. Lopez-Calahorra, D. Velasco & H. Finkelmann. The first asymmetrically β-polysubstituted porphyrin-based hexagonal columnar liquid crystal. *Chem. Commun.* **2002**, 2348-2349.

(96) A. Segade, M. Castella, F. López-Calahorra & D. Velasco. Synthesis and Characterization of Unsymmetrically β-Substituted Porphyrin Liquid Crystals: Influence of the Chemical Structure on the Mesophase Ordering. *Chem. Mater.* **2005,** *17*, 5366-5374.

(97) S. Sengupta, S. Uemura, S. Patwardhan, V. Huber, F. C. Grozema, L. D. A. Siebbeles, U. Baumeister & F. Würthner. Columnar Mesophases Based on Zinc Chlorophyll Derivatives Functionalized with Peripheral Dendron Wedges. *Chem. Eur. J.* **2011,** *17*, 5300-5310.

(98) J. L. Serrano, *Metallomesogens : synthesis, properties, and applications*. VCH: Weinheim; New York, **1996**.

(99) S. Kumar, Monomeric Discotic Liquid Crystals. In *Chemistry of Discotic Liquid Crystals*, S. Kumar, Ed. CRC Press: **2010**; pp 49-360.

(100) X. Zhou, S. W. Kang, S. Kumar, R. R. Kulkarni, S. Z. D. Cheng & Q. Li. Self-Assembly of Porphyrin and Fullerene Supramolecular Complex into Highly Ordered Nanostructure by Simple Thermal Annealing. *Chem. Mater.* **2008,** *20*, 3551-3553.

(101) B. Wu, K. Chen, Y. Deng, J. Chen, C. Liu, R. Cheng & D. Chen. Broad Hexagonal Columnar Mesophases Formation in Bioinspired Transition-Metal Complexes of Simple Fatty Acid meta-Octaester Derivatives of meso-Tetraphenyl Porphyrins. *Chem. Eur. J.* **2015,** *21*, 3671-3681.

(102) M. Kimura, Y. Saito, K. Ohta, K. Hanabusa, H. Shirai & N. Kobayashi. Self-Organization of Supramolecular Complex Composed of Rigid Dendritic Porphyrin and Fullerene. *J. Am. Chem. Soc.* **2002,** *124*, 5274-5275.

(103) J. Miao & L. Zhu. Hydrogen Bond-Assisted Supramolecular Self-Assembly of Doubly Discotic Supermolecules Based on Porphyrin and Triphenylene. *Chem. Mater.* **2010,** *22*, 197-206.

(104) D. W. Bruce, D. A. Dunmur, L. S. Santa & M. A. Wali. Mesomorphic metalloporphyrins showing calamitic mesophases. *J. Mater. Chem.* **1992,** *2*, 363-364.

(105) D. W. Bruce, M. A. Wali & Q. M. Wang. Calamitic nematic liquid crystal phases from Zn complexes of 5, 15-disubstituted porphyrins. *J. Chem. Soc., Chem. Commun.* **1994**, 2089-2090.

(106) Q. M. Wang & D. W. Bruce. Control of intermolecular porphyrin [small pi]-[small pi] interactions: low-melting liquid-crystal porphyrins with calamitic mesophases. *Chem. Commun.* **1996**, 2505-2506.

(107) C. J. Wilson, D. A. Wilson, R. W. Boyle & G. H. Mehl. The design and investigation of porphyrins with liquid crystal properties at room temperature. *J. Mater. Chem. C* **2013,** *1*, 144-150.

(108) F. Camerel, G. Ulrich, J. Barberá & R. Ziessel. Ionic Self-Assembly of Ammonium-Based Amphiphiles and Negatively Charged Bodipy and Porphyrin Luminophores. *Chem. Eur. J.* **2007,** *13*, 2189-2200.

(109) A. Concellón, M. Bucoş, J. L. Serrano, P. Romero & M. Marcos. Supramolecular liquid crystalline dendrimers with a porphyrin core and functional carboxylic acid dendrons. *RSC Adv.* **2016,** *6*, 65179-65185.

(110) G. McDermott, S. M. Prince, A. A. Freer, A. M. Hawthornthwaite-Lawless, M. Z. Papiz, R. J. Cogdell & N. W. Isaacs. Crystal structure of an integral membrane light-harvesting complex from photosynthetic bacteria. *Nature* **1995,** *374*, 517-521.

(111) T. Pullerits & V. Sundström. Photosynthetic Light-Harvesting Pigment−Protein Complexes: Toward Understanding How and Why. *Acc. Chem. Res.* **1996,** *29*, 381-389.

(112) A. M. van Oijen, M. Ketelaars, J. Köhler, T. J. Aartsma & J. Schmidt. Unraveling the Electronic Structure of Individual Photosynthetic Pigment-Protein Complexes. *Science* **1999,** *285*, 400-402.

(113) G. J. Hedley, A. Ruseckas & I. D. W. Samuel. Light Harvesting for Organic Photovoltaics. *Chem. Rev.* **2017,** *117*, 796-837.

(114) M. R. Wasielewski. Photoinduced electron transfer in supramolecular systems for artificial photosynthesis. *Chem. Rev.* **1992,** *92*, 435-461.

(115) D. Gust, T. A. Moore & A. L. Moore. Mimicking Photosynthetic Solar Energy Transduction. *Acc. Chem. Res.* **2001,** *34*, 40-48.

(116) D. Gust, T. A. Moore & A. L. Moore. Molecular mimicry of photosynthetic energy and electron transfer. *Acc. Chem. Res.* **1993,** *26*, 198-205.

(117) D. Gust, T. A. Moore & A. L. Moore. Realizing artificial photosynthesis. *Faraday Discuss.* **2012,** *155*, 9-26.

(118) V. Balzani, P. Ceroni, M. Maestri & V. Vicinelli. Light-harvesting dendrimers. *Current Opinion in Chemical Biology* **2003,** *7*, 657-665.

(119) A. Adronov & J. M. J. Frechet. Light-harvesting dendrimers. *Chem. Commun.* **2000**, 1701-1710.

(120) W.-S. Li & T. Aida. Dendrimer Porphyrins and Phthalocyanines. *Chem. Rev.* **2009,** *109*, 6047-6076.

(121) N. Nishiyama, W.-D. Jang & K. Kataoka. Supramolecular nanocarriers integrated with dendrimers encapsulating photosensitizers for effective photodynamic therapy and photochemical gene delivery. *New. J. Chem.* **2007,** *31*, 1074-1082.

(122) D.-L. Jiang & T. Aida. Morphology-Dependent Photochemical Events in Aryl Ether Dendrimer Porphyrins: Cooperation of Dendron Subunits for Singlet Energy Transduction. *J. Am. Chem. Soc.* **1998,** *120*, 10895-10901.

(123) M. Kimura, T. Shiba, M. Yamazaki, K. Hanabusa, H. Shirai & N. Kobayashi. Construction of Regulated Nanospace around a Porphyrin Core. *J. Am. Chem. Soc.* **2001,** *123*, 5636-5642.

(124) E. M. Harth, S. Hecht, B. Helms, E. E. Malmstrom, J. M. J. Fréchet & C. J. Hawker. The Effect of Macromolecular Architecture in Nanomaterials: A Comparison of Site Isolation in Porphyrin Core Dendrimers and Their Isomeric Linear Analogues. *J. Am. Chem. Soc.* **2002,** *124*, 3926-3938.

(125) S. Hecht, N. Vladimirov & J. M. J. Fréchet. Encapsulation of Functional Moieties within Branched Star Polymers: Effect of Chain Length and Solvent on Site Isolation. *J. Am. Chem. Soc.* **2001,** *123*, 18-25.

(126) S. Hecht, H. Ihre & J. M. J. Fréchet. Porphyrin Core Star Polymers: Synthesis, Modification, and Implication for Site Isolation. *J. Am. Chem. Soc.* **1999,** *121*, 9239-9240.

(127) W. R. Dichtel, S. Hecht & J. M. J. Fréchet. Functionally Layered Dendrimers: A New Building Block and Its Application to the Synthesis of Multichromophoric Light-Harvesting Systems. *Org. Lett.* **2005,** *7*, 4451-4454.

(128) F. Loiseau, S. Campagna, A. Hameurlaine & W. Dehaen. Dendrimers Made of Porphyrin Cores and Carbazole Chromophores as Peripheral Units. Absorption Spectra, Luminescence Properties, and Oxidation Behavior. *J. Am. Chem. Soc.* **2005,** *127*, 11352-11363.

(129) T. H. Xu, R. Lu, X. P. Qiu, X. L. Liu, P. C. Xue, C. H. Tan, C. Y. Bao & Y. Y. Zhao. Synthesis and Characterization of Carbazole-Based Dendrimers with Porphyrin Cores. *Eur. J. Org. Chem.* **2006,** *2006*, 4014-4020.

(130) K. Albrecht, Y. Kasai, A. Kimoto & K. Yamamoto. The Synthesis and Properties of Carbazole−Phenylazomethine Double Layer-Type Dendrimers. *Macromolecules* **2008,** *41*, 3793-3800.

(131) K. Albrecht, Y. Kasai, Y. Kuramoto & K. Yamamoto. A fourth-generation carbazole-phenylazomethine dendrimer as a size-selective host for fullerenes. *Chem. Commun.* **2013,** *49*, 865-867.

(132) T. Imaoka, N. Inoue & K. Yamamoto. Electron-transfer through potential gradient based on a dendrimer architecture. *Chem. Commun.* **2012,** *48*, 7235-7237.

(133) K. Onitsuka, H. Kitajima, M. Fujimoto, A. Iuchi, F. Takei & S. Takahashi. Platinum-acetylide dendrimers possessing a porphyrin core. *Chem. Commun.* **2002**, 2576-2577.

(134) X.-F. Duan, J.-L. Wang & J. Pei. Nanosized π-Conjugated Molecules Based on Truxene and Porphyrin: Synthesis and High Fluorescence Quantum Yields. *Org. Lett.* **2005,** *7*, 4071-4074.

(135) W. R. Dichtel, J. M. Serin, C. Edder, J. M. J. Fréchet, M. Matuszewski, L.-S. Tan, T. Y. Ohulchanskyy & P. N. Prasad. Singlet Oxygen Generation via Two-Photon Excited FRET. *J. Am. Chem. Soc.* **2004,** *126*, 5380-5381.

(136) M. A. Oar, J. M. Serin, W. R. Dichtel, J. M. J. Fréchet, T. Y. Ohulchanskyy & P. N. Prasad. Photosensitization of Singlet Oxygen via Two-Photon-Excited Fluorescence Resonance Energy Transfer in a Water-Soluble Dendrimer. *Chem. Mater.* **2005,** *17*, 2267-2275.

(137) M. A. Oar, W. R. Dichtel, J. M. Serin, J. M. J. Fréchet, J. E. Rogers, J. E. Slagle, P. A. Fleitz, L.-S. Tan, T. Y. Ohulchanskyy & P. N. Prasad. Light-Harvesting Chromophores with Metalated Porphyrin Cores for Tuned Photosensitization of Singlet Oxygen via Two-Photon Excited FRET. *Chem. Mater.* **2006,** *18*, 3682-3692.

(138) S. R. Trenor, A. R. Shultz, B. J. Love & T. E. Long. Coumarins in Polymers: From Light Harvesting to Photo-Cross-Linkable Tissue Scaffolds. *Chem. Rev.* **2004,** *104*, 3059-3078.

(139) X. Ren, M. E. Kondakova, D. J. Giesen, M. Rajeswaran, M. Madaras & W. C. Lenhart. Coumarin-Based, Electron-Trapping Iridium Complexes as Highly Efficient and Stable Phosphorescent Emitters for Organic Light-Emitting Diodes. *Inorg. Chem.* **2010,** *49*, 1301-1303.

(140) P. Kotchapradist, N. Prachumrak, T. Sunonnam, R. Tarsang, S. Namuangruk, T. Sudyoadsuk, T. Keawin, S. Jungsuttiwong & V. Promarak. N-coumarin derivatives as hole-transporting emitters for high efficiency solution-processed pure green electroluminescent devices. *Dyes Pigm.* **2015,** *112*, 227-235.

(141) A. Gaspar, M. J. Matos, J. Garrido, E. Uriarte & F. Borges. Chromone: A Valid Scaffold in Medicinal Chemistry. *Chem. Rev.* **2014,** *114*, 4960-4992.

(142) C. Bazzicalupi, C. Caltagirone, Z. Cao, Q. Chen, C. Di Natale, A. Garau, V. Lippolis, L. Lvova, H. Liu, I. Lundström, M. C. Mostallino, M. Nieddu, R. Paolesse, L. Prodi, M. Sgarzi & N. Zaccheroni. Multimodal Use of New Coumarin-Based Fluorescent Chemosensors: Towards Highly Selective Optical Sensors for Hg2+ Probing. *Chem. Eur. J.* **2013,** *19*, 14639-14653.

(143) N. Hidetsugu, T. Shunsuke & K. Shigekazu. Thermal and Dielectric Properties of Liquid Crystals with a Coumarin Skeleton. *Bull. Chem. Soc. Jpn.* **1983,** *56*, 3571-3377.

(144) Y. Li, X. Chen, P. Chen, Z. An & J. Li. Synthesis and mesomorphic properties of 7-alkoxybezopyrano[2,3-c]pyrazol-3-one. *Liq. Cryst.* **2010,** *37*, 1549-1557.

(145) P. Chen, Y. Li, X. Chen & Z. An. Synthesis, mesomorphic and gelation properties of 7-alkoxycoumarin-3-carbonyl hydrazine. *Liq. Cryst.* **2012,** *39*, 1393-1401.

(146) K. M. Mahadevan, H. N. Harishkumar, J. N. Masagalli & H. T. Srinivasa. Synthesis and Liquid Crystal Property of New Fluoro Coumarin Carboxylates. *Mol. Cryst. Liq. Cryst.* **2013,** *570*, 20-35.

(147) H. T. Srinivasa, H. N. Harishkumar & B. S. Palakshamurthy. New coumarin carboxylates having trifluoromethyl, diethylamino and morpholino terminal groups: Synthesis and mesomorphic characterisations. *J. Mol. Struct.* **2017,** *1131*, 97-102.

(148) J. Buchs, M. Gabler, D. Janietz & H. Sawade. Coumarin-based emissive liquid crystals. *Liq. Cryst.* **2014,** *41*, 1605-1618.

(149) M. K. Paul, Y. D. Singh, A. Dey, S. K. Saha, S. Anwar & A. P. Chattopadhyay. Coumarin based emissive rod shaped new schiff base mesogens and their zinc(II) complexes: synthesis, photophysical, mesomorphism, gelation and DFT studies. *Liq. Cryst.* **2016,** *43*, 343-360.

(150) A. Trajkovska, C. Kim, K. L. Marshall, T. H. Mourey & S. H. Chen. Photoalignment of a Nematic Liquid Crystal Fluid and Glassy−Nematic Oligofluorenes on Coumarin-Containing Polymer Films. *Macromolecules* **2006,** *39*, 6983-6989.

(151) C. Kim, A. Trajkovska, J. U. Wallace & S. H. Chen. New insight into photoalignment of liquid crystals on coumarin-containing polymer films. *Macromolecules* **2006,** *39*, 3817-3823.

(152) M. Obi, S. y. Morino & K. Ichimura. Factors Affecting Photoalignment of Liquid Crystals Induced by Polymethacrylates with Coumarin Side Chains. *Chem. Mater.* **1999,** *11*, 656-664.

(153) P. O. Jackson, M. O'Neill, W. L. Duffy, P. Hindmarsh, S. M. Kelly & G. J. Owen. An Investigation of the Role of Cross-Linking and Photodegradation of Side-Chain Coumarin Polymers in the Photoalignment of Liquid Crystals. *Chem. Mater.* **2001,** *13*, 694-703.

(154) Y. Tian, E. Akiyama, Y. Nagase, A. Kanazawa, O. Tsutsumi & T. Ikeda. Liquid crystalline coumarin polymers, 1. Synthesis and properties of side-group liquid crystalline polymers with coumarin moieties. *Macromol. Chem. Phys.* **2000,** *201*, 1640-1652.

(155) V. K. Gupta & N. L. Abbott. Design of Surfaces for Patterned Alignment of Liquid Crystals on Planar and Curved Substrates. *Science* **1997,** *276*, 1533-1536.

(156) M. Bucoş, T. Sierra, A. Golemme, R. Termine, J. Barberá, R. Giménez, J. L. Serrano, P. Romero & M. Marcos. Multifunctional Supramolecular Dendrimers with an s-Triazine Ring as the Central Core: Liquid Crystalline, Fluorescence and Photoconductive Properties. *Chem. Eur. J.* **2014,** *20*, 10027-10037.

(157) E. Cavero, J. L. Serrano, R. Giménez & M. Piñol. Liquid crystalline dendrimers based on cinnamates and coumarins. *Liq. Cryst.* **2016,** *43*, 1408-1421.

(158) A. R. A. Palmans, P. Smith & C. Weder. Polarizing Energy Transfer in Photoluminescent Conjugated Polymers with Covalently Attached Sensitizers. *Macromolecules* **1999,** *32*, 4677-4685.

(159) S. L. Gilat, A. Adronov & J. M. J. Fréchet. Modular Approach to the Accelerated Convergent Growth of Laser Dye-Labeled Poly(aryl ether) Dendrimers Using a Novel Hypermonomer. *J. Org. Chem.* **1999,** *64*, 7474-7484.

(160) S. L. Gilat, A. Adronov & J. M. J. Fréchet. Light Harvesting and Energy Transfer in Novel Convergently Constructed Dendrimers. *Angew. Chem. Int. Ed.* **1999,** *38*, 1422-1427.

(161) A. Adronov, S. L. Gilat, J. M. J. Fréchet, K. Ohta, F. V. R. Neuwahl & G. R. Fleming. Light Harvesting and Energy Transfer in Laser−Dye-Labeled Poly(aryl ether) Dendrimers. *J. Am. Chem. Soc.* **2000,** *122*, 1175-1185.

(162) A. Adronov, D. R. Robello & J. M. J. Fréchet. Light harvesting and energy transfer within coumarin-labeled polymers. *J. Polym. Sci. Part A: Polym. Chem.* **2001,** *39*, 1366-1373.

(163) A. Cerqueira, V. Almodôvar, M. Neves & A. Tomé. Coumarin–Tetrapyrrolic Macrocycle Conjugates: Synthesis and Applications. *Molecules* **2017,** *22*, 994.

(164) E. Blasco, M. Wegener & C. Barner-Kowollik. Photochemically Driven Polymeric Network Formation: Synthesis and Applications. *Adv. Mater.* **2017**, 1604005.

(165) Y. Chujo, K. Sada & T. Saegusa. Polyoxazoline having a coumarin moiety as a pendant group. Synthesis and photogelation. *Macromolecules* **1990,** *23*, 2693-2697.

(166) Q. Fu, L. Cheng, Y. Zhang & W. Shi. Preparation and reversible photo-crosslinking/photo-cleavage behavior of 4-methylcoumarin functionalized hyperbranched polyester. *Polymer* **2008,** *49*, 4981-4988.

(167) L. Zhao, D. A. Loy & K. J. Shea. Photodeformable Spherical Hybrid Nanoparticles. *J. Am. Chem. Soc.* **2006,** *128*, 14250-14251.

(168) J. He, Y. Zhao & Y. Zhao. Photoinduced bending of a coumarin-containing supramolecular polymer. *Soft Matter* **2009,** *5*, 308-310.

(169) J. He, L. Tremblay, S. Lacelle & Y. Zhao. Preparation of polymer single chain nanoparticles using intramolecular photodimerization of coumarin. *Soft Matter* **2011,** *7*, 2380-2386.

(170) W. Fan, X. Tong, G. Li & Y. Zhao. Photoresponsive liquid crystalline polymer single-chain nanoparticles. *Polym. Chem.* **2017,** *8*, 3523-3529.

(171) M. V. S. N. Maddipatla, D. Wehrung, C. Tang, W. Fan, M. O. Oyewumi, T. Miyoshi & A. Joy. Photoresponsive Coumarin Polyesters That Exhibit Cross-Linking and Chain Scission Properties. *Macromolecules* **2013,** *46*, 5133-5140.

(172) J. Lee, M. V. S. N. Maddipatla, A. Joy & B. D. Vogt. Kinetics of UV Irradiation Induced Chain Scission and Cross-Linking of Coumarin-Containing Polyester Ultrathin Films. *Macromolecules* **2014,** *47*, 2891-2898.

(173) H.-J. Knölker & K. R. Reddy. Isolation and Synthesis of Biologically Active Carbazole Alkaloids. *Chem. Rev.* **2002,** *102*, 4303-4428.

(174) J. Li & A. C. Grimsdale. Carbazole-based polymers for organic photovoltaic devices. *Chem. Soc. Rev.* **2010,** *39*, 2399-2410.

(175) J. V. Grazulevicius, P. Strohriegl, J. Pielichowski & K. Pielichowski. Carbazole-containing polymers: synthesis, properties and applications. *Prog. Polym. Sci.* **2003,** *28*, 1297-1353.

(176) K. Karon & M. Lapkowski. Carbazole electrochemistry: a short review. *J. Solid State Electrochem.* **2015,** *19*, 2601-2610.

(177) M. Manickam, P. Iqbal, M. Belloni, S. Kumar & J. A. Preece. A Brief Review of Carbazole-Based Photorefractive Liquid Crystalline Materials. *Isr. J. Chem.* **2012,** *52*, 917-934.

(178) K. Kawaguchi, M. Shishido & Y. Imanishi. Synthesis, structure, and excimer formation of cholesteric liquid crystals containing carbazolyl groups covalently linked to a cholesterol group. *J. Phys. Chem.* **1988,** *92*, 4806-4811.

(179) Y. Shimizu, K. Shigeta & S. Kusabayashi. Mesomorphic and Photoconducting Behavior of 2-(2-Hydroxy-4-alkoxybenzylideneamino)-9-methylcarbazoles. *Mol. Cryst. Liq. Cryst.* **1986,** *140*, 105-117.

(180) A. Dobarro, D. Velasco, V. v. Arnim & H. Finkelmann. Synthesis of symmetric and asymmetric carbazolyl monomers and their siloxane polymers. Effect of the 2,3,6,7,9-substitution in the carbazole unit on its mesomorphic behaviour. *Macromol. Chem. Phys.* **1997,** *198*, 2563-2581.

(181) K. Irie, S. Machida, T. Ikegami, N. Tanaka, H. Miyasaka, Y. Shimizu & A. Itaya. Photophysical properties of a carbazolyl mesogen of 8PCzC as revealed by absorption, fluorescence, and transient absorption measurements. *Photochemical & Photobiological Sciences* **2005,** *4*, 128-134.

(182) M. Sonntag & P. Strohriegl. Synthesis of a novel liquid crystalline bisindenocarbazole derivative. *Liq. Cryst.* **2007,** *34*, 49-57.

(183) M. Sonntag & P. Strohriegl. Synthesis and characterization of novel conjugated bisindenocarbazoles. *Tetrahedron* **2006,** *62*, 8103-8108.

(184) M. Sonntag & P. Strohriegl. Novel bisindenocarbazole derivative exhibiting a nematic mesophase. *Tetrahdron Lett.* **2006,** *47*, 8313-8317.

(185) Y. Li, Y. Wu, S. Gardner & B. S. Ong. Novel Peripherally Substituted Indolo[3,2-b]carbazoles for High-Mobility Organic Thin-Film Transistors. *Adv. Mater.* **2005,** *17*, 849-853.

(186) M. Manickam, M. Belloni, S. Kumar, S. K. Varshney, D. S. Shankar Rao, P. R. Ashton, J. A. Preece & N. Spencer. The first hexagonal columnar discotic liquid crystalline carbazole derivatives induced by noncovalent [small pi]-[small pi] interactions. *J. Mater. Chem.* **2001,** *11*, 2790-2800.

(187) M. Manickam, S. Kumar, J. A. Preece & N. Spencer. The first hexagonal columnar discotic liquid crystalline carbazole derivative. *Liq. Cryst.* **2000,** *27*, 703-706.

(188) E. Perea, F. López-Calahorra & D. Velasco. First carbazole-based lamellar liquid crystal system. *Liq. Cryst.* **2002,** *29*, 421-428.

(189) E. Perea, F. López-Calahorra, D. Velasco & H. Finkelmann. Polysubstituted N-Arylcarbazoles as Discotic Molecules. *Mol. Cryst. Liq. Cryst.* **2001,** *365*, 695-702.

(190) F. Camerel, B. Donnio & R. Ziessel. Liquid-crystalline functional carbazole and naphthalene platforms. *Soft Matter* **2011,** *7*, 412-428.

(191) V. Percec, M. Obata, J. G. Rudick, B. B. De, M. Glodde, T. K. Bera, S. N. Magonov, V. S. K. Balagurusamy & P. A. Heiney. Synthesis, structural analysis, and visualization of poly(2-ethynyl-9-substituted carbazole)s and poly(3-ethynyl-9-substituted carbazole)s containing chiral and achiral minidendritic substituents. *J. Polym. Sci. Part A: Polym. Chem.* **2002,** *40*, 3509-3533.

(192) R. Zhang, X. Zeng, B. Kim, R. J. Bushby, K. Shin, P. J. Baker, V. Percec, P. Leowanawat & G. Ungar. Columnar Liquid Crystals in Cylindrical Nanoconfinement. *ACS Nano* **2015,** *9*, 1759-1766.

(193) Y. Zhang, T. Wada & H. Sasabe. A new synthetic approach to macrocyclic molecules and main-chain polymers containing carbazole moieties. *Chem. Commun.* **1996**, 621-622.

(194) L. Wang, Y. Zhang, T. Wada & H. Sasabe. Photorefractive effect in a photoconductive electro‐optic carbazole trimer. *Appl. Phys. Lett.* **1996,** *69*, 728-730.

(195) S.-H. Jung, W. Pisula, A. Rouhanipour, H. J. Räder, J. Jacob & K. Müllen. A Conjugated Polycarbazole Ring around a Porphyrin. *Angew. Chem. Int. Ed.* **2006,** *45*, 4685-4690.

(196) B. Schmaltz, A. Rouhanipour, H. J. Räder, W. Pisula & K. Müllen. Filling the Cavity of Conjugated Carbazole Macrocycles with Graphene Molecules: Monolayers Formed by Physisorption Serve as a Surface for Pulsed Laser Deposition. *Angew. Chem. Int. Ed.* **2009,** *48*, 720-724.

(197) S.-i. Kawano, Y. Ishida & K. Tanaka. Columnar Liquid-Crystalline Metallomacrocycles. *J. Am. Chem. Soc.* **2015,** *137*, 2295-2302.

(198) S. Castelar, P. Romero, J. L. Serrano, J. Barberá & M. Marcos. Multifunctional ionic hybrid poly(propyleneimine) dendrimers surrounded by carbazole dendrons: liquid crystals, optical and electrochemical properties. *RSC Adv.* **2015,** *5*, 65932-65941.

(199) S. Castelar, J. Barberá, M. Marcos, P. Romero, J. L. Serrano, A. Golemme & R. Termine. Supramolecular dendrimers based on the self-assembly of carbazole-derived dendrons and triazine rings: liquid crystal, photophysical and electrochemical properties. *J. Mater. Chem. C* **2013,** *1*, 7321-7332.

(200) I. Gracia, B. Feringán, J. L. Serrano, R. Termine, A. Golemme, A. Omenat & J. Barberá. Functional Carbazole Liquid-Crystal Block Codendrimers with Optical and Electronic Properties. *Chem. Eur. J.* **2015,** *21*, 1359-1369.

(201) I. Gracia, J. L. Serrano, J. Barberá & A. Omenat. Functional organogelators formed by liquid-crystal carbazole-containing bis-MPA dendrimers. *RSC Adv.* **2016,** *6*, 39734-39740.

(202) P. L. Burn, S. C. Lo & I. D. W. Samuel. The Development of Light-Emitting Dendrimers for Displays. *Adv. Mater.* **2007,** *19*, 1675-1688.

(203) Z. a. Li, Y. Liu, G. Yu, Y. Wen, Y. Guo, L. Ji, J. Qin & Z. Li. A New Carbazole-Constructed Hyperbranched Polymer: Convenient One-Pot Synthesis, Hole-Transporting Ability, and Field-Effect Transistor Properties. *Adv. Funct. Mater.* **2009,** *19*, 2677-2683.

(204) K. Albrecht, K. Matsuoka, K. Fujita & K. Yamamoto. Carbazole Dendrimers as Solution-Processable Thermally Activated Delayed-Fluorescence Materials. *Angew. Chem. Int. Ed.* **2015,** *54*, 5677-5682.

(205) F. Liu, J.-h. Zou, Q.-y. He, C. Tang, L.-h. Xie, B. Peng, W. Wei, Y. Cao & W. Huang. Carbazole end-capped pyrene starburst with enhanced electrochemical stability and device performance. *J. Polym. Sci. Part A: Polym. Chem.* **2010,** *48*, 4943-4949.

(206) R. M. Adhikari, R. Mondal, B. K. Shah & D. C. Neckers. Synthesis and Photophysical Properties of Carbazole-Based Blue Light-Emitting Dendrimers. *J. Org. Chem.* **2007,** *72*, 4727-4732.

(207) R. M. Adhikari, L. Duan, L. Hou, Y. Qiu, D. C. Neckers & B. K. Shah. Ethynylphenyl-Linked Carbazoles as a Single-Emitting Component for White Organic Light-Emitting Diodes. *Chem. Mater.* **2009,** *21*, 4638-4644.

(208) J. Li, T. Zhang, Y. Liang & R. Yang. Solution-Processible Carbazole Dendrimers as Host Materials for Highly Efficient Phosphorescent Organic Light-Emitting Diodes. *Adv. Funct. Mater.* **2013,** *23*, 619-628.

(209) H. Ren, J. Li, R. Wang, T. Zhang, Z. Gao & D. Liu. Synthesis and luminescent properties of perylene bisimide-cored dendrimers with carbazole surface groups. *Polymer* **2011,** *52*, 3639-3646.

(210) J. Lu, P. F. Xia, P. K. Lo, Y. Tao & M. S. Wong. Synthesis and Properties of Multi-Triarylamine-Substituted Carbazole-Based Dendrimers with an Oligothiophene Core for Potential Applications in Organic Solar Cells and Light-Emitting Diodes. *Chem. Mater.* **2006,** *18*, 6194-6203.

(211) C. C. Lee, M. k. Leung, P. Y. Lee, T. L. Chiu, J. H. Lee, C. Liu & P. T. Chou. Synthesis and Properties of Oxygen-Linked N-Phenylcarbazole Dendrimers. *Macromolecules* **2012,** *45*, 751-765.

(212) P. Moonsin, N. Prachumrak, R. Rattanawan, T. Keawin, S. Jungsuttiwong, T. Sudyoadsuk & V. Promarak. Carbazole dendronised triphenylamines as solution processed high Tg amorphous hole-transporting materials for organic electroluminescent devices. *Chem. Commun.* **2012,** *48*, 3382-3384.

(213) T. Xu, R. Lu, X. Liu, X. Zheng, X. Qiu & Y. Zhao. Phosphorus(V) Porphyrins with Axial Carbazole-Based Dendritic Substituents. *Org. Lett.* **2007,** *9*, 797-800.

(214) T. Xu, R. Lu, X. Liu, P. Chen, X. Qiu & Y. Zhao. Synthesis and Characterization of Subporphyrins with Dendritic Carbazole Arms. *Eur. J. Org. Chem.* **2008,** *2008*, 1065-1071.

(215) J. Ding, J. Gao, Y. Cheng, Z. Xie, L. Wang, D. Ma, X. Jing & F. Wang. Highly Efficient Green-Emitting Phosphorescent Iridium Dendrimers Based on Carbazole Dendrons. *Adv. Funct. Mater.* **2006,** *16*, 575-581.

(216) M. C. Tang, D. P. K. Tsang, M. M. Y. Chan, K. M. C. Wong & V. W. W. Yam. Dendritic Luminescent Gold(III) Complexes for Highly Efficient Solution-Processable Organic Light-Emitting Devices. *Angew. Chem. Int. Ed.* **2013,** *52*, 446-449.

(217) S. Li, G. Zhong, W. Zhu, F. Li, J. Pan, W. Huang & H. Tian. Dendritic europium complex as a single dopant for white-light electroluminescent devices. *J. Mater. Chem.* **2005,** *15*, 3221-3228.

(218) J. Ding, B. Wang, Z. Yue, B. Yao, Z. Xie, Y. Cheng, L. Wang, X. Jing & F. Wang. Bifunctional Green Iridium Dendrimers with a “Self-Host” Feature for Highly Efficient Nondoped Electrophosphorescent Devices. *Angew. Chem. Int. Ed.* **2009,** *48*, 6664-6666.

(219) K. A. Knights, S. G. Stevenson, C. P. Shipley, S.-C. Lo, S. Olsen, R. E. Harding, S. Gambino, P. L. Burn & I. D. W. Samuel. A rapid route to carbazole containing dendrons and phosphorescent dendrimers. *J. Mater. Chem.* **2008,** *18*, 2121-2130.

(220) P. Taranekar, J. Y. Park, D. Patton, T. Fulghum, G. J. Ramon & R. Advincula. Conjugated Polymer Nanoparticles via Intramolecular Crosslinking of Dendrimeric Precursors. *Adv. Mater.* **2006,** *18*, 2461-2465.

(221) P. Taranekar, T. Fulghum, D. Patton, R. Ponnapati, G. Clyde & R. Advincula. Investigating Carbazole Jacketed Precursor Dendrimers: Sonochemical Synthesis, Characterization, and Electrochemical Crosslinking Properties. *J. Am. Chem. Soc.* **2007,** *129*, 12537-12548.

(222) D. L. Patton, P. Taranekar, T. Fulghum & R. Advincula. Electrochemically Active Dendritic−Linear Block Copolymers via RAFT Polymerization: Synthesis, Characterization, and Electrodeposition Properties. *Macromolecules* **2008,** *41*, 6703-6713.

(223) J. Y. Park, R. Ponnapati, P. Taranekar & R. C. Advincula. Carbazole Peripheral Poly(benzyl ether) Dendrimers at the Air−Water Interface: Electrochemical Cross-Linking and Electronanopatterning. *Langmuir* **2010,** *26*, 6167-6176.

(224) M. J. L. Felipe, R. R. Ponnapati, R. B. Pernites, P. Dutta & R. C. Advincula. Synthesis and Electrografting of Dendron Anchored OEGylated Surfaces and Their Protein Adsorption Resistance. *ACS Appl. Mater. Interfaces* **2010,** *2*, 3401-3405.

(225) M. J. Felipe, P. Dutta, R. Pernites, R. Ponnapati & R. C. Advincula. Electropolymerized bioresistant coatings of OEGylated dendron carbazoles: Design parameters and protein resistance SPR studies. *Polymer* **2012,** *53*, 427-437.

(226) C. Kaewtong, G. Jiang, M. J. Felipe, B. Pulpoka & R. Advincula. Self-Assembly and Electrochemical Oxidation of Polyamidoamine−Carbazole Dendron Surfmer Complexes: Nanoring Formation. *ACS Nano* **2008,** *2*, 1533-1542.

(227) P.-F. Cao, L.-H. Rong, A. de Leon, Z. Su & R. C. Advincula. A Supramolecular Polyethylenimine-Cored Carbazole Dendritic Polymer with Dual Applications. *Macromolecules* **2015,** *48*, 6801-6809.

(228) P. H. J. Kouwer, W. F. Jager, W. J. Mijs & S. J. Picken. The Nematic Lateral Phase: A Novel Phase in Discotic Supramolecular Assemblies. *Macromolecules* **2001,** *34*, 7582-7584.

(229) P. H. J. Kouwer, W. F. Jager, W. J. Mijs & S. J. Picken. Charge Transfer Complexes of Discotic Liquid Crystals: A Flexible Route to a Wide Variety of Mesophases. *Macromolecules* **2002,** *35*, 4322-4329.

(230) B. Jiang, S.-W. Yang & W. E. Jones. Conjugated Porphyrin Polymers: Control of Chromophore Separation by Oligophenylenevinylene Bridges. *Chem. Mater.* **1997,** *9*, 2031-2034.

(231) P. N. Murgatroyd. Theory of space-charge-limited current enhanced by Frenkel effect. *J. Phys. D* **1970,** *3*, 151.

(232) P. M. Borsenberger, L. Pautmeier & H. Bässler. Charge transport in disordered molecular solids. *J. Chem. Phys* **1991,** *94*, 5447-5454.

(233) M. Inoue, H. Monobe, M. Ukon, V. F. Petrov, T. Watanabe, A. Kumano & Y. Shimizu. Fast charged carrier mobility of a triphenylene-based polymer film possessing nematic order. *Opto-Electron. Rev.* **2005,** *13*, 303-308.

(234) N. Hoshino. Liquid crystal properties of metal–salicylaldimine complexes.: Chemical modifications towards lower symmetry1Dedicated to Professor Daryle H. Busch.1. *Coord. Chem. Rev.* **1998,** *174*, 77-108.

(235) A. S. Mocanu, M. Amela-Cortes, Y. Molard, V. Circu & S. Cordier. Liquid crystal properties resulting from synergetic effects between non-mesogenic organic molecules and a one nanometre sized octahedral transition metal cluster. *Chem. Commun.* **2011,** *47*, 2056-2058.

(236) S. R. Collinson & D. W. Bruce, Metallomesogens—Supramolecular Organization of Metal Complexes in Fluid Phases. In *Perspectives in Supramolecular Chemistry*, John Wiley & Sons, Ltd.: **2007**; pp 285-369.

(237) P. Wu, A. K. Feldman, A. K. Nugent, C. J. Hawker, A. Scheel, B. Voit, J. Pyun, J. M. J. Fréchet, K. B. Sharpless & V. V. Fokin. Efficiency and Fidelity in a Click-Chemistry Route to Triazole Dendrimers by the Copper(I)-Catalyzed Ligation of Azides and Alkynes. *Angew. Chem. Int. Ed.* **2004,** *43*, 3928-3932.

(238) R. K. Iha, K. L. Wooley, A. M. Nyström, D. J. Burke, M. J. Kade & C. J. Hawker. Applications of Orthogonal "Click" Chemistries in the Synthesis of Functional Soft Materials. *Chem. Rev.* **2009,** *109*, 5620-5686.

(239) U. Tunca. Orthogonal multiple click reactions in synthetic polymer chemistry. *J. Polym. Sci. Part A: Polym. Chem.* **2014,** *52*, 3147-3165.

(240) J. A. Johnson, M. G. Finn, J. T. Koberstein & N. J. Turro. Construction of Linear Polymers, Dendrimers, Networks, and Other Polymeric Architectures by Copper-Catalyzed Azide-Alkyne Cycloaddition "Click" Chemistry. *Macromol. Rapid Commun.* **2008,** *29*, 1052-1072.

(241) P. Lundberg, C. J. Hawker, A. Hult & M. Malkoch. Click Assisted One-Pot Multi-Step Reactions in Polymer Science: Accelerated Synthetic Protocols. *Macromol. Rapid Commun.* **2008,** *29*, 998-1015.

(242) M. V. Walter & M. Malkoch. Simplifying the synthesis of dendrimers: accelerated approaches. *Chem. Soc. Rev.* **2012,** *41*, 4593-4609.

(243) M. Arseneault, C. Wafer & J.-F. Morin. Recent Advances in Click Chemistry Applied to Dendrimer Synthesis. *Molecules* **2015,** *20*, 9263.

(244) H. Vedala, Y. Chen, S. Cecioni, A. Imberty, S. Vidal & A. Star. Nanoelectronic Detection of Lectin-Carbohydrate Interactions Using Carbon Nanotubes. *Nano Letters* **2011,** *11*, 170-175.

(245) N. F. Mott & R. W. Gurney, *Electronic processes in ionic crystals*. The Clarendon Press: New York, **1940**.

Chapter 2

Ionic Liquid Crystal Dendrimers as Proton Conductors

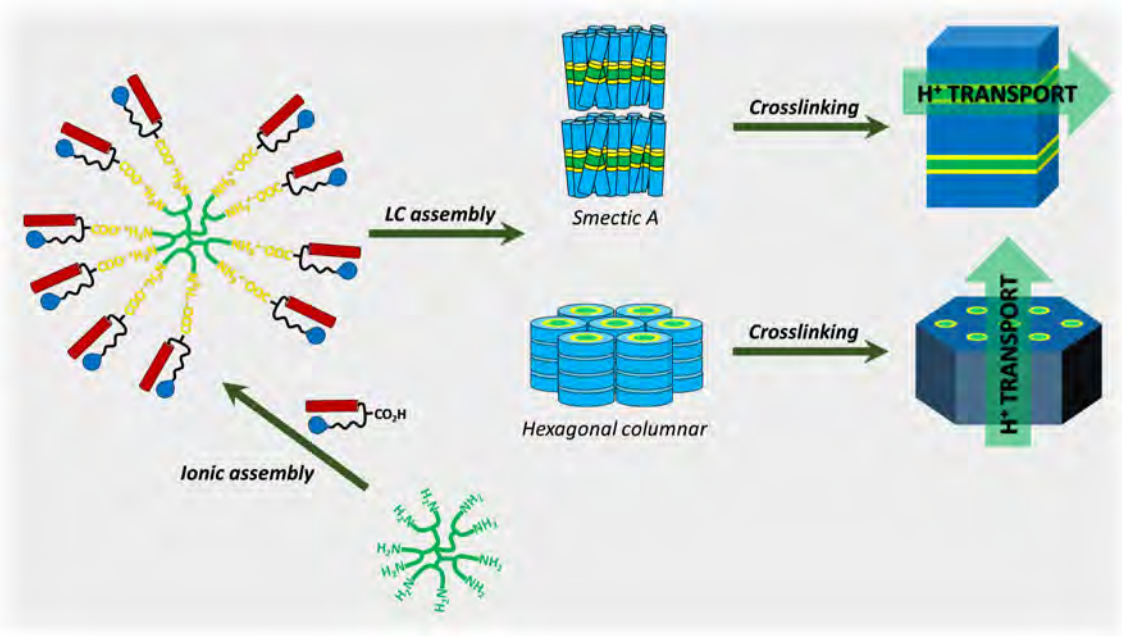

Abstract. *We have successfully developed a new strategy for the preparation of proton conductive materials using ionic LC dendrimers combined with a crosslinking reaction based on coumarin photodimerization. All the materials showed good proton conductive properties as the LC arrangement leads to the presence of ionic nanosegregated areas (formed by the ion pairs) that favor proton conduction.*

“Inspiration exists, but it has to find you working.”

Pablo Picasso

1. INTRODUCTION

1.1 Ion Transport in Liquid Crystals

Ion transport is an important phenomenon in both biological process and advanced device technologies. A great variety of organic electrolytes have been developed for ion batteries, fuel cells and dye-sensitized solar cells, where the efficient transport of ions is essential. High ionic conductivities have been obtained with organic liquids based on polar low molecular weight molecules.[1] As an alternative to liquid electrolytes, solid-state electrolytes have been used to improve mechanical stability.[2] However, the performance of solid-state electrolytes is limited due to their low ion conduction.

To overcome this problem, the use of liquid crystals (LCs) has been found to be a versatile approach for the development of ion transporting materials.[3, 4] The nanosegregated LC phases provide efficient transport of ions through the well-organized channels formed in columnar, smectic or bicontinuous cubic phases (**Figure 1.1**).[5-8] Columnar and smectic arrangements may lead to the formation of 1D and 2D channels (respectively) capable of transporting ions. For 3D ion transport, bicontinuous cubic phases with gyroid nanochannels have been reported. Therefore, LC materials may have potential as new functional electrolytes for electrochemical devices; for example, in lithium-ion batteries (transport of Li^+ ions), dye-sensitized solar cells (transport of I^-/I^{3-} redox couple) or fuel cells (proton transport).

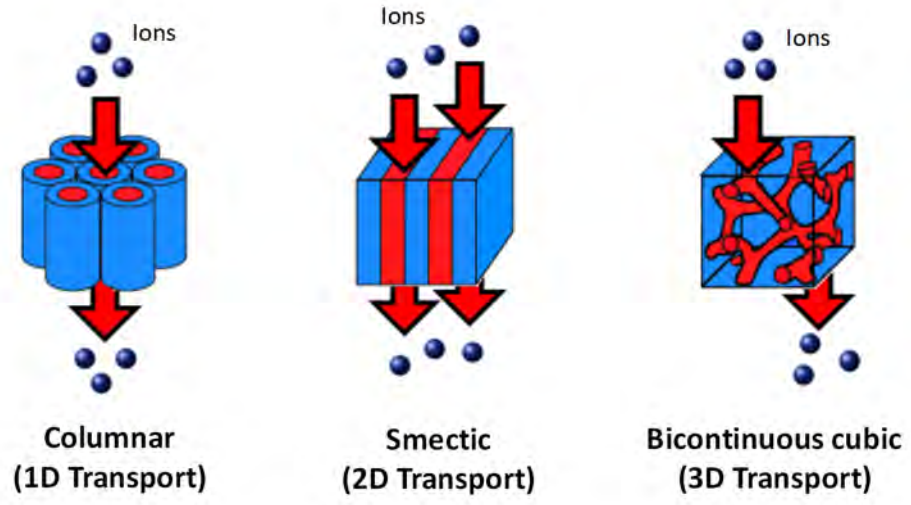

Figure 1.1 Ion transport in nanostructured LC phases

One of the limiting factors of using LCs is the orientation of the nanostructured LCs phases because ion conductivity depends on the macroscopic degree of order of the LC phase. Due to the dynamic nature of LCs, it is possible to align columnar and smectic phases in order to orient the 1D and 2D ion channels. However, bicontinuous cubic LC phases are very attractive as their 3D interconnected channels offer effective ion conduction even in non-aligned samples. Several strategies for LC alignment have been developed. For instance, highly aligned ion conductors have been prepared with the help of surface treatments,[9, 10] electric fields,[11] and magnetic fields.[12, 13] In addition, azobenzene-containing LC molecules can be oriented by photoirradiation with linearly polarized light.[14]

There are two types of LC materials that exhibit ion conductivity. The first type is LC molecules with ionic moieties (ionic liquid crystals). The second type is ionic complexes that consist of non-ionic LC molecules complexed with ionic salts.

1.1.1 Ionic Liquid Crystals

Ionic LCs are mesogenic molecules that contain cationic, anionic or zwitterionic moieties.[15] Imidazolium, ammonium, phosphonium, ammonium sulfobetain, phosphonic acid and sulfonic acid units have been used in the design of LCs for ion transport.[16-19] Moreover, lithium salts, acid molecules or iodide ions have been incorporated into the ionic nanochannels to enhance the ion conductive properties.

Kato and coworkers made pioneering research on ionic columnar LCs forming 1D channels prepared by self-organization of imidazolium-containing molecules (**Figure 1.2**).[20] In these structures, the imidazolium part forms a 1D ionic pathway inside the column. The ionic conductivities were studied in macroscopic aligned samples obtained by shearing the material on glass substrates. Ionic conductivities parallel to the columnar axis were higher than those perpendicular to the axis. Moreover, ionic conductivities were enhanced by introducing a variety of lithium salts.[21]

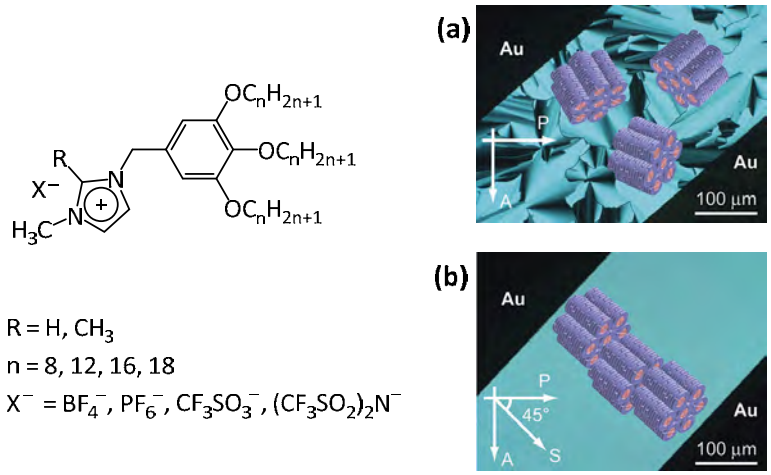

Figure 1.2 Chemical structure of ionic columnar LCs. POM images and schematic representations of the LC arrangement: **(a)** before sheraring and **(b)** after shearing the material along the direction perpendicular to the gold electrodes. (Adapted from reference 20)

The same research group prepared imidazolium-based LC molecules bearing three azobenzene groups that exhibited anisotropic ion conduction in the smectic phase.[14] In addition, this molecular design allowed the photoinduced orientation of the 2D ionic pathways to be perpendicular to the substrate, which is the most efficient organization for a practical application of these electrolyte materials.

Bicontinous cubic LC phases were also employed for the preparation of 3D ion-conductive materials by self-organization of ammonium and phosphonium salts (**Figure 1.3**).[22] The ionic conductivities in the cubic phases were higher than those obtained in the randomly oriented columnar phases due to the formation of 3D interconnected ionic channels.[23]

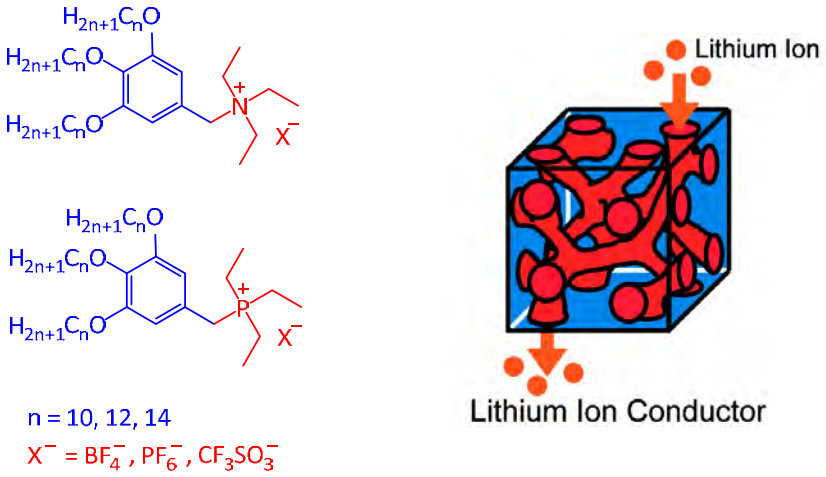

Figure 1.3 Chemical structure of ionic bicontinous cubic LCs. (Adapted from reference 23)

Moreover, nanostructured LC phases can be stabilized by photopolymerization to maintain the anisotropic ion transport over a longer period of time. Crosslinking of polymerizable LC monomers in their mesophase can yield nanostructured, thermally and mechanically stable membrane materials with permanent pathways for ion transport. Rod- and disk-shaped ionic LCs containing polymerizable groups such as methacrylate, acrylate, and 1,3-diene groups have been prepared to obtain ionic LC materials forming permanent 1D, 2D and 3D ion nanochannels.[10, 24, 25] For instance, Osuji and coworkers developed ion-conductive polymer films with 1D channels that were aligned perpendicular or parallel to the film surface.[12, 13] Polymer films were prepared by photopolymerization of the acrylate groups in the oriented hexagonal columnar mesophase (**Figure 1.4**). The oriented films showed a remarkable increase (two orders of magnitude) in their ionic conductivity compared with the unaligned films.

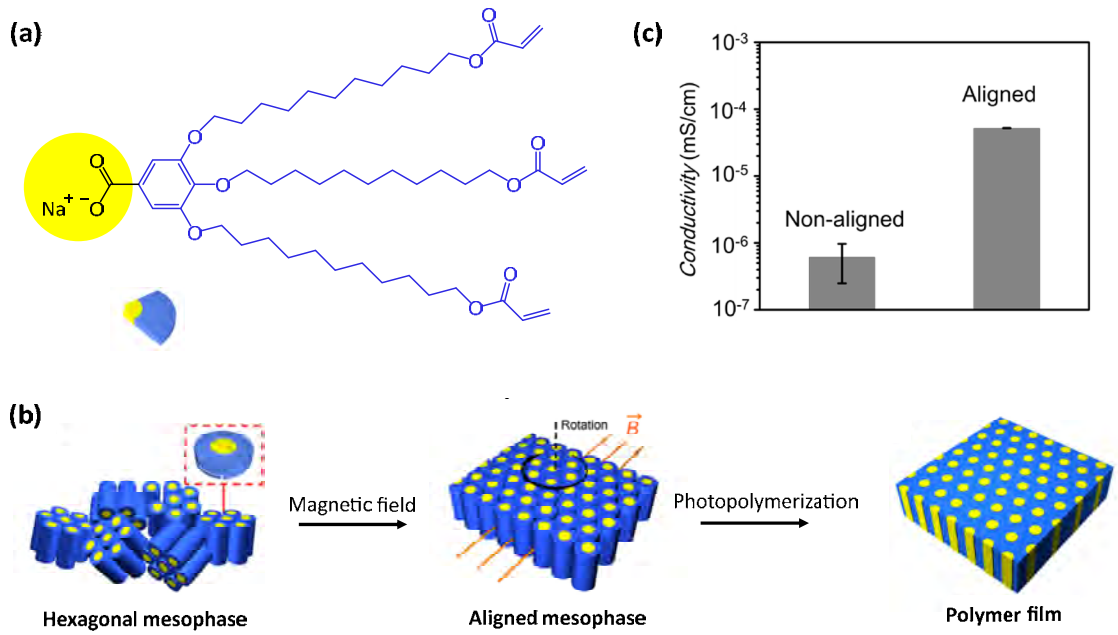

Figure 1.4 (a) Chemical structure of ionic columnar LC, **(b)** schematic representation of the preparation of a LC polymer film with vertically oriented 1D channels, **(c)** ionic conductivity of the non-aligned and aligned polymer films. (Adapted from reference 12)

1.1.2 Ionic Complexes of Non-Ionic Liquid Crystals and Salts

This second type of ion conductive material consists of non-ionic LC molecules with crown ethers, oligo(ethylene oxide), cyclic carbonates or diol moieties that are

complexed with alkaline-metal salts or organic onium salts. These ionic complexes consist of two molecular components which interact through ionic interactions and are able to self-assemble into nanostructured channels. One of the first examples was reported by Kimura *et al.* They described lithium ion conduction in a crown ether-based LC and photoresponsive ion conduction on photoisomerization of azobenzene unit (**Figure 1.5**).[26-28]

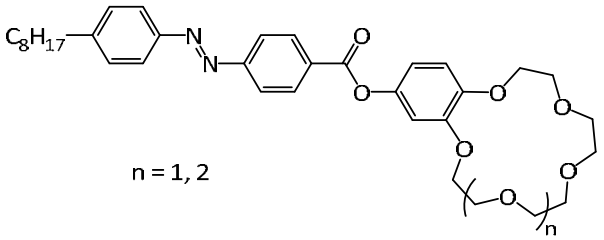

Figure 1.5 Chemical structure of crowned azobenzene LC

Percec *et al.* reported supramolecular columnar assemblies with 1D ion conductive pathways in the center of the columns by using a taper-shaped dendron containing either crown ether or oligo(ethylene oxide) moieties (**Figure 1.6**). These molecules, that were complexed with sodium and potassium triflates, showed ionic conductivities of 10^{-7}–10^{-10} S·cm^{-1}. However, ionic conductivities were lower than expected because no macroscopic alignment had been achieved.[29, 30]

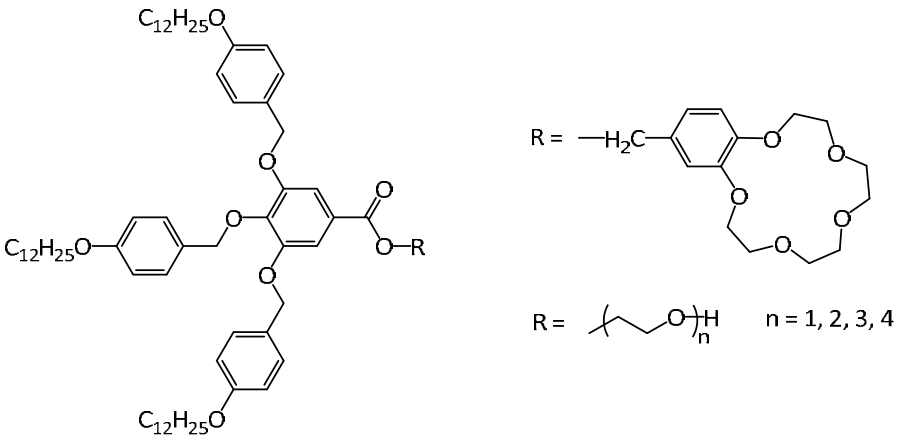

Figure 1.6 Chemical structure of a taper-shaped dendron containing crown ether and oligo(ethylene oxide) moieties.

Kato and coworkers designed 2D ion conductors based on smectic LCs containing poly(ethylene glycol) complexed with lithium salts (**Figure 1.7**). Ionic conductivities of the order of 10^{-4} S·cm^{-1} were achieved in the smectic mesophase at 150 °C for the macroscopically aligned sample. However, the non-aligned sample showed lower conductivities (10^{-7} S·cm^{-1}).[9, 31-33]

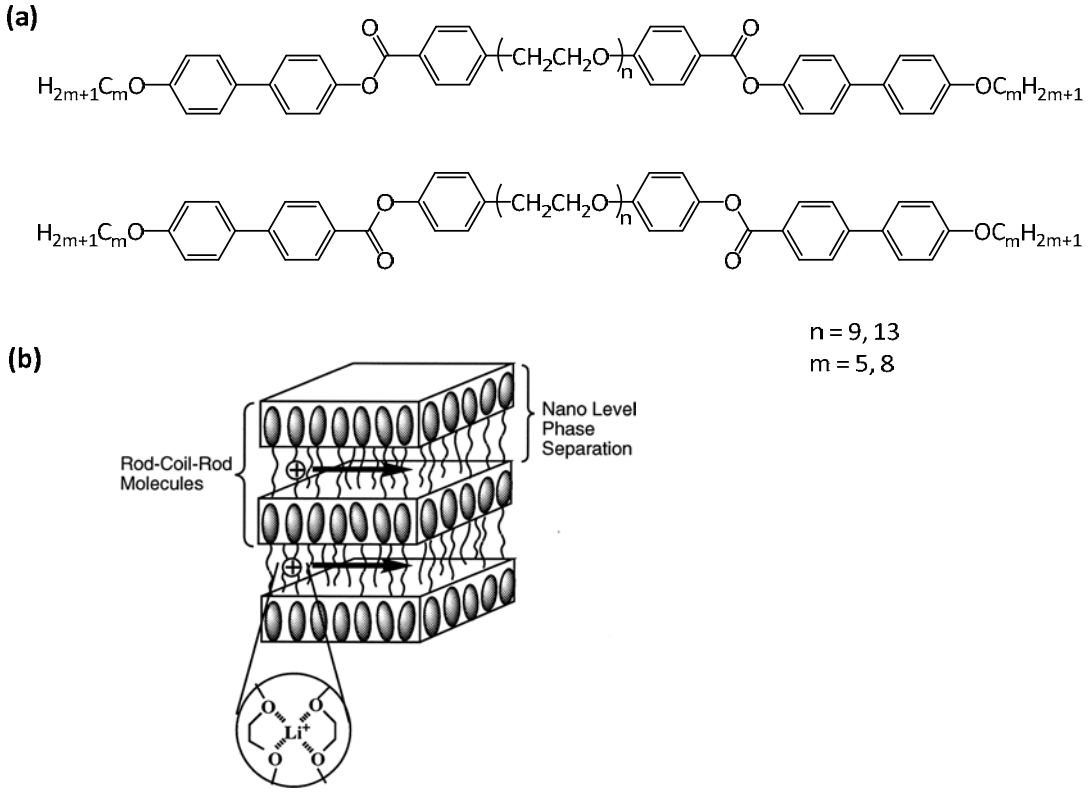

Figure 1.7 Chemical structure of smectic LCs containing poly(ethylene glycol), **(b)** schematic representation of ion conduction for the complex of the mesogenic dimer and the lithium salt. (Adapted from reference 32)

Cho *et al.* reported a LC dendron mixed with lithium triflate that showed ion conductive properties (**Figure 1.8a**). The mixture displayed both hexagonal columnar and bicontinuous cubic mesophases on heating. Due to the increase in dimensionality of conduction pathways in the cubic mesophase, the conductivities were one order of magnitude higher than those obtained in the columnar phase. [34, 35] The same authors also reported the self-assembly of *Janus* dendrimers with lithium triflate in a bicontinuous cubic phase with ion conductivities of about 10^{-7} S·cm^{-1} (**Figure 1.8b**).[36]

In addition, carbonate derivatives have been widely used as LC-based electrolytes for lithium-ion batteries due to their strong dipole moment and the possibility to coordinate to lithium ion.[37, 38] For instance, Kato *et al.* designed a fan-shaped molecule with a propylene carbonate moiety that formed nanosegregated hexagonal columnar LC phase upon complexation with lithium triflate.[11] The columnar assemblies were aligned by applying AC electric field. After applying the electric field, the ionic conductivity became 4.3 times higher than that measured for the polydomain sample. This result suggests that the monodomain orientation

of the columns parallel to the electric field facilitates ion conduction through 1D self-organized conductive paths along the columnar axes.

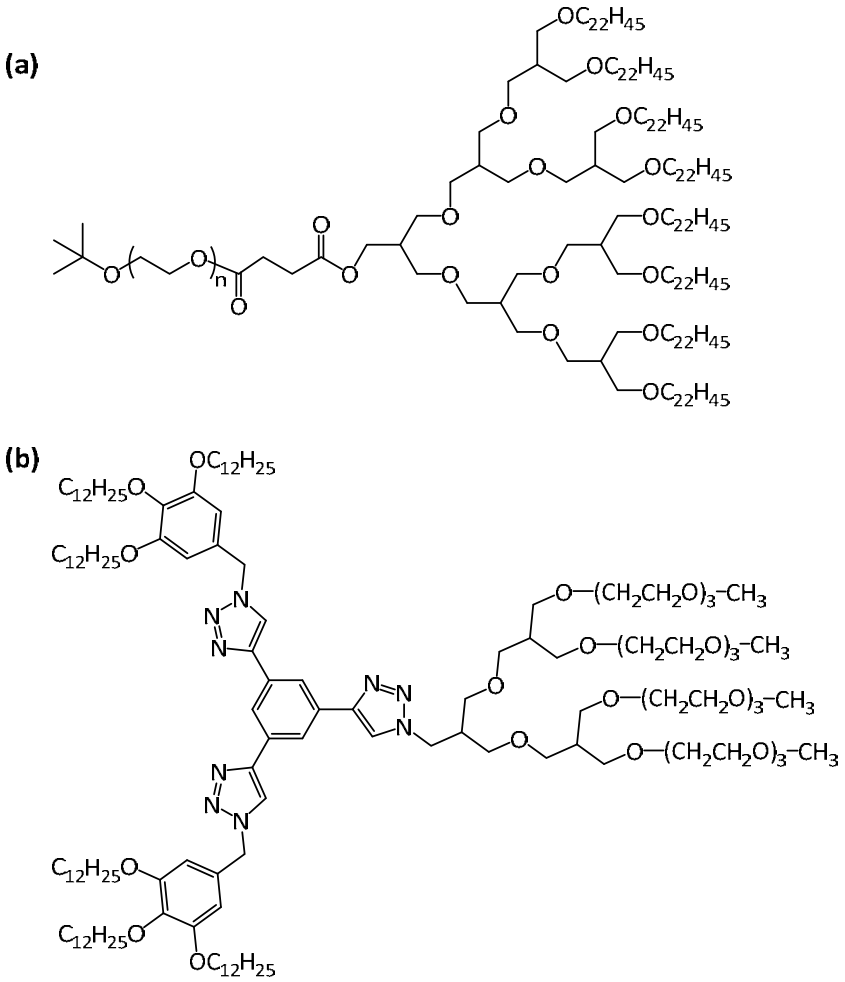

Figure 1.8 Chemical structure of the: **(a)** LC dendron and **(b)** LC *Janus* dendrimer.

A new family of LC ion conductors was developed by mixing organic onium salts and LC molecules containing functional groups that can interact with them. One of the first examples was reported by Kato's research group and it consisted of smectic mixtures of imidazolium-based salts and calamitic LC molecules containing hydroxyl groups. The intermolecular interactions between the hydroxyl groups and the ionic salt enhanced the miscibility and led to the formation of nanosegregated layered structures.[39, 40] The same research group prepared 1D proton conductive pathways by using columnar LC mixtures of fan-shaped mesogenic molecules containing hydroxyl groups and imidazolium salts (**Figure 1.9**).[41] The organic salt was incorporated into the inner part of the column. The oriented structures were also preserved into polymer films by *in situ* photopolymerization.[42] Anisotropic 1D ion conduction was achieved for the aligned columnar polymer films.

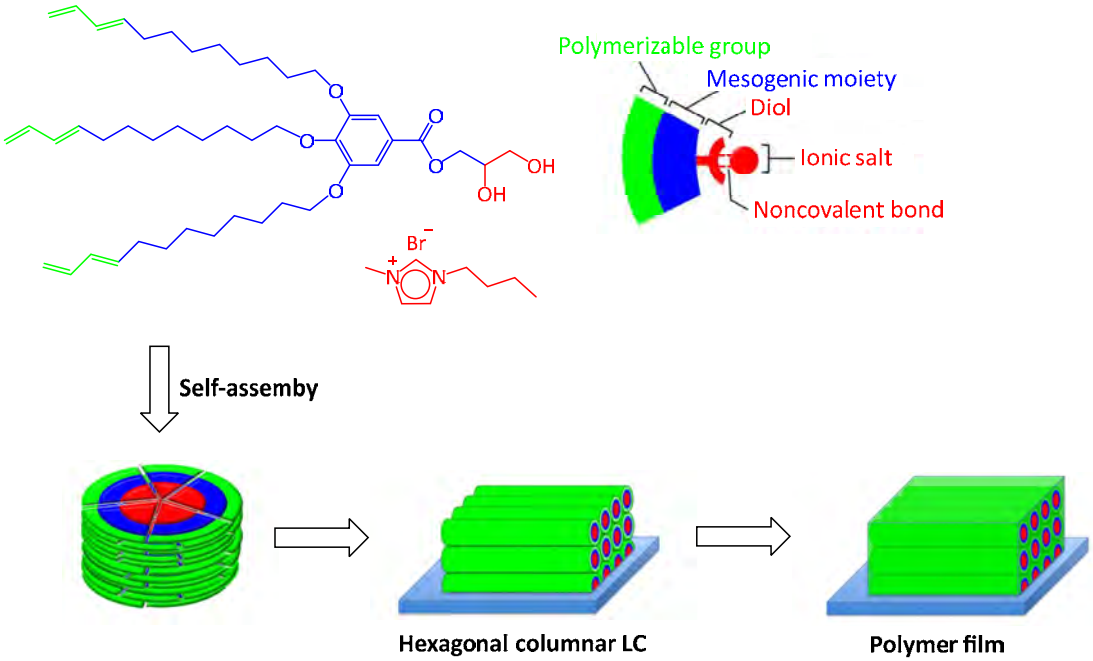

Figure 1.9 Schematic representation of the strategy for the preparation of 1D ion-conductive polymer films with planar alignment of the columns composed of mesogenic molecules having diol moieties and imidazolium salts. (Adapted from reference 42)

Two-component smectic LCs containing carbonate derivatives and imidazolium salts have been applied as electrolytes in dye-sensitized solar cells. In these materials, the I^-/I_3^- redox couple is generated by mixing a imidazolium iodide salt with iodide (**Figure 1.10**).[43-45] The prepared dye-sensitized solar cells converted light to electricity at temperatures of up to 120 °C, making them attractive for the development of solar cells. Ion conductivities for these devices are typically between 10^{-2} and 10^{-3} S·cm^{-1}.

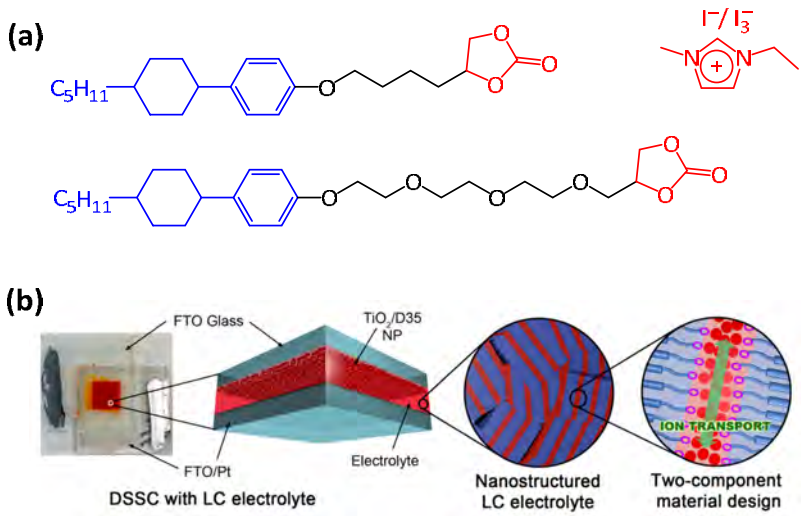

Figure 1.10 (a) Chemical structure of the two-component LC electrolytes. **(b)** Schematic illustration of the LC dye-sensitized solar cells and the proposed organization of the two-component nanostructured electrolyte. (Adapted from reference 43)

1.2 Ionic Liquid Crystal Dendrimers

LC dendrimers represent an attractive tool for the preparation of functional materials as they combine, in a single molecule, the inherent properties of the dendrimer scaffold with the anisotropic properties provided by the LC state.[46, 47] LC dendrimers are generally prepared by the introduction of promesogenic units at the periphery of a preformed dendrimer.[48, 49] However, it is also possible to design LC dendrimers without any promesogenic unit. Ionic LC dendrimers are the most interesting examples; the nanosegregation between polar and apolar regions was the driving force for the formation of the observed mesophases.

Poly(propyleneimine) (PPI) and poly(amidoamine) (PAMAM) dendrimers are excellent candidates for ionic functionalization because they contain amine groups at the periphery that can be ionically attached with carboxylic acids by a proton-transfer reaction.[50] The first example was reported by Tomalia and coworkers showing lyotropic LC behavior with a material resulting from ionic interactions between PPI dendrimer and octanoic acid.[51] Later, Tsiourvas *et al.* described the LC properties of a new family of ionic dendrimers derived from the protonation of PPI with a cholesterol-based carboxylic acid (**Figure 1.11a**).[52] In a similar way, Ujiie *et al.* prepared ionic LC dendrimers derived from PAMAM dendrimer and stearic, palmitic and myristic acids (**Figure 1.11b**).[53]

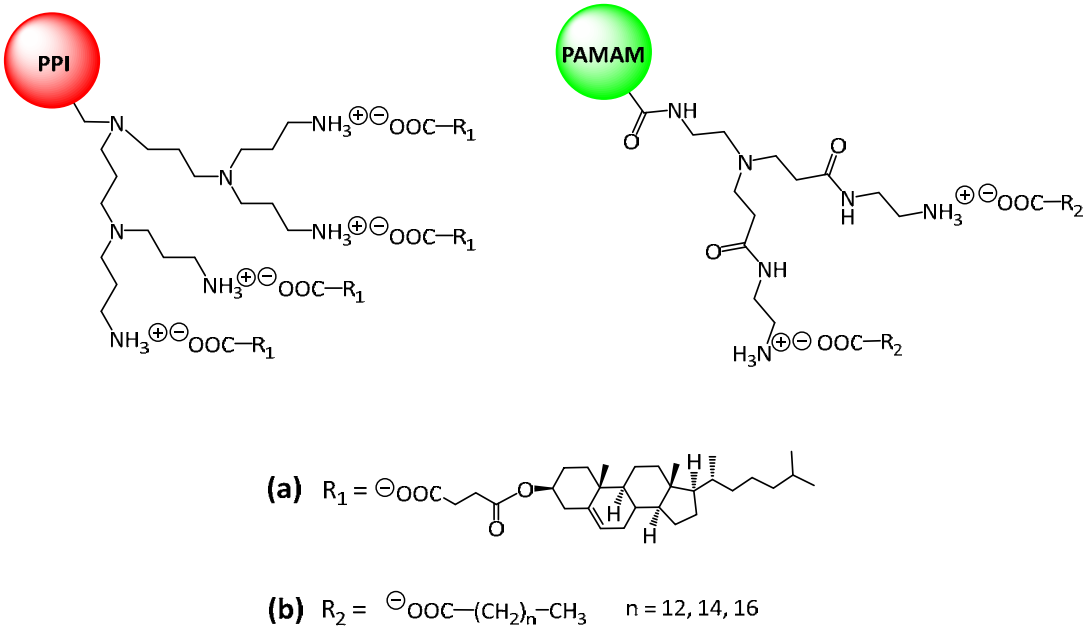

Figure 1.11 Chemical structure of ionic LC dendrimers.

Our research group has described several examples of ionic LC dendrimers that were prepared by mixing aliphatic carboxylic acids containing perhydrogenated or semifluorinated alkyl chains with PAMAM and PPI dendrimers of different generations.[54-57] In these materials, microsegregation plays a key role and the molecule is divided into three parts: the central dendritic part, an ionic continuum formed by the ion pairs, and the terminal alkyl chains of the carboxylic acids (**Figure 1.12**). This well-defined segregation in layers is responsible for the smectic LC behavior in most of the dendrimers. Columnar phases also appeared for the higher generation derivatives.

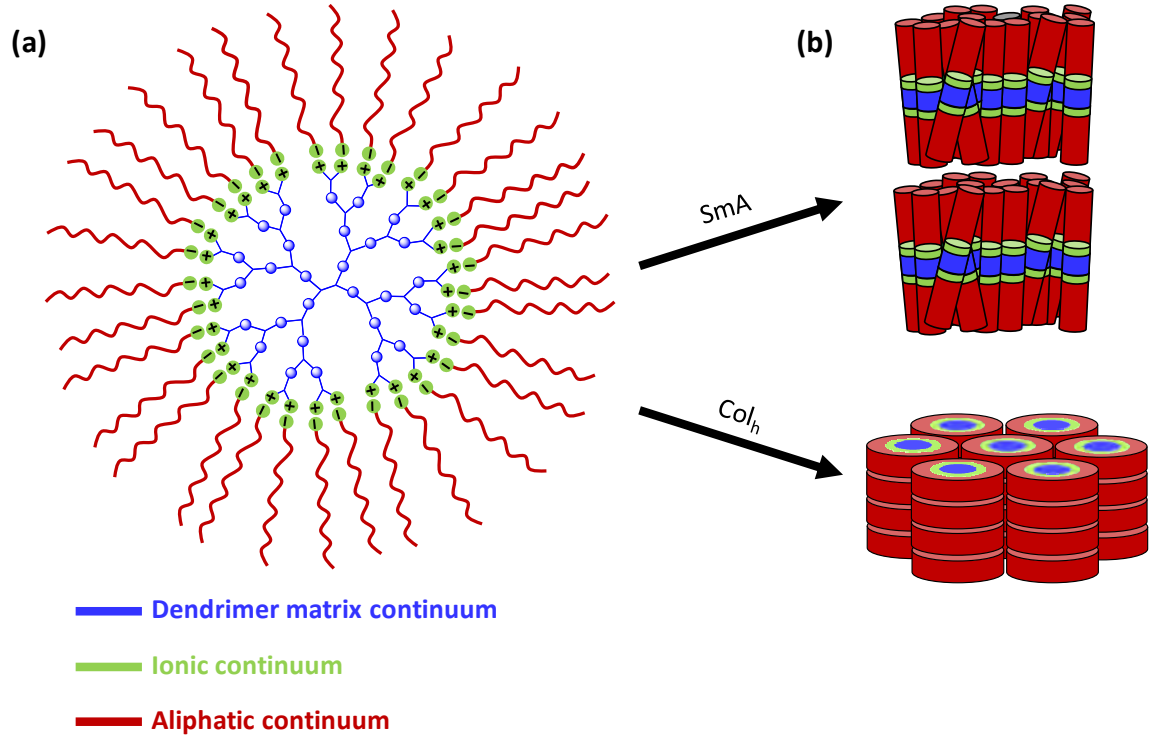

Figure 1.12 Schematic representation of: **(a)** ionic dendrimers constituted by proton transfer between amine and carboxylic acid groups, and **(b)** molecular organization in the smectic A and hexagonal columnar mesophase.

Ionic interactions have also been employed to attach several functional units at the dendrimer periphery, such as azobenzene or oxadiazole derivatives.[58-61] The LC properties of these compounds are very similar to those obtained for the covalent analogues. Consequently, ionic functionalization appears to be an effective and easy approach to obtain LC dendrimers which avoids the time-consuming synthetic procedures associated with the preparation of the covalent derivatives. In addition, the simplicity of the ionic synthetic procedure (compared to the covalent one) has

enabled the preparation of a big family of PPI dendrimers functionalized with bent-core molecules.[62, 63]

Very recently, a new family of ionic hybrid LC dendrimers has been reported by complexation between PPI dendrimer and carboxylic acid dendrons bifunctionalized with promesogenic units and carbazole as luminescent and hole-transporting moiety (**Figure 1.13**).[64] All the ionic dendrimers displayed LC behavior with good luminescent and electrochemical properties.

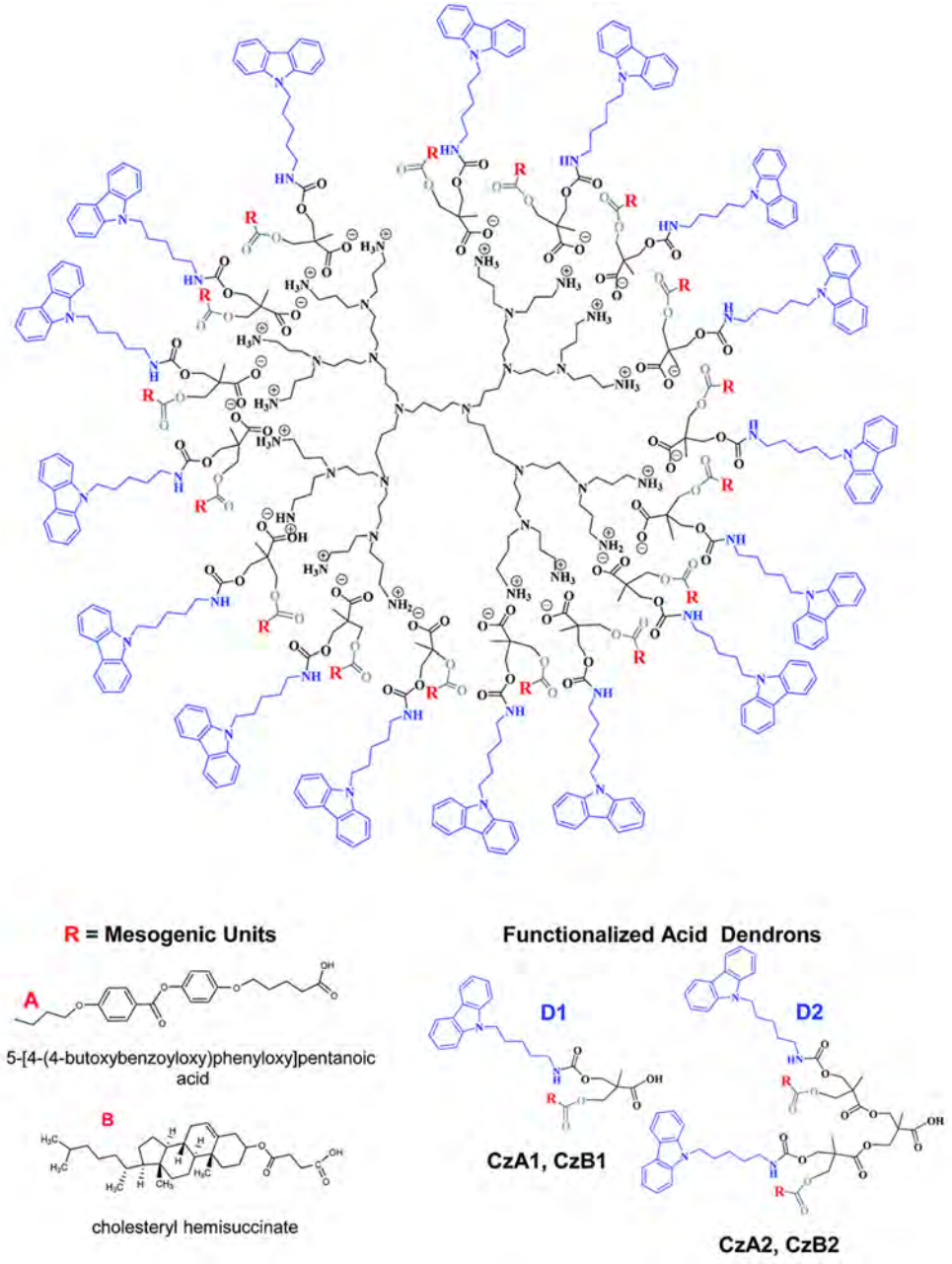

Figure 1.13 Schematic representation of the ionic hybrid LC dendrimers with carbazole functional units. (Adapted from reference 64)

2. PROTON CONDUCTIVE MATERIALS FORMED BY COUMARIN PHOTOCROSSLINKED IONIC LIQUID CRYSTAL DENDRIMERS[‖]

2.1 Objectives

As mentioned in the Introduction, ion conductive materials have been reported with low-molecular-weight mesogenic compounds that were stabilized by photocrosslinking to maintain the ionic conductivity over a longer period of time. The formation of ionic nanosegregated areas in ionic LC dendrimers (formed by ionic salts) allowed us to envision the possibility of obtaining ionic conductivity.

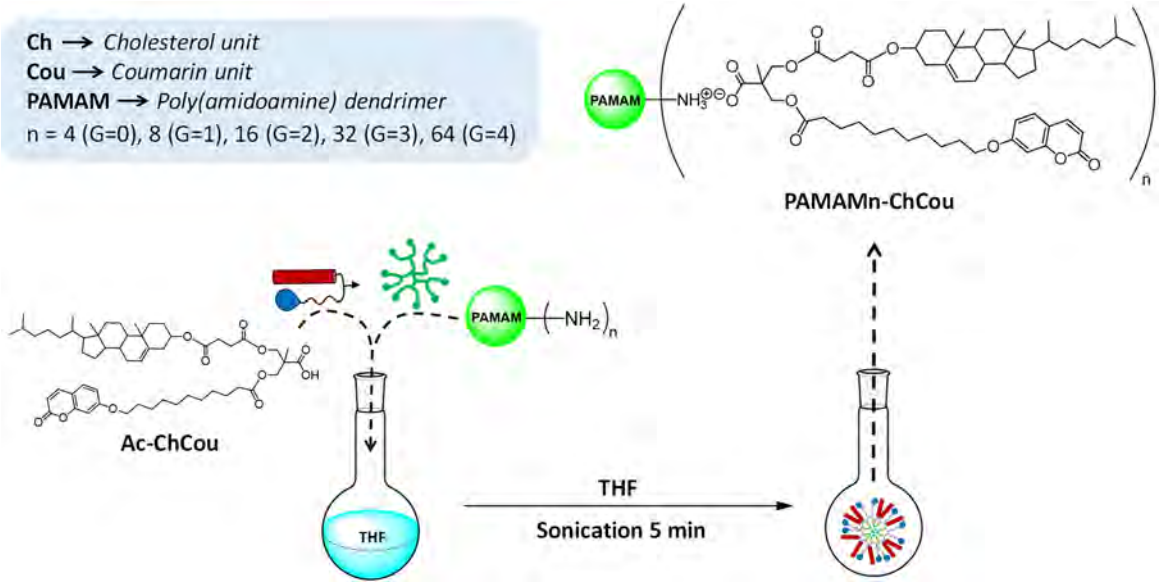

Figure 2.1 Schematic representation of the ionic self-assembly process to prepare the ionic LC dendrimers and the nomenclature of the ionic dendrimers.

To develop 1D and 2D proton conductive materials, we have examined the supramolecular LC organization of ionic dendrimers. A new family of ionic hybrid dendrimers were synthesized from PAMAM dendrimer generations 0 to 4 (bearing 4, 8, 16, 32 or 64 NH_2 terminal groups) (**Figure 2.1**). PAMAM was surrounded by carboxylic acid dendrons bifunctionalized with a promesogenic unit (cholesteryl

[‖] Published in: A. Concellon, T. Liang, A. P. H. J. Schenning, J. L. Serrano, P. Romero & M. Marcos. Proton-conductive materials formed by coumarin photocrosslinked ionic liquid crystal dendrimers. *J. Mater. Chem. C* **2018**, *6*, 1000-1007.
This work was carried out in collaboration with Prof. Albert Schenning (Eindhoven University of Technology, The Netherlands) during a 4 months stay financed by MINECO (EEBB-I-17-12040).

hemisuccinate) and coumarin moieties. Coumarin moieties were chosen as reactive groups for the crosslinking reaction. Upon UV irradiation, coumarins undergo [2+2] cycloaddition to yield cyclobutane dimers. It does not require an initiator or catalyst and side reactions are avoidable. It was expected, the ionic pathways were not disrupted after coumarin photodimerization, thus nanostructured, thermally and mechanically stable membrane materials with permanent pathways for proton transport were obtained (**Figure 2.2**).

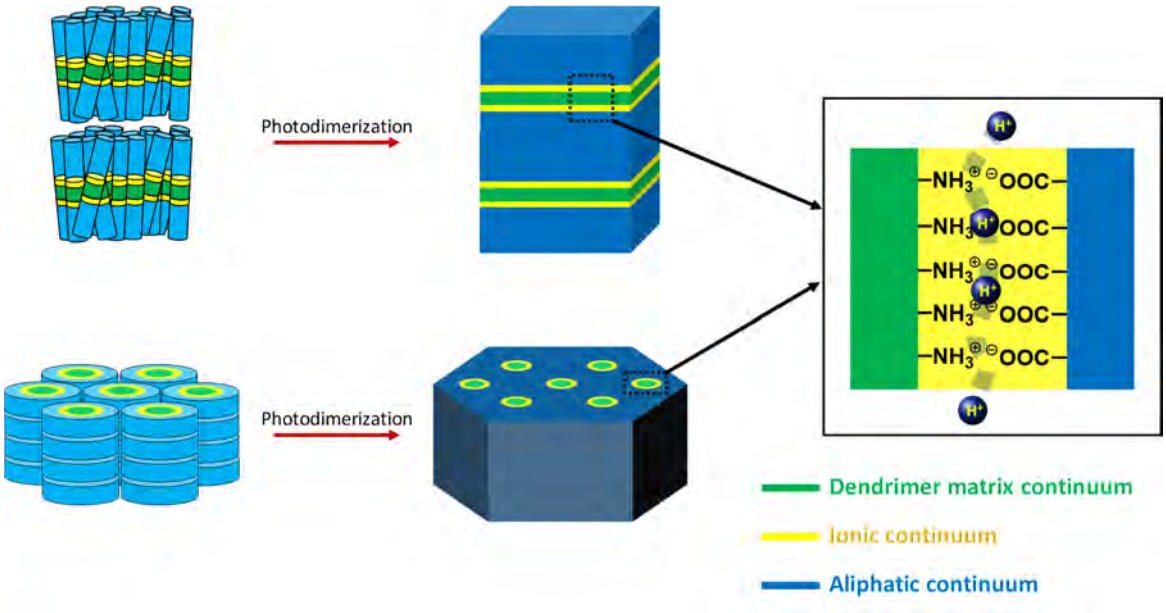

Figure 2.2 Schematic representation of the strategy followed for the preparation of 1D and 2D proton conductive materials based on ionic LC dendrimers.

2.2 Results and discussion

2.2.1 Synthesis and Characterization of Ionic Dendrimers

The carboxylic acid dendron (**Ac-ChCou**) was prepared by DCC esterification between monomer bisMPA protected by a benzyl ester group and cholesteryl hemisuccinate (**Scheme 2.1**). The hydroxyl group was subsequently reacted with a carboxylic acid containing the coumarin unit. Finally, the benzyl ester group was removed efficiently by catalytic hydrogenolysis.

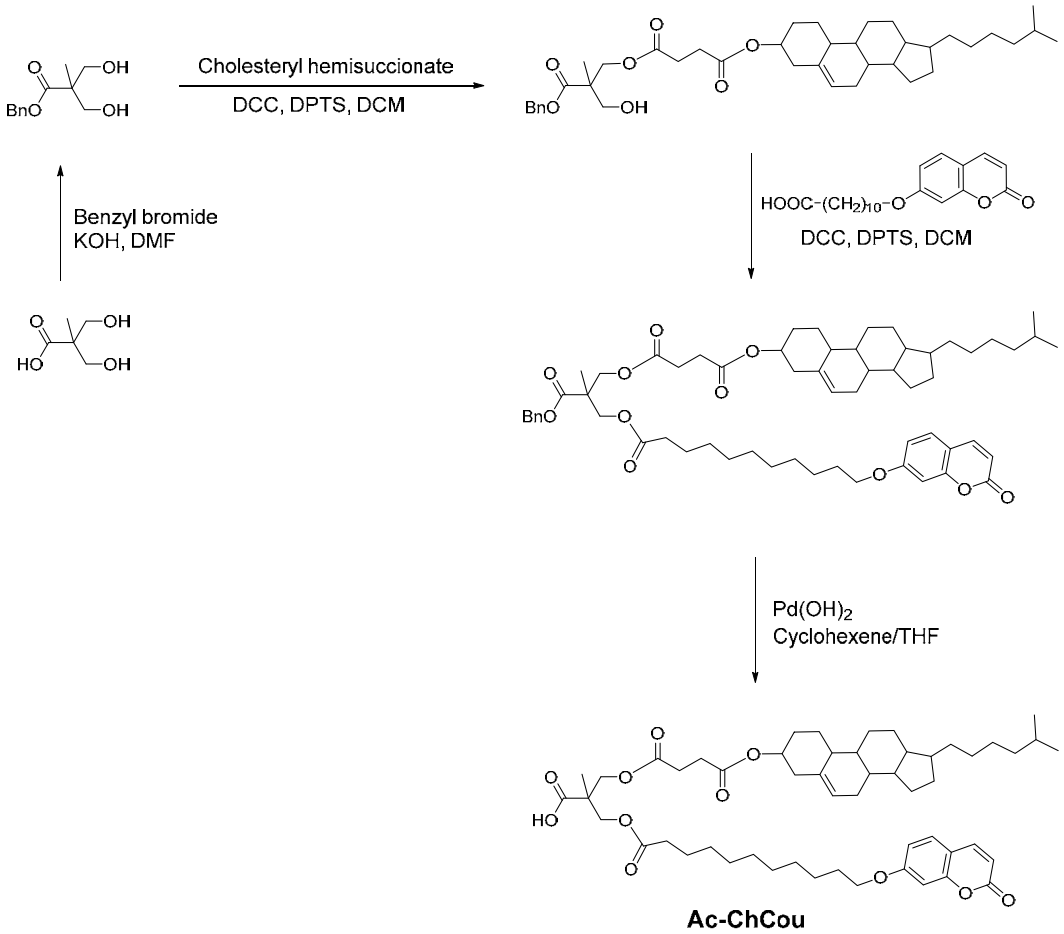

Scheme 2.1 Synthetic route for the preparation of **Ac-ChCou**.

Ionic dendrimers were prepared by mixing a THF solution of **Ac-ChCou** with a solution of the corresponding generation of the PAMAM dendrimer in the stoichiometry necessary to functionalize all terminal amine groups. The mixture was ultrasonicated for 5 min, then the THF was slowly evaporated at room temperature and the sample was dried under vacuum at 40 °C until the weight

remained constant. The formation of ionic interactions between the PAMAM dendrimer and the dendron acids was studied by FTIR and NMR.

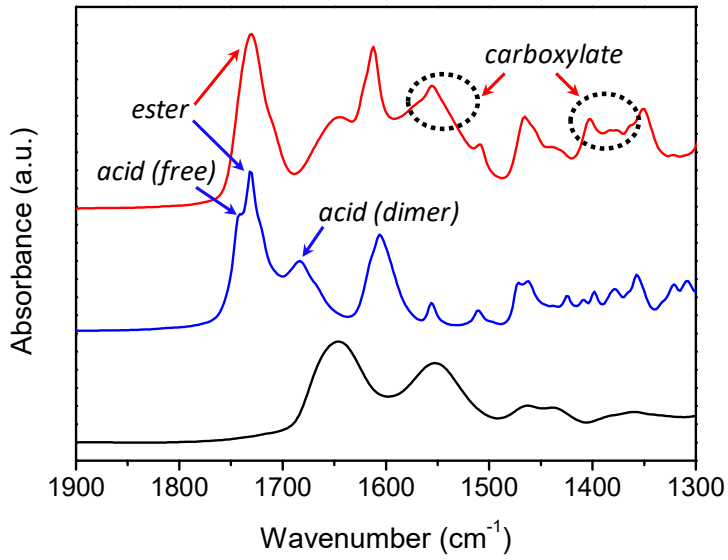

Figure 2.3 FTIR spectra (C=O *st.* region) of **PAMAM16** (black line), **Ac-ChCou** (blue line), and **PAMAM16-ChCou** (red line).

As a representative example that demonstrates the formation of the ionic salts, the FTIR spectra of **Ac-ChCou**, **PAMAM16** and the corresponding ionic dendrimer are shown in **Figure 2.3**. In the spectrum of **Ac-ChCou**, three C=O stretching bands appeared at 1683, 1730 and 1741 cm^{-1}. The band at 1730 cm^{-1} is assigned to the ester groups, whereas the bands at 1686 and 1741 cm^{-1} correspond to the dimeric and free form of the carboxylic acid group, respectively. In the spectrum of **PAMAM16-ChCou** the signals at 1686 and 1741 cm^{-1} were replaced by two new bands at around 1550 and 1400 cm^{-1} due to the asymmetric and symmetric stretching modes of the carboxylate group.

The ^{1}H NMR spectra recorded in $CDCl_3$ clearly show the formation of the ionic assemblies. As a representative example, the ^{1}H NMR spectra of the dendron **Ac-ChCou**, the third generation PAMAM dendrimer (**PAMAM32**) and the ionic dendrimer **PAMAM32-ChCou** complex are shown in **Figure 2.4**. In the initial dendron, the acid proton signal was very broad and barely visible in the ^{1}H spectrum, thus this signal could not be used to determine the formation of the salt. The protons close to the ionic pairs experienced the highest chemical shifts. For instance, the proton signals of diastereotopic methylene (H_P and $H_{P'}$) moved to a higher field after the formation of the salts. Protonation of terminal amine groups

of the PAMAM dendrimer was also confirmed the appearance of the NH_3^+ broad signal at 5.20–4.00 ppm. The absence of the $CH_2C\underline{H_2}$-NH_2 (H_α, δ= 2.77 ppm) and $C\underline{H_2}CH_2$-NH_2 (H_β, δ= 3.22 ppm) signals and the appearance of the $CH_2C\underline{H_2}$-NH_3^+ (H_α, δ= 3.13 ppm) and $C\underline{H_2}CH_2$-NH_3^+ (H_β, δ= 3.52 ppm) signals also confirm the quantitative protonation of terminal amine groups.

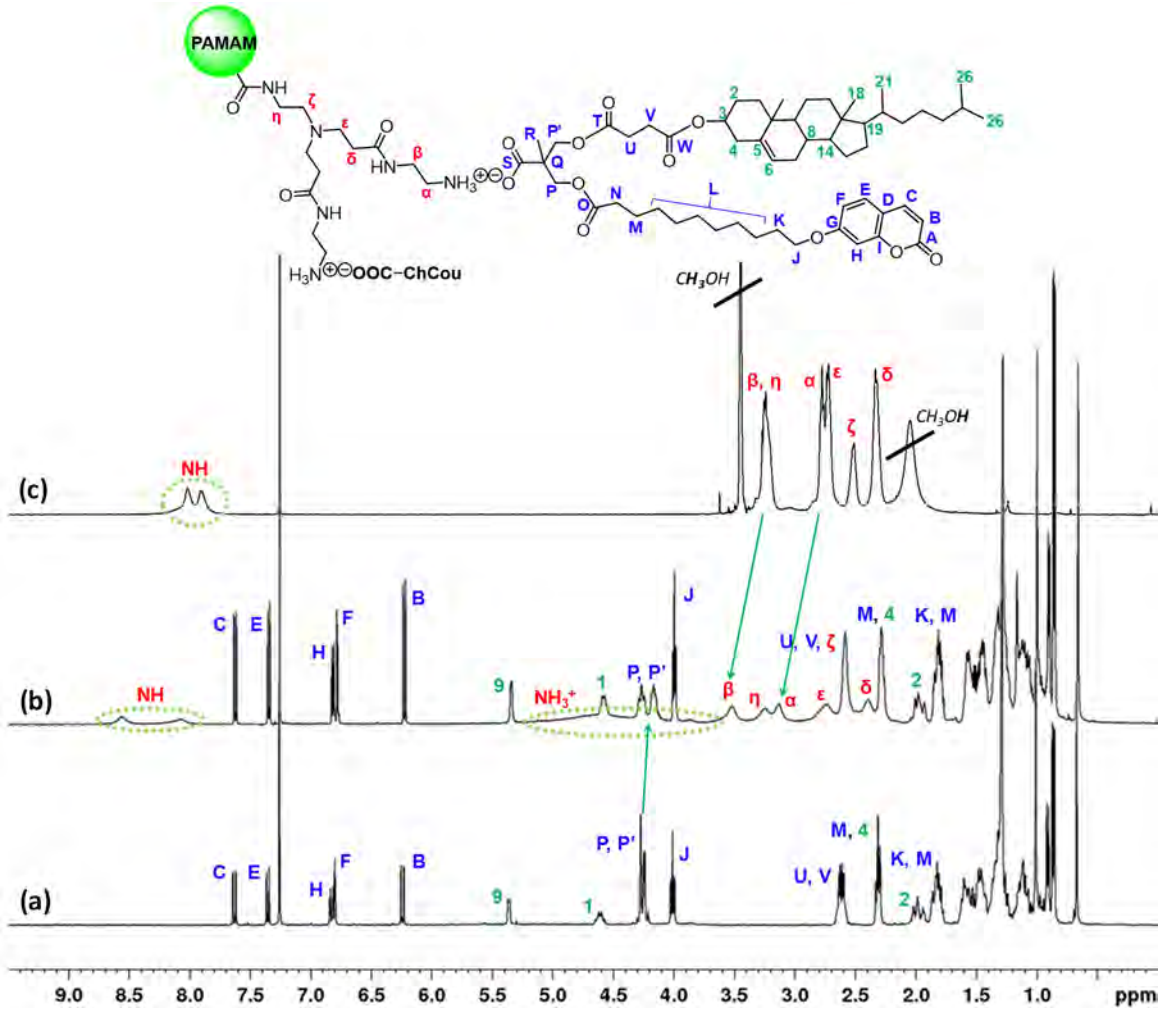

Figure 2.4 ^{1}H NMR spectra ($CDCl_3$, 400 MHz) of: **(a) Ac-ChCou, (b) PAMAM32-ChCou**, and **(c) PAMAM32**.

^{1}H-^{1}H NOESY experiments were also employed to study the formation of these ionic dendrimers in solution. The main feature of NOESY is its ability to provide in a single experiment all the correlations between nuclei which are physically close in space, thus making it a very valuable tool for determining whether supramolecular interactions were established between **Ac-ChCou** dendron and the **PAMAM** dendrimer. The ^{1}H-^{1}H NOESY spectrum of **PAMAM32-ChCou** is shown in **Figure 2.5**. Significant cross-peaks were observed between the diastereotopic protons of **Ac-ChCou** (H_P and $H_{P'}$) and H_α and H_β protons of the terminal branches of PAMAM,

indicating that these groups were close in space because of the ionic pair formation. Besides this, H_P and $H_{P'}$ docked closely with the terminal NH_3^+ groups of PAMAM.

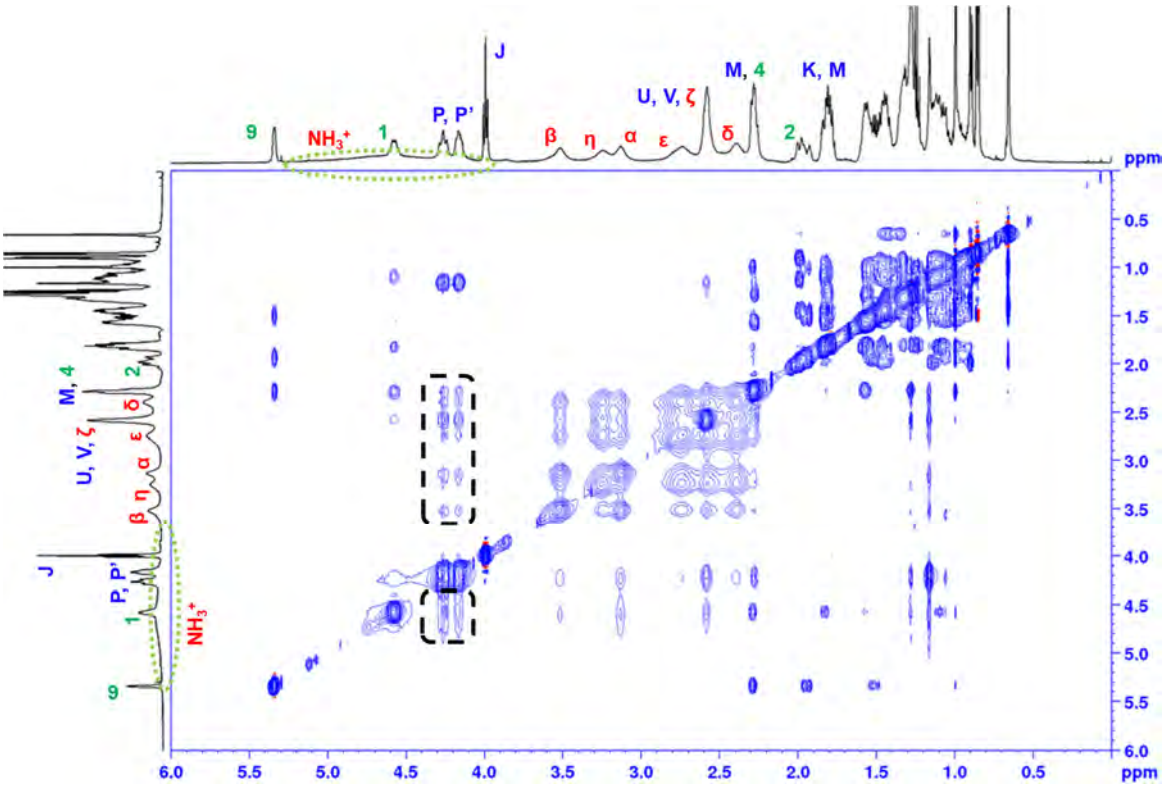

Figure 2.5 ^{1}H-^{1}H NOESY spectrum of **PAMAM32-ChCou** ($CDCl_3$, 298 K, t_{mix} = 200 ms).

In the ^{13}C NMR spectra (**Figure 2.6**) the carboxyl group signal (C_S) of the acid shifts from 176.98 to 178.18, indicating the formation of carboxylate (COO^-). Likewise, the deprotonation of carboxylic acid was also corroborated by the displacement of the methylic carbon (C_Q), the methyl carbon (C_R) and the methylene carbons (C_P and $C_{P'}$) to lower field. In addition, when terminal amine groups of PAMAM are protonated, the methylene carbons (C_α and C_β) move from 41.6/42.4 to 39.7/37.7, respectively (data confirmed by ^{1}H-^{13}C HSQC experiments).

The ^{13}C cross-polarization magic-angle spinning (^{13}C CPMAS) NMR spectra were recorded at room temperature for the ionic hybrid dendrimers (**Figure 2.7**). The downfield shift of the carboxylic carbon (C_S) signal of **PAMAM16-ChCou** provides strong evidence for the formation of the carboxylate anion.

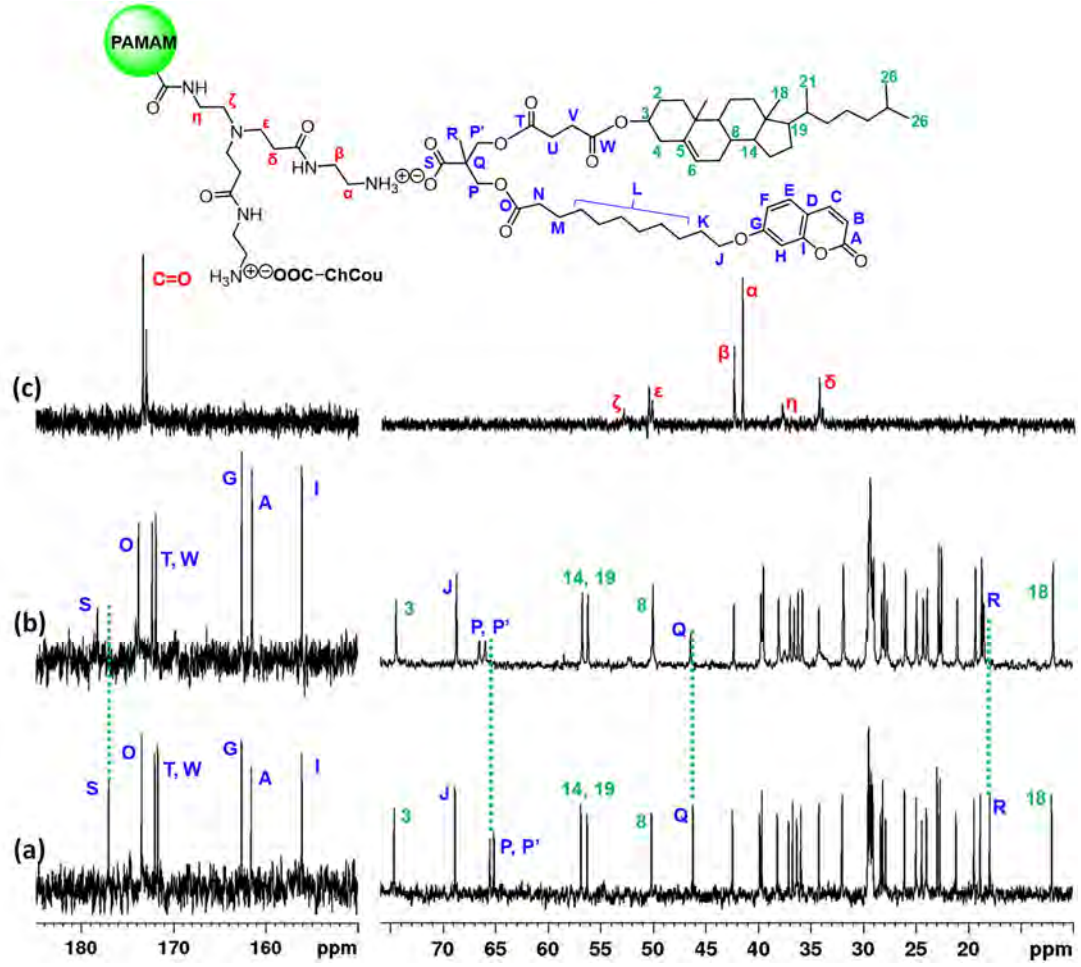

Figure 2.6 ^{13}C NMR spectra ($CDCl_3$, 100 MHz) of: **(a) Ac-ChCou, (b) PAMAM32-ChCou**, and **(c) PAMAM32**.

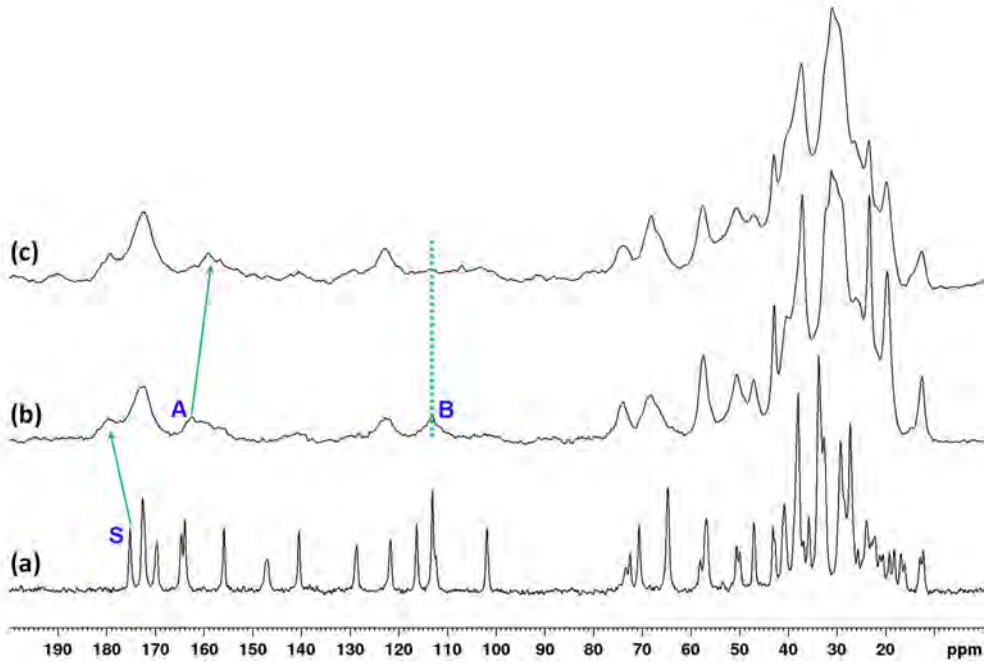

Figure 2.7 ^{13}C CPMAS NMR spectra of: **(a) Ac-ChCou**, **(b)** ionic dendrimer **PAMAM16-ChCou**, and **(c)** ionic dendrimer **PAMAM16-ChCou** after photodimerization.

2.2.2 Thermal Properties and Mesogenic Behavior

The thermal stability of the ionic dendrimers was studied by thermogravimetric analysis (TGA). All the samples showed good thermal stability and in all cases the 5% weight loss temperature ($T_{5\%}$) was detected at temperatures more than 100 ºC above the isotropization point (**Table 2.1**).

Table 2.1 Thermal properties and structural parameters

	$T_{5\%}$ [a] (ºC)	Phase transitions[b]	d_{obs} [c] (Å)	*h k l*[d]	Structural parameters
Ac-ChCou	190	g 9 N 70[e] I	-	-	-
PAMAM4-ChCou	188	g 6 SmA 65[e] I	42.7	1 0 0	d = 42.7 Å
			4.5 (br)		$\varnothing$ = 14.5 Å
PAMAM8-ChCou	203	g 27 SmA 74 (0.9) I	43.2	1 0 0	d = 43.3 Å
			21.7	2 0 0	$\varnothing$ = 20.9 Å
			4.5 (br)		
PAMAM16-ChCou	209	g 21 SmA 63[e] I	46.2	1 0 0	d = 46.2 Å
			23.1	2 0 0	$\varnothing$ = 28.8 Å
			4.5 (br)		
PAMAM32-ChCou	200	g 18 SmA 75[e] I	41.1	1 0 0	d = 41.1 Å
			4.5 (br)		$\varnothing$ = 43.5 Å
PAMAM64-ChCou	198	g 29 Col_h 81[e] I	49.3	1 0 0	a = 56.7 Å
			28.2	1 1 0	h_d = 44.0 Å
			4.5 (br)		

[a] Temperature at which 5% mass lost is detected in the thermogravimetric curve.

[b] DSC data of the second heating process at a rate of 10 ºC/min. Temperatures are read at the maximum of the peak, and enthalpies (kJ/mol) are in brackets. g: glass, SmA: smectic A mesophase, Col_h: hexagonal columnar mesophase, I: isotropic liquid.

[c] *d* value calculated according to Bragg's equation.

[d] Miller indices.

[e] POM data.

Thermal transitions and mesomorphic properties were studied by polarized optical microscopy (POM), differential scanning calorimetry (DSC) and X-ray diffraction (XRD) (**Figure 2.8**). Three cycles were carried out in DSC experiments and data were taken from the second cycle. In some cases, temperatures were taken from POM observations because transition peaks were not detected in DSC curves.

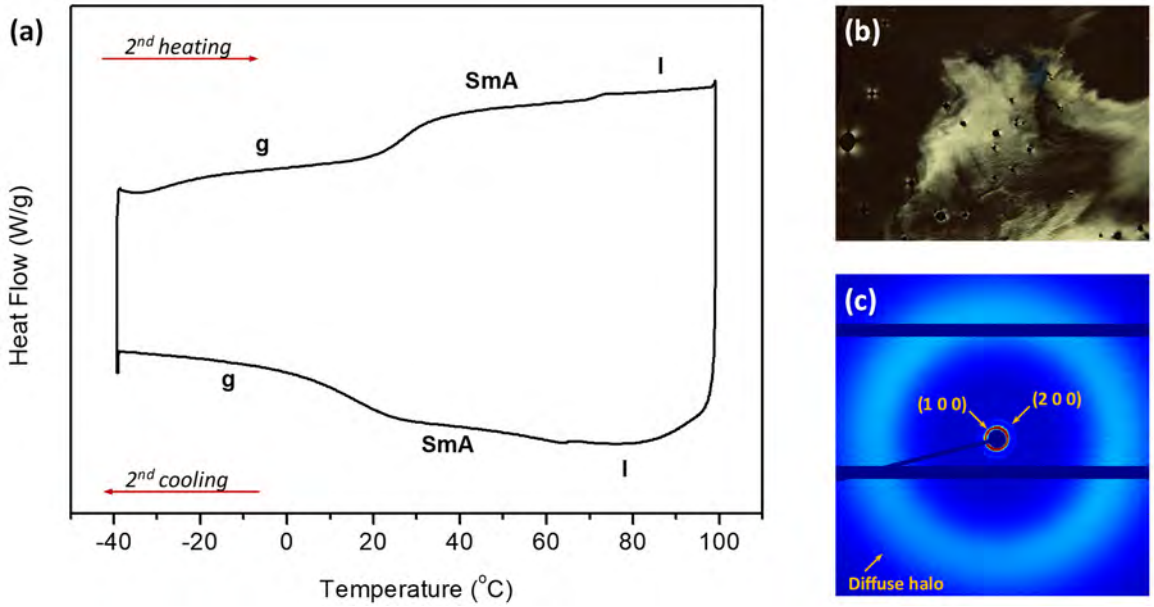

Figure 2.8 (a) DSC traces corresponding to the second scan for **PAMAM8-ChCou** (10 °C/min, Exo down). **(b)** POM microphotograph observed in the cooling process at room temperature for **PAMAM8-ChCou**. **(c)** Room temperature XRD pattern of **PAMAM8-ChCou**.

Dendron **Ac-ChCou** displayed a enantiotropic nematic mesophase, which was observed at room temperature by POM on applying mechanical stress to the sample. The XRD pattern of the nematic phase contained diffuse scattering at low angles and a diffuse halo at high angles corresponding to the intermolecular short-range interactions between molecules.

All the ionic dendrimers displayed liquid crystalline behavior. The DSC curves showed only a glass transition freezing the mesomorphic order at room temperature. Dendrimers for generations G= 0–3 exhibited a smectic A mesophase that was identified by POM on applying mechanical stress to the sample showing birefringent textures. However, the G= 4 ionic dendrimer **PAMAM64-ChCou**, surrounded by 64 dendrons **Ac-ChCou**, exhibited a hexagonal columnar mesophase. The smectic A and hexagonal columnar nature of the mesophases was confirmed by XRD.

In G= 0–3 ionic dendrimers, the XRD patterns were constituted by a diffuse halo in the wide angle region, corresponding to the short-range correlations between the conformationally disordered alkyl chains, and by one or two sharp maxima in the small angle region. These sharp maxima evidence a long-range lamellar packing of molecules, and when there were two low-angle maxima in the reciprocal spacing

ratio 1:2, they can be assigned to the first and second order reflections. The layer spacings (*d*) of the SmA mesophase were obtained by applying Bragg's law and they are gathered in **Table 2.1**.

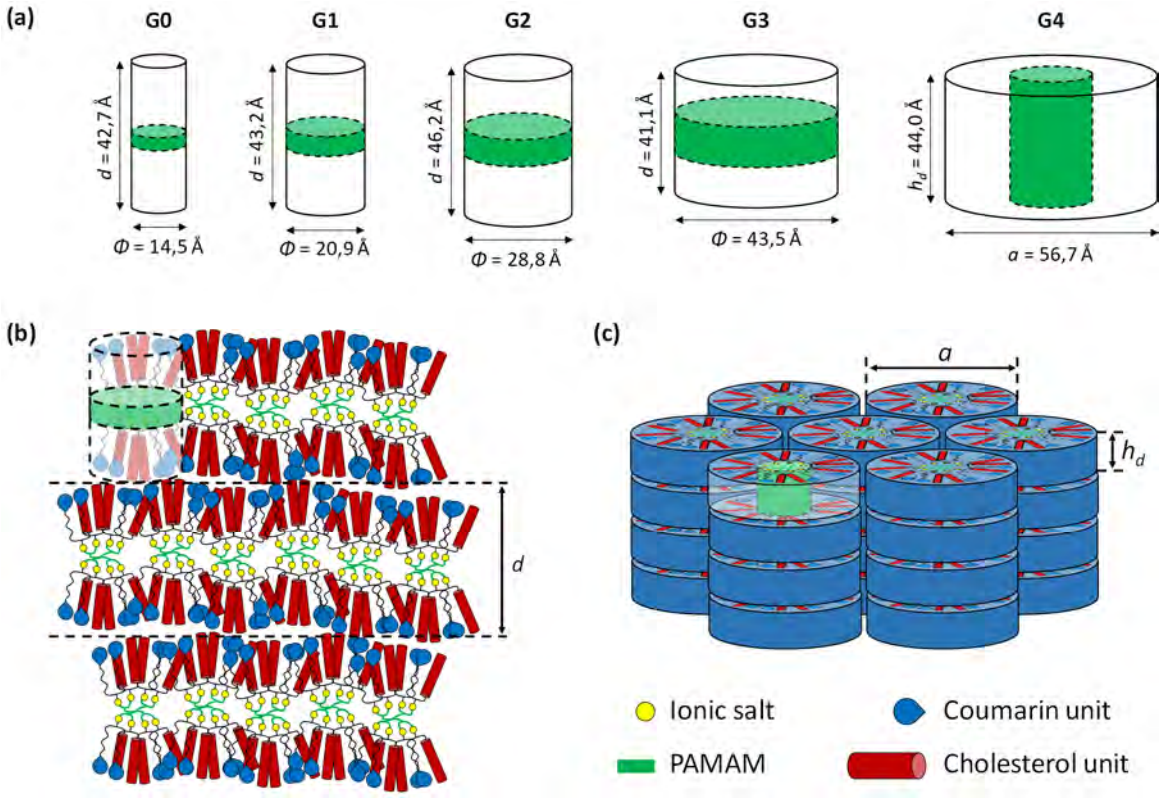

Figure 2.9 (a) Variation of the elementary ionic dendrimer cylinder as a function of generation number. Proposed arrangement of the ionic dendrimers **(b)** in the smectic A mesophase, and **(c)** in the hexagonal columnar mesophase.

The XRD pattern obtained for the G= 4 ionic dendrimer was consistent with a hexagonal columnar mesophase. It exhibited a diffuse maximum corresponding to a distance of about 4.5 Å between the conformationally disordered aliphatic chains. In the low-angle region the XRD pattern showed a set of two sharp reflections in the reciprocal ratio of 1 : 1/√3. These two reflections can be assigned to the reflections (100) and (110) of a hexagonal columnar arrangement with a lattice parameter (*a*) of 56.7Å.

On the basis of our previous works on LC dendrimers,[48, 49] we propose a cylinder-shaped conformation of the G= 0–3 dendrimers, in which the dendrimer matrix occupies the central section whereas the ionic pairs extend up and down with the dendrons statistically distributed (**Figure 2.9**). To gain insight into the molecular arrangement and the packing in the mesophase, it is possible to make some

theoretical calculations using the experimentally measured spacings (*d*) and the molecular weight values (*M*). The density *ρ* of a smectic mesophase can be calculated by the formula:[54]

$$\rho = \frac{4 \cdot 10^{24} \cdot M}{\pi \cdot d \cdot N_A \cdot \emptyset^2}$$

where *Ø* is the diameter of the cylinder and N_A is the Avogadro's number. Assuming that the density of organic compounds is around 1 g/cm^3, it is possible to estimate the diameter *Ø* in Å of the cylindrical dendritic molecules. The results of these calculations show that the diameter of the cylinder increases with the increase in the generation of the dendrimer due to the predominant spreading of the dendritic branches of PAMAM in the plane perpendicular to the cylinder axis to accommodate all the dendrons. Indeed, the height of the molecular cylinder (*d*) remains practically constant for all the G=0–3 dendrimers, whereas the cylinder diameter (*Ø*) increases from one generation to the next one. This can be explained if the dendritic matrix strongly deforms in the directions parallel to the smectic layers upon increasing the generation number. However, the growth of the diameter has a limit where the supermolecule undergoes conformational changes because the cylinder does not have enough space to accommodate the increasing number of fuctional units. The flexibility of the dendrimer matrix allows a molecular conformation in which the dendrons extend radially from the central dendrimer nucleus (**Figure 2.9**). The supramolecular organization of these disk-like molecules in columns gives rise to the observed hexagonal columnar mesomorphism. As for the smectic mesophases, simple calculations can be carried out for the columnar mesophases to gain an insight into the packing in the LC phase. These calculations enable estimated values for the mean disk thickness (h_d) with the formula:[54]

$$h_d = \frac{20 \cdot M}{\sqrt{3} \cdot 6.023 \cdot a^2}$$

A comparison of h_d with *a* indicates that the shape of the dendrimer in the mesophase is more appropriately described as a flattened cylinder than a disk. The arrangement of these disks within supramolecular organizations gives rise to cylindrical columns and therefore to the hexagonal columnar mesophase (**Figure 2.9**).

2.2.3 Absorption and Emission Properties

The UV-Vis absorption and fluorescence spectra of the ionic dendrimers were recorded on dilute solutions (10^{-5} to 10^{-7} M) in THF and in thin films at room temperature. Relevant data are collected in **Table 2.2**.

Table 2.2 Photophysical data

	λ_{abs}^{THF} (log ε)[a]	$\lambda_{abs}^{film\ a}$	$\lambda_{em}^{THF\ b}$	ϕ_F [c]
Ac-ChCou	324 (4.13)	323	384	0.48
PAMAM4-ChCou	323 (4.72)	323	384	0.45
PAMAM8-ChCou	323 (5.03)	323	384	0.46
PAMAM16-ChCou	324 (5.32)	323	383	0.51
PAMAM32-ChCou	323 (5.61)	323	384	0.58
PAMAM64-ChCou	323 (5.94)	323	384	0.56

[a] Maximum of the absorption band in nm (ε: extinction coefficient in $M^{-1}\cdot cm^{-1}$)

[b] Maximum of the emission band in nm.

[c] Quantum yields in THF relative to anthracene (ϕ_F= 0.27 in ethanol)

The ionic dendrimers present identical absorption spectra in THF solution with a band at 323 nm related to the π–π* transition of the coumarin units (**Figure 2.10**). The UV-Vis absorption spectra in solid thin film showed that the absorption band was broader respect to the corresponding THF solutions, due to aggregation of the coumarin units. The fluorescence emission spectra in THF solution exhibited one band at 384 nm. The fluorescence quantum yields (ϕ_F) of the ionic dendrimers were measured with anthracene (ϕ_F= 0.27 in ethanol) as standard, obtaining moderate quantum yield values in the range of 0.45–0.58. In general, the quantum yields increase upon increasing the generation. The fluorescence emission in solid thin film was also recorded and compared to the data from THF solutions, the emission peak appeared broader and red-shifted by ca. 50 nm.

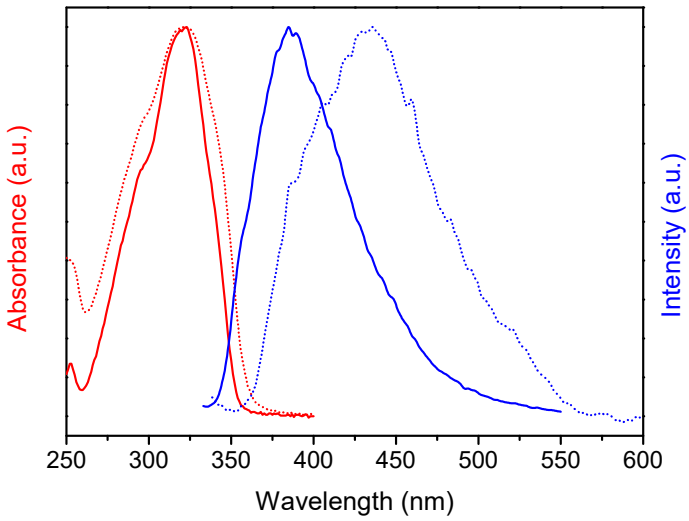

Figure 2.10 Absorption (red) and emission (blue) spectra of **PAMAM64-ChCou** in THF solution (solid lines) and in thin film (dot lines).

2.2.4 Polymer Network Formation by Coumarin Photodimerization

Photodimerization of coumarin units was employed for the crosslinking process by locking the LC arrangement. Exposure of the films to 365 nm UV irradiation caused a decrease of the π–π* band due to photoinduced [2+2] cycloaddition (so-called photodimerization) of the coumarin units. After 30 min of light irradiation only slight changes were further detected in the UV-Vis spectra (**Figure 2.11a**). To examine the structural details of the photo-crosslinking process, irradiated films were studied by FTIR and ^{13}C CPMAS. Irradiation at 365 nm results in coumarin photodimerization as indicated by the decrease in the intensity of the C=C stretching band at 1620 cm^{-1} and the shift of the C=O stretching band from 1730 to 1750 cm^{-1} (**Figure 2.11b**).[65] After photodimerization, the band at 1730 cm^{-1} did not completely disappear because it comprises contributions from the cholesteryl hemisuccinate ester groups. This reaction can also be followed by ^{13}C CPMAS which showed the disappearance of the peak at 113 ppm (C_B), which corresponds to the C=C moieties (**Figure 2.7**). Additionally, after coumarin photodimerization the signal at 163 ppm (C_A) is shifted upfield due to the formation of the cyclobutane ring.[66]

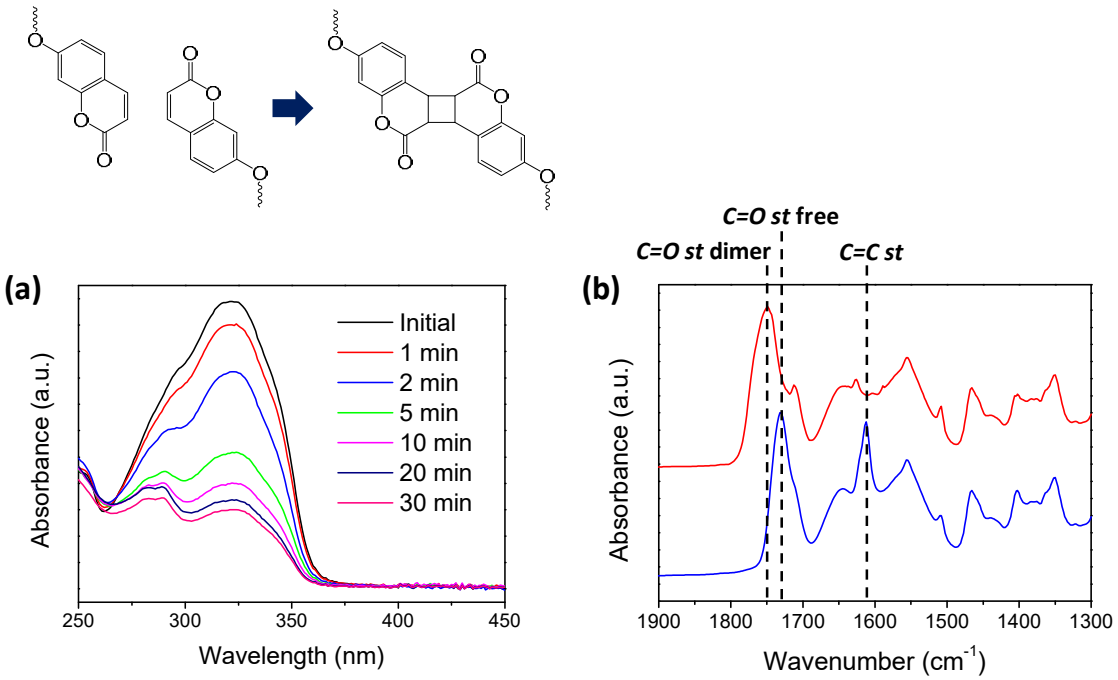

Figure 2.11 Coumarin photodimerization reaction: **(a)** UV-Vis absorption spectra of a UV-irradiated **PAMAM64-ChCou** film at different times, **(b)** FTIR spectra of **PAMAM16-ChCou** before (blue) and after (red) coumarin photodimerization.

The crosslinking of the smectic or columnar ionic dendrimers gave rise to a LC polymer network, whose lattice spacings are significantly smaller (ca. 5 Å) that those of the starting "single" dendrimer (**Figure 2.12**). These results suggest that the ionic pathways have not been disrupted after coumarin photodimerization, thus this reaction can be used to lock in the arrangement of the LC phase.

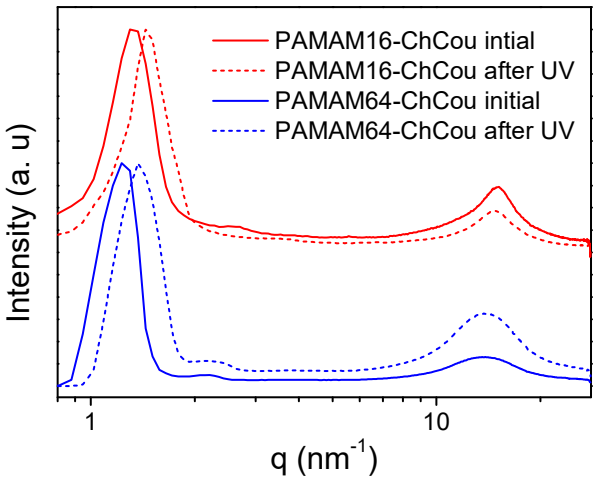

Figure 2.12 1D XRD profiles of **PAMAM16-ChCou** and **PAMAM64-ChCou** before and after photodimerization.

2.2.5 Proton Conduction Properties

The proton conductivity was measured using electrochemical impedance spectroscopy in samples consisting of films sandwiched between ITO-coated electrodes. The typical impedance response (Nyquist plots) consisted of a suppressed semicircle in the high-frequency region and an incline straight line in the low-frequency range (**Figure 2.13**).

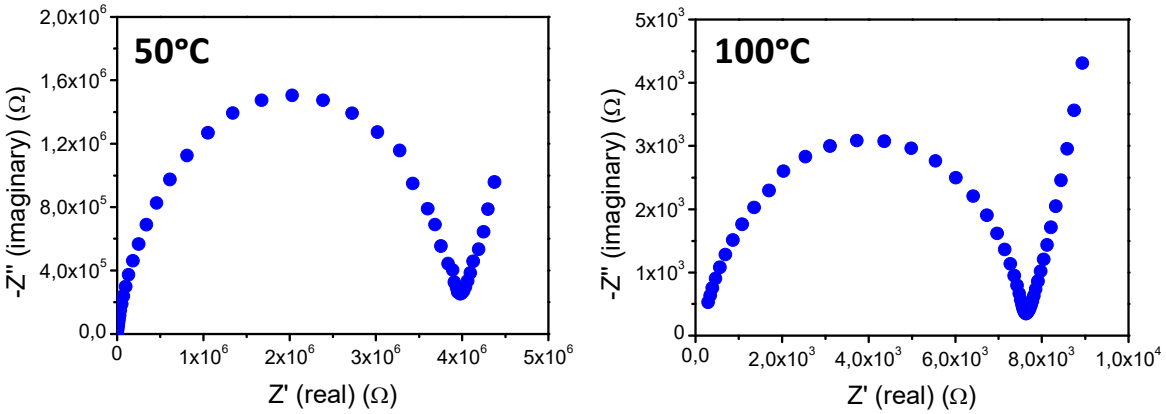

Figure 2.13 Nyquist plots of **PAMAM64-ChCou** at 50 °C and 100 °C.

Because protons have to travel between two electrodes, in anisotropic materials the measured conductivity depends on the macroscopic degree of order and the orientation of the phase with respect to the electrodes. Initially, a random orientation of the samples (polydomain) was observed between electrodes in just prepared cells. Thus, several alignment procedures (shearing or thermal treatments) were performed in an effort to obtain long-range, uniform planar or homeotropic alignment over large areas of the SmA or Col_h samples, respectively. As a representative example, the proton conductivities of **PAMAM64-ChCou** before and after thermal annealing are shown in **Figure 2.14a**. The ionic conductivities after annealing are approximately one order of magnitude higher than those of the films without annealing. This result suggests that thermal treatments favor columnar arrangement perpendicular to the electrodes, having a decisive influence on the proton conductivity.

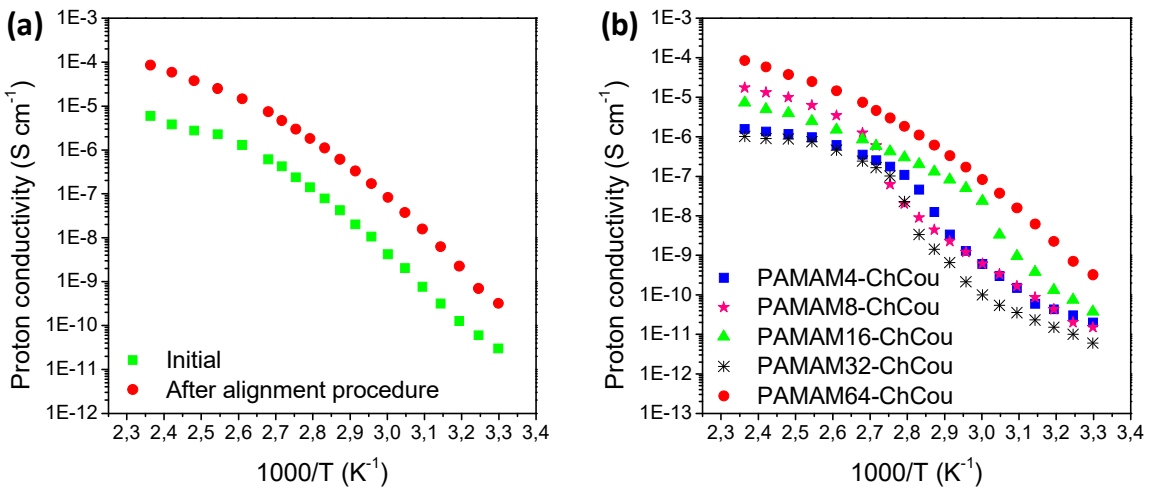

Figure 2.14 Proton conductivities as a function of the temperature of: **(a) PAMAM64-ChCou**, and **(b)** all ionic dendrimers.

In **Figure 2.14b**, the proton conductivities (after alignment) were compared among the different generations of the ionic dendrimers. Interestingly, the G= 4 ionic dendrimer exhibits the highest conductivity. This result can be understood by keeping in mind that the G= 4 dendrimer displayed a hexagonal columnar phase whereas G= 0–3 presented smectic A mesomorphism. Most likely, the supramolecular organization of **PAMAM64-ChCou** may facilitate the protonic charge transport due to the presence of 1D nanochannels. On the other hand, there are no big differences in the ionic conductivities for the G= 0–3 ionic dendrimers. Therefore, these results suggest that the hexagonal columnar organization in the LC state clearly favors proton conduction.

The proton conductivities after coumarin photodimerization were estimated by taking compounds **PAMAM64-ChCou**, which exhibits a hexagonal columnar mesophase, and **PAMAM16-ChCou**, with a smectic A mesophase, as representative examples (**Figure 2.15**). It is remarkable that after crosslinking both dendrimers showed a decrease in conductivities similar to the previously reported polymerizable LCs whose conductivities reduced about one order of magnitude after polymerization due to the decrease in the mobility of ionic moieties.[10, 67]

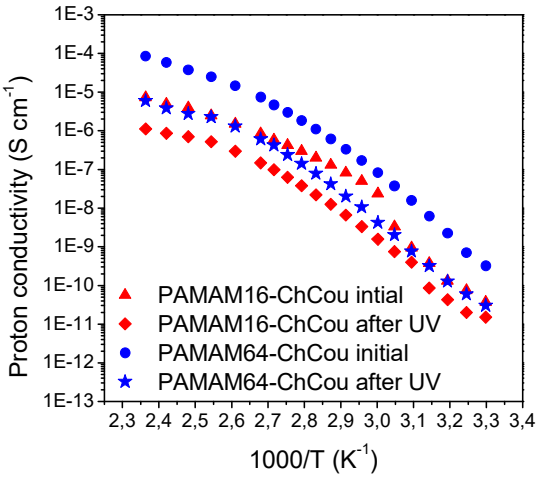

Figure 2.15 Proton conductivities as a function of the temperature of **PAMAM16-ChCou** and **PAMAM64-ChCou** before and after photodimerization.

2.3 Conclusions

A new strategy for the preparation of proton conductive materials has been developed using ionic LC dendrimers combined with a crosslinking reaction based on coumarin photodimerization. 1D and 2D ionic nanosegregated assemblies can be obtained in a modular approach using different generation dendrimers. The use of coumarin photodimerization imparts a new tool to fabricate mechanical stable ionic materials.

All ionic materials showed good proton conductivity and it is expected that macroscopic alignment will enhance this. The proton conduction in these ionic LC dendrimers may open a new path in the search for electrolyte materials for the preparation of electrochemical devices.

3. EXPERIMENTAL PART

3.1 Characterization Techniques

3.1.1 Materials

Poly(amidoamine) dendrimers (PAMAM) were purchased from Dendritech, Inc. Cholesteryl hemisuccinate and the rest of reagents were purchased from Sigma-Aldrich and used as received without further purification. Anhydrous THF and DCM were purchased from Scharlab and dried using a solvent purification system.

3.1.2 Structural Characterization

Infrared spectroscopy experiments were obtained on a Bruker Vertex 70 FT-IR spectrophotometer using KBr pellets.

Solution **nuclear magnetic resonance** experiments were carried out on Bruker Avance spectrometers operating at 500/400 MHz for ^{1}H and 125/100 for ^{13}C, using standard pulse sequences. Chemical shifts are given in ppm relative to TMS and the residual solvent peak was used as internal reference.

Solid-state **nuclear magnetic resonance** experiments were performed in a Bruker Avance III WB400 spectrometer using a double resonance (^{1}H-X) probe with a rotor of 4 mm or 2.5 mm diameter, and the spinning frequency was set to 12 kHz or 20 kHz, respectively. For the former, the ^{1}H and ^{13}C $\pi/2$ pulse length were 3 and 4.3 µs, respectively, the CP contact time was 3 ms and the recycle delay was 7 s. For the latter, the ^{1}H and ^{13}C pulse length were 8 and 5.7 µs, respectively, the CP contact time was 1.5 ms and the recycle delay was 5 s. The pulse sequence employed consisted of ramped cross-polarization with spinal-64 decoupling. Data were acquired at 298 K and chemical shifts are referenced to TMS using adamantane (^{13}C: δ= 29.45 ppm) as secondary standard.

Elemental analysis was performed using a Perkin-Elmer 2400 microanalyzer.

MALDI-TOF mass spectrometry was performed on an Autoflex mass spectrometer (Bruker Daltonics) using dithranol as matrix.

3.1.3 Liquid Crystal Characterization

Mesogenic behavior was investigated by **polarized-light optical microscopy** using an Olympus BH-2 polarizing microscope fitted with a Linkam THMS600 hot stage.

Thermogravimetric analysis was performed using a Q5000IR from TA Instruments at heating rate of 10 °C/min under nitrogen atmosphere.

Thermal transitions were determined by **differential scanning calorimetry** using a DSC Q20 or Q2000 from TA Instruments with powdered samples (2−5 mg) sealed in aluminum pans under nitrogen atmosphere. Glass transition temperatures (T_g) were determined at the half-height of the baseline jump, and first-order transition temperatures were read at the maximum of the corresponding peak.

X-ray diffraction was also performed with a Ganesha Lab Instrument equipped with a GeniX-Cu ultralow divergence source producing X-ray photons with a wavelength of 1.54 Å and a flux of 1×10^8 ph/s. Scattering patterns were collected using a Pilatus 300 K silicon pixel detector. The beam center and the q range were calibrated using the diffraction peaks of silver behenate. Powdered samples were placed in Lindemann glass capillaries (1 mm diameter).

3.1.4 Optical Properties

Ultraviolet-visible spectra were recorded on an ATI-Unicam UV4-200 spectrophotometer.

Fluorescence measurements were recorded on a Perkin-Elmer LS 50B fluorescence spectrophotometer.

All the measurements were performed in dilute THF solutions (10^{-5} to 10^{-7} M) using quartz cuvettes. Thin films for UV-Vis absorption experiments were prepared by casting from THF solutions (1 mg/mL) onto quartz substrates. Films for fluorescence measurements were prepared between two quartz plates by heating the compounds above their isotropization temperature and cooling down to RT.

3.1.5 Proton Conductive Properties

Electrochemical impedance spectroscopy was recorded on an Autolab potentiostat equipped with a temperature controller in the frequency range from 1 Hz to 1 MHz (applied voltage: 10 mV). The conductivities were studied as a function of temperature between 30 and 150 °C with 5 °C intervals. For the preparation of the cells for ionic conductivities, the appropriate amount of the ionic dendrimer was placed on a ITO electrode that was sandwiched with another ITO electrode controlling the thickness by using glass spacers (20 μm). The cell was heated up to a few degrees above the melting point of the liquid crystal and the cell was pressed to obtain the thin film.

After the preparation of the cell, a random orientation of the layers (SmA) or columns (Col_h) was observed between electrodes. Smectic samples were mechanically sheared within the cell in order to obtain a planar alignment of the layers (smectic layers aligned perpendicular to the electrodes). On the other hand, homeotropic alignment of the columnar mesophase was attainable after slow cooling down to room temperature (0.05 °C/min) from the isotropic liquid.

The impedance spectrum can be modeled as an equivalent circuit and divided into imaginary (*Z''*) and real (*Z'*) components. The resistance (R_b) was estimated from the intersection of the real axis (*Z'*) and the semicircle of the impedance spectrum. The proton conductivities σ (S/cm) were calculated with the formula:

$$\sigma = d/(R_b \cdot A)$$

where *d* (cm) is the thickness of the film, *A* (cm^2) is the area of the film and R_b (Ω) is the resistance of the sample.

Photocrosslinking of coumarin units (photodimerization) was carried out by exposing the aligned LC system to 365 nm LED light (ThorsLab) for 30 min.

3.2 Synthetic Procedures

3.2.1 Synthesis of the Coumarin Functional Unit

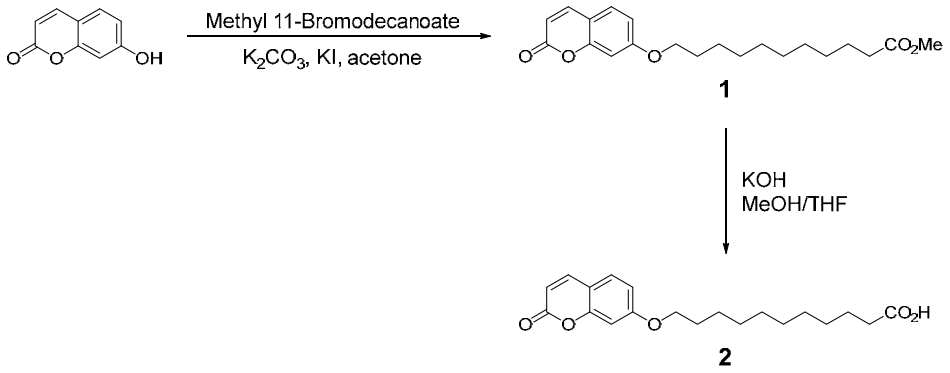

Methyl 11-((2-oxo-2*H*-chromen-7-yl)oxy)undecanoate (1). A mixture of 7-hydroxy-2*H*-chromen-2-one (3 g, 18.5 mmol), methyl 11-bromoundecanoate (5.68 g, 20.35 mmol), potassium carbonate (5.11 g, 37.00 mmol) and a teaspoon of potassium iodide in acetone (175 mL) was stirred and heated to reflux for 12 h. The reaction was allowed to cool down to room temperature and the solvent was evaporated under reduced pressure. The residue was dissolved in DCM and washed with water and brine. The organic layer was dried over anhydrous magnesium sulfate and the solvent was evaporated. The crude product was recrystallized in ethanol. Yield: 93%. IR (KBr, ν, cm^{-1}): 2923 (C-H), 1744 (C=O), 1612, 1463 (Ar), 1232, 1126 (C-O). ^{1}H NMR ($CDCl_3$, 400 MHz, δ, ppm): 7.63 (d, *J*= 9.4 Hz, 1H), 7.6 (d, *J*= 8.5 Hz, 1H), 6.88-6.76 (m, 2H), 6.24 (d, *J*= 9.5 Hz, 1H), 4.00 (t, *J*= 6.5 Hz, 2H), 3.66 (s, 3H), 2.30 (t, *J*= 7.5 Hz, 2H), 1.85-1.74 (m, 2H), 1.67-1.55 (m, 2H), 1.51-1.21 (m, 12H). ^{13}C NMR ($CDCl_3$, 100 MHz, δ, ppm): 176.53, 162.58, 161.47, 156.07, 143.61, 128.83, 113.16, 113.05, 112.50, 101.46, 68.79, 51.60, 34.24, 29.58, 29.47, 29.43, 29.35, 29.26, 29.10, 26.07, 25.07.

11-((2-Oxo-2*H*-chromen-7-yl)oxy)undecanoic acid (2). An aqueous solution of potassium hydroxide (5.45 g, 10 mL) was added to a solution of compound **1** (4.5 g, 12.48 mmol) in methanol and THF (50 mL and 5 mL, respectively). The mixture was stirred and heated under reflux for 2 h. Then, the crude product was precipitated by addition of concentrated hydrochloric acid until pH 2 and it was filtered. The product was recrystallized in ethanol. Yield: 91%. IR (KBr, ν, cm^{-1}): 3133 (O-H), 1719, 1699 (C=O), 1619 1508, 1466 (Ar), 1205, 1139 (C-O). ^{1}H NMR ($CDCl_3$, 400 MHz, δ, ppm): 7.63 (d, *J*= 9.5 Hz, 1H), 7.35 (d, *J*= 8.4 Hz, 1H), 6.87-6.77 (m, 2H),

6.24 (d, *J*= 9.4 Hz, 1H), 4.00 (t, *J*= 7.0 Hz, 2H), 2.34 (t, *J*= 7.5 Hz, 2H), 1.87-1.75 (m, 2H), 1.68-1.58 (m, 2H), 1.51-1.22 (m, 12H). ^{13}C NMR ($CDCl_3$, 100 MHz, δ, ppm): 179.23, 162.59, 161.55, 156.06, 143.65, 128.83, 113.19, 113.03, 112.51, 101.47, 68.80, 34.05, 29.55, 29.43, 29.39, 29.32, 29.16, 29.08, 26.05, 24.81.

3.2.2 Synthesis of the Bifunctional Dendron

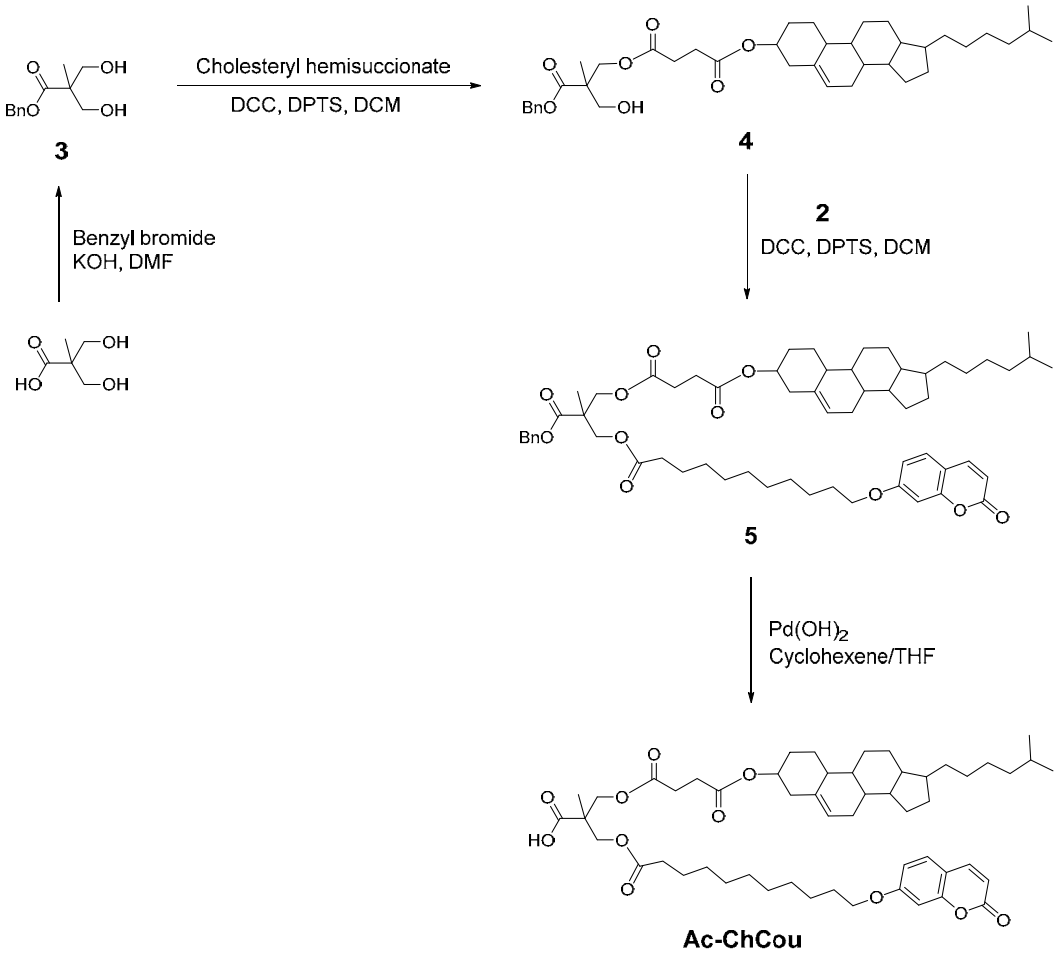

Benzyl 2,2'-bis(hydroxymethyl)propanoate (3). 2,2'-Bis(hydroxymethyl) propionic acid (10 g, 74.55 mmol) and potassium hydroxide (5.02 g, 89.46 mmol) were dissolved in DMF (75 mL). The mixture was heated at 100 °C for 1 h and then benzyl bromide (15.3 g, 89.46 mmol) was added. After stirring for 12 h at 100 °C, DMF was distilled off. The residue was dissolved in DCM and washed with brine. The crude product was recrystallized in toluene. Yield: 59%. IR (KBr, ν, cm^{-1}): 3362 (OH), 3037 (=C-H), 2940 (C-H), 1706 (C=O), 1223, 1041 (C-O). ^{1}H NMR ($CDCl_3$, 400 MHz, δ, ppm): 7.42-7.28 (m, 5H), 5.21 (s, 2H), 3.93 (dd, *J*= 10.5 Hz, *J*= 6.9 Hz, 2H), 3.73 (dd,

J= 11.3 Hz, *J*= 6.3 Hz, 2H), 2.91 (t, *J*= 6.6 Hz, 2H), 1.08 (s, 3H). ^{13}C NMR ($CDCl_3$, 100 MHz, δ, ppm): 175.86, 135.84, 128.77, 128.44, 127.98, 68.42, 66.82, 49.37, 17.23.

Benzyl-protected monofunctionalized dendron (4). Compound **3** (1.00 g, 4.46 mmol), cholesteryl hemisuccinate (2.17 g, 4.46 mmol) and 4-(dimethylamino) *p*-toluenesulfonate (0.70 g, 2.23 mmol) were dissolved in anhydrous DCM (100 mL). The reaction flask was cooled in an ice bath and flushed with argon, then *N,N'*-dicyclohexylcarbodiimide (1.01 g, 4.91 mmol) was added dropwise. The mixture was stirred at RT for 24 h under argon atmosphere. The white precipitate was filtered off and washed with DCM. The solvent was evaporated and the crude product was purified by flash column chromatography on silica gel using DCM as eluent and gradually changing the composition of the eluent to DCM/ethyl acetate (19:1). Yield: 66%. IR (KBr, ν, cm^{-1}): 3516 (OH), 2954 (C-H), 1722 (C=O), 1254, 1055 (C-O).^{1}H NMR ($CDCl_3$, 400 MHz, δ, ppm): 7.41-7.28 (m, 5H), 5.36 (d, *J*= 3.6 Hz, 1H), 5.20 (d, *J*= 12.4 Hz, 1H), 5.16 (d, *J*= 12.4 Hz, 1H), 4.68-4.54 (m, 1H), 4.39 (d, *J*= 11.2 Hz, 1H), 4.25 (d, *J*= 11.2 Hz, 1H), 3.77-3.65 (m, 2H), 2.60-2.51 (m, 4H), 2.31 (d, *J*= 7.7 Hz, 2H), 2.06-0.81 (m, 41H), 0.68 (s, 3H). ^{13}C NMR ($CDCl_3$, 100 MHz, δ, ppm): 174.31, 172.63, 171.72, 139.64, 135.78, 128.75, 128.47, 128.15, 122.91, 74.64, 66.83, 66.05, 65.00, 56.82, 56.26, 50.14, 48.43, 42.44, 39.86, 39.65, 38.18, 37.08, 36.71, 36.32, 35.93, 32.03, 31.98, 29.49, 29.18, 28.37, 28.15, 27.85, 24.42, 23.96, 22.96, 22.71, 21.16, 19.44, 18.85, 17.71, 11.99.

Benzyl-protected bifunctionalized dendron (5). Compound **2** (0.96 g, 2.77 mmol), the monofunctional dendron (**4**) (1.75 g, 2.53 mmol) and 4-(dimethylamino) *p*-toluenesulfonate (0.39 g, 1.26 mmol) were dissolved in anhydrous DCM (75 mL). The reaction flask was cooled in an ice bath and flushed with argon, then *N,N'*-dicyclohexylcarbodiimide (0.63 g, 3.03 mmol) was added dropwise. The mixture was stirred at RT for 24 h under argon atmosphere. The white precipitate was filtered off and washed with DCM. The solvent was evaporated and the crude product was purified by flash column chromatography on silica gel using DCM as eluent and gradually changing the composition of the eluent to DCM/ethyl acetate (19:1). Yield: 90%. IR (KBr, ν, cm^{-1}): 2934 (C-H), 1741 (C=O), 1613, 1467 (Ar), 1231, 1156 (C-O). ^{1}H NMR ($CDCl_3$, 400 MHz, δ, ppm): 7.63 (d, *J*= 9.4 Hz, 1H), 7.40-7.27 (m, 6H), 6.86-6.77 (m, 2H), 6.24 (d, *J*= 9.5 Hz, 1H), 5.40-5.30 (m, 1H), 5.16 (s, 2H), 4.66-4.54 (m, 1H), 4.31-4.16 (m, 4H), 4.00 (t, *J*= 6.5 Hz, 2H), 2.60-2.48 (m, 4H), 2.30 (d, *J*= 7.7 Hz, 2H), 2.22 (t, *J*= 7.6 Hz, 2H), 2.04-0.80 (m, 54H), 0.67 (s, 3H). ^{13}C NMR

($CDCl_3$, 100 MHz, δ, ppm): 173.35, 172.69, 171.94, 171.56, 162.59, 161.41, 156.10, 143.57, 139.71, 135.76, 128.82, 128.72, 128.47, 128.27, 122.86, 113.15, 113.08, 112.51, 101.49, 74.55, 68.81, 66.94, 65.77, 65.43, 56.84, 56.29, 50.17, 46.55, 42.46, 39.88, 39.66, 38.20, 37.10, 36.72, 36.33, 35.93, 34.18, 32.04, 32.00, 29.62, 29.51, 29.46, 29.36, 29.24, 29.13, 28.37, 28.16, 27.88, 26.10, 24.94, 24.42, 23.98, 22.96, 22.70, 21.17, 19.45, 18.86, 17.91, 12.00.

Bifunctionalized dendron Ac-ChCou. Compound **5** and $Pd(OH)_2/C$ (20% wt.) were dissolved in a mixture of THF-cyclohexene (1:3) under reflux. After 12 h, the catalyst was filtered off using Celite® and carefully washed with DCM. The solvent was evaporated and the crude product was purified by flash column chromatography on silica gel using DCM as eluent and gradually changing the composition of the eluent to ethyl acetate. Yield: quantitative. IR (KBr, ν, cm^{-1}): 3228 (OH), 3044 (=C-H), 2932 (C-H), 1741, 1730, 1683 (C=O), 1604, 1507, 1466 (Ar), 1252, 1165 (C-O). ^{1}H NMR ($CDCl_3$, 400 MHz, δ, ppm): 7.63 (d, *J*= 9.5 Hz, 1H), 7.36 (d, *J*= 8.5 Hz, 1H), 6.89-6.75 (m, 2H), 6.24 (d, *J*= 9.5 Hz, 1H), 5.40-5.30 (m, 1H), 4.68-4.54 (m, 1H), 4.32-4.18 (m, 4H), 4.01 (t, *J*= 6.5 Hz, 2H), 2.69-2.54 (m, 4H), 2.36-2.25 (m, 4H), 2.04-0.80 (m, 54H), 0.67 (s, 3H). ^{13}C NMR ($CDCl_3$, 100 MHz, δ, ppm): 176.98, 173.40, 171.97, 171.65, 162.61, 161.57, 156.07, 143.65, 139.70, 128.84, 122.87, 113.20, 113.05, 112.53, 101.50, 74.62, 68.82, 65.50, 65.12, 56.83, 56.30, 50.16, 46.21, 42.46, 39.87, 39.66, 38.19, 37.10, 36.72, 36.33, 35.94, 34.22, 32.04, 32.00, 29.58, 29.48, 29.40, 29.33, 29.23, 29.19, 29.09, 28.37, 28.16, 27.87, 26.07, 24.96, 24.43, 23.99, 22.96, 22.70, 21.17, 19.45, 18.86, 17.89, 12.00. MS (MALDI$^+$, dithranol, m/z): calcd. for $C_{56}H_{82}O_{11}$, 930.6; found, 953.6 $[M+Na]^+$, 975.6 $[M-H+2Na]^+$. Anal. calcd. for $C_{56}H_{82}O_{11}$: C, 72.23%; H, 8.88%. Found: C, 72.00%; H, 8.94%.

3.2.3 Synthesis of the Ionic Dendrimers

Ionic dendrimers were prepared following the previously described methodology.[50, 54] A solution of **Ac-ChCou** in anhydrous THF was added to a solution of the corresponding generation of the PAMAM dendrimer, in approximately 1:1 (primary amine groups:carboxylic acid groups) stoichiometry. The mixture was ultrasonicated for 5 min, and then it was slowly evaporated at

room temperature and dried in vacuum at 40 °C until the weight remained constant.

PAMAM4-ChCou. IR (KBr, ν, cm^{-1}): 3258 (N-H), 3069 (=C-H), 2930 (C-H), 1729, 1645 (C=O), 1611 (Ar), 1555 (COO^-_{asym}), 1406 (COO^-_{sym}), 1158 (C-O). ^1H NMR ($CDCl_3$, 400 MHz, δ, ppm): 8.71-8.50 (m, 4H), 7.63 (d, *J*= 9.5 Hz, 4H), 7.35 (d, *J*= 8.6 Hz, 4H), 6.85-6.76 (m, 8H), 6.23 (d, *J*= 9.5 Hz, 4H), 5.39-5.29 (m, 4H), 4.68-4.47 (m, 4H), 4.36-4.08 (m, 16H), 4.00 (t, *J*= 6.5 Hz, 8H), 3.65-3.43 (m, 4H), 3.22-3.02 (m, 4H), 3.00-2.23 (m, 52H), 2.05-0.74 (m, 216H), 0.66 (s, 12H). ^{13}C NMR ($CDCl_3$, 100 MHz, δ, ppm): 178.40, 173.80, 172.31, 172.02, 162.60, 161.49, 156.08, 143.65, 139.71, 128.86, 122.87, 113.16, 113.04, 112.52, 101.49, 74.62, 68.81, 68.12, 66.80, 66.15, 56.83, 56.32, 50.58 (detected by ^1H-^{13}C HSQC, H_ζ-C_ζ), 50.15, 49.98 (detected by ^1H-^{13}C HSQC, H_ε-C_ε), 46.59, 42.46, 39.87, 39.66, 39.28 (detected by ^1H-^{13}C HSQC, H_η-C_η), 39.10 (detected by ^1H-^{13}C HSQC, H_α-C_α), 38.20, 37.40 (detected by ^1H-^{13}C HSQC, H_β-C_β), 37.10, 36.73, 36.34, 35.95, 34.38, 32.85 (detected by ^1H-^{13}C HSQC, H_δ-C_δ), 32.05, 31.99, 29.65, 29.56, 29.47, 29.44, 29.34, 29.22, 29.13, 28.38, 28.16, 27.87, 26.10, 25.76, 25.06, 24.43, 24.02, 22.97, 22.71, 21.18, 19.45, 18.86, 18.64, 12.00.

PAMAM8-ChCou. IR (KBr, ν, cm^{-1}): 3260 (N-H), 3070 (=C-H), 2928 (C-H), 1728, 1644 (C=O), 1610 (Ar), 1555 (COO^-_{asym}), 1406 (COO^-_{sym}), 1158 (C-O). ^1H NMR ($CDCl_3$, 400 MHz, δ, ppm): 8.74-8.47 (m, 8H), 8.21- 8.06 (m, 4H), 7.63 (d, *J*= 9.5 Hz, 8H), 7.36 (d, *J*= 8.6 Hz, 8H), 6.89-6.74 (m, 16H), 6.24 (d, *J*= 9.5 Hz, 8H), 5.43-5.27 (m, 8H), 4.69-4.49 (m, 8H), 4.39-4.09 (m, 32H), 4.00 (t, *J*= 6.5 Hz, 16H), 3.62-3.45 (m, 16H), 3.37-3.04 (m, 24H), 2.90-2.19 (m, 120H), 2.07-0.76 (m, 432H), 0.66 (s, 24H). ^{13}C NMR ($CDCl_3$, 100 MHz, δ, ppm):178.02, 173.74, 172.25, 171.90, 162.59, 161.51, 156.06, 143.66, 139.70, 128.85, 122.86, 113.16, 113.03, 112.51, 101.48, 74.59, 68.80, 56.82, 56.30, 52.28 (detected by ^1H-^{13}C HSQC, H_ζ-C_ζ), 50.18 (detected by ^1H-^{13}C HSQC, H_ε-C_ε), 50.14, 42.45, 39.86, 39.65, 39.34 (detected by ^1H-^{13}C HSQC, H_α-C_α), 38.18, 37.75 (detected by ^1H-^{13}C HSQC, H_η-C_η), 37.40 (detected by ^1H-^{13}C HSQC, H_β-C_β), 37.09, 36.72, 36.33, 35.94, 34.35, 34.10 (detected by ^1H-^{13}C HSQC, H_δ-C_δ), 32.04, 31.98, 29.63, 29.55, 29.51, 29.45, 29.42, 29.32, 29.11, 28.37, 28.15, 27.86, 26.09, 25.03, 24.42, 24.01, 22.96, 22.71, 21.17, 19.45, 18.86, 18.54, 11.99.

PAMAM16-ChCou. IR (KBr, ν, cm^{-1}): 3261 (N-H), 3069 (=C-H), 2929 (C-H), 1729, 1645 (C=O), 1610 (Ar), 1555 (COO^-_{asym}), 1406 (COO^-_{sym}), 1158 (C-O). ^1H NMR ($CDCl_3$, 400 MHz, δ, ppm): 8.82-8.45 (m, 16H), 8.27-7.96 (m, 12H), 7.63 (d, *J*= 9.5 Hz, 17H),

7.35 (d, *J*= 8.6 Hz, 16H), 6.87-6.74 (m, 32H), 6.23 (d, *J*= 9.5 Hz, 16H), 5.40-5.28 (m, 16H), 4.70-4.46 (m, 16H), 4.38-4.08 (m, 64H), 3.99 (t, *J*= 6.5 Hz, 32H), 3.65-3.41 (m, 32H), 3.37-3.03 (m, 56H), 2.88-2.16 (m, 264H), 2.08-0.75 (m, 864H), 0.66 (s, 48H). ^{13}C NMR ($CDCl_3$, 100 MHz, δ, ppm): 173.73, 172.26, 171.86, 162.59, 161.48, 156.05, 143.66, 139.70, 128.86, 122.84, 113.14, 113.02, 112.51, 101.48, 74.55, 68.80, 68.10, 66.64, 66.05, 56.82, 56.31, 52.30 (detected by ^{1}H-^{13}C HSQC, H_ζ-C_ζ), 50.36 (detected by ^{1}H-^{13}C HSQC, H_ε-C_ε), 50.14, 46.51, 42.44, 39.86, 39.64, 39.56 (detected by ^{1}H-^{13}C HSQC, H_α-C_α), 38.19, 37.78 (detected by ^{1}H-^{13}C HSQC, H_η-C_η), 37.52 (detected by ^{1}H-^{13}C HSQC, H_β-C_β), 37.09, 36.71, 36.33, 35.93, 34.35, 34.17 (detected by ^{1}H-^{13}C HSQC, H_δ-C_δ), 31.98, 29.65, 29.56, 29.47, 29.33, 29.12, 28.36, 28.15, 27.86, 26.10, 25.74, 25.04, 24.42, 24.01, 22.96, 22.70, 21.16, 19.45, 18.86, 18.65, 11.99.

PAMAM32-ChCou. IR (KBr, ν, cm^{-1}): 3260 (N-H), 3069 (=C-H), 2929 (C-H), 1729, 1645 (C=O), 1610 (Ar), 1554 (COO^-_{asym}), 1405 (COO^-_{sym}), 1160 (C-O). ^{1}H NMR ($CDCl_3$, 400 MHz, δ, ppm): 8.72-8.38 (m, 32H), 8.29-7.96 (m, 28H), 7.63 (d, *J*= 9.5 Hz, 32H), 7.35 (d, *J*= 8.6 Hz, 32H), 6.85-6.74 (m, 64H), 6.22 (d, *J*= 9.5, 32H), 5.39-5.28 (m, 32H), 4.64-4.50 (m, 32H), 4.36-4.05 (m, 128H), 3.99 (t, *J*= 6.5 Hz, 64H), 3.65-3.37 (m, 64H), 3.37-3.00 (m, 120H), 2.93-2.19 (m, 552H), 2.09-0.75 (m, 1728H), 0.66 (s, 96H). ^{13}C NMR ($CDCl_3$, 100 MHz, δ, ppm): 178.59, 173.82, 172.35, 171.93, 162.61, 161.48, 156.08, 143.66, 139.73, 128.88, 122.85, 113.15, 113.04, 112.54, 101.52, 74.58, 68.82, 66.49, 66.26, 56.85, 56.37, 52.58 (detected by ^{1}H-^{13}C HSQC, H_ζ-C_ζ), 50.33 (detected by ^{1}H-^{13}C HSQC, H_ε-C_ε), 50.18, 46.60, 42.47, 39.89, 39.69 (detected by ^{1}H-^{13}C HSQC, H_α-C_α), 39.67, 38.21, 37.80 (detected by ^{1}H-^{13}C HSQC, H_η-C_η), 37.75 (detected by ^{1}H-^{13}C HSQC, H_β-C_β), 37.12, 36.74, 36.36, 35.96, 34.38, 34.25 (detected by ^{1}H-^{13}C HSQC, H_δ-C_δ), 32.05, 29.85, 29.67, 29.59, 29.49, 29.36, 29.27, 29.15, 28.38, 28.16, 27.88, 26.12, 25.06, 24.44, 24.05, 22.96, 22.71, 21.19, 19.46, 18.88, 18.63, 12.01.

PAMAM64-ChCou. IR (KBr, ν, cm^{-1}): 3260 (N-H), 3069 (=C-H), 2929 (C-H), 1729, 1645 (C=O), 1610 (Ar), 1555 (COO^-_{asym}), 1406 (COO^-_{sym}), 1158 (C-O). ^{1}H NMR ($CDCl_3$, 400 MHz, δ, ppm): 8.84-8.48 (m, 64H), 8.23-7.94 (m, 60H), 7.63 (d, *J*= 9.5 Hz, 64H), 7.35 (d, *J*= 8.6 Hz, 64H), 6.90-6.69 (m, 128H), 6.23 (d, *J*= 9.5 Hz, 64H), 5.42-5.26 (m, 64H), 4.69-4.49 (m, 64H), 4.39-4.04 (m, 256H), 3.97 (t, *J*= 6.5 Hz, 128H), 3.67-2.99 (m, 376H), 2.96-2.13 (m, 1128H), 2.10-0.75 (m, 3456H), 0.70 (s, 192H). ^{13}C NMR ($CDCl_3$, 100 MHz, δ, ppm): 178.08, 173.70, 172.23, 171.82, 162.59, 161.49, 156.05,

143.68, 139.69, 128.87, 122.84, 113.14, 113.01, 112.51, 101.48, 74.54, 68.80, 68.10, 66.53, 56.81, 56.32, 52.14 (detected by ^{1}H-^{13}C HSQC, H_{ζ}-C_{ζ}), 50.20 (detected by ^{1}H-^{13}C HSQC, H_{ε}-C_{ε}), 50.14, 46.49, 42.44, 39.86, 39.64, 39.41 (detected by ^{1}H-^{13}C HSQC, H_{α}-C_{α}), 38.19, 37.57 (detected by ^{1}H-^{13}C HSQC, H_{η}-C_{η}), 37.52 (detected by ^{1}H-^{13}C HSQC, H_{β}-C_{β}), 37.09, 36.71, 36.33, 35.94, 34.34, 31.98, 29.65, 29.57, 29.47, 29.33, 29.13, 28.37, 28.15, 27.86, 26.10, 25.74, 25.04, 24.42, 24.02, 22.96, 22.70, 21.17, 19.45, 18.86, 18.59, 11.99.

4. REFERENCES

(1) J. Y. Song, Y. Y. Wang & C. C. Wan. Review of gel-type polymer electrolytes for lithium-ion batteries. *J. Power Sources* **1999,** *77*, 183-197.

(2) W. H. Meyer. Polymer Electrolytes for Lithium-Ion Batteries. *Adv. Mater.* **1998,** *10*, 439-448.

(3) T. Kato, M. Yoshio, T. Ichikawa, B. Soberats, H. Ohno & M. Funahashi. Transport of ions and electrons in nanostructured liquid crystals. *Nat. Rev. Mater.* **2017,** *2*, 17001.

(4) M. Yoshio & T. Kato, Liquid Crystals as Ion Conductors. In *Handbook of Liquid Crystals*, Second ed.; J. W. Goodby, P. J. Collings, T. Kato, C. Tschierske, H. Gleeson & P. Raynes, Eds. Wiley-VCH Verlag GmbH & Co. KGaA: **2014**; Vol. 8, pp 727-749.

(5) T. Kato, N. Mizoshita & K. Kishimoto. Functional liquid-crystalline assemblies: Self-organized soft materials. *Angew. Chem. Int. Ed.* **2006,** *45*, 38-68.

(6) T. Kato. Self-Assembly of Phase-Segregated Liquid Crystal Structures. *Science* **2002,** *295*, 2414-2418.

(7) T. Kato. From Nanostructured Liquid Crystals to Polymer-Based Electrolytes. *Angew. Chem. Int. Ed.* **2010,** *49*, 7847-7848.

(8) T. Kato, T. Yasuda, Y. Kamikawa & M. Yoshio. Self-assembly of functional columnar liquid crystals. *Chem. Commun.* **2009**, 729-739.

(9) Y. Iinuma, K. Kishimoto, Y. Sagara, M. Yoshio, T. Mukai, I. Kobayashi, H. Ohno & T. Kato. Uniaxially Parallel Alignment of a Smectic A Liquid-Crystalline Rod−Coil Molecule and Its Lithium Salt Complexes Using Rubbed Polyimides. *Macromolecules* **2007,** *40*, 4874-4878.

(10) M. Yoshio, T. Kagata, K. Hoshino, T. Mukai, H. Ohno & T. Kato. One-Dimensional Ion-Conductive Polymer Films: Alignment and Fixation of Ionic Channels Formed by Self-Organization of Polymerizable Columnar Liquid Crystals. *J. Am. Chem. Soc.* **2006,** *128*, 5570-5577.

(11) H. Shimura, M. Yoshio, A. Hamasaki, T. Mukai, H. Ohno & T. Kato. Electric-Field-Responsive Lithium-Ion Conductors of Propylenecarbonate-Based Columnar Liquid Crystals. *Adv. Mater.* **2009,** *21*, 1591-1594.

(12) X. Feng, M. E. Tousley, M. G. Cowan, B. R. Wiesenauer, S. Nejati, Y. Choo, R. D. Noble, M. Elimelech, D. L. Gin & C. O. Osuji. Scalable Fabrication of Polymer Membranes with Vertically Aligned 1 nm Pores by Magnetic Field Directed Self-Assembly. *ACS Nano* **2014,** *8*, 11977-11986.

(13) X. Feng, S. Nejati, M. G. Cowan, M. E. Tousley, B. R. Wiesenauer, R. D. Noble, M. Elimelech, D. L. Gin & C. O. Osuji. Thin Polymer Films with Continuous Vertically Aligned 1 nm Pores Fabricated by Soft Confinement. *ACS Nano* **2016,** *10*, 150-158.

(14) B. Soberats, E. Uchida, M. Yoshio, J. Kagimoto, H. Ohno & T. Kato. Macroscopic Photocontrol of Ion-Transporting Pathways of a Nanostructured Imidazolium-Based Photoresponsive Liquid Crystal. *J. Am. Chem. Soc.* **2014,** *136*, 9552-9555.

(15) K. Goossens, K. Lava, C. W. Bielawski & K. Binnemans. Ionic Liquid Crystals: Versatile Materials. *Chem. Rev.* **2016,** *116*, 4643-4807.

(16) J. Sakuda, M. Yoshio, T. Ichikawa, H. Ohno & T. Kato. 2D assemblies of ionic liquid crystals based on imidazolium moieties: formation of ion-conductive layers. *New. J. Chem.* **2015,** *39*, 4471-4477.

(17) F. Xu, K. Matsumoto & R. Hagiwara. Effects of Alkyl Chain Length on Properties of 1-Alkyl-3-methylimidazolium Fluorohydrogenate Ionic Liquid Crystals. *Chem. Eur. J.* **2010,** *16*, 12970-12976.

(18) Y. Uchida, T. Matsumoto, T. Akita & N. Nishiyama. Ion conductive properties in ionic liquid crystalline phases confined in a porous membrane. *J. Mater. Chem. C* **2015,** *3*, 6144-6147.

(19) M. Yoshio, T. Mukai, K. Kanie, M. Yoshizawa, H. Ohno & T. Kato. Liquid-Crystalline Assemblies Containing Ionic Liquids: An Approach to Anisotropic Ionic Materials. *Chem. Lett.* **2002,** *31*, 320-321.

(20) M. Yoshio, T. Mukai, H. Ohno & T. Kato. One-Dimensional Ion Transport in Self-Organized Columnar Ionic Liquids. *J. Am. Chem. Soc.* **2004,** *126*, 994-995.

(21) Y. Masafumi, I. Takahiro, S. Harutoki, K. Takayoshi, H. Atsushi, M. Tomohiro, O. Hiroyuki & K. Takashi. Columnar Liquid-Crystalline Imidazolium Salts. Effects of Anions and Cations on Mesomorphic Properties and Ionic Conductivities. *Bull. Chem. Soc. Jpn.* **2007,** *80*, 1836-1841.

(22) T. Ichikawa, M. Yoshio, A. Hamasaki, T. Mukai, H. Ohno & T. Kato. Self-Organization of Room-Temperature Ionic Liquids Exhibiting Liquid-Crystalline Bicontinuous Cubic Phases: Formation of Nano-Ion Channel Networks. *J. Am. Chem. Soc.* **2007,** *129*, 10662-10663.

(23) T. Ichikawa, M. Yoshio, A. Hamasaki, S. Taguchi, F. Liu, X. b. Zeng, G. Ungar, H. Ohno & T. Kato. Induction of Thermotropic Bicontinuous Cubic Phases in Liquid-Crystalline Ammonium and Phosphonium Salts. *J. Am. Chem. Soc.* **2012,** *134*, 2634-2643.

(24) T. Ichikawa, M. Yoshio, A. Hamasaki, J. Kagimoto, H. Ohno & T. Kato. 3D Interconnected Ionic Nano-Channels Formed in Polymer Films: Self-Organization and Polymerization of Thermotropic Bicontinuous Cubic Liquid Crystals. *J. Am. Chem. Soc.* **2011,** *133*, 2163-2169.

(25) K. Hoshino, M. Yoshio, T. Mukai, K. Kishimoto, H. Ohno & T. Kato. Nanostructured ion-conductive films: Layered assembly of a side-chain liquid-crystalline polymer with an imidazolium ionic moiety. *J. Polym. Sci. Part A: Polym. Chem.* **2003,** *41*, 3486-3492.

(26) K. Kimura, T. Suzuki & M. Yokoyama. Photoresponsive ionic conductivity of polymer composite films containing azobenzene liquid crystal. *J. Phys. Chem.* **1990,** *94*, 6090-6093.

(27) K. Kimura, M. Hirao & M. Yokoyama. Synthesis of a crowned azobenzene liquid crystal and its application to thermoresponsive ion-conducting films. *J. Mater. Chem.* **1991,** *1*, 293-294.

(28) H. Tokuhisa, M. Yokoyama & K. Kimura. Photoresponsive Ion-Conducting Behavior of Polysiloxanes Carrying a Crowned Azobenzene Moiety at the Side Chain. *Macromolecules* **1994,** *27*, 1842-1846.

(29) V. Percec, G. Johansson, J. Heck, G. Ungarb & S. V. Battyb. Molecular recognition directed self-assembly of supramolecular cylindrical channel-like architectures from 6,7,9,10,12,13,15,16-octahydro-1,4,7,10,13-pentaoxabenzocyclopentadecen-2-ylmethyl 3,4,5-tris(p-dodecyloxybenzyloxy)benzoate. *J. Chem. Soc., Perkin Trans. 1* **1993**, 1411-1420.

(30) V. Percec, J. A. Heck, D. Tomazos & G. Ungar. The influence of the complexation of sodium and lithium triflate on the self-assembly of tubular-supramolecular architectures displaying a columnar mesophase based on taper-shaped monoesters of oligoethylene oxide with 3,4,5-tris[p-(n-dodecan-1-yloxy)benzyloxy]benzoic acid and of their polymethacrylates. *J. Chem. Soc., Perkin Trans. 2* **1993**, 2381-2388.

(31) T. Ohtake, K. Ito, N. Nishina, H. Kihara, H. Ohno & T. Kato. Liquid-Crystalline Complexes of a Lithium Salt with Twin Oligomers Containing Oxyethylene Spacers. An Approach to Anisotropic Ion Conduction. *Polym. J.* **1999,** *31*, 1155-1158.

(32) T. Ohtake, M. Ogasawara, K. Ito-Akita, N. Nishina, S. Ujiie, H. Ohno & T. Kato. Liquid-Crystalline Complexes of Mesogenic Dimers Containing Oxyethylene Moieties with LiCF3SO3: Self-Organized Ion Conductive Materials. *Chem. Mater.* **2000,** *12*, 782-789.

(33) T. Ohtake, Y. Takamitsu, K. Ito-Akita, K. Kanie, M. Yoshizawa, T. Mukai, H. Ohno & T. Kato. Liquid-Crystalline Ion-Conductive Materials: Self-Organization Behavior and Ion-Transporting Properties of Mesogenic Dimers Containing Oxyethylene Moieties Complexed with Metal Salts. *Macromolecules* **2000,** *33*, 8109-8111.

(34) B. K. Cho, A. Jain, S. M. Gruner & U. Wiesner. Mesophase Structure-Mechanical and Ionic Transport Correlations in Extended Amphiphilic Dendrons. *Science* **2004,** *305*, 1598-1601.

(35) B. K. Cho. Spontaneous bulk organization of molecular assemblers based on aliphatic polyether and/or poly(benzyl ether) dendrons. *Polym. J.* **2012,** *44*, 475-489.

(36) J. W. Choi & B. K. Cho. Degree of chain branching-dependent assemblies and conducting behavior in ionic liquid crystalline Janus dendrimers. *Soft Matter* **2011,** *7*, 4045-4049.

(37) J. Sakuda, E. Hosono, M. Yoshio, T. Ichikawa, T. Matsumoto, H. Ohno, H. Zhou & T. Kato. Liquid-Crystalline Electrolytes for Lithium-Ion Batteries: Ordered Assemblies of a

Mesogen-Containing Carbonate and a Lithium Salt. *Adv. Funct. Mater.* **2015,** *25*, 1206-1212.

(38) R. L. Kerr, S. A. Miller, R. K. Shoemaker, B. J. Elliott & D. L. Gin. New Type of Li Ion Conductor with 3D Interconnected Nanopores via Polymerization of a Liquid Organic Electrolyte-Filled Lyotropic Liquid-Crystal Assembly. *J. Am. Chem. Soc.* **2009,** *131*, 15972-15973.

(39) M. Yoshio, T. Mukai, K. Kanie, M. Yoshizawa, H. Ohno & T. Kato. Layered Ionic Liquids: Anisotropic Ion Conduction in New Self-Organized Liquid-Crystalline Materials. *Adv. Mater.* **2002,** *14*, 351-354.

(40) A. Yamashita, M. Yoshio, B. Soberats, H. Ohno & T. Kato. Use of a protic salt for the formation of liquid-crystalline proton-conductive complexes with mesomorphic diols. *J. Mater. Chem. A* **2015,** *3*, 22656-22662.

(41) H. Shimura, M. Yoshio, K. Hoshino, T. Mukai, H. Ohno & T. Kato. Noncovalent Approach to One-Dimensional Ion Conductors: Enhancement of Ionic Conductivities in Nanostructured Columnar Liquid Crystals. *J. Am. Chem. Soc.* **2008,** *130*, 1759-1765.

(42) A. Yamashita, M. Yoshio, S. Shimizu, T. Ichikawa, H. Ohno & T. Kato. Columnar nanostructured polymer films containing ionic liquids in supramolecular one-dimensional nanochannels. *J. Polym. Sci. Part A: Polym. Chem.* **2015,** *53*, 366-371.

(43) D. Högberg, B. Soberats, S. Uchida, M. Yoshio, L. Kloo, H. Segawa & T. Kato. Nanostructured Two-Component Liquid-Crystalline Electrolytes for High-Temperature Dye-Sensitized Solar Cells. *Chem. Mater.* **2014,** *26*, 6496-6502.

(44) D. Högberg, B. Soberats, R. Yatagai, S. Uchida, M. Yoshio, L. Kloo, H. Segawa & T. Kato. Liquid-Crystalline Dye-Sensitized Solar Cells: Design of Two-Dimensional Molecular Assemblies for Efficient Ion Transport and Thermal Stability. *Chem. Mater.* **2016,** *28*, 6493-6500.

(45) D. Högberg, B. Soberats, M. Yoshio, Y. Mizumura, S. Uchida, L. Kloo, H. Segawa & T. Kato. Self-Assembled Liquid-Crystalline Ion Conductors in Dye-Sensitized Solar Cells: Effects of Molecular Sensitizers on Their Performance. *ChemPlusChem* **2017,** *82*, 834-840.

(46) S. Hernández-Ainsa, M. Marcos & J. L. Serrano, Dendrimeric and Hyperbranched Liquid Crystal Structures. In *Handbook of Liquid Crystals*, Second ed.; J. W. Goodby, P. J. Collings, T. Kato, C. Tschierske, H. Gleeson & P. Raynes, Eds. Wiley-VCH Verlag GmbH & Co. KGaA: **2014**; Vol. 7, pp 259-300.

(47) B. M. Rosen, C. J. Wilson, D. A. Wilson, M. Peterca, M. R. Imam & V. Percec. Dendron-Mediated Self-Assembly, Disassembly, and Self-Organization of Complex Systems. *Chem. Rev.* **2009,** *109*, 6275-6540.

(48) M. Marcos, R. Martín-Rapún, A. Omenat & J. L. Serrano. Highly congested liquid crystal structures: dendrimers, dendrons, dendronized and hyperbranched polymers. *Chem. Soc. Rev.* **2007,** *36*, 1889-1901.

(49) J. Barberá, B. Donnio, L. Gehringer, D. Guillon, M. Marcos, A. Omenat & J. L. Serrano. Self-organization of nanostructured functional dendrimers. *J. Mater. Chem.* **2005,** *15*, 4093-4105.

(50) V. Chechik, M. Zhao & R. M. Crooks. Self-Assembled Inverted Micelles Prepared from a Dendrimer Template: Phase Transfer of Encapsulated Guests. *J. Am. Chem. Soc.* **1999,** *121*, 4910-4911.

(51) S. E. Friberg, M. Podzimek, D. A. Tomalia & D. M. Hedstrand. A Non-Aqueous Lyotropic Liquid Crystal with a Starburst Dendrimer as a Solvent. *Molecular Crystals and Liquid Crystals Incorporating Nonlinear Optics* **1988,** *164*, 157-165.

(52) D. Tsiourvas, T. Felekis, Z. Sideratou & C. M. Paleos. Ionic liquid crystals derived from the protonation of poly(propylene imine) dendrimers with a cholesterol-based carboxylic acid. *Liq. Cryst.* **2004,** *31*, 739-744.

(53) S. Ujiie, Y. Yano & A. Mori. Liquid-Crystalline Branched Polymers having Ionic Moieties. *Mol. Cryst. Liq. Cryst.* **2004,** *411*, 483-489.

(54) R. Martín-Rapún, M. Marcos, A. Omenat, J. Barberá, P. Romero & J. L. Serrano. Ionic Thermotropic Liquid Crystal Dendrimers. *J. Am. Chem. Soc.* **2005,** *127*, 7397-7403.

(55) M. Marcos, R. Martín-Rapún, A. Omenat, J. Barberá & J. L. Serrano. Ionic Liquid Crystal Dendrimers with Mono-, Di- and Trisubstituted Benzoic Acids. *Chem. Mater.* **2006,** *18*, 1206-1212.

(56) S. Hernández-Ainsa, J. Barberá, M. Marcos & J. L. Serrano. Effect of the Phobic Segregation between Fluorinated and Perhydrogenated Chains on the Supramolecular Organization in Ionic Aromatic Dendrimers. *Chem. Mater.* **2010,** *22*, 4762-4768.

(57) S. Hernández-Ainsa, M. Marcos, J. Barberá & J. L. Serrano. Philic and Phobic Segregation in Liquid-Crystal Ionic Dendrimers: An Enthalpy–Entropy Competition. *Angew. Chem. Int. Ed.* **2010,** *49*, 1990-1994.

(58) M. Marcos, R. Alcalá, J. Barberá, P. Romero, C. Sánchez & J. L. Serrano. Photosensitive ionic nematic liquid crystalline complexes based on dendrimers and hyperbranched polymers and a cyanoazobenzene carboxylic acid. *Chem. Mater.* **2008,** *20*, 5209-5217.

(59) S. Hernández-Ainsa, R. Alcalá, J. Barberá, M. Marcos, C. Sánchez & J. L. Serrano. Ionic azo-codendrimers: influence of the acids contents in the liquid crystalline properties and the photoinduced optical anisotropy. *Eur. Polym. J.* **2011,** *47*, 311-318.

(60) S. Hernández-Ainsa, R. Alcalá, J. Barberá, M. Marcos, C. Sánchez & J. L. Serrano. Ionic photoresponsive azo-codendrimer with room temperature mesomorphism and high photoinduced optical anisotropy. *Macromolecules* **2010,** *43*, 2660-2663.

(61) S. Hernández-Ainsa, J. Barberá, M. Marcos & J. L. Serrano. Liquid Crystalline Ionic Dendrimers Containing Luminescent Oxadiazole Moieties. *Macromolecules* **2012,** *45*, 1006-1015.

(62) J. Vergara, N. Gimeno, M. Cano, J. Barberá, P. Romero, J. L. Serrano & M. B. Ros. Mesomorphism from Bent-Core Based Ionic Dendritic Macromolecules. *Chem. Mater.* **2011,** *23*, 4931-4940.

(63) M. Cano, A. Sánchez-Ferrer, J. L. Serrano, N. Gimeno & M. B. Ros. Supramolecular Architectures from Bent-Core Dendritic Molecules. *Angew. Chem. Int. Ed.* **2014,** *53*, 13449-13453.

(64) S. Castelar, P. Romero, J. L. Serrano, J. Barberá & M. Marcos. Multifunctional ionic hybrid poly(propyleneimine) dendrimers surrounded by carbazole dendrons: liquid crystals, optical and electrochemical properties. *RSC Adv.* **2015,** *5*, 65932-65941.

(65) A. Trajkovska, C. Kim, K. L. Marshall, T. H. Mourey & S. H. Chen. Photoalignment of a Nematic Liquid Crystal Fluid and Glassy−Nematic Oligofluorenes on Coumarin-Containing Polymer Films. *Macromolecules* **2006,** *39*, 6983-6989.

(66) M. V. S. N. Maddipatla, D. Wehrung, C. Tang, W. Fan, M. O. Oyewumi, T. Miyoshi & A. Joy. Photoresponsive Coumarin Polyesters That Exhibit Cross-Linking and Chain Scission Properties. *Macromolecules* **2013,** *46*, 5133-5140.

(67) K. Kishimoto, M. Yoshio, T. Mukai, M. Yoshizawa, H. Ohno & T. Kato. Nanostructured Anisotropic Ion-Conductive Films. *J. Am. Chem. Soc.* **2003,** *125*, 3196-3197.

Chapter 3

Nanoporous Materials Based on Supramolecular Liquid Crystal Dendrimers

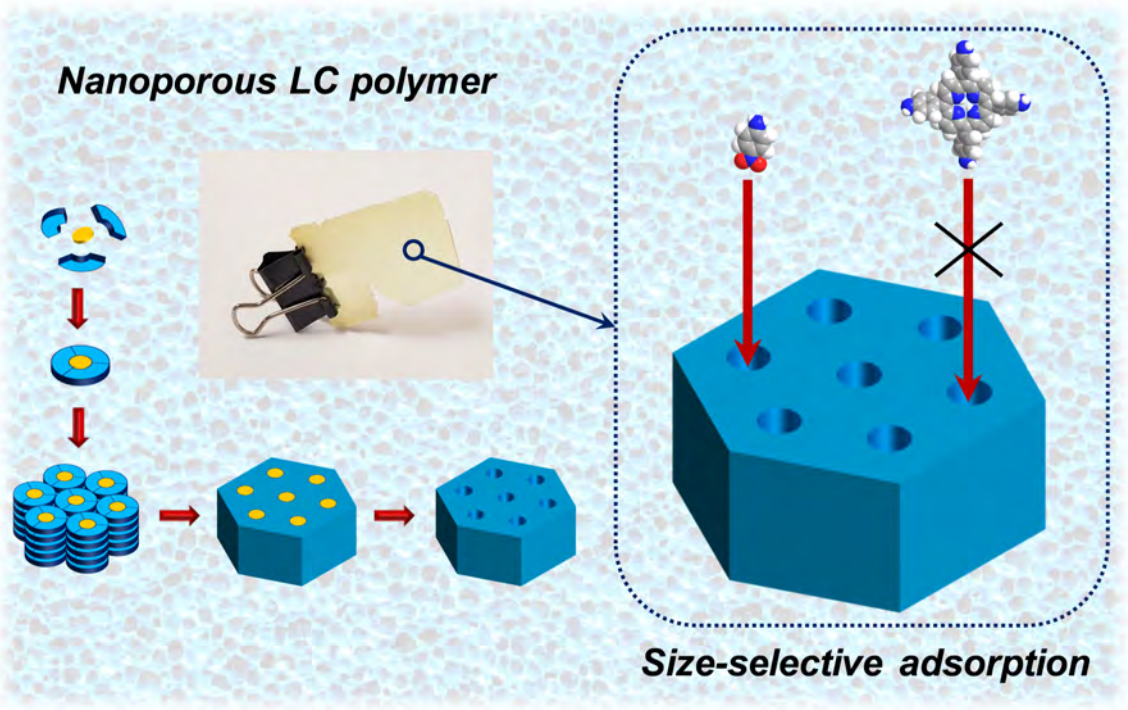

Abstract. *We report an easy and versatile method to obtain nanostructured porous materials by using hydrogen-bonded columnar LC dendrimers, whose order is fixed by coumarin photodimerization. The obtained nanoporous materials show remarkable size selectivity in adsorption experiments because our strategy allows us to control the size of the pores and, consequently, the adsorption selectivity of the obtained polymers. Moreover, the obtained nanoporous polymers are highly versatile because their adsorption selectivity can be tuned on demand by in situ chemical treatment of the polymer films.*

“Above all, don’t fear difficult moments.
The best comes from them.”

Rita Levi-Montalcini

1. INTRODUCTION

1.1 Nanoporous Materials

Nanoporous materials, with a pore size of 100 nm or smaller, have attracted considerable attention due to their commercial use in areas such as filtration, separation, catalysis and drug delivery. The nanosized pores permit the discrimination between molecules and ions based on size and shape. Mimicking biological cell membranes, material scientists have prepared different nanoporous materials mostly based on inorganic systems such as silica, zeolites and metals.[1-4] However, the use of organic polymeric materials, which are much easier to modify and tune for specific applications, has been less often considered.[5-7] Among polymeric materials, those derived from the microphase separation of block copolymers have been broadly exploited. It is well known that diblock copolymers are able to undergo microphase separation in the solid state leading to different morphologies such as spheres, cylinders, and lamellaes.[8, 9] Nanopores can be created by removing one of these blocks.[10, 11] However, this strategy results in a variety of pore shapes and sizes ranging from 5 to 50 nm.[12]

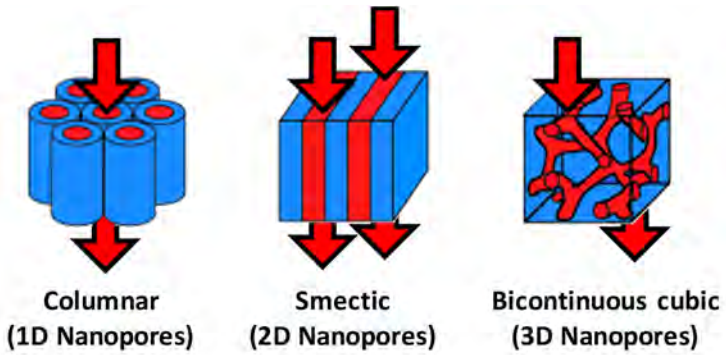

Figure 1.1 Nanoporous materials with different geometries prepared by different LC phases.

In an attempt to create smaller pore dimensions, many groups have started to investigate the use of polymerizable supramolecular liquid crystals (LCs) to prepare porous materials with pore sizes of around 1 nm.[13-15] LC mesophases can be fixed into a polymer network by using reactive LCs that can be (photo)polymerized. Both lyotropic and thermotropic LCs have been used for the preparation of nanoporous materials. The morphology of the nanopores can be controlled by the careful choice of the mesophase (**Figure 1.1**). Two-dimensional (2D) morphologies with pores in the directions within the layer plane can be obtained by using smectic LCs.

Columnar mesophases can be used to create one-dimensional (1D) pores in the direction of the columnar axes. Lyotropic LCs in the bicontinuous cubic mesophase have been used for the preparation of polymer networks with three-dimensional (3D) interwoven nanopores.

This introduction will be focus on the most significant developments in the field of nanoporous polymers based on thermotropic LCs.

1.1.1 Columnar Mesophases (1D Pores)

The first nanoporous material containing 1D pores was described by Kim and coworkers.[16] It consisted of a benzotri(imidazole) template connected by hydrogen bonding with three polymerizable trialkoxybenzoic acid acrylates (**Figure 1.2**). This hydrogen-bonded complex displayed a hexagonal columnar phase which was locked by photopolymerization to obtain a polymer network. In order to remove the template, this polymer network was extracted with acidified methanol to break the hydrogen bonds. Preliminary gas-permeability measurements demonstrated the porous nature of the prepared material.

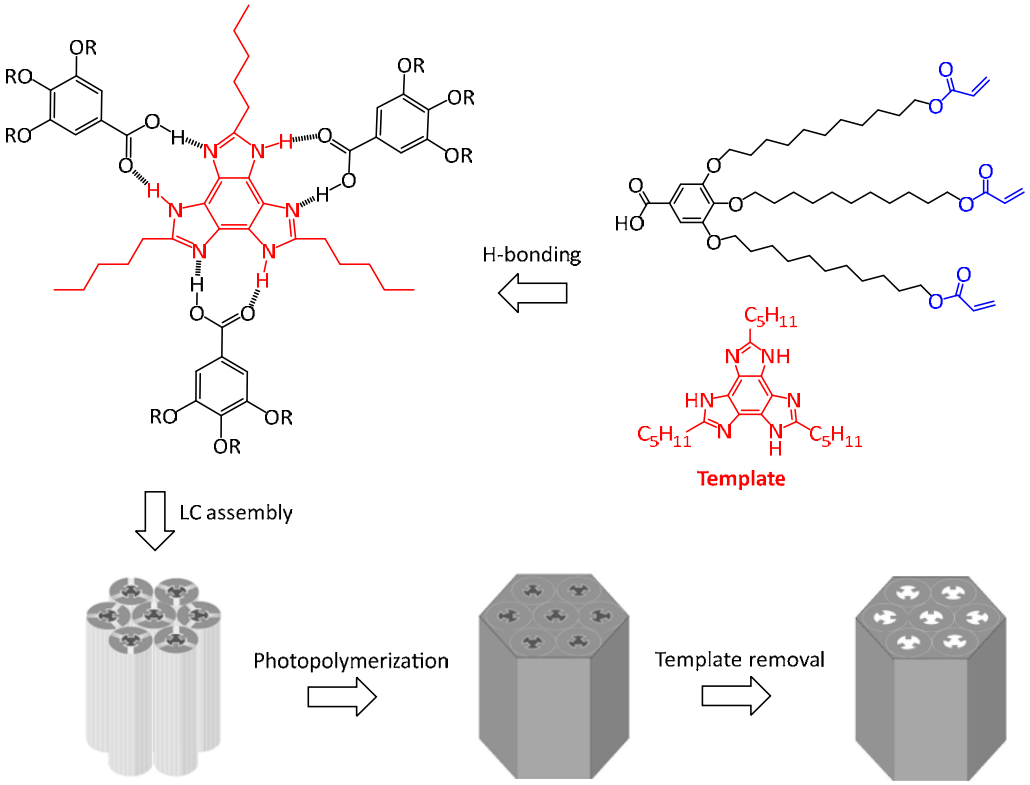

Figure 1.2 Schematic representation of the procedure for the fabrication of nanoporous materials. (Adapted from reference 16)

Ishida *et al.* prepared nanoporous polymers by using the same benzoic acid derivative and chiral amino alcohols as templates (**Figure 1.3**).[17, 18] Polymer networks with helical pores were obtained after photopolymerization of the chiral columnar structure and subsequent template removal. Different dyes and salts were adsorbed by the obtained nanoporous material.[19]

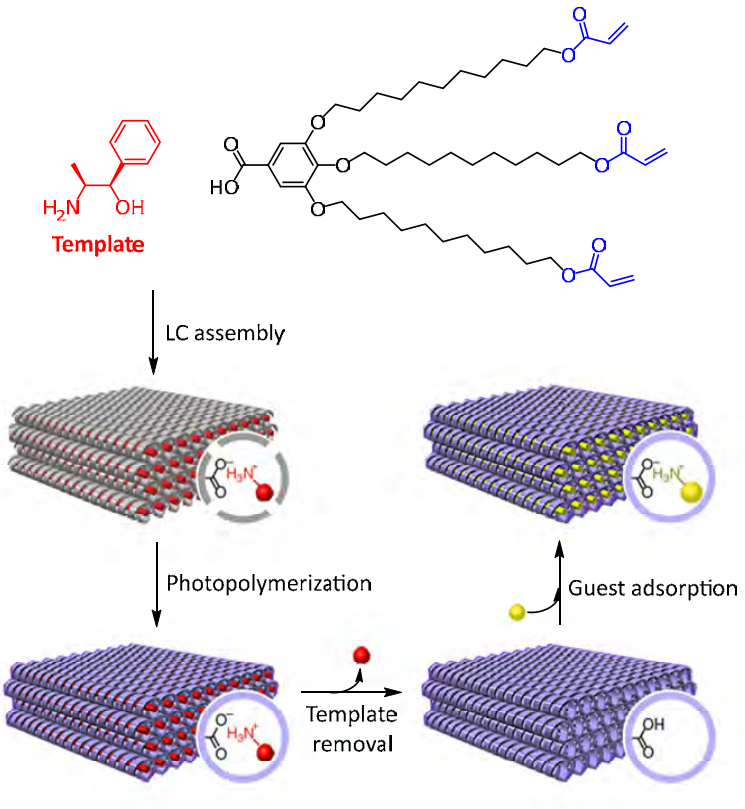

Figure 1.3 Preparation of nanoporous polymers with helical pores. (Adapted from reference 19)

Sijbesma's research group followed a similar template approach to prepare the 1D nanoporous materials based on a hydrogen-bonded complex of tris(benzimidazolyl)benzene and three gallic acid derivatives. The system was crosslinked using an acyclic diene metathesis reaction. Subsequent template removal resulted in a porous material which was able to selectively bind sodium and potassium cations from aqueous solution.[20]

By also using tris(benzimidazolyl)benzene as template and natural unsaturated fatty acids, Osuji and coworkers reported on the preparation of nanoporous polymers with a pore diameter of 12–15 Å (**Figure 1.4**). After template removal with base treatment, anionic pores, used to adsorb a variety of dyes, were obtained. Only cationic dyes smaller than 18 Å were adsorbed, demonstrating size and charge selectivity of the prepared nanoporous materials.[21]

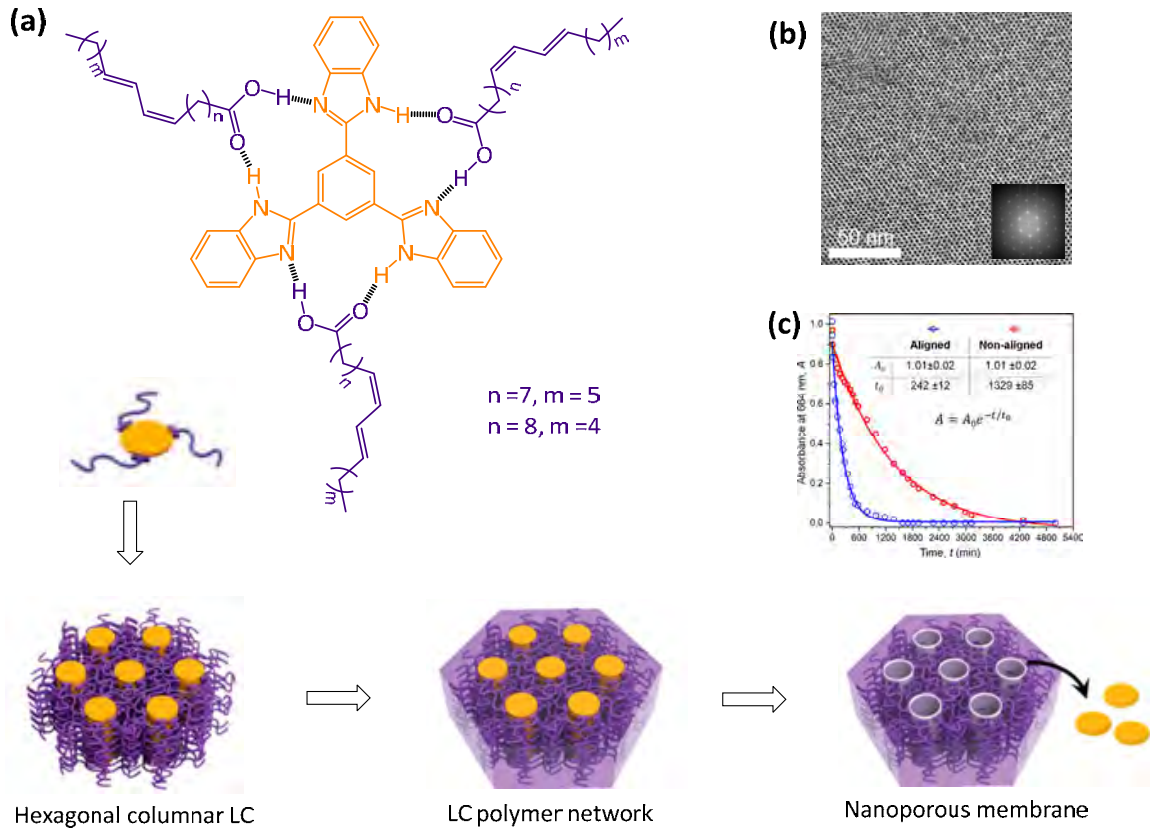

Figure 1.4 (a) Schematic representation of the fabrication of nanoporous polymers from renewable natural fatty acids. **(b)** TEM micrograph of a sectioned nanoporous polymer showing the hexagonal morphology (Inset: Fourier transform image). **(c)** UV-Vis absorbance of methylene blue solutions as a function of time during adsorption into aligned and nonaligned nanoporous polymers. (Adapted from reference 21)

In the previous examples, the hydrogen bonds were formed between a core molecule and polymerizable carboxylic acids obtaining polymers with all the pores functionalized with carboxylic acids or carboxylate groups. Alternatively, Lee *et al.* described the preparation of nanoporous materials with pyridine groups at the pore surface.[22] In a similar way, our research group published hexagonal columnar hydrogen-bonded complexes which were used for the preparation of nanoporous materials. They consisted of a tricarboxylic acid acting as the template and three peripherial promesogenic units containing acetamidopyridine moieties (**Figure 1.5**).[23] Nanoporous polymers with basic functionalities at the pore surface were prepared after crosslinking by thiol-ene UV-initiated 'click' reaction and subsequent elimination of the template. These nanopores were able to adsorb certain acid dyes and also acted as molds for the synthesis of silver nanoparticles with controlled sizes.

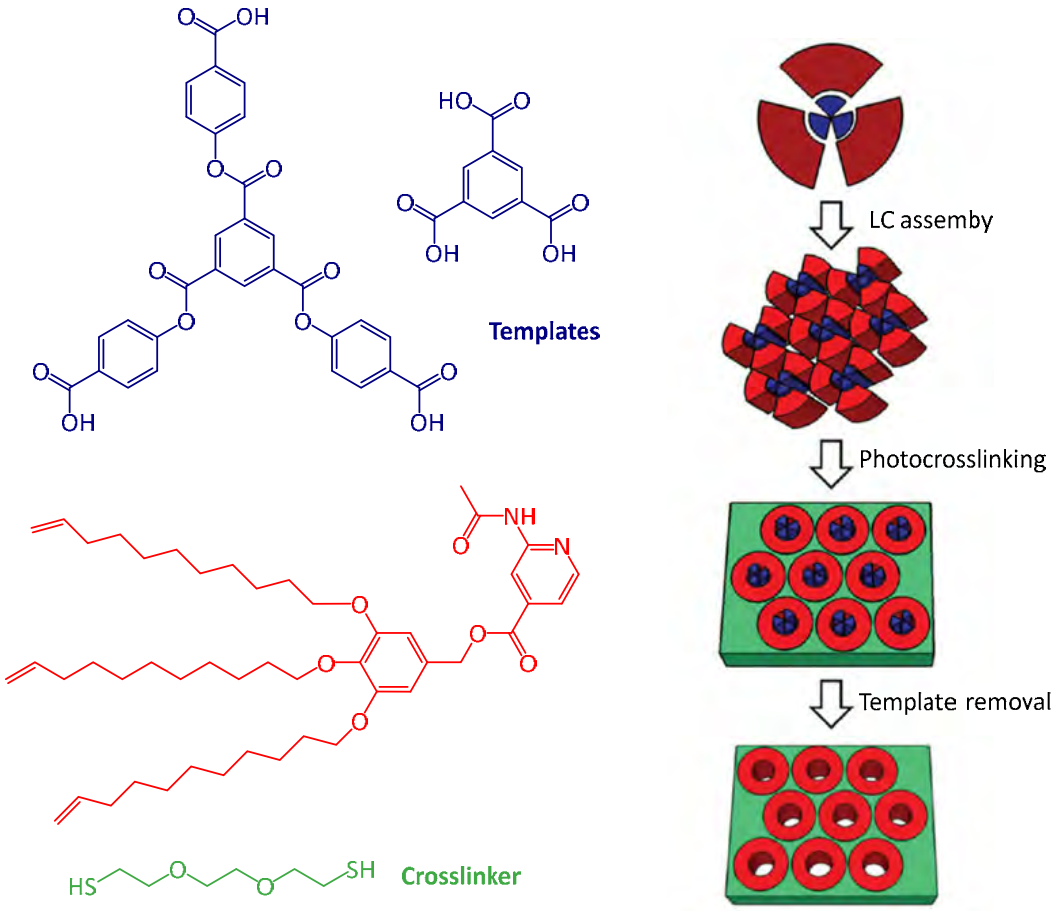

Figure 1.5 Preparation of nanoporous polymers using thiol-ene 'click' chemistry. (Adapted from reference 23)

Nonetheless, other approaches have been developed for the preparation of nanoporous materials without removing the template. Percec's research group reported a cone-shaped dendron containing a dipeptide that self-assembles in nanometer-sized hollow columns that were used as ion channels.[24] Similarly, Kato and coworkers reported a rosette-like structure formed by hydrogen-bonded folates that exhibits cation transporting properties based on tunneling through the supramolecular macrocycles.[25]

Despite the promising properties of columnar nanoporous polymers, columnar mesophases still suffer from the disadvantage that orientationally uniform domains are often hard to obtain. The columns must be aligned homeotropically (perpendicular to the surface) in the initial mesophase as any deviation would result in deactivation of the pores. Thus, the highly aligned polymer films were prepared with the help of surface treatments[26] or using a magnetic field (**Figure 1.6**).[19, 21, 27, 28]

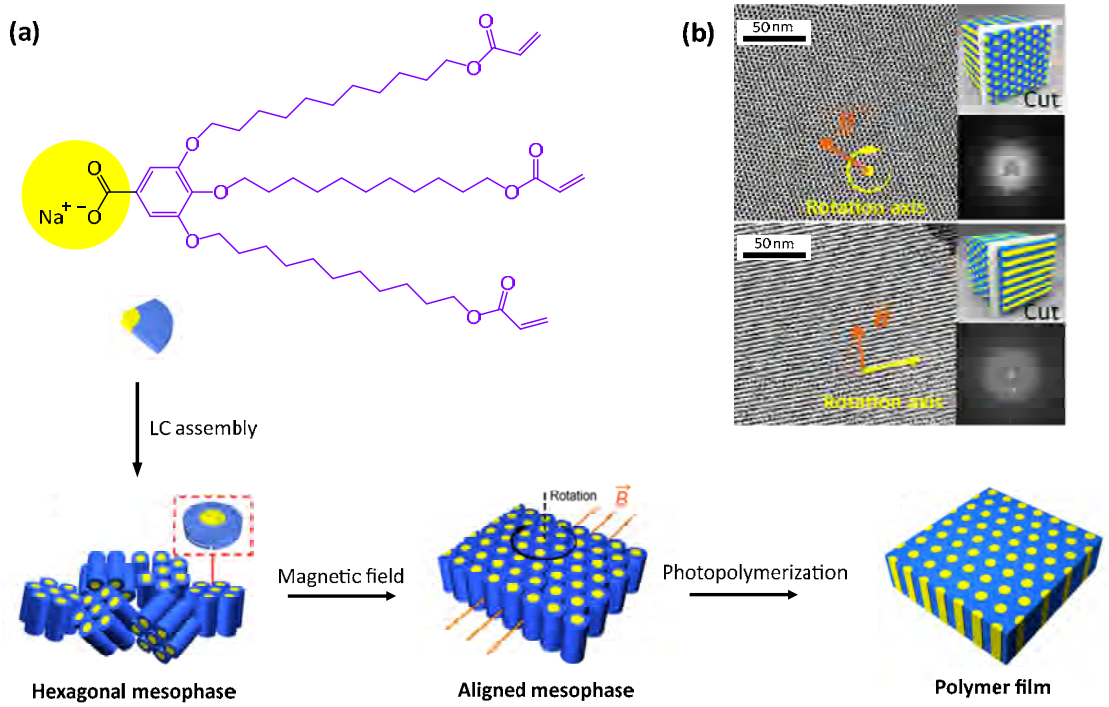

Figure 1.6 (a) Schematic representation of the alignment of a hexagonal columnar mesophase in a magnetic field. **(b)** TEM images of the aligned films microtomed perpendicular (top) or parallel (bottom) parallel to the rotation axis. (Adapted from reference 27)

1.1.2 Smectic Mesophases (2D Pores)

Smectic LCs have often been used for the preparation of 2D nanoporous polymers. However, it is not possible to use the same approach as the one applied in columnar LCs because the polymerized regions, that are not covalently connected to each other, are squashed after removal of the template. To solve this problem, Kishikawa *et al.* developed a new methodology to prepare lamellar nanoporous polymers (**Figure 1.7**).[29] This approach involved introducing "nanopillars" between the layers to avoid squashing after removal of the template. A small fraction of this "nanopillar" was added and this LC mixture was photopolymerized to lock the smectic arrangement into a polymer network. After template removal, nanoporous multilayer structures were obtained. They did not collapse when held, a result of being reinforced by the "nanopillar" units.

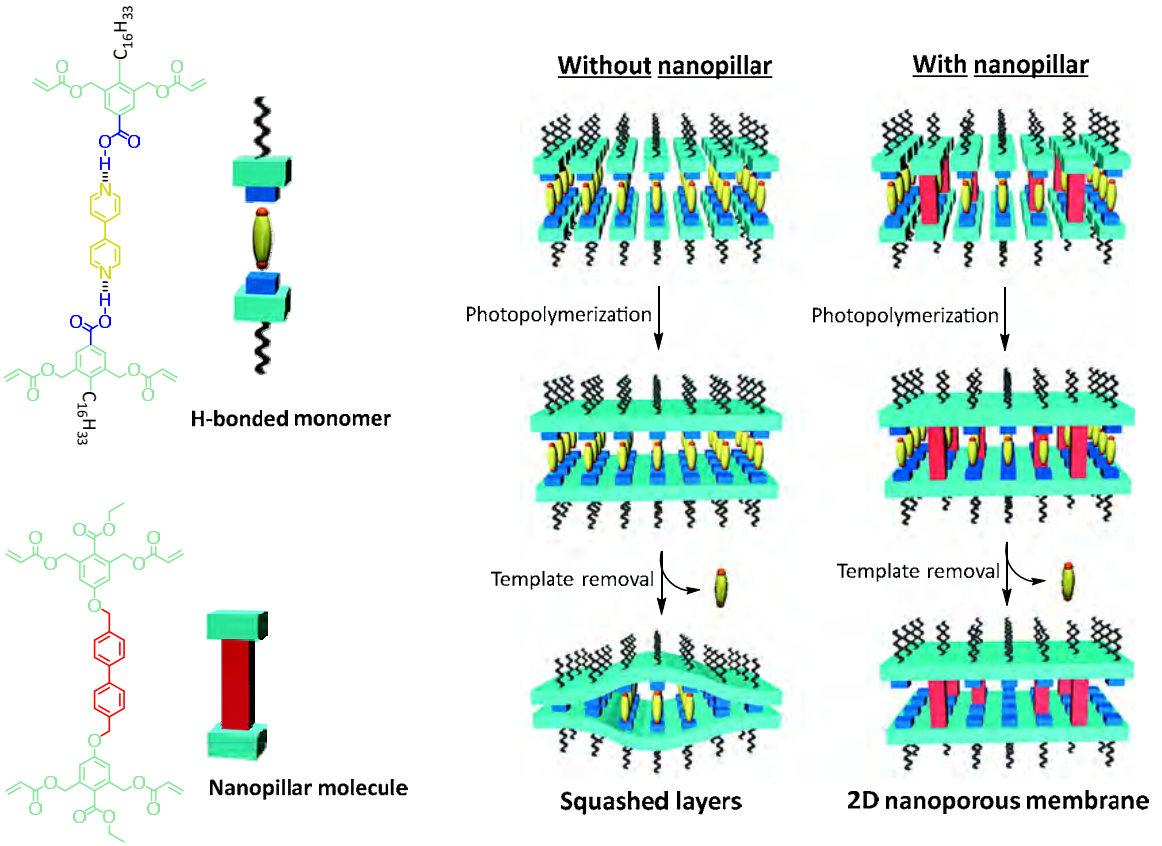

Figure 1.7 Chemical structures of the supramolecular monomer and the nanopillar molecule (left). Schematic representation of the formation of the polymer network with and without nanopillars to obtain 2D nanopores. (Adapted from reference 29)

The same year, Broer and coworkers described a similar approach based on a mixture of two LCs, a hydrogen-bonded dimer and a covalent crosslinker (**Figure 1.8**).[30] A polymer network was created by photopolymerization to lock in the smectic structure. After alkaline treatment of the hydrogen-bonded polymer network, a nanoporous polymer with 2D nanopores was obtained. With this strategy, the nanopores, of approximately 1 nm and with anionic charge, are able to selectively adsorb cationic dyes over anionic and larger cations.[31] Moreover, modification of the crosslinker by introducing a photoresponsive azobenzene unit resulted in a decrease of the smectic layer spacing of the nanoporous network upon UV light exposure. This decrease of the layer spacing led to an alteration of the pore size which permitted control over the adsorption of cations and cationic dyes with light.[32]

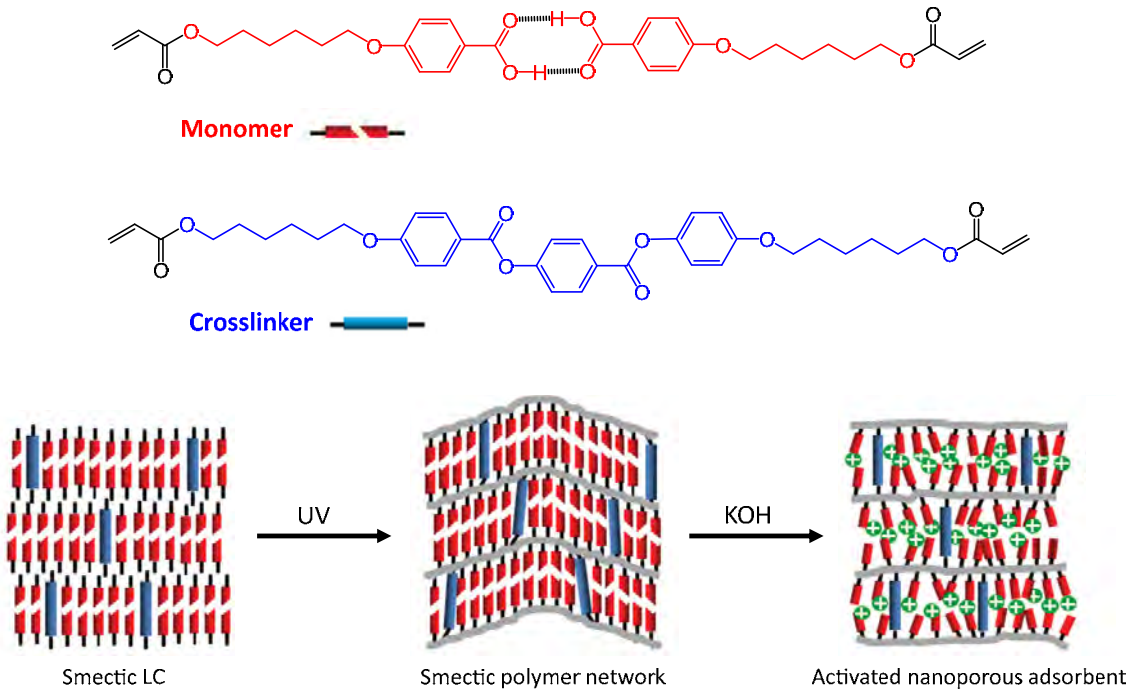

Figure 1.8 Schematic representation of the formation of the nanoporous polymeric material based on smectic LCs. (Adapted from reference 30)

Apart from the selective adsorption of cationic dyes, these smectic nanoporous materials were also used for the synthesis of silver nanoparticles by Schenning's research group.[33, 34] This silver nanoparticles were prepared by filling the nanopores with silver ions which were subsequently reduced with sodium borohydride (**Figure 1.9**). The obtained nanoparticles were almost monodisperse and they concluded that it was possible to control the size of the particles by varying the length of the crosslinker.

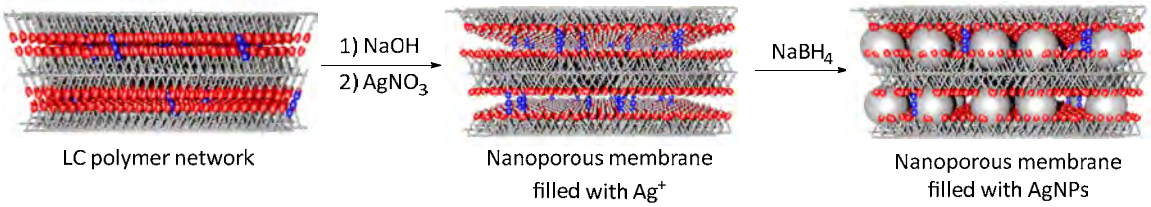

Figure 1.9 Schematic representation for the fabrication of silver nanoparticles (AgNPs) by using nanoporous smectic liquid crystalline polymer networks. (Adapted from reference 33).

Recently, the same research group reported anisotropic anhydrous proton conduction in similar polymer networks.[35] Addition of more crosslinker improved the integrity of the polymer network, resulting in more ordered 2D nanostructures with higher conductivity. Despite exhibiting low proton conductivity values (10^{-7} $S \cdot cm^{-1}$), the polymer films showed anisotropic proton conduction with 54 times

higher conductivity in the direction perpendicular to the molecular director (**Figure 1.10**).

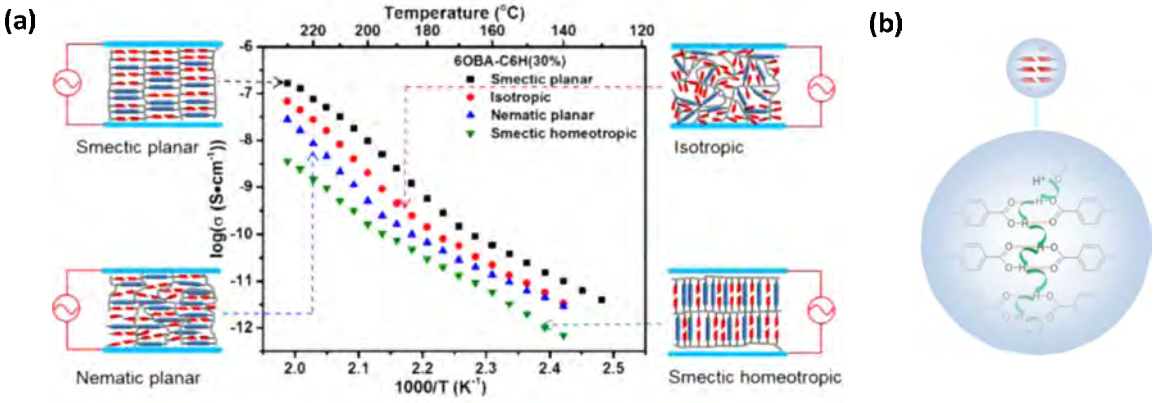

Figure 1.10 (a) Anhydrous proton conductivities as a function of the temperature of the smectic planar, nematic planar, isotropic, and smectic homeotropic polymer films. **(d)** Schematic illustration of the proton transfer pathway in a smectic polymer film. (Adapted from reference 35)

Very recently, Mulder *et al.* developed a new methodology to fabricate and postmodify lamellar nanoporous materials based on dynamic covalent imine chemistry (**Figure 1.11**).[36] The reversibility of the imine bonds made the system appealing as the size and chemical nature of the pore interior could be tuned on demand by *in situ* chemical modification.

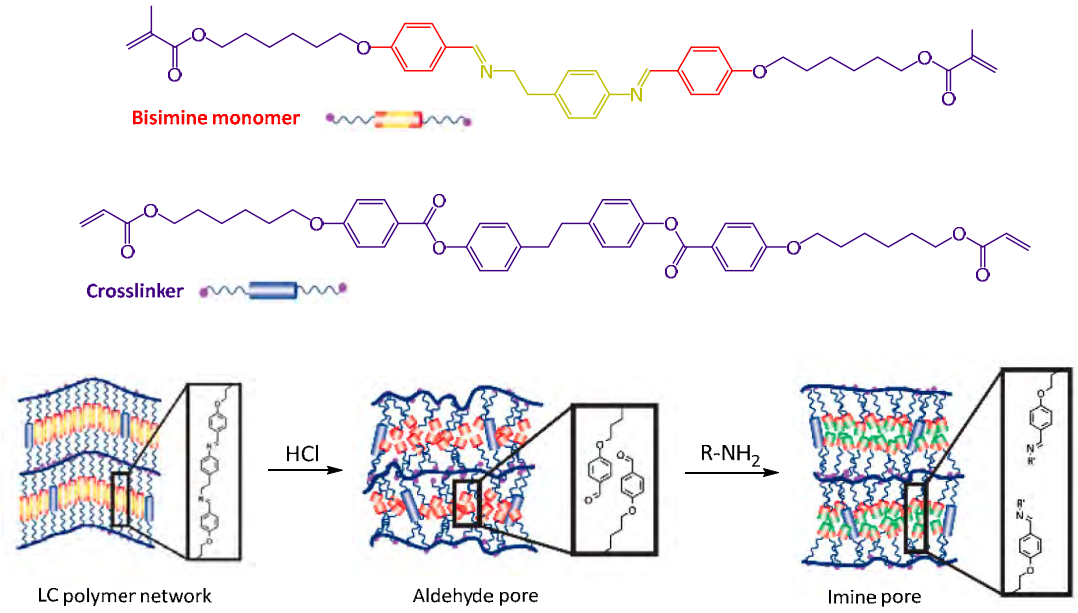

Figure 1.11 Schematic representation of the nanoporous polymer and the chemical modification of its pore interior. (Adapted from reference 36)

1.2 Supramolecular Liquid Crystal Dendrimers

The functionalization of the dendrimer periphery is the most widely used approach for the synthesis of LC dendrimers.[37] However, new LC dendritic structures can also be prepared using a rigid central platform surrounded by several functional dendrons. With this synthetic strategy, two different approaches to new materials have been described. The first one is based on non-covalent interactions, while the second one consists of the preparation of covalently bonded supermolecular structures.

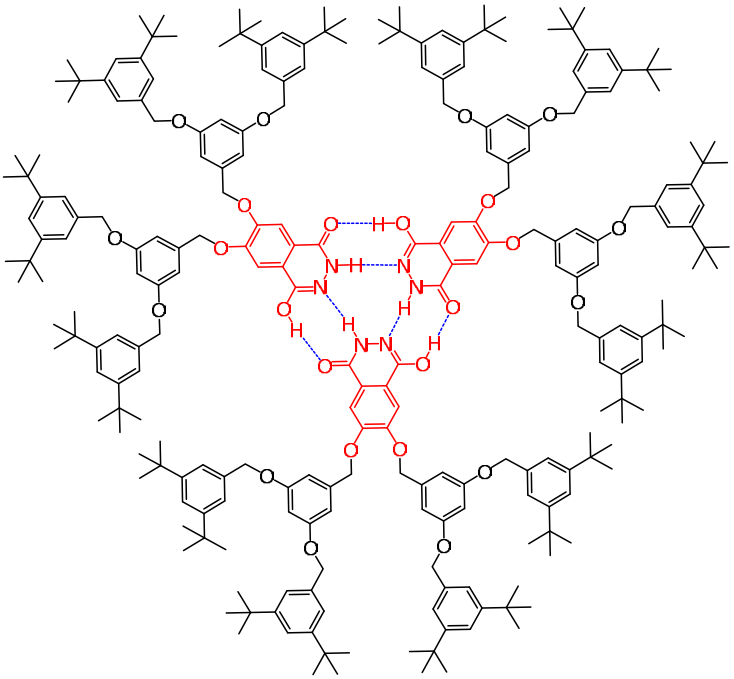

Figure 1.12 First example of hydrogen-bonded dendrimer reported by Lehn and coworkers.

Some examples of the covalent approach have been reported, using central cores complex structures such as polyaromatic scaffolds, macrocycles, and functional fullerene derivatives, among others.[38-42] The adequate functionalization of these platforms results in dendrimers resembling disk-shaped mesogenic molecules which display columnar mesomorphism. However, the larger and more complex structures still require major synthetic efforts and this is often plagued by low yields and high polydispersity. The second strategy is based on supramolecular chemistry, which allows the preparation of dendrimers by a self-assembly process based on non-covalent interactions, such as hydrogen bonding interactions or electrostatic interactions (**Figure 1.12**).[43, 44]

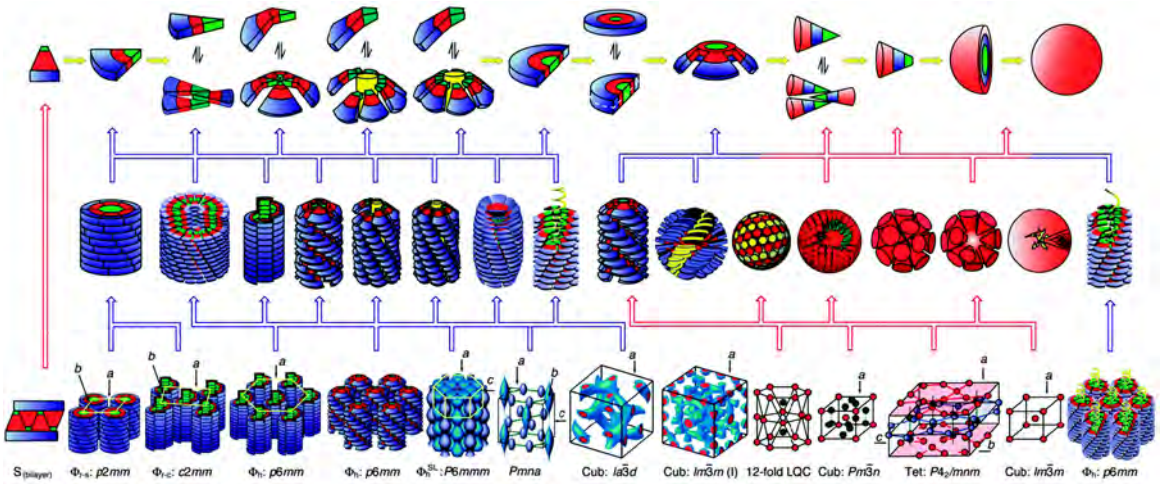

Figure 1.13 LC arrangements formed *via* self-assembly and self-organization of Percec-type dendrons. (Adapted from reference 46)

Percec and coworkers have investigated the self-assembly of structurally perfect dendrons with pre-programmed shapes into supramolecular cylindrical and spherical dendrimers, which then self-organize into various LC mesophases (**Figure 1.13**).[45, 46] The novelty of this approach relies on the simplicity of the molecular geometry and the versatility of the structural modification.

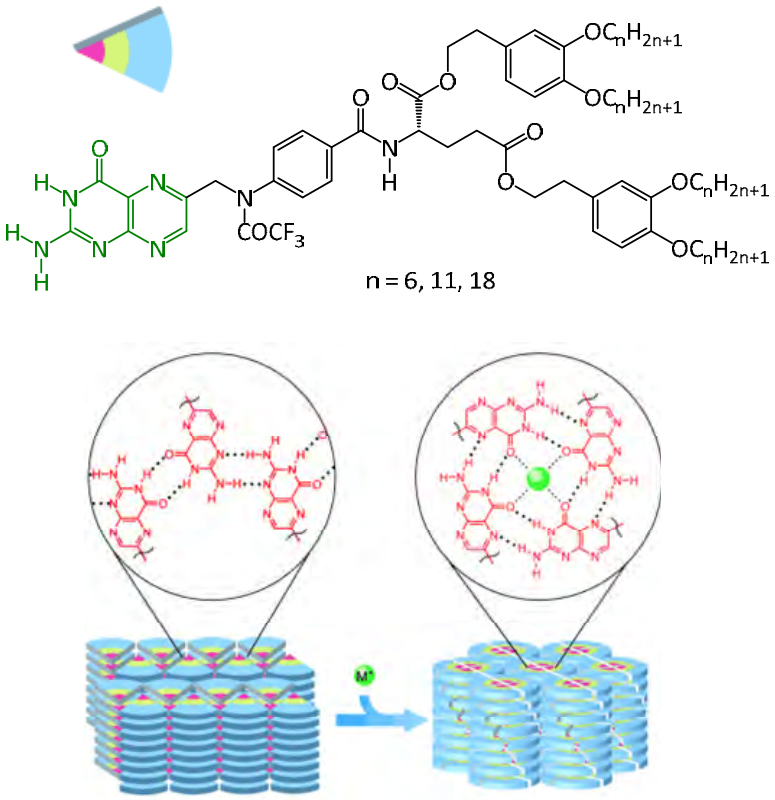

Figure 1.14 Structural changes of supramolecular LC dendrimers based on folic acid derivatives. (Adapted from reference 47)

Kato's research group reported dendrons containing folic acid derivatives in their apexes capable of self-organizing into a smectic LC phases.[47, 48] Addition of alkali metals as templates produced rosette tetrameric structures which exhibited hexagonal columnar phases (**Figure 1.14**).

Kishikawa *et al.* reported urea-containing dendrons which self-organized in columnar LC phases *via* hydrogen bonding between the urea moieties.[49] Aida and coworkers developed fan-shaped dendrons having amide groups in proximity to the polar phthalonitrile core (**Figure 1.15**).[50-52] These dendrons self-assembled into columnar LC phases, with the phtalonitrile moieties pointing undirectionally along the columnar axis, and stabilized by hydrogen bonding of the amides. Lehmann *et al.* also reported supramolecular hexagonal columnar LC dendrimers based on oligo(phenylenevinylene) as their central core.[53] The pyridyl groups in the three cavities served as binding sites for polycatenar dendrons through hydrogen bonding.

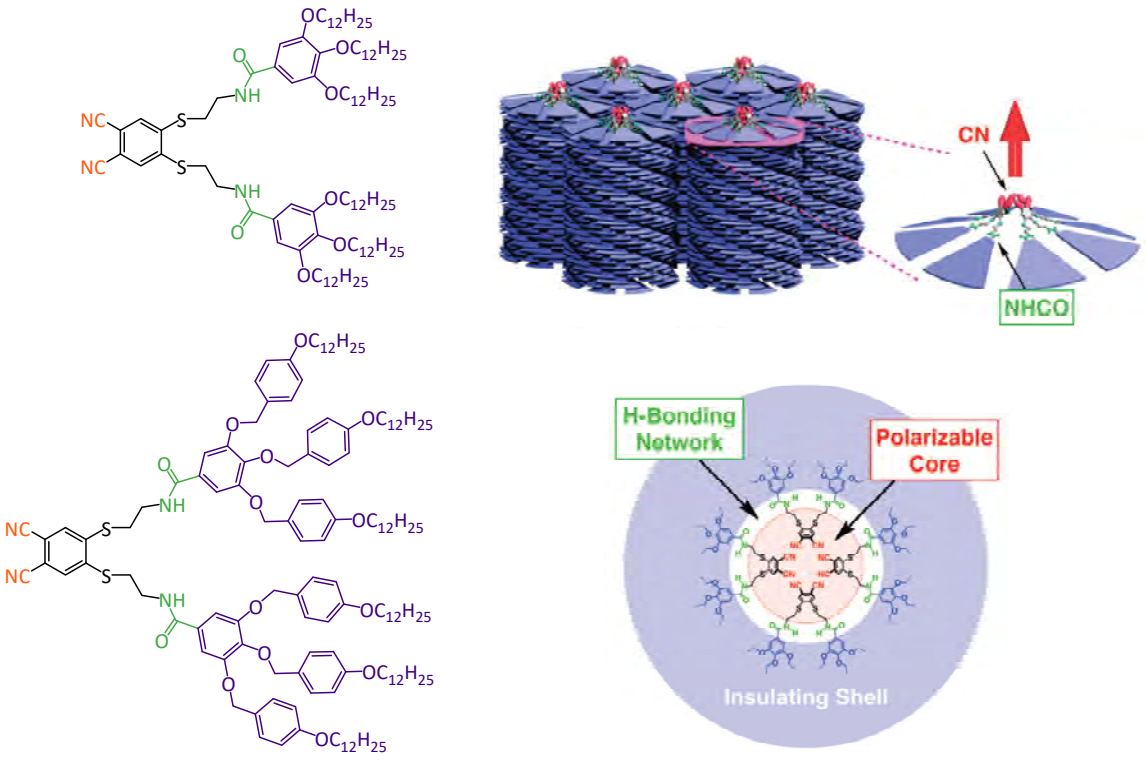

Figure 1.15 Chemical structure of phtalonitrile-based columnar LC dendrimers and their arrangement in the hexagonal columnar phase. (Adapted from reference 51)

Our research group developed supramolecular dendritic structures by using a melamine derivative capable of forming hydrogen-bonded complexes with Percec-

type and V-shaped dendrons. All the complexes displayed hexagonal columnar phases.[54, 55] However, different columnar arrangements were obtained depending on the ratio between the central core and the peripheral dendrons.[56, 57] So far, columnar LC dendrimers based on hydrogen bonding interactions between a tris(triazolyl)triazine derivative and three Percec-type dendrons were also prepared.[58]

Following this general approach, we have described new types of LC dendrimers functionalized with carbazole, coumarin and pyrene groups as fluorescent moieties.[59-61] The supramolecular complexes were prepared through hydrogen bonding between a melamine or a porphyrin central cores and peripheral bifunctional dendrons derived from bisMPA.

2. SIZE-SELECTIVE ADSORPTION IN NANOPOROUS POLYMERS FROM COUMARIN PHOTOCROSSLINKED COLUMNAR LIQUID CRYSTALS[§]

2.1 Objectives

Herein, we report on the preparation of nanoporous polymers by using two hydrogen-bonded complexes that displayed hexagonal columnar mesomorphism. The materials used in this work consist of a melamine (**M**) or tris(triazolyl)triazine (**T**) core hydrogen-bonded to three dendrons derived from a 3,4,5-trialkoxycarboxylic acid bearing coumarin moieties (**d_1Cou**) (**Figure 2.1**). Coumarin was chosen as reactive group for the crosslinking reaction. Upon irradiation at 350 nm, coumarins undergo [2+2] cycloaddition to yield cyclobutane dimers. It does not require an initiator or catalyst and side reactions are avoided.

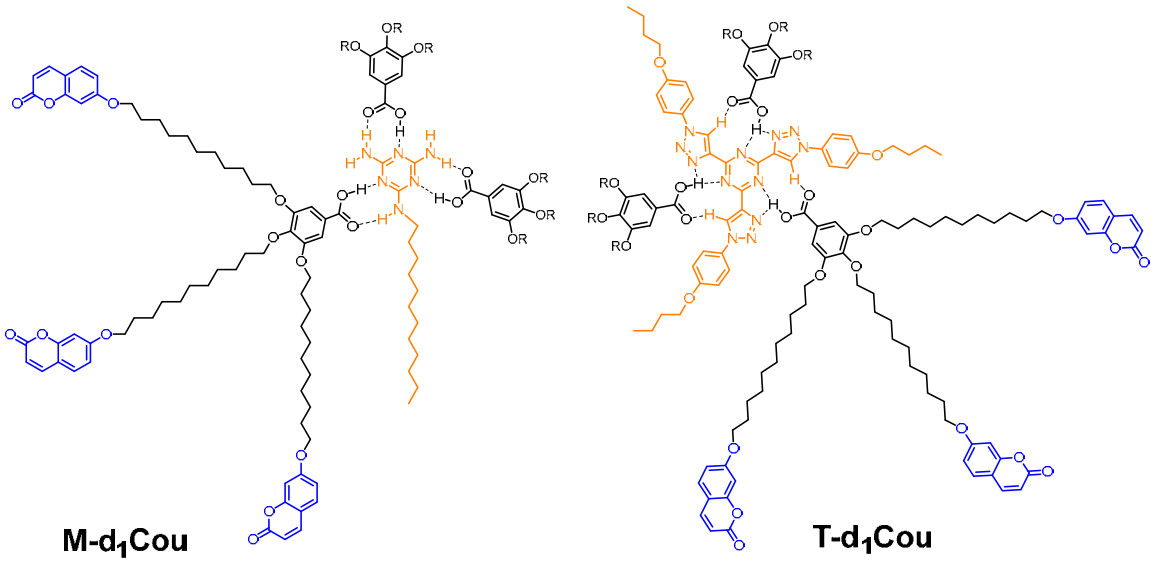

Figure 2.1 Chemical structure of the hydrogen-bonded complexes.

The nanoporous materials were obtained by using the hexagonal columnar complexes, crosslinking *via* coumarin photodimerization, followed by quantitative template removal (**Figure 2.2**). To our knowledge, this is the first report of

[§] Published in: A. Concellón, A. P. H. J. Schenning, P. Romero, M. Marcos & J. L. Serrano. Size-selective adsorption in nanoporous polymers from coumarin photocrosslinked columnar liquid crystals. *Macromolecules* **2018**, *51*, 2349-2358.
This work was carried out in collaboration with Prof. Albert Schenning (Eindhoven University of Technology, The Netherlands) during a 4 months stay financed by MINECO (EEBB-I-17-12040).

mesophase fixation by coumarin photodimerization for preparing nanoporous polymers instead of the more common photopolymerization of (meth)acrylates or 1,3-dienyl groups. Furthermore, the use of both templates allowed us to control the pore size and, accordingly, to tune the adsorption selectivity of the nanoporous polymers.

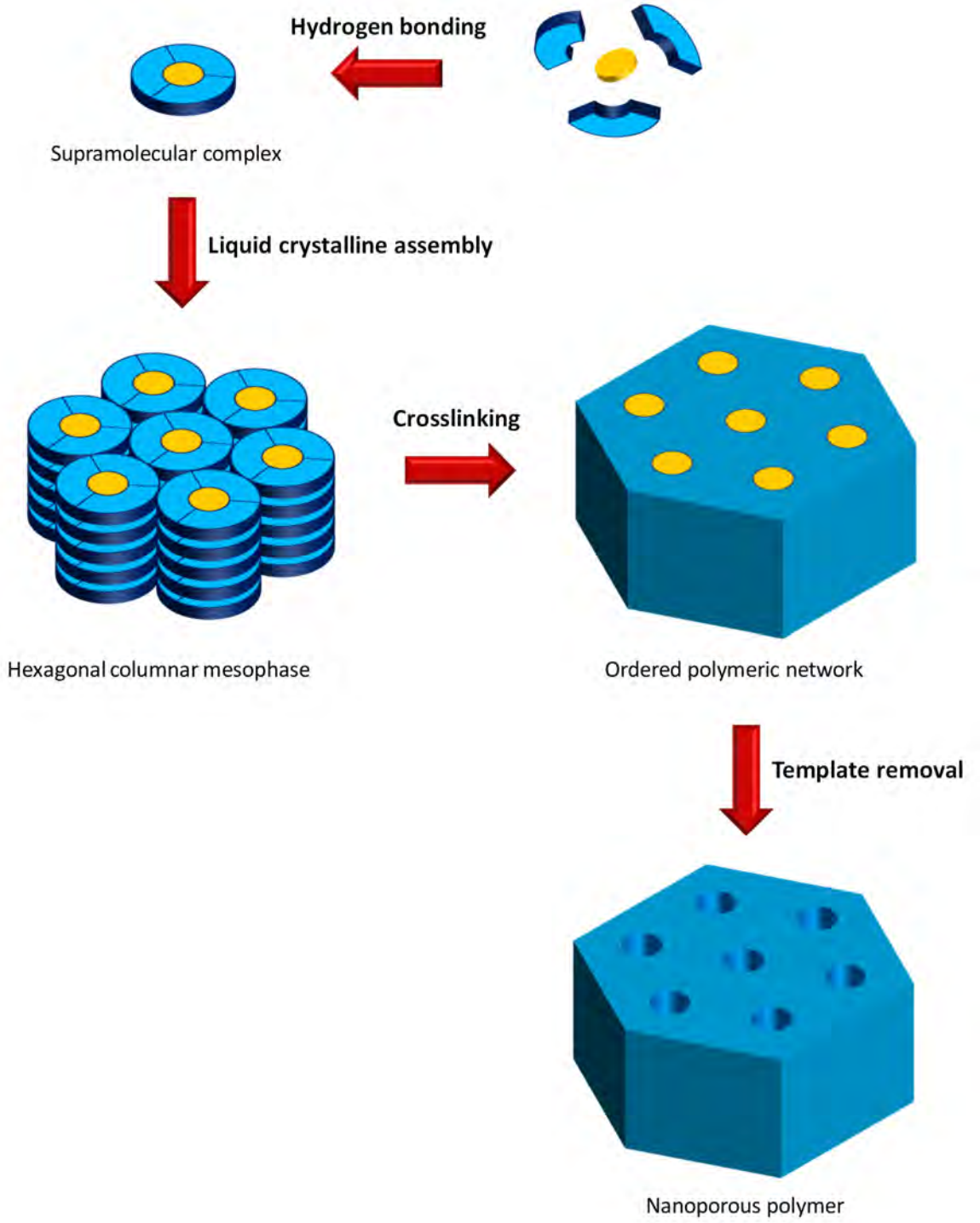

Figure 2.2 Schematic representation of the process for the preparation of the nanoporous materials.

2.2 Results and Discussion

2.2.1 Preparation and Characterization of Supramolecular Complexes

The melamine core (**M**) and the tris(triazolyl)triazine core (**T**) were synthesized following previously reported procedures.[55, 58] The synthesis of the carboxylic acid bearing coumarin moieties (**d_1Cou**) was described in *Chapter 1*.

The hydrogen-bonded complexes were prepared by dissolving **d_1Cou** and the corresponding core (**M** or **T**) in a 1:3 ratio in DCM followed by slow evaporation of the solvent under continuous stirring at room temperature. The resulting mixtures were heated to the isotropic state and cooled down slowly to room temperature. The formation of intermolecular hydrogen bonds in the complexes was study by FTIR and NMR.

FTIR spectra of the complexes displayed several changes with respect to **d_1Cou** and the cores due to the formation of specific interactions between the carboxylic acid and **M** or **T** (**Figure 2.3**). In the **d_1Cou** spectrum, a C=O stretching band appeared at 1670 cm^{-1}, which corresponds to the dimeric form of the carboxylic acid. In the FTIR spectra of **M-d_1Cou** and **T-d_1Cou**, this C=O stretching band was shifted respectively to 1687 and 1695 cm^{-1} due to hydrogen bonding interactions between complementary **d_1Cou** and **M** or **T**.

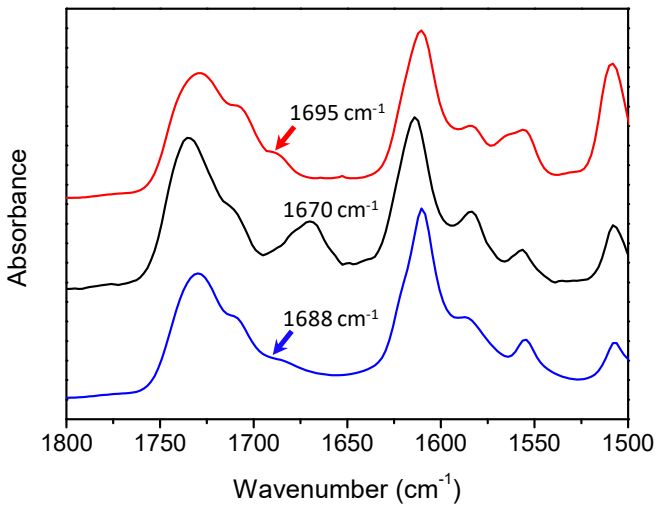

Figure 2.3 FTIR spectra (C=O st. region) of **d_1Cou** (black line), **M-d_1Cou** (blue line), and **T-d_1Cou** (red line).

The ^{1}H NMR spectra of the complexes also proved the hydrogen bonds formation in the complexes, assuming that there is a rapid equilibrium between the complex and its components. In general, proton signals involved in hydrogen bonds, as well as those that are close to the complexing groups, experienced correlated changes in their chemical shifts (**Figure 2.4**). The formation of hydrogen bonds in the **M-d$_1$Cou** complex was assessed by the downfield shift of the N–H proton (H_α and H_ε) signals of the **M** core as these protons are involved in the hydrogen bonds with **d$_1$Cou**. In the case of **T-d$_1$Cou**, the triazole protons (H_3) experienced a downfield displacement, indicating that these protons interact through hydrogen bonding with the carbonyl group of **d$_1$Cou**. Besides, it is particularly noteworthy that in both complexes the protons close to the hydrogen bonds experience slight displacements. These shift variations of the signals of the main protons involved in complex formation are listed in **Table 2.1**.

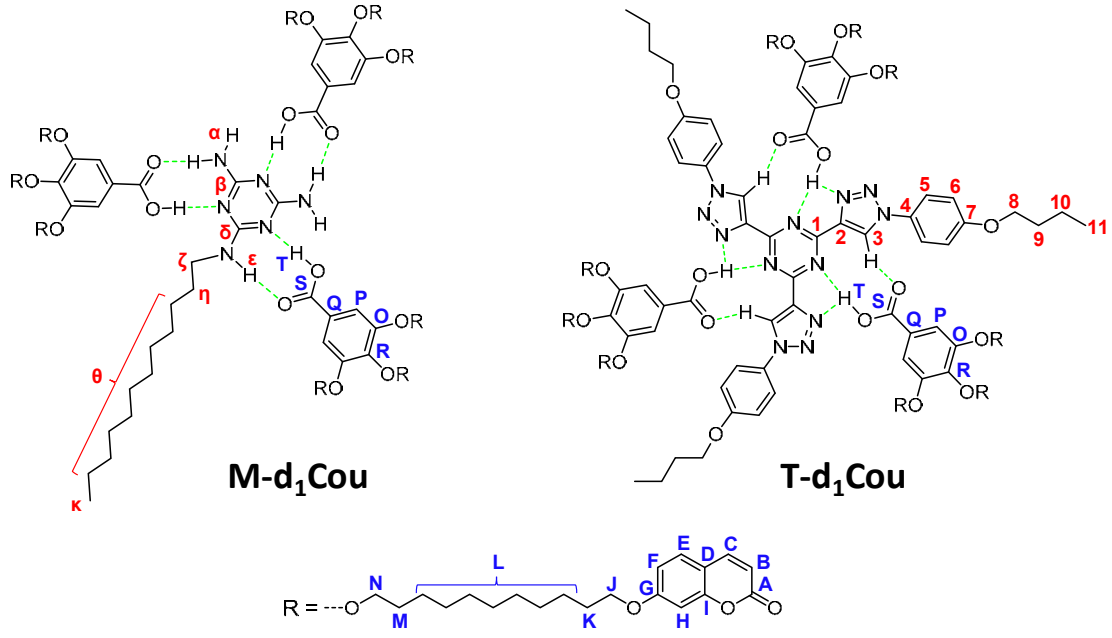

Table 2.1 Main shifts in the ^{1}H NMR spectra (500MHz, CD_2Cl_2) of the 1:3 complexes (changes in chemical shift are shown in brackets, *: not detected)

	H_T	H_P	H_α	H_ε	H_ζ	H_3	H_5	H_6
M			4.89	4.98	3.30			
T						8.86	7.64-7.58	6.98-6.92
d$_1$Cou	*	7.32						
M-d$_1$Cou	4.66	7.30 (-0.02)	6.04 (+1.15)	6.30 (+1.32)	3.36 (+0.06)			
T-d$_1$Cou	*	7.30 (-0.02)				9.04 (+0.18)	7.80-7.76 (+0.17)	7.11-7.07 (+0.14)

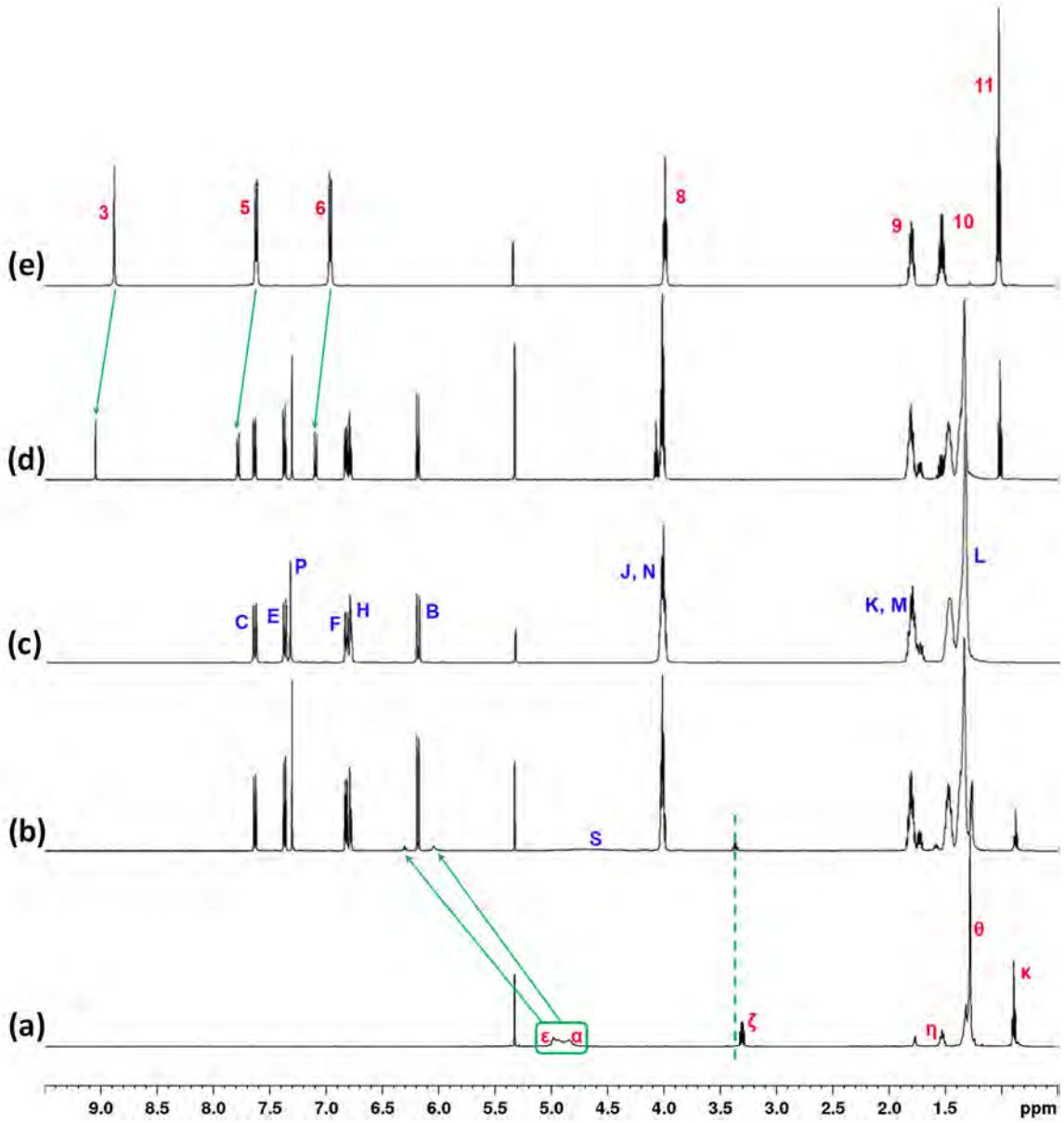

Figure 2.4 ^{1}H NMR spectra in CD_2Cl_2 solution at 25 °C of **(a) M**, **(b)** 1:3 complex **M-d$_1$Cou**, **(c) d$_1$Cou**, **(d)** 1:3 complex **T-d$_1$Cou**, and **(e) T**.

On the other hand, variations in the chemical shifts of the ^{13}C signals of the carbon atoms involved in the formation of hydrogen bonds were also observed. In particular, the ^{13}C signals of the carboxylic acid group of **d$_1$Cou** are shifted by -0.62 ppm (for **M-d$_1$Cou**) or -1.40 ppm (for **T-d$_1$Cou**) after complexation. The shift variations of the signals of the main carbons involved in complex formation are listed in **Table 2.2**.

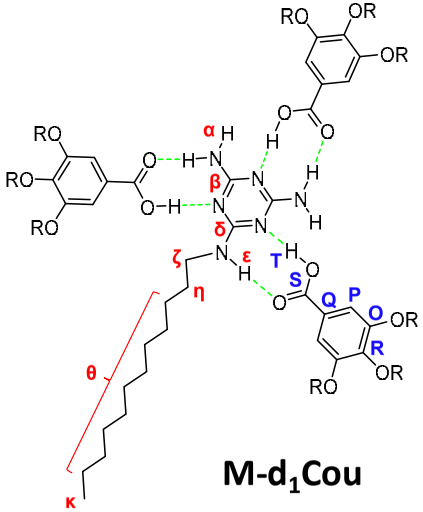

M-d$_1$Cou

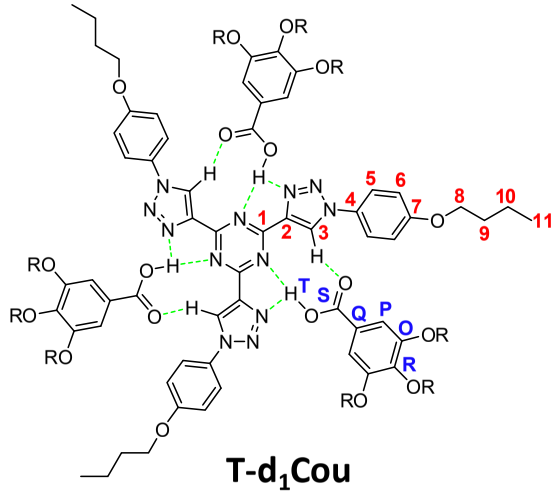

T-d$_1$Cou

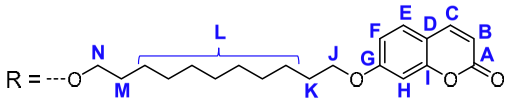

Table 2.2 Main shifts in the ^{13}C NMR spectra (500MHz, CD_2Cl_2) of the complexes (the changes in chemical shift are shown in brackets)

	C_S	C_R	C_Q	C_P	C_O	$C_{\delta,\beta}$	C_ζ	C_1	C_2	C_3	C_4	C_5	C_6	C_7
M						167.39	41.06							
T								167.26	146.22	126.04	130.14	122.60	115.81	160.40
d$_1$Cou	171.19	143.43	124.12	108.74	153.34									
M-d$_1$Cou	170.57 (-0.62)	142.95 (-0.48)	125.32 (+1.20)	108.60 (-0.14)	153.29 (-0.05)	164.73 (-2.66)	41.26 (+0.20)							
T-d$_1$Cou	169.79 (-1.40)	143.29 (-0.14)	124.19 (+0.07)	108.71 (-0.03)	153.35 (+0.01)			170.57 (-0.62)	142.95 (-0.48)	125.32 (+1.20)	108.60 (-0.14)	153.29 (-0.05)	164.73 (-2.66)	41.26 (+0.20)

The formation of the 1:3 hydrogen-bonded complexes was also confirmed by solid state ^{13}C cross-polarization magic-angle spinning (^{13}C CPMAS) NMR spectroscopy; see **Figure 2.5** as a representative example. It is noteworthy that the peak corresponding to the carbonyl group of the noncomplexed acid (C_S) (172.5 ppm) is broadened and shifted in the spectrum of the complexes. Moreover, the signals for some carbon atoms, of both the **d_1Cou** and the cores, are significantly shifted upon complexation, but it is difficult to assign these shifts due to signal overlap.

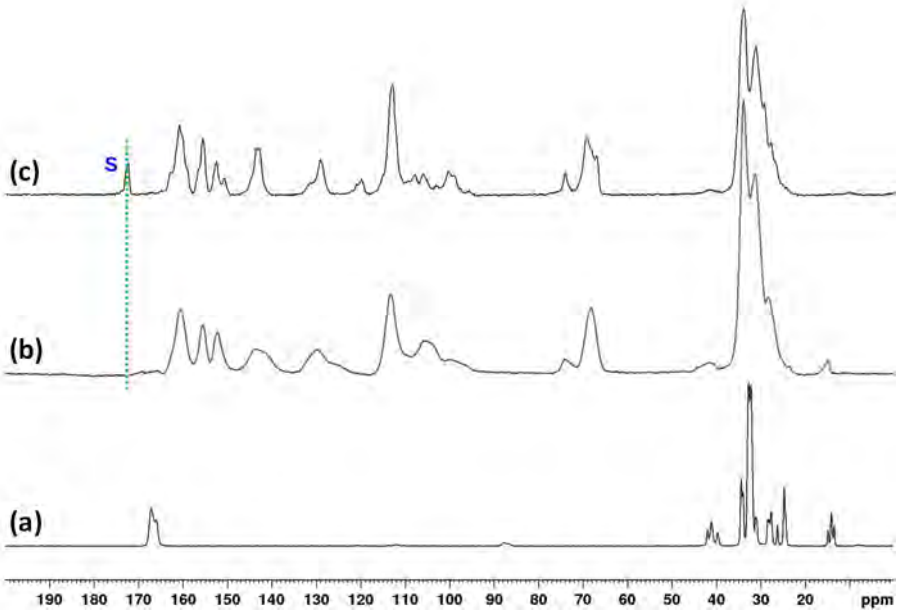

Figure 2.5 ^{13}C CPMAS NMR spectra of **(a) M**, **(b)** complex **M-d_1Cou**, and **(c) d_1Cou**. All the spectra were recorded at room temperature.

2.2.2 Thermal Properties and Mesogenic Behavior

The thermal stability of all the two hydrogen-bonded complexes was studied by thermogravimetric analysis (TGA). All the samples showed good thermal stability, and in all cases the 2% weight loss temperature ($T_{2\%}$) was detected more than 150 °C above the isotropization point. The thermal transitions and mesomorphic properties were studied by polarizing optical microscopy (POM) and differential scanning calorimetry (DSC). The results are summarized in **Table 2.3**.

All the complexes were obtained as homogeneous materials with mesomorphic behavior, as observed by POM (**Figure 2.6a**). For the two compounds the DSC curves were reproducible after the first heating and show only one peak corresponding to the clearing point and a glass transition, which freezes the

mesomorphic order at room temperature (**Figure 2.6b**). Besides, the complex **T-d$_1$Cou** showed some tendency to crystallize because the mesophase undergoes a cold crystallization during the heating process.

Table 2.3 Thermal properties and structural parameters

	$T_{2\%}$ [a] (°C)	Phase transitions[b]	*d* (Å)	*h k l*	Structural parameters[c]
M[d]	218	Cr 112 (SmA 36) I	–		
T[e]	241	g 59 I	–		
d$_1$Cou[f]	242	g 28 Cr 89 I	–		
M-d$_1$Cou	248	g 16 Col$_h$ 87 I	31.2	1 0 0	*a* = 36.1 Å
			18.1	1 1 0	*c* = 5.3 Å[g]
			15.7	2 0 0	
			4.5 (br)		
T-d$_1$Cou	292	g 9 Col$_h$ 58 Cr 86 I	33.4	1 0 0	*a* = 38.4 Å
			19.1	1 1 0	*c* = 5.2 Å[g]
			4.6 (br)		

[a] Temperature at which 2% mass lost is detected in the thermogravimetric curve.

[b] DSC data of the second heating process at a rate of 10 °C/min. g: glass, Cr: crystal, SmA: smectic A mesophase, Col$_h$: hexagonal columnar mesophase, I: isotropic liquid.

[c] $a = \left(2/\sqrt{3}\right)\left((d_{10}) + \sqrt{3}(d_{11}) + \sqrt{4}(d_{20}) + \sqrt{7}(d_{21}) + \cdots\right)/n_{reflections}$

[d] Monotropic LC described in reference 55. Reported thermal properties: Cr 103 (SmA 39) I.

[e] Compound described in reference 58. Reported thermal properties: g 60 I.

[f] Data from *Chapter 1.*

[g] Calculated *c* value.

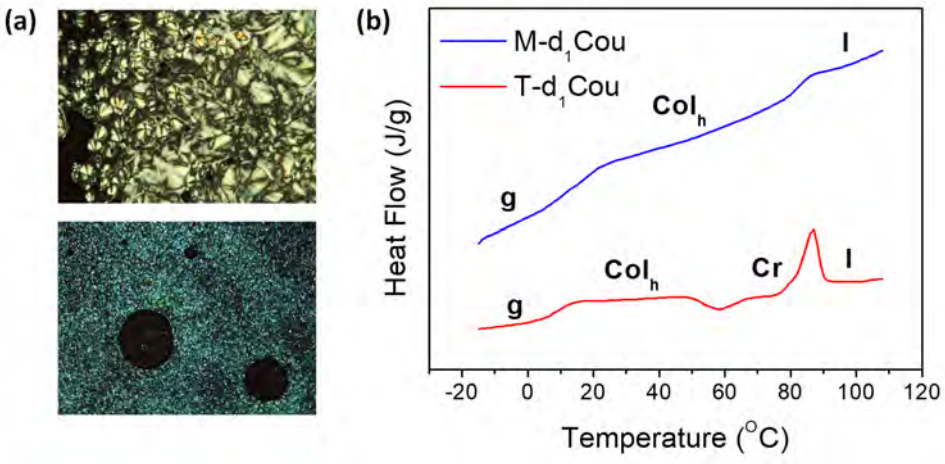

Figure 2.6 (a) POM microphographs for 1:3 **M-d$_1$Cou** (top) and **T-d$_1$Cou** (bottom) 1:3 complexes, **(b)** DSC traces corresponding to the second heating scan (10 °C/min, exo down).

The assignment of the type of mesophase and the determination of the lattice parameters was achieved by X-ray diffraction (XRD). The XRD patterns of **M-d$_1$Cou** and **T-d$_1$Cou** contain three reflections in the low-angle region in a ratio 1 : 1/√3 : 1/√4 (**Figure 2.7**). These three reflections can be assigned to the reflections (100), (110), and (200) of a hexagonal columnar arrangement; the lattice parameters (a) are gathered in **Table 2.3**. Also, a broad diffuse halo is observed in the high-angle region, which is characteristic of the liquid-like order of the hydrocarbon chains at around 4.5 Å. The relationship between the density (ρ) of the complexes in the mesophase and the measured lattice parameters is given by the equation:

$$\rho = \frac{M \cdot Z}{N_A \cdot V}$$

where M is the molar mass, Z is the number of molecules in the unit cell, N_A is Avogadro's number, and V is the unit cell volume ($V = a^2 \cdot \sqrt{3}/2 \cdot c \cdot 10^{-24}$). On considering the XRD parameters and assuming ρ = 1 g cm^{-3}, which is reasonable for liquid crystals, and Z=1 (each column slice contains one molecule of the supramolecular complex), we estimated mean stacking distances (c) of around 5.25 Å, which are reasonable values for columnar mesophases with an irregular stacking of the disks. Therefore, these calculations are in good agreement with the formation of discotic 1:3 complexes with one complex per stacking unit.

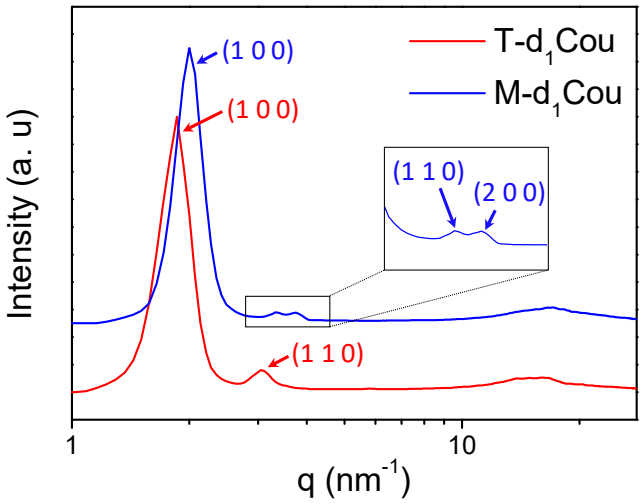

Figure 2.7 1D XRD profiles of 1:3 **M-d$_1$Cou** and **T-d$_1$Cou** complexes.

2.2.3 Network Formation by Coumarin Photodimerization

Once the supramolecular complexes were characterized, the next step consisted of the preparation of crosslinked films. Coumarin units were employed for the crosslinking process by photoinduced [2+2] cycloaddition (so-called photodimerization) in order to lock in the LC arrangement of the complexes. The coumarin photodimerization was monitored by several techniques such as UV-Vis spectroscopy, FTIR, and ^{13}C CPMAS.

The UV-Vis spectra of **M-d$_1$Cou** and **T-d$_1$Cou** in thin film show an intense band at 320 nm related to the π–π* band of the coumarin units (see **Figure 2.8a** as a representative example). Exposure of the supramolecular complexes films to 365 nm UV irradiation caused [2+2] cycloaddition of the coumarin units, and this was consistent with the remarkable decrease of the π–π* band. After 30 min of light irradiation only slight changes were further detected in the UV-Vis spectra (**Figure 2.8b**).

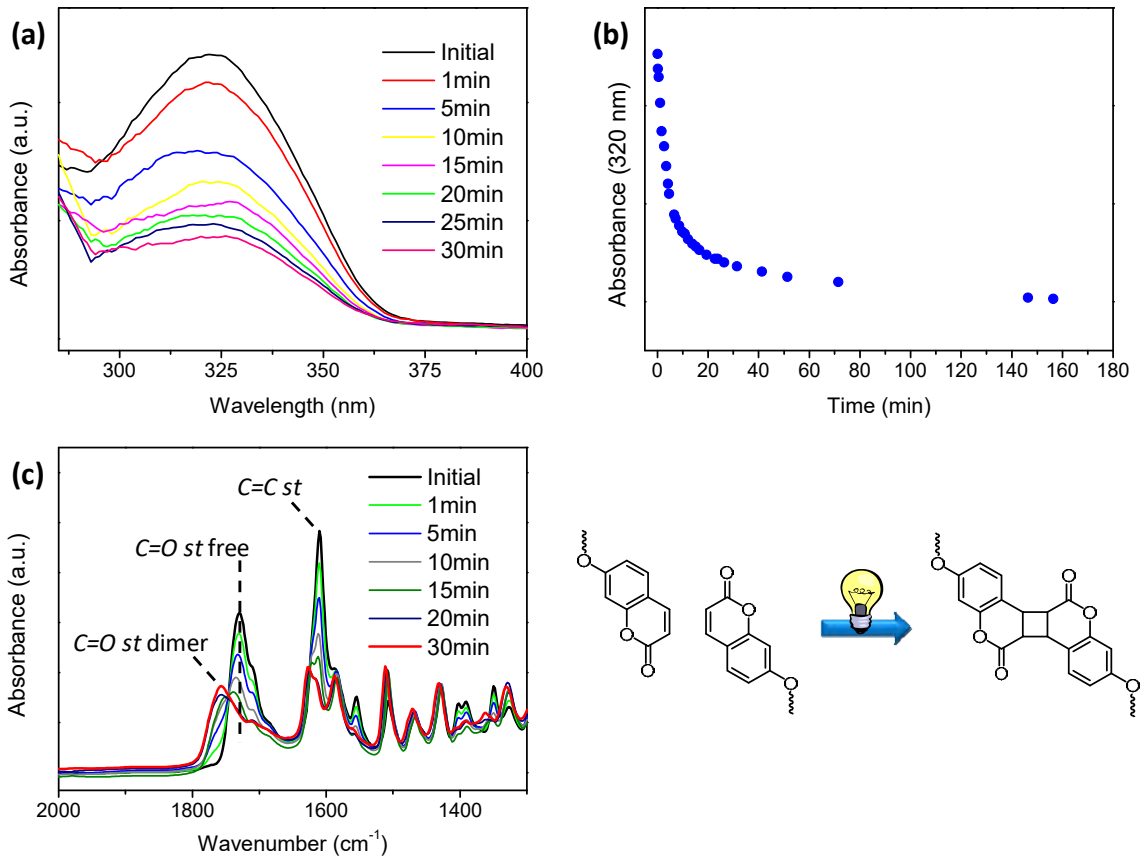

Figure 2.8 Coumarin photodimerization reaction: **(a)** UV-Vis absorption spectra of a UV-irradiated **M-d$_1$Cou** film for different times, **(b)** change of absorbance over time for a UV-irradiated **M-d$_1$Cou** film and **(c)** IR spectra of a UV-irradiated **M-d$_1$Cou** film for different times.

To examine the structural details of the photocrosslinking process, irradiated films were studied by FTIR and ^{13}C CPMAS. Irradiation at 365 nm results in coumarin photodimerization as indicated by the decrease the intensity of the C=C stretching band at 1620 cm^{-1} and the shift of the C=O stretching band from 1730 to 1750 cm^{-1} (**Figure 2.8c**). This reaction can also be followed by ^{13}C CPMAS which shows the increase of the intensity of the peak at 44 ppm, which corresponds to the cyclobutane ring. Additionally, coumarin photodimerization decreases the intensity of the signals at 149 ppm (C_C) and 113 ppm (C_B), which corresponds to the C=C of the coumarin (**Figure 2.9**). Insolubility of the obtained polymer films in common organic solvents, such as dichloromethane, chloroform, tetrahydrofuran, acetone, ethanol, or methanol, confirmed a high degree of coumarin photocrosslinking to fixate the liquid crystal order.

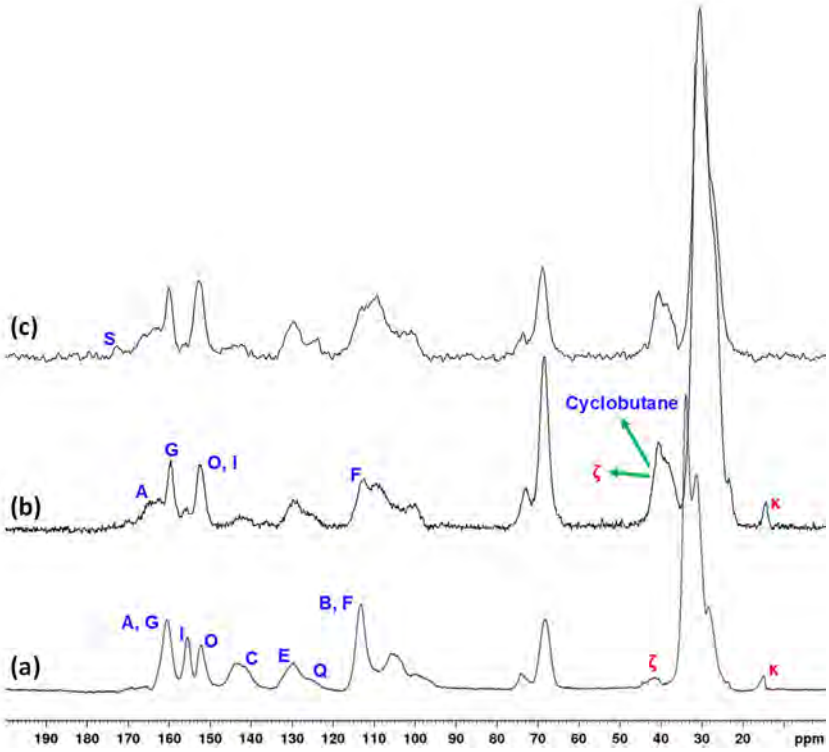

Figure 2.9 ^{13}C CPMAS NMR spectra of **(a)** complex **M-d$_1$Cou**, **(b)** **M**-based polymer, and **(c)** **M**-based nanoporous polymer. All the spectra were recorded at room temperature.

The XRD diffraction patterns of the complexes after coumarin photodimerization showed retention of the hexagonal columnar arrangement, but the lattice spacings were slightly decreased (ca. 4 Å) and broadened (**Figure 2.10**). In both cases, the (110) and (200) reflections could no longer be observed in film due to broadening. These results indicate that coumarin photodimerization can be used to form a crosslinked polymer network and lock in the morphology of the LC phase.

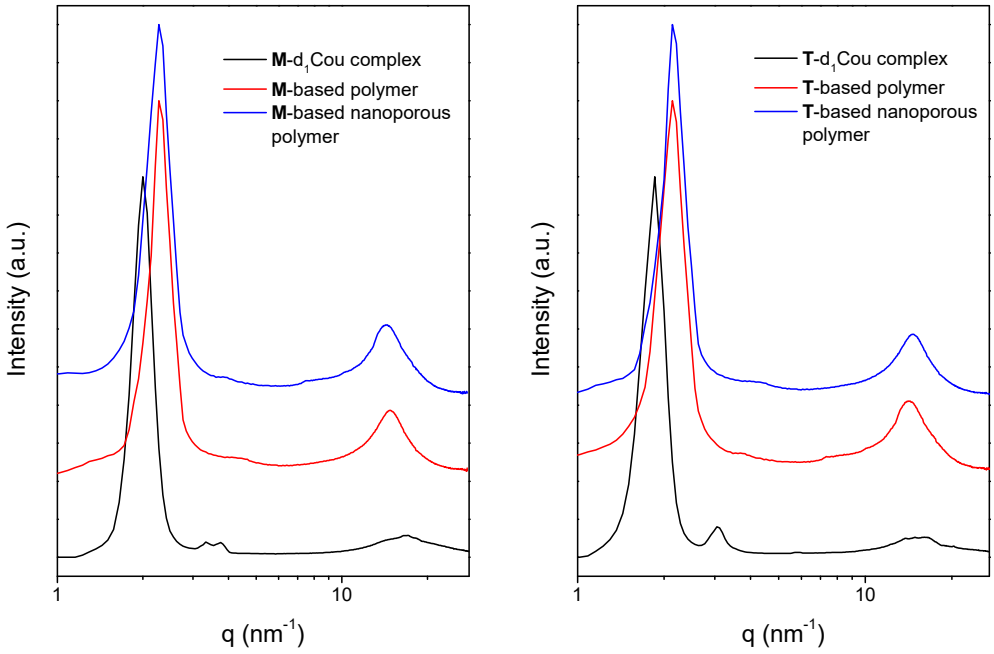

Figure 2.10. 1D XRD profiles of hydrogen bonded complexes, polymers (with template), and nanoporous polymer (after template removal).

2.2.4 Nanoporous Polymer Formation by Template Removal

Self-standing nanoporous polymers were prepared by chemical treatment of the polymer films with 3 M hydrochloric acid solution in ethanol (**Figure 2.11**). The removal of the template was confirmed by FTIR, gravimetry, ^{13}C CPMAS, and XPS measurements.

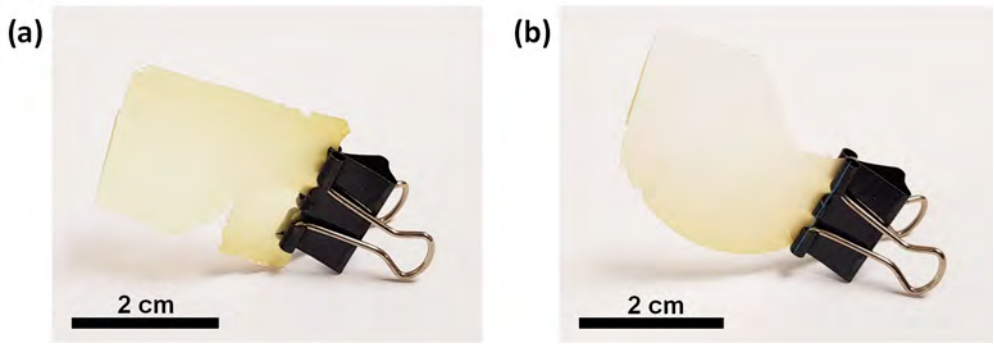

Figure 2.11 (a) M-based and **(b) T**-based self-standing nanoporous polymers.

The efficacy of **M** or **T** removal was verified by FTIR spectroscopy (**Figure 2.12**). After template elimination, –COOH functionalities were expected to be at the pore surface. The IR spectra of the nanoporous polymers showed a new band at around 1675 cm^{-1} related to free carboxylic acid groups, indicating elimination of the

templates. Quantitative templates removal was also confirmed by ^{13}C CPMAS analysis (**Figure 2.9**) which showed the disappearance of the signal corresponding to the methyl carbon of the melamine core (C_K). Additionally, a new peak at 173 ppm related to the non-complexed carboxylic acid group (C_S) indicated template elimination.

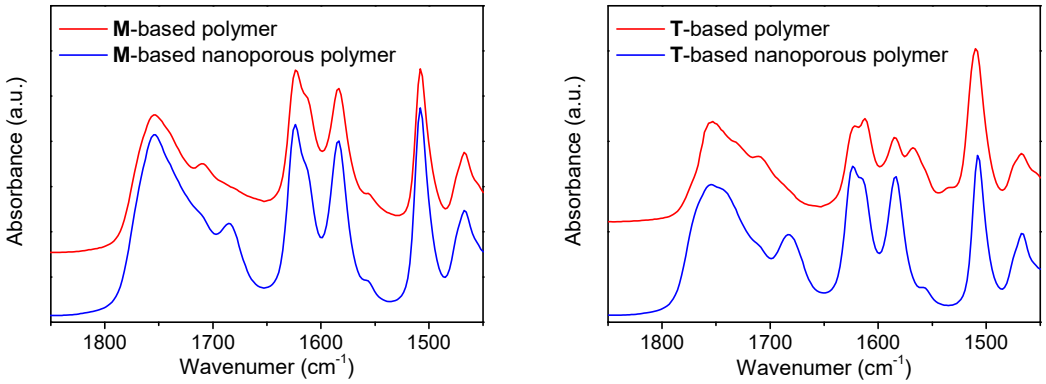

Figure 2.12 FTIR spectra of the initial polymers (with template) and nanoporous polymers (after template removal).

Another method to quantify template removal is gravimetry. Polymer films were weighted before and after the chemical treatment with HCl. The films showed a decrease in mass equal to a template removal of 97±2% for **M**-based nanoporous polymer and 96±2% for **T**-based nanoporous polymer. XPS depth scans were performed by subsequent sputter cycles (etching) in order to quantify the nitrogen-to-carbon ratio throughout the thickness of the chemical treated films. The N/C ratio *versus* sputter time (depth) is presented in **Figure 2.13**. Before template removal, all the films showed a constant N/C composition. However, nitrogen was no longer detected in the nanoporous polymers, indicating quantitative elimination of the templates.

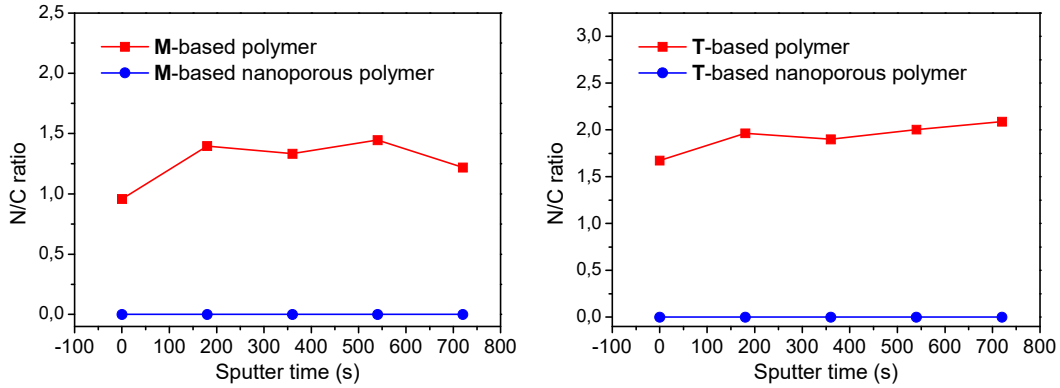

Figure 2.13 Nitrogen-to-carbon ratio of the initial polymers (with template) and nanoporous polymers (after template removal) as a function of the sputter time (depth).

After removal of the template, the structural properties were investigated by XRD. The diffraction patterns of the films showed that lattice parameters of the porous polymers were the same as the native polymer film (**Figure 2.10**). The bulk material retained its hexagonal columnar arrangement even after template removal due to the crosslinking of coumarin units. These results indicate structural integrity and the formation of nanopores with an estimated pore diameter of around 5 and 10 Å for **M**- or **T**-based nanoporous polymers, respectively (**Figure 2.14**).

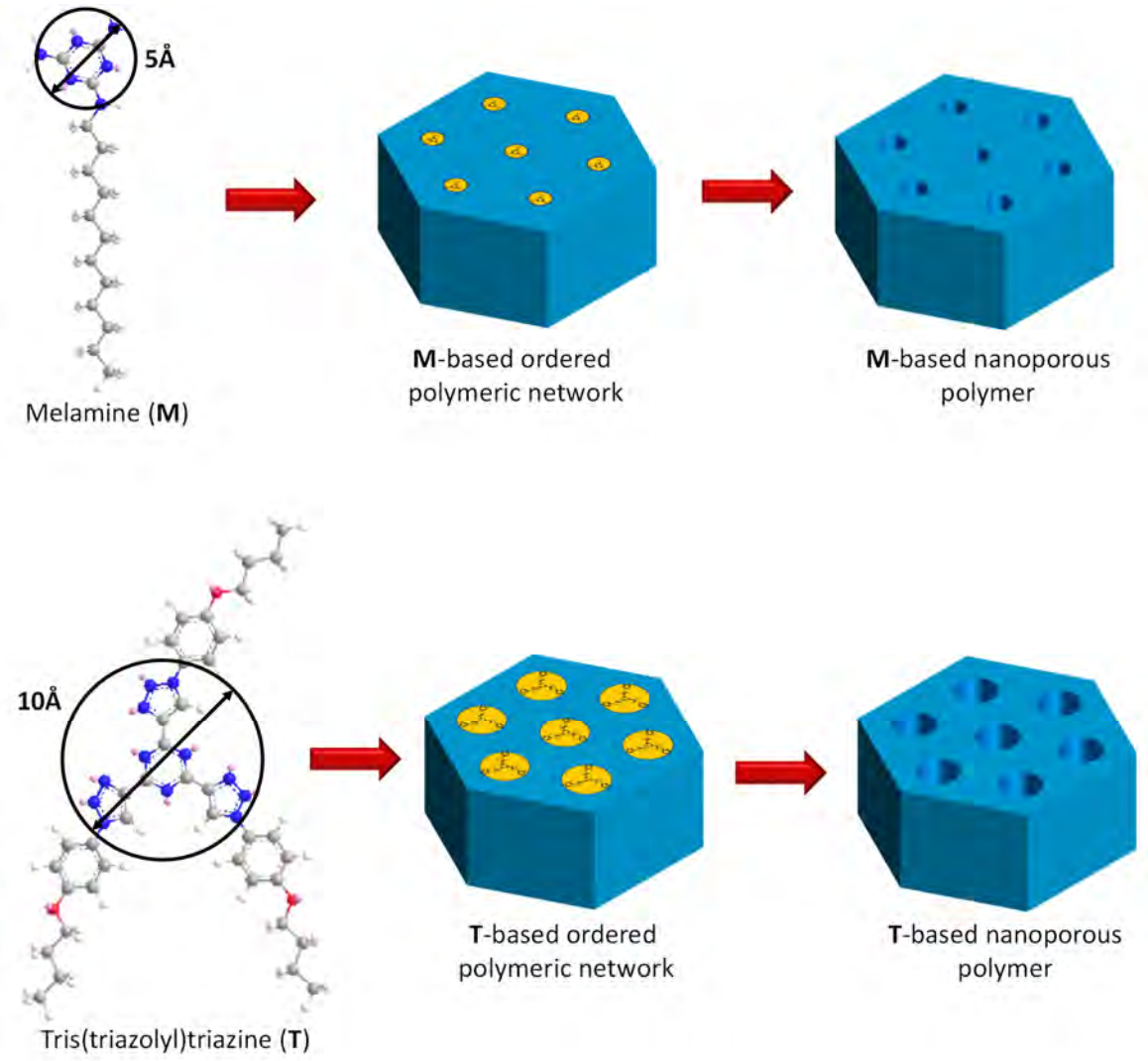

Figure 2.14 MM2 energy-minimized structure and diameter of **M** and **T** central cores. Schematic illustration of the obtained nanoporous polymers with different pore sizes.

2.2.5 Selective Adsorption of Molecules or Ions

2.2.5.1 *Selective Adsorption of Neutral Molecules*

The use of **M**- and **T**-based nanoporous polymers with –COOH functionalities at the pore surface for selective uptake of organic molecules was studied. For this purpose, a variety of molecules with $–NH_2$ functional groups and different sizes were selected: *p*-nitroaniline (pNA, size= 6×4 Å), 1-aminopyrene (APy, size= 9×8 Å) and *meso*-tetra(*p*-aminophenyl)porphine (TAPP, size= 18×18 Å). The adsorption capacity and kinetics of **M**- and **T**-based porous polymer was investigated by UV-Vis spectroscopy (**Figure 2.15**). Control experiments were carried out by immersing polymer films (without template removal) in pNA, APy, and TAPP solutions. The solutions with the polymer films had nearly the same absorbance as the initial solutions, revealing its inability to adsorb molecules without template removal. Adsorption occurs inside the pore and not on the exterior surface of the film.

In the case of the **M**-based adsorbent with a pore size of around 5 Å, only pNA was adsorbed by the –COOH functionalized pores. This evidences that size-selective adsorption is possible with this polymer. The adsorption kinetics was studied following the absorbance of pNA at 372 nm over time and shows that adsorption reached a plateau within 8–10 h. The capacity of pNA adsorption was also investigated; 24% of the carboxylic acid groups were occupied by pNA, which corresponds to 0.72 per disk (each disk consists of three carboxylic acids).

In the case of the **T**-based adsorbent, with a pore size of around 10 Å, both pNA and APy molecules were adsorbed. TAPP uptake in the –COOH functionalized pores is precluded by size exclusion of the larger TAPP relative to pNA or APy. The adsorption kinetics was also studied revealing that a plateau is reached in 8–10 h. The occupation degree of the carboxylic acid groups with pNA and APy was 42% (1.26 per disk) and 27% (0.81 per disk), respectively. It is noteworthy that the adsorption capacity of the **T**-based adsorbent is higher than the **M**-based adsorbent due to its larger pore size.

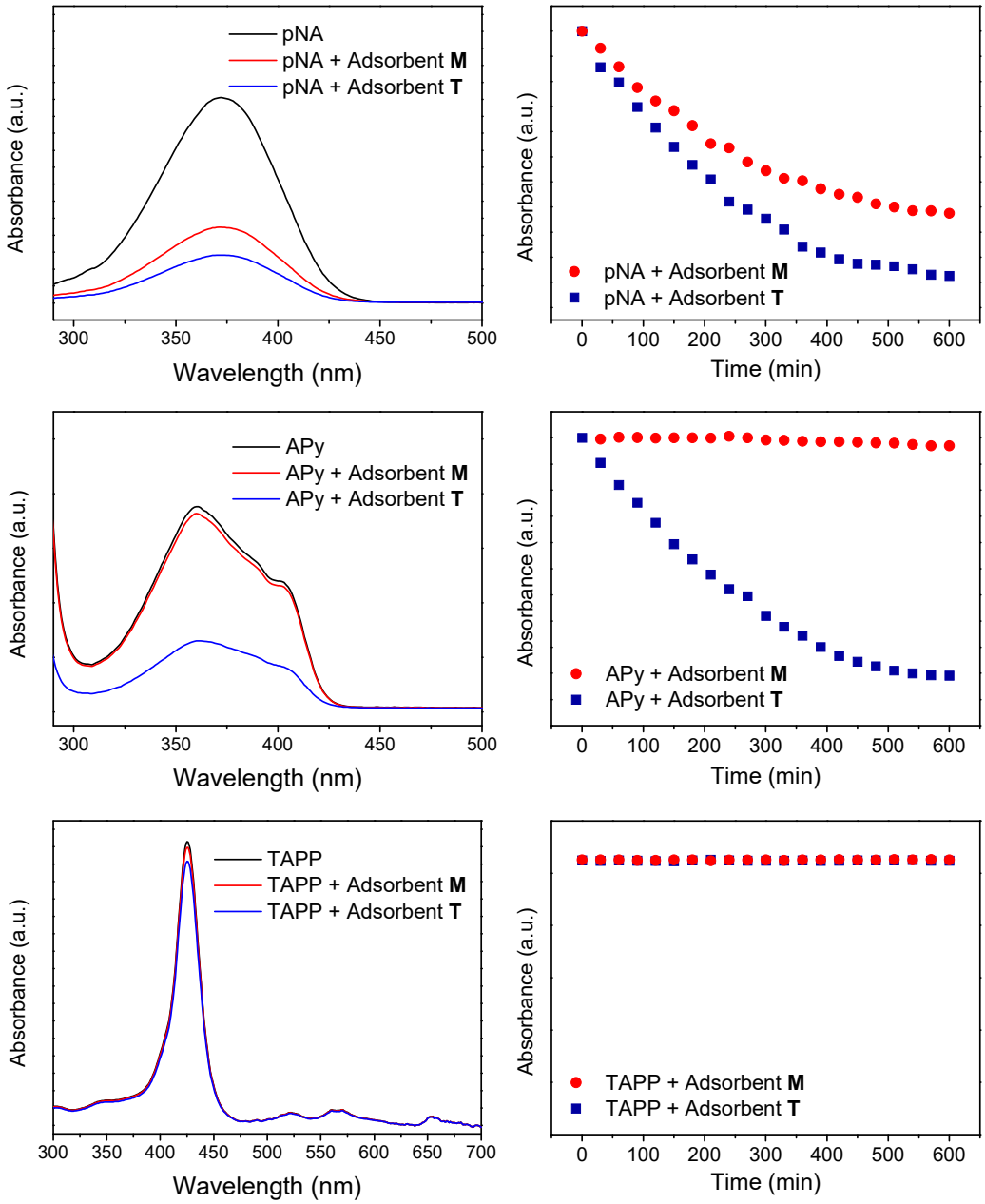

Figure 2.15 UV-Vis spectra before and after adsorption of pNA, APy, and TAPP with **M**- and **T**-based adsorbents (left). Adsorption kinetics of pNA, APy, and TAPP (right).

Desorption is important to reuse the adsorbent and to recover valuable adsorbates. It was investigated by UV-Vis spectroscopy with fresh, completely pNA filled adsorbents. **M**- and **T**-based adsorbents are able to hold the major fraction of pNA in deionized water. However, after immersing the adsorbents in potassium hydroxide 0.1 M (aq.), the carboxylate moieties are deprotonated and pNA is removed from the adsorbents. Additionally, the adsorption-desorption was investigated several times, revealing that it is reversible in three repeating cycles (**Figure 2.16**), and thus it is possible to reuse these adsorbents many times.

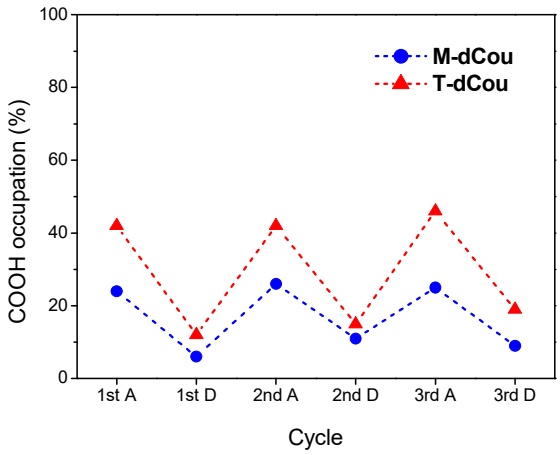

Figure 2.16. Occupation degree of adsorption sites (COOH) with pNA during three adsorption (A)-desorption (D) cycles.

2.2.5.2 *Preparation of Anionic Nanoporous Polymers with Different Counter Cations in the Pore*

Nanoporous polymers with carboxylic acid functionalized pores were treated with 0.1 M aqueous solutions of the hydroxide salts of Li^+, Na^+, K^+, Cs^+ and NH_4^+ ions for 5 h. The formation of porous polymers with –COOLi, –COONa, –COOK, –COOCs, and –$COONH_4$ groups at the pore surface was confirmed by FTIR. The COOH *st.* band was shifted from 1685 to 1560 and 1404 cm^{-1} (**Figure 2.17**).

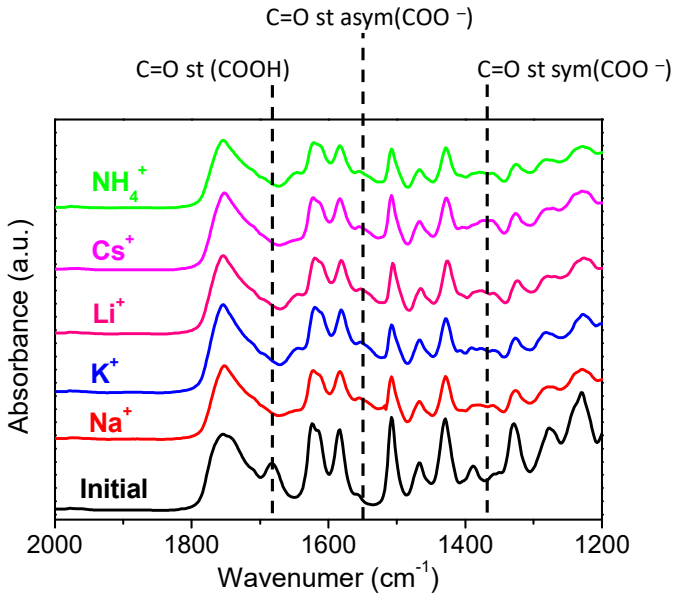

Figure 2.17 FTIR spectra of the **M**-based nanoporous polymer after exposure to different hydroxide salts.

2.2.5.3 *Selective Adsorption of Cationic Dyes*

The adsorbents with –COOK functionalities at the pore surface were then used to selective adsorption of ionic dyes. Selective adsorption of molecular species in water with different sizes and charges was carried out with methylene blue (MB), methyl orange (MO), and rhodamine B (RhB). MB and RhB are positively charged dyes, while MO is negatively charged. Their estimated sizes are 6×13 Å (MB), 12×16 Å (RhB), and 5×12 Å (MO).

First, the ability of adsorbing ionic dyes was studied when –COOK functionalized nanoporous polymers where immersed in MB aqueous solution. Dye adsorption was monitored by UV-Vis spectroscopy (**Figure 2.18**). MB was adsorbed by the porous polymer as determined by the decrease of the absorption intensity at 665 nm. The solutions turned from deep blue to less blue, while the film became blue, indicating that the cationic dye is adsorbed from solution. The adsorption capacity was calculated; 9% for **M**-based adsorbent (0.27 per disk) and 19% for **T**-based adsorbent (0.47 per disk) of the –COOK groups were associated with MB.

Figure 2.18 also shows the result of the simultaneous adsorption of MB and MO in water. The initial UV-Vis spectrum showed two bands: one at 465 nm belonging to MO and the second at 665 nm belonging to MB. After equilibration with the nanoporous polymers, the UV-Vis spectra showed a stable band for MO but a loss of the MB band. The color of the solution changed from green to yellow after equilibration. The observed selectivity can be ascribed to the difference in the charge of the species.

The size selectivity of the nanopores was demonstrated by simultaneous adsorption of MB and RhB from aqueous solutions (**Figure 2.18**). After equilibration, the color of the solutions changed from violet to pink, and the UV-Vis absorption band of MB decreased and the RhB absorption band remained constant. RhB uptake in the pores is significantly precluded by size exclusion of the larger dye RhB relative to MB.

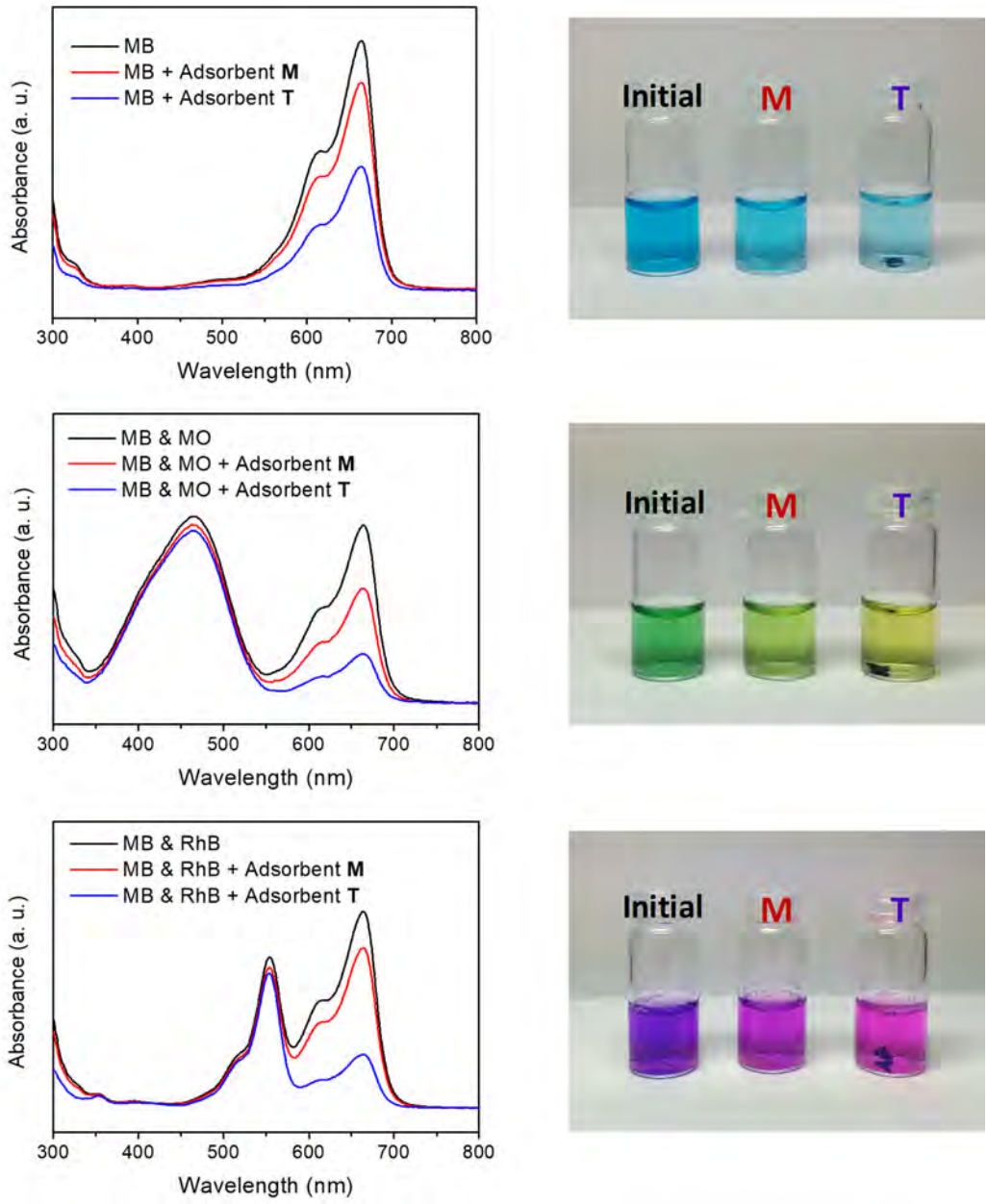

Figure 2.18 UV-Vis spectra before and after adsorption of MB, MB&MO, and MB&RhB with **M**- and **T**-based adsorbents (left). Vials of MB, MB&MO, and MB&RhB before and after adsorption with **M**- or **T**-based adsorbents (right).

Desorption was investigated with fresh, completely MB filled **M**- and **T**-based adsorbents in deionized water. The solution became only slightly blue, indicating minor desorption of MB. Nevertheless, after immersing the adsorbents in hydrochloric acid 3 M (aq.), the solution suddenly became blue indicating desorption of MB. At low pH, the carboxylate moieties are protonated and MB is removed from the adsorbents. Moreover, the adsorption-desorption was investigated several times by UV-Vis spectroscopy, which revealed that it is

reversible in three repeating cycles (**Figure 2.19**), indicating that these adsorbents can be use many times.

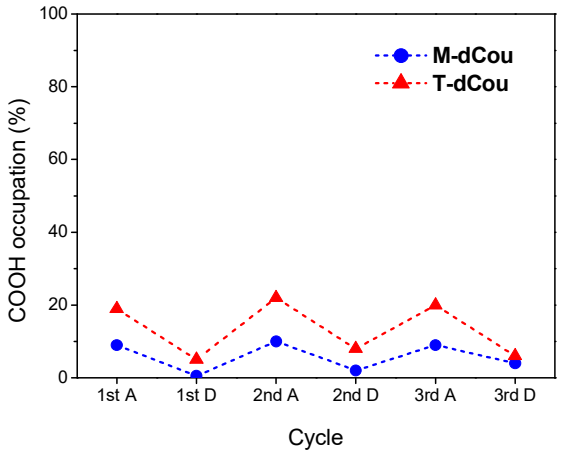

Figure 2.19. Occupation degree of adsorption sites (COO^-) with MB during three adsorption (A)-desorption (D) cycles.

2.3 Conclusions

We have successfully developed a new strategy to obtain self-standing nanoporous polymers based on the fixation of columnar mesophases by coumarin photodimerization. The size of the pores can be controlled by careful choice of the utilized template. The nanoporous materials with carboxylic acids at the pore surface demonstrate remarkable size selectivity in adsorption experiments. In addition, the chemical nature of the pore can be tuned by *in situ* treatment with potassium hydroxide. After this base treatment the polymers are able to adsorb cationic dyes and to selectively adsorb cationic dyes over anionic and larger cations. The adsorbed molecules can be desorbed by acid or base treatment thus it is possible to reuse these nanoporous polymers.

Our results clearly suggest that these polymers with hexagonal columnar nanopores may be useful in a wide range of applications including molecular recognition, filtration, separation, or catalysis. Future work will be focused on obtaining homeotropically aligned polymer films and on developing helical nanoporous polymers for chiral separation.

3. EXPERIMENTAL PART

3.1 Characterization Techniques

3.1.1 Materials

All commercially available reagents were purchased from Sigma-Aldrich and used as received. Anhydrous THF and DCM were purchased from Scharlab and dried using a solvent purification system.

3.1.2 Structural Characterization

Infrared spectroscopy (IR) spectra were obtained on a FTS 6000 spectrophotometer from Bio-Rad equipped with Specac Golden gate diamond ATR; 50 scans at a resolution of 4 cm^{-1} were carried out.

Solution nuclear magnetic resonance (NMR) experiments were carried out on Bruker Avance spectrometers operating at 500 MHz for ^{1}H and 125 for ^{13}C, using standard pulse sequences. Chemical shifts are given in ppm relative to TMS, and this was used as internal reference.

Solid-state **nuclear magnetic resonance** (NMR) experiments were performed in a Bruker Avance III WB400 spectrometer using a double resonance (^{1}H–X) probe with a rotor of 4 or 2.5 mm diameter, and the spinning frequency was set to 12 or 20 kHz, respectively. For the former, the ^{1}H and ^{13}C $\pi/2$ pulse lengths were 3 and 4.3 µs, respectively, the CP contact time was 3 ms and the recycle delay was 7 s. For the latter, the ^{1}H and ^{13}C pulse lengths were 8 and 5.7 µs, respectively, the CP contact time was 1.5 ms, and the recycle delay was 5 s. The pulse sequence employed consisted of ramped cross-polarization with spinal-64 decoupling. Data were acquired at 298 K, and chemical shifts are referenced to TMS using adamantane (^{13}C: δ= 29.45 ppm) as secondary standard.

Elemental analysis was performed using a Perkin-Elmer 2400 microanalyzer.

The **X-ray photoelectron spectroscopy** (XPS) measurements were carried out with a Thermo Scientific K-Alpha, equipped with a monochromatic small-spot X-ray

source and a 180° double focusing hemispherical analyzer with a 128-channel detector. Spectra were obtained using an aluminum anode (Al K_α = 1486.6 eV) operating at 72 W and a sport size of 400 µm. Survey scans were measured at a constant pass energy of 200 eV and region scans at 50 eV. The background pressure was 2×10^{-9} mbar and during measurement 3×10^{-7} mbar argon because of the charge compensation for the dual beam source.

3.1.3 Liquid Crystal Characterization

Mesogenic behavior was investigated by **polarized-light optical microscopy** (POM) using an Olympus BH-2 polarizing microscope fitted with a Linkam THMS600 hot stage.

Thermogravimetric analysis (TGA) was performed using a Q5000IR from TA Instruments at heating rate of 10°C/min under nitrogen atmosphere.

Thermal transitions were determined by **differential scanning calorimetry** (DSC) using a DSC Q20 or Q2000 from TA Instruments with powdered samples (2−5 mg) sealed in aluminum pans. Glass transition temperatures (T_g) were determined at the half-height of the baseline jump, and first-order transition temperatures were read at the maximum of the corresponding peak.

X-ray diffraction (XRD) was performed with a Ganesha Lab Instrument equipped with a GeniX-Cu ultralow divergence source producing X-ray photons with a wavelength of 1.54 Å and a flux of 1×10^8 ph/s. Scattering patterns were collected using a Pilatus 300 K silicon pixel detector. The beam center and the *q* range were calibrated using the diffraction peaks of silver behenate. Powdered samples were placed in Lindemann glass capillaries (1 mm diameter).

3.1.4 Optical properties

Ultraviolet-visible spectra were recorded on an Shimadzu UV-3102 spectrophotometer.

3.2 Synthetic procedures

3.2.1 Synthesis of the Tris(triazolyl)triazine Central Core

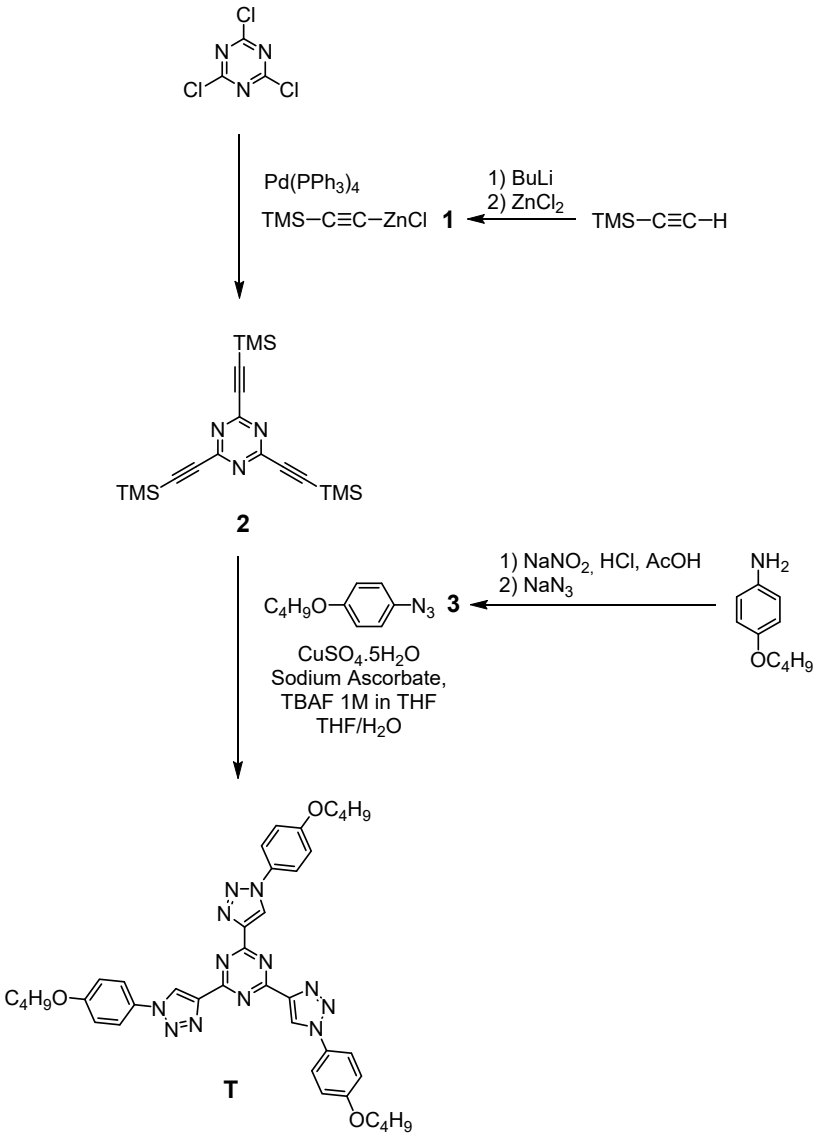

((Trimethylsilyl)ethynyl)zinc chloride (1). A mixture of (trimethylsilyl)acetylene (12.5 mL, 86.5 mmol) in anhydrous THF (50 mL) was cooled at -78 °C in a Schlenk flask. Then, a 2.5 M solution of *n*-butyllithium in THF (34.6 mL, 86.5 mmol) was added dropwise to the mixture and it was kept stirring at -78 °C. After 30 min, a solution of anhydrous zinc chloride (12 g, 86.5 mmol) in THF (60 mL) was added carefully. The resulting mixture was slowly warmed to room temperature and used in the next reaction without further purification.

2,4,6-Tris((trimethylsilyl)ethynyl)-1,3,5-triazine (2). The obtained solution of ((trimethylsilyl)ethynyl)zinc chloride (**1**) (86.5 mmol) was added dropwise to a mixture of cyanuric chloride (3.22 g, 17.3 mmol) and $Pd(PPh_3)_4$ (1.01 g, 0.87 mmol) in anhydrous THF (40 mL) and the mixture was kept stirring at RT for 3 h. Then the crude was poured into hydrochloric acid a 1 M (aq.) (175 mL) and extracted three times with ether. The combined organic phases were dried over anhydrous magnesium sulfate. The solution was filtered and the solvent was removed under reduced pressure. The crude product was recrystallized in methanol. Yield: 53%. IR (KBr, ν, cm^{-1}): 2169 (C≡C), 1480 (C=N). ^{1}H NMR ($CDCl_3$, 298K, 400 MHz, δ, ppm): 0.27 (s, 27H). ^{13}C NMR ($CDCl_3$, 298K, 100 MHz, δ, ppm): 159.72, 102.21, 100.5, -0.83.

1-Azido-4-butoxybenzene (3): A mixture of 4-butoxyaniline (2.6 mL, 15.1 mmol), water (40 mL), glacial acetic acid (90 mL), and concentrated hydrochloric acid (8 mL) was cooled in an ice bath. A 2 M aqueous solution of sodium nitrite (9 mL) was added dropwise to the mixture and it was kept stirring in the ice bath. Then, a solution of sodium azide (1.10 g, 16.9 mmol) in water (10 mL) was slowly added. The reaction was stirred at 0 °C for 90 min and the mixture was then extracted twice with DCM. The combined organic phases were washed twice with sodium hydroxide 10% (aq.). Then, the organic phase was washed with brine and dried over anhydrous magnesium sulfate. The product was purified by flash chromatography on silica gel using hexane as eluent. Yield: 89%. (KBr, ν, cm^{-1}): 2111 (N_3), 1504 (Ar), 1230, 1011 (C-O). ^{1}H NMR ($CDCl_3$, 298K, 400 MHz, δ, ppm): 7.01-6.93 (m, 2H), 6.91-6.86 (m, 2H), 3.95 (t, *J*= 7.0 Hz, 2H), 1.83-1.72 (m, 2H), 1.53-1.40 (m, 2H), 0.97 (t, *J*= 7.0 Hz, 3H). ^{13}C NMR (CD_2Cl_2, 298K, 100 MHz, δ, ppm): 156.72, 132.18, 120.10, 116.2, 68.23, 31.44, 19.41, 14.0.

2,4,6-Tris(1-(4-butoxyphenyl)-1,2,3-triazol-4-yl)-1,3,5-triazine (T). A Schlenk flask was charged with compound **2** (1.0 g, 2.71 mmol), 1-azido-4-butoxybenzene (**3**) (1.61 g, 8.41 mmol), sodium ascorbate (0.16 g, 0.82 mmol), copper (II) sulfate pentahydrate (0.10 g, 0.39 mmol) and THF/H_2O (1:1, 35 mL). The reaction flask was degassed by three freeze-pump-thaw cycles and flushed with argon. The reaction mixture was stirred at RT for 5 min and then tetrabutylammonium fluoride (1 M in THF, 8.4 mL) was added. The reaction was stirred at RT in the dark overnight. Then, the mixture was poured into water and extracted with DCM. The combined organic phases were dried over anhydrous magnesium sulfate. The solution was filtered

and the solvent was removed under reduced pressure. The product was purified by flash chromatography on silica gel using DCM as eluent. Finally, the crude product was recrystallized in ethanol. Yield: 42%. IR (KBr, ν, cm^{-1}): 1611, 1566, 1513 (Ar), 1247, 1169 (C-O). ^{1}H NMR (CD_2Cl_2, 298K, 400 MHz, δ, ppm): 8.86 (s, 3H), 7.64-7.58 (m, 6H), 6.98-6.92 (m, 6H), 3.97 (t, *J*= 7.0 Hz, 6H), 1.83-1.74 (m, 6H), 1.56-1.47 (m, 6H), 1.00 (t, *J*= 7.0Hz, 9H). ^{13}C NMR (CD_2Cl_2, 298K, 100 MHz, δ, ppm): 167.26, 160.40, 146.22, 130.14, 126.04, 122.60, 115.81, 68.70, 31.62, 19.62, 14.01. MS (MALDI$^+$, dithranol, m/z): calcd. for $C_{39}H_{42}N_{12}O_3$, 726.4; found, 749.5 $[M+Na]^+$, 1475.9 $[2M+Na]^+$.

3.2.2 Synthesis of the Melamine Central Core

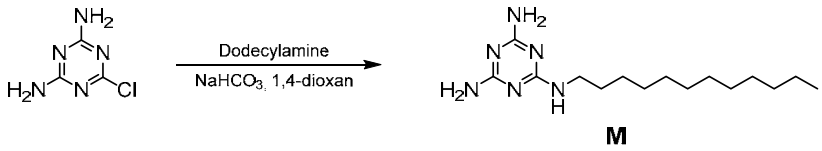

M

2,4-diamino-6-dodecylamino-1,3,5-triazine (M). A mixture of 2-chloro-4,6-diamino-1,3,5-triazine (2.77 g, 19 mmol), dodecylamine (3.52 g, 19 mmol) and sodium hydrogencarbonate (1.60 g, 19 mmol) in 1,4-dioxan (75 mL) was refluxed under argon atmosphere for 6 h. The reaction mixture was poured into water and the precipitate was filtered off and washed with water. The crude product was purified by flash column chromatography on silica gel using DCM/methanol (10:1) as eluent. Then, the product was recrystallized in ethanol. Yield: 53%. IR (KBr, ν, cm^{-1}): 3495, 3440, 3330, 1665. ^{1}H NMR (CD_2Cl_2, 298K, 400 MHz, δ, ppm): 5.09-4.68 (m, 5H), 3.36-3.23 (m, 2H), 1.58-1.44 (m, 2H), 1.44-1.17 (m, 18H), 0.8 (t, *J*= 6.7 Hz, 3H). ^{13}C NMR (CD_2Cl_2, 298K, 100 MHz, δ, ppm): 167.39, 41.06, 32.52, 30.39, 30.21, 29.96, 27.51, 23.28, 14.45. Anal. calcd. for $C_{15}H_{30}N_6$: C, 61.22%; H, 10.20%; N, 28.57%. Found: C, 61.00%; H, 10.55%; N, 28,37%.

3.2.3 Preparation of the Hydrogen-Bonded Complexes

For the preparation of the hydrogen-bonded complexes, the required amounts of the carboxylic acid **d_1Cou** and the corresponding core **M** or **T** were weighted (3:1 molar ratio) and dissolved in anhydrous DCM. The solvent was slowly evaporated at RT, and the mixtures were dried under vacuum at 30 °C for at least 2 days. Finally, the mixtures were heated to their isotropic states and then cooled down slowly to room temperature before used for further experiments.

M-d_1Cou. IR (KBr, ν, cm^{-1}): 3347 (N-H), 3086 (=C-H), 2921 (C-H), 1728, 1688 (C=O), 1610, 1589, 1553, 1510 (Ar), 1223, 1116 (C-O). ^{1}H NMR (CD_2Cl_2, 298K, 500 MHz, δ, ppm): 7.69-7.59 (m, 9H), 7.40-7.33 (m, 9H), 7.30 (s, 6H), 6.86-6.75 (m, 18H), 6.30 (t, *J*= 5.6 Hz, 1H), 6.22-6.14 (m, 9H), 6.11-5.96 (m, 4H), 4.66 (s_{broad}, 1H), 4.11-3.91 (m, 36H), 3.45-3.25 (m, 2H), 1.88-1.68 (m, 36H), 1.62-1.18 (m, 146H), 0.87 (t, *J*= 7.0 Hz, 3H). ^{13}C NMR (CD_2Cl_2, 298K, 125 MHz, δ, ppm): 170.57, 164.73, 162.90, 161.36, 156.41, 153.29, 143.82, 142.95, 129.20, 125.32, 113.24, 113.17, 112.85, 108.60, 101.66, 73.85, 69.59, 69.20, 41.26, 32.35, 30.77, 30.11, 30.03, 30.00, 29.96, 29.80, 29.78, 29.77, 29.46, 29.43, 27.27, 26.51, 26.40, 26.36, 23.11, 14.30.

T-d_1Cou. IR (KBr, ν, cm^{-1}): 3079 (=C-H), 2920 (C-H), 1729, 1695 (C=O), 1611, 1582, 1555, 1505 (Ar), 1226, 1117 (C-O). ^{1}H NMR (CD_2Cl_2, 298K, 500 MHz, δ, ppm): 9.04 (s, 3H), 7.84-7.75 (m, 6H), 7.69-7.59 (m, 9H), 7.41-7.33 (m, 9H), 7.30 (s, 6H), 7.13-7.07 (m, 6H), 6.87-6.75 (m, 18H), 6.22-6.15 (m, 9H), 4.11-3.96 (m, 42H), 1.89-1.68 (m, 42H), 1.60-1.22 (m, 152H), 1.01 (t, *J*= 7.4 Hz, 6H). ^{13}C NMR (CD_2Cl_2, 298K, 125 MHz, δ, ppm): 169.79, 167.29, 162.91, 161.39, 160.46, 156.42, 153.35, 146.26, 143.84, 143.29, 130.19, 129.21, 126.12, 124.19, 122.66, 115.87, 113.24, 113.18, 112.85, 108.71, 101.66, 73.88, 69.62, 69.21, 68.75, 31.65, 30.77, 29.96, 29.77, 29.43, 26.49, 26.36, 19.64, 14.02.

3.3 Experimental Procedures

3.3.1 Preparation of the Liquid Crystalline Polymer Networks

Poly(vinyl alcohol) (PVA) sacrificial layers were prepared onto glass substrates in order to facilitate network extraction after coumarin photodimerization. LC films were prepared by sandwiching a small amount of the supramolecular complex between two PVA-coated glass substrates using silicon spacers of 10 µm. The system was heated to the isotropic state and slowly cooled down to RT (0.1 ºC/min). Then, the system was irradiated with a 365 nm LED light (ThorsLab) for 30 min (15 min each side). Finally, the system was immersed in water to dissolve the PVA layer in order to obtain the polymer films floating at the water surface. Then the films were dried under vacuum at RT for 5 h.

3.3.2 Preparation of the Nanoporous Polymers by Template Elimination

For the elimination of **M** or **T** templates, polymer films were immersed in 5 ml of hydrochloric acid 3 M (ethanol solution) under orbital oscillation for 24 h. Then the films were washed with water, ethanol and dried under vacuum at RT 5 h to produce the nanoporous polymers.

3.3.3 Selective Adsorption of Neutral Molecules

p-Nitroaniline, 1-aminopyrene, and *meso*-tetra(*p*-aminophenyl)porphine were dried prior to use and dissolved at a known concentration in methanol to get relatives absorbances of approximately 1. The nanoporous polymers were cut into small pieces of approximately 1.0 mg, and were immersed in the *p*-nitroaniline, 1-aminopyrene, or *meso*-tetra(*p*-aminophenyl)porphine solutions. The films were allowed to adsorb the molecules at RT overnight. The adsorption behavior was monitored by UV-Vis spectroscopy, and the dye concentration was calculated using the peak maximum.

The sizes of *p*-nitroaniline, 1-aminopyrene, and *meso*-tetra(*p*-aminophenyl) porphine were calculated by the MM2 force field method using the Chem3D software package.

3.3.4 Preparation of Anionic Nanoporous Polymers with Different Counter Cations in the Pore

The nanoporous polymers were cut into small pieces of approximately 1.0 mg, and were immersed in 0.1 M aqueous solutions of the hydroxide salts of Li^+, Na^+, K^+, Cs^+ and NH_4^+ ions for 5 h. They were quickly washed with a few milliliters of distilled water to remove the residual base and them they were dried under vacuum at RT for 5 h.

3.3.5 Selective Adsorption of Cationic Dyes

The dyes (methylene blue, methyl orange and rhodamine B) were dried prior to use and dissolved at a known concentration in distilled water to get relatives absorbances of approximately 1. The nanoporous polymers were cut into small pieces of approximately 1.0 mg, and were immersed in potassium hydroxide 0.1 M (aq.) to deprotonate the carboxylic acid moieties. They were quickly washed with a few milliliters of distilled water to remove the residual base, and subsequently, they were added to the dye solution. The films were allowed to adsorb the molecules at RT overnight. The adsorption behavior was monitored by UV-Vis spectroscopy, and the dye concentration was calculated using the peak maximum.

The sizes of methylene blue, methyl orange, and rhodamine B were calculated by the MM2 force field method using the Chem3D software package.

4. REFERENCES

(1) J. Zhang & C. M. Li. Nanoporous metals: fabrication strategies and advanced electrochemical applications in catalysis, sensing and energy systems. *Chem. Soc. Rev.* **2012,** *41*, 7016-7031.

(2) M. Shah, M. C. McCarthy, S. Sachdeva, A. K. Lee & H.-K. Jeong. Current Status of Metal–Organic Framework Membranes for Gas Separations: Promises and Challenges. *Ind. Eng. Chem. Res.* **2012,** *51*, 2179-2199.

(3) J. Gascon, F. Kapteijn, B. Zornoza, V. Sebastián, C. Casado & J. Coronas. Practical Approach to Zeolitic Membranes and Coatings: State of the Art, Opportunities, Barriers, and Future Perspectives. *Chem. Mater.* **2012,** *24*, 2829-2844.

(4) K. Na, M. Choi & R. Ryoo. Recent advances in the synthesis of hierarchically nanoporous zeolites. *Microporous Mesoporous Mat.* **2013,** *166*, 3-19.

(5) J. R. Holst, A. Trewin & A. I. Cooper. Porous organic molecules. *Nat. Chem.* **2010,** *2*, 915-920.

(6) J. Tian, P. K. Thallapally & B. P. McGrail. Porous organic molecular materials. *CrystEngComm* **2012,** *14*, 1909-1919.

(7) D. Wu, F. Xu, B. Sun, R. Fu, H. He & K. Matyjaszewski. Design and Preparation of Porous Polymers. *Chem. Rev.* **2012,** *112*, 3959-4015.

(8) Y. Mai & A. Eisenberg. Self-assembly of block copolymers. *Chem. Soc. Rev.* **2012,** *41*, 5969-5985.

(9) C. M. Bates & F. S. Bates. 50th Anniversary Perspective: Block Polymers—Pure Potential. *Macromolecules* **2017,** *50*, 3-22.

(10) M. A. Hillmyer, Nanoporous Materials from Block Copolymer Precursors. In *Block Copolymers II*, V. Abetz, Ed. Springer Berlin Heidelberg: Berlin, Heidelberg, **2005**; pp 137-181.

(11) C. G. Gamys, J. M. Schumers, C. Mugemana, C. A. Fustin & J. F. Gohy. Pore-Functionalized Nanoporous Materials Derived from Block Copolymers. *Macromol. Rapid Commun.* **2013,** *34*, 962-982.

(12) H. Ahn, S. Park, S. W. Kim, P. J. Yoo, D. Y. Ryu & T. P. Russell. Nanoporous Block Copolymer Membranes for Ultrafiltration: A Simple Approach to Size Tunability. *ACS Nano* **2014,** *8*, 11745-11752.

(13) A. P. H. J. Schenning, Y. C. González-Lemus, I. K. Shishmanova & D. J. Broer. Nanoporous membranes based on liquid crystalline polymers. *Liq. Cryst.* **2011,** *38*, 1627-1639.

(14) D. J. Broer, C. M. W. Bastiaansen, M. G. Debije & A. P. H. J. Schenning. Functional Organic Materials Based on Polymerized Liquid-Crystal Monomers: Supramolecular Hydrogen-Bonded Systems. *Angew. Chem. Int. Ed.* **2012,** *51*, 7102-7109.

(15) J. Lugger, D. Mulder, R. Sijbesma & A. Schenning. Nanoporous Polymers Based on Liquid Crystals. *Materials* **2018,** *11*, 104.

(16) H. K. Lee, H. Lee, Y. H. Ko, Y. J. Chang, N. K. Oh, W. C. Zin & K. Kim. Synthesis of a Nanoporous Polymer with Hexagonal Channels from Supramolecular Discotic Liquid Crystals. *Angew. Chem. Int. Ed.* **2001,** *40*, 2669-2671.

(17) Y. Ishida, S. Amano, N. Iwahashi & K. Saigo. Switching of Structural Order in a Cross-Linked Polymer Triggered by the Desorption/Adsorption of Guest Molecules. *J. Am. Chem. Soc.* **2006,** *128*, 13068-13069.

(18) Y. Ishida, H. Sakata, A. S. Achalkumar, K. Yamada, Y. Matsuoka, N. Iwahashi, S. Amano & K. Saigo. Guest-Responsive Covalent Frameworks by the Cross-Linking of Liquid-Crystalline Salts: Tuning of Lattice Flexibility by the Design of Polymerizable Units. *Chem. Eur. J.* **2011,** *17*, 14752-14762.

(19) C. Li, J. Cho, K. Yamada, D. Hashizume, F. Araoka, H. Takezoe, T. Aida & Y. Ishida. Macroscopic ordering of helical pores for arraying guest molecules noncentrosymmetrically. *Nat. Commun.* **2015,** *6*, 8418.

(20) G. M. Bögels, J. A. M. Lugger, O. J. G. M. Goor & R. P. Sijbesma. Size-Selective Binding of Sodium and Potassium Ions in Nanoporous Thin Films of Polymerized Liquid Crystals. *Adv. Funct. Mater.* **2016,** *26*, 8023-8030.

(21) X. Feng, K. Kawabata, G. Kaufman, M. Elimelech & C. O. Osuji. Highly Selective Vertically Aligned Nanopores in Sustainably Derived Polymer Membranes by Molecular Templating. *ACS Nano* **2017,** *11*, 3911-3921.

(22) J. H. Lee. Fabrication of conjugated polymeric nanochannels from star-shaped supramolecular liquid crystals containing two different photoreactive groups. *Liq. Cryst.* **2014,** *41*, 738-746.

(23) I. Gracia, P. Romero, J. L. Serrano, J. Barberá & A. Omenat. Templated nanoporous membranes based on hierarchically self-assembled materials. *J. Mater. Chem. C* **2017,** *5*, 2033-2042.

(24) V. Percec, A. E. Dulcey, V. S. K. Balagurusamy, Y. Miura, J. Smidrkal, M. Peterca, S. Nummelin, U. Edlund, S. D. Hudson, P. A. Heiney, H. Duan, S. N. Magonov & S. A. Vinogradov. Self-assembly of amphiphilic dendritic dipeptides into helical pores. *Nature* **2004,** *430*, 764-768.

(25) N. Sakai, Y. Kamikawa, M. Nishii, T. Matsuoka, T. Kato & S. Matile. Dendritic Folate Rosettes as Ion Channels in Lipid Bilayers. *J. Am. Chem. Soc.* **2006,** *128*, 2218-2219.

(26) M. Yoshio, T. Kagata, K. Hoshino, T. Mukai, H. Ohno & T. Kato. One-Dimensional Ion-Conductive Polymer Films: Alignment and Fixation of Ionic Channels Formed by Self-Organization of Polymerizable Columnar Liquid Crystals. *J. Am. Chem. Soc.* **2006,** *128*, 5570-5577.

(27) X. Feng, M. E. Tousley, M. G. Cowan, B. R. Wiesenauer, S. Nejati, Y. Choo, R. D. Noble, M. Elimelech, D. L. Gin & C. O. Osuji. Scalable Fabrication of Polymer Membranes with Vertically Aligned 1 nm Pores by Magnetic Field Directed Self-Assembly. *ACS Nano* **2014,** *8*, 11977-11986.

(28) X. Feng, S. Nejati, M. G. Cowan, M. E. Tousley, B. R. Wiesenauer, R. D. Noble, M. Elimelech, D. L. Gin & C. O. Osuji. Thin Polymer Films with Continuous Vertically Aligned 1 nm Pores Fabricated by Soft Confinement. *ACS Nano* **2016,** *10*, 150-158.

(29) K. Kishikawa, A. Hirai & S. Kohmoto. Fixation of Multilayered Structures of Liquid-Crystalline 2:1 Complexes of Benzoic Acid Derivatives and Dipyridyl Compounds and the Effect of Nanopillars on Removal of the Dipyridyl Molecules from the Polymers. *Chem. Mater.* **2008,** *20*, 1931-1935.

(30) C. L. Gonzalez, C. W. M. Bastiaansen, J. Lub, J. Loos, K. Lu, H. J. Wondergem & D. J. Broer. Nanoporous Membranes of Hydrogen-bridged Smectic Networks with Nanometer Transverse Pore Dimensions. *Adv. Mater.* **2008,** *20*, 1246-1252.

(31) H. P. C. van Kuringen, G. M. Eikelboom, I. K. Shishmanova, D. J. Broer & A. P. H. J. Schenning. Responsive Nanoporous Smectic Liquid Crystal Polymer Networks as Efficient and Selective Adsorbents. *Adv. Funct. Mater.* **2014,** *24*, 5045-5051.

(32) H. P. C. van Kuringen, Z. J. W. A. Leijten, A. H. Gelebart, D. J. Mulder, G. Portale, D. J. Broer & A. P. H. J. Schenning. Photoresponsive Nanoporous Smectic Liquid Crystalline Polymer Networks: Changing the Number of Binding Sites and Pore Dimensions in Polymer Adsorbents by Light. *Macromolecules* **2015,** *48*, 4073-4080.

(33) A. Longo, D.-J. Mulder, H. P. C. van Kuringen, D. Hermida-Merino, D. Banerjee, D. Dasgupta, I. K. Shishmanova, A. B. Spoelstra, D. J. Broer, A. P. H. J. Schenning & G. Portale. On the Dimensional Control of 2 D Hybrid Nanomaterials. *Chem. Eur. J.* **2017,** *23*, 12534-12541.

(34) D. Dasgupta, I. K. Shishmanova, A. Ruiz-Carretero, K. Lu, M. Verhoeven, H. P. C. van Kuringen, G. Portale, P. Leclère, C. W. M. Bastiaansen, D. J. Broer & A. P. H. J. Schenning. Patterned Silver Nanoparticles embedded in a Nanoporous Smectic Liquid Crystalline Polymer Network. *J. Am. Chem. Soc.* **2013,** *135*, 10922-10925.

(35) T. Liang, H. P. C. van Kuringen, D. J. Mulder, S. Tan, Y. Wu, Z. Borneman, K. Nijmeijer & A. P. H. J. Schenning. Anisotropic Dye Adsorption and Anhydrous Proton Conductivity in Smectic Liquid Crystal Networks: The Role of Cross-Link Density, Order, and Orientation. *ACS Appl. Mater. Interfaces* **2017,** *9*, 35218-35225.

(36) D. J. Mulder, L. M. W. Scheres, J. Dong, G. Portale, D. J. Broer & A. P. H. J. Schenning. Fabrication and Postmodification of Nanoporous Liquid Crystalline Networks via Dynamic Covalent Chemistry. *Chem. Mater.* **2017,** *29*, 6601-6605.

(37) S. Hernández-Ainsa, M. Marcos & J. L. Serrano, Dendrimeric and Hyperbranched Liquid Crystal Structures. In *Handbook of Liquid Crystals*, Second ed.; J. W. Goodby, P. J. Collings, T. Kato, C. Tschierske, H. Gleeson & P. Raynes, Eds. Wiley-VCH Verlag GmbH & Co. KGaA: **2014**; Vol. 7, pp 259-300.

(38) J. van Herrikhuyzen, P. Jonkheijm, A. P. H. J. Schenning & E. W. Meijer. The influence of hydrogen bonding and [small pi]-[small pi] stacking interactions on the self-assembly properties of C3-symmetrical oligo(p-phenylenevinylene) discs. *Org. Biomol. Chem.* **2006,** *4*, 1539-1545.

(39) R. I. Gearba, D. V. Anokhin, A. I. Bondar, W. Bras, M. Jahr, M. Lehmann & D. A. Ivanov. Homeotropic Alignment of Columnar Liquid Crystals in Open Films by Means of Surface Nanopatterning. *Adv. Mater.* **2007,** *19*, 815-820.

(40) Ž. Tomović, J. van Dongen, S. J. George, H. Xu, W. Pisula, P. Leclère, M. M. J. Smulders, S. De Feyter, E. W. Meijer & A. P. H. J. Schenning. Star-Shaped Oligo(p-phenylenevinylene) Substituted Hexaarylbenzene: Purity, Stability, and Chiral Self-assembly†. *J. Am. Chem. Soc.* **2007,** *129*, 16190-16196.

(41) J. Jiménez, A. Laguna, E. Gascón, J. A. Sanz, J. L. Serrano, J. Barberá & L. Oriol. New Liquid Crystalline Materials Based on Two Generations of Dendronised Cyclophosphazenes. *Chem. Eur. J.* **2012,** *18*, 16801-16814.

(42) M. Lehmann, P. Maier, M. Grüne & M. Hügel. Crowded Star Mesogens: Guest-Controlled Stability of Mesophases from Unconventional Liquid-Crystal Molecules. *Chem. Eur. J.* **2017,** *23*, 1060-1068.

(43) M. Suárez, J. M. Lehn, S. C. Zimmerman, A. Skoulios & B. Heinrich. Supramolecular Liquid Crystals. Self-Assembly of a Trimeric Supramolecular Disk and Its Self-Organization into a Columnar Discotic Mesophase. *J. Am. Chem. Soc.* **1998,** *120*, 9526-9532.

(44) T. Kato, N. Mizoshita & K. Kishimoto. Functional Liquid-Crystalline Assemblies: Self-Organized Soft Materials. *Angew. Chem. Int. Ed.* **2006,** *45*, 38-68.

(45) B. M. Rosen, C. J. Wilson, D. A. Wilson, M. Peterca, M. R. Imam & V. Percec. Dendron-Mediated Self-Assembly, Disassembly, and Self-Organization of Complex Systems. *Chem. Rev.* **2009,** *109*, 6275-6540.

(46) H. J. Sun, S. Zhang & V. Percec. From structure to function via complex supramolecular dendrimer systems. *Chem. Soc. Rev.* **2015,** *44*, 3900-3923.

(47) K. Kanie, M. Nishii, T. Yasuda, T. Taki, S. Ujiie & T. Kato. Self-assembly of thermotropic liquid-crystalline folic acid derivatives: hydrogen-bonded complexes forming layers and columns. *J. Mater. Chem.* **2001,** *11*, 2875-2886.

(48) T. Kato. Self-Assembly of Phase-Segregated Liquid Crystal Structures. *Science* **2002,** *295*, 2414-2418.

(49) K. Kishikawa, S. Nakahara, Y. Nishikawa, S. Kohmoto & M. Yamamoto. A Ferroelectrically Switchable Columnar Liquid Crystal Phase with Achiral Molecules: Superstructures and Properties of Liquid Crystalline Ureas. *J. Am. Chem. Soc.* **2005,** *127*, 2565-2571.

(50) A. S. Tayi, A. Kaeser, M. Matsumoto, T. Aida & S. I. Stupp. Supramolecular ferroelectrics. *Nat. Chem.* **2015,** *7*, 281-294.

(51) D. Miyajima, F. Araoka, H. Takezoe, J. Kim, K. Kato, M. Takata & T. Aida. Ferroelectric Columnar Liquid Crystal Featuring Confined Polar Groups Within Core–Shell Architecture. *Science* **2012,** *336*, 209-213.

(52) D. Miyajima, F. Araoka, H. Takezoe, J. Kim, K. Kato, M. Takata & T. Aida. Columnar Liquid Crystal with a Spontaneous Polarization along the Columnar Axis. *J. Am. Chem. Soc.* **2010,** *132*, 8530-8531.

(53) M. Lehmann & P. Maier. Shape-Persistent, Sterically Crowded Star Mesogens: From Exceptional Columnar Dimer Stacks to Supermesogens. *Angew. Chem. Int. Ed.* **2015,** *54*, 9710-9714.

(54) L. Alvarez, J. Barbera, L. Puig, P. Romero, J. L. Serrano & T. Sierra. Supramolecular chirality of columnar mesophases consisting of H-bonded complexes of melamine and polycatenar benzoic acids. *J. Mater. Chem.* **2006,** *16*, 3768-3773.

(55) J. Barberá, L. Puig, P. Romero, J. L. Serrano & T. Sierra. Propeller-like Hydrogen-Bonded Banana−Melamine Complexes Inducing Helical Supramolecular Organizations. *J. Am. Chem. Soc.* **2006,** *128*, 4487-4492.

(56) F. Vera, J. Barberá, P. Romero, J. L. Serrano, M. B. Ros & T. Sierra. Orthogonal Action of Noncovalent Interactions for Photoresponsive Chiral Columnar Assemblies. *Angew. Chem. Int. Ed.* **2010,** *49*, 4910-4914.

(57) F. Vera, R. M. Tejedor, P. Romero, J. Barberá, M. B. Ros, J. L. Serrano & T. Sierra. Light-Driven Supramolecular Chirality in Propeller-Like Hydrogen-Bonded Complexes That Show Columnar Mesomorphism. *Angew. Chem. Int. Ed.* **2007,** *46*, 1873-1877.

(58) B. Feringán, P. Romero, J. L. Serrano, R. Giménez & T. Sierra. Supramolecular Columnar Liquid Crystals Formed by Hydrogen Bonding between a Clicked Star-Shaped s-Triazine and Benzoic Acids. *Chem. Eur. J.* **2015,** *21*, 8859-8866.

(59) S. Castelar, J. Barberá, M. Marcos, P. Romero, J. L. Serrano, A. Golemme & R. Termine. Supramolecular dendrimers based on the self-assembly of carbazole-derived dendrons and triazine rings: liquid crystal, photophysical and electrochemical properties. *J. Mater. Chem. C* **2013,** *1*, 7321-7332.

(60) M. Bucoş, T. Sierra, A. Golemme, R. Termine, J. Barberá, R. Giménez, J. L. Serrano, P. Romero & M. Marcos. Multifunctional Supramolecular Dendrimers with an s-Triazine Ring as the Central Core: Liquid Crystalline, Fluorescence and Photoconductive Properties. *Chem. Eur. J.* **2014,** *20*, 10027-10037.

(61) A. Concellón, M. Bucoş, J. L. Serrano, P. Romero & M. Marcos. Supramolecular liquid crystalline dendrimers with a porphyrin core and functional carboxylic acid dendrons. *RSC Adv.* **2016,** *6*, 65179-65185.

Chapter 4

Novel Dendritic Architectures for Biomedical Applications

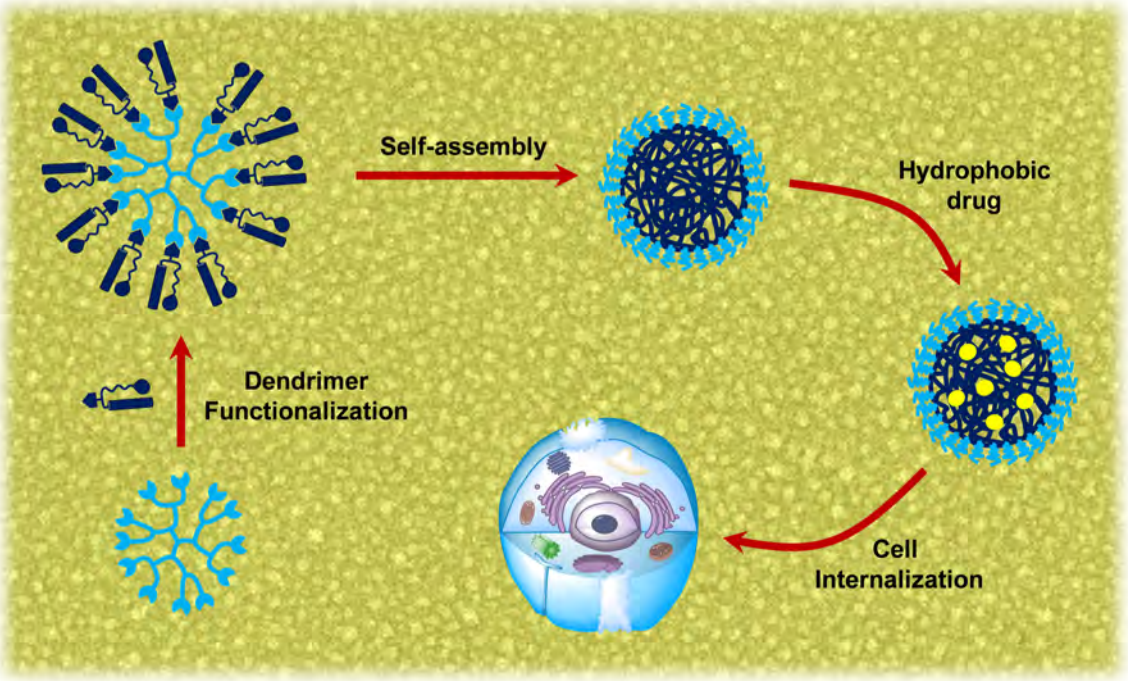

Abstract. *We report the synthesis and characterization of a novel class of amphiphilic dendrimers from a hydrophilic PAMAM dendrimer functionalized with hydrophobic bisMPA first generation dendrons bearing cholesterol and coumarin moieties. As demonstrated by TEM and DLS, these dendrimers are capable of forming stable spherical micelles in water with diameters of 18–40 nm, depending on the generation of the dendrimer. In addition, these spherical micelles permitted the encapsulation of hydrophobic drugs and at the same time provided intracellular fluorescent traceability due to the presence of coumarin units in their chemical structure. Therefore, these dendrimers are interesting nanocarriers for applications in nanotechnology and biomedicine.*

“If you always do what you always did,
you will always get what you always got”

Albert Einstein

1. INTRODUCTION

1.1 Self-Assembly of Amphiphilic Block Copolymers

The design of efficient drug delivery vehicles is a true challenge in polymer and materials science. Since the concept of physical drug encapsulation within polymeric aggregates was introduced, a significant number of polymer assemblies have been identified. In particular, the construction of amphiphilic block copolymer-based drug carriers is a subject of great interest and is a stimulating topic of interdisciplinary research in chemistry, biology and materials science.[1-6]

In aqueous media, self-assembly of amphiphilic block copolymers to minimize energetically unfavorable hydrophobic-water interactions can lead to a variety of polymeric nanostructures, such as micelles or vesicles (**Figure 1.1**).[7-11] Formation of these various morphologies, as well as their size, has been demonstrated to be highly dependent on the composition, molecular geometry and relative block lengths of the block copolymers.

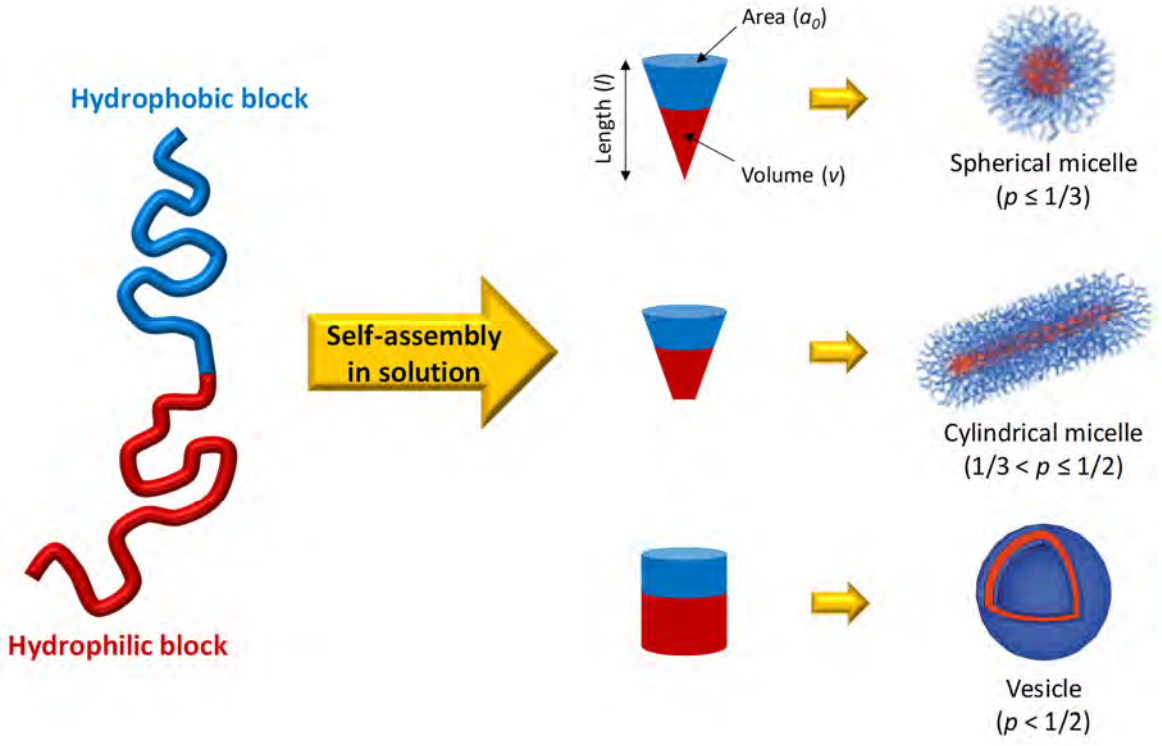

Figure 1.1 Different morphologies formed by amphiphilic block copolymers depending on the packing parameter (p).

The packing parameter (p), introduced by Israelachvili *et al.* in their theory of self-assembly of small molecule amphiphiles,[12] can be used to predict the assembled

morphologies. The packing parameter describes the geometry of an amphiphile and it is calculated by the equation:

$$p = \frac{v}{a_0 \times l}$$

where v is the volume of the hydrophobic chain, a_0 is the area occupied by the hydrophilic headgroup, and l is the length of the molecule. As a general rule, amphiphiles with *p* values below 0.5 result in highly curved aggregates such as spherical and cylindrical micelles, while bilayer formation is favored with increasing *p* values up to *p*= 1.

Spherical micelles typically exhibit core-shell architectures in which the hydrophilic shell affords water solubility, while the hydrophobic core provides an ideal location for encapsulation of hydrophobic molecules. As far as intravenous delivery of chemotherapeutic agents is concerned, polymeric micelles are perfect instruments to solubilize hydrophobic drugs, infiltrate the body with a minimal immunogenic response and target diseased tissues, thus releasing the drug payload at its destination while minimizing damage to healthy tissues.[13-15]

Polymeric vesicles, so-called polymersomes, originate from closing bilayers forming a central aqueous compartment which is enclosed by an amphiphilic copolymer bilayer membrane. The hydrophobic chains create a wall membrane stabilized by the hydrophilic chains forming internal and external shells. Polymer vesicles are also excellent candidates for drug delivery as they offer the benefit of simultaneous encapsulation of hydrophilic compounds in their aqueous cavities and the insertion of hydrophobic molecules within their membrane.[16, 17]

1.2 Amphiphilic Dendrimers as Drug Delivery Systems

In the field of amphiphilic polymers, dendrimers are ideal candidates for biomedical applications due to their flawless macromolecular structure and exact number of functional groups. For this reason, dendritic amphiphiles capable of forming well-defined nanostructures in water have been thoroughly investigated.[18-22] One of the first examples was reported by Tomalia's research group and it consisted of a hydrophobic dendritic core surrounded by an hydrophilic shell.[23] These compounds self-assembled in water, generating micelles composed of only one molecule (unimolecular micelles). Such systems can encapsulate hydrophobic drugs or dyes in their dendritic structure, and they can be easily internalized by cells due to their small diameters of 5–20 nm.[24, 25]

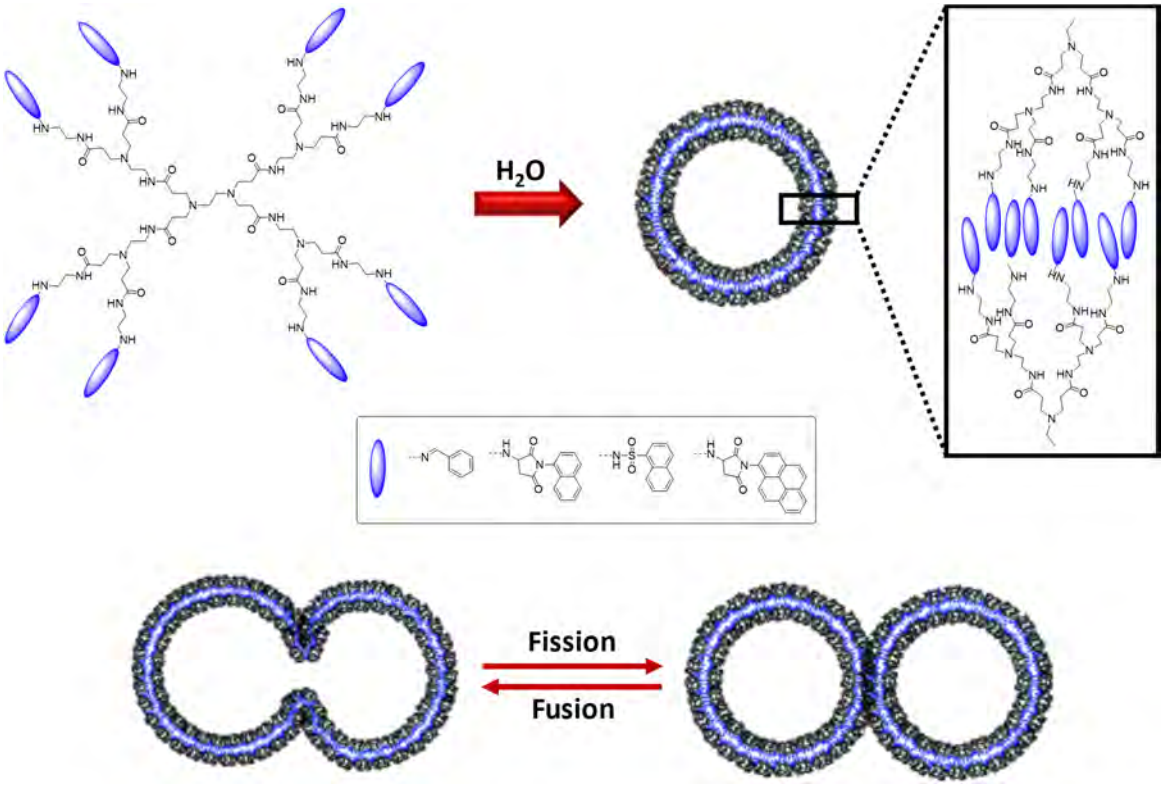

Figure 1.2 Chemical structure of PAMAM derivatives functionalized with chromophores and a schematic illustration of vesicle formation.

Wang *et al.* synthesized amphiphilic PAMAM dendrimers by periphery functionalization with phenyl, naphthyl, pyrenyl, and dansyl chromophores (**Figure 1.2**).[26] Low generation dendrimers (G= 0–3) self-organized in water into vesicles, while higher generations (G= 4–5) did not form ordered aggregates. This self-organization was induced by the π-π interactions of the peripheral aromatic

chromophores and hydrogen bonding interactions of the PAMAM core. Moreover, a large number of “twins” and “quins” vesicular aggregates consisting of two and five vesicles, respectively, were observed.

Our research group synthesized new amphiphilic dendritic architectures from commercial hyperbranched bisMPA polyesters (Boltorn®) and amino-terminated bisMPA dendrons.[27] These compounds were totally biocompatible, and their high number of terminal amino groups made them efficient systems in terms of complex formation with DNA and internalization inside mesenchymal stem cells. Efficient transfection on mesenchymal stem cells was found to be generation dependent.

Lee *et al.* synthesized an amphiphilic dendritic structure consisting of a rigid aromatic core functionalized with carbohydrate-branched dendrons and a hydrophobic alkyl chain (**Figure 1.3**).[28] Such compounds self-assembled in aqueous solution into well-defined nanofibers with uniform diameters. Interestingly, these cylindrical objects reversibly transformed into spherical objects after the addition of guest molecules such as Nile Red.

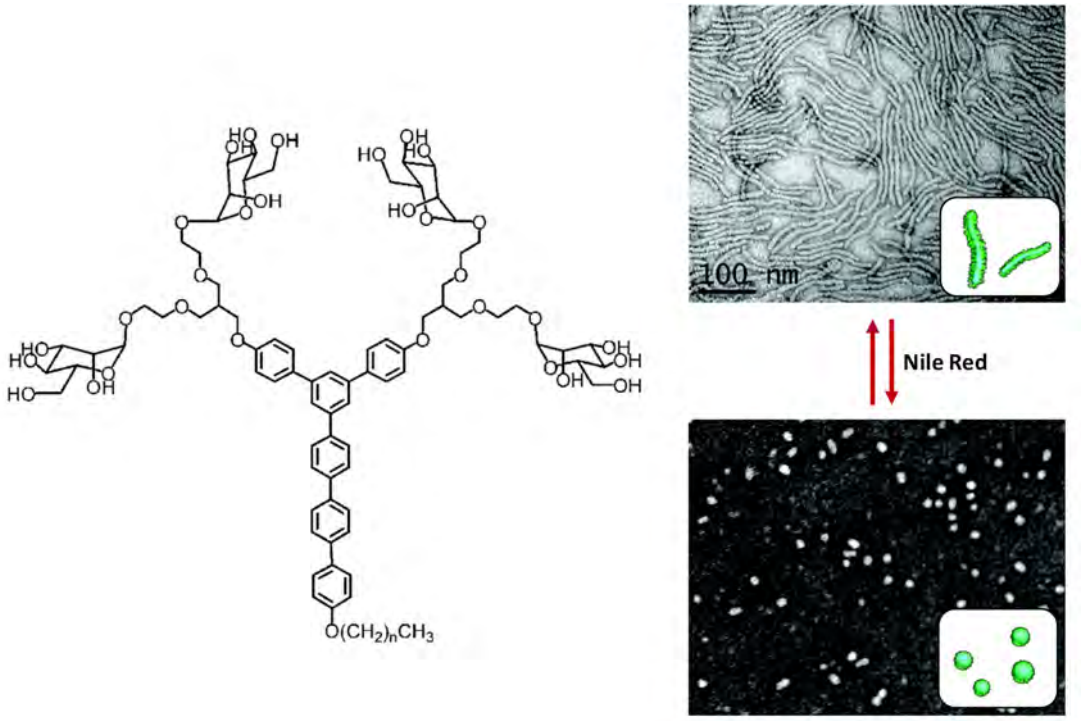

Figure 1.3 Chemical structure of the amphiphilic dendron and TEM images of the reversible transformation of cylindrical micelles into spherical micelles.

Percec and coworkers reported an extensive library of amphiphilic *Janus* dendrimers which demonstrated facile self-assembly in water to form stable

vesicles.[29] These systems were prepared by coupling of two antagonistic parts, one is hydrophilic and the second one is hydrophobic. Similarly, our research group described a series of Janus dendrimers which self-assembled in water forming different morphologies depending on the hydrophilic/hydrophobic balance. These dendrimers could encapsulate several hydrophobic drugs, increasing their water solubility without altering their therapeutic activity.[30-32]

Meijer's research group reported the synthesis of new amphiphilic structures by combining a well-defined polystyrene block with PPI dendrons (G= 1–5).[33] In the aqueous phase, these linear-dendritic block copolymers formed different assemblies (from spherical micelles to vesicles) depending on the generation of the dendron (**Figure 1.4**).

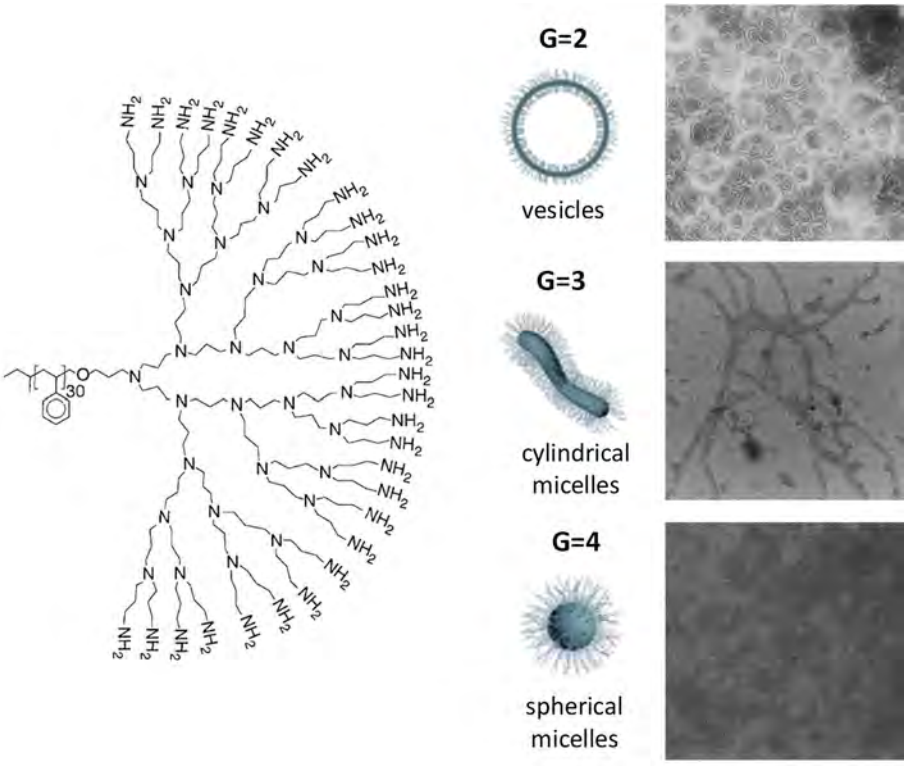

Figure 1.4 Chemical structure of the linear dendritic block copolymers and TEM images of the different self-assemblies.

Our research group reported aqueous assemblies (cylindrical micelles, sheet-like micelles, tubular micelles or vesicles) based on amphiphilic linear-dendritic block copolymers composed of poly(ethylene glycol) and dendrons based on bisMPA functionalized at the periphery with 4-cyanoazobenzene moieties (**Figure 1.5**).[34] Theoretical simulations of these systems predicted the disruption of the

macromolecular assemblies by photoisomerization thus facilitating the release of encapsulated molecules.[35]

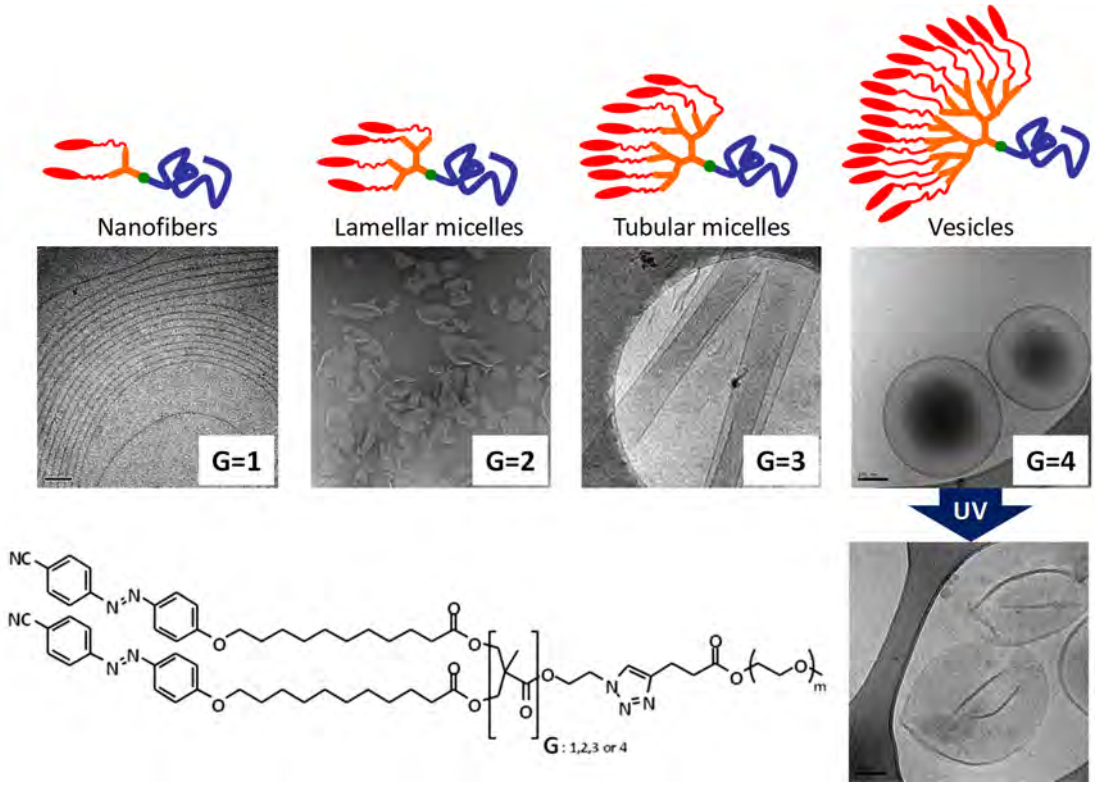

Figure 1.5 Cryo-TEM images showing the morphological evolution of the linear dendritic block copolymers self-assemblies in water.

Additionally, these vesicles were loaded with both hydrophobic and hydrophilic fluorescent probes to demonstrate that the distortion of the bilayer membrane under low intensity UV irradiation increases its permeability to the encapsulated molecules (**Figure 1.6**).[36-38]

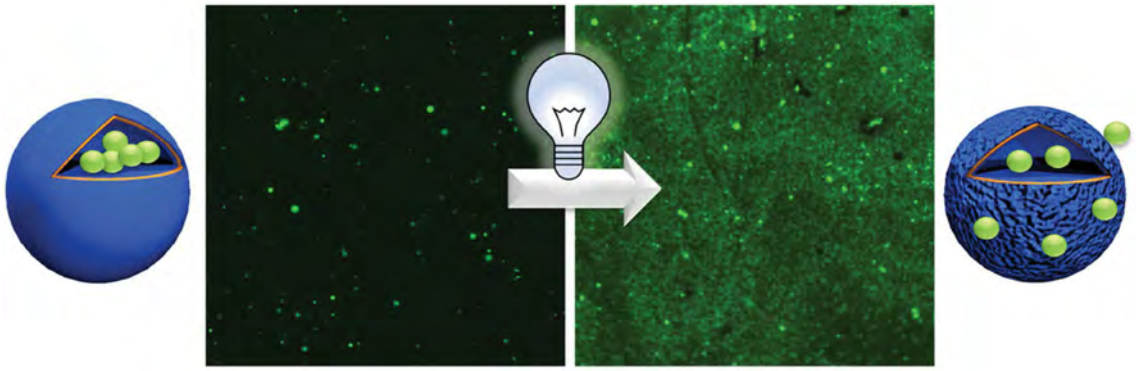

Figure 1.6 Confocal fluorescence microscopy images showing the light stimulated release of Rhodamine B upon UV irradiation of loaded vesicles.

Very recently, Malkoch *et al.* reported the synthesis a new family of amphiphilic linear-dendritic block copolymers (**Figure 1.7**). They consisted of a hydrophilic poly(ethylene glycol) block and a fourth generation bisMPA dendron functionalized with hydrophobic cholesterol groups.[39] Spherical assemblies with therapeutically relevant properties were successfully created in water. These nanocarriers allowed the encapsulation of one or two anticancer drugs and also provided intracellular fluorescent traceability. Moreover, these nanocarriers were proven to penetrate the cancerous cell membranes and deliver the cargo of drugs into the nuclei as well as the cytoplasm and mitochondria.

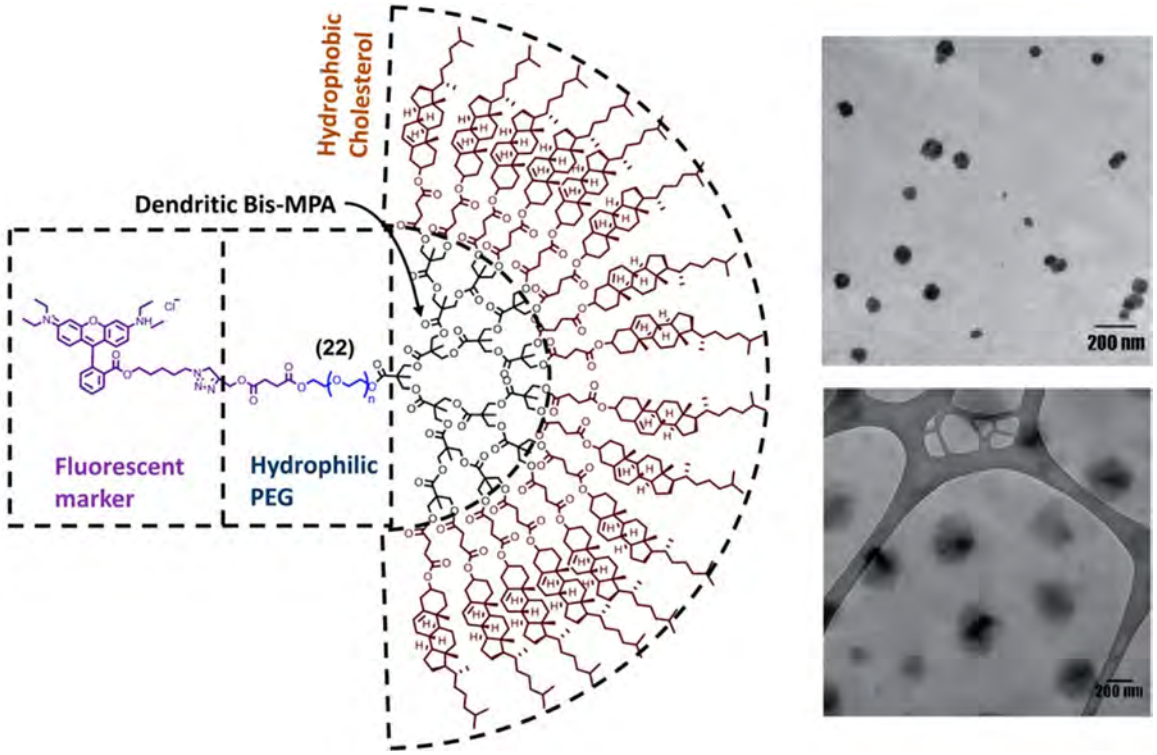

Figure 1.7 Chemical structure and TEM images of the fluorescent linear dendritic block copolymer self-assemblies reported by Malkoch *et al.*

All the aqueous assemblies were obtained from covalent dendritic systems, but ultimately the frequently time-consuming synthetic procedures required to synthesize the dendrimers might reduce their practical feasibility in controlled drug release. Therefore, an effective approach to obtain self-assembled systems in water would consist of using supramolecular (ionic) interactions to functionalize a dendritic core. For instance, our research group reported ionic amphiphilic PAMAM dendrimers bearing aliphatic chains that self-assembled in water generating different nanostructures (**Figure 1.8**). Micelles, lamellae, and nanospheres were found depending on the generation of the dendrimer, the length of the acid, and

the number of fatty acids introduced in the PAMAM core. Furthermore, these nanostructures were sensitive to pH and were capable of trapping both hydrophobic and hydrophilic molecules.[40-42] Our research group has also prepared ionic PAMAM dendrimers decorated with hydrophilic chains that were able to form complexes with DNA.[43]

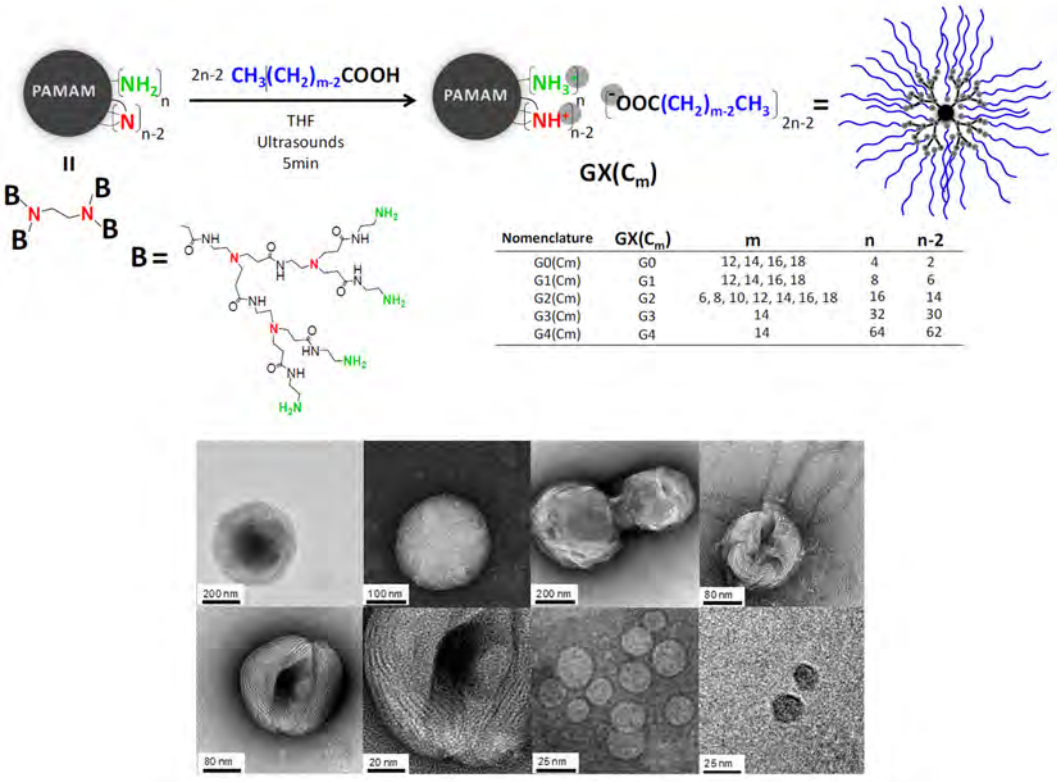

Nomenclature	GX(C_m)	m	n	n-2
G0(Cm)	G0	12, 14, 16, 18	4	2
G1(Cm)	G1	12, 14, 16, 18	8	6
G2(Cm)	G2	6, 8, 10, 12, 14, 16, 18	16	14
G3(Cm)	G3	14	32	30
G4(Cm)	G4	14	64	62

Figure 1.8 Schematic synthetic route, chemical structure, and TEM images of the self-assemblies in water prepared with ionic dendrimers.

2. LUMINESCENT DENDRIMERS AS DRUG DELIVERY SYSTEMS

2.1 Objectives

Polymeric nanocarriers have attracted much attention during the past decade because they are able to carry large quantities of therapeutic drugs to their final destination, effectively protect their cargo from the body and more importantly, the body from the cargo. Among the vast variety of molecules investigated in this context, dendrimers have shown great potential for the design of efficient vehicles for drug delivery. Our research group reported the self-assembly behaviour in water of a series of amphiphilic dendrimers consisting of PAMAM which was ionically functionalized with different amounts of fatty acids. All these dendrimers formed well-defined nanobjects in water and were able to encapsulate a hydrophobic drug (plitidepsin).[40] However, as drug delivery systems, these amphiphilic dendrimers lacked an important feature, as it is *in vitro* and *in vivo* traceability.

In contrast to earlier strategies, we have prepared polymeric nanocarriers that were designed to express traceable fluorescent groups with the potential capacity to carry a large cargo of hydrophobic drugs. This was accomplished by preparing two families of amphiphilic hybrid dendrimers from a hydrophilic PAMAM dendrimer (**Figure 2.1**). PAMAM was surrounded by a hydrophobic bisMPA first generation dendron bearing cholesterol and coumarin moieties. The cholesterol was selected due to its hydrophobic character as well as its excellent self-assembly properties, while the coumarin was selected as a fluorescent label. **PAMAMn-ChCou** derivatives consist of ionic dendrimers coming from the ionic functionalization of PAMAM generations 0 to 4 (bearing 4, 8, 16, 32 or 64 terminal groups). **PAMAMn-*cov*-ChCou** dendrimers come from the covalent fuctionalization of the second and fourth generation PAMAM dendrimer (bearing 16 or 64 terminal groups).

This chapter describes the synthesis, characterization and liquid crystalline properties of these amphiphilic dendrimers. Since these materials were targeted as controlled release systems, we also present a detail characterization of the corresponding self-assemblies in water by transmission electron microscopy (TEM)

and dynamic light scattering (DLS). Additionally, the cytotoxicity *in vitro* of these polymeric nanocarriers has been tested.

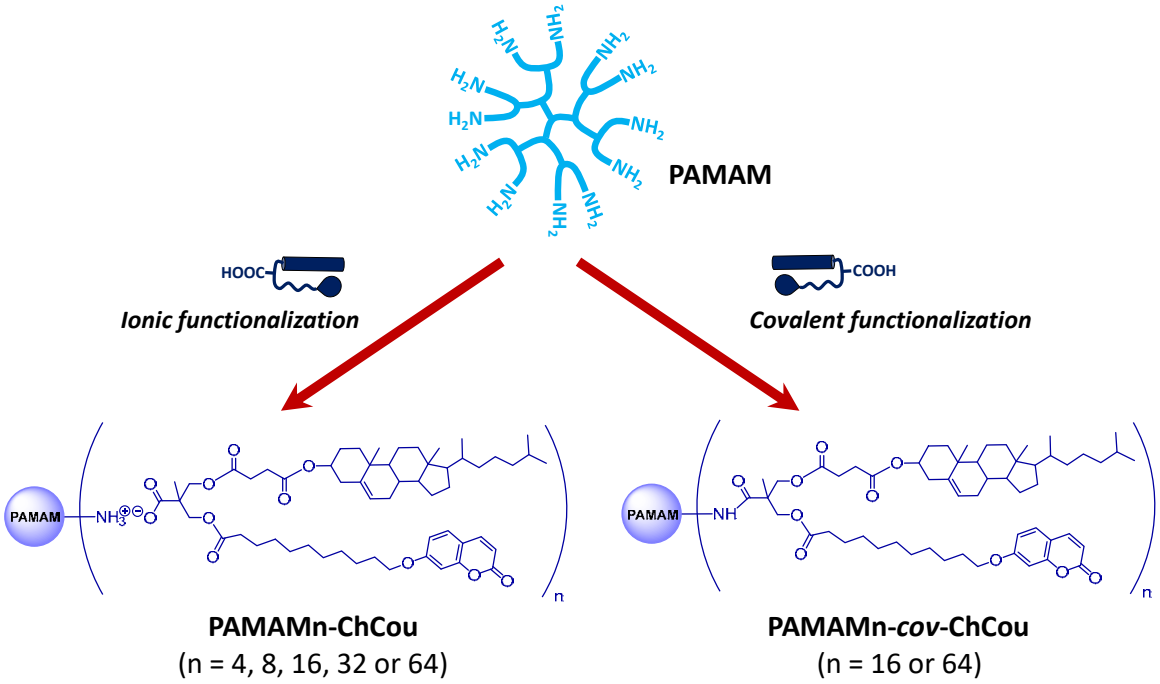

Figure 2.1 Schematic representation of the ionic and covalent functionalization of PAMAM dendrimer.

2.2 Results and discussion

2.2.1 Synthesis and Characterization of Dendrimers

The syntesis of the carboxylic acid dendron (**Ac-ChCou**) and the ionic dendrimers **PAMAMn-ChCou** (n= 0–4) was described in Chapter 2. The covalent derivatives (**PAMAMn-*cov*-ChCou**) were synthesized by the coupling of carbonyldiimidazol (CDI)-activated carboxylic acid group of **Ac-ChCou** with the terminal amine groups of the corresponding generation of **PAMAM** (**Scheme 2.1**). The chemical structures of **PAMAMn-*cov*-ChCou** was determined by FTIR, NMR spectroscopy, MALDI-TOF mass spectroscopy, size exclusion chromatography (SEC), and elemental analysis.

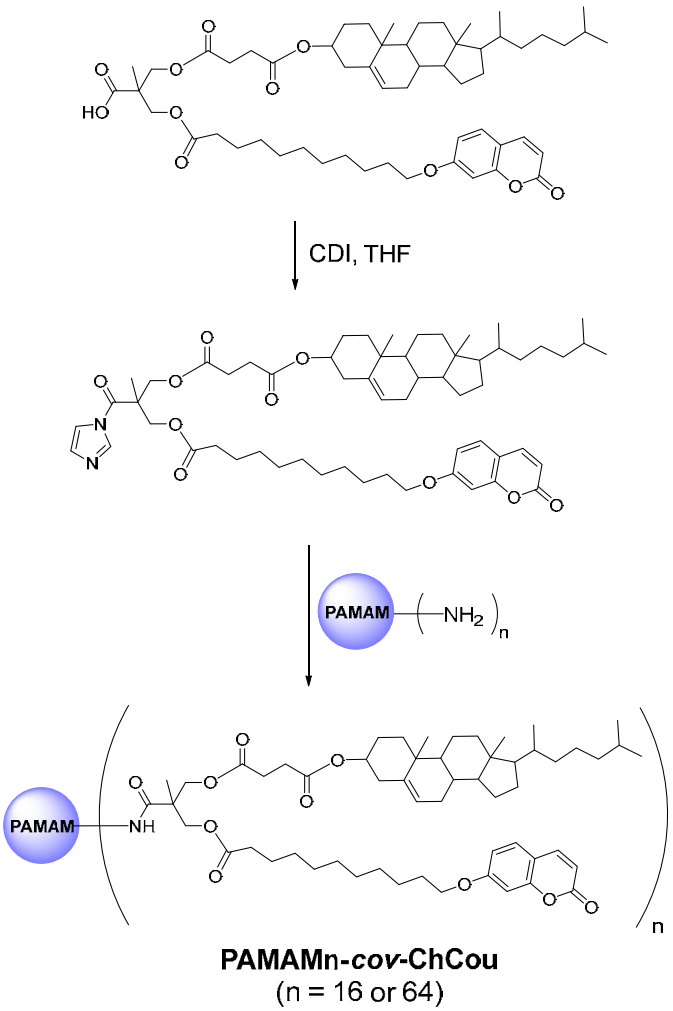

Scheme 2.1 Synthesis of **PAMAMn-*cov*-ChCou** covalent dendrimers.

The FTIR spectra clearly confirmed the formation of the covalent dendrimers. As a repesentative example, the FTIR spectra of **Ac-ChCou**, **PAMAM16** and the corresponding covalent dendrimer are shown in **Figure 2.2**. In the spectrum of

PAMAM16-cov-ChCou, the bands at 1730 and 1683 cm^{-1} corresponding to the dimeric form and free form of the carboxylic acid group of **Ac-ChCou** were replaced by a band at 1646 cm^{-1} due to the stretching of the amide carbonyl groups.

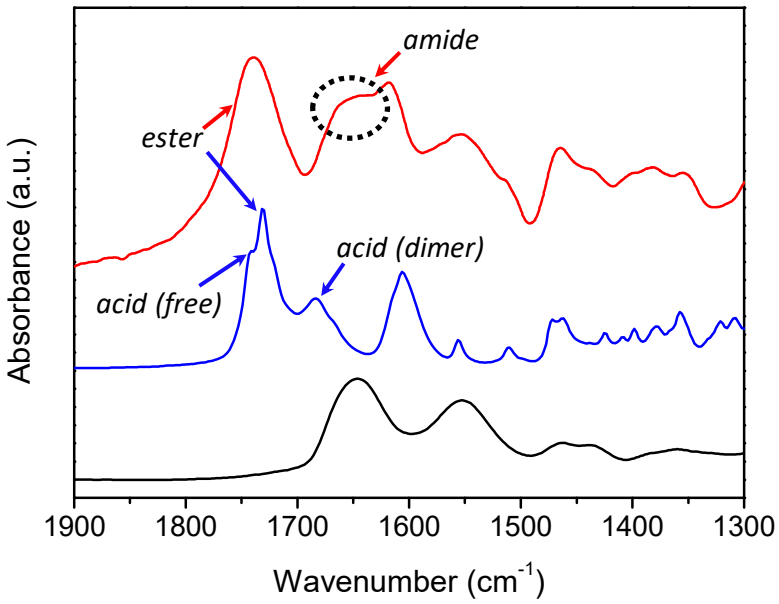

Figure 2.2 FTIR spectra (C=O *st.* region) of **PAMAM16** (black line), **Ac-ChCou** (blue line) and **PAMAM16-*cov*-ChCou** (red line).

Further evidence for the formation of the covalent dendrimers was visible in ^{1}H NMR spectra, as can be seen in **Figure 2.3**, where the absence of the $CH_2C\underline{H}_2$-NH_2 (H_α, δ= 2.77 ppm) and $C\underline{H}_2CH_2$-NH_2 (H_β, δ= 3.22 ppm) signals and the appearance of the $CH_2C\underline{H}_2$-NHCO (H_α, δ= 3.32 ppm) and $C\underline{H}_2CH_2$- NHCO (H_β, δ= 3.32 ppm) signals confirm a quantitative functionalization of terminal amine groups of PAMAM.

In the ^{13}C NMR spectra, formation of the amide groups was confirmed by the absence of the carboxyl group signal of the acid (C_S, δ= 176.98 ppm) and the appearance of a carbon signal from the amide carbonyl groups (C_S, δ= 172.16 ppm) (**Figure 2.3**).

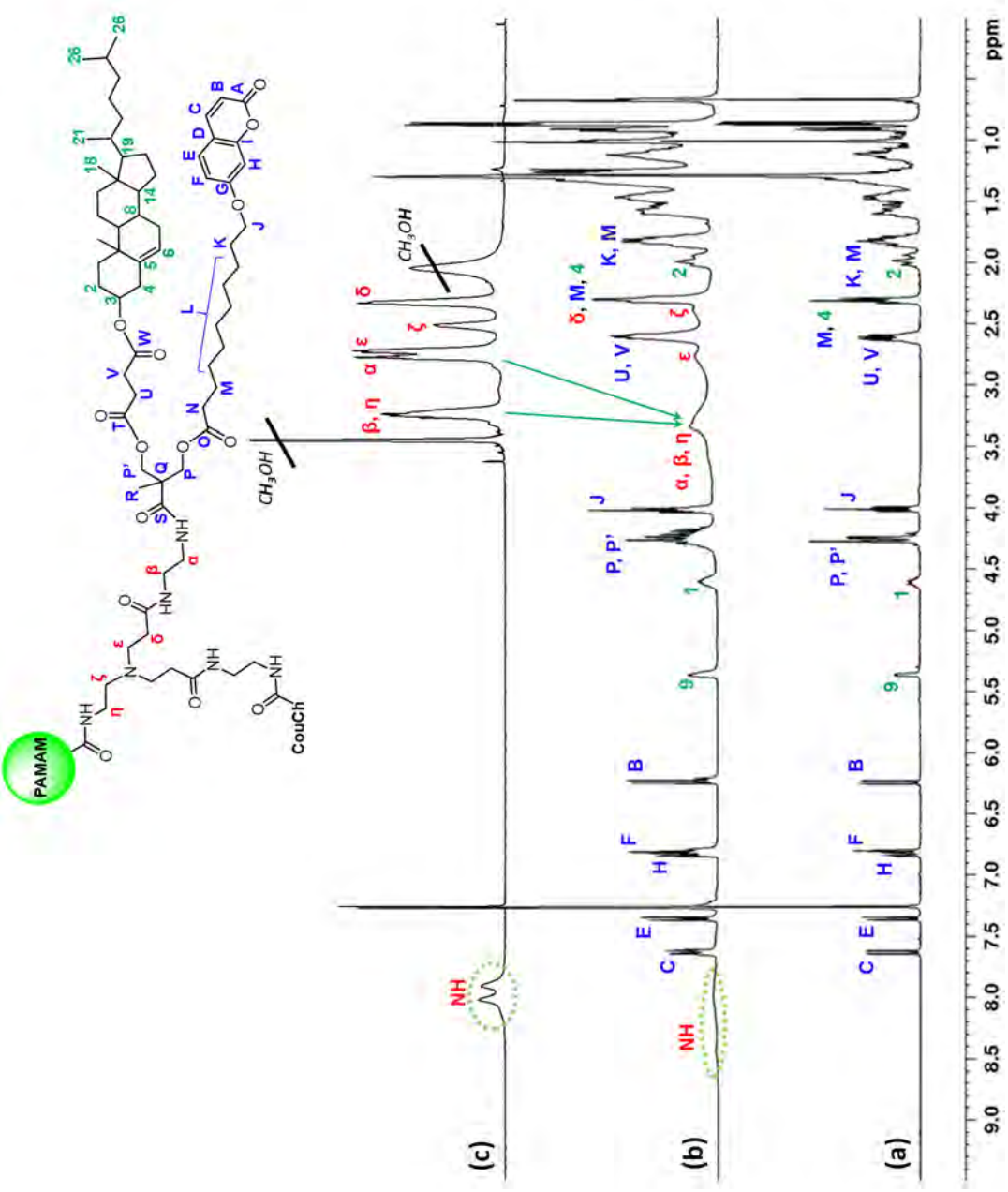

Figure 2.3 ^{1}H (left) and ^{13}C (right) NMR spectra in $CDCl_3$ solution at 25° C of: **(a) Ac-ChCou**, **(b)** covalent dendrimer **PAMAM*64-cov*-ChCou** and **(c)** PAMAM.

The complete functionalization of **PAMAMn-*cov*-ChCou** was also confirmed by SEC and MALDI-TOF MS. The effective functionalization of the PAMAM dendrimers with **Ac-ChCou** was assessed by SEC traces based on monomodal and narrow molar mass distributions as well as the shift of the molecular weight distribution peak towards lower retention times which indicated **PAMAMn-*cov*-ChCou** formation (**Figure 2.4a**). The MALDI-TOF mass spectrum of **PAMAM16-*cov*-ChCou** revealed the presence of an intense peak at 18167.1 corresponding to the fully functionalized dendrimer (**Figure 2.4b**). The rest of the peaks are associated with statistical defects present in the original **PAMAM16** dendrimer.[44, 45] On the other hand, the high molecular weight of **PAMAM64-*cov*-ChCou** (Exact Mass: 73815.6) precluded its measurement by MALDI-TOF MS. This behaviour has previously been observed in other covalent dendrimers with high molecular weight.[46, 47]

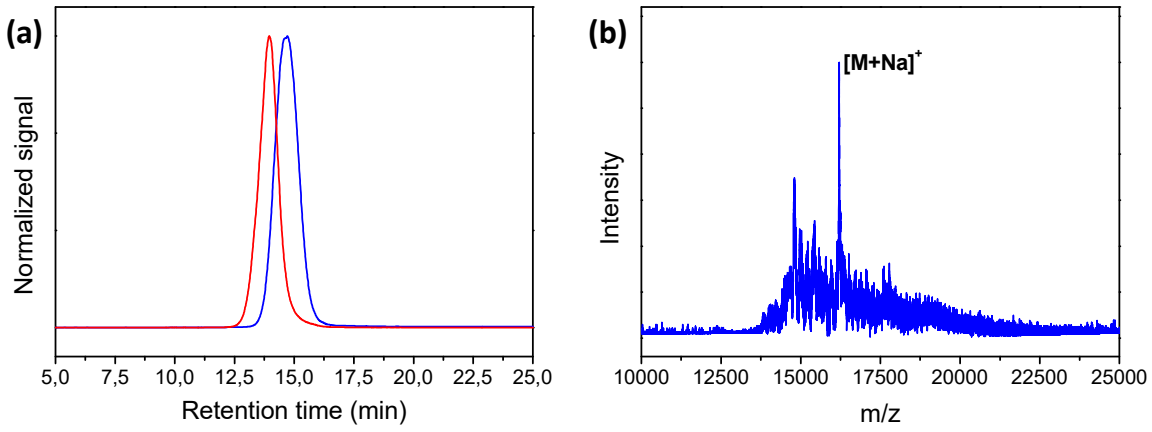

Figure 2.4 (a) MALDI-TOF mass spectrum of **PAMAM16-*cov*-ChCou**. **(b)** SEC traces of: **PAMAM16-*cov*-ChCou** (blue), and **PAMAM64-*cov*-ChCou** (red).

2.2.2 Thermal Properties and Mesogenic Behavior

The thermal stability and liquid crystalline properties of **Ac-ChCou** and ionic dendrimers (**PAMAMn-ChCou**) were described in *Chapter 2*. However, the most relevant data has been included in **Table 2.1** for comparative purposes.

The thermal stability of the covalent dendrimers (**PAMAMn-*cov*-ChCou**) was studied by thermogravimetric analysis (TGA). All the samples showed good thermal stability and in all cases the 5% weight loss temperature ($T_{5\%}$) was detected at temperatures more than 100 °C above the isotropization point (**Table 2.1**).

Table 2.1 Thermal properties and structural parameters

	$T_{5\%}$ [a] (°C)	Phase transitions[b]	d_{obs} [c] (Å)	*h k l* [d]	Structural parameters
PAMAM16-*cov*-ChCou	244	g 25 SmA 71[e] I	46.5	1 0 0	d = 46.8 Å
			23.5	2 0 0	
			4.5 (br)		
PAMAM16-ChCou[f]	209	g 21 SmA 63[e] I	46.2	1 0 0	d = 46.2 Å
			23.1	2 0 0	
			4.5 (br)		
PAMAM64-*cov*-ChCou	217	g 35 Col_h 87[e] I	53.3	1 0 0	a = 61.5 Å
			30.8	1 1 0	
			4.5 (br)		
PAMAM64-ChCou[f]	198	g 29 Col_h 81[e] I	49.3	1 0 0	a = 56.7 Å
			28.2	1 1 0	
			4.5 (br)		

[a] Temperature at which 5% mass lost is detected in the thermogravimetric curve.

[b] DSC data of the second heating process at a rate of 10 °C/min. g: glass, SmA: smectic A mesophase, Col_h: hexagonal columnar mesophase, I: isotropic liquid.

[d] Miller indices.

[e] POM data

[f] Data from Chapter 2

The thermal transitions and mesomorphic properties were studied by polarized optical microscopy (POM), differential scanning calorimetry (DSC) and X-ray diffraction (XRD). Both **PAMAM16-*cov*-ChCou** and **PAMAM64-*cov*-ChCou** displayed liquid crystalline behavior showing birrefringent textures by POM (**Figure 2.5**). The DSC curves showed only a glass transition freezing the mesomorphic order at room temperature.

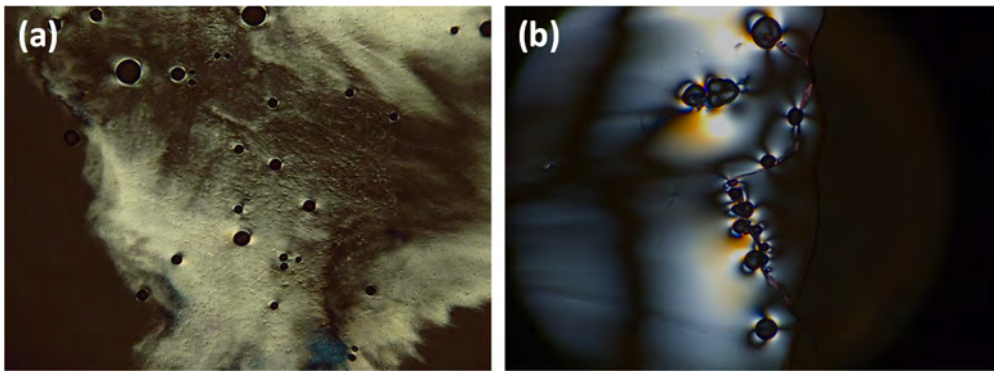

Figure 2.5 POM microphotographs observed in the cooling process at room temperature for: **(a) PAMAM16-*cov*-ChCou**, and **(b) PAMAM64-*cov*-ChCou**.

The nature of the mesophases was identified by XRD. The XRD patterns of **PAMAM16-*cov*-ChCou** contained in the low-angle region one sharp maximum that could be assigned to the first order reflection from a lamellar structure. In the high-angle region, a broad diffuse halo was detected at 4.5 Å which corresponds to the short-range correlations between the conformationally disordered alkyl chains (**Figure 2.6a**). This kind of XRD pattern is characteristic of a smectic A mesophase due to orthogonal character of the mesophase deduced from the presence of homeotropic domains in the textures observed by POM. It has been previously shown that these kinds of ionic and covalent dendrimers assemble into a smectic A layer, adopting a cylindrical shape, in which the substitutents are statistically located upward and downward with respect to the dendrimeric matrix.[46, 48]

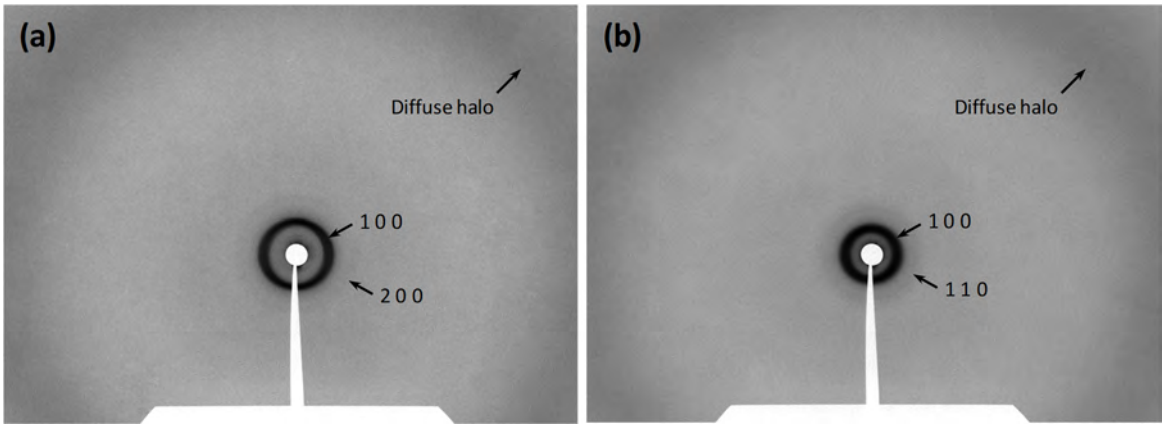

Figure 2.6 Room temperature XRD pattern of: **(a) PAMAM16-*cov*-ChCou** in the SmA mesophase, and **(b) PAMAM64-*cov*-ChCou** in the Col_h mesophase.

The XRD patterns obtained for **PAMAM64-*cov*-ChCou** showed two reflections in the low-angle region with a ratio of 1 : 1/√3, which could be assigned to the reflections (100) and (110) of a hexagonal columnar mesophase (**Figure 2.6b**). In the high-angle region, a typical diffuse halo at 4.5 Å, related to the conformationally disordered aliphatic chains, was detected. In this case, the flexibility of the dendrimer matrix allowed a molecular conformation in which substituents extend radially from the central dendrimer core. The supramolecular organization of these disk-like molecules in columns gives rise to the observed Col_h mesomorphism.[49, 50]

The structural parameters of the covalent dendrimers (**PAMAMn-*cov*-ChCou**) and that of their analogous ionic dendrimers (**PAMAMn-ChCou**) do not vary to a great extent (**Table 2.1**). The slightly higher *d* and *a* values obtained for the covalent dendrimers gives evidence of a higher mobility present in the case of ionic

dendrimers where the moieties can fluctuate in position and slightly penetrate into the dendrimer matrix. By contrast, covalent compounds moieties occupy fixed positions. The same tendency has been previously described in other similar dendrimers.[51]

2.2.3 Self-Assembly of the Dendrimers in Water

Self-assembled structures of the dendrimers were prepared by the co-solvent method using THF/water and following the micellization process by turbidimetry. Dendrimers were first dissolved in THF and then water was slowly added, and at some point, the water addition caused a sudden jump in turbidity which indicated that the dendrimer self-assembly had started (**Figure 2.7**). Once turbidity reached an almost constant value, the resulting dispersion was dialyzed against water to remove the organic solvent. **PAMAM4-ChCou**, **PAMAM8-ChCou** and **PAMAM16-ChCou** precipitated during dialysis, which pointed to the collapse of the assemblies in water. Nevertheless, stable dispersions were obtained for the rest of the dendrimers after storing for a few weeks. Because of this, any further study was limited to **PAMAM32-ChCou**, **PAMAM64-ChCou, PAMAM16-*cov*-ChCou** and **PAMAM64-*cov*-ChCou**.

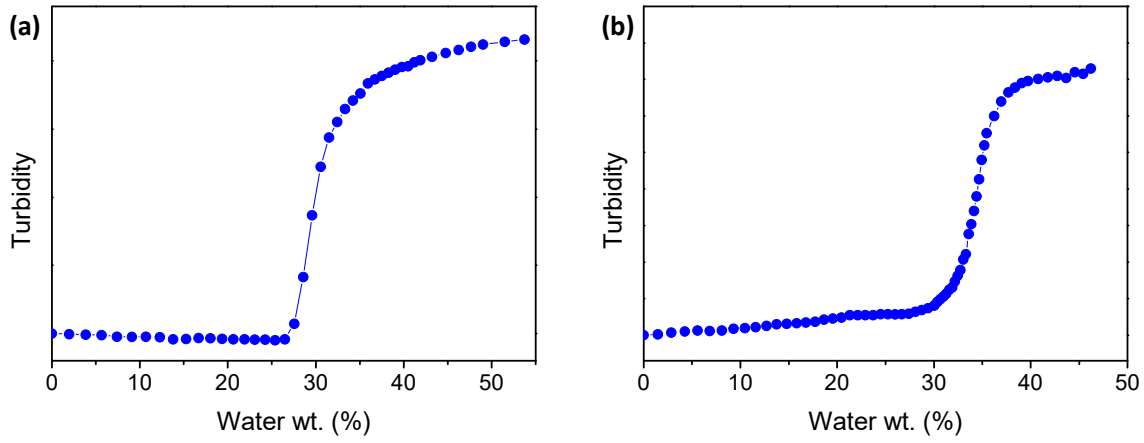

Figure 2.7 Turbidity evolution of: **(a) PAMAM16-*cov*-ChCou**, and **(b) PAMAM16-ChCou** (Turbidity of the THF solutions *versus* amount of water added).

The critical aggregation concentration (CAC) in water, measured by the concentration of the amphiphilic macromolecule above which the macromolecule chains start to associate, was determined by fluorescence using Nile Red as a polarity sensitive probe (**Figure 2.8**).[36] Samples of amphiphilic dendrimers were

stirred overnight together with Nile Red at room temperature and the emission spectra of Nile Red were registered from 560 to 700 nm. The calculated CAC values were typical for polimeric spherical micelles and are gathered in **Table 2.2**.

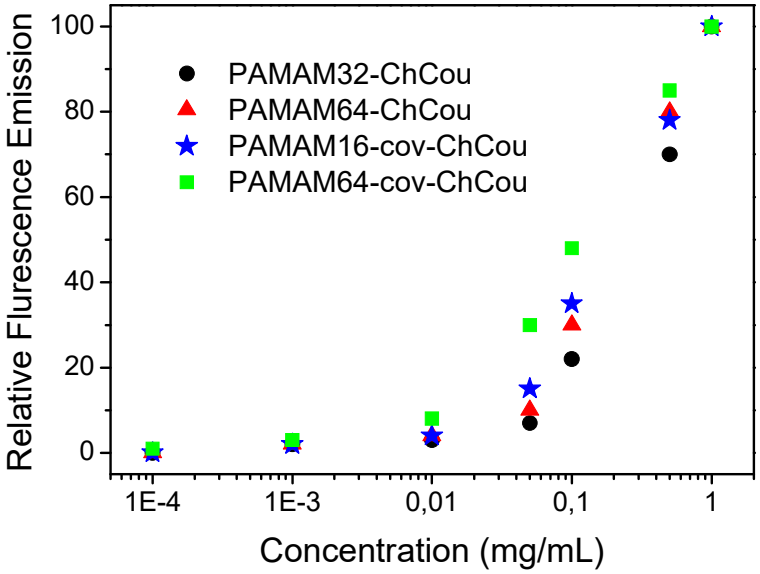

Figure 2.8 Fluorescence intensity of Nile Red at 606 nm (λ_{exc} = 550 nm) *versus* dendrimer concentration.

The morphology of the **PAMAM32-ChCou**, **PAMAM64-ChCou,** **PAMAM16-*cov*-ChCou**, and **PAMAM64-*cov*-ChCou** self-assemblies was first investigated by transmission electron microscopy (TEM) (**Figure 2.9**). TEM images showed the presence of spherical micelles whose diameter (D_h^{TEM} in **Table 2.2**) depended on the generation on the dendrimer.

Table 2.2 CAC values and average size diameters (D_h) of the spherical micelles.

	CAC (μg/mL)	D_h^{TEM} (nm)[a]	D_h^{DLS} (nm)[b]
PAMAM32-ChCou	65	23 ± 4	28 ± 8
PAMAM64-ChCou	46	30 ± 5	38 ± 10
PAMAM16-*cov*-ChCou	28	18 ± 3	24 ± 6
PAMAM64-*cov*-ChCou	19	40 ± 6	47 ± 13

[a] Average size diameter obtained by TEM from 200 individual micelles.

[b] Average size diameter obtained by DLS from number size distributions.

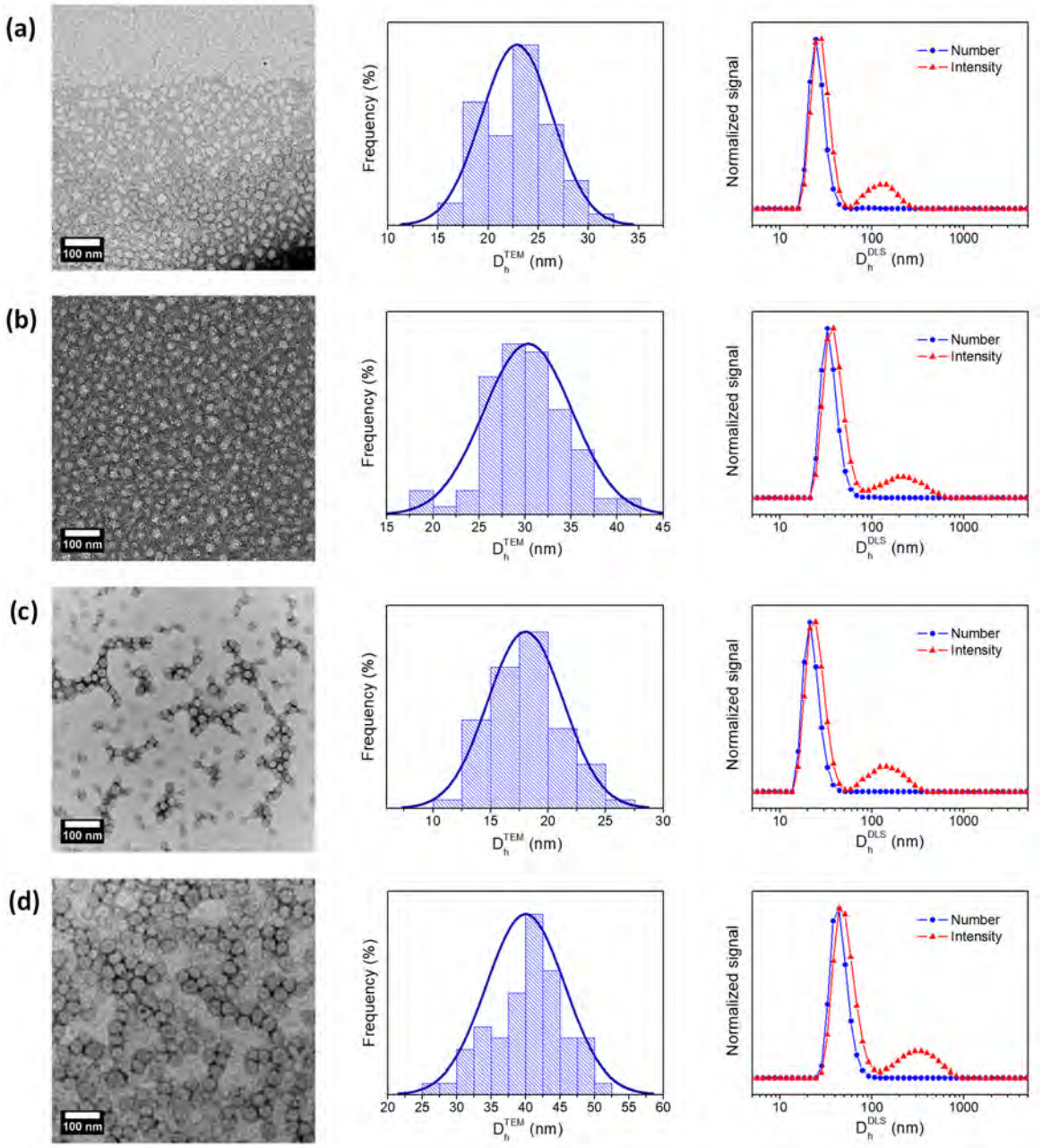

Figure 2.9 TEM images, histogram obtained by TEM from 200 individual micelles, and DLS measurements (number and intensity distributions) from water suspensions of: **(a) PAMAM32-ChCou**, **(b) PAMAM64-ChCou, (c) PAMAM16-*cov*-ChCou,** and **(d) PAMAM64-*cov*-ChCou.**

The average size of the micelles was also determined by dynamic light scattering (DLS) and the hydrodynamic diameters (D_h^{DLS} in **Table 2.2**) were in good agreement with TEM observations. Two distributions were found in the intensity DLS measurements, one corresponding to single micelles and a second distribution, less intense, was attributed to aggregation of single micelles forming a more complex aggregate (**Figure 2.9**). However, it should be mentioned that these aggregates

were observed in a lesser number than single micelles (see the number size distributions obtained by DLS in **Figure 2.9**). Number distributions emphasize the species with the highest number of particles (which often tend to be the smaller ones), while intensity distributions emphasize the species with the largest scattering intensity contributing to the overall result (which often tend to be the larger particles).

2.2.4 Absorption and Emission Properties of the Self-Assemblies

The optical properties of the self-assemblies were evaluated by UV-vis spectroscopy (**Figure 2.10**). The spectra of the amphiphilic dendrimers in THF solution showed the characteristic profile of the coumarin chromophore which includes an intense band at 323 nm related to the π-π* transition. The spectra of the micelles in water (1 mg/mL) showed broad and bathochromic shifting of the π-π* band in contrast to the results of the dendrimers in THF.

The fluorecent traceability of the self-assemblies was evaluated by fluorescence spectroscopy (**Figure 2.10**). The emission spectra of the amphiphilic dendrimers in THF exhibited one band at 384 nm, while the spectra of the micelles in water showed a bathochromic shift of around 15 nm, compared to the results of the dendrimers in THF.

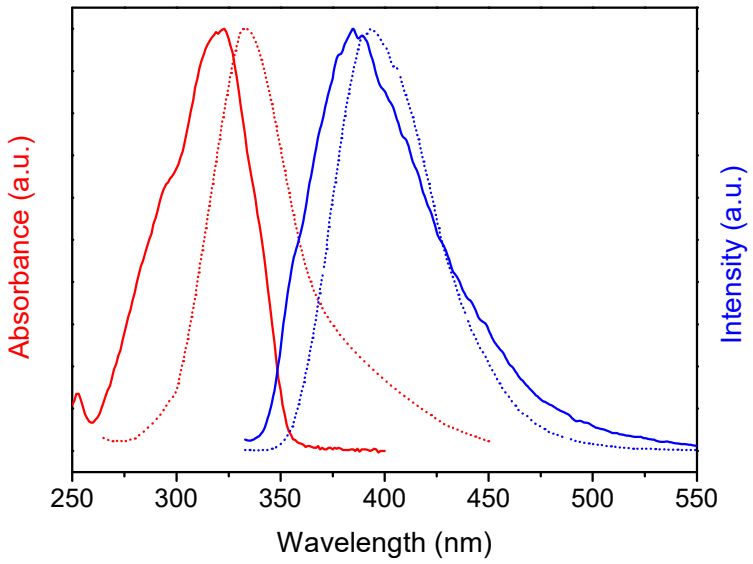

Figure 2.10 Absorption (red) and emission (blue) spectra of **PAMAM64-*cov*-ChCou** self-assemblies (dot lines) and in THF solution (solid lines).

2.2.5 Cytotoxicity of the Self-Assemblies

The cytotoxicity of the amphiphilic dendrimers was tested in cell cultures using the HeLa (Human cervix cancer) cell line. Among the great variety of cell viability essays, we selected the *Alamar Blue* assay. With this assay, Alamar Blue (blue color) is reduced to resorufin (red color) upon entering living cells. The amount of reduced *Alamar Blue* is directly proportional to the number of metabolically active cells in the culture, which can be quantified spectrophotometrically. The cell viabiliy curves for all the amphiphilic dendrimers are shown in **Figure 2.11**.

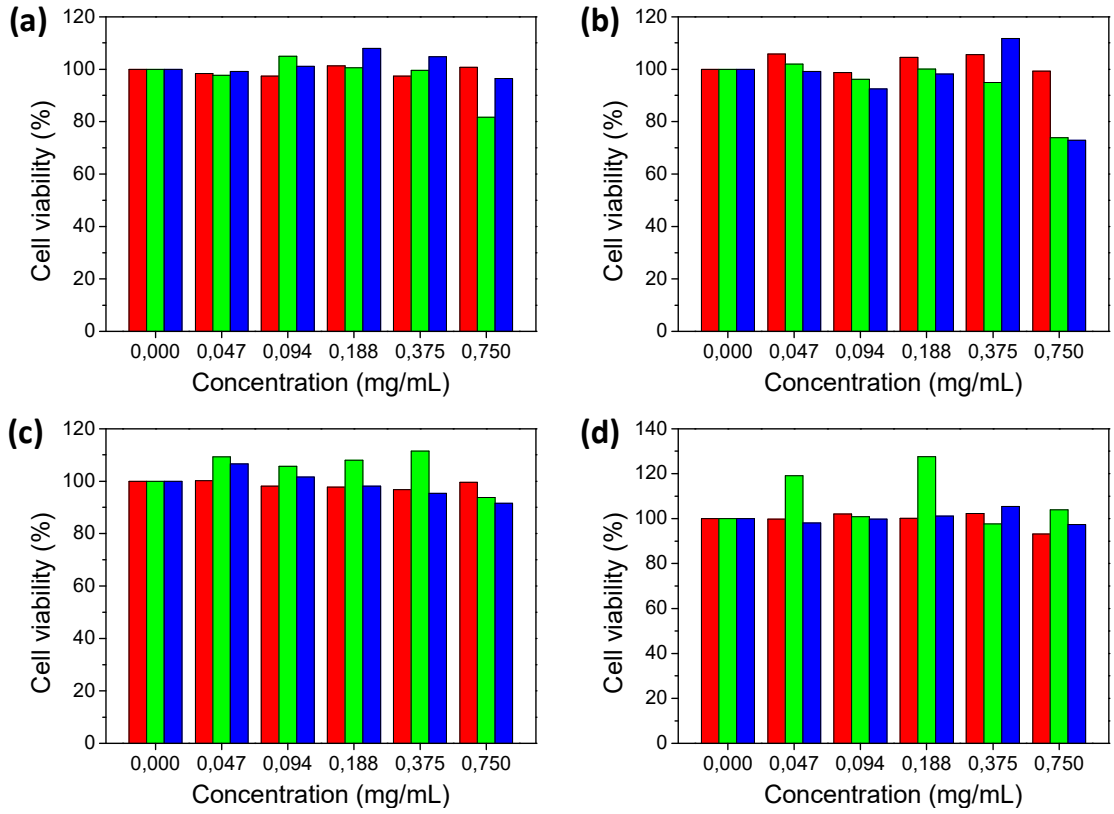

Figure 2.11 Cell viability in HeLa cell line of: **(a) PAMAM32-ChCou**, **(b) PAMAM64-ChCou**, **(c) PAMAM16-*cov*-ChCou**, and **(d) PAMAM64-*cov*-ChCou** self-assemblies at increasing the concentration after 24 h (red bars), 48 h (green bars), and 72 h (blue bars) incubation times.

In general, there was not a decrease in cell viability after 72 h of cell culture in the presence of increasing concentrations of the self-assemblies from 0.05 to 0.75 mg/mL. Although similar cell viability values were obtained, different behavior was observed in the decay of the curves. The **PAMAM32-ChCou** and **PAMAM64-ChCou** self-assemblies showed a viability decay of up to 80% after 72 h of cell culture. This result indicates that the cytotoxic effect is less pronunced on the covalent-based self-assemblies (**PAMAM16-*cov*-ChCou** and **PAMAM64-*cov*-ChCou**) than on the ionic-based self-assemblies (**PAMAM32-ChCou** and **PAMAM64-ChCou**).

2.3 Conclusions

We have reported a series of amphiphilic hybrid dendrimers that consisted of a PAMAM dendrimer functionalized with a coumarin-containing bisMPA dendron. All the compounds exhibited mesogenic behavior with smectic A or hexagonal columnar mesophases depending on the generation of the dendrimer. Moreover, these amphiphilic dendrimers can self-assemble in water producing spherical micelles whose size can be modulated by the generation of the dendrimer. Additionally, these nanocarriers presented the important feature of traceability due to the presence of coumarin fluorescent moieties in the chemical structure of the dendrimer.

We have also tested the cell viability *in vitro* of the micelles as a function of their concentration in HeLa cell line. All the micelles have proven to be non-toxic below 0.75 mg/mL. Therefore, we can conclude that these types of amphiphilic dendrimers may be useful in the preparation of fluorescent polymeric nanocarriers for biomedical applications. Future work will be focused on the study of these amphiphilic dendrimers for effective loading and delivering of hydrophobic drugs.

3. EXPERIMENTAL PART

3.1 Characterization Techniques

3.1.1 Materials

Poly(amidoamine) dendrimers (PAMAM) were purchased from Dendritech, Inc. All the reagents were purchased from Sigma-Aldrich and used as received without further purification. Anhydrous THF was purchased from Scharlab and dried using a solvent purification system.

3.1.2 Structural Characterization

Infrared Spectroscopy spectra were obtained on a Bruker Vertex 70 FT-IR spectrophotometer using KBr pellets.

Solution **Nuclear Magnetic Resonance** experiments were carried out on Bruker Avance spectrometers operating at 400 MHz for ^{1}H and 100 for ^{13}C, using standard pulse sequences. Chemical shifts are given in ppm relative to TMS and the residual solvent peak was used as internal reference.

Elemental Analysis was performed using a Perkin-Elmer 2400 microanalyzer.

MALDI-TOF Mass Spectrometry was performed on an Autoflex mass spectrometer (Bruker Daltonics) using dithranol as matrix.

Size Exclusion Chromatography was carried out on a Waters e2695 Alliance liquid chromatography system equipped with a Waters 2424 evaporative light scattering detector using two Styragel® columns, HR4 and HR1 from Waters. Measurements were performed in THF using a flow of 1 mL/min and poly(methyl methacrylate) (PMMA) narrow molar mass standards.

3.1.3 Liquid Crystal Characterization

Mesogenic behavior was investigated by **Polarized-Light Optical Microscopy** using an Olympus BH-2 polarizing microscope fitted with a Linkam THMS600 hot stage.

Thermogravimetric Analysis was performed using a Q5000IR from TA instruments at heating rate of 10 °C/min under nitrogen atmosphere.

Thermal transitions were determined by **Differential Scanning Calorimetry** using a DSC Q2000 from TA instruments with powdered samples (2–5 mg) sealed in aluminum pans. Glass transition temperatures (T_g) were determined at the half height of the baseline jump, and first order transition temperatures were read at the maximum of the corresponding peak.

X-Ray Diffraction was performed with an evacuated Pinhole camera (Anton-Paar) operating a point-focused Ni-filtered Cu-K_α beam. The patterns were collected on flat photographic films perpendicular to the X-ray beam. Powdered samples of the supramolecular complexes were placed in Lindemann glass capillaries (0.9 mm diameter).

3.1.4 Optical Properties

Ultraviolet-visible spectra were recorded on an ATI-Unicam UV4-200 spectrophotometer.

Fluorescence measurements were recorded on a Perkin-Elmer LS 50B fluorescence spectrophotometer.

All the measurements were performed in dilute THF solutions (10^{-5} to 10^{-7} M) using quartz cuvettes.

3.1.5 Characterization of the Self-Assemblies

Transmission Electron Microscopy was performed using JEOL-2000 FXIII electron microscope operating at 200 kV. For the preparation of TEM samples, 5 µL of a 0.5

mg/mL water dispersions of the self-assemblies were deposited onto carbon-coated copper grids, and the water was then removed by capillarity using filter paper. The samples were stained with uranyl acetate and the grid was left to dry overnight under vacuum. The 0.5 mg/mL suspension was prepared by diluting the former suspension with Milli-Q water.

Dynamic Light Scattering measurements were carried out in a Malvern Instrument Nano ZS using a He–Ne laser with a 633 nm wavelength, a detector angle of 173° at 25 °C. The self-assemblies concentrations were 0.10 mg/mL and size measurements were performed at least three times on each sample to ensure reproducibility.

3.2 Synthetic Procedures

The syntesis of the carboxylic acid dendron (**Ac-ChCou**) and the ionic dendrimers **PAMAMn-ChCou** (n= 0–4) was described in Chapter 2.

3.2.1 Synthesis of the Covalent Dendrimers

The synthesis of the covalent dendrimers (**PAMAMn-*cov*-ChCou**, n= 16 and 64) was performed following a previously described method.[52] Carbonyldiimidazol (CDI) (1.03 eq.) was slowly added to a solution of **Ac-ChCou** (1.00 eq.) in anhydrous THF. The reaction mixture was stirred at RT for 1 h under a stream of argon. The mixture was transferred to a Schlenk flask containing the corresponding PAMAM dendrimer (1.00 eq. terminal amino groups), and it was heated at 40 °C for 72 h. Then the reaction mixture was partially evaporated and carefully precipitated using cold methanol. The dendrimer was dried in a vacuum at RT for 48 h.

PAMAM16-*cov*-ChCou. Yield: 55 %. IR (KBr, ν, cm^{-1}): 3316 (N-H), 3085 (=C-H), 2931 (C-H), 1739, 1646 (C=O), 1613 (Ar), 1158 (C-O). ^{1}H NMR ($CDCl_3$, 400 MHz, δ, ppm): 8.25-7.74 (m, 44H), 7.68-7.58 (m, 16H), 7.39-7.33 (m, 16H), 6.88-6.73 (m, 32H), 6.28-6.17 (m, 16H), 5.45-5.31 (m, 16H), 4.68-4.49 (m, 16H), 4.37-4.08 (m, 64H), 4.05-3.93 (m, 32H), 3.53-3.00 (m, 88H), 2.94-2.20 (m, 264H), 2.04-0.64 (m, 910H). ^{13}C NMR ($CDCl_3$, 100 MHz, δ, ppm): 173.57, 173.36, 172.16, 171.94, 171.74, 162.66, 161.37, 156.14, 143.62, 143.58, 139.77, 128.90, 128.84, 122.87, 113.20, 113.14, 112.58, 101.61, 74.63, 68.86, 56.90, 56.39, 50.25, 46.29, 46.20, 42.51, 39.94, 39.70, 38.25, 37.16, 36.77, 36.39, 35.96, 34.33, 34.26, 32.06, 29.56, 29.46, 29.37, 29.25, 29.17, 29.10, 28.38, 28.17, 27.92, 26.12, 26.07, 25.06, 24.99, 24.46, 24.08, 22.95, 22.71, 21.22, 19.47, 18.90, 17.95, 12.03. MS (MALDI$^+$, dithranol, m/z): calcd. for $C_{1038}H_{1600}N_{58}O_{204}$, 18143.7; found, 18167.1 $[M+Na]^+$. Anal. calcd. for $C_{1038}H_{1600}N_{58}O_{204}$: C, 68.67%; H, 8.88%; N, 4.47%. Found: C, 68.50%; H, 8.65%; N, 5.00%.

PAMAM64-*cov*-ChCou. Yield: 68 %. IR (KBr, ν, cm^{-1}): 3307 (N-H), 3080 (=C-H), 2933 (C-H), 1741, 1641 (C=O), 1613, 1555 (Ar), 1158 (C-O). ^{1}H NMR ($CDCl_3$, 400 MHz, δ, ppm): 8.67-7.81 (m, 188H), 7.67-7.59 (m, 64H), 7.40-7.32 (m, 64H), 6.88-6.74 (m, 128H), 6.29-6.18 (m, 64H), 5.41-5.26 (m, 64H), 4.70-4.47 (m, 64H), 4.34-4.07 (m,

256H), 4.07-3.90 (m, 128H), 3.52-3.03 (m, 376H), 2.90-2.17 (m, 1128H), 2.05-0.63 (m, 3648H). ^{13}C NMR ($CDCl_3$, 100 MHz, δ, ppm): 173.45, 173.36, 172.14, 172.02, 171.95, 171.65, 171.57, 162.67, 161.46, 156.15, 143.60, 143.51, 139.78, 128.86, 128.83, 122.87, 113.19, 113.15, 113.11, 112.60, 101.62, 74.63, 68.87, 56.91, 56.40, 50.26, 46.46, 46.32, 42.53, 39.95, 39.71, 38.25, 37.17, 36.79, 36.39, 35.96, 34.30, 32.08, 29.59, 29.49, 29.35, 29.28, 29.16, 29.12, 28.38, 28.18, 27.93, 26.12, 26.09, 25.03, 24.46, 24.05, 22.95, 22.71, 21.23, 19.47, 18.90, 18.15, 17.93, 12.03. Anal. calcd. for $C_{4206}H_{6496}N_{250}O_{828}$: C, 68.44%; H, 8.87%; N, 4.74%. Found: C, 68.82%; H, 9.00%; N, 4.62%.

3.3 Experimental Procedures

3.3.1 Preparation of the Self-Assemblies in Water

Milli-Q water was gradually added to a solution of 5 mg/mL of the corresponding dendrimer in THF, and the self-assembly process was followed by measuring the loss of intensity of transmitted light at 650 nm due to scattering (turbidimetry) as a function of the water content. At a critical water value, a sudden increase of turbidity occurs coinciding with the onset of polymer self-assembly. When a constant value of turbidity was reached, the mixture was dialyzed against water to remove THF using a Spectra/Por® dialysis membrane (MWCO 1000) for 4 days. Water suspensions of the self-assemblies were obtained with concentrations around 1.5 mg/mL.

3.3.2 Determination of the Critical Aggregation Concentration (CAC)

Critical aggregation concentration (CAC) was determined by fluorescence spectroscopy using Nile Red as the probe as follows.[36] 119 µL of a solution of Nile Red in dichloromethane (5×10^{-6} M) was added into a series of flasks and then the solvent evaporated. Afterwards, water suspensions of the self-assemblies, prepared by diluting the former suspension, were added to each flask with concentrations ranging from 1.0×10^{-4} to 1.0 mg/mL. In each flask a final concentration of 1.0×10^{-6} M of Nile Red was reached and the resulting suspensions were stirred overnight at room temperature to reach equilibrium before fluorescence was measured. The emission spectra of Nile Red were registered from 560 to 700 nm while exciting at 550 nm.

3.3.3 Cell Line and Cell Culture

Human cervix cancer cell line HeLa (kindly obtained from Cancer Research UK Cell services) was maintained in DMEM Low-Glucose (with 1 g/L *D*-Glucose, *L*-Glutamine and pyruvate; Gibco) supplemented with 10% FBS and 1%

penicillin–streptomycin–amphotericin at 37 °C and 5% CO_2 in a humidified atmosphere.

3.3.4 Citotoxicity Studies: *Alamar Blue Assay*

Cells were seeded at a density of 5×10^3 cells per well in 96 multiwell culture plates. After 24 h of incubation, the culture medium was removed, and 100 µL of DMEMc plus the corresponding self-assemblies dispersion in water was added (final dendrimer concentration was 0.05-0.75 mg/mL). Incubation with the self-assemblies was carried out at three different time periods (24, 48 and 72 h). After each incubation time, the solutions were replaced by a 10% v/v *Alamar Blue* dye solution (Thermo Fisher) in fresh DMEMc. Upon entering living cells, resazurin (active ingredient of *Alamar Blue*, blue color) is reduced to resorufin (red compound). After incubation for 1.5 h at 37 °C, changes in viability were detected by absorbance measurement at 570 nm, using 600 nm as a reference wavelength, on a Multiskan GO (ThermoScientific) plate reader. Cells incubated with 100 µL of DMEMc plus the corresponding percentage of milli-Q water (without containing self-assemblies) were used as control. Cytotoxicity is expressed as the relative viability of the cells incubated with the self-assemblies compared to control cells (considered as 100% viability). A total of three replicates per concentration were assayed. The following equation was used to calculate the cell viability:

$$\% = 100 \times \frac{(O_2 \times A_1) - (O_1 \times A_2)}{(O_2 \times P_1) - (O_1 \times P_2)}$$

O_1: molar extinction coefficient of *Alamar Blue* at 570 nm.
O_2: molar extinction coefficient of oxidized *Alamar Blue* at 600 nm.
A_1: Absorbance of test wells at 570 nm.
A_2: Absorbance of test wells at 600 nm.
P_1: Absorbance of positive growth control well at 570 nm.
P_2: Absorbance of positive growth control well at 600 nm.

4. REFERENCES

(1) M. Elsabahy & K. L. Wooley. Design of polymeric nanoparticles for biomedical delivery applications. *Chem. Soc. Rev.* **2012,** *41*, 2545-2561.

(2) A. Rösler, G. W. M. Vandermeulen & H.-A. Klok. Advanced drug delivery devices via self-assembly of amphiphilic block copolymers. *Adv. Drug Deliv. Rev.* **2012,** *64*, 270-279.

(3) Y. Yan, G. K. Such, A. P. R. Johnston, J. P. Best & F. Caruso. Engineering Particles for Therapeutic Delivery: Prospects and Challenges. *ACS Nano* **2012,** *6*, 3663-3669.

(4) J. Nicolas, S. Mura, D. Brambilla, N. Mackiewicz & P. Couvreur. Design, functionalization strategies and biomedical applications of targeted biodegradable/biocompatible polymer-based nanocarriers for drug delivery. *Chem. Soc. Rev.* **2013,** *42*, 1147-1235.

(5) M. Chen & M. Yin. Design and development of fluorescent nanostructures for bioimaging. *Progress in Polymer Science* **2014,** *39*, 365-395.

(6) A. Kowalczuk, R. Trzcinska, B. Trzebicka, A. H. E. Müller, A. Dworak & C. B. Tsvetanov. Loading of polymer nanocarriers: Factors, mechanisms and applications. *Progress in Polymer Science* **2014,** *39*, 43-86.

(7) G. Riess. Micellization of block copolymers. *Prog. Polym. Sci.* **2003,** *28*, 1107-1170.

(8) K. Letchford & H. Burt. A review of the formation and classification of amphiphilic block copolymer nanoparticulate structures: micelles, nanospheres, nanocapsules and polymersomes. *Eur. J. Pharm. Biopharm.* **2007,** *65*, 259-269.

(9) T. Smart, H. Lomas, M. Massignani, M. V. Flores-Merino, L. R. Perez & G. Battaglia. Block copolymer nanostructures. *Nano Today* **2008,** *3*, 38-46.

(10) A. Blanazs, S. P. Armes & A. J. Ryan. Self-assembled block copolymer aggregates: from micelles to vesicles and their biological applications. *Macromol. Rapid Commun.* **2009,** *30*, 267-277.

(11) Y. Mai & A. Eisenberg. Self-assembly of block copolymers. *Chem. Soc. Rev.* **2012,** *41*, 5969-5985.

(12) J. N. Israelachvili, D. J. Mitchell & B. W. Ninham. Theory of self-assembly of hydrocarbon amphiphiles into micelles and bilayers. *J. Chem. Soc. Faraday Trans.* **1976,** *72*, 1525-1568.

(13) N. Kamaly, Z. Xiao, P. M. Valencia, A. F. Radovic-Moreno & O. C. Farokhzad. Targeted polymeric therapeutic nanoparticles: design, development and clinical translation. *Chem. Soc. Rev.* **2012,** *41*, 2971-3010.

(14) J. Gong, M. Chen, Y. Zheng, S. Wang & Y. Wang. Polymeric micelles drug delivery system in oncology. *J. Control. Release* **2012,** *159*, 312-323.

(15) H. Wei, R.-X. Zhuo & X.-Z. Zhang. Design and development of polymeric micelles with cleavable links for intracellular drug delivery. *Progress in Polymer Science* **2013,** *38*, 503-535.

(16) R. Bleul, R. Thiermann & M. Maskos. Techniques To Control Polymersome Size. *Macromolecules* **2015,** *48*, 7396-7409.

(17) X. Hu, Y. Zhang, Z. Xie, X. Jing, A. Bellotti & Z. Gu. Stimuli-Responsive Polymersomes for Biomedical Applications. *Biomacromolecules* **2017,** *18*, 649-673.

(18) S.-E. Stiriba, H. Frey & R. Haag. Dendritic Polymers in Biomedical Applications: From Potential to Clinical Use in Diagnostics and Therapy. *Angew. Chem. Int. Ed.* **2002,** *41*, 1329-1334.

(19) E. R. Gillies & J. M. J. Frechet. Designing macromolecules for therapeutic applications: Polyester dendrimer-poly(ethylene oxide) "bow-tie" hybrids with tunable molecular weight and architecture. *J. Am. Chem. Soc.* **2002,** *124*, 14137-14146.

(20) T. Wei, C. Chen, J. Liu, C. Liu, P. Posocco, X. Liu, Q. Cheng, S. Huo, Z. Liang, M. Fermeglia, S. Pricl, X.-J. Liang, P. Rocchi & L. Peng. Anticancer drug nanomicelles formed by self-assembling amphiphilic dendrimer to combat cancer drug resistance. *PNAS* **2015,** *112*, 2978-2983.

(21) S. E. Sherman, Q. Xiao & V. Percec. Mimicking Complex Biological Membranes and Their Programmable Glycan Ligands with Dendrimersomes and Glycodendrimersomes. *Chem. Rev.* **2017,** *117*, 6538-6631.

(22) F. Liko, F. Hindré & E. Fernandez-Megia. Dendrimers as Innovative Radiopharmaceuticals in Cancer Radionanotherapy. *Biomacromolecules* **2016,** *17*, 3103-3114.

(23) G. R. Newkome, C. N. Moorefield, G. R. Baker, M. J. Saunders & S. H. Grossman. Unimolecular Micelles. *Angew. Chem. Int. Ed.* **1991,** *30*, 1178-1180.

(24) M. Liu, K. Kono & J. M. J. Fréchet. Water-soluble dendritic unimolecular micelles:: Their potential as drug delivery agents. *J. Control. Release* **2000,** *65*, 121-131.

(25) X. Fan, Z. Li & X. J. Loh. Recent development of unimolecular micelles as functional materials and applications. *Polym. Chem.* **2016,** *7*, 5898-5919.

(26) B.-B. Wang, X. Zhang, X.-R. Jia, Z.-C. Li, Y. Ji, L. Yang & Y. Wei. Fluorescence and Aggregation Behavior of Poly(amidoamine) Dendrimers Peripherally Modified with Aromatic Chromophores: the Effect of Dendritic Architectures. *J. Am. Chem. Soc.* **2004,** *126*, 15180-15194.

(27) A. Lancelot, R. González-Pastor, A. Concellón, T. Sierra, P. Martín-Duque & J. L. Serrano. DNA Transfection to Mesenchymal Stem Cells Using a Novel Type of Pseudodendrimer Based on 2,2-Bis(hydroxymethyl)propionic Acid. *Bioconjugate Chem.* **2017,** *28*, 1135-1150.

(28) J.-H. Ryu, E. Lee, Y.-b. Lim & M. Lee. Carbohydrate-Coated Supramolecular Structures: Transformation of Nanofibers into Spherical Micelles Triggered by Guest Encapsulation. *J. Am. Chem. Soc.* **2007,** *129*, 4808-4814.

(29) V. Percec, D. A. Wilson, P. Leowanawat, C. J. Wilson, A. D. Hughes, M. S. Kaucher, D. A. Hammer, D. H. Levine, A. J. Kim, F. S. Bates, K. P. Davis, T. P. Lodge, M. L. Klein, R. H. DeVane, E. Aqad, B. M. Rosen, A. O. Argintaru, M. J. Sienkowska, K. Rissanen, S. Nummelin & J. Ropponen. Self-Assembly of Janus Dendrimers into Uniform Dendrimersomes and Other Complex Architectures. *Science* **2010,** *328*, 1009-1014.

(30) J. Movellan, P. Urbán, E. Moles, J. M. de la Fuente, T. Sierra, J. L. Serrano & X. Fernàndez-Busquets. Amphiphilic dendritic derivatives as nanocarriers for the targeted delivery of antimalarial drugs. *Biomaterials* **2014,** *35*, 7940-7950.

(31) E. Fedeli, A. Lancelot, J. L. Serrano, P. Calvo & T. Sierra. Self-assembling amphiphilic Janus dendrimers: mesomorphic properties and aggregation in water. *New. J. Chem.* **2015,** *39*, 1960-1967.

(32) A. Lancelot, R. Clavería-Gimeno, A. Velázquez-Campoy, O. Abian, J. L. Serrano & T. Sierra. Nanostructures based on ammonium-terminated amphiphilic Janus dendrimers as camptothecin carriers with antiviral activity. *Eur. Polym. J.* **2017,** *90*, 136-149.

(33) J. C. M. van Hest, D. A. P. Delnoye, M. W. P. L. Baars, M. H. P. van Genderen & E. W. Meijer. Polystyrene-Dendrimer Amphiphilic Block Copolymers with a Generation-Dependent Aggregation. *Science* **1995,** *268*, 1592-1595.

(34) J. del Barrio, L. Oriol, C. Sanchez, J. Luis Serrano, A. Di Cicco, P. Keller & M.-H. Li. Self-assembly of linear-dendritic diblock copolymers: from nanofibers to polymersomes. *J. Am. Chem. Soc.* **2010,** *132*, 3762-3769.

(35) Y.-L. Lin, H.-Y. Chang, Y.-J. Sheng & H.-K. Tsao. Photoresponsive polymersomes formed by amphiphilic linear–dendritic block copolymers: generation-dependent aggregation behavior. *Macromolecules* **2012,** *45*, 7143-7156.

(36) E. Blasco, J. del Barrio, C. Sánchez-Somolinos, M. Piñol & L. Oriol. Light induced molecular release from vesicles based on amphiphilic linear-dendritic block copolymers. *Polym. Chem.* **2013,** *4*, 2246-2254.

(37) E. Blasco, J. L. Serrano, M. Piñol & L. Oriol. Light responsive vesicles based on linear–dendritic block copolymers using azobenzene–aliphatic codendrons. *Macromolecules* **2013,** *46*, 5951-5960.

(38) H. García-Juan, A. Nogales, E. Blasco, J. C. Martínez, I. Šics, T. A. Ezquerra, M. Piñol & L. Oriol. Self-assembly of thermo and light responsive amphiphilic linear dendritic block copolymers. *Eur. Polym. J.* **2016,** *81*, 621-633.

(39) O. C. J. Andrén, Y. Zhang, P. Lundberg, C. J. Hawker, A. M. Nyström & M. Malkoch. Therapeutic Nanocarriers via Cholesterol Directed Self-Assembly of Well-Defined Linear-Dendritic Polymeric Amphiphiles. *Chem. Mater.* **2017,** *29*, 3891-3898.

(40) E. Fedeli, S. Hernandez-Ainsa, A. Lancelot, R. Gonzalez-Pastor, P. Calvo, T. Sierra & J. L. Serrano. Nanoobjects formed by ionic PAMAM dendrimers: hydrophilic/lipophilic modulation and encapsulation properties. *Soft Matter* **2015,** *11*, 6009-6017.

(41) S. Hernández-Ainsa, E. Fedeli, J. Barberá, M. Marcos, T. Sierra & J. L. Serrano. Self-assembly modulation in ionic PAMAM derivatives. *Soft Matter* **2014,** *10*, 281-289.

(42) S. Hernández-Ainsa, J. Barberá, M. Marcos & J. L. Serrano. Nanoobjects coming from mesomorphic ionic PAMAM dendrimers. *Soft Matter* **2011,** *7*, 2560-2568.

(43) J. Movellan, R. González-Pastor, P. Martín-Duque, T. Sierra, J. M. de la Fuente & J. L. Serrano. New Ionic bis-MPA and PAMAM Dendrimers: A Study of Their Biocompatibility and DNA-Complexation. *Macromol. Biosci.* **2015,** *15*, 657-667.

(44) L. P. Tolić, G. A. Anderson, R. D. Smith, H. M. Brothers, R. Spindler & D. A. Tomalia. Electrospray ionization Fourier transform ion cyclotron resonance mass spectrometric characterization of high molecular mass Starburst™ dendrimers. *Int. J. Mass. Spectrom. Ion Process* **1997,** *165-166*, 405-418.

(45) J. Peterson, V. Allikmaa, J. Subbi, T. Pehk & M. Lopp. Structural deviations in poly(amidoamine) dendrimers: a MALDI-TOF MS analysis. *Eur. Polym. J.* **2003,** *39*, 33-42.

(46) J. Barberá, M. Marcos & J. L. Serrano. Dendromesogens: Liquid Crystal Organizations versus Starburst Structures. *Chem. Eur. J.* **1999,** *5*, 1834-1840.

(47) M. D. McKenna, J. Barberá, M. Marcos & J. L. Serrano. Discotic Liquid Crystalline Poly(propylene imine) Dendrimers Based on Triphenylene. *J. Am. Chem. Soc.* **2005,** *127*, 619-625.

(48) R. Martín-Rapún, M. Marcos, A. Omenat, J. Barberá, P. Romero & J. L. Serrano. Ionic Thermotropic Liquid Crystal Dendrimers. *J. Am. Chem. Soc.* **2005,** *127*, 7397-7403.

(49) M. Marcos, R. Giménez, J. L. Serrano, B. Donnio, B. Heinrich & D. Guillon. Dendromesogens: Liquid Crystal Organizations of Poly(amidoamine) Dendrimers versus Starburst Structures. *Chem. Eur. J.* **2001,** *7*, 1006-1013.

(50) M. Marcos, R. Martín-Rapún, A. Omenat, J. Barberá & J. L. Serrano. Ionic Liquid Crystal Dendrimers with Mono-, Di- and Trisubstituted Benzoic Acids. *Chem. Mater.* **2006,** *18*, 1206-1212.

(51) S. Hernández-Ainsa, J. Barberá, M. Marcos & J. L. Serrano. Liquid Crystalline Ionic Dendrimers Containing Luminescent Oxadiazole Moieties. *Macromolecules* **2012,** *45*, 1006-1015.

(52) V. Martinez, S. Mecking, T. Tassaing, M. Besnard, S. Moisan, F. Cansell & C. Aymonier. Dendritic Core−Shell Macromolecules Soluble in Supercritical Carbon Dioxide. *Macromolecules* **2006,** *39*, 3978-3979.

Chapter 5

Resumen y Conclusiones

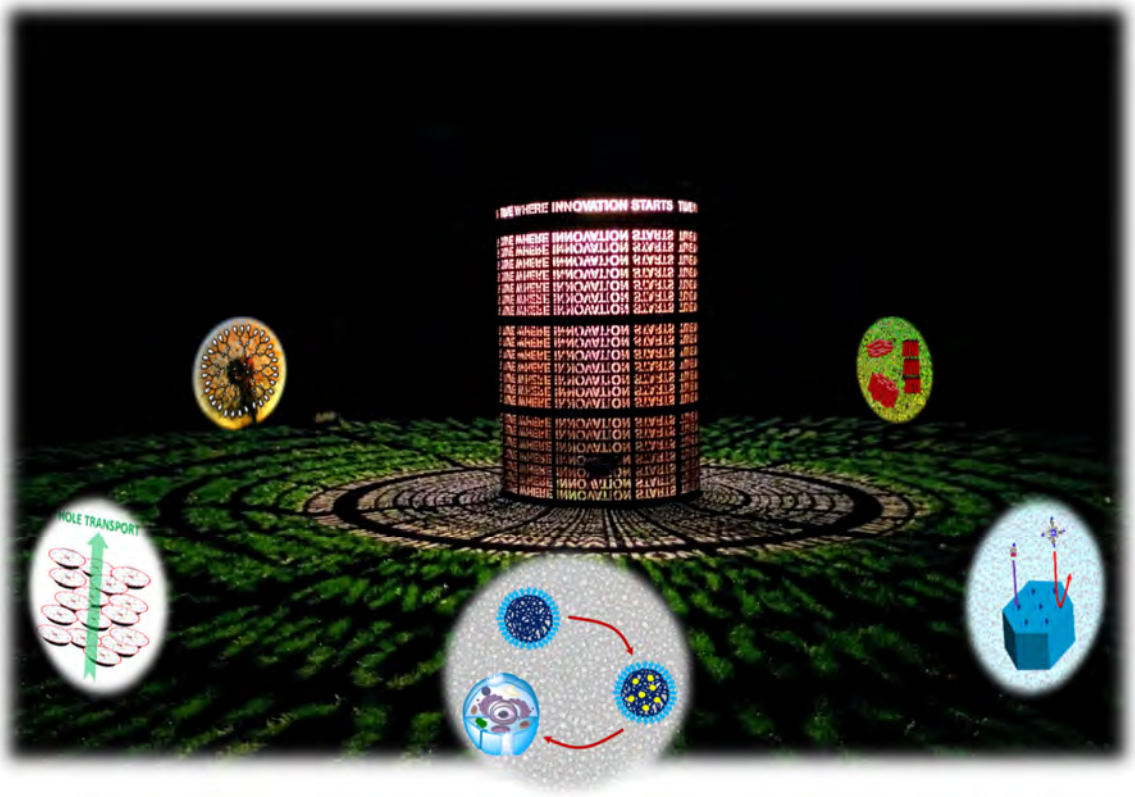

Abstract. *Recapitulación en castellano de los resultados y conclusiones más relevantes obtenidos en cada capítulo.*

When a student asked Linus Pauling if his proposed research could possibly work, Pauling quoted an old physics text problem: "If you are walking through a forest and come upon a cube of gold that is one foot on each side, should you try and pick it up? Answer: No, you should not, because the cube would weigh about 1200 pounds." Smiling, Pauling said, "But of course you should try and pick it up. Any fool would!"

Acc. Chem. Res. **1995,** 28, 91.

MATERIALES FUNCIONALES AVANZADOS BASADOS EN DENDRÍMEROS CRISTALES LÍQUIDOS: Nuevas Arquitecturas Dendríticas con Aplicaciones en Ciencia de Materiales y Biomedicina

Los **dendrímeros** constituyen en la actualidad un área de extraordinario interés en la investigación de **materiales funcionales**. El uso de los **cristales líquidos** como agentes capaces de promover la ordenación de las unidades activas presentes dentro de la estructura dendrítica puede dar lugar a la creación de un nuevo tipo de materiales orgánicos con aplicaciones tanto en Ciencia de Materiales como en Biomedicina.

El objetivo principal de esta tesis ha sido la **obtención de nuevos materiales funcionales a partir de dendrímeros cristales líquidos** para su aplicación como semiconductores orgánicos, para la obtención de materiales conductores de protones, para la preparación de membranas nanoporosas y para aplicaciones biomédicas.

CAPÍTULO 1: Semiconductores orgánicos basados en dendrímeros cristales líquidos con núcleo de porfirina

Los materiales orgánicos resultan muy atractivos en el campo de la **electrónica molecular** para la fabricación de celdas fotovoltaicas (OPVs), diodos orgánicos emisores de luz (OLEDs) o transistores orgánicos de efecto campo (OFETs). Estos dispositivos, cuya capa activa está basada en moléculas orgánicas π-conjugadas, requieren de una estructura interna bien organizada para poder desempeñar óptimamente su función. Los cristales líquidos pueden ser empleados como una valiosa herramienta para el desarrollo y procesado de materiales funcionales en los que el control de la organización molecular sea esencial para la mejora de determinadas propiedades.

En este contexto, se sintetizaron y caracterizaron dendrímeros que poseen un núcleo de porfirina y unidades funcionales de cumarina en la periferia mediante

química covalente. Estos sistemas, que son mucho más estables en comparación con los supramoleculares, presentaron un comportamiento cristal líquido nemático discótico. Además, presentaron efecto antena, con una eficiencia de aprox. 20%, donde las cumarinas de la periferia actúan como dadores al núcleo central de porfirina. También estos compuestos presentaron altos valores de movilidad de carga (los más altos descritos hasta la fecha para este tipo de mesofase).

Pese a los buenos resultados obtenidos, los sistemas covalentes presentan una síntesis y purificación laboriosa. Por ello, se buscó la mejora de su síntesis por medio de química 'click', obteniendo una nueva familia de productos con rendimientos superiores al 75%. Utilizando esta nueva aproximación, se sintetizaron dendrímeros con núcleo de porfirina y con unidades de carbazol en la periferia. Así mismo, la modificación de la estructura química de la cumarina permitió aumentar la eficiencia del efecto antena (>90%).

CAPÍTULO 2: Dendrímeros cristales líquidos iónicos como materiales conductores de protones

El desarrollo de **sistemas de almacenamiento electroquímico de energía fácilmente transportable** es un área de intensa investigación hoy en día. Para la construcción de este tipo de dispositivos es necesario el desarrollo de nuevos electrolitos que proporcionen un eficiente transporte de iones. La nanosegregación presente en las organizaciones cristal líquido es una prometedora estrategia para la preparación de nuevos electrolitos sólidos ya que las moléculas con comportamiento mesógeno pueden tener partes iónicas, que puedan dar lugar a canales iónicos, permitiendo un transporte de iones.

En este capítulo se evaluó por primera vez el uso de dendrímeros cristales líquidos iónicos para la preparación de materiales conductores mono- y di-mensionales de protones. Para ello, se sintetizó una nueva familia de dendrímeros cristales líquidos iónicos basados en la unión de núcleos de poli(amidoamina) (PAMAM) con un dendron bifuncional que contiene unidades fotodimerizables de cumarina. La preparación se ha realizado siguiendo una aproximación supramolecular (enlace

iónico), que ha demostrado ser sencilla, cuantitativa y versátil si se compara con la preparación mediante química covalente.

Todos los dendrímeros presentaron comportamiento cristal líquido que puede ser modulado modificando la generación del núcleo de PAMAM utilizado, dando lugar a mesofases esmécticas A para generaciones bajas y a mesofases columnares hexagonales al aumentar la generación.

La reacción de fotodimerización de las unidades de cumarina se utilizó como reacción de entrecruzamiento para obtener redes poliméricas cristal líquido. Todos los materiales preparados presentaron buenas propiedades de conducción ya que el orden cristal líquido lleva a la formación de áreas nanosegregadas que favorecen el transporte de protones.

CAPÍTULO 3: Materiales nanoporosos basados en dendrímeros cristales líquidos supramoleculares

Los **materiales nanoporosos** despiertan un gran interés debido a sus aplicaciones en campos diversos como son la filtración y purificación de aguas, procesos de separación, catálisis o almacenamiento de gases. Para preparación de sistemas con poros del orden de 1 nm o inferior, los cristales líquidos suponen una prometedora herramienta ya que combinan una autoorganización en dimensiones nanoscópicas junto con un fácil procesado en dimensiones macroscópicas.

Con este objetivo, se sintetizaron y caracterizaron complejos supramoleculares (*via* enlaces de hidrógeno) a partir de diferentes moléculas plantilla y un dendrón funcional que contiene unidades fotodimerizables de cumarina. Estos complejos supramoleculares presentaron mesomorfismo columnar hexagonal y con ellos fue posible obtener redes poliméricas mediante un proceso de fotodimerización de las unidades de cumarina. Las redes obtenidas conservaron el mesomorfismo columnar exhibido por los complejos supramoleculares.

Posteriormente, tras la eliminación de las moléculas plantilla por tratamiento químico, se obtuvieron polímeros porosos con poros de tamaño controlado que mantienen el orden inducido por el empaquetamiento cristal líquido presente en las redes poliméricas precursoras. Los materiales porosos obtenidos demostraron

ser capaces de discriminar entre distintas moléculas en función de su tamaño. Además, debido a la presencia de ácidos carboxílicos en la superficie del poro, fue posible modificar la "química del poro", pudiendo variar la selectividad de la membrana hacia determinados analitos.

CAPÍTULO 4: Nuevas arquitecturas dendríticas para aplicaciones biomédicas

El **transporte y liberación de fármacos** permiten tratar diversas enfermedades de forma más específica reduciendo de esta forma los efectos secundarios de los tratamientos. Para ello se requiere el uso de nano-transportadores poliméricos. De entre todas las variedades de polímeros capaces de autoensamblarse en agua, los dendrímeros son unos prometedores candidatos ya han sido descritos como "cajas moleculares" con varias aplicaciones farmacéuticas como potenciadores de la solubilidad, agentes de contraste en imagen por resonancia magnética, transporte de fármacos, terapia fotodinámica, etc.

En este contexto, se sintetizaron y caracterizaron dendrímeros híbridos covalentes e iónicos a partir de dendrímeros comerciales de poli(amidoamina) (PAMAM) y un dendrón bifuncional que contiene cumarina. La naturaleza hidrófila de estos dendrímeros les confiere un carácter anfífilo que les permite autoensamblarse en agua generando micelas esféricas. Además, la incorporación en la estructura química de los dendrímeros de un cromofóro fluorescente (cumarina) dota a estas micelas de luminiscencia sin necesidad de un marcador externo.

ADVANCED FUNCTIONAL MATERIALS BASED ON LIQUID CRYSTAL DENDRIMERS: NOVEL DENDRITIC ARCHITECTURES FOR APPLICATIONS IN MATERIAL SCIENCE AND BIOMEDICINE

Alberto Concellón Allueva

Memoria presentada en la Universidad de Zaragoza para optar al Grado de Doctor

Dpto. Química Orgánica
Facultad de Ciencias – ICMA
Universidad de Zaragoza – CSIC

Zaragoza, Abril 2018